frontiers | Research Topics

The sun seen with the atacama large mm and sub-mm array (ALMA) - first results

Edited by
Costas E. Alissandrakis, Timothy Bastian, Masumi Shimojo and Alexander Nindos

Published in
Frontiers in Astronomy and Space Sciences

ISSN 1664-8714
ISBN 978-2-8325-2506-7
DOI 10.3389/978-2-8325-2506-7

About Frontiers

Frontiers is more than just an open access publisher of scholarly articles: it is a pioneering approach to the world of academia, radically improving the way scholarly research is managed. The grand vision of Frontiers is a world where all people have an equal opportunity to seek, share and generate knowledge. Frontiers provides immediate and permanent online open access to all its publications, but this alone is not enough to realize our grand goals.

Frontiers journal series

The Frontiers journal series is a multi-tier and interdisciplinary set of open-access, online journals, promising a paradigm shift from the current review, selection and dissemination processes in academic publishing. All Frontiers journals are driven by researchers for researchers; therefore, they constitute a service to the scholarly community. At the same time, the *Frontiers journal series* operates on a revolutionary invention, the tiered publishing system, initially addressing specific communities of scholars, and gradually climbing up to broader public understanding, thus serving the interests of the lay society, too.

Dedication to quality

Each Frontiers article is a landmark of the highest quality, thanks to genuinely collaborative interactions between authors and review editors, who include some of the world's best academicians. Research must be certified by peers before entering a stream of knowledge that may eventually reach the public - and shape society; therefore, Frontiers only applies the most rigorous and unbiased reviews. Frontiers revolutionizes research publishing by freely delivering the most outstanding research, evaluated with no bias from both the academic and social point of view. By applying the most advanced information technologies, Frontiers is catapulting scholarly publishing into a new generation.

What are Frontiers Research Topics?

Frontiers Research Topics are very popular trademarks of the *Frontiers journals series*: they are collections of at least ten articles, all centered on a particular subject. With their unique mix of varied contributions from Original Research to Review Articles, Frontiers Research Topics unify the most influential researchers, the latest key findings and historical advances in a hot research area.

Find out more on how to host your own Frontiers Research Topic or contribute to one as an author by contacting the Frontiers editorial office: frontiersin.org/about/contact

The sun seen with the atacama large mm and sub-mm array (ALMA) - first results

Topic editors

Costas E. Alissandrakis — University of Ioannina, Greece
Timothy Bastian — National Radio Astronomy Observatory, United States
Masumi Shimojo — National Astronomical Observatory of Japan (NAOJ), Japan
Alexander Nindos — University of Ioannina, Greece

Citation

Alissandrakis, C. E., Bastian, T., Shimojo, M., Nindos, A., eds. (2023). *The sun seen with the atacama large mm and sub-mm array (ALMA) - first results*. Lausanne: Frontiers Media SA. doi: 10.3389/978-2-8325-2506-7

Table of contents

frontiers | Frontiers in Astronomy and Space Sciences

TYPE Editorial
PUBLISHED 26 January 2023
DOI 10.3389/fspas.2023.1138626

OPEN ACCESS

EDITED AND REVIEWED BY:
Scott William McIntosh,
National Center for Atmospheric Research (UCAR), United States

*CORRESPONDENCE
Costas E. Alissandrakis,
calissan@uoi.gr

SPECIALTY SECTION
This article was submitted to Stellar and Solar Physics, a section of the journal Frontiers in Astronomy and Space Sciences

RECEIVED 05 January 2023
ACCEPTED 09 January 2023
PUBLISHED 26 January 2023

CITATION
Alissandrakis CE, Bastian T, Shimojo M and Nindos A (2023), Editorial: The Sun seen with the Atacama Large mm and sub-mm array (ALMA)—First results[1].
Front. Astron. Space Sci. 10:1138626.
doi: 10.3389/fspas.2023.1138626

Editorial: The Sun seen with the Atacama Large mm and sub-mm array (ALMA)—First results[1]

Costas E. Alissandrakis[1]*, Timothy Bastian[2], Masumi Shimojo[3,4] and Alexander Nindos[1]

[1]Department of Physics, University of Ioannina, Ioannina, Greece, [2]National Radio Astronomy Observatory (NRAO), Charlottesville, VA, United States, [3]National Astronomical Observatory of Japan, Mitaka, Japan, [4]Department of Astronomical Science, The Graduate University for Advanced Studies (SOKENDAI), Mitaka, Japan

KEYWORDS

ALMA, Sun, Solar mm radio emission, Solar atmosphere, quiet Sun, Solar active regions, Solar prominences, Solar flares

Editorial on the Research Topic
The Sun Seen with the Atacama Large mm and sub-mm Array (ALMA)—first results

The Atacama Large Millimeter and submillimeter Array (ALMA; Wootten and Thompson, 2009) is a unique general-purpose radio interferometer for exploring the Universe at millimeter (mm) and sub-millimeter (sub-mm) wavelengths.

Observing the Sun with ALMA is not straightforward, due to the high intensity of its emission, its motion (both the apparent motion across the sky and the differential rotation), its size which is larger than the field of view of a single ALMA antenna, and its highly variable emission as a result of a multitude of phenomena, ranging from oscillations to flares. After a significant testing and commissioning effort, ALMA developed solar observing capability, with the first usable data coming out of the commissioning period in December 2015 (see **Figure 1** for an example). The possibility of user proposals opened with Cycle 4 (October 2016—September 2017 and the first scientific solar observations were carried out in December 2016.

When the call for this Research Topic was launched, more than 50 refereed articles using ALMA solar observations had been published. It was thus time to put together these first results in a Research Topic that would serve both as a report of hitherto accomplishments and as a guide for the future. The response was enthusiastic, with practically all research groups implicated in solar ALMA observing responding positively. We would like to express our sincere thanks to all colleagues, authors and reviewers, that worked hard to make this Research Topic possible and we hope that it will become a reference for future work.

This Research Topic includes 12 contributions with more than 50 authors. We start with an overview of solar observing with ALMA, by Bastian et al., in which the authors describe the challenges of using the instrument for solar observing, its capabilities and limitations, as well as the prospects for the future, as ALMA is evolving and improving rapidly. The review of quiet

1 Dedicated to the memory of our good friend and colleague Rob Rutten (1942-2022).

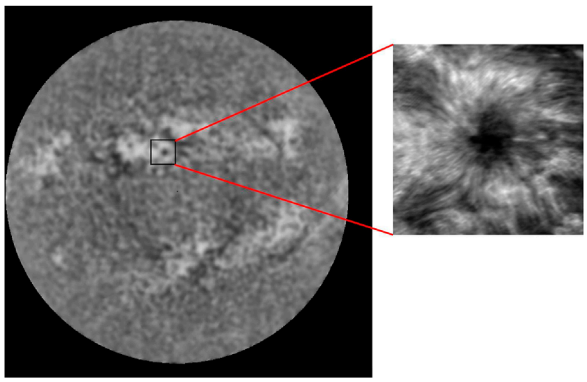

FIGURE 1
ALMA images of the Sun at 1.3 mm (band 6). Left: Full disk image obtained by scanning with a single dish; the spatial resolution is $30''$. Right: High resolution ($1''$) image of the region around the sunspot, obtained in interferometric mode with mosaicking. Both images were obtained on 18 December 2015, during the commissioning period and were processed by the authors for better visibility of the disk features.

Sun ALMA observations by Alissandrakis et al. comes next, where the results on the temperature structure of the chromosphere, the chromospheric network and spicules are presented, followed by the research article by Tarr et al., which compares the 3 mm brightness temperature with the Hα line width in the weak solar network.

Small-scale dynamic phenomena and oscillations are an important issue for solar physics, and the relevant ALMA results are reviewed by Nindos et al. Recent advances in numerical computations have produced sophisticated magnetohyrodynamic models of the solar chromosphere and their possible signatures at mm-wavelengths are discussed in the review by Wedemeyer et al. that follows.

Prominences and filaments are a basic ingredient of the solar chromosphere, and their properties derived from ALMA observations are discussed in the review by Heinzel et al. In a related research article that follows, da Silva Santos et al. present the results of their study of an active region filament observed by ALMA and IRIS.

Active regions are places with concentrated magnetic flux, which play a crucial role in energetic solar phenomena. Their properties, as revealed with ALMA, are reviewed by Loukicheva and Reardon. In two related research articles, Abe et al. analyze their observations of time variations of the chromospheric temperature in a plage, while de Oliveira e Silva et al. discuss the modeling of active regions with 3-dimensional magnetic field extrapolations.

Although no ALMA observations of solar flares have been published yet, Fleishman et al. share their thoughts on what we can learn from mm/submm observations in a mini review. The Research Topic concludes with an article on the radio emission from supra-arcade downflows by Zurbriggen et al.

As this Research Topic was near completion, our good friend and colleague Robert Rutten passed away. Rob was involved in the early stages of this Research Topic. He was a distinguished researcher and educator, pioneer in many aspects of Solar Physics, including the appearance of Hα features in ALMA images (Rutten, 2017), with brilliant ideas and acute but constructive criticism. He will be remembered by the entire solar physics community, and we dedicate this Research Topic to his memory.

Author contributions

All authors listed have made a substantial, direct, and intellectual contribution to the work and approved it for publication.

Acknowledgments

This work makes use of the following ALMA data: ADS/JAO. ALMA. 2011.0.00020. SV ALMA is a partnership of ESO (representing its member states), NSF (United States) and NINS (Japan), together with NRC (Canada), MOST and ASIAA (Taiwan), and KASI (Republic of Korea), in cooperation with the Republic of Chile. The Joint ALMA Observatory is operated by ESO, AUI/NRAO and NAOJ.

Conflict of interest

The authors declare that the research was conducted in the absence of any commercial or financial relationships that could be construed as a potential conflict of interest.

Publisher's note

References

Rutten, R. J. (2017). Solar H-alpha features with hot onsets. III. Long fibrils in Lyman-alpha and with ALMA. *Astron. Astroph.* 598, A89. doi:10.1051/0004-6361/201629238

Wootten, A., and Thompson, A. R. (2009). The Atacama Large millimeter/submillimeter Array. *IEEE Proc.* 97, 1463–1471. doi:10.1109/JPROC.2009.2020572

frontiers | Frontiers in Astronomy and Space Sciences

TYPE Review
PUBLISHED 17 October 2022
DOI 10.3389/fspas.2022.977368

OPEN ACCESS

EDITED BY
Abhishek Kumar Srivastava,
Indian Institute of Technology (BHU), India

REVIEWED BY
Nicole Vilmer,
Centre National de la Recherche Scientifique (CNRS), France
Divya Oberoi,
Tata Institute of Fundamental Research, India

*CORRESPONDENCE
T. S. Bastian,
tbastian@nrao.edu

SPECIALTY SECTION
This article was submitted to Stellar and Solar Physics, a section of the journal Frontiers in Astronomy and Space Sciences

RECEIVED 24 June 2022
ACCEPTED 25 August 2022
PUBLISHED 17 October 2022

CITATION
Bastian TS, Shimojo M, Bárta M, White SM and Iwai K (2022), Solar observing with the Atacama large millimeter-submillimeter array. *Front. Astron. Space Sci.* 9:977368. doi: 10.3389/fspas.2022.977368

Solar observing with the Atacama large millimeter-submillimeter array

T. S. Bastian[1]*, M. Shimojo[2,3], M. Bárta[4], S. M. White[5] and K. Iwai[6]

[1]National Radio Astronomy Observatory, Charlottesville, VA, United States, [2]National Astronomical Observatory of Japan, Mitaka, Japan, [3]Department of Astronomical Science, The Graduate University for Advanced Studies (SOKENDAI), Mitaka, Japan, [4]Astronomical Institute of the Czech Academy of Sciences, Ondřejov, Czechia, [5]Space Vehicles Directorate, Air Force Research Laboratory, Albuquerque, NM, United Sates, [6]Institute for Space-Earth Environmental Research, Nagoya University, Nagoya, Japan

The Atacama Large Millimeter-submillimeter Array (ALMA), sited on the high desert plains of Chajnantor in Chile, has opened a new window onto solar physics in 2016 by providing continuum observations at millimeter and sub-millimeter wavelengths with an angular resolution comparable to that available at optical (O), ultraviolet (UV), extreme ultraviolet (EUV), and X-ray wavelengths, and with superior time resolution. In the intervening years, progress has been made testing and commissioning new observing modes and capabilities, in developing data calibration strategies, and in data imaging and restoration techniques. Here we review ALMA current solar observing capabilities, the process by which a user may propose to use the instrument, and summarize the observing process and work flow. We then discuss some of the challenges users may encounter in imaging and analyzing their data. We conclude with a discussion of additional solar observing capabilities and modes under consideration that are intended to further exploit the unique spectral coverage provided by ALMA.

KEYWORDS

instrumentation, millimeter-submillimeter wavelengths, solar observing, calibration, data analysis, ALMA

1 Introduction

The Atacama Large Millimeter-submillimeter Array (ALMA) is a high-performance, general-purpose telescope that has opened a new frontier of astrophysics, offering fundamentally new observations at mm-λ and submm-λ. ALMA first became available to the wider scientific community more than a decade ago, at the end of 2011 (ALMA observing Cycle 0) but it was not until 5 years later in late 2016 that solar observations first became available with ALMA (observing Cycle 4), Since then, the solar physics community has embarked on a number of ambitious solar observing programs, providing new insights into outstanding problems in solar physics. Results from several of these programs are presented in the Frontiers collection of articles and reviews entitled "The Sun Seen with the Atacama Large mm and sub-mm Array (ALMA)—First Results ".

Solar observing with ALMA is not without challenges. First, a number of technical barriers needed to be overcome to enable solar observing—and continue to be addressed as new observing modes and capabilities are considered. Second, as an interferometer the imaging and data reduction techniques employed by ALMA are not necessarily familiar to the wider solar community and a learning curve must be surmounted. In fact, solar imaging and reduction techniques remain under development in some cases. Hence, the ALMA solar user community is small, but growing. Finally, as a new window onto the Sun, the observations themselves pose interesting challenges to our understanding of physical processes on the Sun!

In the remainder of this section we introduce the key attributes of ALMA and summarize the basic elements of the technical and operational approach to observing the Sun. Readers may wish to consult additional resources: a general overview of the instrument may be found in Wootten and Thompson (2009) while details regarding solar observing and data calibration are presented by Shimojo et al. (2017) and White et al. (2017). In Section 2 we summarize ALMA's current observing capabilities, with an emphasis on new capabilities that have been commissioned since Cycle 4. In Section 3 we discuss the process by which an interested scientist may propose to observe with ALMA. We then describe, for successful observing programs, the observing process and the subsequent work flow leading to data delivery to the observer. In Section 4 we discuss some of the lessons learned from experience with ALMA imaging and data analysis. In Section 5 we discuss future observing modes and capabilities that will enhance solar science with ALMA. We conclude in Section 6.

1.1 Organization of the observatory

Before describing the instrument itself we briefly describe the organization of the observatory. The observatory is fundamentally international in nature, a partnership between the United States National Science Foundation, the European Organization for Astronomical research in the Southern Hemisphere, and the National Institutes of Natural Sciences of Japan, in cooperation with the Republic of Chile. Management of the of the observatory is consolidated under the Joint ALMA Observatory (JAO[1]). The JAO is based in Santiago, Chile, and is responsible for operating, maintaining, enhancing, and optimizing ALMA on behalf of the wider scientific community. The JAO organizes and oversees calls for proposals and their review, executes approved observing programs, and archives the data. The telescope itself is sited approximately 1,500 km north of Santiago at the Array Operations Site (AOS). Telescope operations are supported and maintained from the Operations Support Facility (OSF) at a distance of about 30 km from the AOS. The OSF also supports assembly, integration, and verification of technology before it is moved to the AOS.

The ALMA scientific community is supported by ALMA Regional Centers (ARCs) affiliated with each ALMA partner.[2] These are operated by the National Radio Astronomy Observatory (NRAO) on behalf of North America, the European Southern Observatory (ESO) on behalf of its member states, and the National Astronomical Observatory of Japan (NAOJ) on behalf of East Asia. The North American and East Asia ARCs are co-located with their national observatories whereas the European ARC follows a distributed model of seven ARC nodes coordinated from ESO headquarters in Garching. The ARC node with responsibilities for the European solar community is based in Ondrejov, Czech Republic. The ARCs are each advised by scientific advisory committees to ensure that user concerns and priorities are known and addressed. The overall observatory is advised by the ALMA Scientific Advisory Committee.

The role of the ARCs or ARC nodes in the workflow of a given project is discussed in greater detail in Section 3. It is important to note that the ARCs also play an important role in education and outreach. For example, the ARCs are used to organize ALMA Community Workshops prior to each call for proposal. The goal of those meetings is to help the local community with proposal preparation.

1.2 Overview of the instrument

ALMA is located on the Chajnantor plateau of the Chilean Andes at a latitude of − 23°, a longitude of − 67.8°, and an elevation of over 5,000 m (Figure 1). It is a general-purpose telescope designed to operate at mm-λ and submm-λ in order to address an extremely broad program of astrophysics—from cosmology, to star and planet formation, to astrochemistry. ALMA is an interferometer comprising an array of antennas that sample the Fourier transform of the brightness distribution within the field of view. A given pair of antennas measures a single Fourier component, an amplitude and a phase referred to as a complex *visibility*, corresponding to a spatial frequency defined by the antenna spacing and orientation. A given antenna spacing is referred to as an antenna *baseline*. Long antenna baselines measure small angular scales and short baselines measure large angular scales in the brightness distribution. The Fourier

1 See https://www.almaobservatory.org.

2 The roles and responsibilities of the ARCs can be found at https://almaobservatory.org/en/about-alma/global-collaboration.

FIGURE 1
ALMA is an array composed of 50 × 12 m movable antennas (left background), 12 × 7 m fixed antennas (right foreground), and 4 × 12 m total power antennas. Credit: NRAO/AUI/NSF.

domain in which the measurements are made is referred to as the aperture plane or the *uv* plane, where *u* and *v* refer to the coordinates of antenna baselines, typically measured in wavelength units. An array of N antennas has $N(N-1)/2$ independent baselines. The instantaneous *uv* sampling provided by an array is sometimes referred to as the "snapshot" *uv* coverage. For sources that are static in time, one can exploit the fact that the array geometry, as viewed from the source, changes due to Earth's rotation, allowing the *uv* plane sampling to be filled in with time. This technique is referred to as Earth rotation aperture synthesis.

ALMA has a total of 66 high performance antennas. The 12-m array is composed of 50 × 12 m antennas and is reconfigurable. That is, the antennas may be moved to change the distribution of baselines and, hence, sampling in the *uv* plane in order to change the angular resolution and surface brightness sensitivity of the instrument. Baseline lengths can be as small as 15 m and as large as 16 km although for solar observing, array configurations are currently restricted to the four most compact configurations of the ten array configurations in general use (see Table 2). With all 50 antennas operative in the 12-m array, a total of 1,225 independent baselines are available. The field of view (FOV) of the 12-m array is determined by the response of a single antenna which, to first order may be described by a modified Airy function with a main lobe and sidelobes. The main lobe is well described by a Gaussian. ALMA antennas are of Cassegrain design; accounting for the taper of the antenna illumination pattern and blockage by the subreflector and the quadrupod support structure, the HPBW of the Gaussian main beam—also referred to as the primary beam—is given by $\theta_{FOV} = 1.13\lambda/D = 19.42''\lambda_{mm}$. The Atacama Compact Array (ACA) comprises 12 × 7 m antennas and four 12 m total power antennas. The 7 m antennas are fixed and provide lower-resolution imaging to complement that provided by the 12-m array, or it can be used in a standalone mode. In the case of solar observations, the array of 7 m antennas is used to supplement the angular coverage provided by the 12-m array as discussed further in Section 2. The FOV of a 7 m antenna is $\theta_{FOV} = 33.3''\lambda_{mm}$. The four 12 m antennas are available for making total power measurements. These play an important role in solar observing by effectively filling in the smallest spatial frequencies that are not otherwise measured by the 12-m array and the 7 m array of antennas as we discuss further in Sections 2.5, 4.4.

Interferometric (INT) observations made by with the 12-m array use the Baseline Correlator (BLC) to produce visibility data. The ACA correlator may be used to correlate antennas in the 7-m array. Alternatively, as is the case for solar observations (see Section 1.3.3 below), correlations between antennas in the ACA and the 12-m array may be processed together through the BLC. Continuum observations are performed using the ALMA Time Domain Mode (TDM). A given target is observed in two frequency ranges above and below the local oscillator (LO) frequency—the upper and lower sidebands. Each side band is subdivided into two spectral windows, each of 2 GHz bandwidth. Hence, a total of four spectral windows is observed with a combined bandwidth of 8 GHz. Available observing bands and spectral windows are summarized in Table 1. Each spectral window is currently fixed in frequency as a result of the gain reduction approach adopted (see Section 1.3.1). The TDM mode coarsely channelizes each spectral window into 128 frequency channels. During calibration and data reduction these are corrected for the instrument response across the spectral window (bandpass correction), edited to remove radio frequency interference or unwanted atmospheric lines, and then averaged to form pseudo-continuum frequency bands.

ALMA antennas measure two orthogonal senses of linear polarization simultaneously, X and Y. All solar observations are currently made in dual-polarization mode. That is, the BLC produces correlations between antennas i and j as X_iX_j and Y_iY_j visibilities. The two linearly polarized correlations are generally summed to produce visibilities in total intensity (the Stokes I parameter). The two may be differenced as a means of estimating the thermal noise (Shimojo et al., 2017). The implementation of full polarimetry for solar observations is currently under study (Section 5.1).

1.3 Challenges posed by the Sun

The Sun poses a number of challenges for a general purpose instrument not specifically designed and optimized for solar observing. These challenges are over and above the already considerable challenges of observing in the mm/submm-λ range. Among them are:

TABLE 1 ALMA solar observing bands.

Freq. Band	ν_{LO} (GHz)	λ_{LO} (mm)	Spw 0 (GHz)	spw 1 (GHz)	Spw 2 (GHz)	Spw 3 (GHz)
3	100	3	92–94	94–96	104–106	106–108
5	198	1.51	190–192	192–194	202–204	204–206
6	239	1.25	229–231	231–233	245–247	247–249
7	346.6	0.86	338.6–340.6	340.6–342.6	350.6–352.6	352.6–345.6

- The Sun is an intense emitter, so much so that it causes ALMA receivers to go into compression and for electronic elements along the signal path to saturate unless provisions are made.
- The Sun is a moving target, not only because of its apparent motion across the sky, but also because of its (differential) rotation.
- The Sun is much larger than the FOV of a single ALMA antenna, which is $< 20''$ at a wavelength of 1 mm, for example.
- Emission from the Sun is highly variable as a result of a variety of phenomena, ranging from chromospheric oscillations to flares.

We now briefly summarize how each of these challenges have been addressed.

1.3.1 Antenna gain reduction

The ALMA antennas were carefully designed to allow them to safely point at the Sun. However, to avoid compression of the receivers and saturation along the electronic signal path, two steps are taken:

(1) The gain of the SIS mixers in ALMA receivers is reduced by changing the voltage bias and/or the local oscillator (LO) current—the so-called "mixer detuned" or "mixer debiased" (MD) mode. The decrease in receiver gain provides greater headroom for the receivers to operate without going into compression. However, to ensure correct calibration transfer, both the Sun and calibrator sources must be observed in MD mode.
(2) There is still an enormous differential in the power entering the system when observing the Sun and observing calibrator sources, which are typically compact quasars or planets. Stepped attenuators along the signal path are used to set signal powers to optimum levels during an instrumental setup scan on the solar target. For all subsequent calibrator scans, the attenuators settings are reduced by a known and fixed amount on each antenna. In this way, robust phase transfer is ensured.

As shown by Shimojo et al. (2017) these modifications allow observations of quiet Sun and active region phenomena. Observations of solar flares are another matter, one that we discuss in Section 5.4. A consequence of using the MD mode is an increase in system temperature which lowers the system sensitivity when observing calibrator sources, as least for bands 3, 5, and 6. For gain calibrators, it is highly desirable to observe a bright quasar (> 1 Jy) relatively close to the Sun (< 15 deg). Between late June and early July, there are no such bright quasars near the Sun, a period of time that should therefore be avoided for solar observing. In practice, it is rare that suitable array configurations are available for solar observing at this time because the larger configurations are favored during Chilean winter.

1.3.2 Apparent source motion

The Sun and other solar system objects—planets, comets, asteroids—all display apparent motion. Their apparent position on the celestial sphere is described by an ephemeris. In the case of the Sun, the *ALMA Solar Ephemeris Generator*[3] is a convenient tool for preparing the solar ephemeris needed for observations on any specified date. The *Ephemeris Generator* takes into account solar rotation via a standard or user-specified solar rotation model, as well as target offsets relative to the center of the solar disk. ALMA scheduling blocks link the user-specified solar ephemeris to the online system, allowing it to point and track the solar target of interest as discussed further in Section 3.

1.3.3 Mapping a large field of view

The FOV of a single 12 m ALMA antenna is small compared to the angular diameter of the Sun, or even compared with the typical scale of an active region (few arcmin). There are two issues:

- In order to increase the size of the angular domain mapped by ALMA, mosaicking techniques must be used (Cornwell and Fomalont, 1989; Sault et al., 1996)). Mosaicking entails sequentially sampling a user-specified grid of array

3 The ALMA Solar Ephemeris Generator was developed by Ivica Skokić and is available at http:celestialscenes.com/alma/coords/CoordTool.html.

pointings to increase the effective FOV. The spacing between discrete pointings is set to ensure Nyquist sampling or better. Mosaic pointing patterns are referenced to the user-specified solar ephemeris.

- A related issue is that, as an interferometer, ALMA acts as a high-pass filter. While the maximum antenna baselines set the angular resolution of the array, the minimum antenna baselines determine the largest angular scales measured by the array. As seen in Table 2, the maximum recoverable scale measured by a given configuration of the 12 m array are all significantly less than the FOV! Two measures were implemented to mitigate this state of affairs:
  (i) Solar observations use both the antennas in the 12-m array and those in the ACA as a combined array to perform interferometric (INT) observations. That is, all antenna baselines – 7 m × 7 m, 7 m × 12 m, and 12 m × 12 m are correlated in the BLC. In doing so, measurements on shorter baselines and larger angular scales are available and may be helpful in some circumstances (see Section 4.1).
  (ii) Solar observers are provided with contemporaneous fast-scan total power (TP) maps of the full disk of the Sun (Phillips et al., 2015; White et al., 2017)). These maps can be used to "fill in" the largest angular scales that are otherwise not measured by the interferometric array.

We return to some of the subtleties associated with these mitigation strategies in Section 4.4.

1.3.4 Time resolution

Solar emission at mm-λ and submm-λ varies over a wide range of time scale, from <1 s to minutes, hours, and days. Depending on a given user's science objectives, it may be necessary to resolve this time variability on the relevant time scale. If it is acceptable to average over time variability, one can exploit Earth rotation synthesis to improve sampling of the *uv* plane somewhat with the available distribution of antennas. However, if the user wishes to resolve variable emission on time scales of minutes or less, the uv coverage does not change appreciably over the relevant time scale and the user is effectively constrained to snapshot *uv* coverage. For many types of science, this trade-off is acceptable: the quality of the imaging is compromised but the source variability of interest is resolved.

2 ALMA solar observing capabilities

We now summarize ALMA's solar observing modes and capabilities, current as of Cycle 9 in 2022–2023. We emphasize that development of additional modes and capabilities is ongoing, as discussed further in Section 5. We note that while a number of software packages may be used to image ALMA data, the most powerful and well-supported is the *Common Astronomical Software Applications*[4] (CASA) package. We make occasional reference to specific tasks or functions found in CASA.

2.1 Frequency bands

Four frequency bands are currently supported by ALMA for continuum solar observing (Table 1). Bands 3 and 6 were the first to be commissioned and were offered to the community in 2016 (Cycle 4). Testing and commissioning of solar continuum observations in ALMA Band 7 (346.6 GHz, 0.86 mm) were completed in 2018 and were made available to the community in 2019 as part of ALMA Cycle 7. Solar continuum observations in Band 5 (198 GHz, 1.51 mm) were commissioned in 2019 and were to be made available in 2020 for ALMA Cycle 8. Owing to the pandemic, however, Cycle 7 observations ended prematurely with the shutdown of the telescope in March 2020 and Cycle 8 was effectively canceled. The telescope was restarted in 2021 and the observing cycle number was reset to Cycle 8. Science observations recommenced in October 2021.

Two MD modes were initially commissioned for Bands 3, 5, and 6. MD1 was initially designed for observations of the quiet Sun and MD2 for observations of active regions. In practice, however, it is found that MD2 results in more linear receiver performance although it comes at the cost of higher system temperature T_{sys} (~ 800, 700, and 800 K, respectively). In the case of Band 7, no stable voltage de-bias settings were found. Hence, nominal receiver settings are used for band 7 observations although the stepped attenuators are optimized for solar observing. On one hand, T_{sys} remains low (~ 200 K); on the other, the system is in mild compression (~ 15%).

2.2 Array configurations

Four of the ten possible 12-m array configurations are available for solar observing as shown in Table 2. Check marks indicate that the configuration is available for solar observations. There are two reasons for this restriction: first, at mm-λ and submm-λ precipitable water vapor in the sky introduces phase variations to the wavefront incident on each antenna that can propagate into the visibilities as image motion and/or a loss of coherence unless corrected. ALMA uses water vapor radiometers (WVRs) on each antenna to measure brightness temperature variations of the sky, a proxy for the phase variations (Nikolic et al., 2013) that may be used to make antenna-based phase corrections. Unfortunately, the WVRs saturate when pointing at the Sun and such corrections are

4 https://casa.nrao.edu.

TABLE 2 ALMA angular resolution and maximum recoverable scale.

Configuration	Band	3	5	6	7
	ν (GHz)/λ (mm)	100/3	198/1.51	239/1.25	346.6/0.86
ACA	θ_{res}(arcsec)	11.6	6.77	5.45	3.63
	θ_{MRS} (arcsec)	66.0	36.1	29.0	19.3
C-1	θ_{res}(arcsec)	3.38	1.83	1.47	0.98
	θ_{MRS} (arcsec)	28.5	15.4	12.4	8.25
C-2	θ_{res}(arcsec)	2.30	1.24	1.00	0.67
	θ_{MRS} (arcsec)	22.6	12.2	9.81	6.54
C-3	θ_{res}(arcsec)	1.42	0.77	0.62	
	θ_{MRS} (arcsec)	16.2	8.73	7.02	
C-4	θ_{res}(arcsec)	0.92			
	θ_{MRS} (arcsec)	11.2			

TABLE 3 Total power map scaling.

Band	White et al. (2017)	Alissandrakis et al. (2022)
3	7,300 K	7,347 K
5		6,532 K
6	5,900 K	6,347 K
7		6,085 K

therefore not available for solar observations. Instead, self-calibration techniques must be used to correct phase variations (Section 5). However, for self-calibration to be effective, the loss of coherence due to phase fluctuations, which increases with baseline length, must not be so extreme as to render the technique ineffective because it relies on a plausible initial model of the source. Hence, the maximum array configurations in each available frequency band is chosen to ensure that self-calibration techniques can be used in most cases to correct for phase fluctuations introduced by the sky.

A second issue is that as the array configuration increases in size with a fixed number of antennas, sampling in the *uv* plane becomes increasingly sparse. Since *uv* coordinates are measured in wavelength units, it is also the case that the sampling becomes increasingly diluted with increasing frequency. This is readily seen in Table 2 which shows the array resolution and the maximum recoverable scale[5] θ_{MRS} for each frequency band and configuration. While the angular resolution improves for a given configuration as one moves to higher frequencies, or as one increases the size of the array configuration at a fixed frequency, the price paid is poorer sampling of the Fourier domain. This is an important consideration when imaging a target like the Sun, which emits on angular scales ranging from the available resolution to scales much larger than the FOV of a given antenna. The configurations offered for solar use therefore represent a compromise between angular resolution and the density of *uv* sampling.

It is important to note, however, that any of the four 12-m array configurations available to solar observers may be used in combination with the ACA 7-m array. That is, solar observations make use of a single heterogeneous array that includes available 12-m array antennas and ACA 7 m antennas. The reason for doing so is readily apparent from Table 2: θ_{MRS} for any band and any configuration is less than the FOV. Inclusion of the ACA 7 m antennas provides sampling up to angular scales comparable with the nominal FOV; and as previously noted, full-disk total power maps are also available to fill in emission on the largest angular scales. We return to issues related to the use of the heterogenous array in Section 4.1.

2.3 Time resolution

The time resolution initially offered to the solar community for Cycle 4 was 2 s. This was reduced to 1 s beginning with Cycle 7. ALMA provides a much higher snapshot imaging cadence than is typically available at UV/EUV wavelengths from space missions such as the *Solar Dynamics Observatory*(SDO; 12 s)

5 The maximum recoverable scale is $\theta_{MRS} \approx 203\lambda_{mm}/L_5$ arcsec, where L_5 is the radius in meters within which 5% of the baselines in a given configuration reside. L_5 is 9.1, 21.4, 27.0, 36.6, and 54.1 for the ACA, C-1, C-2, C-3, and C-4 configurations, respectively.

and the *Interface Region Imaging Spectrograph* (IRIS; 20 s). A study led funded by the European Southern Observatory is exploring opportunities for even higher time resolution imaging, as well as the use of larger antenna configurations to enable higher angular resolution imaging (Section 5).

2.4 Mosaicking

The mosaicking technique was introduced in Section 1.3.3 The upper limit to the number of pointings in a given mosaic is currently limited to 150 for both solar and non-solar observations. An example of a large format mosaic is shown in Figure 2. The minimum time per pointing for solar observations is 7.6 s, including overhead for moving the antennas from one point to another. Therefore, including calibration, more than 20 min is required for a single large format mosaic. More limited mosaics can, of course, be executed but users must weigh the tradeoffs between the desired FOV, the time required to execute a given mosaic, and the time scale on which the source may change. An example of a ten-pointing mosaic is shown in Section 4.1.

2.5 Fast-scan total power mapping

Full-disk TP maps supplement interferometric (INT) observations. These provide broader context images for the INT data and provide the means of "filling in" short *uv* spacings, critical if absolute brightness temperatures are needed. The most straightforward technique for combining TP and INT data is "feathering" (Cotton, 2015). See Section 4.4 for further discussion about combining TP and INT data.

As described by White et al. (2017) a double-circle pattern is employed to scan a region centered on the Sun that is 2,400″ in diameter (see Figure 3 for an example). The resolution of the map is determined by the resolution of the 12 m total power antenna: 58.3″, 29.3″, 24.3″, and 16.7″ at Bands 3, 5, 6, and 7, respectively. The time required to produce a full disk map depends on the frequency band: e.g., 13 min for Band 3 and 17 min for Band 6. Calibration of the full disk maps is challenging. Non-repeatability between specific instances led White et al. (2017) to suggest best-values for the quiet Sun brightness temperature at the center of the solar disk based on an aggregation of many test observations. Recently, Alissandrakis et al. (2022) performed an analysis of the center-to limb brightening of ALMA full-disk TP maps in Bands 3, 6, and 7 and showed that Bands 6 and 7 could be cross-calibrated against Band 3 in a self-consistent manner. Table 3 shows the quiet Sun brightness temperature originally recommended by White et al. (2017) and those resulting from the analysis of Alissandrakis et al. (2022). Ultimately, quiet Sun brightness measurements should be referenced to an independent standard such as the Moon.

The time required to produce full-Sun maps (10–20 min) is typically longer than the time scale of many dynamic phenomena of interest. There is also a significant mismatch between the time resolution available for INT data (1 s) and the TP mapping time. It is not possible to drive the TP antennas at higher rates to produce higher-cadence maps and so the field of view must be reduced to decrease the mapping time. In Cycle 9, therefore, a

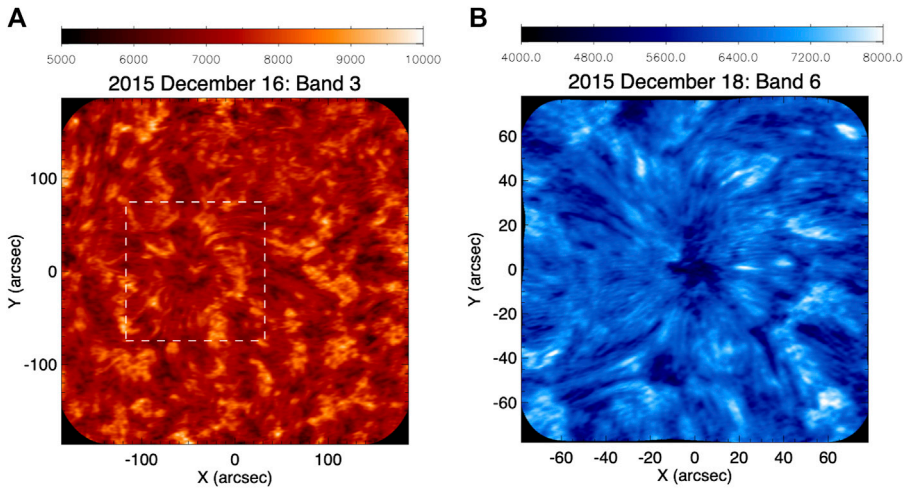

FIGURE 2
Examples of large-format mosaics from ALMA science verification data. **(A)**: a 149-pt mosaic in Band 3 (3 mm) of a sunspot-containing active region. **(B)**: a 149-pt mosaic in Band 6 (1.25 mm) of the same sunspot 2 days later. The equivalent field of view of the Band 6 image is shown on the Band 3 as a dashed-line box. Note the difference in brightness temperature scale. See also Shimojo et al. (2017).

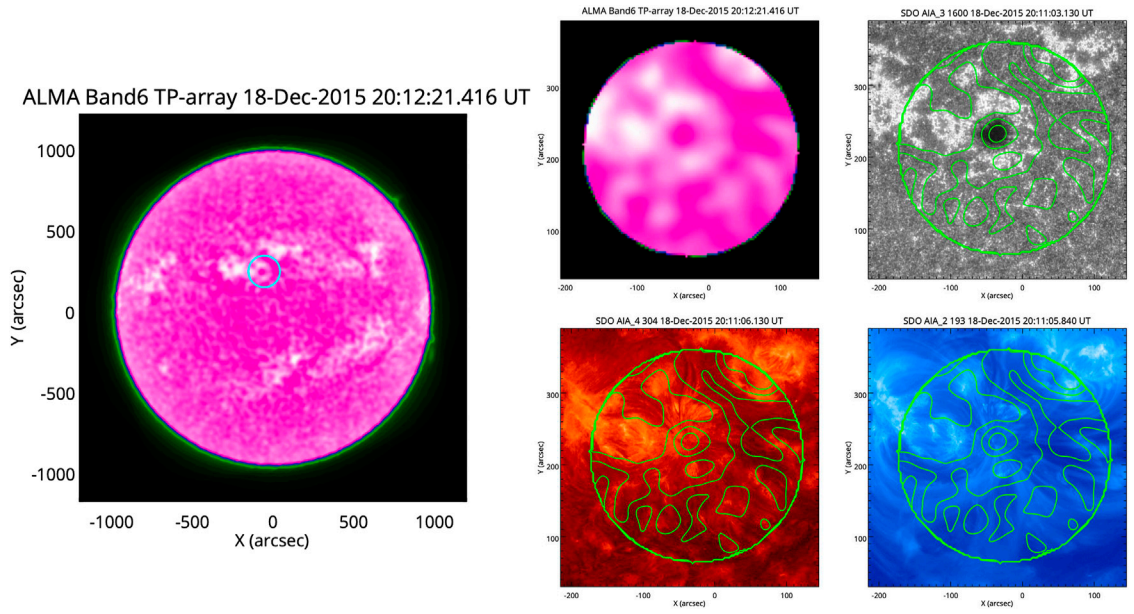

FIGURE 3
Simulated FRM data. Left panel: Full disk TP image obtained with Band 6 on 18 December 2015. The circle indicates the field of view of FRM with 300″ diameter. Right panels: Simulated FRM image and UV/EUV images. Upper Left: Simulated FRM image with 300″ diameter FoV. Upper Right: UV continuum (1700Å band). Lower Left: He II 304Å Band, Lower Right: Fe XII 193 Å Band. Green contours show the FRM image. Examples of a total power full disk map (left) and FRM map (middle, top). The Band 6 total power map was acquired during commissioning in December 2015. The FRM map was made using the TP map in simulation.

second fast-scanning TP mapping mode has been made available to solar observers: Fast Regional Mapping (FRM). The intent of the FRM mode is the same as that of the full-Sun maps: to obtain short-spacing data that is complementary to the INT data, but on a time scale that is more closely commensurate with changes in the source. Therefore, the coordinates of the field center are the same as the target coordinates of the interferometric observation. Moreover, the scan pattern of the FRM released in ALMA-Cycle 9 is the double-circle pattern, which is the same as for the full-Sun map, and the shape of the field of view is a circle. The observer only needs to specify the need for FRM observations in support of a particular science goal, and specify the diameter of the mapping domain. See Figure 3 for an example of FRM mapping using simulated data. Additional scan patterns are under development: the use of a Lissajous scan patterns allows rectangular mapping domains.

The size of the field of view and the mapping cadence is a trade-off that depends on the science objectives. Test observations in Band 6 found that map durations are 11, 21, 32, and 63 s for map diameters of 100″, 200″, 300″, and 600”, respectively, consistent with detailed simulations. FRM maps can therefore be obtained on a cadence comparable to SDO or IRIS imaging observations, for example. FRM observations are available simultaneously with INT observations but, similar to INT observations, FRM observations must be periodically interrupted for calibration. In addition, at beginning and end of an FRM observation, full-Sun maps are obtained for flux calibration. Therefore, an FRM observation always includes numerous regional maps and two full-disk maps. The FRM maps are calibrated against the full-disk maps in two steps: the full disk brightness is scaled to the recommended quiet-Sun value near the center of the disk and the FRM maps are then scaled from the full-disk maps at the appropriate offset. Since it is assumed that the brightness of the reference point does not change significantly during the observations, the diameter of the FRM mapping domain should be chosen to include quiet Sun as the reference point. Hence, a mapping region ≥200” is recommended, in general.

2.6 System issues

Unfortunately, a number of system issues have affected solar data at various times to varying degrees. All issues have related to pointing or tracking. Once identified, most issues have been addressed and subsequent observations have been unaffected. From a scientific perspective, it has usually been possible to recover from the errors introduced by these issues but it is important for users, especially users of archival data, to be aware of them. The first affects Cycle 4 data observed in December 2016. Instead of tracking the user-specified ephemeris the system simply tracked the

center of the solar disk; i.e., it did not take any user-specified target offsets into account or track with solar rotation. At this time, the Sun was in solar minimum and most programs were to observe the quiet solar chromosphere. Some observers were able to correct their data for the lack of rotational tracking and address their science objectives but for others their science objectives were compromised. The problem was corrected and additional operational checks were put into place to verify that targeting is indeed as requested by the PI.

A second issue is related to the reference coordinates assigned to a given observations. As an ephemeris object, the geocentric coordinates of the source change continuously in time. Hence, a reference coordinate corresponding to the appropriate reference time is assigned. For observations in Cycles 4 and 5, the coordinates were determined using the CASA task *fixplanets* using the antenna POINTING table in measurement set. These were found to be inaccurate by as much as 30". Since Cycle 6 the ephemeris table is used directly using the CASA *phasecenter* function of the *msmetadata* tool (*msmd.phasecenter*(). Archival data should be processed using up-to-date scripts.

In Cycle 7, residual pointing effects were traced to general relativistic (GR) corrections for light bending near the Sun.[6] The most important of these occurred as the result of the misapplication of GR delay corrections for target offsets within 920″ of the solar barycenter. The error results in a radial pointing offset that is a function of the desired target offset. Figure 4 shows that the radial pointing offset increasing linearly with target offset from 0″ to ≈ 55″ and then decreases with increasing target offset, dropping below 5″ for radial offsets $>5'$. The error is not present for targets on the solar limb. This problem persisted until March 2020 but has now been corrected. Users should use source names beginning with "Sun" (case insensitive) to ensure that GR corrections are disabled for solar observations. In many cases, the offset introduced by this issue does not seriously compromise science objectives because the pointing error is <10" in many cases. However, if ALMA images are being compared with data from other missions and observatories they must obviously be corrected in order to properly co-align the data. For mosaics, it appears that while the reference pointing established by the ephemeris is affected, offset pointings relative to the reference were not.

A related error originates in the 30 s cadence at which GR delay corrections were made. For an ephemeris object like the Sun there is a drift of the target relative to the pointing offset that is "reset" with every GR delay event, resulting in a pointing ramp every 30 s. The magnitude of the effect is of order 1″ and can be corrected through self-calibration or cross-correlation. Figure 5 shows an example. Not only were interferometric data affected by the GR delay corrections, antenna pointing was, too. The maximum antenna pointing error occurs at the limb and is 1.85". It has no impact on source positions and is small compared to the primary beam in Band 3 but can affect the primary beam correction for Bands 6 and 7.

Finally, full disk TP maps have been subject to small timing errors that manifest as low-level artifacts at the solar limb as pointed out by Alissandrakis et al. (2017). This will soon be corrected with the use of higher-performance 12 m antennas for TP mapping and updates to the relevant software.

3 ALMA solar program workflow

The life-cycle of any ALMA project, from an initial idea up to publication of the results, is schematically drawn in Figure 6. Here, we discuss elements of proposal preparation, proposal review, solar observing, data calibration, and quality assurance (QA). Issues related to data imaging and analysis are discussed in Section 4.

The life-cycle of a given science program formally begins by with the submission of a proposal for observing time in response to an ALMA call for proposals. Calls are issued on an annual basis in March and the proposal deadline is in April. Proposal preparation and submission is referred to as Phase I. Investigators are notified of the disposition of their proposal in August. Should the proposal be successful in the subsequent evaluation (see Section 3.3 below), so called Scheduling Blocks (SBs) are generated from technical details specified in the proposal. This procedure works mostly automatically, with a small adjustments made by the Contact Scientist (CS) and the observatory staff in cooperation with the project Principal Investigator (PI). This is called Phase II. An SB is later converted to a Python script loaded by ALMA during observations. An observing cycle lasts 1 year, beginning on October 1. Solar observations are only possible with a limited number of array configurations (Table 2) and so users should be aware of the array configuration schedule[7] during the course of the year.

The primary interface between ALMA and the user is an ARC. Depending on nationality, users will be affiliated with a given ARC. From the user point of view there are three important components of the ARC support: the Helpdesk system, the Contact Scientist (CS), and Data Analysts (DAs). While the

6 See the knowledgebase article at https://help.almascience.org/kb/articles/what-is-a-cycle-7-solar-data-issue-i-should-be-aware-of for details.

7 ALMA antenna configuration schedules can be found at https://almascience.eso.org/observing/observing-configuration-schedule.

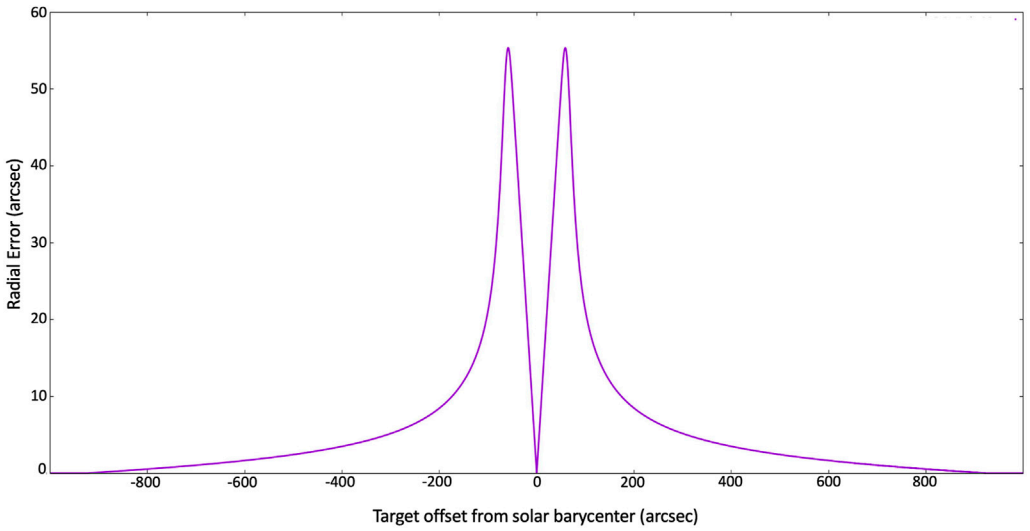

FIGURE 4
The radial position error of the target as a function of target offset from the solar barycenter. Figure provided to the authors by N. Phillips (ESO) and reproduced with permission.

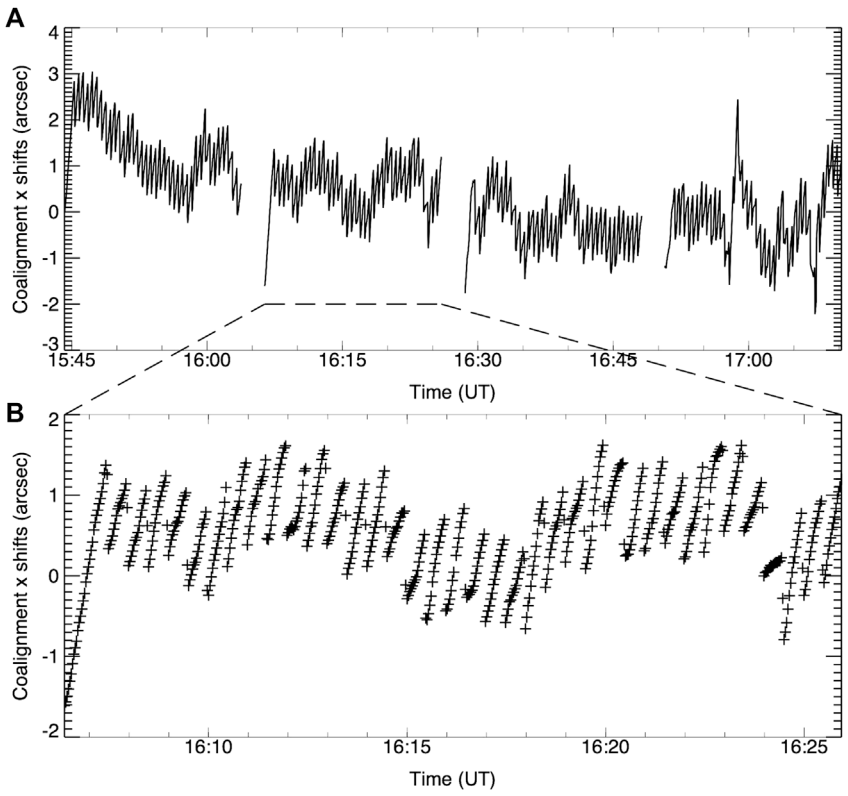

FIGURE 5
Example of the pointing ramping that results from the application of the GR delay tracking correction every 30 s. The **(A)** shows the change in pointing for the duration of an SB. The **(B)** shows a detail in which the ramping is vividly illustrated.

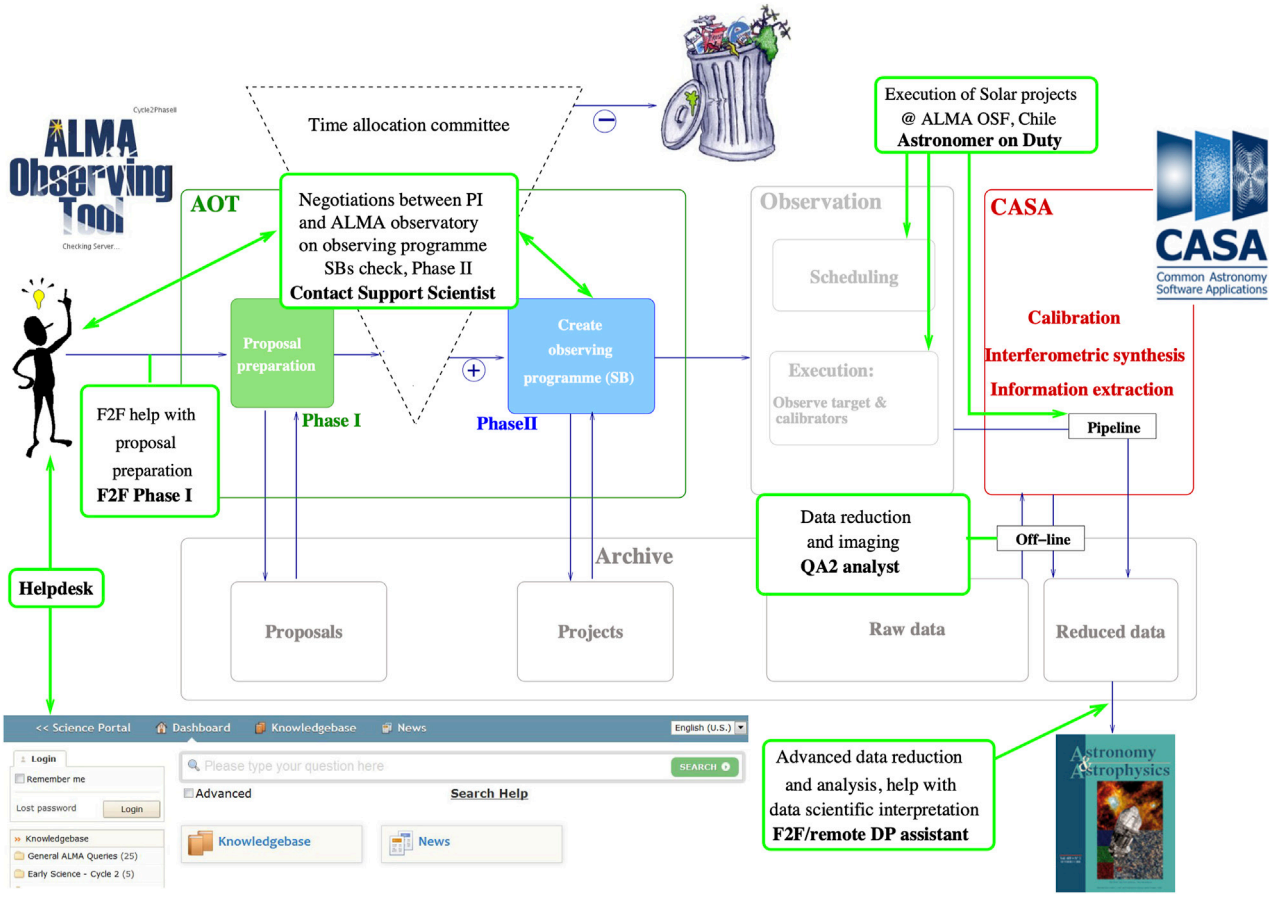

FIGURE 6
Schematic representation of the workflow of a project from proposal development and submission to data reduction and analysis.

Helpdesk is open to user queries anytime it also contains a rich knowledgebase that can be consulted. The CS is an ARC astronomer assigned to a given project when it is accepted, i.e., before the Phase II starts. The communication between the PI and CS starts by opening a project-dedicated Helpdesk ticket—the ARC will do so on PI's behalf. Following the successful execution of an observation, the relevant ARC is responsible for calibrating the data and performing quality assurance. DAs perform these functions as we discuss further below.

Solar observations with ALMA often coordinate with other ground-based or space-based telescopes and observatories. Hence, careful coordination between the PI and JAO science operations is necessary (Section 3.4) After the observations are executed by JAO science operations the raw data are transferred to the ARCs for processing. This includes calibration, reference imaging, and quality assurance (QA) assessment. This process typically lasts several weeks following an observations. Should the data pass the QA, they are delivered to the PI. The PI receives (1) raw data, (2) calibration and imaging scripts (Python) together with the master scriptForPI.py, and the products—FITS files with the images, one per each Execution Block, both for interferometric (INT) and total power (TP) observations. Additional post-processing (e.g., INT + TP data combination, time-domain imaging with self-calibration loop, etc.) is the PI's responsibility; however, the ARCs can provide assistance and in some cases and the advice of ARC astronomers can be solicited at any time via the ALMA Helpdesk system.

3.1 Proposal preparation and submission

An ALMA proposal is prepared and submitted using the ALMA Observing Tool (OT).[8] It is a Java-based GUI application.

8 The ALMA OT, as well as the user manual and online tutorials, is available at https://almascience.nrao.edu/proposing/observing-tool or at https://almascience.eso.org/proposing/observing-tool.

In brief, it contains a set of query pages where the PI describes the project setup:

- Basic information about the project: PI, co-investigators, title, scientific category. There are five science categories:
  (1) Cosmology and the high redshift universe
  (2) Galaxies and galactic nuclei
  (3) ISM, star formation and astrochemistry
  (4) Circumstellar disks, exoplanets and the solar system
  (5) Stellar evolution and the Sun
- Science goals (SGs): one per target and observing band (e.g., "Prominence in Band 3"). For each SG one must provide:
  – Spectral setup
  – Field setup
  – Control and performance
  – Technical justification.
- Scientific justification

Proposers are encouraged to consult the ALMA Proposer's Guide.[9] As noted in Section 2.6, users should prefix each source name with "Sun" to ensure that the system handles relativistic corrections correctly. We briefly summarize key elements of an SG.

The *Spectral setup* currently allows only the "single continuum" frequency bands specified in Table 1. The spectral windows within a given frequency band are fixed; i.e., one cannot change the LO frequency to place them elsewhere in the frequency band. Observations of the same target may be performed in more than a single band—for each, a separate SG must be defined. ALMA cannot observe multiple frequency bands simultaneously (see Section 5). The best that can be done at present is to perform back-to-back observation of the same field consecutively in different frequency bands.

The *Field setup* for each SG can be more complicated: one can chose between single pointing (SP) and a mosaic. An SP has a FOV approximately defined by the size of the primary beam of a 12-m antenna. Should a larger FOV be required to meet science objectives, a mosaic must be requested (Section 1.2.3, Section 2.4) and the user must specify the angular size of the domain to be imaged. The OT automatically calculates the number of discrete antenna pointings required in the mosaic. Nyquist sampling is the default spacing between pointings. Any unique combination of spectral and field setup requires a separate SG. Beginning in Cycle 9 (2022) the fast regional mapping (FRM; Section 2.5) capability became available. The OT allows users to define the circular area to be scanned with relatively high cadence encompassing the interferometric image. To avoid the Fourier aliasing, it is recommended that users select a region that is twice the size of the interferometric FOV. For the purposes of proposal preparation, a representative solar ephemeris must be uploaded for each SG in the field setup. As described below, the ephemeris actually used by a given solar observing program must be provided one or 2 days before a given program is executed. All target pointings—SP, mosaic, and FRM—are referenced to the user-provided ephemeris.

Control and performance parameters in the OT are used by the user to specify the desired angular resolution or an acceptable range of angular resolutions for the project. Coupled with the desired spectral setup, the appropriate array configuration(s) will be determined. Sensitivity parameters for an SG can often be ignored since there is no lack of signal on solar targets, in general. Exceptions do occur, however; for example, solar prominences at high frequencies, as they can be quite optically thin. The default integration time of 2 s is sufficient in most cases. The maximum time of a single realization of the observation of the given SG (the so-called Execution Block–EB; see below) is 2 h. Note, that this period means ~ 1.5 h on the science target, the rest is spent on instrument setup and calibration.

The Technical justification is used to justify each SG setup and to demonstrate its feasibility. It is highly recommended that proposers specify and justify any requests that may have an operational impact: for example, that back-to-back execution of particular SBs is required, or that coordination with another telescope will be needed. An excellent resource for technical aspects of ALMA is the Technical Handbook,[10] which is updated each observing cycle.

The key component of an ALMA proposal is the scientific justification. It is of critical importance as it makes the scientific case for an allocation of telescope time to address the stated science goals. Solar proposers should be aware that not all reviewers are necessarily solar experts. The proposal should provide enough context and background for a non-expert to understand the science goals. The scientific justification is the largest determinant in whether a given proposal receives a time allocation!

Before a proposal can be submitted it must be "validated". That is, it is checked by the OT for completeness and feasibility within the constraints imposed on solar observing programs. For example, the validator does not allow you to observe the Sun in Band 9 or to use C-7 array configuration (as implied from selecting an angular resolution that requires an array configuration that is not allowed). Upon validation, a proposal may be submitted.

9 The ALMA Proposer's Guide is updated each observing cycle and is available at https://almascience.eso.org/documents-and-tools.

10 The ALMA Technical Handbook is available at https://almascience.eso.org/documents-and-tools.

3.2 Proposal review

Before 2021 a large number of ALMA Review Panels (ARPs) was allocated to the five different science categories based on proposal pressure within each category. Typically a minimum of 2 ARPs and a maximum of 6 was allocated to each category to review and rank each proposal within that category. The ALMA Program Review Committee (APRC), comprising APR Chairs, then convened to perform a final review of proposal rankings and to determine which large proposals would be accepted. Large proposals are those requiring allocations of more than 50 h of time on the 12-m array.

Beginning with Cycle 8 (2021) the JAO adopted a Distributed Peer Review (DPR) system. The process is "double blind": reviewers do not know the identities of the proposing team and proposers do not know the identities of proposal reviewers. All proposals are evaluated and ranked using the DPR process with the exception of large proposals, which continue to be evaluated by the APRC. All PIs, or a designated co-investigator, must review ten proposals for each proposal they submit.[11] Since a given solar proposal is being evaluated by peers who also submitted proposals, not all of whom are solar experts, it is important to ensure that a proposal is understandable to non-experts.

Most proposers are affiliated with one of the four ALMA partners. Those who are not may still propose for observing time under "open skies." A total of 5% of the available observing time is available to unaffiliated observers.[12] ALMA typically receives 1700-1800 proposals for each observing cycle. Of these, only a few dozen proposals are typically submitted by the solar community. The instrument is highly over-subscribed with only 15%–20% of submitted proposals approved for a time allocation and so the number of solar programs observed to date is not large.

3.3 Solar observing process

Solar observing in practice has evolved since first becoming available in late-2016. Initially, solar programs were executed in a "campaign mode." While this was a convenient and flexible way to maximize the number of programs scheduled within the campaign period, they relied on the presence of solar scientists at the ALMA OSF. A reliance on external solar scientists, especially if several array configurations were required, was deemed unsustainable. In more recent years, the execution of solar programs is coordinated through the PI, the CS, and the Astronomer on Duty (AoD).

Several days before a given observation can potentially be executed, the PI opens a "Target of Opportunity" (ToO) ticket using the Helpdesk, in which the PI briefly describes the details of observation, including the target coordinates, whether to track solar rotation, and any constraints that might impact operations—e.g., whether possible loss of complementary TP maps compromises the science goal or is tolerable, whether back-to-back observations of some blocks are absolutely essential or not, etc. The ToO ticket should be updated before each potential execution of an SB. The AoD is currently responsible for generating the solar ephemeris based on information provided by the PI in the ToO ticket, and for any changes to the orientation of a mosaic, if one or more is requested. Before the actual observation takes place, its execution is simulated, the results of which are reviewed and approved by the PI and CS. If a given SG is being supported by an external observatory or mission, the PI is responsible for coordinating such support.

As described above, each SG defined in the OT proposal (Phase I) is automatically transformed into an SB during the Phase II. The SBs represent a complete observation setup but critical information must still be provided. As noted, an ephemeris must be generated shortly before an SB is executed. In addition, it is usually the case that calibrator sources are left unspecified until the observing window is approximately known. The CS is responsible for ensuring that appropriate calibrator sources are specified in the SB. Each execution of an SB (which may be executed more than once) is called an Execution Block (EB). The SB (or its EB realization) consists of smaller elements—scans and subscans. The SB for an INT observation typically contains scans for pointing, flux, and band-pass calibration at the beginning of each EB followed by multiple science-target scans interleaved with gain calibration and atmospheric calibration scans (see Shimojo et al. (2017), Figure 4), for a schematic figure of the EB structure. In the case of mosaic observations, scans are further broken down into subscans, one for each instance of a distinct pointing. In parallel to INT observations, fast scan TP mapping is performed with one or more total power antennas to provide full disk maps and/or FRM maps.

3.4 Solar data calibration and quality assurance

Once successfully executed, data from an observing program are entered into the ALMA data archive. A copy of the ALMA data archive is available at each ARC. The data of a given PI are calibrated and assessed by DAs at the relevant ARC. Many non-solar observations are sufficiently standard that they can be automatically processed (pipeline processing). Solar observations are non-standard and are manually calibrated using specialized scripts and utilities.

11 Additional details regarding DPR process and policies may be found at https://almascience.nrao.edu/documents-and-tools/cycle9/principles-review-process.

12 See https://almascience.nrao.edu/documents-and-tools/cycle9/alma-user-policies for additional details regarding user policies.

Briefly, data calibration entails solving for the instrumental (complex) gain of each antenna and applying it to source data in order to infer the "true" amplitudes and phases of the complex visibilities. This is typically done by observing a gain calibrator, usually a point-like source or a source of known structure, with a precisely known location and flux density. Taking a point-like source as an example, the source amplitude of each baseline should be that of the source itself and the phase should be zero (Fourier transform of a δ-function). For a given frequency, time, and polarization only N complex gain solutions are needed whereas N(N-1)/2 observations are available. The system is highly over-determined for a large-N array like ALMA and the gains are determined using a non-linear least-squares approach. In general, the flux density of the gain calibrator is not known *a priori* and it must be referenced to an observation of a flux calibrator that has a well-established and stable flux density. This is not possible for the Sun. For non-solar observations the source is too weak to contribute to system noise and the *system temperature*, T_{sys}, is dominated by receiver noise, spillover, etc. However, when observing the Sun the source itself contributes the bulk of the system noise, referred to as the *antenna temperature,* T_{ant}. In order to calibrate the flux scale of solar visibility data it is necessary to measure T_{ant}. Therefore, while observations of a gain calibrator provide phase solutions, the amplitude scale must be established using the ALMA Calibration Device at periodic intervals throughout a solar observations. Further details are available in Shimojo et al. (2017).

Additional calibrations are necessary: at the beginning of an observation an antenna pointing calibration is performed, delay calibration, and the relative sideband gains. In addition, as noted in Section 1, ALMA observes in four spectral windows, each 2 GHz in bandwidth and channelized into 128 frequency channels. A bandpass calibrator is therefore also observed at the beginning of an EB to deduce the relative variation of amplitude and phase across each spectral window so that it can be removed before averaging frequencies to form pseudo-continuum datasets. Additional calibrations, e.g., baseline calibration, are performed by science operations as needed.

After data calibration data analysts image each spectral window and polarization of each EB to: (i) Ensure that the data are of sufficient quality to meet the science requirements defined in the proposal (Quality Assurance level 2 – QA2), and (ii) Serve as a starting point for more advanced data analysis; e.g., time-domain imaging, self-calibration, feathering, etc. The QA2 process involves—in addition to data selection (flagging), calibration, basic imaging and image inspection—final consistency checks of the entire dataset. QA2 has sometimes revealed issues with the approach to data reduction or have fed back into telescope operations. For example, as described in Section 2.6 it was determined that the procedure used to set reference coordinates was inaccurate for data acquired in Cycle 4 and Cycle 5. The reduction script used by the DAs was therefore revised and updated to correct the issue. More recently, it was determined that, for single pointing data the reference images used standard gridding as the default which resulted in the use of the 7 m primary beam rather than the appropriately weighted primary beam response of the heterogeneous array. In any case, caution should be exercised when using the reference images for scientific analysis.

4 ALMA solar imaging and data analysis

Current ALMA solar observing capabilities provide a great deal of flexibility in terms of frequency band selection, angular resolution, time resolution, and image size. As described in the previous section, data calibration is handled by the ARCs and is generally robust. Observers must then confront myriad issues related to solar imaging and data analysis. The Sun is arguably the most difficult imaging problem possible for ALMA because while interferometers are at their best with compact discrete sources, the Sun fills any field of view with relatively-low-contrast structure on all spatial scales. Furthermore, it is dynamic on a range of time scales and solar observers generally cannot take advantage of Earth rotation aperture synthesis to help fill in spatial scales missing from any snapshot observation as those of sidereal sources can. A major challenge is to produce high quality images that recover the critical angular scales needed to address the science objectives of interest. In this section we summarize some of the challenges and subtleties associated with imaging and analyzing ALMA solar observations. They include the use of the heterogeneous array, data weights, self-calibration, and combining single dish total power data with interferometric data.

4.1 Heterogeneous array

As summarized in Section 4, solar observations with ALMA are performed by the 12-m array in combination with the ACA; that is, as a heterogeneous array comprising both 12 and 7 m antennas. The intent is to maximize the range of spatial scales to which the observations are sensitive. On the other hand, the use of different antenna sizes, with different fields of view and weighting (Section 4.3), introduces subtleties that are not yet fully understood. The effective use of the heterogeneous array is still an area of active investigation.

For a single pointing, the use of the heterogeneous array is straightforward but there are subtleties. The use of the

appropriate gridding function ("mosaic" or "mosaicft") is necessary in order to handle visibility gridding for the different antenna sizes correctly. For sources on the solar disk, emission fills the primary beam (and beyond) for all telescopes. The issue of primary beam correction becomes somewhat complicated because the 7 and 12 m telescopes have primary beams of different sizes, and therefore do not "see" the same region of the Sun. In the case of a single-pointing observation, the standard procedure is to produce a map from the visibilities, deconvolve the result, then apply a primary beam correction to the deconvolved image, but neither the 7 m nor the 12 m primary beam, nor any hybrid, truly represents the appropriate correction. The correct imaging path for this case may be to have a model of the sky that is then convolved with the spatial response of each pair of telescopes, using the primary beams appropriate to each telescope, to form visibilities, and the model is then iteratively corrected to make the modeled visibilities, or the corresponding map, match the telescope data. Such a process is not currently available in CASA, but may be needed to optimally exploit ALMA solar data.

Mosaicking works well in many cases but there appear to be failure modes that are not fully understood. The problem has been recently explored by da Silva Santos et al. (2022). Figure 7 shows a deconvolution of a small mosaic produced by CASA, using CASA's "mosaic" gridding option, with an alternate approach in which the individual pointings are each mapped separately and then combined in the image plane using a linear mosaic technique and an appropriate primary beam. For this dataset most CASA images of an 80-second loop of 10-pointing mosaics have either bright or dark features that corrupt the map, and thus one cannot reliably produce time-resolved mosaics; the alternate technique, however, works reliably. The reason for the failure of CASA imaging may be due to the fact that the mosaic gridding technique limits the field of view to within a certain distance of the pointing center, but, e.g., the field of view of the 7 m antennas is larger than the field of view of the 12 m antennas, and thus there is emission outside the 12 m gridded area that is sampled by the data, and is aliased into the gridded region, but this needs to be investigated further.

Some users may find that their goals are adequately addressed by using the 12-m array alone, which greatly simplifies the data reduction and avoids some of the pitfalls described above, which are not fully understood. Others may wish to use the heterogeneous array as two homogeneous arrays: the 12-m array together with the ACA. It is straightforward to feather images made with the 12-m array, the ACA, and a TP map, again avoiding some of the issues raised by using mixed antenna pairs.

4.2 Self-calibration

Self-calibration is a technique (e.g., Cornwell and Fomalont (1989)) where the source itself is used to determine corrections to antenna-based gains. Gain errors are most often due to atmospheric "seeing" and, as such, are dominated by phase errors. As discussed in Section 2.2, ALMA makes use of WVR measurements as a proxy for phase fluctuations at each antenna for non-solar observations. This capability is not available for solar observations because the WVRs saturate when pointing at the Sun. An active topic of research is to develop an alternative proxy for phase fluctuations, such as observations of the Sun in the wing of the 183 GHz water absorption line in Band 5 (see Section 5.5). Solar observations must therefore rely on self-calibration techniques in the interim.

Experience to date suggests that a hierarchical approach to self-calibration is effective, where the average image of a scan is used as the initial source model to deduce average phase corrections. The corrected data are imaged and deconvolved to produce a new source model. This is used to determine phase corrections on a shorter time scale. This can proceed iteratively until corrections on time scales as short as the integration time are deduced.

The self-calibration of mosaic data is somewhat less straightforward but the same hierarchical approach can work well. The difference is that it is often useful to perform the first iteration of self-calibration by determining average corrections for an entire mosaic before determining solutions for each pointing separately, using the mosaic as the model.

4.3 Data weights

Data weights enter into the imaging problem in two ways: i) the weight assigned to each visibility in forming an image through Fourier inversion, and ii) the weight assigned to each antenna beam in a mosaic. The weight assigned to a visibility measured by antenna i and j is $1/\sigma_{ij}^2$, where σ_{ij}^2 is the statistical variance of the measurement. For solar observations, the system noise is dominated by the source (the Sun) and the variance is of order $\sigma_{ij} \sim (T_{ant,i}T_{ant,j}/A_iA_j)(k_B/\Delta\nu\Delta t)$ where $T_{ant,i}$ is the antenna temperature of antenna i and A_i is its effective area. All other things being equal, visibilities in a homogeneous array are given approximately the same weight (e.g., the 12-m array). However, for a heterogeneous array, we have visibility measurement with 7 m × 7 m antennas, 7 m × 12 m antennas, and 12 m × 12 m antennas. The weights for each of these pairings therefore scale as $(7/12)^4$: $(7/12)^2$: 1, or roughly 1/9:1/3:1. For a heterogeneous array of, say, 10 ACA antennas and 45 antennas from the 12-m array, the total number of baselines would be 1,485. Of these, only 45 would be 7 m × 7 m pairs (3%) and 450 would be 7 m × 12 m pairs (30%). Coupled with the visibility weights, 7 m × 7 m correlations have very little impact on imaging and even the (weighted) 7 m × 12 m correlations come in at the ~ 10% level.

In the case of mosaic imaging, user should be aware of a second subtlety, namely, the so-called primary beam correction.

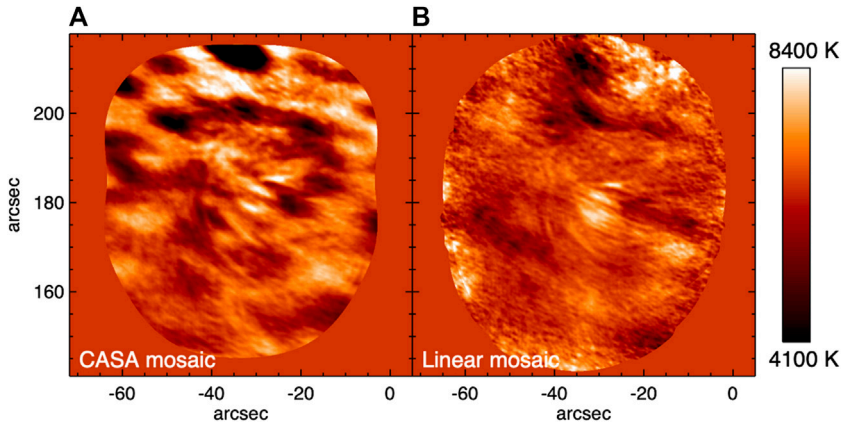

FIGURE 7
Example of a small mosaic formed from ten discrete pointings in 80 s. **(A)**: The image produced by joint deconvolution of the ten pointings in CASA. **(B)**: The image produced by imaging each pointing separately and combining them linearly.

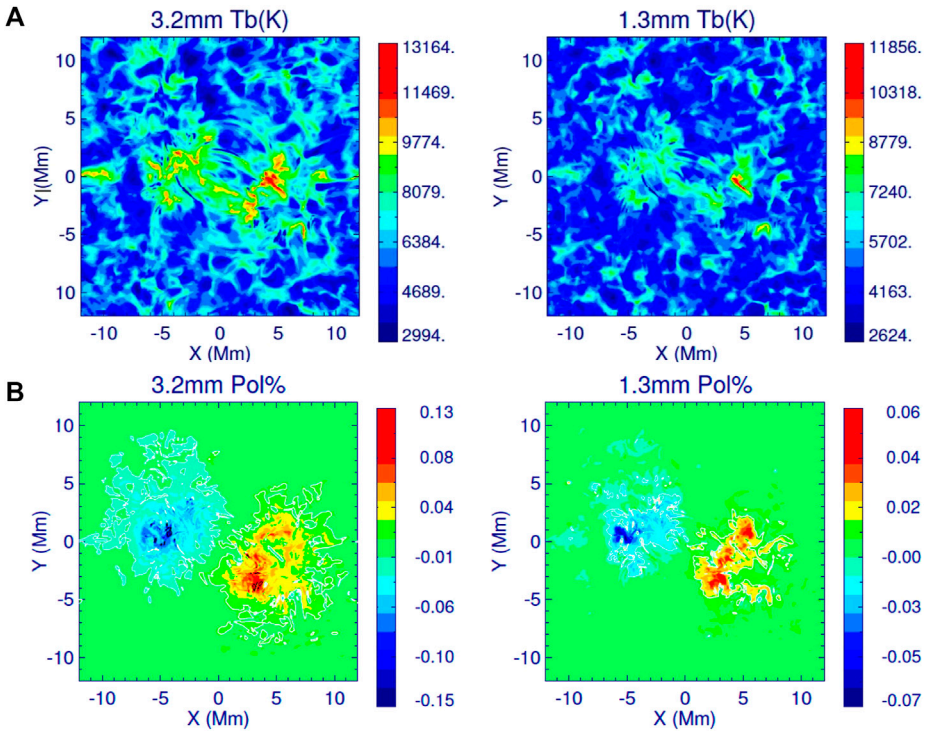

FIGURE 8
Model brightness temperature distributions for a bipolar regions in Band 3 and Band 6 **(A)** and the corresponding degree of circular polarization **(B)**. After Loukitcheva et al. (2017).

The primary beam correction is formed from the grid of pointings on the sky as $\Sigma_k B(\theta - \theta_k)/\sigma_k^2$, where B is the primary beam response. Consider a mosaic formed with a homogeneous array. The weight assigned to the antenna primary beam for each pointing k is approximately the same for all antennas. Since the variance depends on T_{ant}, and T_{ant} may change significantly with k, the weight assigned to each pointing may also vary. An extreme example is given by a Band 7 mosaic

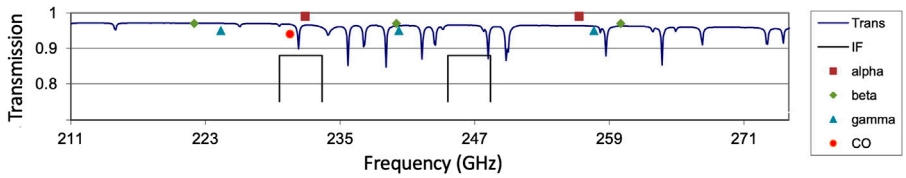

FIGURE 9
Lines present in the ALMA Band 6 frequency range. The blue line indicates the atmospheric transmission and the black brackets indicate the current locations of the upper and lower sidebands for solar observing. The legend indicates the frequencies of the Hα, Hβ, and Hγ radio recombination lines as well as CO. Note that the lower sideband was selected to include H30α recombination line and the CO J = 2-1 line. Adapted from an unpublished figure provided to the authors by R. Hills.

on the solar limb. As noted in Section 1.1, Band 7 uses nominal receiver settings and T_{sys} is consequently small (200 K). When pointing on the solar disk the system noise is therefore dominated by T_{ant}, the variance is high, and the weight assigned to that pointing is low. When the pointing is such that the limb only partially fills the beam, or the pointing is above the limb and the Sun contributes little emission to the system, the variance is low and the corresponding weight is high. This can lead to a distorted mosaic beam where the emission of interest is down-weighted relative to pointings above the limb! Users may therefore wish to correct their mosaic with a uniform weight applied to each pointing or even use weights proportional to the fractional filling factor of the Sun, although the latter idea has not been tested.

A minor issue is that if a heterogeneous array is used, the effective primary beam (FOV) differs from that of a single antenna in a homogeneous array. The response of a single baseline with identical antennas is the same as that of a single antenna, while the response of a 7 m × 12 m baseline is geometric mean of the two antenna power patterns. The effective FOV is the weighted sum of the relevant FOV for each baseline. The net effect is to slightly broaden the 12-m array FOV ($< 10\%$).

4.4 Combining interferometric and single dish data

An interferometer cannot measure angular scales greater than that measured by the minimum antenna baseline. In the absence of total power information, also known as the "zero-spacing flux," ALMA measures the distribution of brightness relative to the mean. The mean brightness of the background Sun is of order 6,000–8,000 K, far in excess of the low-contrast variation against the mean. The restoration of total power information to ALMA images is critical if absolute brightness temperatures are important to the science objectives.

To zeroeth order, simply adding a constant brightness offset to an image, corresponding to the mean brightness, largely corrects for the absence of short spatial frequencies and this approach may indeed be sufficient for single-pointing imaging on the solar disk. For mosaic images, however, this is not necessarily sufficient. Solar observations with ALMA provide low-resolution full-disk maps of the Sun that are observed contemporaneously with interferometric observations using one or more of the 4 TP antennas. Calibrated TP maps contain the correct flux on all scales ranging from the 12 m primary beam size to the scale of the Sun in any given frequency band. Hence, by combining TP observations with interferometric data, one can recover the largest angular scales.

While it is possible, in principle, to first perform data combination in the uv domain followed by image deconvolution, it is perhaps more straightforward to reverse the order and to use a technique called "feathering" (e.g., Cotton 2015). Briefly, feathering begins with TP and interferometric maps, MTP and MINT, that embody low angular frequencies and high angular frequencies, respectively. The TP map must be coaligned with the interferometric map. It is convenient to cutout an imaging domain of the TP map that is perhaps twice the size of the INT map. The two are then Fourier transformed, $FT(MTP)$ and $FT(MINT)$, as is the 12 m primary beam FT(B), taken to be Gaussian. A mask is then formed from FT(B) as $m = 1 - FT(B)$ and the sum $FT(MTP) + mFT(MINT)$ is formed. The use of the mask is to smoothly weight down angular scales measured by the interferometer that overlap with those measured by the single dish TP map. The sum is then inverse-Fourier transformed $FT^{-1}(FT(MTP) + mFT(MINT))$, yielding the combined image.

This approach works well in many cases; e.g., mosaics on the solar disk. However, it has shortcomings when imaging the solar limb. Two factors come into play: first, fast-scan total power maps sometimes have artefacts at the limb due to residual scan timing errors. It is undesirable to propagate these into the combined image. Second, as seen from Table 2, the minimum angular scales measured by the 12-m array decrease with frequency band and array size. While the heterogeneous array mitigates this to some extent, the degree of overlap between the TP data and interferometric data in the *uv* domain, and the

density of interferometric sampling in the region of overlap, both decrease with increasing frequency and array size. As a result, angular scales between the 12-m array MRS and the 12 m FOV are increasingly poorly sampled.

5 Future capabilities and observing modes

ALMA capabilities currently support a wide range of solar science but additional capabilities will no doubt further enrich the scientific possibilities. We briefly summarize several new instrumental capabilities that are under active consideration and then briefly touch on possible observing modes that do not depend on the development technical or data reduction capabilities but, rather, depend on observatory policy and science operations.

5.1 Polarimetry

ALMA currently supports full polarimetry for non-solar observing. A longstanding goal has been to implement support of polarimetry for solar observations. Efforts are currently underway to enable polarimetry in Band 3. Polarimetry involves measuring cross-hand as well as parallel-hand correlations on each antenna baseline *ij*: i.e., X_iX_j, Y_iY_j, X_iY_j, and Y_iX_j. Formation of the Stokes polarization parameters requires measuring the phase difference between the *X* and *Y* polarization channels and measuring instrumental polarization embodied by "polarization leakage" terms for each antenna. The challenge has been to demonstrate that the necessary quantities can be measured using the MD mode with sufficient accuracy to ensure that the polarization signals are robust.

The Stokes V parameter is of primary interest. It offers a diagnostic of the chromospheric magnetic field in active regions and flares. Modeling suggests (Loukitcheva et al., 2017; Loukitcheva, 2020) that 3 mm may be the most promising wavelength to focus on such efforts (Figure 8), at least initially, as it produces the highest degree of polarization of available frequency bands. Hence, initial efforts have gone into testing polarization observation in Band 3 with the intent of making Band 3 solar polarimetry a supported mode. However, testing is ongoing at the time of this writing and it is not yet known when the mode will become available.

5.2 Spectral line observing

Spectral line detections would significantly widen the diagnostic value of ALMA observations for studying the chromosphere, since they would permit line-of-sight velocity information that is missing from continuum observations (Figure 9). As reviewed by Wedemeyer et al. (2016), while such lines have been observed at high millimeter frequencies, there are significant potential issues.

The two best candidates for line detection are hydrogen recombination lines (e.g., H26α at 353.6 GHz) and CO rotational transitions (e.g., CO 3–2 at 345 GHz). The difficulty in detecting such lines is the fact that they are strongly pressure-broadened in the chromosphere, which reduces their contrast with the continuum. Thus, recombination lines were detected in emission by Clark et al. (2000a,b) in single-dish observations at 662.4 (H21α) and 888.0 (H19α) GHz, but only at and above the solar limb where pressure is lower, not against the solar disk. An additional complication in interpreting the spectra at these frequencies is the presence of numerous terrestrial atmospheric absorption lines. ALMA interferometer data should improve on these results since the relatively large beam of the single-dish maps (~ 19") requires averaging over a large area of extended limb, resulting in a line peak 10% above continuum level, whereas ALMA can achieve sub-arcsecond resolution (assuming successful treatment of the sharp solar limb, as discussed above). Clark et al. (2000b) argued that the line width of the core of the recombination lines from above the limb seemed to scale roughly with frequency, from about 550 MHz at H21α to 700 MHz at H19α. If this scaling continued down to ALMA Band 7, we might expect a width of order 300 MHz for H26α, but we note that the H21α/H19α values were a factor of about 3 narrower than expected from theory (Hoang-Binh et al., 1987). As discussed earlier, ALMA can center a single baseband 2 GHz wide on a spectral line, with a frequency resolution of 16 MHz in standard solar observing mode, which would be adequate to measure a line 300 MHz wide, but perhaps not a line that is several times wider with reduced contrast to the continuum.

There are, to this point, no confirmed detections of CO lines on the Sun at mm/submm – λ. The detections have been made so far mostly in the infrared (e.g., Ayres et al. (2006)) where a dense concentration of easily-observable CO rovibrational absorption lines occurs. Conventionally CO molecule formation requires temperatures of at most 3500 K, so one might expect CO to be preferentially detected in cool regions such as sunspot umbrae, but in fact CO can regularly be detected off-limb at heights where temperatures are expected to be much higher. An interpretation of this result is that CO forms in cool pockets such as the rarefaction phases of large-amplitude acoustic waves propagating through the chromosphere, or in the wake of chromospheric shocks. These interpretations carry the implication that CO formation is highly dynamic. ALMA observations can help to test these models, but this will require time-resolved spectral-line mapping in order to track the dynamics of CO features. CO lines are also expected to be pressure-broadened, and may form lower in the chromosphere than the recombination lines, where pressure is higher. However, the higher mass of the CO molecule should reduce the broadening, as found in simulations reported by

Wedemeyer et al. (2016). CO lines may be detected in absorption or emission, depending on the temperature profile in the region where they are found.

5.3 Additional frequency bands

Solar observing with ALMA is currently limited to four frequency bands. The use of additional frequency bands is highly desirable but requires significant testing and commissioning time. Two bands of interest are Band 1 (35–50 GHz; 7 mm) and Band 4 (125–163 GHz; 2.1 mm). Band 1 (Huang et al., 2016) is an entirely new capability, not just for the solar community but for the astronomical community at large. First light with Band 1 receivers was achieved in August 2021. The goal is to make Band 1 available to the wider community in Cycle 10 (October 2023) but use by the solar community must await solar testing and commissioning. While Band 4 is part of the original suite of ALMA receivers, it has not been available for solar use. It would fill the gap between Band 3 and Band 5. Extending coverage to Band 8 (385–500 GHz; 0.7 mm) is also under consideration.

Bands 9 (602–720 GHz), and 10 (787–950 GHz) are also of considerable interest. They are the most promising frequency bands for spectral line work. However, their use is problematic for solar INT observing. First, exceptional weather conditions are required for high-frequency observing under any circumstances. Daytime observing in Bands 9 and 10 is currently prohibited. Second, Bands 9 and 10 are double-sideband receivers and so the observing strategy may be more complicated than the MD mode used currently. On the other hand, the system temperatures for these bands is higher than for the lower frequency receivers (ranging from a few × 100 K for Band 8 to > 1000 K for Bands 9 and 10) which may simplify their use. Both policy and technical challenges would need to be overcome to exploit them for interferometric solar observations. We note, however, that full disk TP mapping in Band 9 was demonstrated (see (Bastian et al., 2018), Figure 3) during commissioning and science verification in 2015 through a sky opacity $\tau \sim 1$!

5.4 Flare mode observations

Observations of flares at mm-λ and submm-λ offers the potential of fundamentally new insights into energy release, particle acceleration, and emission mechanism on the Sun (see Fleishman et al., this Frontier collection). Implementation of flare mode observing confronts us with additional challenges, however. While the MD mode has successfully enabled observations of quiescent solar phenomena, it is not designed to handle the much higher flux densities produced by solar flares. Alternatives must be explored.

It is likely that solar filters installed on the ALMA Calibration Device on each antenna will be at least part of the approach. The solar filters were the initial solution adopted by ALMA to manage solar signals. However, as detailed by Shimojo et al. (2017) the filters have a number of undesirable properties that led to the development of MD mode observing instead. The solar filter is placed in front of a given receiver in order to attenuate the incident signal. The nominal amount of attenuation is $4+2\lambda_{mm}$ dB, amounting to signal reductions by factors of 10, 5, 3.5, and 3 for bands 3, 5, 6, and 7, respectively.[13]

The antenna temperature is $T_{ant} = SA_e/2k_B \approx 124S_{SFU}$ K where S_{SFU} is the flux density in solar flux units (10^{-19} ergs s^{-1} cm^{-2} Hz^{-1}), $A_e = \eta A$ is the effective area of the antenna, and k_B is Boltzmann's constant. For the non-flaring Sun, $T_{ant} \sim T_B \sim 6{,}000 - 8000$ K. With the signal attenuation factors as given, ALMA could accommodate flares of order 600, 250, 160, and 120 SFU within the antenna beam for bands 3, 5, 6, and 7, respectively. This may be sufficient to observe many flares but may be problematic for some: the so-called "sub-THz" component of certain flares displays an inverted spectrum (Krucker et al., 2013). That is, the flux density increases with frequency and the system may saturate in the higher frequency bands. Preliminary tests of the filters in Band 7 indicate that the degree of attenuation is less than nominal, possibly exacerbating the problem. Alternative, or additional, strategies may be necessary to observe flares. Possibilities include the use of MD mode in tandem with solar filters and/or off-pointing the antennas so that a given flare occurs in a sidelobe of the antenna response. The first sidelobe of the 12-m antennas is a factor of 100 less sensitive than the center of the main response lobe. It is expected that testing and commissioning efforts for solar mode flare observations will begin in the coming year.

5.5 High angular resolution

Solar observations are currently restricted to the four most compact array configurations for reasons given in Section 2.2. This limits the available angular resolution to ≈ 0.6" – 0.9". On the other hand, the high brightness of solar emission can also yield opportunities that are impossible for "standard" interferometry of relatively weak targets for which the implicit assumption is that we need rather long observing (total signal

13 A preliminary assessment of the solar filters for Band 7 showed that the attenuation introduced by the filters did not necessarily conform to expectations. In addition, single-dish TP maps made through the solar filters show poorer contrast than maps made without the filter. A painstaking assessment of the filters lies ahead.

integration) times to reach a sufficiently high signal to noise ratio (SNR). Since the image integration in "standard" interferometry is typically performed over periods greatly exceeding the time-scale of the phase variations, the resulting image is blurred and the resolution (long-duration coherence) is lost unless provisions are made–the use of the WVRs and self-calibration. Phase variations occur on time scales of seconds to tens of second. Depending on the details of seeing conditions and the array configuration, these may largely manifest as low order distortions of the snapshot solar images: e.g., image wander and warping. These distortions can be, to a large extent, distinguished and separated from the true dynamics of the Sun: the large-scale solar structures change at much longer timescale (minutes) than the integration time or the time scale of phase variations over the array. The Sun allows a good SNR to be achieved even on the shortest integration times (currently 1 s, but as short as 0.16 s in principle), which enable time series of relatively sharp, but distorted images, to be obtained instead of a single blurry image by, in effect, freezing the phase variations. Self-calibration techniques are a well-established and tested means of mitigating phase variations in solar data, even in the absence of WVR corrections. It is anticipated that higher angular resolution imaging with ALMA is possible by extending observations to larger array configurations. Higher angular resolution imaging is the subject an ESO ALMA Development Study that started in July 2022.

5.6 Standalone total power mapping

ALMA science operations currently provides TP full-disk and/or FRM maps as a complement to the interferometric observations. The full disk TP maps have been exploited scientifically in their own right (Alissandrakis et al., 2017, 2020, 2022; Brajša et al., 2018; Selhorst et al., 2019; Sudar et al., 2019). There is interest in the solar community of using TP antennas in a mode that is independent of the 12-m array or ACA. A particularly attractive possibility is to perform multi-band TP or FRM mapping in standalone mode, possibly even in bands not currently supported for INT observing. As noted above, full disk TP mapping in Band 9 has been successfully demonstrated. Support of such a mode would require a policy change by the JAO as well as changes to the OT and operations.

5.7 Science sub-arrays

It is currently not possible to observe the Sun in more than one frequency band simultaneously. One might suppose that time sharing between two or mode frequency bands might be a promising strategy but the time overheads in switching frequency bands is prohibitive and significant changes would be needed to SBs. A more feasible approach may be the use of antenna subarrays, where the antennas of the 12-m array are distributed among two or more groups of antennas that operate as independent arrays. A user could allocate half of the antennas to one subarray and half to another; or divide them into three arrays with comparable number of antennas. However, since the number of antenna baselines and, therefore, *uv* samples is ~ $N^2/2$ the *uv* coverage provided by a given subarray quickly degrades with the number of subarrays and so users would need to consider carefully the advantages and disadvantages of the approach.

6 Concluding remarks

ALMA is a remarkable instrument that has opened a new wavelength regime for exploration. Solar observations with ALMA have been possible since late-2016 but the number of programs that have been successfully executed has been relatively modest. There are several reasons for this: i) as a general purpose instrument used by the entire astronomy and astrophysics community, competition for observing time is fierce—only a few solar observing programs are observed per cycle; ii) as an interferometer, ALMA is not necessarily familiar to segments of the solar community—a learning curve must be surmounted through education and outreach; iii) the data can be challenging to reduce and analyze—progress on establishing and sharing "best practices" is ongoing.

Nevertheless, as the solar community becomes increasingly knowledgable about solar observing at mm/submm-λ and as new observing modes and capabilities continue to be developed, the scientific impact of ALMA will continue to increase. This is particularly true in light of next-generation instruments coming online at other wavelengths; e.g., the Daniel K. Inouye Solar Telescope (DKIST), operating at O/IR wavelengths. Powerful synergies are available that will only increase the impact of ALMA.

Author contributions

TB authored the bulk of the manuscript. MB wrote Section 3 and contributed Section 2.6 and Section 5.5. MS contributed Sections 2.5 and 5.1. SW contributed to Section 2.6, and wrote Sections 4.1 and 5.2. All authors discussed and revised the manuscript and contributed numerous comments and corrections.

Funding

MB acknowledges support by projects 20-09922J and 21-16808J by the GACR, and project LM2015067 by the Ministry of education of the Czech Republic. SW acknowledges support from AFOSR grant 20-RV-COR-026.

Acknowledgments

We wish to thank our friend and colleague, Prof. Richard Hills, now deceased, for both his important contributions to, and his unstinting encouragement for, making solar observations with ALMA a reality. We thank the reviewers for their careful reading of the manuscript and for their constructive comments. ALMA is a partnership of ESO (representing its member states), NSF (USA) and NINS (Japan), together with NRC (Canada), MOST and ASIAA (Taiwan), and KASI (Republic of Korea), in cooperation with the Republic of Chile. The Joint ALMA Observatory is operated by ESO, AUI/NRAO and NAOJ. The National Radio Astronomy Observatory is a facility of the National Science Foundation operated under cooperative agreement by Associated Universities, Inc. This article made use of the following ALMA data: ADS/JAO.ALMA#2011.0.00020.SV.

Conflict of interest

The authors declare that the research was conducted in the absence of any commercial or financial relationships that could be construed as a potential conflict of interest.

Publisher's note

References

Alissandrakis, C. E., Bastian, T. S., and Nindos, A. (2022). A first look at the submillimeter sun with alma. *Astron. Astrophys.* 661, L4. doi:10.1051/0004-6361/202243774

Alissandrakis, C. E., Nindos, A., Bastian, T. S., and Patsourakos, S. (2020). Modeling the quiet sun cell and network emission with ALMA. *Astron. Astrophys.* 640, A57. doi:10.1051/0004-6361/202038461

Alissandrakis, C. E., Patsourakos, S., Nindos, A., and Bastian, T. S. (2017). Center-to-limb observations of the sun with alma . implications for solar atmospheric models. *Astron. Astrophys.* 605, A78. doi:10.1051/0004-6361/201730953

Ayres, T. R., Plymate, C., and Keller, C. U. (2006). Solar carbon monoxide, thermal profiling, and the abundances of c, o, and their isotopes. *Astrophys. J. Suppl. Ser.* 165, 618–651. doi:10.1086/504847

Bastian, T. S., Bárta, M., Brajša, R., Chen, B., Pontieu, B. D., Gary, D. E., et al. (2018). Exploring the sun with alma. *Messenger* 171, 25–30.

Brajša, R., Sudar, D., Benz, A. O., Skokić, I., Bárta, M., De Pontieu, B., et al. (2018). First analysis of solar structures in 1.21 mm full-disc alma image of the sun. *Astron. Astrophys.* 613, A17. doi:10.1051/0004-6361/201730656

Clark, T. A., Naylor, D. A., and Davis, G. R. (2000a). Detection and limb brightening of the h i n=20-19 rydberg line in the submillimetre spectrum of the sun. *Astron. Astroph.* 357, 757–762.

Clark, T. A., Naylor, D. A., and Davis, G. R. (2000b). Detection of the h i n=22-21 rydberg line in emission at the solar submillimetre limb. *Astron. Astroph.* 361, L60–L62.

Cornwell, T., and Fomalont, E. B. (1989). "Self-calibration," in *Synthesis imaging in radio astronomy of astronomical society of the pacific conference series*. Editors R. A. Perley, F. R. Schwab, and A. H. Bridle, 6, 185.

Cotton, W. (2015). *Obit memo 41: Image combination by feathering*. Tech. rep. Charlottesville, VA: National Radio Astronomy Observatory.

da Silva Santos, J. M., White, S. M., Reardon, K., Cauzzi, G., Gunár, S., Heinzel, P., et al. (2022). Subarcsecond imaging of a solar active region filament with alma and iris. *Front. Astron. Space Sci.* 9, 898115. doi:10.3389/fspas.2022.898115

Hoang-Binh, D., Brault, P., Picart, J., Tran-Minh, N., and Vallee, O. (1987). Ion-collision broadening of solar lines in the far-infrared and submillimeter spectrum. *Astron. Astroph.* 181, 134–137.

Huang, Y. D. T., Morata, O., Koch, P. M., Kemper, C., Hwang, Y.-J., Chiong, C.-C., et al. (2016). "The atacama large millimeter/sub-millimeter array band-1 receiver," in *Modeling, systems engineering, and project management for astronomy VI of society of photo-optical instrumentation engineers (SPIE) conference series*. Editors G. Z. Angeli and P. Dierickx, 9911, 99111V. doi:10.1117/12.2232193

Krucker, S., Giménez de Castro, C. G., Hudson, H. S., Trottet, G., Bastian, T. S., Hales, A. S., et al. (2013). Solar flares at submillimeter wavelengths. *Astron. Astrophys. Rev.* 21, 58. doi:10.1007/s00159-013-0058-3

Loukitcheva, M. (2020). Measuring magnetic field with atacama large millimeter/submillimeter array. *Front. Astron. Space Sci.* 7, 45. doi:10.3389/fspas.2020.00045

Loukitcheva, M., White, S. M., Solanki, S. K., Fleishman, G. D., and Carlsson, M. (2017). Millimeter radiation from a 3d model of the solar atmosphere. ii. chromospheric magnetic field. *Astron. Astrophys.* 601, A43. doi:10.1051/0004-6361/201629099

Nikolic, B., Bolton, R. C., Graves, S. F., Hills, R. E., and Richer, J. S. (2013). Phase correction for ALMA with 183 GHz water vapour radiometers. *Astron. Astrophys.* 552, A104. doi:10.1051/0004-6361/201220987

Phillips, N., Hills, R., Bastian, T., Hudson, H., Marson, R., and Wedemeyer, S. (2015). "Fast single-dish scans of the sun using alma," in *Revolution in astronomy with ALMA: The third year of astronomical society of the pacific conference series*. Editors D. Iono, K. Tatematsu, A. Wootten, and L. Testi, 499, 347.

Sault, R. J., Stavley-Smith, L., and Brouw, W. N. (1996). An approach to interferometric mosaicing. *Astron. Astrophys. Suppl. Ser.* 120, 375–384. doi:10.1051/aas:1996287

Selhorst, C. L., Simões, P. J. A., Brajša, R., Valio, A., Giménez de Castro, C. G., Costa, J. E. R., et al. (2019). Solar polar brightening and radius at 100 and 230 GHz observed by ALMA. *Astrophys. J.* 871, 45. doi:10.3847/1538-4357/aaf4f2

Shimojo, M., Bastian, T. S., Hales, A. S., White, S. M., Iwai, K., Hills, R. E., et al. (2017). Observing the sun with the atacama large millimeter/submillimeter array (alma): High-resolution interferometric imaging. *Sol. Phys.* 292, 87. doi:10.1007/s11207-017-1095-2

Sudar, D., Brajša, R., Skokić, I., and Benz, A. O. (2019). Centre-to-limb brightness variations from the atacama large millimeter-submillimeter array (alma) full-disk solar images. *Sol. Phys.* 294, 163. doi:10.1007/s11207-019-1556-x

Wedemeyer, S., Bastian, T., Brajša, R., Hudson, H., Fleishman, G., Loukitcheva, M., et al. (2016). Solar science with the atacama large millimeter/submillimeter array—A new view of our sun. *Space Sci. Rev.*, 200, 1–73. doi:10.1007/s11214-015-0229-9

White, S. M., Iwai, K., Phillips, N. M., Hills, R. E., Hirota, A., Yagoubov, P., et al. (2017). Observing the sun with the atacama large millimeter/submillimeter array (alma): Fast-scan single-dish mapping. *Sol. Phys.* 292, 88. doi:10.1007/s11207-017-1123-2

Wootten, A., and Thompson, A. R. (2009). The atacama large millimeter/submillimeter array. *Proc. IEEE* 97, 1463–1471. doi:10.1109/JPROC.2009.2020572

frontiers | Frontiers in Astronomy and Space Sciences

TYPE Review
PUBLISHED 11 October 2022
DOI 10.3389/fspas.2022.981320

OPEN ACCESS

EDITED BY
Dipankar Banerjee,
Indian Institute of Astrophysics, India

REVIEWED BY
Souvik Bose,
Lockheed Martin Solar and Astrophysics Laboratory (LMSAL), United States
Debi Prasad Choudhary,
California State University, Northridge, United States

*CORRESPONDENCE
Costas E. Alissandrakis,
calissan@uoi.gr

SPECIALTY SECTION
This article was submitted to Stellar and Solar Physics, a section of the journal Frontiers in Astronomy and Space Sciences

RECEIVED 29 June 2022
ACCEPTED 05 September 2022
PUBLISHED 11 October 2022

CITATION
Alissandrakis CE, Bastian TS and Brajša R (2022), The quiet sun at mm wavelengths as seen by ALMA. *Front. Astron. Space Sci.* 9:981320. doi: 10.3389/fspas.2022.981320

The quiet sun at mm wavelengths as seen by ALMA

Costas E. Alissandrakis[1]*, T. S. Bastian[2] and Roman Brajša[3]

[1]Department of Physics, University of Ioannina, Ioannina, Greece, [2]National Radio Astronomy Observatory (NRAO), Charlottesville, VA, United States, [3]Hvar Observatory, Faculty of Geodesy, University of Zagreb, Zagreb, Croatia

Solar observations at sub-mm, mm and cm wavelengths offer a straightforward diagnostic of physical conditions in the solar atmosphere because they yield measurement of brightness temperature which, for optically thick features, equals intrinsic temperature - much unlike solar diagnostics in other spectral ranges. The Atacama Large Millimeter and sub-millimeter Array (ALMA) has therefore opened a new, hitherto underexplored, spectral window for studying the enigmatic solar chromosphere. In this review we discuss initial ALMA studies of the quiet chromosphere that used both single-dish and compact-array interferometric observing modes. We present results on the temperature structure of the chromosphere, comparison with classic empirical models of the chromosphere, and observations of the chromospheric network and spicules. Furthermore, we discuss what may be expected in the future, since the ALMA capabilities continuously expand and improve towards higher angular resolution, wavelength coverage, and polarization measurement for magnetometry.

KEYWORDS

ALMA, sun, solar mm radio emission, quiet sun, chromosphere, chromospheric network

1 Introduction

Traditionally, the term "quiet Sun" refers to the solar atmosphere outside of solar active regions and during times free of transient energetic events such as flares and coronal mass ejections. Despite decades of study at optical (O), ultraviolet (UV), and extreme ultraviolet (EUV) wavelengths, a detailed understanding of the quiet Sun has remained elusive. ALMA has now opened a new window onto the Sun: millimeter- and submillimeter-wavelength observations of the Sun with angular and time resolutions that are orders of magnitude better than was previously possible, comparable to those available at O/UV/EUV wavelengths. The Atacama Large Millimeter and sub-millimeter Array (ALMA, Wootten and Thompson, 2009) offers new and complementary diagnostics of solar phenomena, including the quiet Sun. In this review we present and assess ALMA observations of the quiet Sun (QS). We do not treat transient phenomena and oscillations, which are the subject of the review by Nindos et al., in this special Research Topic collection. Comparisons with radiative Magnetohydrodynamics (rMHD) models are addressed in the review by Wedemeyer et al., included in this special Research Topic collection.

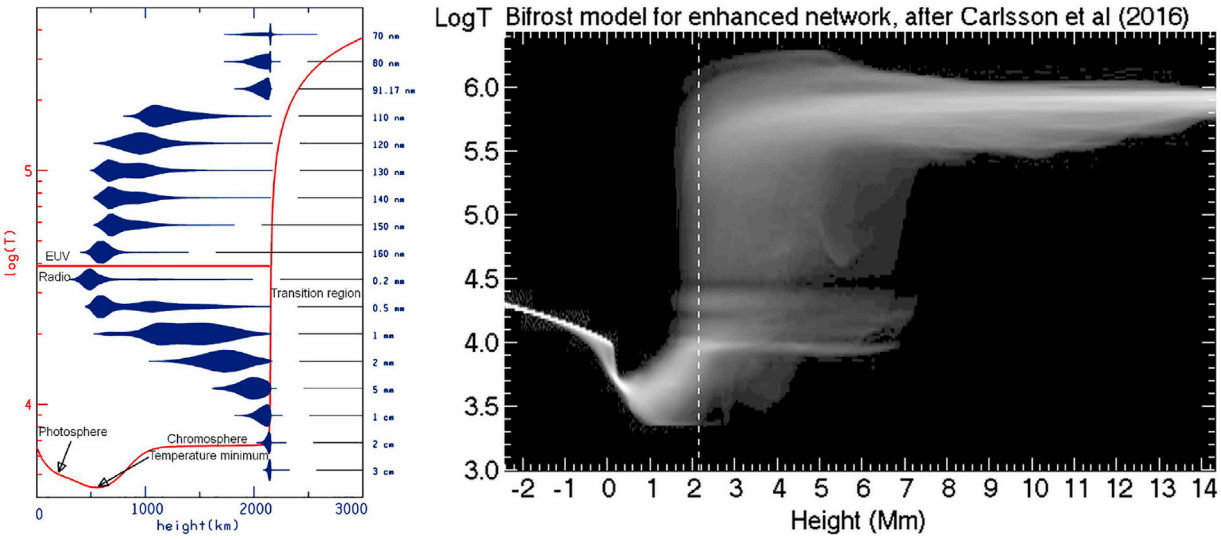

FIGURE 1
The temperature as a function of height and the formation height of mm-λ emission (Left) The electron temperature as a function of height (red line) according to model C7, adapted from Avrett and Loeser (2008). The contribution to the continuum intensity is plotted in blue for wavelengths 0.2–30 mm (below the red horizontal line) and the extreme ultraviolet wavelengths, marked at the right. (Right) Probability density function of the temperature as a function of height from Bifrost simulations of an enhanced network region. The vertical dashed line is at 2.14 Mm. Adapted from the lower panel of figure 10 of Carlsson et al. (2016).

We start with a brief description of O/UV observations of the QS in order to put the mm-λ observations in perspective (Section 2) and then we discuss what ALMA can offer to our understanding of the physical processes involved (Section 3). We proceed with the presentation of results obtained from low resolution full-disk ALMA observations, on the morphology (Section 4.1), on empirical models of the solar atmosphere (Section 4.2) and on the formation height of the emission (Section 4.3). The results from high resolution interferometric observations are discussed in Section 5, for disk (Section 5.1) and limb (Section 5.2) structures, whereas the appearance of limb structures on the disk is discussed in Section 5.3. We conclude with a brief discussion and some thoughts about the prospects of future observations of the quiet Sun with ALMA.

2 The quite sun in optical and EUV wavelengths

The solar atmosphere is commonly described in terms of the visible *photosphere*; the *chromosphere*, the thin layer visible in Hα during eclipses; and the *corona*, the extended atmosphere of the Sun visible in white light during eclipses. The *transition region* refers to material that lies at the interface between the chromosphere and the corona. Of particular interest here is the chromosphere because it is from this medium that radiation at mm and submm wavelength originates as we now discuss.

As a first approximation, the physical parameters of the solar atmosphere can be assumed to vary with height only. This is because gravity produces a strong stratification and thus the radial density gradient is much larger than the horizontal, at least in the lower atmospheric layers. This assumption has led to the classic one-dimensional atmospheric models, often multi-component to describe various atmospheric features (see the reviews by Shibasaki et al., 2011 and Alissandrakis, 2020 for more details). The temperature structure of the solar atmosphere according to one such model is plotted in red in the left panel of Figure 1. Once the temperature and density structure are known, one can compute the opacity and the effective height of formation of the radiation at a particular wavelength; this is also plotted in the left panel of the same figure, in the form of contribution functions, which give the distribution of the observed emission with height and are equal to the height derivative of the emergent intensity, dI_ν/dh. We note that the solar mm radio emission comes from the chromosphere, possibly extending down to the temperature minimum at sub-mm wavelengths. We further note that extreme ultraviolet (EUV) continuum emission also comes from the same atmospheric layers (upper part of Figure 1, top left), thus images in these two spectral ranges are expected to show similar structures; hence, combining mm and EUV continuum data can potentially provide improved diagnostics.

With the advent of fast numerical computations, a number of sophisticated tools have been developed for 3D solar atmospheric modeling (see review by Wedemeyer et al., included in this

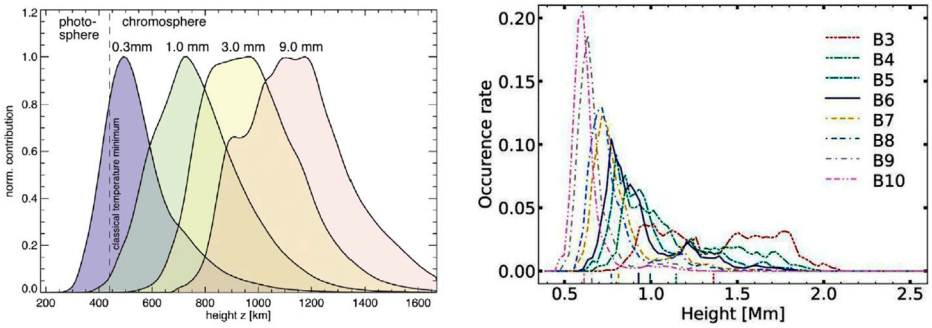

FIGURE 2
Contribution functions for mm-λ. (Left) Contribution functions at four wavelengths between 0.3 and 9.0 mm at the center of the solar disk according to Wedemeyer et al. (2016). Reprinted by permission from: Springer Nature, Space Science Reviews, © 2019. (Right) QS contribution functions for the ALMA frequency bands according to Eklund et al. (2021). Reproduced with permission © ESO.

special Research Topic collection). Such models clearly demonstrate the complex structure and the dynamics of the upper layers of the solar atmosphere (see below). An example of the deduced temperature structure is given in the right panel of Figure 1, from a simulation of an enhanced network region by Carlsson et al. (2016). It is interesting that transition region temperatures, from various features, appear in an extended range of heights that go beyond 2.14 Mm (dashed line), predicted by Avrett and Loeser (2008). Although this particular model may not be representative of the average QS, which includes inter-network regions, it is still indicative.

The average contribution functions computed from such a model at mm-λ are displayed in the left panel of Figure 2 (see also figure 3 in Wedemeyer et al., this special Research Topic collection). They are similar to the predictions of the 1D model, putting again the formation height of mm emission above the temperature minimum and into the chromosphere. More recently, numerical simulations under local thermodynamic equilibrium by Martínez-Sykora et al. (2020) gave average formation heights of 0.9 Mm (with a standard deviation of 0.7 Mm) for the 1.2 mm emission and 1.8 Mm (standard deviation of 1 Mm) for the 3 mm emission, whereas computations by the same authors under non-equilibrium hydrogen ionization gave greater heights and a much smaller height difference: 2.67 ± 1.08 Mm for 1.2 mm emission and 2.78 ± 1.09 Mm for 3 mm emission. Finally, Eklund et al. (2021) computed contribution functions for all ALMA frequency bands (Figure 2, right) and predicted lower heights: 0.9 Mm for the QS at 1.2 and 1.3 Mm at 3 mm. Observational evidence on the formation height is discussed in Section 4.3.

Of course, anyone who has seen a solar image knows that horizontal structure is very important. Briefly, horizontal structure in the solar atmosphere comes from the interplay of two factors: one of them is mass motions and the other is the magnetic field. Magnetohydrodynamics (MHD), which is a good (but not perfect) approximation for the solar atmosphere, tells us that the result of the interaction depends on the energy density of each factor: when the magnetic energy density (which is the same as the magnetic pressure) is much larger than the energy density of the plasma (which includes thermal and kinetic energy or, alternatively gas and dynamic pressure), the plasma flows along the magnetic field lines of force (see, e.g., Alissandrakis, 2020, also Carlsson et al., 2019, for a more detailed discussion). This is the case in the chromosphere and the corona, where we see spectacular structures that map the magnetic field, as well as in sunspots.[1]

As we go down to the photosphere, the density increases faster than the magnetic field (Gary, 2001), and thus the plasma dominates in that atmospheric layer. Here convective motions on two scales, the *granulation* (see, e.g., figure 5 in Alissandrakis, 2020) and the larger *supergranulation* determine the horizontal structure, with the latter pushing and compressing the magnetic field at the borders of the supergranules, thus forming the *chromospheric network*. This particular cellular structure, although detectable in photospheric velocity maps, manifests itself mainly in the chromosphere, hence its name.

At the chromospheric level, the network appears in the form of bright structures, well visible in the core of the Ca II K and Hα lines, known as *bright mottles* (coarse or fine depending on the spatial resolution of the instrument; see the reviews by Beckers, 1968, 1972 and Tsiropoula et al., 2012). It is also visible in all chromospheric spectral lines and continua, such as the Mg II k line at 2796 Å, observed by the *Interface Region Imaging Spectrograph* (IRIS) and the UV continua centered at 1600 and 1700 Å spectral bands observed by the *Atmospheric Imaging Assembly* (AIA), aboard the *Solar Dynamics Observatory* (SDO). Figure 3 shows such images, together with a magnetogram from the *Helioseismic*

1 This comparison is often made in terms of the plasma parameter β, which is the ratio of the gas pressure to the magnetic pressure.

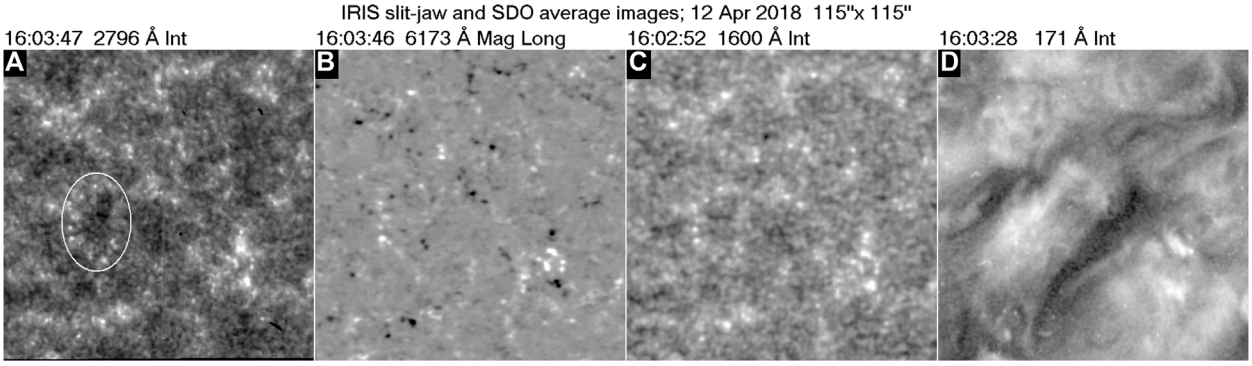

FIGURE 3
Images of a quiet Sun region: **(A)** in the Mg II k line; **(B)** an HMI magnetogram, saturated at ± 50 G; **(C)** in the AIA 1600 Å band and **(D)** in the AIA 171 Å band. Images have been averaged over 20 min, to reduce the effect of 5-min oscillations which is very prominent at 2796 and 1600 Å. The white ellipse in panel a marks a prominent supergranulation sell. Figure made by the authors from IRIS, AIA and HMI data.

and Magnetic Imager (HMI) aboard SDO and an AIA image in the 171 Å band. We note the cellular arrangement of the network structures and their association with regions of enhanced magnetic field. We also note that the structures disappear in the 171 Å image, illustrating the well-know fact that the network becomes diffuse in the transition region and disappears in the low corona (Reeves et al., 1974); apparently, this is a result of fanning out of the magnetic field, and of field lines closing at low heights.

In addition to the bright mottles, Hα images show absorbing features dubbed as *dark mottles*[2]. These structures appear on top of the bright mottles and are best visible in the blue wing of the Hα line, suggesting ascending motions (see top panel of figure 9 in Alissandrakis, 2020). As the quality of the observations improves, new results and new names appear in the literature; for example, Langangen et al. (2008) reported dark features on the solar dik, in the blue wing of the Ca II IR line, and so did Rouppe van der Voort et al. (2009) for same line and Hα; these *rapid blueshifted events* were identified as the counterpart of type II spicules (see below); still, these structures look very much like classic dark mottles seen at high resolution. Dark mottles are hard to see in other chromospheric lines or continua (see, however, Bose et al., 2019, 2021), probably because they are geometrically and optically thin.

The form of dark mottles, particularly in images far from the center of the disk, suggests predominantly radial structures; they appear as *spicules* beyond the limb (Figure 4); they are slender (300–1,000 km) plasma jets with speeds of tens of km s^{-1} to > 100 km s^{-1}, which protrude well up into the corona, reaching heights above 10 Mm (Macris, 1957; Beckers, 1968, 1972; Tsiropoula et al., 2012; see also bottom panel of figure 9 and figure 10 in Alissandrakis, 2020). Ordinary spicules have life times of ~ 10 min, while of order 10^7 spicules are active on the Sun at any given time. They collectively carry ~ 100 times the mass flux of the solar wind into the low solar atmosphere Beckers, 1968, 1972). The mechanisms of their origin and their role in the energy and mass budgets of the outer solar atmosphere and solar wind is therefore a topic of considerable interest. Recent progress on refining their physical properties has largely been driven by O/UV observations from space-based instrumentation: *Hinode*/SOT and IRIS. These have led to the recognition of two classes of spicules, type I and type II (de Pontieu et al., 2007) the latter being prevalent in coronal holes and the quiet Sun. Type II spicules are narrower, short-lived (a few tens of s) and faster than type I spicules. Spicules are much more extended in the He II 304 Å line, where they are usually referred to as *macrospicules* (Bohlin et al., 1975).

In spite of many decades of research, the origin of spicules is still a subject of debate. As disk mottles are clearly associated with the network, a magnetic association is very likely; what is not clear is whether they are a result of reconnection, as suggested a long time ago by Pikel'Ner (1969), see also Samanta et al. (2019), or some other mechanism, such as the leakage of photospheric oscillations expelling plasma along the magnetic field lines, (De Pontieu et al., 2004), or even a consequence of ambipolar diffusion (Martínez-Sykora et al., 2017; Carlsson et al., 2019).

It turns out that the quiet Sun is not that quiet after all. As the spatial and temporal resolution of our instruments improve, more and more kinds of small-scale transient events are detected (see, e.g., the recent works by Kleint and Panos, 2022; Saqri et al., 2022; Shokri et al., 2022; Purkhart and Veronig, 2022). Such events have been given various names, too many to mention them all, and a possible source of confusion.

2 Some authors use the term *fibrils* instead of mottles; however, classically, fibrils are elongated structures seen in active regions where the magnetic field has a strong horizontal component.

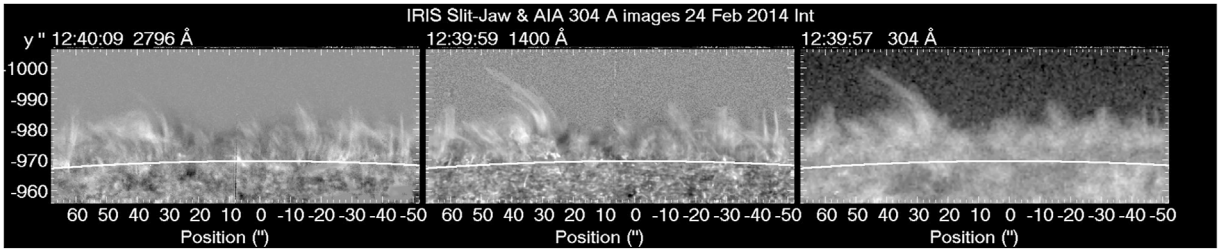

FIGURE 4
Spicules beyond the limb near the south pole of the sun, as seen in IRIS slit-jaw images with a bandwidth of 4 Å around the Mg II 2796 Å k line (left), and with a spectral width of 55 Å in the 1400 Å band which includes the Si IV lines (center), as well as in an AIA image in the He II 304 Å line (right). Time-averaged images have been subtracted from the original IRIS data for better visibility of spicules. The white arc marks the solar limb. Solar south is up. The spatial resolution of IRIS ia about 4 times better than that of AIA. Figure made by the authors from IRIS and AIA data.

In the EUV, events with energies as low as 10^{24} erg (e.g. Purkhart and Veronig, 2022) have been reported, which puts them inside the range of *nanoflares*, proposed by Parker (1988) as the mechanism of coronal heating (see Section 7 in Alissandrakis, 2020 for a brief discussion). ALMA observations have revealed many such events that are discussed in detail in the review by Nindos et al., included in this special Research Topic collection.

3 Why ALMA?

Continuum observations of the quiet Sun at mm-λ and submm-λ have been performed for decades, serving as a powerful complement to optical O/UV/EUV observations. Indeed, Linsky (1973) compiled quiet Sun measurements from λ = 1–20 mm made during the 1960s and cross-calibrated them against the Moon, resulting in a useful compendium used in models for many years; e.g., the well-known semi-empirical models of Vernazza et al. (1981). The primary advantages of observations in the mm/submm-λ regime are well known: 1) The sources of opacity are well understood: at mm-λ the opacity is dominated by H and He free-free absorption; at submm-λ H^- free-free absorption (collisions between electrons and neutral hydrogen) becomes non-negligible and is an additional source of opacity. 2) The radiation at these wavelengths is emitted under conditions of local thermodynamic equilibrium and the source function is therefore Planckian. Furthermore, the Rayleigh-Jeans approximation is valid and the observed intensity (or brightness temperature) is linearly proportional to the kinetic temperature of the emitting plasma for optically thick emission. Bastian et al. (2017) pointed out, however, that the degree of ionization for H and He can depart significantly from conditions expected for ionization equilibrium. As a consequence, while the source function can be in LTE, the opacity may be far from its LTE value. 3) Finally, the radiative transfer of continuum radiation at these wavelengths is straightforward.

The obvious and persistent disadvantage to observing in the mm/submm-λ regime has been that observations have largely been made with single dishes for which the angular resolution was poor (see Linsky, 1973 and references therein for early measurements as well as Lindsey et al., 1984, 1986, 1990, 1992; Bastian et al., 1993). Occasionally, interferometers with limited numbers of antennas have been used to observe the Sun as a means of improving the angular resolution (e.g., Horne et al., 1981; White et al., 2017), but the ability to image was absent or relatively poor. Eclipse observations with single dishes or interferometers have also been exploited to garner high resolution information, but it was necessarily in one dimension (Lindsey et al., 1983; Roellig et al., 1991; Belkora et al., 1992). In addition to the limitations imposed by poor angular resolution, time-resolved observations were infrequent.

Gary (1996), Loukitcheva et al., 2004, Loukitcheva et al., 2015), and Benz (2009) reviewed many pre-ALMA quiet Sun brightness temperature measurements and compared the observational results with the results of various theoretical models. The quiet Sun emission in the wavelength range from λ = 0.85 mm to λ = 8 mm was measured by Bastian et al. (1993), White et al. (2006), Brajša et al. (2007a,b), and Iwai et al. (2017) and in the wavelength range 0.7–5 mm various measurements were summarized by White et al. (2017). In the wavelength range 0.7–5 mm the quiet Sun brightness temperature varies from 5000 to 8000 K (White et al., 2017). As expected, there is an average trend of the brightness temperature increase with wavelength, although some scatter of the results and measurement uncertainties are present.

Interferometric maps of the quiet Sun in the mm-range were first produced by White et al. (2006) and Loukitcheva et al. (2006). They used the 10-element Berkeley-Illinois-Maryland Association Array (BIMA) in its most compact D-configuration, to obtain $\sim 10''$ resolution. Images from BIMA and the Combined Array for Research in Millimeter-wave Astronomy (CARMA) at 3.5 and 3.3 mm wavelengths are

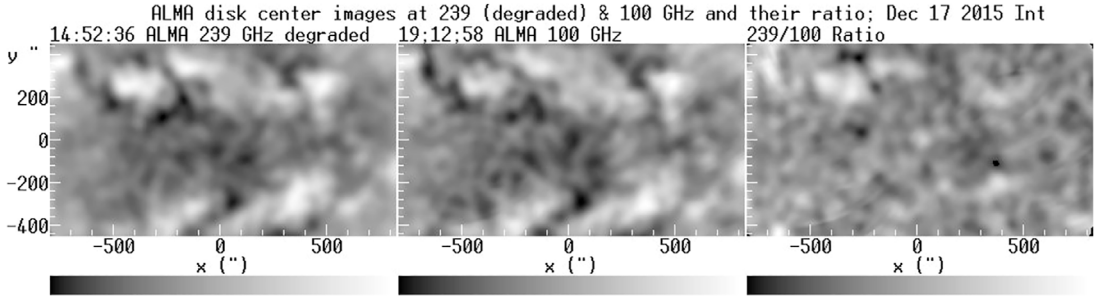

FIGURE 5
A region near the center of the disk observed with ALMA in full-disk mode on 17 December 2015: Degraded 239 GHz image, 100 GHz image, and their ratio. Values range from 6000 to 7380 K, 6860–8380 K and 0.83 to 0.93, respectively. From Alissandrakis et al. (2017), reproduced with permission © ESO.

shown in figure 5 of Shibasaki et al. (2011). In all cases the chromospheric network, delineated in the TRACE continuum images or the photospheric magnetograms, is the dominant structure in the radio images.

ALMA represents a significant step forward (see Wedemeyer et al., 2016). For the first time it provides the scientific community with high-fidelity imaging of the Sun at sub-arcsecond angular resolution, allowing detailed comparisons with images made in the O/UV/EUV wavelength regimes. In addition, it does so with an imaging cadence as short as 1 s. ALMA therefore offers a fundamentally new tool for studying the quiet Sun chromosphere in a manner that is fully commensurate with the capabilities currently available at other wavelengths. ALMA therefore offers powerful new observations of the quiet solar chromosphere that, particularly when made jointly with O/UV/EUV observations, provide new insights and constraints on our understanding of chromospheric phenomena. Bastian et al., in a review article included in this special Research Topic collection, provide a comprehensive summary of current ALMA capabilities for solar observing as well as capabilities anticipated to be available in the coming years. Technical details regarding solar observing with ALMA are given by Shimojo et al. (2017) and White et al. (2017).

4 Full-disk ALMA observations

ALMA provides both high resolution interferometric imaging and lower resolution full-disk imaging. The latter does not only serve to determine the background brightness for interferometric images, but also give a global view of the Sun, not available in the high resolution images due to their small field of view. Thus full-disk images give information on all kinds of solar phenomena not yet imaged in interferometric mode; moreover, they provide accurate measurements on the variation of the brightness temperature from the center of the disk to the limb which, in turn, is important for solar atmospheric models.

4.1 Morphology and comparison with other wavelength ranges

Several full-disk images were obtained during the ALMA solar commissioning observations in December 2015 at 239 and 100 MHz. Alissandrakis et al. (2017) compared images obtained on December 17 in both bands with Hα images from the GONG network, 1600 Å images from AIA/SDO and magnetograms from HMI/SDO and noted that plage regions were the most prominent feature on the disk. A large sunspot was clearly visible at 239 and barely discernible at 100 GHz. Prominences were well visible beyond the limb, but large-scale neutral lines rather than filaments were seen on the disk, as darker-than-average features.

They also noted that the chromospheric network is well visible at 239 GHz and very similar to the AIA 1600 and 304 Å images, with a slightly better correlation with 1600 Å. Moreover, they computed the 239/100 GHz intensity ratio, after smoothing the 239 GHz images to the 100 GHz resolution (Figure 5) and reported a range of values from 0.83 to 0.93 and a spectral index in the range of −0.21 to −0.083. The ratio was higher for the active region plage in the upper part of the figure, which had a flat spectrum, but not for the faculae in the lower part of the figure, whereas the dark lanes between the faculae were indistinguishable in the ratio image. Alissandrakis et al. (2020) made similar comparisons with Band 7 (0.85 mm) ALMA images (see their figures 1, 2).

Brajša et al. (2018) analyzed a full-disc solar ALMA image at 1.21 mm obtained on 18 December 2015, during the same CSV-EOC (Commissioning and Science Verification - Extension of Capabilities) campaign. The ALMA image was calibrated and compared with full-disc solar images from the same day in Hα line, in He I 1083 nm line core, and with various SDO images

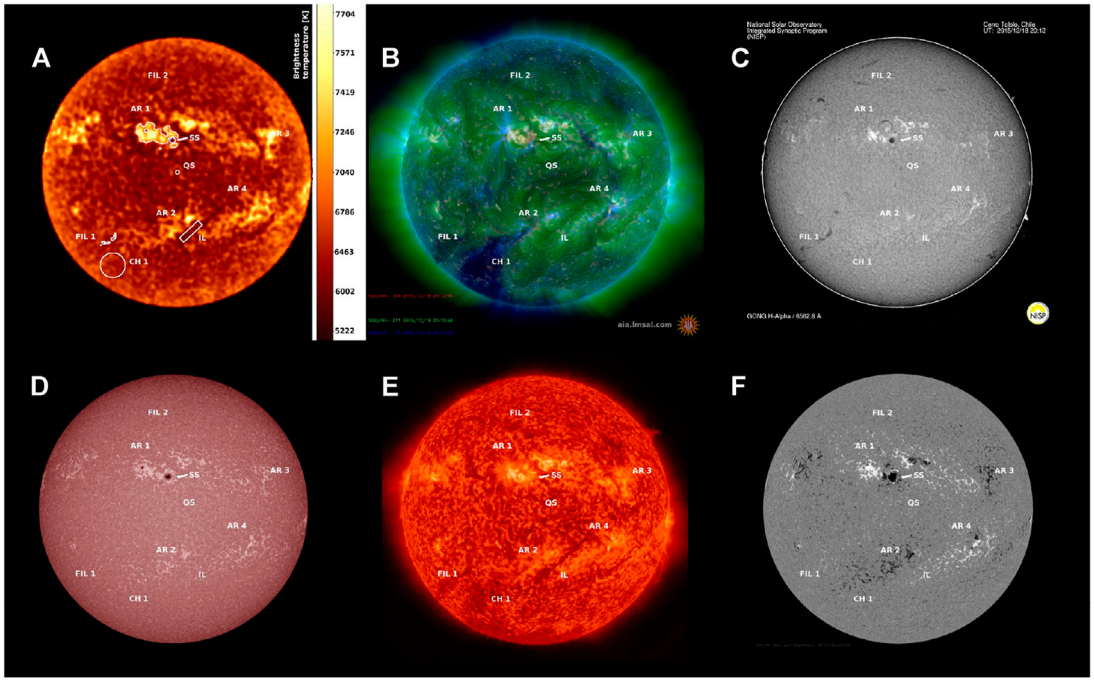

FIGURE 6
Images of the Sun from different instruments taken on 18 December 2015 **(Top row) (A)**: ALMA intensity map at 248 GHz (λ = 1.21 mm, 20 h 12 m 21s). The brightness temperature in K is given on the intensity bar on the right. **(B)**: SDO composite image from AIA 30.4 nm, AIA 21.1 nm, AIA 17.1 nm instruments (20 h 12 m 58s UT). **(C)**: Hα filtergram from Cerro Tololo Observatory, NISP (20 h 12 m UT). **(Bottom row) (D)**: SDO AIA 170.0 nm filtergram. **(E)**: SDO AIA 30.4 nm filtergram. **(F)**: SDO HMI magnetic field. Several regions of interest are encircled by white lines: AR indicates the position of active regions, FIL shows the position of filaments, SS shows the position of the sunspot, QS shows the position of the central quiet Sun region, IL indicates the position of magnetic inversion line, while CH is the position of the coronal hole. Adapted from Brajša et al. (2018). Reproduced with permission © ESO.

(AIA at 170, 30.4, 21.1, 19.3, and 17.1 nm and HMI magnetogram). The brightness temperatures of various structures were determined by averaging over corresponding regions of interest in the calibrated ALMA image. Positions of the quiet Sun, active regions, prominences on the disc, magnetic inversion lines, coronal holes and coronal bright points were identified in the ALMA image (Figure 6). At the wavelength of 1.21 mm, active regions appear as bright areas (but sunspots are dark), while prominences on the disc and coronal holes are not discernible from the quiet Sun background, despite having slightly less intensity than surrounding quiet Sun regions. Magnetic inversion lines appear as large, elongated dark structures and coronal bright points correspond to ALMA bright points. The identification of coronal bright points in the ALMA image was one of the most important new result of that study. The great majority of all coronal bright points from the EUV image correspond to the He I 1083 nm dark points (75%) and to the ALMA 1.21 mm bright points (82%). Moreover, all ALMA 1.21 mm bright points show a well-defined relationship with magnetic structures (100% correspondence), mostly with small-scale bipolar magnetic regions and in some cases with small unipolar magnetic regions.

Brajša et al. (2021) investigated small-scale ALMA bright features in the quiet Sun region using a full-disk solar image produced with single-dish ALMA measurements (1.21 mm, 248 GHz) performed on 18 December 2015. The selected quiet Sun region was compared with the EUV and soft X-ray images and with the magnetograms (Figure 7). We note that with the GOES-13 SXI (Solar X-ray Imager)-FM1 filter soft X-rays are detected, which are caused by the bremsstrahlung of the hot plasma from the chromosphere and corona. In the quiet Sun region, enhanced emission seen in the ALMA was almost always associated with a strong line-of-sight magnetic field. Four coronal bright points were identified and one typical case was studied in detail (Figure 7). Other small-scale ALMA bright features were most likely associated with magnetic network elements and plages.

The question of visibility of features in Hα, Ly-α and ALMA has been addressed by Rutten (2017; see also Rutten and Rouppe van der Voort, 2017; Rutten et al., 2019), under the working hypothesis that the observed ubiquitous long Hα fibrils are contrails from propagating heating events. Application of a recipe that assumes momentary Saha-Boltzmann extinction during their hot onset to millimeter wavelengths, suggests that

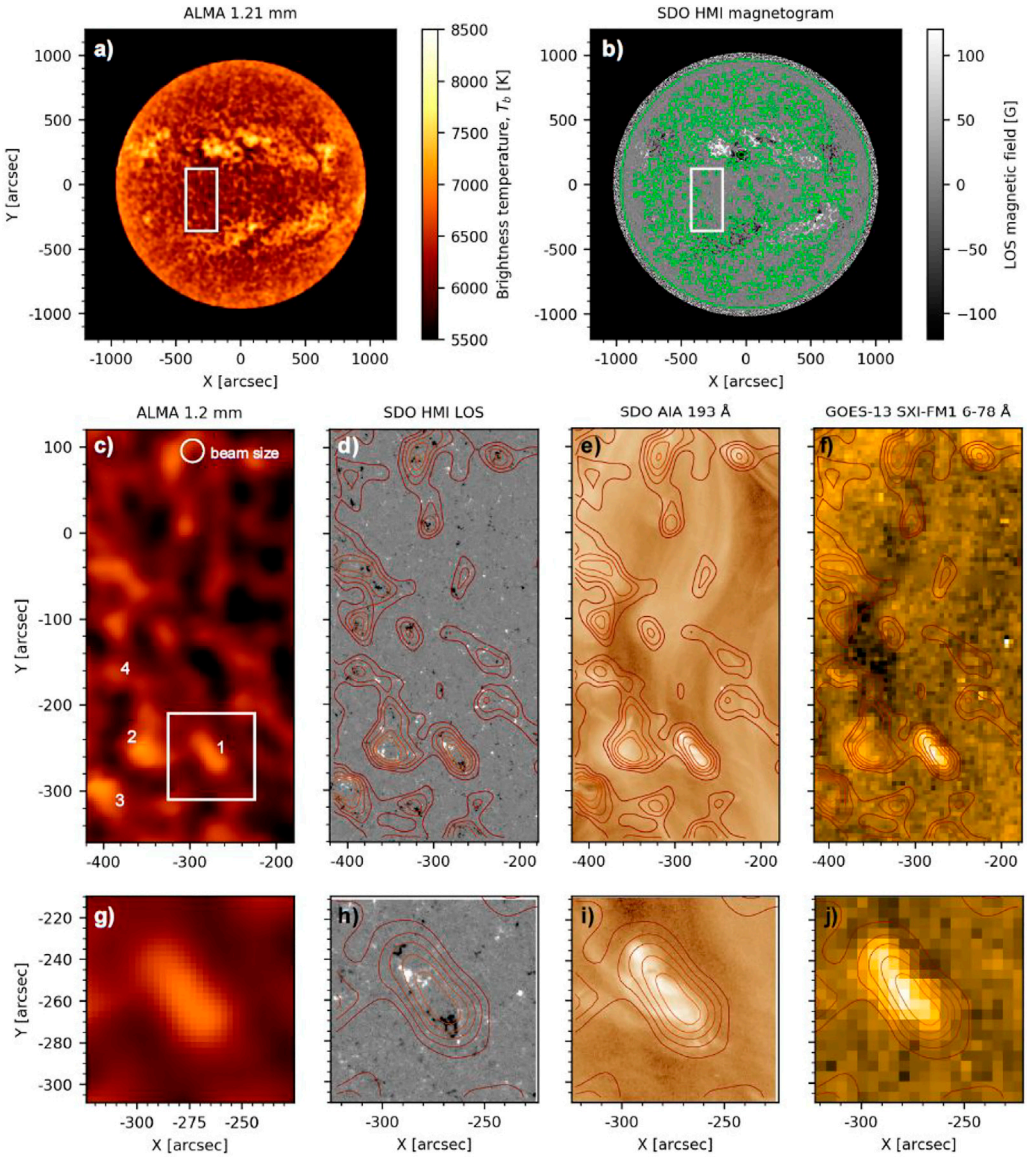

FIGURE 7
Different views of coronal bright points: 1.21 mm (ALMA), magnetic field, EUV, soft X-rays. **(a)**: Single-dish ALMA 248 GHz (1.21 mm, Band 6), **(b)**: SDO/HMI magnetogram, with white box outlining the quiet Sun area shown in panels in the middle row. Both images were taken on 18 December 2015 at 20:12 UT. Magnetogram intensity was clipped at ±120 G and ALMA contours of 6500 K were overlaid in green color. **(c)**: the ALMA image of the quiet Sun shown enlarged and compared with **(d)**: SDO/HMI magnetogram, **(e)**: SDO/AIA 193 Å filtergram, and **(f)**: GOES-13 SXI tin (Sn) filter image, with ALMA contours overlaid (levels at 6300, 6400, 6500, 6600 and 6700 K) **(g–j)**: enlargements of a single ALMA bright feature, marked in the white rectangle in panel **(c)**, at the same wavelengths as in the middle row. The beam size of the single-dish ALMA measurements, 26″, is given in the panel **(c)**. Reproduced from Brajša et al. (2021) with permission © ESO.

ALMA should observe Hα-like fibril canopies, not acoustic shocks underneath. Therefore, anything opaque in Hα will be at least similarly opaque at mm wavelengths. Rutten (2017) concluded that mm contrail fibrils would be yet more opaque than the Hα ones, constituting yet denser canopies. In short, Rutten (2017) predicted that the ALMA quiet-Sun is mostly chromospheric canopies, not appearing the same as in Hα, but opaque as in Hα.

A good dark-dark correspondence (sunspot and small filaments) and bright-bright correspondence (plages) between the two images was indeed found by Brajša et al. (2021). However, the relationship between Hα core and high-resolution ALMA images in the millimeter wavelength range is more complicated, since these authors found examples of both types of behavior, correlation and anticorrelation. Some small-scale, bright ALMA features have bright Hα counterparts, and

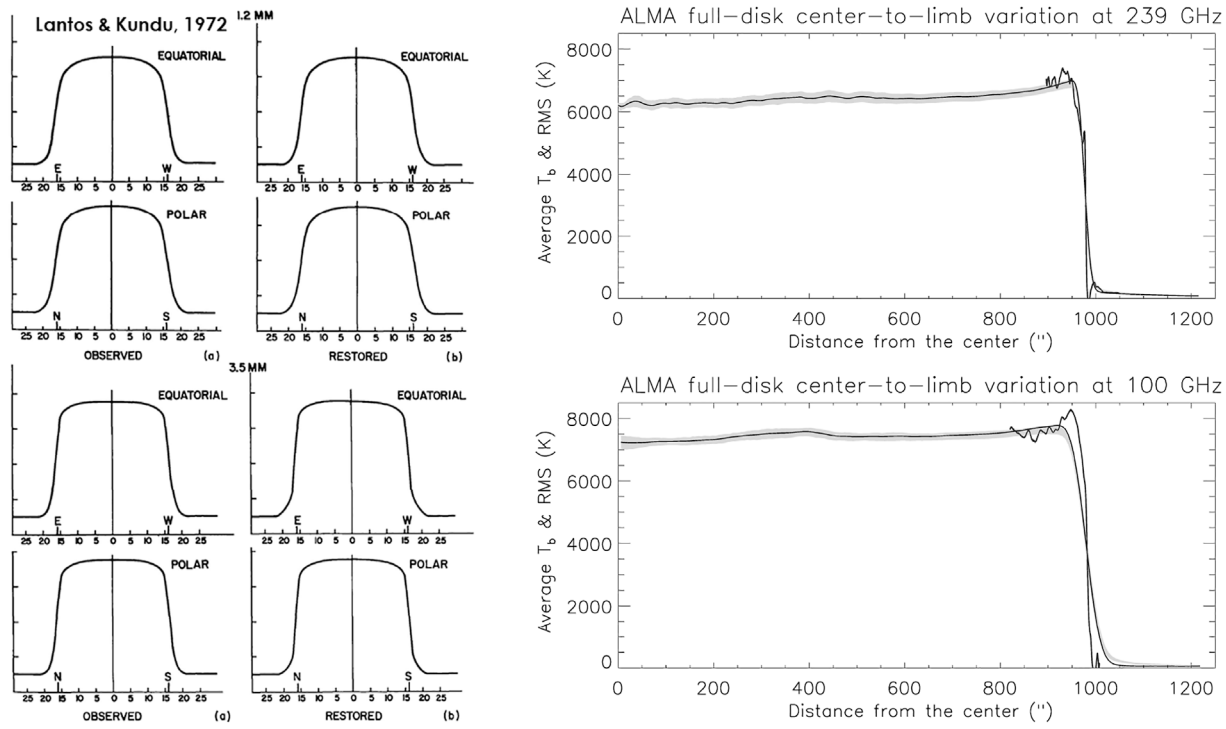

FIGURE 8
Old and new Center-to-limb variation (CLV) curves). Left: CLV curves at 1.2 and 3 mm (250 and 100 GHz respectively) from Lantos and Kundu (1972). Reproduced with permission © ESO. Right: CLV curves for 239 and 100 GHz form ALMA full-disk images from Alissandrakis et al. (2017). The gray band shows the measured values ± the corresponding rms. The superposed blue curves near the limb are from high resolution ALMA images. Curves in black show the CLV after correction for diffuse light. Reproduced with permission © ESO.

some have dark Hα counterparts (including fibrils). Moreover, examples of a bright-dark and a dark-bright correlation between the Hα wing sum and ALMA image were reported. We can thus conclude that, while some of the predictions of Rutten (2017) have been qualitatively confirmed using ALMA observations, there are notable exceptions.

4.2 Center-to-limb variation and atmospheric models

The first imaging observations of the Sun in the mm range were made in the 70s, with the 36-ft radio telescope of the National Radio Astronomy Observatory in Tucson, Arizona (Buhl and Tlamicha, 1970; Kundu, 1970, 1971, 1972; Kundu and McCullough, 1972). This instrument provided resolution of 3.5′, 1.2′ and 1.2′ at 9 mm, 3.5 and 1.2 mm respectively. Analyzing the center-to-limb variation (CLV) of the brightness temperature and taking into account the effect of the instrumental beam, Lantos and Kundu (1972) found limb darkening both at 1.2 and 3 mm (Figure 8, left). As solar atmospheric models predict limb brightening at these wavelengths, Lantos and Kundu (1972) had to invoke absorbing structures (spicules) in order to match the models with the observations.

ALMA full-disk images are much more precise than the old 36-ft images and the first analysis of commissioning observations by Alissandrakis et al. (2017) showed clear limb brightening both in Band 3 (100 MHz, 3 mm) and in Band 6 (250 GHz, 1.26 mm), available at that time (right panel of Figure 8). Moreover, Alissandrakis et al. (2017) combined the measurements of brightness temperature, T_b, as a function of the cosine of the heliocentric distance, μ, from both frequency bands to a single curve T_b (μ_{ref}), by reducing all values to a common reference frequency of 100 GHz; they also extended their frequency range by including measurements by Bastian et al. (1993) at 350 GHz and found a linear relation between T_b and μ_{100}. Subsequently, they inverted the equation of transfer,

$$T_b(\mu) = \int_0^\infty T_e(\tau)\, e^{-\tau/\mu}\, d\tau/\mu \qquad (1)$$

where τ is the optical depth, to obtain the electron temperature, T_e as a function of τ_{ref}.

The inversion was done by noting that a linear (or polynomial) T_e (log τ_{100}) relation leads also to a linear (or

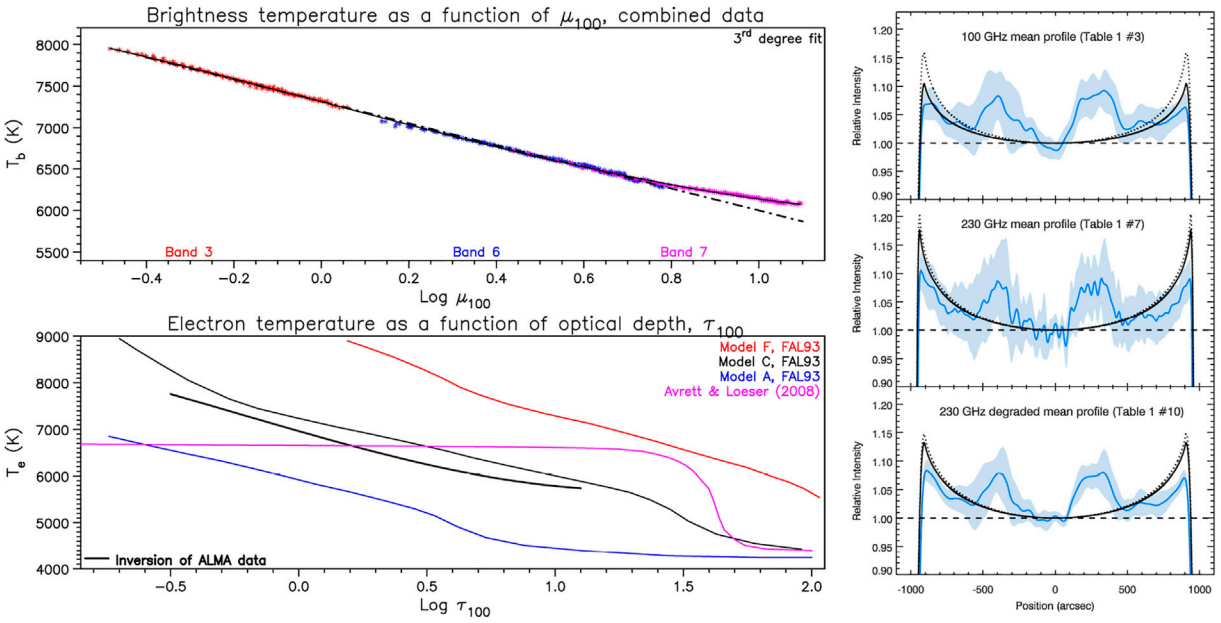

FIGURE 9
Atmospheric modeling from ALMA CLV data Left, top: Combined CLV curve, T_e (log τ_{100}), from ALMA Band 3, Band 6 and Band 7 observations obtained in January 2020, adapted from Alissandrakis et al. (2022). The solid line shows a third degree fit and the dash-dotted line shows a linear fit up to log μ_{100} = 0.8. Reproduced with permission © ESO. Left, bottom: The electron temperature as a function of optical depth (thick black line) obtained from the inversion of the CLV curve. Also shown are the predictions of atmospheric models discussed in the text. Adapted from Alissandrakis et al. (2022). Right: Comparison between observed CLV (blue curves) and the predictions of models C (dotted lines) and SSC (continuous black lines). The dashed line represents the quiet Sun. From Selhorst et al., 2019 © AAS, reproduced with permission.

polynomial) T_b (log μ_{100}) relation, thus the coefficients of the former can be computed from the coefficients of the latter, determined from a fit to the observed data. For example, a third degree polynomial expression for the electron temperature:

$$T_e(\tau) = a_0 + a_1 \ln\tau + a_2 \ln^2\tau + a_3 \ln^3\tau, \tag{2}$$

gives a brightness temperature of:

$$\begin{aligned} T_b(\mu) = {} & a_0 + a_1 C_1 + a_2 C_2 + a_3 C_3 \\ & + (a_1 + 2a_2 C_1 + 3a_3 C_2)\ln\mu \\ & + (a_2 + 3a_3 C_1)\ln^2\mu \\ & + a_3 \ln^3\mu, \end{aligned} \tag{3}$$

with.

$$C_1 = -0.577216, \tag{4}$$

$$C_2 = 1.978112, \quad \text{and} \tag{5}$$

$$C_3 = -5.444874 \tag{6}$$

(see Appendix A in Alissandrakis et al., 2022.)

A similar approach was employed by Alissandrakis et al. (2020) (see their figure 4 for a comparison of the observed CLV with the model); these authors cross-calibrated band 6 with respect to band 3 using the CLV curves, something that was not necessary for the data used by Alissandrakis et al. (2017).

We note that the parameters derived from the fit can be used for the computation of the brightness temperature spectrum at the center of the solar disc. Such a computation was done by Alissandrakis et al. (2020), see their figure 3, and the derived spectrum was compared with older measurements compiled by Loukitcheva et al., 2004, which is a highly inhomogeneous data set and has a lot of scatter. Several points were near the ALMA spectrum, but most of them were below.

In a recent work Alissandrakis et al. (2022) used ALMA Band 7 (347 GHz, 0.86 mm) data instead of the measurements by Bastian et al. (1993); this, more homogeneous data set, revealed a flattening of the T_b (log μ_{100}) curve at large μ, with a third degree polynomial fitting the data better. The results are shown in Figure 9 (left). The left top panel gives the CLV curve derived from the combination of all three available ALMA frequencies and its fit with a third degree curve. The thick black curve in the left bottom panel shows the result of the inversion, which is compared to the predictions of models A (internetork), C (average quiet Sun) and F (network) of Fontenla et al. (1993), as well as of model C7 of Avrett and Loeser (2008). The physical parameters of these models were used to compute τ_{100} as a function of the height, z, and, though the $T_e(z)$ relation, the optical depth as a function of T_e.

The observational result is very close to the prediction of model C of the Fontenla et al. (1993), as already noted by Alissandrakis et al. (2017), and very different from that of the Avrett and Loeser (2008) model, which predicts too small a temperature variation in the chromosphere. The flattening at high optical depths is probably an indication that we approach the region of temperature minimum. As the observations are very close to the model, there is no need to invoke spicule absorption.

In a different approach, Selhorst et al. (2019) compared their CLV measurements of the commissioning observations with model C of Fontenla et al. (1993) and with their own SSC model (Selhorst et al., 2005). As shown in Figure 9 (right), they found that the SSC model gave a better fit to the observations. The same authors reported average polar brightening of 10.5% and 17.8% at 100 and 230 GHz, respectively. Finally, Sudar et al. (2019) fitted the CLV, again from the commissioning data, with a quadratic curve in μ and used their results for image corrections, without performing any comparison with model predictions.

4.3 Formation height and the solar radius

In order to pass from the observationally determined $T_e(\tau)$ to the variation of temperature as a function of height, $T_e(z)$, we need a relation between τ and z. This implicates the opacity and hence the density as a function of height, for which we have no direct observational information; the situation is further complicated by the fact that temperature variations change the degree of ionization and hence the electron density, in a way that is complicated due to departures from local thermodynamic equilibrium (LTE). Thus, no attempt to derive $T_e(z)$ from mm-λ $T_e(\tau)$ has been made yet.

Qualitative information about the formation height can be provided through the comparison of the morphology of ALMA images with images in other spectral regions. Already Alissandrakis et al. (2017) noted the similarity of chromospheric network structures in ALMA and AIA 1600 Å and 304 Å images, putting their formation height between the two; this is consistent with the fact that AIA 304 Å channel is dominated by the He II lines which form around T_e = 50,000 K (O'Dwyer et al., 2010), much above the mm-λ brightness temperature. We note that, in the cm-λ range, where radiation forms higher, Bogod et al. (2015) found a better correlation of RATAN-600 data with 304 Å AIA images.

Indications about the formation height can be obtained from the association of the observed disk center brightness temperature to the electron temperature predicted by models. For model C of Fontenla et al. (1993), this gives heights of 1.09, 1.25 and 1.82 Mm above the τ_{5000} = 1 level, which is the level where the optical depth at 5,000 Å is unity, for radiation at 0.85, 1.26 and 3 mm, respectively.

The solar radius is another indicator of the formation height; however the radius reflects the maximum height of formation rather than the average, the presence of spicules complicate the measurement, while it cannot be accurately determined from the relatively low resolution full-disk ALMA images. Alissandrakis et al. (2020) compiled various height measurements in their Table 4; they gave heights of 2.4 ± 1.7 Mm and 4.2 ± 2.5 Mm above the τ_{5000} = 1 level, for the limb at 1.26 and 3 mm respectively. Both are between the measured heights of the 1600 Å and the 304 Å emissions, but below the heights measured in eclipse observations (see also Section 5.2 below). Selhorst et al. (2019) obtained average values of the solar radius of 965.9 ± 3.2″ at 3 mm and 961.6 ± 2.1″ at 1.26 mm, which correspond to heights above the τ_{5000} = 1 level of 4.6 ± 2.3 Mm and 1.5 ± 1.5 Mm respectively and are within the error margins of Alissandrakis et al. (2020). More recently, Menezes et al. (2022) gave values of 968 ± 3″ for the solar radius at 3 mm and 963 ± 2″ at 1.26 mm, corresponding to heights of 6.1 ± 2.1 Mm and 2.5 ± 1.4 Mm respectively, above the τ_{5000} = 1 level.

5 High resolution ALMA observations

Several ALMA observing sessions focused on quiet Sun regions both on the disk and at the limb. The small field of view of ALMA has not allowed a global view of the Sun at high resolution, while, using mosaicing techniques, two larger regions near the limb were imaged during the commissioning period with fields of view of 60″ by 60″ at 1.26 mm and 190″ by 180″ at 3 mm (Figure 10). Most of the published results are at 3 mm, where atmospheric conditions are more favorable than at 1.26 mm, whereas no high resolution observations in Band 7 (0.85 mm), recently made available for solar observing, have been presented yet.

5.1 Structures on the solar disk and the chromospheric network

The most complete set, covering seven regions from the center of the disk to the limb at 3 mm with a resolution of 2.4″ by 4.5″, is that of Nindos et al. (2018); these authors extended the ALMA field of view to a diameter of 120″, twice that of the nominal and were thus able to make better comparisons with simultaneous AIA 1600 Å and 304 Å images, smoothed to the ALMA resolution (Figure 11). They thus confirmed the association of the bright mm-λ structures to the chromospheric network, discussed in Section 4 and also visible in Figure 10. In a subsequent work, Nindos et al. (2021) presented observations of a very quiet region in both bands 3 and 6, obtained on the same day, with a resolution of 2.7″ by 1.7″ for band 3 and 1.6″ by 0.7″ for band 6 (Figure 12). In addition to the similarity with AIA 1600 Å and 304 Å images,

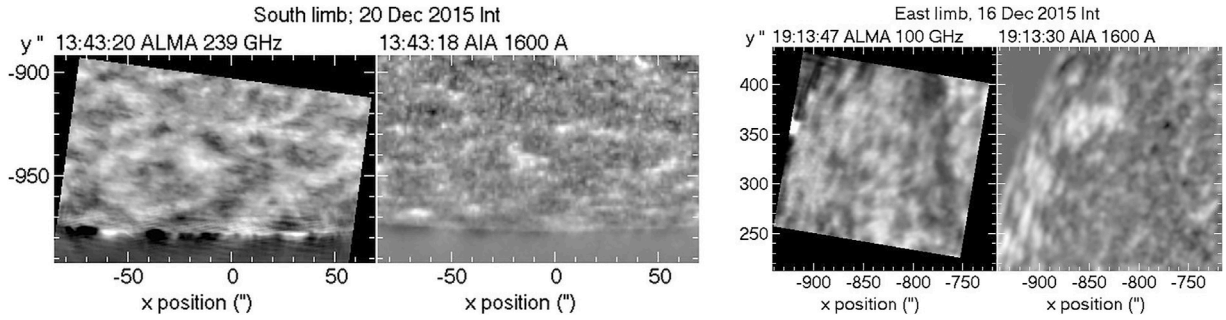

FIGURE 10
ALMA images near the S and E limbs obtained during the commissioning period, together with the corresponding AIA 1600 Å images. A plage region is visible near the E limb. All images have been corrected for CLV, by subtracting 85% of the azimuthally averaged intensity; AIA images were smoothed to the ALMA resolution of 1.76 by 1.01″ at 239 GHz and 5.45 by 4.00″ at 100 GHz. Solar north is up. Figure made by the authors from data set ADS/JAO. ALMA. 2011.0.00020. SV.

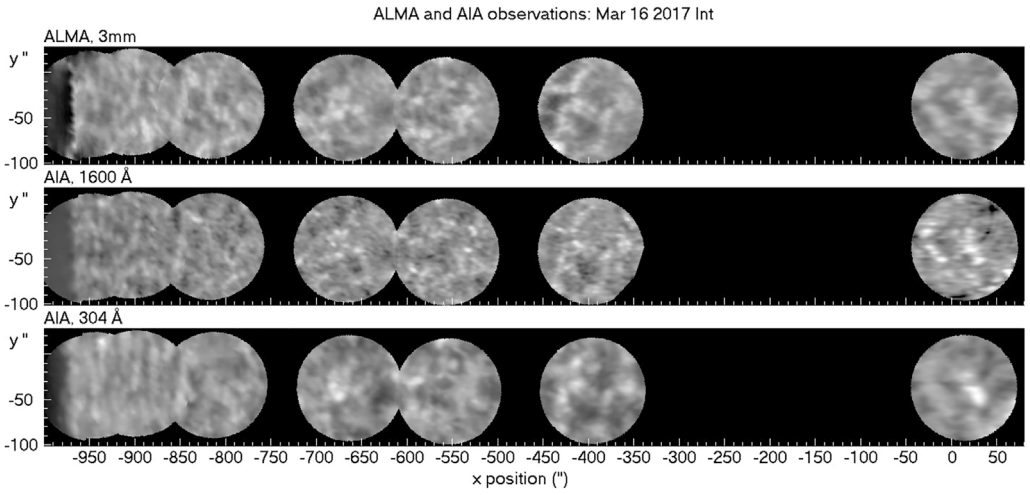

FIGURE 11
ALMA and AIA images of the quiet Sun. Top row: Composite of seven 3 mm ALMA images from the limb (at left) to the center of the disc. Second and third rows: Composites of AIA 1600 and 304 Å images for the same time intervals and FOVs as the ALMA images, convolved with the ALMA beam. The photospheric radius is 964.8″. From Nindos et al., 2018, reproduced with permission © ESO.

Figure 12 reveals a similarity with negative, broadband, Hα images from the GONG network. A similar association of ALMA and Hα features was reported by Alissandrakis et al. (2022) from full-disk 347 MHz (0.85 mm) images. Nindos et al. (2021) attributed this similarity in terms of absorption in Hα by dark mottles (spicules), located above network elements, implying that the mottles are transparent at 3 mm and that ALMA images show the network points below them. An alternative interpretation, in terms of Rutten's (2017) models, is that ALMA sees a part of opaque fibrils. Observationally, it is hard to distinguish between the two; opaque fibrils should appear more elongated than the hitherto images show (see also Figure 14 below), but this could be masked by the ALMA beam (resolution).

Alissandrakis et al. (2020) used the observations presented in the previous paragraph, as well as commissioning data (see their Table 6), to measure the CLV of the brightness temperature for the network and cell interior (internetwork); from that, they computed the electron temperature as a function of the optical depth for these components, as described in Section 4.2. As in the case of the average quiet Sun, they found linear relations between T_e and log τ_{100}. Two segregation schemes were employed, one

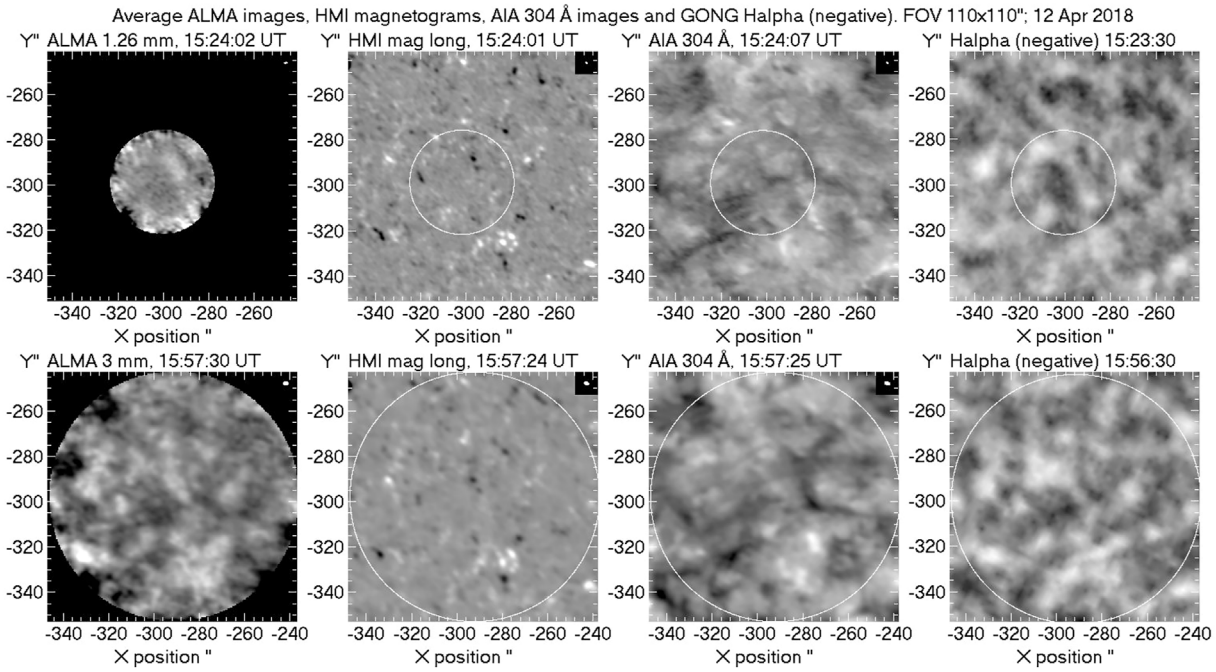

FIGURE 12
Average ALMA images of the network in Band 6 (top-left) and in Band 3 (bottom-left), together with the corresponding HMI magnetograms (saturated at ± 50 G), as well as AIA 304 Å and Hα negative images from GONG. The insert at the top right corner of the images shows the ALMA resolution. The circles in the non-ALMA images mark the ALMA field of view. All images are oriented with the celestial north pointing up (from Nindos et al., 2021, reproduced with permission © ESO).

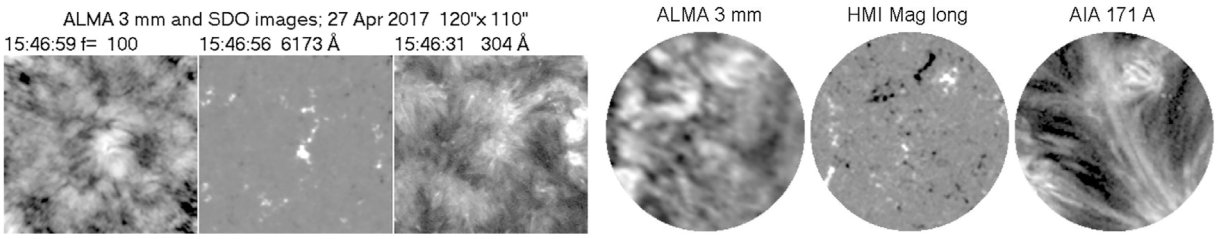

FIGURE 13
ALMA images at 3 mm. Left: A low intensity region at 3 mm from data used by Loukitcheva et al. (2019), together with an HMI magnetogram saturated at ± 200 G and a 304 Å AIA image (prepared by the authors using data from ALMA project 2016.1.00202. S and from SDO). Right: A quiet region at 3 mm together with an HMI magnetogram and a 171 Å AIA image; the diameter of the field of view is ~ 67″ (adapted from Wedemeyer et al., 2020).

attributing equal number of pixels in network and cell interior and another, closer to that used in classic models. The latter gave a network/cell temperature difference of ~ 1550 K (ratio of ~ 1.24), considerably less than ~ 3280 K (ratio of ~ 1.55) predicted from models F and A of Fontenla et al. (1993).

Brightness temperature measurements from interferometric ALMA images at 3 mm were also published by Loukitcheva et al. (2019) and Wedemeyer et al. (2020). Loukitcheva et al. (2019) observed a region 200″ SW of the disk center with 1.6″ resolution and reported an extended low brightness area which they called "chromospheric ALMA hole" (Figure 13, left). As a matter of fact, this was the interior of a large supergranule with an average brightness (deduced from the histograms of their figure 2A) of 6,440 K, considerably below the average cell interior value of

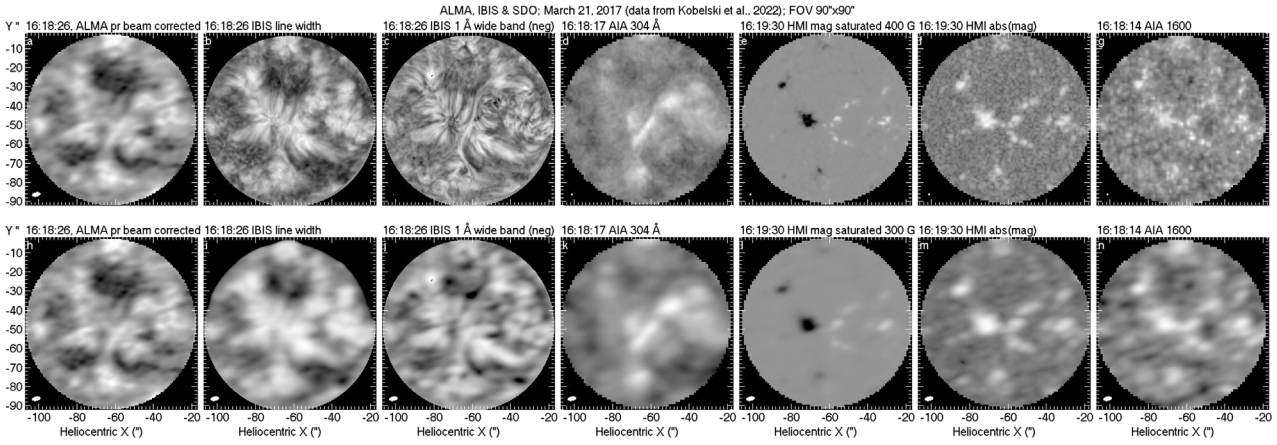

FIGURE 14
ALMA images at 3 mm. Top row: ALMA image together with IBIS Hα images and SDO images; the insert at the lower left corner shows the instrumental resolution (beam). Bottom row: Same as in the upper row, with the images smoothed to the ALMA resolution. Produced by the authors using data from Kobelski et al. (2022) and SDO.

7,060 K used by Alissandrakis et al. (2020), whereas the average brightness of what they called "bright network" was 7,850 K, compared to 7,690 K of Alissandrakis et al. (2020). Another region near the center of the disk was observed with a resolution of 1.4″ by 2.1″ by Wedemeyer et al. (2020) (Figure 13, right), who reported average T_b values of 7,228 and 7,588 K, for cell and network respectively, while their radiative MHD model predicted average values of 6,688 and 7,977 K for the cell and network respectively.

In a recent work, Kobelski et al. (2022) analyzed 3 mm ALMA data of a bipolar region of enhanced network, in conjunction with Hα images obtained with the Interferometric BIdimensional Spectrometer (IBIS), mounted on the Dunn Solar Telescope. They reported a strong association between ALMA emission and Hα line width (see also the article by Tarr et al., in this collection), confirming a similar finding by Molnar et al. (2019) for a plage region. From the publicly available data set of Kobelski et al. (2022) and SDO data we compiled a set of images, displayed in Figure 14. We note that the Hα linewidth image (panels b and i) is very similar to the negative broadband (1 Å) Hα image (panels c and j); this is not unexpected, as dark structures on the disk are known to have broad line profiles. This shows that the finding of Molnar et al. (2019) about the linewidth is one and the same thing with the finding of Nindos et al. (2021) and Alissandrakis et al. (2022) about the broadband Hα images. In addition, these images confirm the association of mm emission with the network features seen in the magnetogram and in the 1600 Å band; moreover, a low brightness region appears in the interior of a large supergranule, north of the image center, similar to the one reported by Loukitcheva et al. (2019).

5.2 Observations of spicules

Spicules, near the limits of instrumental resolution even at O/UV wavelengths, have not been well-studied at mm/submm-λ because the necessary resolution has been unavailable. Nevertheless, interferometric and single disk observations during times of solar eclipses placed constraints on the mean height of the chromospheric "limb extension" at various submm/mm wavelengths during the 1980s and 1990s (see also Section 4.3 above). Lindsey et al. (1983, 1986) showed that the limb extension from 30 to 200μ extended well above heights expected from the hydrostatic, one-dimensional models of Vernazza et al. (1981), a discrepancy that increased with wavelength as established by Labrum et al. (1978); Horne et al. (1981); Wannier et al. (1983) and later confirmed by Roellig et al. (1991); Lindsey et al. (1992); Belkora et al. (1992); Ewell et al. (1993). Braun and Lindsey (1987) interpreted these observations in terms of a purely spicular model where the additional opacity above 1,000 km was provided by a random and dynamic distribution of spicules. Belkora et al. (1992) noted the close correspondence in height between the 3 mm limb extension and the height of Hα spicules. Ewell et al. (1993) pointed out that extant observations of the chromospheric limb extension was in any case consistent with an effective density scale height of 1,200 km.

ALMA provides the necessary angular resolution and time resolution to map the brightness and kinematics of solar spicules at mm/submm-λ directly. These are important for the same reasons that they are for other problems of chromospheric physics (Section 2): observations at these wavelengths can make rather direct measurements of the temperature of spicules where they are

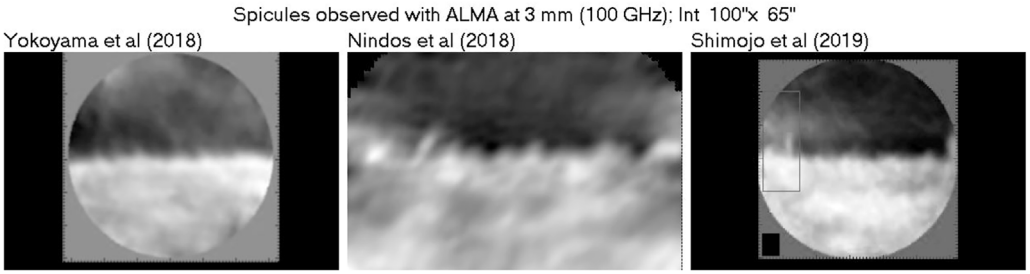

FIGURE 15
The first ALMA observations of spicules at 100 GHz (3 mm). Images reprocessed by the authors for better visibility. Reproduced from figure 11 of Alissandrakis (2020).

optically thick and they can impose constraints on their densities that are wholly independent of O/UV observations.

As a relatively new capability, however, the number of studies of solar spicules has been small in number and scope. Yokoyama et al. (2018) reported the first observations of solar spicules (Figure 15 left). These were obtained at the southern limb at a wavelength of 3 mm with an angular resolution of 2.56" × 1.6". These authors noted the presence of "sawtooth" irregularities on the limb and jet-like activity that appeared to correspond well to IRIS "jet clusters". Interestingly, these limb irregularities seen at 3 mm were well-correlated with absorption observed in the SDO 171Å band; i.e., the EUV emission from plasma at coronal temperatures was absorbed by foreground chromospheric structures (see also Alissandrakis and Valentino, 2019). A dynamic feature rising at 40 km-s^{-1}, showing a brightness excess of just 135 K was determined to have an electron density of 4.6–8.4 × 10^9 cm^{-3}.

The presence of spicules or groups of spicules was also reported by Nindos et al. (2018), see middle panel of Figure 15, who also detected a discrete structure near the resolution of ALMA extending 15″ above the limb with a life time of ~ 10 min and a brightness temperature of ≈ 2600 K; these structures were identical to structures seen in simultaneous Hα images from the GONG network. Shimojo et al. (2020) also reported a dynamic limb feature observed at 3 mm (Figure 15 right) that they interpreted as being a macrospicule. It extended to 15" above the limb with an apparent brightness temperature of 240 K. With a filling factor assumed to be 0.25 the density inferred was ~ 10^{10} cm^{-3}.

Clearly, work to date has only scratched the surface. Spicules are at the current limits of ALMA resolution and there are significant technical difficulties associated with the extraction of accurate brightness temperatures as evidenced by the wide range that has been reported so far. The difficulty has been highlighted by Shimojo et al. (2017) who point out that the bright solar limb causes interferometric "overshoot", strong negative emission that is difficult to remove. Many more observations of spicules are needed in all of the ALMA solar observing bands–from 0.85 to 3 mm–to more comprehensive characterize their temperature, density, and kinematics at these wavelengths as well as their relationship to UV/EUV emission and absorption.

5.3 Visibility of spicules on the disk

Interestingly, no elongated structures in emission or in absorption, reminiscent of spicules appear in Figures 10–12, 14. Elongated structures (Figure 13, left) do appear in the data used by Loukitcheva et al. (2019) (Figure 13, left), but it is not clear if these are spicules or some other kind of loops; still, movies created by the authors from data in the *SALSA* archive (Henriques et al., 2022) did not reveal any motions reminiscent of expanding spicules. A set of compact loops joining opposite magnetic polarities was reported by Wedemeyer et al. (2020), visible in the ALMA and 171 Å images reproduced in Figure 13, right (upper part of the field of view); the same image shows other elongated structures. We add that Chintzoglou et al. (2021) observed a plage region and reported an evolving elongated structure which they identified as a type II spicule.

Using values of physical parameters (T_e, N_e) derived from spicule models in O/UV, it is possible to compute their brightness on the disk at mm-λ. Values from such spicule models were compiled in Table 7 of Alissandrakis et al. (2018). A first look at the table shows that spicules on the disk should appear in emission, since T_e values are above the mm-λ T_b. A simple calculation for a 500 km diameter vertical spicule, located 45° from the center of the disk and at a height of ~ 6000 km (projected distance from the spicule base of 6″) gives, for most models, brightness temperatures of the order of 5,000, 2000 and 1,000 K above the background at 3, 1.26 and 0.86 mm respectively; these values, even if they are corrected for spatial resolution of 1, 2 or 3″, by factors of 0.57, 0.33 and 0.22, respectively, predict that spicules should be prominent on the disk. Still, the "cold model" of Alissandrakis et al. (2018) predicts excess brightness of just 140, 61 and 34 K at the three wavelengths, after correction for instrumental resolution; this would be compatible with the absence of spicules in disk

observations. Obviously, we have a lot to learn about spicules from ALMA.

6 Summary and future prospects

Five years after the first public release of the solar commissioning data, ALMA has provided valuable information that has improved our understanding of the quiet Sun. Both low resolution, full disk images and high resolution interferometric imaging have had their contribution to that end.

Full disk ALMA images, of much better quality than any prior single-dish observations, made possible the comparison of the mm-λ emission in three wavelength bands (Band 3, 3 mm, 100 GHz; Band 6, 1.26 mm, 236 GHz and Band 7, 0.86 mm, 347 GHz) with UV and EUV images of the solar atmosphere from the chromosphere to the corona. Practically all known solar features were identified in such images. In particular, the chromospheric network is very prominent in the QS, and comparison with AIA images puts the formation height of the mm emission between that of the 1600 Å and 304 Å AIA bands, thus confirming that the radiation comes from the chromosphere.

Combined measurements of the brightness temperature variation from the center of the solar disk to the limb in all three ALMA bands made possible the computation of the electron temperature as a function of the optical depth and the comparison with classic atmospheric models; the ALMA results were close to model C of Fontenla et al. (1993) and far from the model C7 of Avrett and Loeser (2008). Moreover, the band 7 data showed some flattening at high optical depth, a possible indication of approach to the temperature minimum.

Interferometric ALMA observations have been published mostly for band 3, with few in band 6. The association of the mm emission with the network is confirmed by these observations, while an association with negative broadband Hα images was also detected. As demonstrated in Figure 14 of this review, this is the same as the association of the emission with the Hα linewidth reported previously. This effect could be interpreted either in terms of Hα structures being transparent at mm-λ, in which case ALMA images lower-lying network elements, or in terms of opaque fibrils, directly observed by ALMA. Some cases of low brightness in the center of large supergranules were also reported.

Few ALMA observations are far from the center of the solar disk. These have allowed the measurement of the network/internetwork brightness ratio and its center-to-limb variation. Comparison with classic theoretical models showed that the network is less bright and the internetwork less dark than the model predictions.

There are only three published observations at the limb, at 3 mm, and all show spicular structure, mostly below the image resolution. Excess brightness temperatures in the range of 240–2000 K were reported, but these values probably suffer from the effects of insufficient spatial resolution and/or clustering of many structures.

ALMA is a fast developing instrument and so are the solar observing modes. For the quiet Sun we anticipate exciting new results as the available frequency bands increase, the spatial resolution improves, the pointing accuracy of interferometric observations is getting better, a more precise absolute calibration of full-disk images is achieved and circular polarization measurements are implemented. For details on the associated instrumentation issues we refer the reader to the article by Bastian et al. in this special Research Topic collection.

The availability of more frequency bands is important for all aspects discussed in this review. For solar atmospheric modeling in particular, we stress the importance ef extending to higher frequencies, which will take us closer to the temperature minimum. The extension to lower frequency bands is also important, as this will take us higher in the chromosphere and into the low chromosphere-corona transition region; it will also bridge the gap between ALMA and Nobeyama, as well as RATAN-600 observations. Intermediate bands (4 and 5) are no less important, as they will fill the frequency range between bands 3 and 6; we note that band 5 is already available, but no results have been published yet.

Improved spatial resolution, which can be achieved with more extended array configurations (at the expense of less precise imaging of large-scale structure) and/or at higher frequencies, will give us a more precise view of the fine structure. This will be a great advantage for limb observation of spicules. From brightness measurements at two or more frequencies with sufficient spatial resolution, it will be straight forward to compute their electron temperature and density. The ideal situation would be to have simultaneous multi-frequency observations, but this is not possible with ALMA, at least not until a sub-array observing mode is developed. Under the current situation we have to be content with statistical analyses of images taken at different times. Improved resolution could also give information on whether features on the disk are elongated, as expected in the case of opaque fibrils, or not, as expected in the case of network structures.

The absolute calibration of full-disk images is a rather complicated issue (see White et al., 2017), and problems in bands 6 and 7 have been reported and remedied by Alissandrakis et al. (2020) and Alissandrakis et al. (2022). Thus the need of a better absolute calibration of ALMA full-disk solar observations, using the moon for example, is imperative.

The pointing of interferometric solar ALMA images has a number of problems, discussed in the Bastian et al. article of this collection. A precise pointing, of the order of $1''$ or better, is important for 1) accurate measurement of position of the limb and of the solar radius and 2) measurement of the shift of ALMA images with respect to images in other wavelengths and magnetograms, that will make possible to compute the height

of the mm-λ emission, as was done by Alissandrakis (2019) for UV/EUV wavelengths.

Circular polarization measurements are of primary interest for regions with high magnetic field, such as sunspots, but the signal might be too low to measure in the quiet Sun. Bogod et al. (2015) reported values of the magnetic field in the range of 40–200 G in the cm-λ range for the QS, from observations with RATAN-600, which would give a polarization degree in the range of 0.22–1.1% at 3 mm. Even if this is not measurable, we will have an upper limit.

Solar ALMA work has greatly benefited from the synergy with ground and space based instruments operating in other wavelengths, such as AIA and HMI on SDO, IRIS, IBIS on the Dunn Solar Telescope and the Goode Solar Telescope (GST). As the ALMA resolution improves, this synergy will be enhanced in the near future with next-generation instruments coming online, such as the Daniel K. Inouye Solar Telescope (DKIST). It is therefore very important to plan coordinated observing campaigns.

Last but not least, the interferometric observations published so far have provided images with a small field of view and in regions mostly near the disk center; we thus lack a global view of what the mm-λ Sun looks like at high resolution. Mosaicking of the full Sun is out of question, but some large fov mosaics could be done, at the expanse of time resolution; in fact, no large mosaics have been attempted since the commissioning observations (Figure 10).

The remedy is one and only: more and more solar observations with ALMA.

Author contributions

All authors listed have made a substantial, direct, and intellectual contribution to the work and approved it for publication.

Funding

RB acknowledges the support by the Croatian Science Foundation under the project 7549 "Millimeter and sub-millimeter observations of the solar chromosphere with ALMA" and by the EU Horizon 2020 project SOLARNET (824135, 2019-2023).

Acknowledgments

The authors thank Prof. Rob Rutten for long and interesting discussions. While this article was in the proof correction stage, Rob passed away at the age of 80. This article is dedicated to his memory. This work makes use of the following ALMA data: ADS/JAO.ALMA.2011.0.00020.SV, ADS/JAO.ALMA2016.1.00202.S and ADS/JAO.ALMA2016.1.00788.S. ALMA is a partnership of ESO (representing its member states), NSF (USA) and NINS (Japan), together with NRC (Canada), MOST and ASIAA (Taiwan), and KASI (Republic of Korea), in cooperation with the Republic of Chile. The Joint ALMA Observatory is operated by ESO, AUI/NRAO and NAOJ. We also used images from AIA/SDO and HMI/SDO and we are grateful to all those that operate these instruments and make their data available to the community. Finally, we thank the authors of Kobelski et al. (2022) for making their data public. The National Radio Astronomy Observatory is a facility of the National Science Foundation operated under cooperative agreement by Associated Universities, Inc.

Conflict of interest

The authors declare that the research was conducted in the absence of any commercial or financial relationships that could be construed as a potential conflict of interest.

Publisher's note

References

Alissandrakis, C. E. (2019). Measurement of the height of the chromospheric network emission from solar dynamics observatory images. *Sol. Phys.* 294, 161. doi:10.1007/s11207-019-1552-1

Alissandrakis, C. E. (2020). Structure of the solar atmosphere: A radio perspective. *Front. Astron. Space Sci.* 7, 74. doi:10.3389/fspas.2020.574460

Alissandrakis, C. E., and Valentino, A. (2019). Structure of the transition region and the low corona from TRACE and SDO observations near the limb. *Sol. Phys.* 294, 96. doi:10.1007/s11207-019-1486-7

Alissandrakis, C. E., Bastian, T. S., and Nindos, A. (2022). A first look at the submillimeter Sun with ALMA. *Astron. Astrophys.* 661, L4. doi:10.1051/0004-6361/202243774

Alissandrakis, C. E., Nindos, A., Bastian, T. S., and Patsourakos, S. (2020). Modeling the quiet Sun cell and network emission with ALMA. *Astron. Astrophys.* 640, A57. doi:10.1051/0004-6361/202038461

Alissandrakis, C. E., Patsourakos, S., Nindos, A., and Bastian, T. S. (2017). Center-to-limb observations of the Sun with ALMA . Implications for solar atmospheric models. *Astron. Astrophys.* 605, A78. doi:10.1051/0004-6361/201730953

Alissandrakis, C. E., Vial, J. C., Koukras, A., Buchlin, E., and Chane-Yook, M. (2018). IRIS observations of spicules and structures near the solar limb. *Sol. Phys.* 293, 20. doi:10.1007/s11207-018-1242-4

Avrett, E. H., and Loeser, R. (2008). Models of the solar chromosphere and transition region from SUMER and HRTS observations: Formation of the extreme-

ultraviolet spectrum of hydrogen, carbon, and oxygen. *Astrophys. J. Suppl. Ser.* 175, 229–276. doi:10.1086/523671

Bastian, T. S., Chintzoglou, G., De Pontieu, B., Shimojo, M., Schmit, D., Leenaarts, J., et al. (2017). A first comparison of millimeter continuum and Mg II ultraviolet line emission from the solar chromosphere. *Astrophys. J.* 845, L19. doi:10.3847/2041-8213/aa844c

Bastian, T. S., Ewell, J., and Zirin, H. (1993). The center-to-limb brightness variation of the sun at lambda = 850 microns. *Astrophys. J.* 415, 364–375. doi:10.1086/173170

Beckers, J. M. (1968). Solar spicules (invited review paper). *Sol. Phys.* 3, 367–433. doi:10.1007/BF00171614

Beckers, J. M. (1972). Solar spicules. *Annu. Rev. Astron. Astrophys.* 10, 73–100. doi:10.1146/annurev.aa.10.090172.000445

Belkora, L., Hurford, G. J., Gary, D. E., and Woody, D. P. (1992). Measurement of the solar limb brightness profile at 3 millimeters during the total eclipse of 1991 july 11. *Astrophys. J.* 400, 692. doi:10.1086/172031

Benz, A. O. (2009). 4.1.1.6 Radio emission of the quiet Sun. *Landolt Börnstein* 4116doi, 103–115. doi:10.1007/978-3-540-88055-4_5

Bogod, V. M., Alissandrakis, C. E., Kaltman, T. I., and Tokhchukova, S. K. (2015). Ratan-600 observations of small-scale structures with high spectral resolution. *Sol. Phys.* 290, 7–20. doi:10.1007/s11207-014-0526-6

Bohlin, J. D., Vogel, S. N., Purcell, J. D., Sheeley, J., Tousey, R., Vanhoosier, M. E., et al. (1975). A newly observed solar feature: Macrospicules in He II 304 Å. *Astrophys. J.* 197, L133. doi:10.1086/181794

Bose, S., Henriques, V. M. J., Joshi, J., and Rouppe van der Voort, L. (2019). Characterization and formation of on-disk spicules in the Ca II K and Mg II k spectral lines. *Astron. Astrophys.* 631, L5. doi:10.1051/0004-6361/201936617

Bose, S., Joshi, J., Henriques, V. M. J., and Rouppe van der Voort, L. (2021). Spicules and downflows in the solar chromosphere. *Astron. Astrophys.* 647, A147. doi:10.1051/0004-6361/202040014

Brajša, R., Benz, A. O., Temmer, M., Jurdana-Šepić, R., Šaina, B., and Wöhl, H. (2007a). An interpretation of the coronal holes' visibility in the millimeter wavelength range. *Sol. Phys.* 245, 167–176. doi:10.1007/s11207-007-9008-4

Brajša, R., Benz, A. O., Temmer, M., Jurdana-Šepić, R., Šaina, B., Wöhl, H., et al. (2007b). On the visibility of coronal holes in microwaves. *Cent. Eur. Astrophys. Bull.* 31, 219.

Brajša, R., Skokić, I., Sudar, D., Benz, A. O., Krucker, S., Ludwig, H. G., et al. (2021). ALMA small-scale features in the quiet Sun and active regions. *Astron. Astrophys.* 651, A6. doi:10.1051/0004-6361/201936231

Brajša, R., Sudar, D., Benz, A. O., Skokić, I., Bárta, M., De Pontieu, B., et al. (2018). First analysis of solar structures in 1.21 mm full-disc ALMA image of the Sun. *Astron. Astrophys.* 613, A17. doi:10.1051/0004-6361/201730656

Braun, D., and Lindsey, C. (1987). A solar chromosphere and spicule model based on far-infrared limb observations. *Astrophys. J.* 320, 898. doi:10.1086/165607

Buhl, D., and Tlamicha, A. (1970). The mapping of the sun at 3.5 MM. *Astron. Astroph.* 5, 102–112.

Carlsson, M., De Pontieu, B., and Hansteen, V. H. (2019). New view of the solar chromosphere. *Annu. Rev. Astron. Astrophys.* 57, 189–226. doi:10.1146/annurev-astro-081817-052044

Carlsson, M., Hansteen, V. H., Gudiksen, B. V., Leenaarts, J., and De Pontieu, B. (2016). A publicly available simulation of an enhanced network region of the Sun. *Astron. Astrophys.* 585, A4. doi:10.1051/0004-6361/201527226

Chintzoglou, G., De Pontieu, B., Martínez-Sykora, J., Hansteen, V., de la Cruz Rodríguez, J., Szydlarski, M., et al. (2021). ALMA and IRIS observations of the solar chromosphere. I. An on-disk type II spicule. *Astrophys. J.* 906, 82. doi:10.3847/1538-4357/abc9b1

De Pontieu, B., Erdélyi, R., and James, S. P. (2004). Solar chromospheric spicules from the leakage of photospheric oscillations and flows. *Nature* 430, 536–539. doi:10.1038/nature02749

de Pontieu, B., McIntosh, S., Hansteen, V. H., Carlsson, M., Schrijver, C. J., Tarbell, T. D., et al. (2007). A tale of two spicules: The impact of spicules on the magnetic chromosphere. *Publ. Astron. Soc. Jpn. Nihon. Tenmon. Gakkai.* 59, S655–S652. doi:10.1093/pasj/59.sp3.S655

Eklund, H., Wedemeyer, S., Szydlarski, M., and Jafarzadeh, S. (2021). The Sun at millimeter wavelengths. III. Impact of the spatial resolution on solar ALMA observations. *Astron. Astrophys.* 656, A68. doi:10.1051/0004-6361/202140972

Ewell, J. M. W., Zirin, H., Jensen, J. B., and Bastian, T. S. (1993). Submillimeter observations of the 1991 july 11 total solar eclipse. *Astrophys. J.* 403, 426. doi:10.1086/172213

Fontenla, J. M., Avrett, E. H., and Loeser, R. (1993). Energy balance in the solar transition region. III. Helium emission in hydrostatic, constant-abundance models with diffusion. *Astrophys. J.* 406, 319. doi:10.1086/172443

Gary, D. E. (1996). "Imaging spectroscopy of the non-flaring sun," in *Radio emission from the stars and the sun*. Editors A. R. Taylor, and J. M. Paredes (San Francisco: Astronomical Society of the Pacific Conference Series), 93, 387.

Gary, G. A. (2001). Plasma beta above a solar active region: Rethinking the paradigm. *Sol. Phys.* 203, 71–86. doi:10.1023/A:1012722021820

Henriques, V. M. J., Jafarzadeh, S., Guevara Gómez, J. C., Eklund, H., Wedemeyer, S., Szydlarski, M., et al. (2022). The Solar ALMA Science Archive (SALSA). First release, SALAT, and FITS header standard. *Astron. Astrophys.* 659, A31. doi:10.1051/0004-6361/202142291

Horne, K., Hurford, G. J., Zirin, H., and de Graauw, T. (1981). Solar limb brightening at 1.3 millimeters. *Astrophys. J.* 244, 340–344. doi:10.1086/158711

Iwai, K., Shimojo, M., Asayama, S., Minamidani, T., White, S., Bastian, T., et al. (2017). The brightness temperature of the quiet solar chromosphere at 2.6 mm. *Sol. Phys.* 292, 22. doi:10.1007/s11207-016-1044-5

Kleint, L., and Panos, B. (2022). Occurrence and statistics of IRIS bursts. *Astron. Astrophys.* 657, A132. doi:10.1051/0004-6361/202142235

Kobelski, A. R., Tarr, L. A., Jaeggli, S. A., Luber, N., Warren, H. P., and Savage, S. (2022). A publicly available multiobservatory data set of an enhanced network patch from the photosphere to the corona. *Astrophys. J. Suppl. Ser.* 261, 15. doi:10.3847/1538-4365/ac6b3b

Kundu, M. R., and McCullough, T. P. (1972). Polarization of solar active regions at 9.5 mm wavelength. *Sol. Phys.* 24, 133–141. doi:10.1007/BF00231091

Kundu, M. R. (1972). Observations of prominences at 3.5 millimeter wavelength. *Sol. Phys.* 25, 108–115. doi:10.1007/BF00155749

Kundu, M. R. (1970). Solar active regions at millimeter wavelengths. *Sol. Phys.* 13, 348–356. doi:10.1007/BF00153556

Kundu, M. R. (1971). Solar radio emission at 1.2 mm wavelength. *Sol. Phys.* 21, 130–136. doi:10.1007/BF00155783

Labrum, N. R., Archer, J. W., and Smith, C. J. (1978). Solar brightness distribution at 3 mm wavelength from observations of the eclipse of 1976 October 23. *Sol. Phys.* 59, 331–343. doi:10.1007/BF00951837

Langangen, Ø., De Pontieu, B., Carlsson, M., Hansteen, V. H., Cauzzi, G., and Reardon, K. (2008). Search for high velocities in the disk counterpart of type II spicules. *Astrophys. J.* 679, L167–L170. doi:10.1086/589442

Lantos, P., and Kundu, M. R. (1972). The quiet sun brightness distributions at millimeter wavelengths and chro mospheric inhomogeneities. *Astron. Astroph.* 21, 119–124.

Lindsey, C. A., Yee, S., Roellig, T. L., Hills, R., Brock, D., Duncan, W., et al. (1990). Submillimeter observations of the sun from the james clerk maxwell telescope. *Astrophys. J.* 353, L53. doi:10.1086/185706

Lindsey, C., Becklin, E. E., Jefferies, J. T., Orrall, F. Q., Werner, M. W., and Gatley, I. (1984). Observations of the brightness profile of the sun in the 30-200 micron continuum. *Astrophys. J.* 281, 862–869. doi:10.1086/162166

Lindsey, C., Becklin, E. E., Jefferies, J. T., Orrall, F. Q., Werner, M. W., and Gatley, I. (1983). Submillimeter extensions of the solar limb determined from observations of the total eclipse of 1981 July 31. *Astrophys. J.* 264, L25–L30. doi:10.1086/183938

Lindsey, C., Becklin, E. E., Orrall, F. Q., Werner, M. W., Jefferies, J. T., and Gatley, I. (1986). Extreme limb profiles of the sun at far-infrared and submillimeter wavelengths. *Astrophys. J.* 308, 448. doi:10.1086/164515

Lindsey, C., Jefferies, J. T., Clark, T. A., Harrison, R. A., Carter, M. K., Watt, G., et al. (1992). Extreme-infrared brightness profile of the solar chromosphere obtained during the total eclipse of 1991. *Nature* 358, 308–310. doi:10.1038/358308a0

Linsky, J. L. (1973). A recalibration of the quiet sun millimeter spectrum based on the moon as an absolute radiometric standard. *Sol. Phys.* 28, 409–418. doi:10.1007/BF00152312

Loukitcheva, M. A., White, S. M., and Solanki, S. K. (2019). Alma detection of dark chromospheric holes in the quiet sun. *Astrophys. J.* 877, L26. doi:10.3847/2041-8213/ab2191

Loukitcheva, M., Solanki, S. K., Carlsson, M., and Stein, R. F. (2004). Millimeter observations and chromospheric dynamics. *Astron. Astrophys.* 419, 747–756. doi:10.1051/0004-6361:20034159

Loukitcheva, M., Solanki, S. K., Carlsson, M., and White, S. M. (2015). Millimeter radiation from a 3D model of the solar atmosphere. I. Diagnosing chromospheric thermal structure. *Astron. Astrophys.* 575, A15. doi:10.1051/0004-6361/201425238

Loukitcheva, M., Solanki, S. K., and White, S. (2006). The dynamics of the solar chromosphere: Comparison of model predictions with millimeter-interferometer observations. *Astron. Astrophys.* 456, 713–723. doi:10.1051/0004-6361:20053171

Macris, C. J. (1957). Recherches sur les spicules de projection sur le disque solaire. *Ann. d'Astrophysique* 20, 179.

Martínez-Sykora, J., De Pontieu, B., de la Cruz Rodriguez, J., and Chintzoglou, G. (2020). the formation height of millimeter-wavelength emission in the solar chromosphere. *Astrophys. J.* 891, L8. doi:10.3847/2041-8213/ab75ac

Martínez-Sykora, J., De Pontieu, B., Hansteen, V. H., Rouppe van der Voort, L., Carlsson, M., and Pereira, T. M. D. (2017). On the generation of solar spicules and Alfvénic waves. *Science* 356, 1269–1272. doi:10.1126/science.aah5412

Menezes, F., Selhorst, C. L., Giménez de Castro, C. G., and Valio, A. (2022). Subterahertz radius and limb brightening of the Sun derived from SST and ALMA. *Mon. Not. R. Astron. Soc.* 511, 877–885. doi:10.1093/mnras/stab3501

Molnar, M. E., Reardon, K. P., Chai, Y., Gary, D., Uitenbroek, H., Cauzzi, G., et al. (2019). Solar chromospheric temperature diagnostics: A joint ALMA-hα analysis. *Astrophys. J.* 881, 99. doi:10.3847/1538-4357/ab2ba3

Nindos, A., Alissandrakis, C. E., Bastian, T. S., Patsourakos, S., De Pontieu, B., Warren, H., et al. (2018). First high-resolution look at the quiet Sun with ALMA at 3mm. *Astron. Astrophys.* 619, L6. doi:10.1051/0004-6361/201834113

Nindos, A., Patsourakos, S., Alissandrakis, C. E., and Bastian, T. S. (2021). ALMA observations of the variability of the quiet Sun at millimeter wavelengths. *Astron. Astrophys.* 652, A92. doi:10.1051/0004-6361/202141241

O'Dwyer, B., Del Zanna, G., Mason, H. E., Weber, M. A., and Tripathi, D. (2010). SDO/AIA response to coronal hole, quiet Sun, active region, and flare plasma. *Astron. Astrophys.* 521, A21. doi:10.1051/0004-6361/201014872

Parker, E. N. (1988). Nanoflares and the solar X-ray corona. *Astrophys. J.* 330, 474. doi:10.1086/166485

Pikel'Ner, S. B. (1969). A mechanism for the formation of chromospheric spicules. *Astron. Zhurnal* 46, 328.

Purkhart, S., and Veronig, A. M. (2022). Nanoflare distributions over solar cycle 24 based on SDO/AIA differential emission measure observations. *Astron. Astrophys.* 661, A149. doi:10.1051/0004-6361/202243234

Reeves, E. M., Foukal, P. V., Huber, M. C. E., Noyes, R. W., Schmahl, E. J., Timothy, J. G., et al. (1974). Observations of the chromospheric network: Initial results from the apollo telescope mount. *Astrophys. J.* 188, L27. doi:10.1086/181423

Roellig, T. L., Becklin, E. E., Jefferies, J. T., Kopp, G. A., Lindsey, C. A., Orrall, F. Q., et al. (1991). Submillimeter solar limb profiles determined from observations of the total solar eclipse of 1988 march 18. *Astrophys. J.* 381, 288. doi:10.1086/170650

Rouppe van der Voort, L., Leenaarts, J., de Pontieu, B., Carlsson, M., and Vissers, G. (2009). On-disk counterparts of type II spicules in the Ca II 854.2 nm and Hα lines. *Astrophys. J.* 705, 272–284. doi:10.1088/0004-637X/705/1/272

Rutten, R. J., Rouppe van der Voort, L. H. M., and De Pontieu, B. (2019). Solar Hα features with hot onsets. IV. Network fibrils. *Astron. Astrophys.* 632, A96. doi:10.1051/0004-6361/201936113

Rutten, R. J., and Rouppe van der Voort, L. H. M. (2017). Solar Hα features with hot onsets. II. A contrail fibril. *Astron. Astrophys.* 597, A138. doi:10.1051/0004-6361/201527560

Rutten, R. J. (2017). Solar H-alpha features with hot onsets. III. Long fibrils in Lyman-alpha and with ALMA. *Astron. Astrophys.* 598, A89. doi:10.1051/0004-6361/201629238

Samanta, T., Tian, H., Yurchyshyn, V., Peter, H., Cao, W., Sterling, A., et al. (2019). Generation of solar spicules and subsequent atmospheric heating. *Science* 366, 890–894. doi:10.1126/science.aaw2796

Saqri, J., Veronig, A. M., Warmuth, A., Dickson, E. C. M., Battaglia, A. F., Podladchikova, T., et al. (2022). Multi-instrument STIX microflare study. *Astron. Astrophys.* 659, A52. doi:10.1051/0004-6361/202142373

Selhorst, C. L., Silva, A. V. R., and Costa, J. E. R. (2005). Solar atmospheric model with spicules applied to radio observation. *Astron. Astrophys.* 433, 365–374. doi:10.1051/0004-6361:20042043

Selhorst, C. L., Simões, P. J. A., Brajša, R., Valio, A., Giménez de Castro, C. G., Costa, J. E. R., et al. (2019). Solar polar brightening and radius at 100 and 230 GHz observed by ALMA. *Astrophys. J.* 871, 45. doi:10.3847/1538-4357/aaf4f2

Shibasaki, K., Alissandrakis, C. E., and Pohjolainen, S. (2011). Radio emission of the quiet sun and active regions (invited review). *Sol. Phys.* 273, 309–337. doi:10.1007/s11207-011-9788-4

Shimojo, M., Bastian, T. S., Hales, A. S., White, S. M., Iwai, K., Hills, R. E., et al. (2017). Observing the sun with the atacama large millimeter/submillimeter array (ALMA): High-resolution interferometric imaging. *Sol. Phys.* 292, 87. doi:10.1007/s11207-017-1095-2

Shimojo, M., Kawate, T., Okamoto, T. J., Yokoyama, T., Narukage, N., Sakao, T., et al. (2020). Estimating the temperature and density of a spicule from 100 GHz data obtained with ALMA. *Astrophys. J.* 888, L28. doi:10.3847/2041-8213/ab62a5

Shokri, Z., Alipour, N., Safari, H., Kayshap, P., Podladchikova, O., Nigro, G., et al. (2022). Synchronization of small-scale magnetic features, blinkers, and coronal bright points. *Astrophys. J.* 926, 42. doi:10.3847/1538-4357/ac4265

Sudar, D., Brajša, R., Skokić, I., and Benz, A. O. (2019). Centre-to-Limb brightness variations from the atacama large millimeter-submillimeter array (ALMA) full-disk solar images. *Sol. Phys.* 294, 163. doi:10.1007/s11207-019-1556-x

Tsiropoula, G., Tziotziou, K., Kontogiannis, I., Madjarska, M. S., Doyle, J. G., and Suematsu, Y. (2012). Solar fine-scale structures. i. spicules and other small-scale, jet-like events at the chromospheric level: Observations and physical parameters. *Space Sci. Rev.* 169, 181–244. doi:10.1007/s11214-012-9920-2

Vernazza, J. E., Avrett, E. H., and Loeser, R. (1981). Structure of the solar chromosphere. III. Models of the EUV brightness components of the quiet sun. *Astrophys. J. Suppl. Ser.* 45, 635–725. doi:10.1086/190731

Wannier, P. G., Hurford, G. J., and Seielstad, G. A. (1983). Interferometric observations of solar limb structure at 2.6 millimeters. *Astrophys. J.* 264, 660–666. doi:10.1086/160639

Wedemeyer, S., Bastian, T., Brajša, R., Hudson, H., Fleishman, G., Loukitcheva, M., et al. (2016). Solar science with the atacama large millimeter/submillimeter array—a new view of our sun. *Space Sci. Rev.*, 200, 1–73. doi:10.1007/s11214-015-0229-9

Wedemeyer, S., Szydlarski, M., Jafarzadeh, S., Eklund, H., Guevara Gomez, J. C., Bastian, T., et al. (2020). The Sun at millimeter wavelengths. I. Introduction to ALMA Band 3 observations. *Astron. Astrophys.* 635, A71. doi:10.1051/0004-6361/201937122

White, S. M., Iwai, K., Phillips, N. M., Hills, R. E., Hirota, A., Yagoubov, P., et al. (2017). Observing the sun with the atacama large millimeter/submillimeter array (ALMA): Fast-scan single-dish mapping. *Sol. Phys.* 292, 88. doi:10.1007/s11207-017-1123-2

White, S. M., Loukitcheva, M., and Solanki, S. K. (2006). High-resolution millimeter-interferometer observations of the solar chromosphere. *Astron. Astrophys.* 456, 697–711. doi:10.1051/0004-6361:20052854

Wootten, A., and Thompson, A. R. (2009). The atacama large millimeter/submillimeter array. *Proc. IEEE* 97, 1463–1471. doi:10.1109/JPROC.2009.2020572

Yokoyama, T., Shimojo, M., Okamoto, T. J., and Iijima, H. (2018). ALMA observations of the solar chromosphere on the polar limb. *Astrophys. J.* 863, 96. doi:10.3847/1538-4357/aad27e

frontiers | Frontiers in Astronomy and Space Sciences

TYPE Original Research
PUBLISHED 11 January 2023
DOI 10.3389/fspas.2022.978405

OPEN ACCESS

EDITED BY
Timothy Bastian,
National Radio Astronomy Observatory, United States

REVIEWED BY
Carlos Guillermo Giménez De Castro,
Mackenzie Presbyterian University, Brazil
Yihua Yan,
National Astronomical Observatories (CAS), China

*CORRESPONDENCE
Lucas A. Tarr,
ltarr@nso.edu

SPECIALTY SECTION
This article was submitted to Stellar and Solar Physics, a section of the journal Frontiers in Astronomy and Space Sciences

RECEIVED 26 June 2022
ACCEPTED 21 December 2022
PUBLISHED 11 January 2023

CITATION
Tarr LA, Kobelski AR, Jaeggli SA, Molnar M, Cauzzi G and Reardon KP (2023), Spatio-temporal comparisons of the hydrogen-alpha line width and ALMA 3 mm brightness temperature in the weak solar network.
Front. Astron. Space Sci. 9:978405.
doi: 10.3389/fspas.2022.978405

Spatio-temporal comparisons of the hydrogen-alpha line width and ALMA 3 mm brightness temperature in the weak solar network

Lucas A. Tarr[1]*, Adam R. Kobelski[2], Sarah A. Jaeggli[1], Momchil Molnar[3,4,5], Gianna Cauzzi[3,6] and Kevin P. Reardon[3,4]

[1]National Solar Observatory, Makawao, HI, United States, [2]NASA MSFC, Huntsville, AL, United States, [3]National Solar Observatory, Boulder, CO, United States, [4]Department of Astrophysical and Planetary Sciences LASP University of Colorado, Boulder, CO, United States, [5]High Altitude Observatory, National Center for Atmospheric Research, Boulder, CO, United States, [6]INAF–Osservatorio Astrofisico di Arcetri, Firenze, Italy

Comparisons between the Atacama Large Millimeter/sub-millimeter Array (ALMA) 3 mm emission and a range of optical and UV solar observations have found the strongest correspondence between the width of the hydrogen alpha line at 656.3 nm and the 3 mm brightness temperature. Previous studies on the oscillatory power of p-modes using ALMA Band 3 and Band 6 data in the 3–5 min period bandpass have found a confusing mix of results, with many reporting a complete lack of the p-mode enhancement typically found in other chromospheric observables. We study these issues using an extensive, publicly available coordinated data set targeting a region of weak network flux near disk center at time SOL 2017-03-17T15:42-16:45. We focus on the Interferometric Bidimensional Spectropolarimeter (IBIS) H-alpha and ALMA 3 mm data series. We confirm the strong correlation between the H-alpha line width and the 3 mm brightness temperature, but find a bimodal relation between the two diagnostics, with a shallower slope of 7.4e-5 Å/K in cooler regions and steeper slope of 1.2e-4 Å/K in hotter regions. The origin of the bimodal distribution is unknown, but does hold for the duration of the observations. Both slopes are steeper than a previously reported value, but this is likely due to systematic differences in the analysis. We then calculate the oscillatory power in the H-alpha and 3 mm data. The IBIS data clearly show the p-mode oscillations in spatially averaged power spectra while the ALMA data do not. However, when we remove IBIS data at times corresponding to the ALMA calibration windows, the spatially averaged power spectra for the two data series are nearly identical, with a Pearson correlation coefficient of 0.9895. Further, the power in the two bands remains strongly correlated when the spatial information is retained but the power is integrated over different temporal frequency bands. We therefore argue that the lack of observed p-modes in the ALMA data may be predominantly due to spectral windowing induced by the timing and duration of the calibration observations. Finally, we find that spatial maps of oscillatory power at 3 mm display the pattern

of magnetic shadows and halos typically displayed by other chromospheric diagnostics.

KEYWORDS

solar chromosphere, solar oscillations, solar physics, solar radio astronomy, solar activity, solar magnetic activity, chromospheric activity, ALMA band 3

1 Introduction

The solar chromosphere is a richly structured and dynamic plasma environment typified by increasing temperature, decreasing density, and the rapid transition of numerous plasma properties with height, such as ionization fraction (towards more highly ionized states) or the ratio of thermal to magnetic energy (towards magnetic dominance) (Bray and Loughhead, 1974; Leake et al., 2014). The chromosphere acts as a conduit for energy to propagate from the mechanical reservoir of the upper convection zone into the corona where it can heat the coronal plasma, accelerate the solar wind, and power flares and eruptions. Determining how the chromosphere is structured is a critical task towards identifying which energy transfer mechanisms are dominant in each type of solar environment—quiet Sun, plage, within coronal holes, at the center of sunspots, etc.—and how they evolve over time. Given the rapid transitions within the chromosphere, multiple radiative diagnostics that are sensitive to different properties of the plasma must be observed at the same time and understood as a whole in order to reconstruct the chromospheric structure.

A longstanding question in solar physics is the nature of chromospheric oscillations and their relative importance for the propagation of energy between the photosphere and the corona (see review by Khomenko and Calvo Santamaria (2013) and references therein). Observations at millimeter wavelengths provide a rather direct measurement of the chromospheric electron temperature and are therefore an important diagnostic of these oscillations (Loukitcheva et al., 2006) especially when obtained with the good spatial and temporal resolution provided by the Atacama Large Millimeter/sub-millimeter Array [ALMA; (Wootten and Thompson, 2009; Hills et al., 2010)]. However, reports of oscillations in the ALMA data sets have so far been rather mixed.

Jafarzadeh et al. (2021) presented results from a wide variety of solar data sets and features observed with Band 3 and Band 6 data during the ALMA Cycle 4 solar campaign. They found evidence what is expected to be nearly ubiquitous enhancement in oscillatory power in 3–5 mHz p-mode range typically found in chromospheric diagnostics (5 and 3 min periodicity, respectively) in just two of the ten data sets they analyzed. The two sets of observations that did contain evidence of chromospheric oscillations were studied in more detail in Nindos et al. (2021), who did detect p-mode power in both Band 3 and Band 6 ALMA data.

Patsourakos et al. (2020) found oscillatory power at p-mode frequencies in their Band 3 quiet Sun observations at multiple heliographic angles in a center-to-limb study. However, when looking for spatial coherence in the oscillatory power, they found no coherence at scales above the ALMA spatial resolution, and reported no correlation with the underlying pattern of either brightness structure or network/internetwork regions. They also reported that frequency-integrated maps of the power spectra in select bands did not reveal the power-shadow or -halo features typically found in photospheric and chromospheric diagnostics (Braun et al., 1992; Brown et al., 1992; Vecchio et al., 2007).

Narang et al. (2022) calculated the oscillatory power in a region of plage using ALMA Band 6 observations, which correspond to lower heights and cooler temperatures relative to Band 3, although there can be significant overlap between the contribution functions for the two channels (Wedemeyer et al., 2016). They investigated the spatially averaged power over the ALMA field of view as well as the spatial distribution of frequency-integrated power in different temporal frequency ranges. Similar to most of the data series analyzed by Jafarzadeh et al. (2021), these authors did not find significant power in the p-mode band of 3–5 min periods. They also did not find any strong correlations between the spatial distribution of oscillatory power in the ALMA data compared to transition region and coronal data sets from the Interface Region Imaging Spectrograph (IRIS) and the Atmospheric Imaging Assembly (AIA) on the Solar Dynamics Observatory (SDO).

Molnar et al. (2021) reported somewhat similar results to the above for power spectra of the Band 3 observations of a region of network flux near an active region. Their plots of the spatially averaged power spectra (e.g., their Figure 14) do not show any prominent peak at p-mode frequencies. They do, however, report fairly strong spatial variations in the power spectra that correlate with different temperature regimes, and all have the same power law trend. They also find several power enhancements above the power law trend in specific bands at higher frequencies, from 10 to 50 mHz.

Chai et al. (2022) found very clear indications of power at 5 mHz in a sunspot umbra with their ALMA Band 3 observations. These oscillations showed good correspondence with simultaneous velocity proxies in the Hα line. At higher

frequencies, umbral and penumbral regions had essential the same spectrum. Their quiet Sun regions did not show any prominent enhancement in the 3–5 mHz range, but did show some excess power around 30 mHz, perhaps similar to the findings of Molnar et al. (2021).

Nindos et al. (2021) included an appendix considering the effect of observation duration and calibration windows on the measured power spectrum. Using a monochromatic source as an example, they found that the windowing effect for their ALMA cycle 4 observations did not reduce the spectral width of the recovered source (which is due to finite frequency resolution), but did reduce the peak power as well as modify the side-lobe size and pattern. We will use a multi-instrument data set to study the effect temporal sampling and calibration windows of the computed power spectrum in more detail.

We present here analysis of a combined data set described in Kobelski et al. (2022) that includes 3 mm (or 100 GHz; Band 3) interferometric observations from the ALMA, sensitive to the chromospheric temperature, and spectral-imaging observations of the hydrogen Hα line at 656.3 nm from the Interferometric Bidimensional Spectropolarimeter [IBIS; (Cavallini, 2006)]; at the Dunn Solar Telescope. The combined data set covers ~60 min of observations of a small, bipolar region of network flux located near disk center on 2017-03-21. The millimeter radiation provides a direct measure of the electron temperature in the chromosphere, but exactly where the emission forms, how it varies based on dynamic phenomena or on the surrounding magnetic structure, and how it relates to other diagnostics is still under investigation (Alissandrakis et al., 2020; Wedemeyer et al., 2020; Narang et al., 2022).

Our aim in this paper is to explore spatial and dynamic correlations in our observations of network magnetic fields. Molnar et al. (2019) found a strong positive correlation between the ALMA 3 mm brightness temperature and the Hα line width in an area of network flux near an active region. A linear fit to the trend gave a slope of 6.12×10^{-5} Å/K. Kobelski et al. (2022) confirmed this strong correlation between the two quantities for a region of weakly enhanced network magnetic field in the quiet Sun. They reported a steeper slope of 1.1×10^{-4} Å/K over a narrower range of observed temperatures, due to their more quiet target region. They also used a slightly different definition of the line width compared to Molnar et al. (2019), which affects the value of slope but not the goodness of fit. In any case, the correspondence between the 3 mm brightness temperature and the width of the Hα line is striking, to the extent that the two observables, when sampled at the same spatial scale, cannot readily be distinguished.

By comparing the power spectra derived from the Hα line width to those derived from the 3 mm data, we argue in this paper that the lack of detected p-modes in the ALMA data in previous studies may be an effect of the windowing due to the timing of calibration data acquisition.

In **Section 2** we describe the observations used in the analysis. In **Section 3** we describe how we prepped the original data, specifically how we characterised the Hα data for use in later analyses. In **Section 4** we discuss properties of the joint distribution of the Hα and 3 mm data series. In **Section 5** we discuss aspects of each time series of data in terms of the average power spectra and spatial distribution of oscillatory power. We briefly discuss the results in **Section 6** and finally conclude in **Section 7**.

2 Observations

The present work uses two data series taken from the more extensive coordinated data set described in Kobelski et al. (2022) [1]. The full data set includes coordinated observations between ALMA and multiple instruments at each of the Dunn Solar Telescope (DST), IRIS, Hinode spacecraft, and SDO facilites; the Nuclear Spectroscopic Telescope Array (NuSTAR) also observed the same solar target within several hours of our observations. The calibration of each data series, the coalignment of all series to each other, and the solar target are fully described in that paper, so here we only provide a short overview of the details relevant to the present work. Kobelski et al. (2022) have made the full data set publicly available at https://share.nso.edu/shared/dkist/ltarr/kolsch/.

ALMA was operated in configuration C43-1 and observations were taken using Band 3, with a central frequency of 100 GHz (3 mm wavelength) and a bandwidth of 18 GHz. With this configuration and frequency, ALMA's spatial resolution is approximately 3″ on the sky, though the beam shape is elliptic. The data series was self-calibrated using the CLEAN algorithm and produced output at a 2 s cadence, or 1,515 spatial maps of the relative brightness temperature ΔT_B over the entire time series. The time series includes five ≈10 minute acquisitions, each separated by 3 min of calibration data. Given the quiet Sun target and its proximity to disk center, we use the mean temperature of 7300 K reported in White et al. (2017) for quiet Sun disk center ALMA 100 GHz observations to define the zero point of these observations, i.e., $T_B = \Delta T_B + 7300$ K. The details of the ALMA data set are described further in Kobelski et al. (2022). The spatial maps show features over approximately a 60″ diameter field of view, see **Figure 1A**. We note, however, that the spatial reconstruction of this interferometric data does not produce a hard cutoff in the field of view. Comparison to the Hα data carried out in §3 does show well-correlated variations out to the edge of the IBIS field of view, which does have a hard cutoff due

1 In keeping with their terminology, we use *data series* to refer to data from a single instrument and *data set* to refer to the entire collection of coaligned data series from all instruments.

to the circular field stop. With this in mind, care must be taken when comparing the two data series.

The dual Fabry-Pérot based IBIS instrument was used to scan the Hα line at 656.3 nm repeatedly, executing 1,800 scans during the observations. Each scan consisted of 26 unequally spaced wavelength positions, using tighter sampling in the line core of ≈12.5 pm and ≈19.1 pm in the line wing, and covering a total of ±2 Å about line center. At each wavelength scan step, IBIS imaged a 2D spatial field of view 90″ in diameter. Each step in the spectral scan lasted .167 s, giving a total cadence of 4.3 s for a single complete scan of the spectral line; i.e., all 26 spectral points over the spatial field of view.

Our primary focus is on the ≈60 min of observations with Band 3 of ALMA, which has a central frequency of 100 GHz or 3 mm in wavelength, and the spatially- and temporally-overlapping imaging-spectroscopic observations of the 656.3 nm Hα line that last ≈120 min in total and completely overlap the ALMA observations. The target was a small, bipolar patch of enhanced network magnetic flux approximately (−60″, −50″) from disk center, observed on 21 March 2017. **Figure 1** presents an overview of the region and our observations. Panel (a) shows the ALMA ΔT_B. Panels (b) and (c) show intensity maps from two of the twenty six positions of the IBIS spectral scan, in the blue wing (656.19 nm) and near the center (656.27 nm) of the Hα line, respectively. The red and blue lines in every panel respectively mark the −50 and +50 Gauss contours of the line of sight magnetic field measured by HMI and pulled from the hmi.M_720s data series. The dark filament that can be seen in the Hα core lies along the polarity inversion line of the small bipole near the center of the IBIS field of view. The filament varies in extent and intensity, persists throughout the observation, and occasionally shows very strong signals in the blue wing around −.8 Å from the line core. Those dynamics will be considered in a separate work.

The magnetic flux in this area was likely associated with the decay of NOAA Active Region 12639 although by the time of our observations it had essentially merged with the background network. In fact, it had decayed substantially since being observed by another group in the ALMA Cycle-4 campaign (Shimizu et al., 2021) 2 days prior to our own observations, a happy coincidence that could be exploited in future studies. While decaying, Kuhar et al. (2018) were able to detect microflaring from this particular region a few hours after our observing window using X-ray data from NuSTAR with a total thermal energy of order a few $\times 10^{26}$ erg. Given their complex spatial and temporal morphology, and the ratio of thermal to non-thermal emission allowed by NuSTAR's sensitivities, these authors conclude that the impulsive events in this region classify as (small) quiet Sun microflares, but not the elementary heating events proposed by Parker (1988).

For use in later analyses we define the set of ALMA times as $\{t_A\}$ and the set of IBIS times as $\{t_I\}$, where times are defined at the center of the integration for ALMA and at the center of each spectral scan for IBIS. These sets exclude "bad" data frames during the calibration windows (ALMA) and periods of bad seeing (IBIS). We then define their set intersection as $\{t_O\} = \{t_A\} \bigcap \{t_I\}$, where the new, "overlapping" set is defined as the set of all closest-in-time pairs (one ALMA, one IBIS) with no repeated times from either data series.

To elaborate further, the ALMA data have a nominal cadence of 2 s, but approximately every 10 min it has an approximately 3 min data gap due to the calibration window. The IBIS data have a nominal cadence of approximately 4.3 s, but have occasional spans of bad data that we do not use due to poor seeing. We wish to pair up elements from each data series. The goal of this task is not to temporally co-align the two data series (for that purpose we would simply interpolate the data), but instead to generate data series with similar characteristics in terms of duration and sampling, from which we may calculate the temporal power spectrum of each series and understand the effect of sampling on these calculated spectra by comparing them to the power spectra calculated from each of the full time series. To achieve the best statistics, we wish to use the maximum number of samples from each data series without using any sample twice. In a very rough sense, this means that every other sample from the ALMA time series will be paired with one IBIS sample. But because the two cadences are not related by an integer multiple, and because there are (independent) data gaps present in each data series, the actual pairing is more erratic. Given the ratio in sampling between the two data series, roughly every 8–10 IBIS timesteps an additional ALMA timestep is skipped, but this is of course modified any time there is missing data from either time series.

The final result of the set intersection produces 685 pairs of samples from the ALMA and IBIS time series, with a (very roughly) 4 s cadence. We do not enforce a maximum allowed time difference between any pair of elements in $\{t_O\}$. The largest temporal offset between any pair of ALMA-IBIS samples is 1.7 s, eight pairs have $\Delta t > 1$ s, and the remaining 677 pairs are essentially evenly distributed between $0 < \Delta t < 1$ s in 0.2 s bins.

3 Hα line width measurements

Following in the footsteps of Molnar et al. (2019) who found the remarkable relation between the width of the Hα line and the 3 mm brightness temperature, we begin by characterizing the Hα line in terms of the minimum intensity, center wavelength (i.e., Doppler velocity), and spectral width.

We characterize the line independently at each spatial location and each time in the data series using the method described in Kobelski et al. (2022)§4.2, which in turn is based on Cauzzi et al. (2009); **Figure 2** shows the various steps in the process where the final result, the line width, is indicated by the red dashed line. The method is, in effect, a version of the full

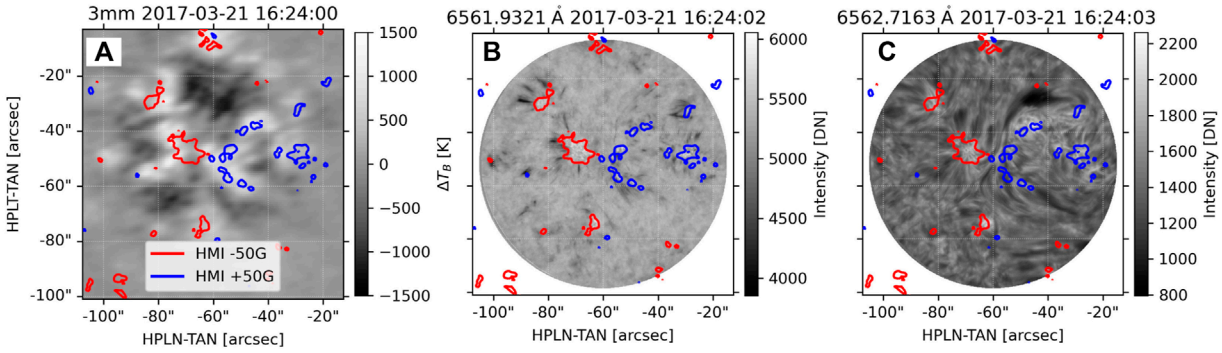

FIGURE 1
(A) ALMA Band 3 brightness temperature relative to the mean temperature, **(B)** intensity in the IBIS Hα blue wing at 656.19 nm, and **(C)** intensity near the Hα line core at 656.27 nm. In all three panels the red and blue contours mark the ±50 Gauss line of sight magnetic field measured by HMI.

width at half max, but modified to isolate only the chromospheric portion of the line profile around the line core. First, we construct a spline-interpolated model (green dashed line) of the measured line profile (blue "+" symbols and straight lines). We define the center wavelength as the center of the best-fit Gaussian (orange) to the central 12 measured points. The intensity minimum (red cross; $I_{\rm min}$) is the value of the spline model at the center wavelength. Next we define an upper threshold as the average intensity at ±.75 Å from the line center (marked by the green and purple dots) using the spline model. The intensity midpoint between the upper threshold and the minimum is marked in each wing of the line by the red stars. The final width $\delta\lambda$ is the distance between them calculated using the spline model, shown as the red dashed line.

We use ±.75 Å to define the upper intensity threshold in order to avoid the influence of a telluric H_2O line at +1.5 Å relative to Hα. In contrast, Molnar et al. (2019) used ±1.0 Å as their upper bound, as their data were obtained under drier atmospheric conditions at the DST and do not appear to suffer from telluric H_2O contamination. The clean signal they obtained throughout the entire line allowed those authors to vary the parameters defining the line width and test the resulting correlation between the width and the ALMA brightness temperature. They found that, while the slope of a linear fit between $\delta\lambda$ and T_B varied depending the parameters, the correlation coefficient was relatively similar. We address this point further in the discussion in §6.

Figure 3 presents an overview of the data analyzed at a single time, 15:42:12 UT. In the top row we plot (a) a spatial map of the ALMA Band 3 relative brightness temperature ΔT_B and b) the calculated IBIS Hα line width $\delta\lambda$ at full IBIS resolution. In panel (c) we show a map of the line width after being convolved with a 2D Gaussian (described next) and interpolated to the locations of the ALMA pixel centers. Panel (d) shows the line-of-sight Doppler velocity of the Hα line at full IBIS resolution.

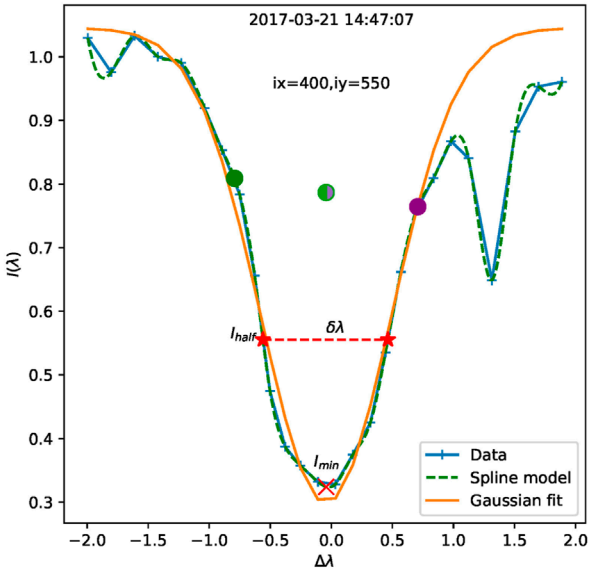

FIGURE 2
Example calculation of the Hα line width. The x-axis is wavelength in Å from the nominal line core, while the y-axis is the profile intensity, normalized to the maximum of the average profile over the whole sample. This figure is reproduced from Kobelski et al. (2022) by permission of the AAS.

Contours of both data sets are shown in Panel (c) [see labels in Panel (a)] and provide a by-eye demonstration of the good correlation between ΔT_B and $\delta\lambda$. An animation of these four panels for the 685 time steps in t_O is available in the online material. Panel (e) shows the joint distribution of T_B and $\delta\lambda$ calculated using only pixels within the red circle from panels (a) and (c), or 2,813 pixels for this single time. This 45″ diameter circle marks the conservatively-defined overlapping FOV for the two instruments, as described below.

We now discuss our methodology for spatially smoothing and interpolating the IBIS data to best match the ALMA data. In general, the ALMA spatial resolution pattern is returned by the CLEAN algorithm as a best-fit ellipse to the primary beam. An equivalent circular Gaussian resolution element can be defined by $\sqrt{b_{\min} b_{\max}}$ where $b_{\min}$ and $b_{\max}$ are the major and minor radii of the ALMA beam projected onto the sky. The beam shape changes over the course of our observations at the 2% level, with maximum, minimum, and median values of the Gaussian FWHM of 3.28″, 3.21″, and 3.236″, respectively.

Instead of using the reported ALMA beam parameters we empirically determine the circular Gaussian kernel that minimizes the RMS difference between the convolved and interpolated IBIS Hα line widths and the ALMA brightness temperature maps. The minimization is performed independently at each time in the overlapping set $\{t_O\}$ and then averaged over the time series to produce a final convolution kernel with standard deviation of 1.28″, or a FWHM of 3.03″. This is comparable to the ALMA beam size determined by CLEAN. As a side effect, during the minimization process we found an additional spatial offset of (1.65″,.22″) between the IBIS and ALMA data series that exists in the Kobelski et al. (2022) data set. The additional offset has been included in all of the present work. We stress that a single spatial offset is applied to the entire self-aligned data series, as opposed to a different offset being applied to each time step; the latter would bias our results. After convolution we interpolate (and therefore down sample) the IBIS data to the same spatial locations as the ALMA pixel centers. The excellent correlation between the ALMA brightness temperature and the Hα line width, together with the higher spatial resolution and the long-duration and uninterrupted nature of IBIS data series, allow us to study the effects of the spatial and temporal features of the ALMA Band 3 data.

4 Joint distribution

Figure 4 shows the joint distribution between the relative brightness temperature ΔT_B, the convolved and interpolated Hα line width, and the convolved and interpolated Doppler velocity for all times in the set $\{t_O\}$. The figure was created with the corner.py python module (Foreman-Mackey, 2016), which produces a rasterized histogram with contours in equal steps of quintiles (20% of the data) in the high-density regions of the distribution function, and individual clouds of points in the lowest (outer) regions with the final 20% of the data. The distribution is generated from all pixels within a 30 pixel (22.5″) radius of the ALMA beam center. We used this rather conservative definition of the cospatial field of view between the instruments in order to avoid oversampling outer regions of the reconstructed ALMA images where the contrast diminishes, and also avoid potential issues at the edges of the IBIS field of view discussed below. This reduced field of view still retains enough pixels, ∼1.92 million throughout the overlapping 685 time steps in the set $\{t_O\}$, to give good statistical weight to our results. Panels (a), (c), and (f) show the 1D distributions of ΔT_B, $\delta\lambda$, and v_{dop}, respectively. Panel (b) shows the joint distribution for $(\Delta T_B, \delta\lambda)$, Panel (d) for $(\Delta T_B, v_{dop})$, and Panel (e) for $(\delta\lambda, v_{dop})$.

The joint distribution between the Hα line width and the 3 mm brightness temperature in **Figure 4B** shows a bimodal distribution, with a low-T_B, low-$\delta\lambda$ cluster and a high-T_B, high-$\delta\lambda$ cluster. The two lobes show different linear trends but have large scatter. We estimated the linear trend of each lobe using the central moment of each distribution core, defined as the inner 20% of the data. This definition primarily excluded the broad, high temperature spread of points in the upper right of the distribution, and the resulting fits should be treated as "by eye." The lower temperature, narrower line width region has a shallower slope of 7.4×10^{-5} Å/K (blue line in the figure), and the higher temperature, larger line width region has a steeper slope of 1.2×10^{-4} Å/K (yellow line). The hotter regions are typically cospatial with the underlying strong magnetic field concentrations (see **Figure 1**). Looking at the animations of **Figure 3** it is clear that the collection of high temperature and broad line width points in the upper right are associated with short-lived dynamic events. A single linear fit to all the data gives a slope of 9.4×10^{-5} Å/K.

The two lobes in the full joint distribution which were used for the low temperature and high temperature fits in **Figure 4** are barely discernible in the joint distribution for individual times, making instantaneous fits unreliable. Given the spread in slopes for the high-T, low-T, and full fits, a reasonable estimate for the uncertainty is simply $\pm 2 \times 10^{-5}$ Å/K. The variation of 2×10^{-5} is consistent with the spread in slopes determined using a single linear fit to the joint distribution at individual times (e.g., without trying to separate into hotter and cooler distributions). On the other hand, the fitted slope at any given individual time has a 95% confidence level of $\approx \pm .15 \times 10^{-5}$ Å/K, so the time variation of the determined slope has much more variation than allowed by the fit to the slope at any particular time. The variation in slope seems to be due to a combination of dynamic events and the relative distribution of hotter versus cooler regions in the small, cospatial FOV; see the animation of **Figure 1** and discussion below.

We generated multiple similar distributions by varying the radius that defines the overlapping field of view for the two data series. As we mentioned in the introduction, ALMA's spatial sensitivity gradually reduces away from the beam center. This causes a reduction in the contrast of T_B with respect to the center of the field of view, in addition to smoothing of the spatial features. For the IBIS data, the variable seeing conditions at the DST during our observations caused the field of view to occasionally shift. Although we corrected these shifts *post facto* during the self-alignment of the IBIS data (17, §2.5.1),

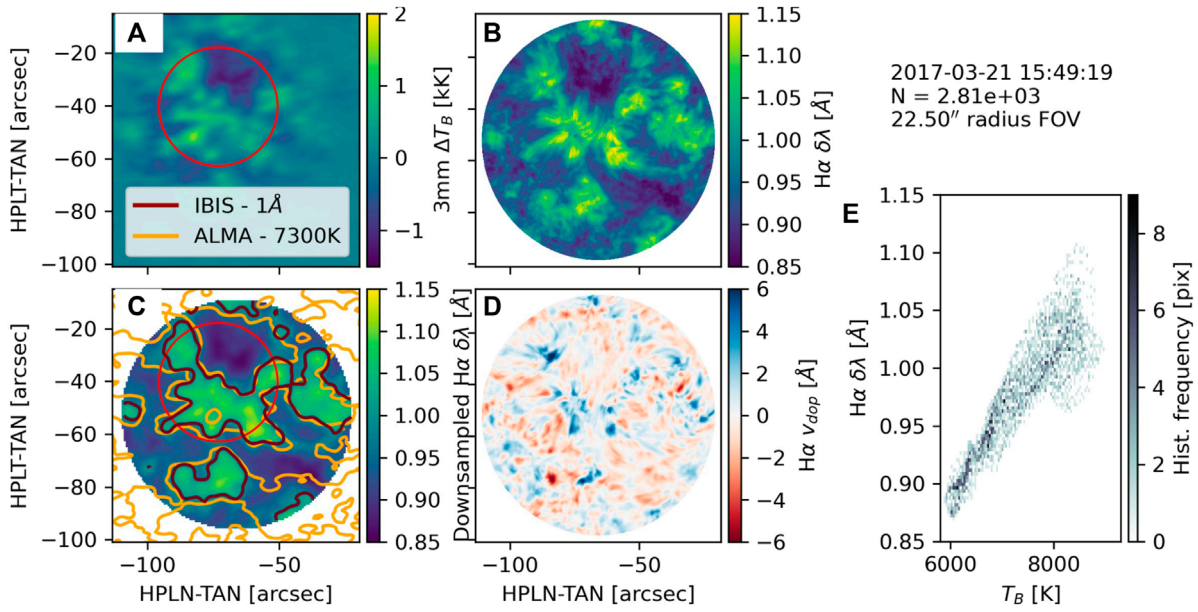

FIGURE 3
Overview of the primary data series used for this study: **(A)** ALMA Band 3 relative brightness temperature ΔT_B; **(B)** full resolution IBIS Hα line width; **(C)** convolved and spatially down-sampled line width; **(D)** full resolution Hα Doppler velocity; and **(E)** the joint probability distribution of brightness temperature and the line width within the 45″ diameter red circle, which is a conservative estimate of the overlapping FOV. **(C)** shows contours of the ALMA 7300 K level (orange) and IBIS 1 Å line width level (dark red). An animation based on **(A–D)** is included in the online material.

they still make the edges of the nominal field of view subject to intermittent data loss[2]. Using a safely smaller field of view, centered on the ALMA beam center, mitigates both of these issues but limits the range of solar features being sampled and consequently can alter the properties of the measured distribution.

In our case, the ALMA FOV is fairly well centered near the north end of the negative polarity on the western side of the underlying magnetic bipole, as seen in Figure 1A, so the area closest to the beam center is slightly biased towards higher temperatures. Immediately north of the beam center is the large, somewhat "W"-shaped region that has the lowest values of temperature, magnetic flux, and line width. The regions of more moderate temperature and line width, with reduced physical contrast, are in fact further out from the ALMA beam center, in the region of reduced instrumental sensitivity. As we increase the area used to generate the distribution, the bimodal lobes in Figure 4B tend to fill in towards each other. The same two-slope character remains, but the "knee" on the bottom side of the distribution becomes even more prominent at the intersection of the two lobes around (−100 K, .95 Å). Note that unlike the ALMA data, there is no *a priori* reason for the IBIS data to trend toward the mean at the edge of the field of view.

In summary, our choice of a 45″ diameter circle to define the cospatial FOV, indicated by the red circle in Figure 3, is our attempt to balance these two competing forms of bias (effects at the edge of the field of view versus uneven sampling of solar features). The most important point is that the main features of the joint distribution $(T_B, \delta\lambda)$ in Figure 4B are essentially unchanged regardless of our chosen field of view, even though the individual underlying 1D distributions can change appreciably: for instance, which peak dominates the Hα line width distribution (.9 Å or 1.05 Å) in panel (c) varies with the FOV as it covers more or less of one of the features. We thus conclude that the bimodal distribution with two different slopes is a real feature of the data, although we are not certain what physical effect would cause it, or if it could be due to some other unknown systematic error.

The joint distributions involving the Doppler velocity also show a change in behavior for the cooler regions versus the hotter regions, Figure 4 Panels (d) and (e). The joint distribution of ALMA with the IBIS Doppler velocity shows essentially no trend below the median ALMA temperature at $\Delta T_B = 0$ and a positive trend above that (Panel d). This same behavior is found in the joint distribution of the IBIS line width and Doppler velocity using only the IBIS data (Panel e), which again gives us confidence that the trend is physical. This may be a signature

2 The solid yellow patch at the bottom of the IBIS FOV in Figure 7A is due to one of these intermittent data losses.

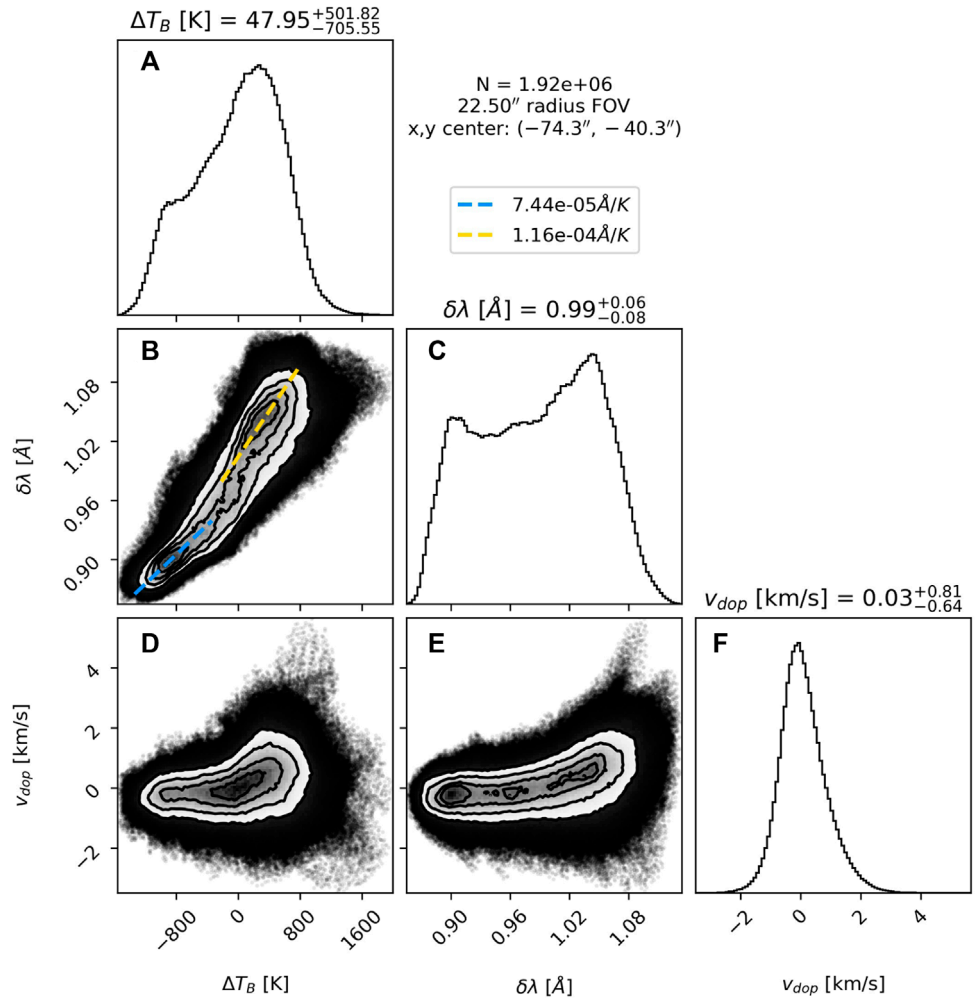

FIGURE 4
1D distribution for the relative Band 3 brightness temperature **(A)**, Hα line width **(C)**, and Hα Doppler velocity **(F)**, and the 2D joint distributions for (ΔT_B,$\delta\lambda$) **(B)** (ΔT_B,v_{dop}) **(D)**, and ($\delta\lambda$,v_{dop}) **(E)**, generated from pixels within a 22.5″ radius from the ALMA beam center. The distributions contain a total of 1.92×10^6 pixels over the 685 joint time steps $\{t_O\}$. The contours in the joint distributions mark the 20% quintiles, e.g., 20% of the data is between each contour, and the remaining 20% (or 3.8×10^5 pixels) are in the outer cloud of individual points. The blue (yellow) dashed lines show fits to the cores of the cooler (hotter) regions. The zero point of the ALMA temperature scale is the average over the data and should be close to the value of 7300 K reported by White et al. (2017).

of hot upflows surrounding magnetic concentrations, possibly with dynamic counterparts, but those details will need to be investigated in a subsequent work.

5 Time series analysis

The IBIS Hα line width data series, with its longer baseline and more continuous coverage, provides a useful reference for understanding the characteristics of the power spectrum of the ALMA 3 mm brightness temperature fluctuations. The ALMA and IBIS data series each have non-uniform temporal sampling due to the intermittent calibration observations (ALMA) and occasional bad atmospheric conditions (IBIS). Both constitute missing data in what are otherwise quite regularly sampled time series, but the character of the missing data is very different between the two data series. For IBIS, the data have short pauses with essentially random spacing and duration, whereas the calibration sequences for ALMA are extensive (3 min) and regular (every 10 min). The latter produces especially strong windowing effects that can significantly affect the interpretation of power spectra generated from the data (VanderPlas, 2018). We therefore used the method of Lomb (1976) and Scargle (1982) as implemented in the astropy.LombScargle package and described in (VanderPlas et al., 2012; VanderPlas and Ivezić, 2015) to estimate the power spectral density (PSD) of each data series. We

calculated the power spectra using the same range of frequencies and spectral bins for all data series, but have verified that this produced identical power spectra to the case of letting the software package algorithmically determine the optimal set of bins.

The astropy package allows for several different normalizations of the PSD. We used the default normalization which, for a time series $s(t)$ sampled at N times $\{t_n\}$, calculates the power spectrum normalized to the total power of the mean subtracted time series:

$$\mathrm{PSD}(f) = \frac{\chi^2_{\mathrm{ref}} - \chi^2(f)}{\chi^2_{\mathrm{ref}}}, \tag{1}$$

$$\text{where} \qquad \chi^2_{\mathrm{ref}} = \sum_n \left\langle (s_n - \langle s \rangle)^2 \right\rangle = \sum_n \langle s_n^2 \rangle - \langle s \rangle^2 \tag{2}$$

is the mean squared deviation, $s_n = s(t_n)$, and $\chi^2(f)$ is the goodness-of-fit of the least-squares fit of a sinusoidal model to the measured data at a given frequency, i.e.

$$\chi^2(f) = \sum_n \Big[s_n - \big[a(f) \sin 2\pi f \big(t_n - \phi_f\big) + b(f) \cos 2\pi f \big(t_n - \phi_f\big) \big] \Big]^2. \tag{3}$$

The standard Lomb-Scargle power spectrum given in Eq. 1 is normalized to the total power in a measured (and mean-subtracted) time series, $\chi^2_{\mathrm{ref}} = \langle s^2 \rangle$ which makes it a measure of the *relative* distribution of power over frequency for a given time series (a single spatial location in the ΔT_B, $\delta\lambda$, or v_{dop} data series). At a given frequency $0 \leq PSD(f) \leq 1$, where 0 would mean that the best-fit model has zero amplitude ($a = b = 0$), and 1 would mean that the entire time series is perfectly fit by a single frequency sinusoid f. For evenly sampled data, the Lomb-Scargle spectrum is related to the Fourier spectrum by

$$\mathrm{PSD}_F(f_i) = \frac{1}{2} \chi^2_{\mathrm{ref}} \mathrm{PSD}(f_i) \tag{4}$$

where $f_i = \frac{i}{T}$ are the typical Fourier frequencies. In this section Figure 5 displays total power in physical units and all the remaining figures use the arbitrary Lomb-Scargle normalized units (ADU).

In Section 5.1, we calculate the spatially averaged power spectra for each data series and compare how temporally downsampling the sets $\{t_A\}$ and $\{t_I\}$ to the set $\{t_O\}$ affects the average power spectra. This analysis provides evidence that at least some of the previously reported lack of oscillatory power in the 3–5 min period range for the 3 mm observations (Jafarzadeh et al., 2021) may be an artifact of the calibration sequences.

We then consider the spatial distribution of oscillatory power computed for each of data series in Section 5.1. Here we see the spatial patterns typically found in other, similar chromospheric data sets. By using temporal and spatial downsampling of the Hα we confirm that the spatial variations in power the ALMA brightness temperature fluctuations follow those for the Hα line width, which provides further evidence that the calibration windows are masking the detection of p-mode power in the ALMA data.

5.1 Spatially averaged power spectra

Figure 5 shows spatial maps of the temporally averaged total fluctuation power for the various data sets in physical units, e.g., $\chi^2_{\mathrm{ref}}(x,y)$ from Eq. 2 evaluated at spatial location (x,y). Panel (a) shows the power in the line width fluctuations, b) in the Doppler velocity, and c) in the brightness temperature, calculated using the full temporal set for each variable ($\{t_I\}$ for IBIS and $\{t_A\}$ for ALMA). Panels (d) and (e) show the average power for the line width and Doppler data using the reduced time series $\{t_O\}$. The spatial average over the FOV for each map is given in the lower right panel of the figure; RMS variations can be obtained by taking the square root of the provided values.

The primary effect of temporally down sampling the IBIS data from $\{t_I\}$ to $\{t_O\}$ is the introduction of the ≈3 min ALMA calibration windows into the IBIS time series. Comparing panels (a) and (d) to (b) and (e), this down sampling appears to have a greater effect on the calculation of power in fluctuations of the line width than for the Doppler velocity. This is borne out by comparing the spatially averaged power in each case, which is reduced by 25% for the former but only 11% for the latter. The power in the ALMA brightness temperature fluctuations bears some resemblance to that of the line width data, particularly the "W" shaped suppressed power near the center of network cell around $(-75'', -30'')$, and some of the brightest kernels in the ALMA data, but the correspondence is not particularly striking.

We next calculated the power spectral density for each of the data series described in Sections 2 and Sections3, i.e., the full resolution ALMA and IBIS data series as well as the temporally and/or spatially down sampled versions of each. We are not concerned with the joint distribution here, so the individual field of view for each instrument was used, as opposed to the 45″ common field of view considered in Section 4. As described by Eq. 1, the power spectrum of a single signal (i.e., a single spatial location) is normalized to its total power. The power spectra at different spatial locations can then be ensemble averaged to determine the relative distribution of power across all frequencies.

Figure 6 shows the spatially averaged power spectral density of the ALMA 3 mm brightness temperature using four different ways of spatially or temporally downsampling the data. The blue curve shows the power spectrum computed using the full temporal cadence $\{t_A\}$ and a 67″ diameter FOV about the beam center. The orange curve is the PSD for the full temporal cadence averaged over a 45″ FOV. The green curve is the PSD

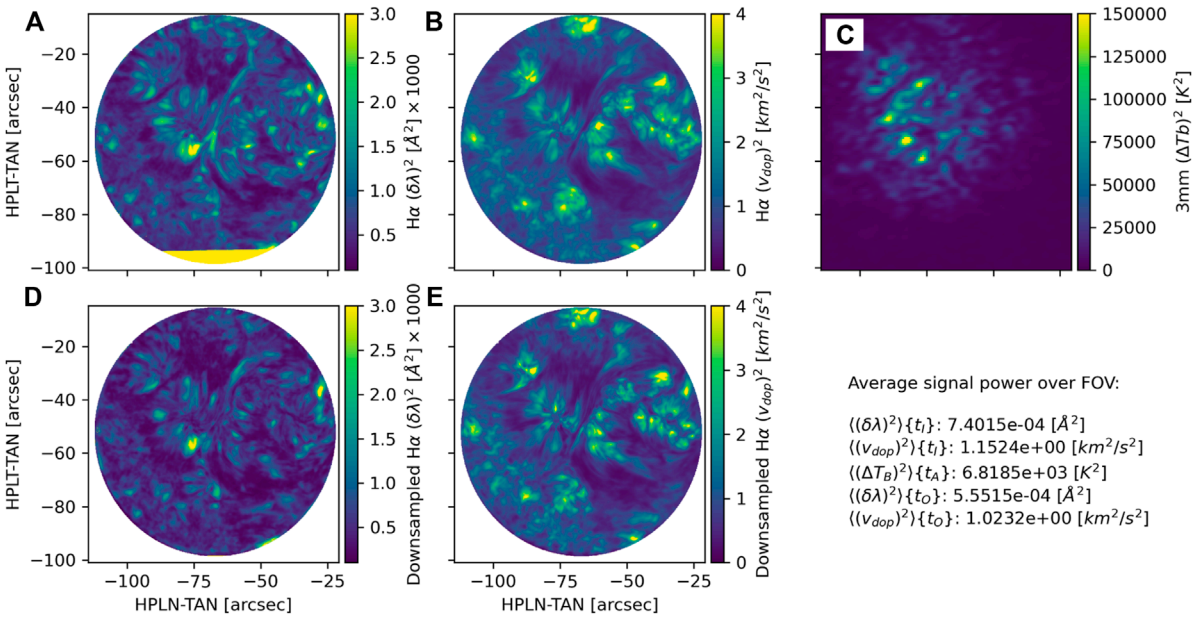

FIGURE 5
Total time-averaged power maps for different data series: **(A)** $\delta\lambda$, **(B)** v_{dop}, **(C)** ΔT_B, each calculated over the respective time series $\{t_I\}$ and $\{t_A\}$. **(D)** and **(E)** repeat the first two panels for the IBIS data, but use the down sampled, overlap time series $\{t_O\}$. The spatially averaged total power is given for each data series in the lower right panel.

calculated with the reduced cadence overlapping time series $\{t_O\}$ and averaged over the 67″ FOV. Finally, the gray curve uses the overlapping set $\{t_O\}$ and smaller FOV.

The power spectra are essentially identical for all cases below about 10 mHz and show an apparent spectral break around 5 mHz, from a shallower to steeper slope. The larger FOV has slightly more power relative to the smaller FOV at high frequencies, above ∼20 mHz. The temporal down sampling has a more dramatic effect, increasing the white-noise floor above about 40 mHz and producing a conspicuous bump at 30 mHz. A similar bump at 30 mHz appears to be present in **Figure 5D** of Chai et al. (2022), which shows power spectra for ALMA in quiet Sun regions. Finally, we note that the strong deviations from the trend at low frequencies, near 1.5 mHz and 2.5 mHz, are artifacts of the time series window function (see VanderPlas (2018)).

In **Figure 7** we repeat the analysis of **Figure 6** for the IBIS Hα line width data with the original resolution and several down sampled versions. The power spectrum for the temporal down sampled ALMA data from **Figure 6** (green curve) is included for context. The black curve is calculated using the IBIS data at full spatial and temporal resolution, the red curve uses the convolved and spatially down sampled IBIS data, and the translucent purple curve uses the spatially and temporally down sampled IBIS data, i.e., IBIS sampled at the ALMA spatial resolution and in the set $\{t_O\}$. Here we see that spatially down sampling has little effect on the power derived from the line width data while temporally down sampling the IBIS data to include the ALMA calibration windows results in power spectral density curves that lie nearly on top of each other. To quantify the above statement, the Pearson correlation coefficient between the temporally-and-spatially down sampled IBIS data and the temporally down sampled ALMA data, i.e., what should be the two most similar data sets, is .9895. For comparison, the correlation coefficient for the full resolution version for each curve (blue line from **Figure 6** to black line from **Figure 7**) is .9731, and the full ALMA series (blue) to spatially reduced IBIS (red) is .9464.

The relative offset between the full temporal IBIS power curve (black or red) and the temporally down sampled power (purple) is due to the standard Lomb-Scargle normalization, which does not include a factor for the number of sampled times N. If present, this factor would differ between the two time series by the ratio of the elements in the set $\{t_I\}$ versus $\{t_O\}$ (that is, 1787 to 685, or roughly 2.6:1), and be uniformly applied over all frequencies, thus producing a constant offset in the log-scaled plot. Because we are currently analyzing only the relative distribution of power over frequency (e.g., the shape of each curve), we opt not to perform any additional normalization when plotting our results in this section. Thus, the difference in number of sampled times from the underlying signal manifests as a constant offset in the log-scaled plots while, at the same time, preserving their shape. In the current context, this actually helps to distinguish between the various power curves: the power spectra resulting from a single continuous signal's time series with two different samplings, but both being well sampled, will be

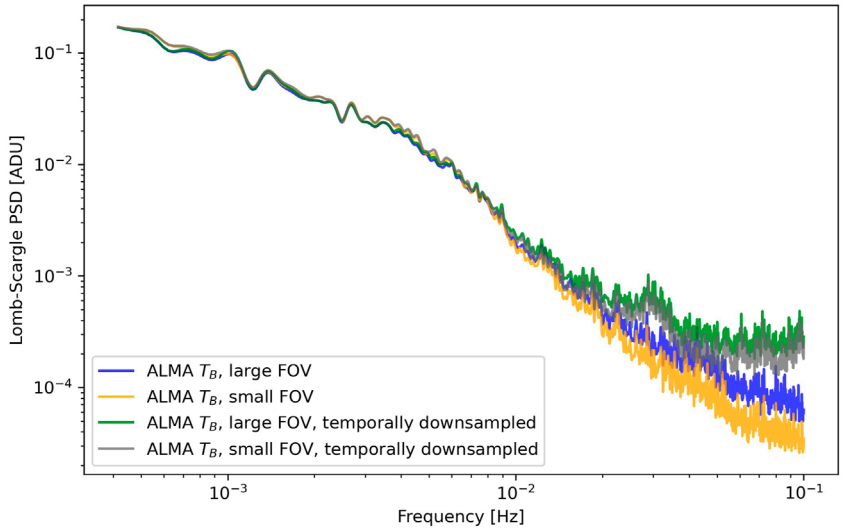

FIGURE 6
Spatially averaged power spectra for different sub-samples of data series. ALMA temperature, large 67″ FOV (blue); ALMA temperature, small 45″ FOV (orange); ALMA temperature large FOV, $\{t_O\}$ (green); ALMA temperature small FOV, $\{t_O\}$ (grey).

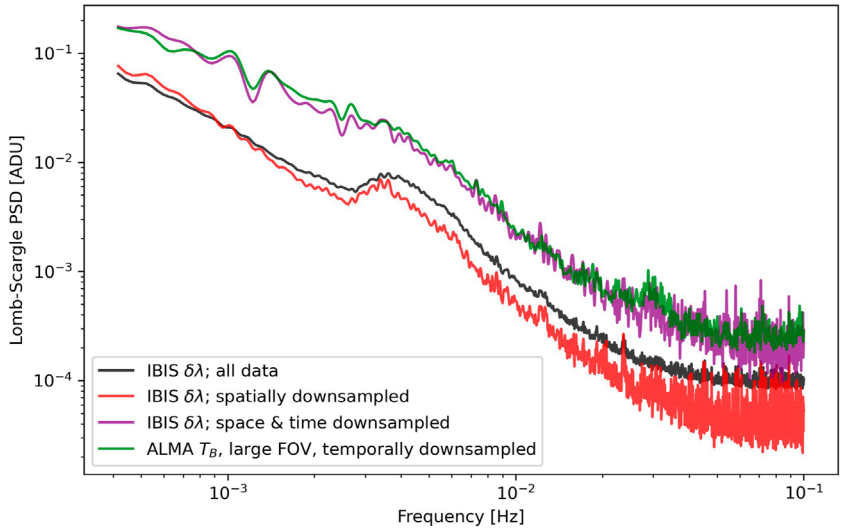

FIGURE 7
Spatially averaged power spectra for different sub-samples of data series. All IBIS line width data (black); spatially down sampled IBIS line width (red); spatially and temporally down sampled IBIS line width (purple); ALMA temporally down sampled temperature 67″ FOV (green).

shifted by the ratio of the sampling, while changes in the shape of the power spectra will be due to under-sampling or windowing effects.

To place each curve on a roughly appropriate physical power scale the relative curves in Figures 6–8 should be divided by the appropriate number of timesteps included in the data set as well as the average power indicated in Figure 5. However, we caution that these temporally unevenly sampled datasets, each of which include some level of spatial coherence that are folded into the spatial average, make a precise calculation of the absolute power a more involved analysis than we are attempting here.

The prominent bump at 4 mHz in the black curve in Figure 7 marks the solar p-mode frequency band in the full resolution Hα line width data. That band contains considerable power across the typical 3 and 5 min oscillation windows. The effect of either spatially or temporally down sampling the data is immediately

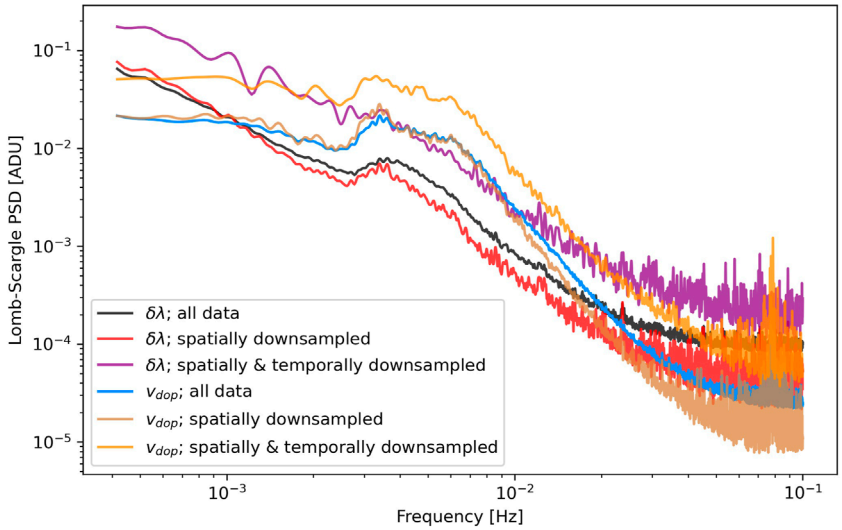

FIGURE 8
Spatially averaged power spectra of the IBIS Doppler velocity time series averaged over the full IBIS field of view for different spatial and temporal sampling schemes. The spectrum derived from the full data set is shown in blue, spatially down sampled in brown (which nearly overlaps the blue line below 10 mHz), and spatially-temporally down sampled in orange. The line width power spectra from **Figure 7** are included for reference.

apparent by comparing the translucent red or purple curves to the black curve. Spatial down sampling the IBIS data does not eliminate the p-mode signal (red), while temporally down sampling the IBIS data does (purple). The temporal down sampling does produce the vertical shift in the line by the ratio of the number of sampled times, as discussed above, while the change in shape is due to undersampling the signal with the new temporal sampling. The temporal down sampling produces a power spectrum that is closely matches the ALMA PSD up to 10 mHz (compare the purple curve to the green curve) and remains well correlated at higher frequencies. Given that the temporal down sampling of ALMA data from 2 to 4 s cadence produced very little change in the resulting power spectrum below ∼10 mHz, this analysis provides strong evidence that the apparent lack of p-modes in the ALMA data is a spectral effect due to the interval and duration of the calibration sequences.

As a final comparison, we calculate the spatially averaged power spectra, including spatially and temporally down sampled versions, of the IBIS Hα Doppler velocity data. The results are shown in **Figure 8** where we also include the curves for the Hα line width for comparison, using the same colors as in **Figure 7**. The power spectrum for the full resolution Doppler data is shown in blue, spatially downsampled in light brown, and both spatially and temporally downsampled in orange. The Doppler velocity power spectra shows markedly different behavior than those for the line width (black, red, purple) or brightness temperature (not shown, but the purple line here is largely the same). The p-mode bump is again prominent in the Doppler data but with a different distribution compared to that in the line width. The temporal down sampling does not appear to suppress the p-modes in the Doppler velocity data as it did for the line width data and, presumably, the ALMA data. However, this may be due to the flat slope of the Doppler power distribution below 2 mHz in the original data combined with the strong apparent oscillations from the windowing function at 1.5 and 2.5 mHz.

5.2 Frequency integrated maps of power spectral density

As mentioned in the introduction, there have been conflicting reports as to how the spatial distribution of power in different frequency bands varies across the ALMA Band 3 field of view. Some authors find substantial variations (Molnar et al., 2021; Chai et al., 2022), others do not (Patsourakos et al., 2020; Narang et al., 2022) or find somewhat ambiguous results (Jafarzadeh et al., 2021). We find ourselves in the former camp, with seemingly well resolved spatial variations in oscillatory power across the field of view. As we will see, the variations in the ALMA brightness temperature align well with those derived from the Hα line width once the two data series were spatially and temporally sampled on the same grids.

In **Figures 9**, **10**, **11**, **12** we show the spatial distribution of power in different temporal frequency bands for each of the data series. **Figure 9** is generated using the full spatio-temporal IBIS Hα Doppler velocity, **Figure 10** the full spatio-temporal IBIS Hα line width, **Figure 11** the ALMA Band3 brightness temperature, and **Figure 12** the IBIS Hα line width after spatial convolution

and interpolation to the ALMA resolution and pixel locations. The sub-panels in each figure show the frequency-integrated power in the ranges: (a) .42–2.78 mHz, (b) 2.78–4.16 mHz, (c) 4.16–8.33 mHz, (d) 2.78–8.33 mHz, (e) 8.33–10 mHz, (f) 10–40 mHz, and (g) 40–100 mHz. Phenomenologically, these bands correspond to (a) low frequencies, (b) the 5 min p-modes, (c) the 3 min p-modes, (d) the total p-mode range, and (e, f, g) three higher frequency bands that attempt to capture the transition from evanescent waves just above the acoustic cutoff (if one can reasonably be defined) to more freely propagating MHD waves in regimes where the WKB[3] approximation is expected to hold, e.g., where the characteristic wavelength of a disturbance is smaller than the typical gradient scale of the medium.

Comparing the Doppler velocity power in different frequency bands in **Figure 9** makes it immediately apparent how the different dynamics correspond to different features on the Sun. The distribution of power in the low frequency band shown in Panel (a) is essentially the inverse of that found in the 5 mHz (c) and higher bands. The areas of highest power at low frequency lie above the stronger network magnetic flux concentrations that can be seen in HMI or Hinode/SP observations (see **Figure 1** and Kobelski et al. (2022); **Figure 2**) but cover a much larger physical area as the magnetic field expands to form the magnetic canopy in the chromosphere. These same regions have suppressed power at higher frequencies, at least up to 40 mHz in panel (f), though this trend has essentially disappeared above that frequency, as seen in panel (g). These features are well known and define the so-called magnetic shadows and acoustic halos (Braun et al., 1992; Brown et al., 1992; Judge et al., 2001; Vecchio et al., 2007; Vecchio et al., 2009). We note that the largest, strongest region does show a compact suppression of power at its center near $(-75'', -50'')$ in the lowest frequency bin, as seen in panel (a), but this behavior in the other magnetic patches is less conclusive.

The distribution of power in the line width data, **Figure 10**, shows a much different pattern. Here the most prominent concentrations of power are seen in the 5 mHz band in the quiet Sun regions to the southeast of the central magnetic bipole. This is also the region with rather moderate line widths, not the large line width regions surrounding the network flux patches, nor the very narrow width region immediately north of the central bipole (**Figure 3**). The strong power in the quiet Sun regions is likely due to acoustic shocks (Vecchio et al., 2009).

The final two figures in this section show the spatial power maps for the ALMA 3 mm brightness temperature, in **Figure 11**, and the convolved, downsampled IBIS Hα line width, in **Figure 12**. According to our results in §4 and §5.1, these two figures should be very similar, and indeed they are. The ALMA data in Panel (a) at low frequencies show a slight enhancement in the central portion of the field of view relative to the surrounding area. This pattern is consistent with the full resolution IBIS Hα line width data in **Figure 10A** and the interpolated data in **Figure 12A**. In contrast, the V-shaped (or heart-shaped) central area of the ALMA field of view shows lesser power than the surrounding areas in all the frequency bands above 3 mHz, panels (b–f). Again, this same pattern is visible in the PSD maps of the sub-sampled IBIS data in bands up to 10 mHz, **Figures 12B–E**, but becomes less apparent the two higher frequency bands. This behavior is consistent with the spatially averaged spectra in **Figure 6**, where the ALMA and IBIS data series match well up to around 10 mHz, then diverge (compare the purple curve to either the blue or orange curve).

At the highest temporal frequencies we consider in **Figure 11G**, the ALMA data shows a strong radial pattern that appears dominated by the sensitivity of the spatial reconstruction more than anything else. Still, some of the features continue to line up between the ALMA and IBIS PSD maps, such as the compact high power point near $(-50'', -40'')$ that is discernable in panels (f) and (g) of **Figures 10–12**.

6 Discussion

We have confirmed the result of Molnar et al. (2019) that the 3 mm brightness temperature and Hα line width are strongly correlated. We find a bimodal distribution in the 2D histogram of these variables, corresponding to hotter network regions and cooler internetwork regions. The Hα line width increases more steeply with respect to the ALMA brightness temperature in hotter regions than in the cooler regions. The slope that we find is different than Molnar et al. (2019), and some change in slope might be due to the different definition of the Hα line width from the IBIS data. The slope and clustering may depend on the variety of observed solar features in the two sets of observations. Our modest network patch, located very close to disk center, has a greatly reduced range of observed ALMA temperatures compared to the somewhat stronger network patch near an active region studied in Molnar et al. (2019) and Molnar et al. (2021). Understanding the underlying reason for the significant variation in the range of observed temperatures in Band 3, even for relatively similar solar features, will require further investigation.

Our use of the intensity at ±.75 Å to set the upper "continuum" threshold introduces crosstalk in the Hα line width measurement when the line is sufficiently broad to suppress the wing intensity at those wavelengths. This appears to cause the metric to saturate at a maximum line width of around 1.2 Å, but also an increasing reduction of the expected line width values for widths above 1.0 Å. The saturation is clearly evident when reprocessing the Molnar et al. (2019) data (from April 2017) to

3 See Weinberg (Weinberg, 1962) for a complete description of applying Wentzle-Kramers-Brillouin approximation to the MHD equations.

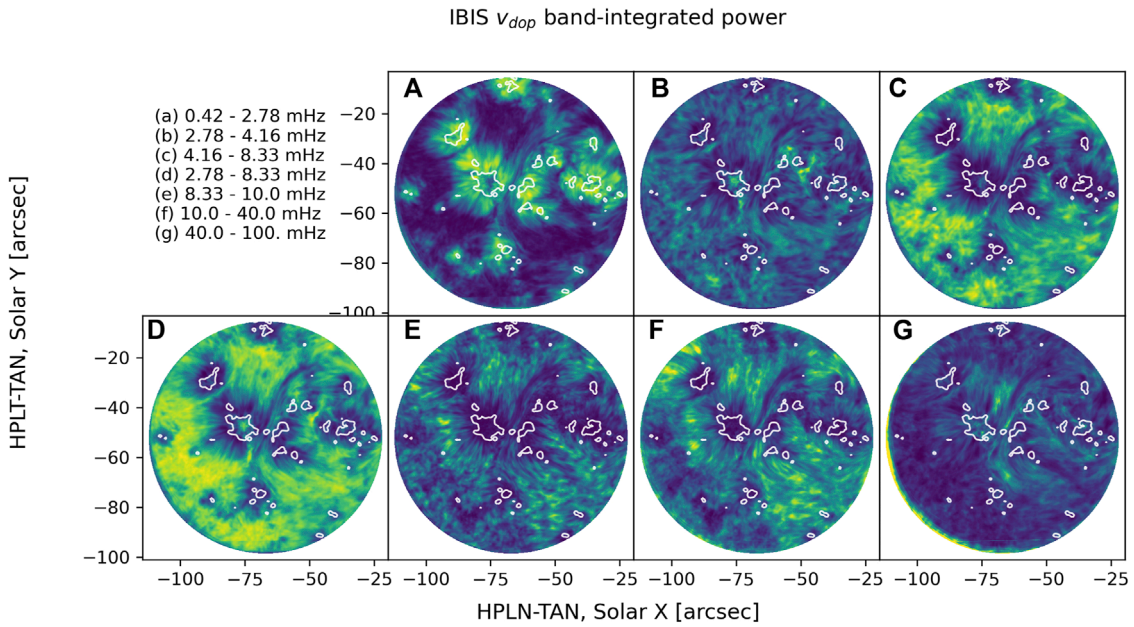

FIGURE 9
Spatial maps of the frequency-integrated power spectral density of the IBIS Hα Doppler velocity over the seven frequency bands indicated in the upper left. These bands correspond to: **(A)** low frequencies; **(B)** 5 min oscillations; **(C)** 3 min oscillations; **(D)** combined p-modes; **(E)** near-cutoff; **(F)** mid frequencies; **(G)** high frequencies. The spatial coordinates correspond to the solar position at the beginning of the ALMA observations at 2017-03-21 15:42:13 UT. Note that the color scale is adjusted separately for each panel as the data span ≈40 dB. Higher power is bright yellow, lower power is dark blue. The white lines are the 50 G contours of unsigned LOS magnetic flux from HMI.

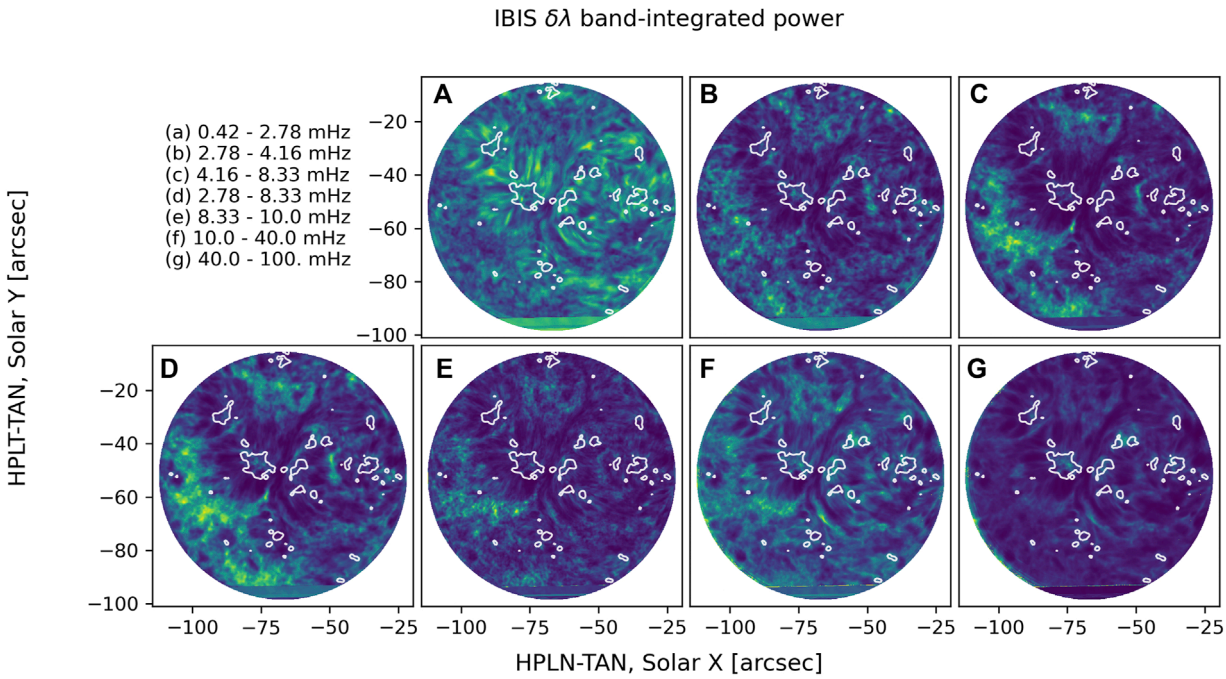

FIGURE 10
The same as **Figure 9** but for the full temporal and spatial resolution IBIS Hα line width. The frequency bands correspond to: **(A)** low frequencies; **(B)** 5 min oscillations; **(C)** 3 minute oscillations; **(D)** combined p-modes; **(E)** near-cutoff; **(F)** mid frequencies; **(G)** high frequencies.

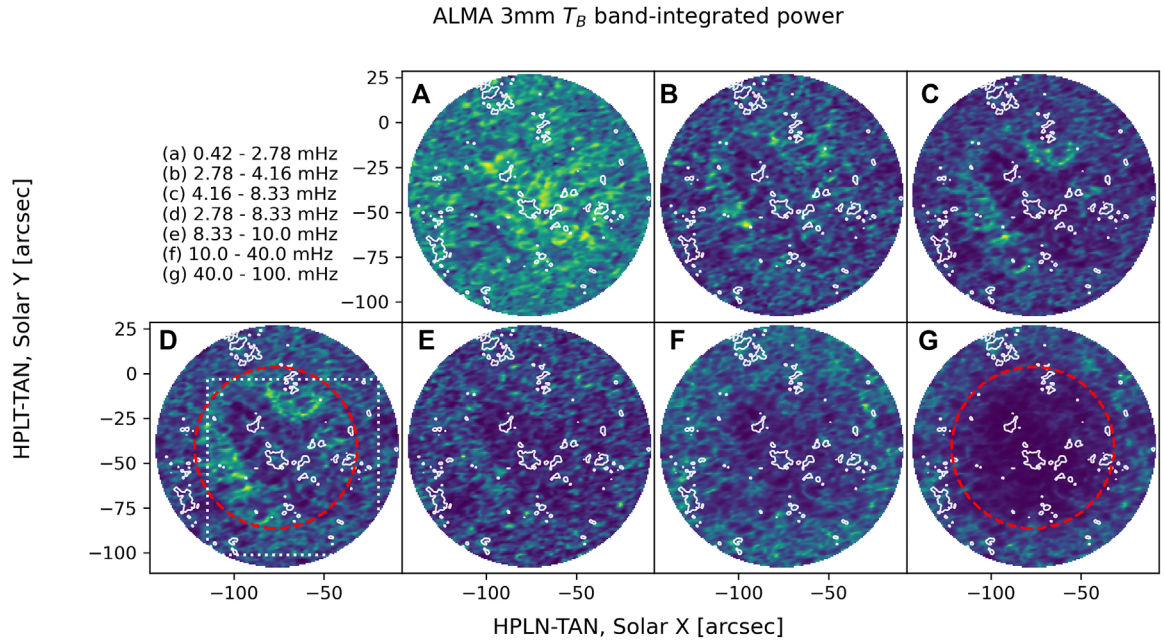

FIGURE 11
Same as **Figure 9** but for the ALMA 3 mm brightness temperature and a slightly larger field of view. The outer boundary has a $67''$ radius while the red dashed circle shows a $45''$ diameter, both relative to the ALMA beam center. The white dotted rectangle in **(D)** indicates the IBIS FOV. The frequency bands correspond to: **(A)** low frequencies; **(B)** 5 min oscillations; **(C)** 3 minute oscillations; **(D)** combined p-modes; **(E)** near-cutoff; **(F)** mid frequencies; **(G)** high frequencies.

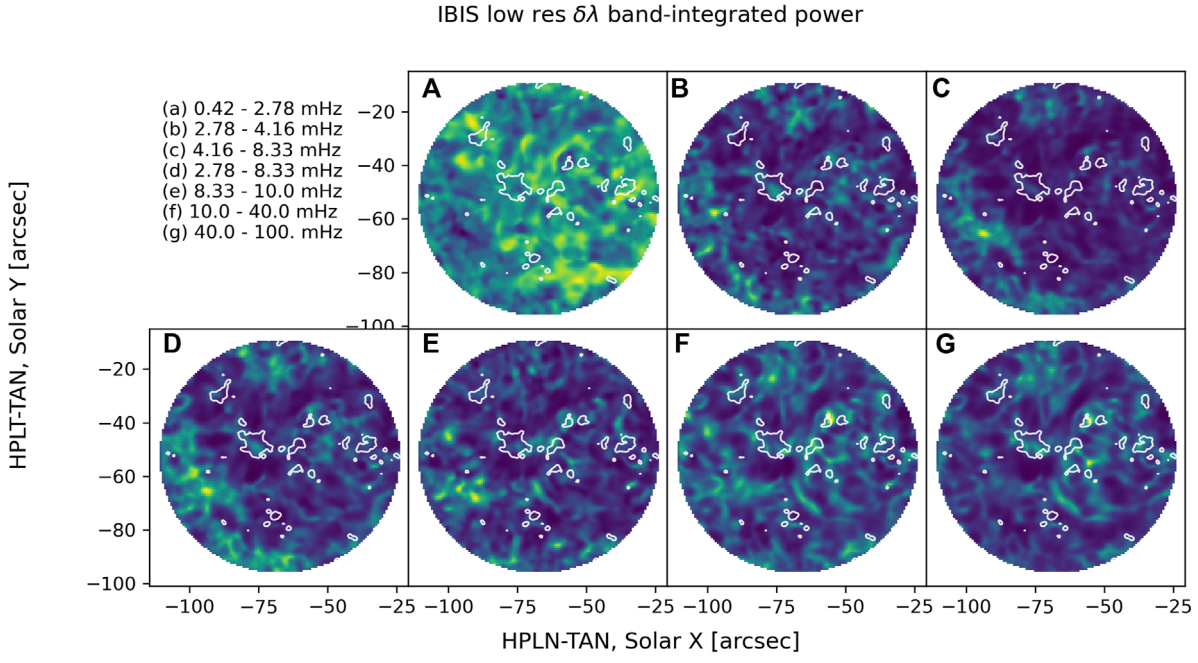

FIGURE 12
Same as **Figure 11** but for the IBIS line width data spatially convolved and downsampled to match ALMA, and temporally subsampled to the overlapping times $\{t_O\}$. The frequency bands correspond to: **(A)** low frequencies; **(B)** 5 min oscillations; **(C)** 3 minute oscillations; **(D)** combined p-modes; **(E)** near-cutoff; **(F)** mid frequencies; **(G)** high frequencies.

more closely match the data and line-fitting parameters in the current analysis. However, the greatly reduced temperature range of the March 2017 data series appears to stay mostly in the linear regime. This makes a direct comparison between the two data sets difficult to interpret. In general, using the wing intensity at ± 1.0 Å or greater in the calculation of the line width is generally preferred as it avoids this saturation effect.

What is certain, despite the disparities just discussed, is that the ALMA Band 3 brightness temperature and Hα are strongly correlated diagnostics. That good correlation provided us with an independent reference to help separate systematic effects in the ALMA data from observed solar behavior in the subsequent power spectral analysis. In particular, we have attempted to address the confusing melange of reports of oscillatory power in the ALMA Band 3 data. In summary, we found:

- When averaged over space, the p-modes are only clearly visible in the IBIS Hα data, and show up clearly in the power spectra of both $\delta\lambda$ and v_{dop}.
- Spatially down sampling IBIS $\delta\lambda$ data to ALMA spatial resolution does not remove p-mode signature.
- Temporally down sampling IBIS $\delta\lambda$ data does remove the obvious p-mode signature.
- The preceding steps make the spatially averaged $\delta\lambda$ and the T_B power spectra match extremely well, especially below 10 mHz.
- Both the spatially averaged ALMA PSD curve and the spatially resolved power maps show little difference for the full versus temporally overlapping subsets below 15 mHz; e.g., temporally downsampling from ∼2 to ∼4 seconds does not significantly alter the ALMA power spectra.
- The spatial maps of ALMA oscillatory power match the maps of spatially and temporally downsampled Hα line width power.
- A conspicuous bump at 30 mHz is present in the temporally downsampled ALMA data, but in no other data series in our data set. It does seem to be present in the average quiet Sun PSD reported in **Figure 5D** of Chai et al. (2022), and in the network flux near an active region reported in Molnar et al. (2021).

In §5.1 we showed that for our data series the lack of significant power in the p-mode bands in the ALMA data is consistent with it being an artifact of the temporal sampling, particularly the duration and spacing of the calibration windows. This conclusion is based on the transition from a clear p-mode signal in the full Hα $\delta\lambda$ power spectrum, as calculated over the entire time series, to a lack of such signature after applying the ALMA calibration windows to the Hα data and then recomputing the spatially averaged power spectrum. The latter now closely matches the ALMA spectrum, as shown in **Figure 7**. This result likely holds for other data series as well. Our conclusion required the combination of the 3 mm brightness temperature and the more continuous Hα line width data.

It is clear from **Figures 12B–D** that the strongest concentrations of p-mode power in the IBIS H α δ λ data are in the quiet Sun just outside the network flux regions, following the typical magnetic shadow/acoustic halo pattern (Braun et al., 1992; Brown et al., 1992; Rajaguru et al., 2013). While less clear in the lower resolution ALMA data, we find that the spatial variation of p-mode power is still present. Loukitcheva et al. (2004) predicted strong p-mode signals at sub-mm wavelengths in non-magnetic atmospheres. This was seemingly confirmed by observations with the BIMA (Loukitcheva et al., 2006). With the preceding arguments, we find that it holds in our data series as well. Significantly, we find spatial distributions in the 3 mm power, and these vary with frequency band in tandem with the line width power maps. Contrarily, Patsourakos et al. (2020) reported no such spatial variation in their band-integrated power maps (see discussion immediately preceding their §2.1).

Chai et al. (2022) found unambiguous detection of 3 min oscillations in sunspot umbra, but not the surrounding penumbra or quiet Sun in the ALMA data. In contrast, cotemporal Hα observations also displayed clear 5 min oscillations in the penumbra, but unfortunately did not extend into the quiet Sun. The ALMA observations had 3.6 min calibration scans in between 10.25 min blocks of on-target observations, similar to our own, which suggests that the lack of a prominent p-mode signature in the quiet Sun could be due to the calibration sequences. However, this could also be influenced by proximity to the sunspot, whose magnetic canopy has a much larger extent compared to our humble bipolar network patch.

Jafarzadeh et al. (2021) provide extensive examples of Lomb-Scargle power spectral density similar to what we have presented in this work. Their examples cover both ALMA Band 3 and Band 6 observations and a wide variety of solar targets. Their power spectra display a similar knee, or apparent spectral break, to that seen in **Figure 6** with no obvious peak at the p-mode frequencies for eight out of the 10 datasets they analyzed (see their **Figure 11**). They attribute the lack of clear p-mode signals to the spatial distribution of strong magnetic elements in and around the FOV in the majority of their datasets: "While we discussed above various possible scenarios to explain these oscillatory behaviours, we conjecture that the lack of 3-min (5.5 mHz) oscillations may be a result of (a) the "umbrella" effect due to the magnetic canopy, (b) power suppression in the presence of strong magnetic fields, (c) significant variations in the height of formation, or (d) waves not displaying temperature fluctuations at these frequencies".

We do find some enhanced p-mode power in our ALMA data in the quiet regions just outside of magnetic network

concentrations, as seen in **Figure 11D**. The magnetic field in the present data set is not markedly different from some of the data sets for which Jafarzadeh et al. (2021) reported a lack of p-mode oscillations. The higher resolution and complementary view provided by the map of PSD derived from the Hα $\delta\lambda$ in **Figure 10D** shows more clearly the familiar pattern of power shadows and halos centered on the magnetic concentrations (Braun et al., 1992; Brown et al., 1992; Judge et al., 2001; Vecchio et al., 2007; Vecchio et al., 2009; Rajaguru et al., 2013). Comparing **Figures 9–11**, the exact pattern of shadows and halos depends on the frequency band of the map and physical properties of the diagnostic, e.g., oscillations in velocity versus intensity, and formation height. In the p-mode band for all diagnostics we find some power at the very center of the strong magnetic patches, surrounded by the lower power shadow, and the strongest power in the quiet regions surrounding the shadows. This is most evident for the strongest magnetic element in our FOV, the negative footpoint of the central bipole at $(-75, -50'')$. In terms of oscillatory power, our small bipolar region acts like a miniature active region, despite the fact that the magnetic concentrations are not strong or large enough to produce even a micropore. Again, this is consistent with previous work (Vecchio et al., 2007). In contrast, Patsourakos et al. (2020) did not find evidence for shadows or halos in their band-integrated power maps, and Narang et al. (2022) also found little spatial variation in the maps of oscillatory power across the field of view in their Band 6 observations targeting a region of plage. While we have not studied Band6 data, given our findings for the Band 3 data, it is possible that the calibration sequences have affected their results.

7 Conclusion

We presented results that combine optical and millimeter wavelength diagnostics using several of the publicly available data series described in Kobelski et al. (2022) and accessible at https://share.nso.edu/shared/dkist/ltarr/kolsch/. By undertaking a joint analysis of two related diagnostics, namely the ALMA Band 3 brightness temperature and the IBIS Hα line width, we found evidence that the previously reported lack of observed p-modes in at least some of the ALMA Band 3 data may be an artifact of the temporal sampling. While we cannot conclusively demonstrate that p-modes are present in our ALMA Band 3 observations, our combined findings of their clear presence in the Hα data, the strong correspondence in the spatially-averaged Hα and ALMA PSDs, and the strong correspondence between the two diagnostics in band-integrated spatial maps are all highly suggestive. This result provides strong motivation for adjusting the operational model for solar observations with ALMA from what was done in Cycle-4. Calibration windows could be shorter and/or less frequent, albeit with an impact on the reliability of the phase corrections. Alternatively, semi-random spacing of calibration windows would reduce temporal windowing artifacts. We also find that spatially resolved maps of oscillatory power in Band 3 data integrated over temporal frequency bands do reveal suppression of power near magnetic concentrations and (slight) enhancements outside of those suppression regions. Given the weakness magnetic field, it is not yet obvious what magnetic configuration is associated with the enhancements.

The spatial pattern in the power maps of the ALMA data correspond well to maps of power generated from the spatially downsampled Hα line width data. However, the variance in the spatial distribution of power is much lower in the downsampled Hα data compared to the original data. Given the strong correlation between the line width and brightness temperature and the nearly equivalent spatially-averaged power spectra of the two data sets once placed on the same spatial and temporal grids, we believe that our identification of magnetic shadows and power halos around the network concentrations in the ALMA data is correct.

Data availability statement

Publicly available datasets were analyzed in this study. This data can be found here: https://share.nso.edu/shared/dkist/ltarr/kolsch/.

Author contributions

Funding for this project was secured by AK (principal investigator) with LT and SJ. The majority of the data analysis was carried out by LT, with supporting data analysis by SJ, KR, AK, MM, and GC. The manuscript was prepared by LT with supporting work from SJ and AK. All authors participated in discussion of the analysis and were responsible for reading and editing the manuscript.

Funding

The work of LT, AK, and SJ was supported in part by NASA Heliophysics Supporting Research grant 80NSSC19K0118. LT, SJ, MM, GC, and KR were supported by the National Solar Observatory (NSO). NSO is managed by the Association of Universities for Research in Astronomy, Inc., and is funded by the National Science Foundation. MM was supported for part of this work by a FINESST fellowship with grant number 80NSSC20K1505 and by the DKIST Ambassador Program, funding for which is provided by the National Solar Observatory,

a facility of the National Science Foundation, operated under Cooperative Support Agreement number AST-1400405. KR also acknowledges the support of NASA under the grant 80NSSC20K1282.

Acknowledgments

The authors thank Nicholas Luber for their help in previous work calibrating the ALMA data used here. This paper makes use of the following ALMA data: ADS/JAO. ALMA#2016.1.00788.S. ALMA is a partnership of ESO (representing its member states), NSF (United States) and NINS (Japan), together with NRC (Canada), MOST and ASIAA (Taiwan), and KASI (Republic of Korea), in cooperation with the Republic of Chile. The Joint ALMA Observatory is operated by ESO, AUI/NRAO and NAOJ. Data in this publication were obtained with the Dunn Solar Telescope of the National Solar Observatory, which is operated by the Association of Universities for Research in Astronomy, Inc., under cooperative agreement with the National Science Foundation. This research has made use of NASA's Astrophysics Data System Bibliographic Services. Analysis was carried out primarily in the Python programming language and made use of the AstroPy (Astropy Collaboration Robitaille et al., 2013; Price-Whelan et al., 2018) and SunPy (The SunPy Community Barnes et al., 2020) packages. Figures were prepared using Matplotlib (Hunter, 2007).

Conflict of interest

The authors declare that the research was conducted in the absence of any commercial or financial relationships that could be construed as a potential conflict of interest.

Publisher's note

All claims expressed in this article are solely those of the authors and do not necessarily represent those of their affiliated organizations, or those of the publisher, the editors and the reviewers. Any product that may be evaluated in this article, or claim that may be made by its manufacturer, is not guaranteed or endorsed by the publisher.

Supplementary material

The Supplementary Material for this article can be found online at: https://www.frontiersin.org/articles/10.3389/fspas.2022.978405/full#supplementary-material

References

Alissandrakis, C. E., Nindos, A., Bastian, T. S., and Patsourakos, S. (2020). Modeling the quiet Sun cell and network emission with ALMA. *Astronomy Astrophysics* 640, A57. doi:10.1051/0004-6361/202038461

Astropy, C., Robitaille, T. P., Tollerud, E. J., Greenfield, P., Droettboom, M., Bray, E., et al. (2013). Astropy: A community Python package for astronomy. *Astronomy Astrophysics* 558, A33. doi:10.1051/0004-6361/201322068

Braun, D. C., Lindsey, C., Fan, Y., and Jefferies, S. M. (1992). Local acoustic diagnostics of the solar interior. *Astrophysical J.* 392, 739. doi:10.1086/171477

Bray, R. J., and Loughhead, R. E. (1974). *The solar chromosphere*. Chapman & Hall.

Brown, T. M., Bogdan, T. J., Lites, B. W., and Thomas, J. H. (1992). Localized sources of propagating acoustic waves in the solar photosphere. *Astrophysical Journall* 394, L65. doi:10.1086/186473

Cauzzi, G., Reardon, K., Rutten, R. J., Tritschler, A., and Uitenbroek, H. (2009). The solar chromosphere at high resolution with IBIS. IV. Dual-line evidence of heating in chromospheric network. *Astronomy Astrophysics* 503, 577–587. doi:10.1051/0004-6361/200811595

Cavallini, F. (2006). IBIS: A new post-focus instrument for solar imaging spectroscopy. *Sol. Phys.* 236, 415–439. doi:10.1007/s11207-006-0103-8

Chai, Y., Gary, D. E., Reardon, K. P., and Yurchyshyn, V. (2022). A study of sunspot 3 minute oscillations using ALMA and GST. *Astrophysical J.* 924, 100. doi:10.3847/1538-4357/ac34f7

Foreman-Mackey, D. (2016). corner.py: Scatterplot matrices in python. *J. Open Source Softw.* 1, 24. doi:10.21105/joss.00024

Hills, R. E., Kurz, R. J., and Peck, A. B. (2010). Alma: Status report on construction and early results from commissioning. *Ground-based Airborne Telesc. III Proc. SPIE* 7733, 773317. doi:10.1117/12.857017

Hunter, J. D. (2007). Matplotlib: A 2d graphics environment. *Comput. Sci. Eng.* 9, 90–95. doi:10.1109/MCSE.2007.55

Jafarzadeh, S., Wedemeyer, S., Fleck, B., Stangalini, M., Jess, D. B., Morton, R. J., et al. (2021). An overall view of temperature oscillations in the solar chromosphere with ALMA. *Philosophical Trans. R. Soc. Lond. Ser. A* 379, 20200174. doi:10.1098/rsta.2020.0174

Judge, P. G., Tarbell, T. D., and Wilhelm, K. (2001). A study of chromospheric oscillations using the SOHO and TRACE spacecraft. *Astrophysical J.* 554, 424–444. doi:10.1086/321383

Khomenko, E., and Calvo Santamaria, I. (2013). Magnetohydrodynamic waves driven by p-modes. *J. Phys. Conf. Ser.* 440, 012048. doi:10.1088/1742-6596/440/1/012048

Kobelski, A. R., Tarr, L. A., Jaeggli, S. A., Luber, N., Warren, H. P., and Savage, S. (2022). A publicly available multiobservatory data set of an enhanced network patch from the photosphere to the corona. *Astrophysical J. Suppl. Ser.* 261, 15. doi:10.3847/1538-4365/ac6b3b

Kuhar, M., Krucker, S., Glesener, L., Hannah, I. G., Grefenstette, B. W., Smith, D. M., et al. (2018). NuSTAR detection of X-ray heating events in the quiet sun. *Astrophysical Journall* 856, L32. doi:10.3847/2041-8213/aab889

Leake, J. E., DeVore, C. R., Thayer, J. P., Burns, A. G., Crowley, G., Gilbert, H. R., et al. (2014). Ionized plasma and neutral gas coupling in the sun's chromosphere and earth's ionosphere/thermosphere. *Space Sci. Rev.* 184, 107–172. doi:10.1007/s11214-014-0103-1

Lomb, N. R. (1976). Least-squares frequency analysis of unequally spaced data. *Astrophysical J. Suppl. Ser.* 39, 447–462. doi:10.1007/BF00648343

Loukitcheva, M., Solanki, S. K., Carlsson, M., and Stein, R. F. (2004). Millimeter observations and chromospheric dynamics. *Astronomy Astrophysics* 419, 747–756. doi:10.1051/0004-6361:20034159

Loukitcheva, M., Solanki, S. K., and White, S. (2006). The dynamics of the solar chromosphere: Comparison of model predictions with millimeter-interferometer observations. *Astronomy Astrophysics* 456, 713–723. doi:10.1051/0004-6361:20053171

Molnar, M. E., Reardon, K. P., Chai, Y., Gary, D., Uitenbroek, H., Cauzzi, G., et al. (2019). Solar chromospheric temperature diagnostics: A joint ALMA-hα analysis. *Astrophysical J.* 881, 99. doi:10.3847/1538-4357/ab2ba3

Molnar, M. E., Reardon, K. P., Cranmer, S. R., Kowalski, A. F., Chai, Y., and Gary, D. (2021). High-frequency wave power observed in the solar chromosphere with IBIS and ALMA. *Astrophysical J.* 920, 125. doi:10.3847/1538-4357/ac1515

Narang, N., Chandrashekhar, K., Jafarzadeh, S., Fleck, B., Szydlarski, M., and Wedemeyer, S. (2022). Power distribution of oscillations in the atmosphere of a plage region. Joint observations with ALMA, IRIS, and SDO. *Astronomy Astrophysics* 661, A95. doi:10.1051/0004-6361/202142080

Nindos, A., Patsourakos, S., Alissandrakis, C. E., and Bastian, T. S. (2021). ALMA observations of the variability of the quiet Sun at millimeter wavelengths. *Astronomy Astrophysics* 652, A92. doi:10.1051/0004-6361/202141241

Parker, E. N. (1988). Nanoflares and the solar X-ray corona. *Astrophysical J.* 330, 474. doi:10.1086/166485

Patsourakos, S., Alissandrakis, C. E., Nindos, A., and Bastian, T. S. (2020). Observations of solar chromospheric oscillations at 3 mm with ALMA. *Astronomy Astrophysics* 634, A86. doi:10.1051/0004-6361/201936618

Price-Whelan, A. M., Sipőcz, B. M., Günther, H. M., Lim, P. L., Crawford, S. M., Conseil, S., et al. (2018). The astropy project: Building an open-science project and status of the v2.0 core package. *Astronomical J.* 156, 123. doi:10.3847/1538-3881/aabc4f

Rajaguru, S. P., Couvidat, S., Sun, X., Hayashi, K., and Schunker, H. (2013). Properties of high-frequency wave power halos around active regions: An analysis of multi-height data from HMI and AIA onboard SDO. *Sol. Phys.* 287, 107–127. doi:10.1007/s11207-012-0180-9

Scargle, J. D. (1982). Studies in astronomical time series analysis. II. Statistical aspects of spectral analysis of unevenly spaced data. *Astrophysical J.* 263, 835–853. doi:10.1086/160554

Shimizu, T., Shimojo, M., and Abe, M. (2021). Simultaneous ALMA-hinode-IRIS observations on footpoint signatures of a soft X-ray loop-like microflare. *Astrophysical J.* 922, 113. doi:10.3847/1538-4357/ac27a4

SunPy, C., Barnes, W. T., Bobra, M. G., Christe, S. D., Freij, N., Hayes, L. A., et al. (2020). The sunpy project: Open source development and status of the version 1.0 core package. *Astrophysical J.* 890(1), 68. doi:10.3847/1538-4357/ab4f7a

VanderPlas, J., Connolly, A. J., Ivezic, Z., and Gray, A. (2012). "Introduction to astroML: Machine learning for astrophysics," in Proceedings of Conference on Intelligent Data Understanding (Piscataway, NJ: IEEE), 47–54. doi:10.1109/CIDU.2012.6382200

VanderPlas, J. T., and Ivezić, Ž. (2015). Periodograms for multiband astronomical time series. *Astrophysical J.* 812, 18. doi:10.1088/0004-637X/812/1/18

VanderPlas, J. T. (2018). Understanding the lomb-scargle periodogram. *Astrophysical Journals* 236, 16. doi:10.3847/1538-4365/aab766

Vecchio, A., Cauzzi, G., Reardon, K. P., Janssen, K., and Rimmele, T. (2007). Solar atmospheric oscillations and the chromospheric magnetic topology. *Astronomy Astrophysics* 461, L1–L4. doi:10.1051/0004-6361:20066415

Vecchio, A., Cauzzi, G., and Reardon, K. P. (2009). The solar chromosphere at high resolution with IBIS. II. Acoustic shocks in the quiet internetwork and the role of magnetic fields. *Astronomy Astrophysics* 494, 269–286. doi:10.1051/0004-6361:200810694

Wedemeyer, S., Bastian, T., Brajša, R., Hudson, H., Fleishman, G., Loukitcheva, M., et al. (2016). Solar science with the Atacama large millimeter/submillimeter array—a new view of our sun. *Space Sci. Rev.* 200, 1–73. doi:10.1007/s11214-015-0229-9

Wedemeyer, S., Szydlarski, M., Jafarzadeh, S., Eklund, H., Guevara Gomez, J. C., Bastian, T., et al. (2020). The Sun at millimeter wavelengths. I. Introduction to ALMA Band 3 observations. *Astronomy Astrophysics* 635, A71. doi:10.1051/0004-6361/201937122

Weinberg, S. (1962). Eikonal method in magnetohydrodynamics. *Phys. Rev.* 126, 1899–1909. doi:10.1103/PhysRev.126.1899

White, S. M., Iwai, K., Phillips, N. M., Hills, R. E., Hirota, A., Yagoubov, P., et al. (2017). Observing the sun with the Atacama large millimeter/submillimeter Array (ALMA): Fast-scan single-dish mapping. *Sol. Phys.* 292, 88. doi:10.1007/s11207-017-1123-2

Wootten, A., and Thompson, A. R. (2009). The Atacama large millimeter/submillimeter Array. *IEEE Proc.* 97, 1463–1471. doi:10.1109/JPROC.2009.2020572

frontiers | Frontiers in Astronomy and Space Sciences

TYPE Review
PUBLISHED 04 October 2022
DOI 10.3389/fspas.2022.981205

OPEN ACCESS

EDITED BY
Mario J. P. F. G. Monteiro,
University of Porto, Portugal

REVIEWED BY
João M. da Silva Santos,
National Solar Observatory,
United States
Tomoko Kawate,
National Institute for Fusion Science,
Japan

*CORRESPONDENCE
Alexander Nindos,
anindos@uoi.gr

SPECIALTY SECTION
This article was submitted to Stellar and Solar Physics,
a section of the journal
Frontiers in Astronomy and Space Sciences

RECEIVED 29 June 2022
ACCEPTED 27 July 2022
PUBLISHED 04 October 2022

CITATION
Nindos A, Patsourakos S, Jafarzadeh S and Shimojo M (2022), The dynamic chromosphere at
millimeter wavelengths.
Front. Astron. Space Sci. 9:981205.
doi: 10.3389/fspas.2022.981205

The dynamic chromosphere at millimeter wavelengths

Alexander Nindos[1]*, Spiros Patsourakos[1], Shahin Jafarzadeh[2,3] and Masumi Shimojo[4,5]

[1]Physics Department, University of Ioannina, Ioannina, Greece, [2]Max Planck Institute for Solar System Research, Göttingen, Germany, [3]Rosseland Centre for Solar Physics, University of Oslo, Oslo, Norway, [4]National Astronomical Observatory of Japan, National Institutes of Natural Sciences, Mitaka, Japan, [5]Department of Astronomical Science, The Graduate University of Advanced Studies (SOKENDAI), Mitaka, Japan

The chromosphere is one of the most complex and dynamic layers of the solar atmosphere. The dynamic phenomena occur on different spatial and temporal scales, not only in active regions but also in the so-called quiet Sun. In this paper we review recent advances in our understanding of these phenomena that stem from the analysis of observations with the Atacama Large Millimeter/submillimeter Array (ALMA). The unprecedented sensitivity as well as spatial and temporal resolution of ALMA at millimeter wavelengths have advanced the study of diverse phenomena such as chromospheric *p*-mode-like and high-frequency oscillations, as well as small-scale, weak episodes of energy release, including shock waves. We review the most important results of these studies by highlighting the new aspects of the phenomena that have revealed as well as the new questions and challenges that have generated.

KEYWORDS

sun solar radio emission, sun chromosphere, sun quiet sun, sun active regions, sun oscillations, sun MHD waves

1 Introduction

The solar chromosphere is traditionally defined as a ~2000-km-thick layer lying above the photosphere. Its emission can be detected in strong optical and UV spectral lines as well as in infrared, millimeter-wavelength (mm-λ) and submillimeter-λ continua (e.g. *see* Rutten, 2007; Carlsson et al., 2019, and references therein). The pertinent spectral observations indicate that the chromosphere is highly inhomogeneous and dynamic. A dominant feature of the quiet chromosphere is the so-called chromospheric network, which consists of narrow bright emission lanes enclosing dark cells (the terms cell interior or internetwork are commonly used for these darker areas). The diameter of individual internetwork areas is about 20,000 km. The network coincides with the borders of supergranules, i.e. large-scale convection cells with similar sizes in the photosphere (Leighton et al., 1962). The network lanes host strong magnetic fields which are deformed and dragged there by the supergranular flows (e.g., Orozco Suárez et al., 2012; Jafarzadeh et al., 2014, and references therein). The most well-known features of the quiet chromosphere when observed in Hα are the spicules which are thin, dark, elongated structures apparently emerging above the network boundaries. Their exact drivers,

however, remain unidentified (Pereira et al., 2012). When seen at the limb, spicules show as bright jet-like features rising to heights of up to ~10,000 km and then either diffuse in the corona or fall down.

In active regions the chromosphere consists of sunspots and their surroundings, plages (i.e. bright regions with magnetic fluxes that are larger than those of the quiet Sun, but smaller than those of sunspots), and a multitude of dark and bright fibril-like features (*see*, e.g., Jafarzadeh et al., 2017a, and references therein). Filaments, i.e. narrow, dark, elongated thread-like features associated with chromospheric material that penetrates into the corona and is suspended by the magnetic field may appear both in and away active regions, along magnetic polarity inversion lines (e.g. *see* Vial and Engvold, 2015, and references therein).

The chromosphere has long been known to deviate from hydrostatic equilibrium (e.g. *see* Zirin, 1988). Furthermore, it is a particularly dynamic layer hosting a multitude of intermittent dynamic phenomena on different spatial and temporal scales. First of all, wave and oscillatory phenomena are ubiquitous throughout the chromosphere (e.g. *see* Jess et al., 2015, and reference therein). Their most traditional manifestation is probably the chromospheric oscillations with periods from three to 5 min. These oscillations may represent the penetration of the photospheric *p*-mode oscillations into the corona (Jefferies et al., 2006). In addition to them, and owing to its inhomogeneous and magnetic nature, a complex picture of wave phenomena, including reflections, interferences, mode conversions and shock waves has been attributed to the chromosphere (e.g. *see* Bogdan et al., 2003; Wedemeyer-Böhm et al., 2009).

Episodes of small-scale energy release are also ubiquitous in the chromosphere, not only in active regions but also in the quiet Sun (e.g. *see* Tsiropoula et al., 2012; Shimizu, 2015; Henriques et al., 2016, and references therein). These may range from small events whose detection limit is determined by the sensitivity and resolution (spatial, spectral, and temporal) of the instrument to microflares and sub-flares. There is no unique name for them in the literature, but in this paper we adopt the term "transient brightenings."

Both the dissipation of magnetic waves (e.g. *see* Hollweg, 1981; De Pontieu et al., 2007b; McIntosh et al., 2011) and the braiding and reconnection of magnetic fields followed by energy release (e.g. *see* Parker, 1988; Klimchuk, 2006; Cirtain et al., 2013) are considered leading candidates for the heating of the upper layers of the solar atmosphere. Therefore both the wave phenomena observed in the chromosphere as well as its transient brightenings (no matter whether the latter are attributed to shock waves or magnetic reconnection) could be relevant to the heating of the chromosphere.

Although several of the observational building blocks of the chromosphere have been established a long time ago, the physics dictating their properties and dynamics is not. Several difficulties have contributed to this situation. First of all the chromosphere is intrinsically complex. It is the layer of the solar atmosphere where the transition from a plasma-dominated regime to a magnetic-field-dominated regime takes place. It is also a region where interactions between ions and neutrals can be relevant. Furthermore, although it is only heated to a few thousand degrees above the photosphere, the higher chromospheric densities, compared to those of the corona, imply that up to two orders of magnitude more energy is required to heat the chromosphere than the corona, making the problem of chromospheric heating much more demanding in terms of energy input compared to coronal heating. Moreover, the small spatial and temporal scales of the chromosphere call for high spatial and temporal resolution observations.

In addition to the above issues, the formation of the chromospheric spectral lines are associated with non-equilibrium effects, for example, non-local thermodynamic equilibrium (NLTE) and time-dependent ionization of hydrogen (*see* Carlsson and Stein, 1992, 2002). The situation is better at millimeter wavelengths; the mm-λ emission of the non-flaring Sun is due to the thermal free-free mechanism under LTE. Therefore, the source function is Planckian and the observed brightness temperature is directly linked to the electron temperature *via* the radiative transfer equation (e.g. *see* Shibasaki et al., 2011; Wedemeyer et al., 2016). Unfortunately, old mm-λ data suffered from low sensitivity, low spatial resolution, and absolute calibration problems, which limited their contributions to understanding the chromosphere and its dynamics.

The relatively recent (since 2016) availability of solar mm-λ observations with ALMA at 3 mm (Band 3) and 1.25 mm (Band 6) offers the potential to significantly advance our knowledge of the chromosphere owing to the instument's unprecedented spatial resolution and sensitivity (Shimojo et al., 2017a; White et al., 2017). So far, several publications reporting ALMA observations have appeared (those published before 2019 have been reviewed by Loukitcheva, 2019) covering diverse subjects, such as the structure of the quiet chromosphere, off-limb and on-disk spicules, comparisons of observations with models, oscillations and small-scale transient phenomena, plages, and sunspots.

In this paper we review the new findings concerning dynamic phenomena in the chromosphere that have been brought by ALMA observations. We do not cover dynamics of spicules because it is a subject of a separate review in this Special Research Topic collection. We also do not cover flares because up to now no ALMA observations of flares have been released (note, however, that the potential of mm-λ observations to clarify open issues in flare research is reviewed by Fleishman et al. in this Special Research Topic collection). The structure of our paper corresponds to the two major sub-topics of the subject (wave phenomena in Section 2 and transient brightenings in Section 3) for which measurable progress has been reported by using ALMA

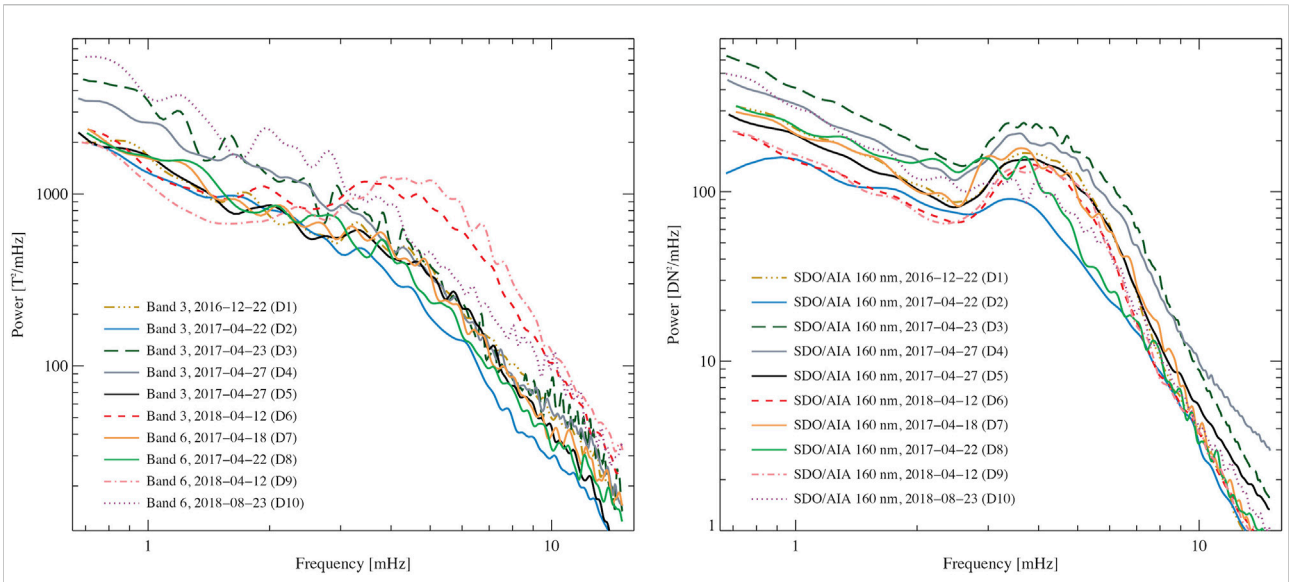

FIGURE 1
Mean power spectra from 10 ALMA datasets (averaged over the entire FOVs) observed in Band 3 and Band 6, sampling the mid-to-upper chromosphere (left) and from their lower chromospheric counterparts observed with SDO/AIA in 1600 Å (right). Images reproduced from Jafarzadeh et al. (2021).

data. We present conclusions and discuss prospects for future work in Section 4.

2 Oscillatory phenomena

2.1 p-mode oscillations

2.1.1 Magnetic environment

The *p*-modes can propagate through both non-magnetic and magnetic environments (known as magneto-acoustic waves in the latter) where the magnetic field acts as a guide for their efficient propagation through the solar atmosphere. These different environments include *1*) sunspot umbrae, resulting in the so-called umbral flashes in the chromosphere due to shock formation (Beckers and Tallant, 1969; Beckers and Schultz, 1972), *2*) sunspot penumbrae, forming running penumbral waves along the magnetic-field lines (Giovanelli, 1972; Löhner-Böttcher et al., 2016), and *3*) small-scale magnetic structures, manifested as point-like or fibrillar features in intensity images (Jafarzadeh et al., 2017b,c).

The characteristic periodicity of *p*-modes in the solar chromosphere has been known to be 3 min through a multitude of studies (e.g. Cram, 1978; Fleck and Schmitz, 1991), either as a "global" property (averaged over a relatively large field of view, FoV), or in specific magnetic structures (e.g., in sunspot umbrae; Centeno et al., 2006; Jess et al., 2020; *see* also Section 2.3). While in the former case, FoVs may often contain both non-magnetic and strong field-concentration regions, the contribution of the non-magnetic environments usually becomes more important in large quiet Sun FoVs where only small scale magnetic concentrations exist, covering a small fraction of the entire area.

The magnetic fields expand with height and bend over their surrounding areas as they extend into the upper atmosphere, creating the so-called magnetic canopies (Gabriel, 1976; Giovanelli and Jones, 1982; Solanki et al., 1991; Rosenthal et al., 2002). The magnetic canopies may be detected through the entire solar atmosphere, and their heights depend on the field strength of their photospheric footpoints (Jafarzadeh et al., 2017a). Thus, such magnetic canopies at chromospheric heights, seen as fibrillar structures in intensity images (in, e.g. Hα spectral line), may obscure the dynamics, including *p*-modes, coming from underneath –the "umbrella effect". However, Rutten (2017) suggested that although the same effect should also exist in mm-λ observations, the dense fibrillar structures may not be visible in brightness temperature images due to their reduced lateral contrast (i.e., an insensitivity to Doppler shifts).

Jafarzadeh et al. (2021) examined ten different ALMA datasets (six in Band 6 and four in Band 3) for the presence of global *p*-modes. They found that only two datasets, out of 10, showed enhanced power at around 4 mHz. Figure 1 shows the mean power spectra of the 10 ALMA datasets (left panel), along with those computed for the same FoVs observed in 1600 Å with the Atmospheric Imaging Assembly (AIA; Lemen et al. (2012), onboard the Solar Dynamics Observatory (SDO; Pesnell et al., 2012). The latter samples heights corresponding to the temperature minimum/lower chromosphere. From these plots

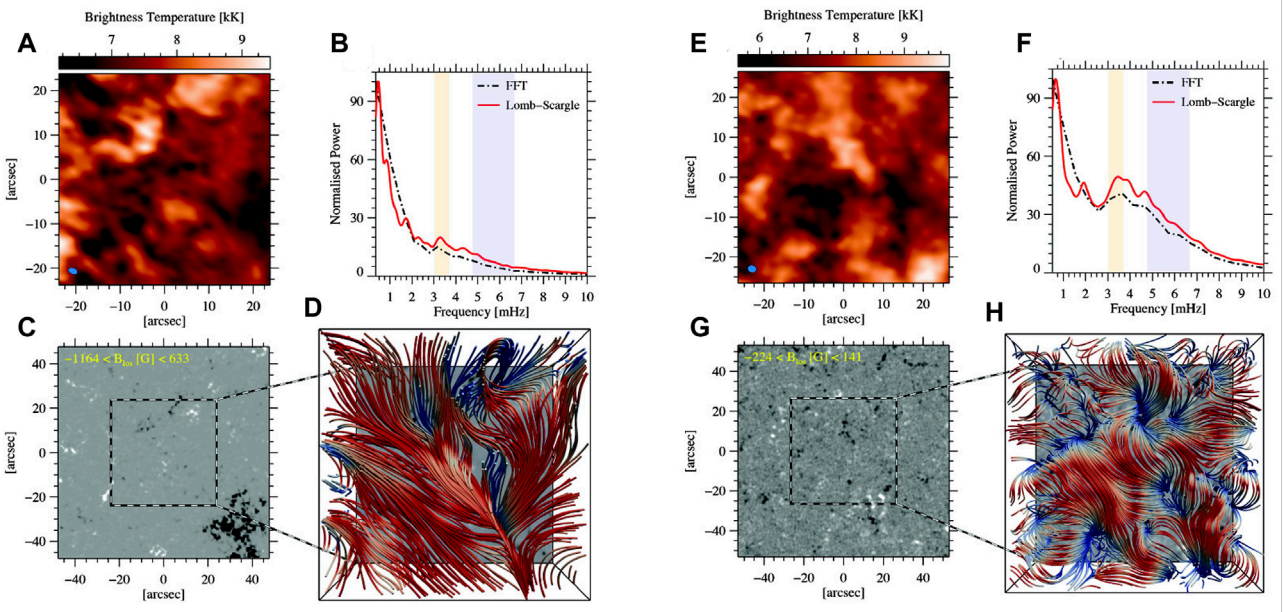

FIGURE 2
Panels **(A–D)**: the 22 December 2016 Band 3 dataset used for the detection of mm-λ oscillations. **(A)** An ALMA brightness temperature map in Band 3. **(B)** Spatially averaged brightness temperature power spectra from FFT (dash-dotted black line) and Lomb-Scargle (solid red line) transforms. Period ranges corresponding to the 3 and 5 min windows (each with a width of 1 min) are respectively depicted with the purple and yellow stripes. **(C)** The SDO/HMI line-of-sight photospheric magnetogram for a FOV twice as large as ALMA's. The ALMA's FOV is marked with the dashed square. **(D)** A top view of the field topology at upper chromosphere heights above the ALMA's FOV. The colors identify inclination angles, from vertical (blue) to horizontal (red). Panels **(E–H)**: same as panels **(A–D)** but for the 12 April 2018 Band 3 dataset. Figure reproduced from Jafarzadeh et al. (2021).

it is obvious that while the global *p*-modes are clearly observed in all ten datasets sampling the low chromosphere, they show up in only two ALMA datasets that sample the upper chromosphere (one in Band 3 and one in Band 6).

Jafarzadeh et al. (2021) additionally calculated magnetostatic potential field extrapolations from photospheric magnetic fields simultaneously observed with the SDO's Helioseismic and Magnetic Imager; (HMI Schou et al., 2012). From the extrapolations, the magnetic topologies associated with the areas observed by ALMA could be inspected. Figure 2 shows observations and calculations for a contrasting pair of such Band 3 observations. For each dataset we show the ALMA brightness temperature map (panels a, e), spatially averaged power spectra (panels b, f), corresponding HMI magnetogram associated to a larger FoV compared to that of ALMA (panels c, g), and a top view of the field topology above the ALMA FoV at upper chromospheric heights (panels d, h). The averaged power spectra are shown from two different spectral analysis methods, Fast Fourier Transform (FFT; Cooley and Tukey 1965) and Lomb-Scargle approach (Lomb, 1976; Scargle, 1982). The latter is particularly relevant since the ALMA observations have a 2–3 min gap between blocks of ≈ 10 min. On the extended photospheric magnetograms, the ALMA FoVs are marked with dashed squares. The randomly plotted magnetic field lines on the field-topology map are colored with the unsigned inclination angle, changing from vertical (dark blue) to horizontal (dark red). Figure 3 shows the same plots as in Figure 2, but for two contrasting datasets sampled in Band 6.

The importance of magnetic field environment in observation of *p*-modes in the mid-to-upper chromosphere (sampled by the ALMA Band 3 and 6 observations) may better be understood when the datasets appearing in Figure 2 for Band 3 and Figure 3 for Band 6, are compared. As evidenced in Figures 2A–D, the photospheric counterpart of the ALMA observations samples a very quiet region, while a strong enhanced-network patch in its immediate vicinity (the lower-right corner) creates the overarching highly inclined magnetic canopy over the entire FoV at the heights sampled by ALMA Band 3. As a result, the averaged power spectrum does not show any power enhancements at around 3–5 mHz. In comparison, when both the ALMA FoV and its surroundings pose very quiet areas in the photosphere (Figures 2E–H), the magnetic topology at chromospheric heights is organized in smaller-scale and less dense loops compared to those rooted in strong kG fields. Thus, the *p*-modes are not fully obscured, resulting in power enhancements in the 3–5 mHz frequency range. The first example shown in Figures 3A–D for ALMA observations in Band 6 refers to a plage area in both ALMA FoV and its surroundings, as illustrated in the HMI magnetogram. Hence, both nearly vertical fields and a dense magnetic canopy can be

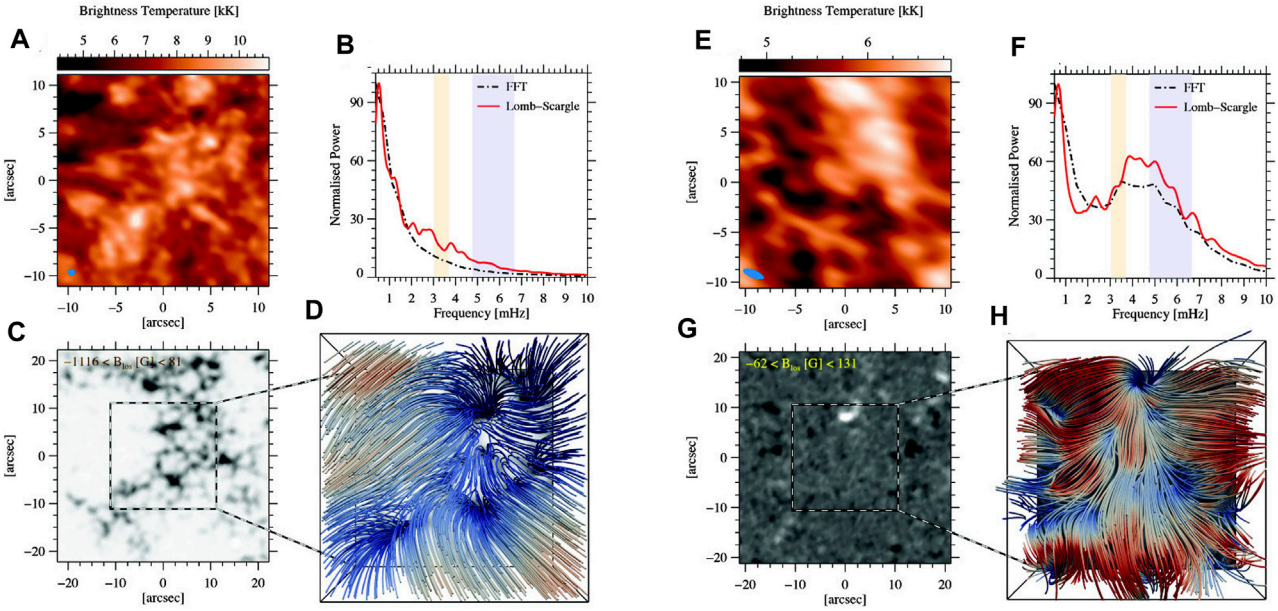

FIGURE 3
Same as Figure 2 but for the 22 April 2017 Band 6 dataset (panels **A**–**D**) and the 12 April 2018 Band 6 dataset (panels **E**–**H**). Figure reproduced from Jafarzadeh et al. (2021).

observed at the heights sampled by the ALMA Band 6. On the other hand, the *p*-modes show well in the other Band 6 dataset presented in Figures 3E–H which corresponds to the same target that was presented in Figures 2E–H.

The absence of power enhancements around 3–5 mHz (thus, lack of *p*-mode detection) could be the result of a combination of various phenomena. In the magnetic canopy regions, both the "umbrella" effect, where the magnetic canopy obscures oscillations coming from lower heights, and possibly the large field inclination angles (Heggland et al., 2011) could be responsible for the absence of *p*-mode observations. In addition, in the strong field concentrations, where the field is nearly vertical at chromospheric heights, acoustic power suppression (known as "magnetic shadows"; Leighton et al., 1962; Title et al., 1992) may develop due to multiple wave-mode conversions at the plasma-$\beta \approx 1$ level(s), where interactions between *p*-mode oscillations and the embedded magnetic fields occur (Moretti et al., 2007; Nutto et al., 2012).

2.1.2 Properties of p-mode oscillations

Patsourakos et al. (2020) and Nindos et al. (2021) analyzed spatially-resolved observations of *p*-mode oscillations in the quiet Sun and deduced their physical characteristics. This was achieved by analysis of the spatially averaged Power Spectral Density (PSD) either for the entire observed FoV or by employing appropriate spatial masks for the cell and network separately. The resulting PSDs for frequency windows encompassing the *p*-mode peaks were fitted by the sum of a linear and log-normal function of the logarithm of frequency meant to reproduce the background and *p*-mode peak, respectively. From the log-normal part of the fitting function, the *p*-mode frequency, amplitude and width were deduced.

In Patsourakos et al. (2020) Band 3 quiet Sun observations with a spatial resolution of typically $2.5'' \times 4.5''$ and a 2-s cadence were analyzed. The employed FoVs were $80'' \times 80''$ and scanned quiet Sun targets from disk center to the limb. Spatially resolved chromospheric oscillations with frequencies of 4.2 ± 1.7 mHz were detected in both cell and network. While individual pixels exhibited brightness temperature fluctuations of up to a few hundred K, the spatially averaged PSDs corresponded to fluctuations in the range 55–75 K, which amounts up to the 1% of the spatio-temporal averaged brightness temperature. A moderate increase of the relative *p*-mode strength (i.e., root mean square, rms, brightness temperature divided by the average brightness temperature) from disk center to limb was also registered.

In Nindos et al. (2021) a quiet Sun region near disk center was observed at both Band 6 and Band 3 at a 1-s cadence. The spatial resolution (FoV) was $1''$, $2''$ ($30'' \times 30''$, $60'' \times 60''$), for Band 6 and Band 3, respectively. The resulting PSDs are given in Figure 4. In both bands, *p*-mode oscillations with frequencies in between 3.6 and 4.4 mHz were found with amplitudes of 103 and 107 K for Band 6 and Band 3, respectively. The associated relative brightness temperature fluctuations with respect to the spatio-

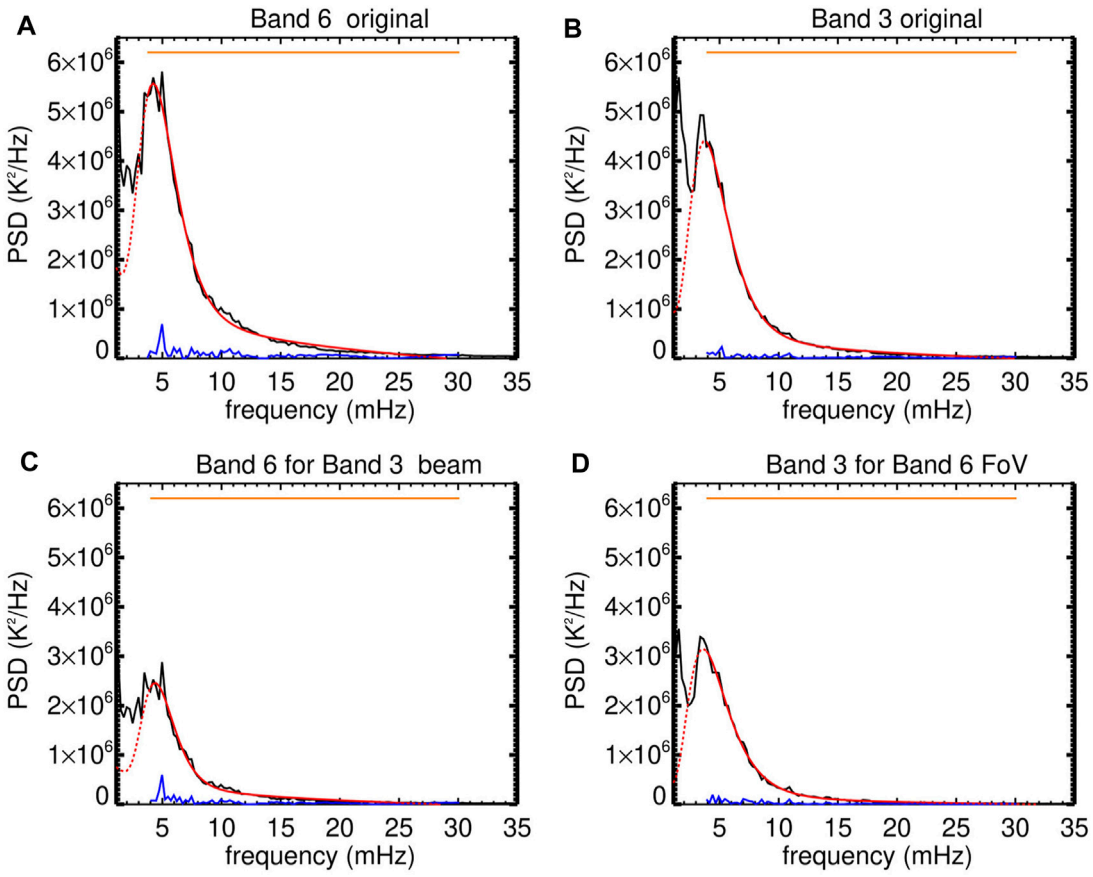

FIGURE 4
Quiet-Sun *p*-mode oscillations observed at 3 and 1.25 mm by ALMA. Black lines correspond to the spatially averaged PSDs, red lines to their fittings, and blue lines to the absolute residuals between the observed PSDs and the associated fittings. Panels **(A,B)** correspond to the original Band 6 and Band 3 observations, panel **(C)** to Band 6 observations at Band 3 spatial resolution and panel **(D)** for Band 3 observations corresponding to the Band 6 FoV (from Nindos et al., 2021). Reproduced with permission © ESO.

temporal average of the brightness temperature were 1.7–1.8%. Bringing the superior ($\sim 1''$) spatial resolution of the Band 6 observations to the resolution of the Band 3 observations ($\sim 2''$) led to a decrease of the rms of the Band 6 oscillations by a factor of 1.6. Furthermore, the reduction of the full Band 3 FoV to that of Band 6 (i.e. factor of four in area reduction) had a smaller effect in the resulting rms of the oscillations (factor of ~1.1).

The *p*-mode oscillations corresponded to the 0.5–0.6 of the spectrum-integrated power (i.e., PSD integral over the entire considered frequency range), which suggests they correspond to a significant fraction of the observed brightness temperature fluctuations. On the other hand, the energy density of the *p*-mode oscillations in Band 6 was about 3×10^{-2} erg cm^{-3}, which is roughly equivalent (*see* Nindos et al., 2021, for details) to a power per unit area that is about an order of magntitude smaller than the energy losses of the quiet chromosphere.

Comparing with previous mm-λ quiet Sun observations at 3.5 mm at a spatial resolution of $10''$ with Berkeley- Illinois-Maryland (BIMA) presented by White et al. (2006) and Loukitcheva et al. (2006), the ALMA observations discussed above, due to their superior spatial resolution, allowed, for the first time, to spatially resolve cell and network oscillations and also to deduce higher oscillation amplitudes.

2.2 High-frequency oscillations

High-frequency oscillations are of particular importance since they can carry a vast amount of energy to the upper solar atmosphere. Such waves, of different magneto-acoustic (magnetohydrodynamic) types, have previously been observed in the ultraviolet to infrared wavelength range and have shown to be energetic enough to potentially heat the solar chromosphere and beyond (De Pontieu et al., 2007a; Kuridze et al., 2012; Kubo

et al., 2016; Jafarzadeh et al., 2017c; Gafeira et al., 2017). However, in the pre-ALMA era most studies, with an exception of that by Okamoto and De Pontieu (2011), have not identified high-frequency waves in the upper chromosphere. Only recently, such high-frequency oscillations have also been detected at millimeter wavelengths, thanks to high-quality observations provided by ALMA. As such, Guevara Gómez et al. (2021) studied the dynamics of small-scale bright features observed with ALMA Band 3 (supposedly sampling heights that correspond to the upper chromosphere). They found that the majority of their small, likely magnetic, structures exhibit oscillations in brightness temperature, size, and horizontal motion, with periods on the order of 90 ± 22 s, 110 ± 12 s, and 66 ± 23 s, respectively.

Recent publications have begun investigating properties of high-frequency oscillations and p-modes at millimeter wavelengths in the solar chromosphere, using state-of-the-art numerical simulations (Eklund et al., 2021b). However, Fleck et al. (2021) showed that such numerical models should be treated with great caution. They compared various simulation codes and found that the height dependence of wave power, particularly for high-frequency waves, varied between the models by up to two orders of magnitude.

2.3 Sunspot oscillations

Sunspot oscillations are one of the most well known oscillatory phenomena in the solar atmosphere. The oscillations are detected as intensity and velocity variations (e.g. *see* the review by Khomenko and Collados, 2015, and references therein). In the umbra, at photospheric heights, oscillations with periods in both the 5-min range and the 3-min range have been established. Higher up in the chromosphere, oscillations with periods of 150–200 s exhibit larger amplitudes and are detected in the inner part of the umbra. Sunspot oscillations are directly linked with the propagation of MHD waves. The 5-min oscillations are thought to be driven by the *p*-modes while the traditional interpretation of the 3-min oscillations considered them as produced by a resonant cavity provided by the sunspot itself (e.g. *see* Bogdan and Judge, 2006; Khomenko and Collados, 2015; Jess et al., 2020). Detection of such chromospheric resonances appears to be challenging (Felipe, 2021) and may depend on the spatial resolution and quality of observations (Jess et al., 2021). It has also been advocated that the 3-min oscillations indicate upward-propagating waves that pass through the gravitationally stratified gas (Felipe et al., 2010; Chae and Goode, 2015). The sunspots' magneto-acoustic oscillations in the solar chromosphere are also responsible for observable changes in coronal plasma composition (Baker et al., 2021; Stangalini et al., 2021).

Using ALMA 3 mm observations, Chai et al. (2022) reported the first detection of spatially resolved 3-min oscillations of the mm-λ emission above the umbra of a sunspot. The detected modulation of the mm-λ emission is linked to the temporal variability of the chromospheric electron temperature through the free-free emission. These authors calculated the spatial distribution of the 3-min power amplitude (*see* Figure 5) which correlated well to similar maps made from observations at several locations along Hα line except at +0.8 Å where the oscillatory power was weak. From the 3-mm and Hα time profiles they found that there was a rather constant phase offset among ALMA brightness temperature and Hα sub-band intensities. Comparison of the properties of the mm-λ oscillations with the acoustic hydrodynamic model by Chae and Goode (2015) revealed that the ALMA intensity fluctuations were consistent with the propagation of an acoustic wave above the umbra. Furthermore, the 3-mm oscillations exhibited a slower rise and faster fall which may indicate nonlinear wave steepening or shock behavior above the umbra.

3 Weak transient activity

3.1 Statistical properties of transient brightenings

In addition to oscillations, several studies have reported transient brightenings in both quiet Sun (Yokoyama et al., 2018; Eklund et al., 2020; Nindos et al., 2020, 2021) and active region (Shimojo et al., 2017b; da Silva Santos et al., 2020; Chintzoglou et al., 2021b; Shimizu et al., 2021) observations with ALMA. In relation to the ALMA frequencies used, most of these reports utilize Band 3 observations with the exception of the papers by Nindos et al. (2021) who presented both Band 3 and Band 6 observations and Chintzoglou et al. (2021a) who analyzed Band 6 data. No observations in Band 7 (0.86 mm) recently made available for solar observing have been published thus far.

Obviously, any meaningful statistics of the properties of such events requires their detection in sufficient numbers. Large numbers of events have indeed been reported by Nindos et al. (2020, 2021), and Eklund et al. (2020). These authors analyzed ALMA quiet Sun data and the identification of their events resulted from the application of algorithms designed for that purpose. Nindos et al. (2020, 2021) applied intensity and temporal thresholds to the light curves of all pixels after they removed the effect of *p*-mode oscillations (*see* section 2.1.2). The resulting active pixels were further constrained by applying a spatial clustering criterion determined by the size of the ALMA beam and combined with a synchrony tolerance of ±2 min between time profile peaks of the selected adjacent pixels. Eklund et al. (2020) searched for intensity peaks in excess of 400 K in the light curves of all pixels. Then the selected pixels

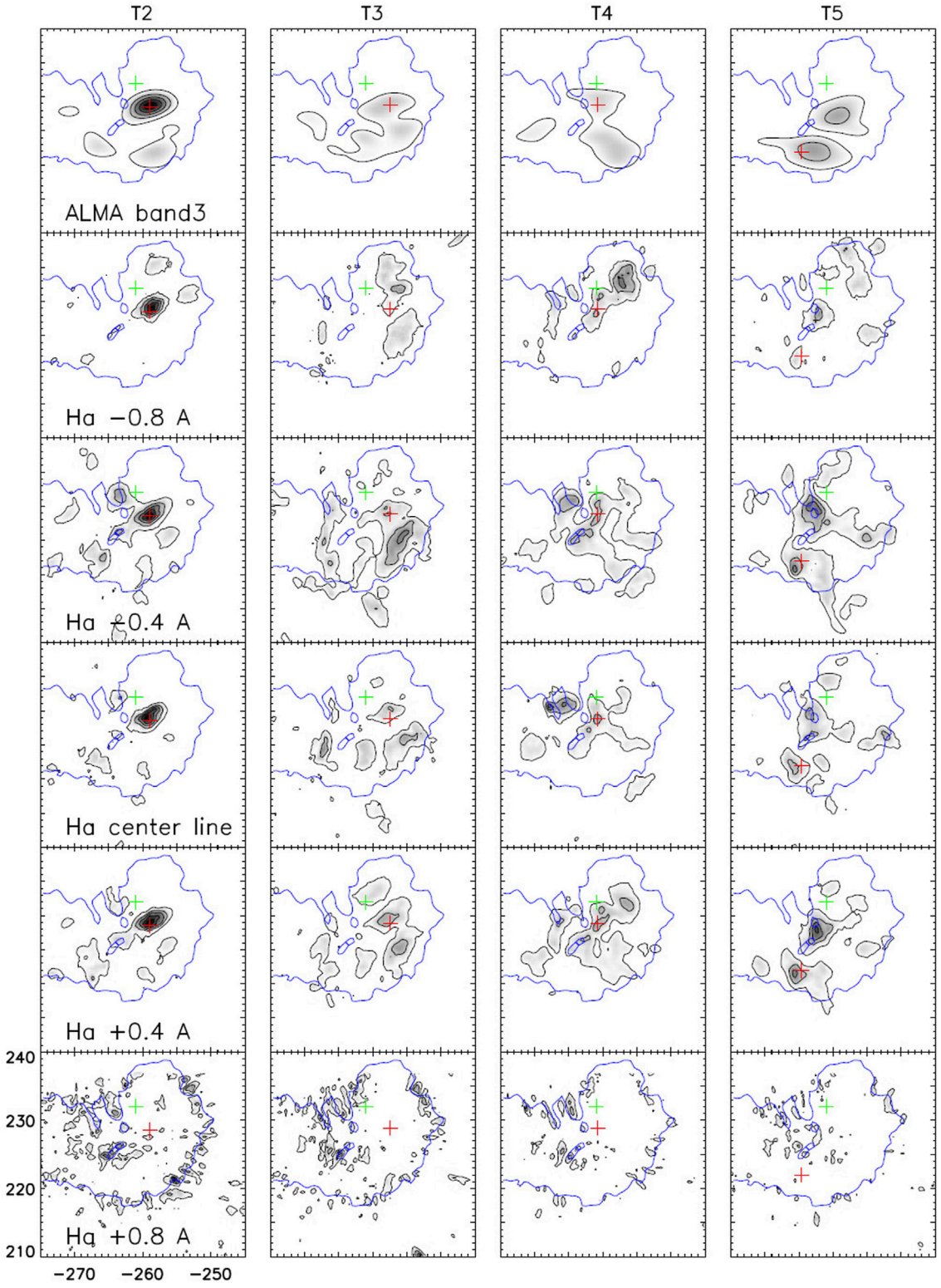

FIGURE 5
Spatial distribution of the 3-min oscillation power amplitude in 3 mm (top row) and in various sub-bands along the Hα line. The columns correspond to different ALMA solar scans, each of duration of about 10 min (from Chai et al., 2022). © AAS. Reproduced with permission.

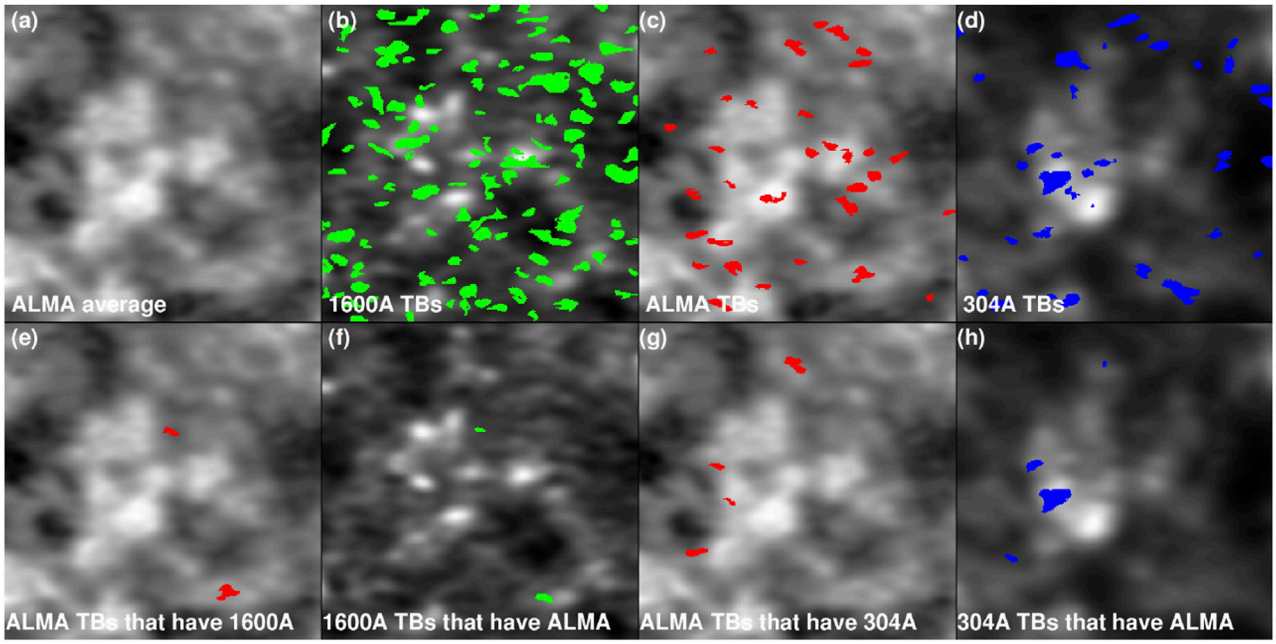

FIGURE 6
The different colors mark the pixels participating in transient brightenings in 1600 Å (green), 3 mm (red) and 304 Å (blue) 10-min data of a quiet Sun region. In panels **(A–D)** all events identified at a given wavelength are displayed. In the bottom row, panels **(E,F)** display the events appearing both at 3 mm and 1600 Å while panels **(G,H)** display the events appearing both at 3 mm and 304 Å (from Nindos et al., 2020). Reproduced with permission © ESO.

were grouped together by employing a *k*-means clustering algorithm.

Nindos et al. (2020) detected a total of 184 3-mm transient events in six quiet Sun regions located from close to the limb to disk center (Nindos et al., 2018), each one observed for about 10 min. Nindos et al. (2021) detected 77 and 115 events at 1.25 and 3 mm, respectively, in a very quiet region that was observed close to disk center for about 40 min. These numbers correspond to occurrence rates per unit area of about [2–5] × 10^{-22} events per cm^2 s. However, the number of ALMA events with AIA counterparts (either at 1600 or 304 Å) was about 6–10 times smaller (*see* Figure 6). This might be due to the different temperature ranges sampled by the ALMA-AIA datasets with the ALMA events probing cooler material whose temperature increase may not be sufficient to give rise to emission in the 304 Å passband. On the opposite side, the AIA events may be rather weak to energize the layers probed by ALMA. Furthermore all ALMA-AIA events in these studies should be optically thick and since 3 mm emission must be coming from higher layers than 1600 Å (Howe et al., 2012; Alissandrakis et al., 2017; Patsourakos et al., 2020), it is not surprising that the higher 3-mm transients do not correlate well with the 1600-Å transients that appear lower down because, at 3 mm, we cannot see down to those heights.

The events detected by Nindos et al. (2020, 2021) exhibited brightness temperature increases from ~40 K to more than 500 K above background levels. Most of them were weak; for example the 3-mm event of Figure 7 can be detected only after the average image is subtracted from each snapshot (compare panels of rows (a) and (b)). They were all of the gradual rise-and-fall type (*see* the bottom panel of Figure 7 for a characteristic example) with mean durations (quantified by the FWHM of the event's light curves) of about 50 s. The gradual nature of the light curves suggests the events result from thermal free-free emission (e.g. *see* Nindos, 2020). Although the presence of nonthermal electrons has been reported in previous studies of microwave transient brightenings (e.g. Gary et al., 1997; Krucker et al., 1997; Nindos et al., 1999), model calculations (White and Kundu, 1992) indicate that one needs to invoke a population of MeV-emitting electrons to obtain appreciable gyrosynchrotron emission at 1–3 mm. We also note that Nindos et al. (2020, 2021) found power-law behavior for the maximum intensity, duration, and size of their brightenings with indices in the interval of 1.93–3.11 which is broadly consistent with those for EUV transient brightenings (e.g. *see* Joulin et al., 2016, and references therein).

Eklund et al. (2020) detected 552 3-mm events in a quiet region that was observed for about 40 min (Wedemeyer et al., 2020). The occurrence rate per unit area of these events was almost two orders of magnitude larger than those reported by Nindos et al. (2020, 2021). This discrepancy could be interpreted in terms of either possible intrinsic differences among the regions

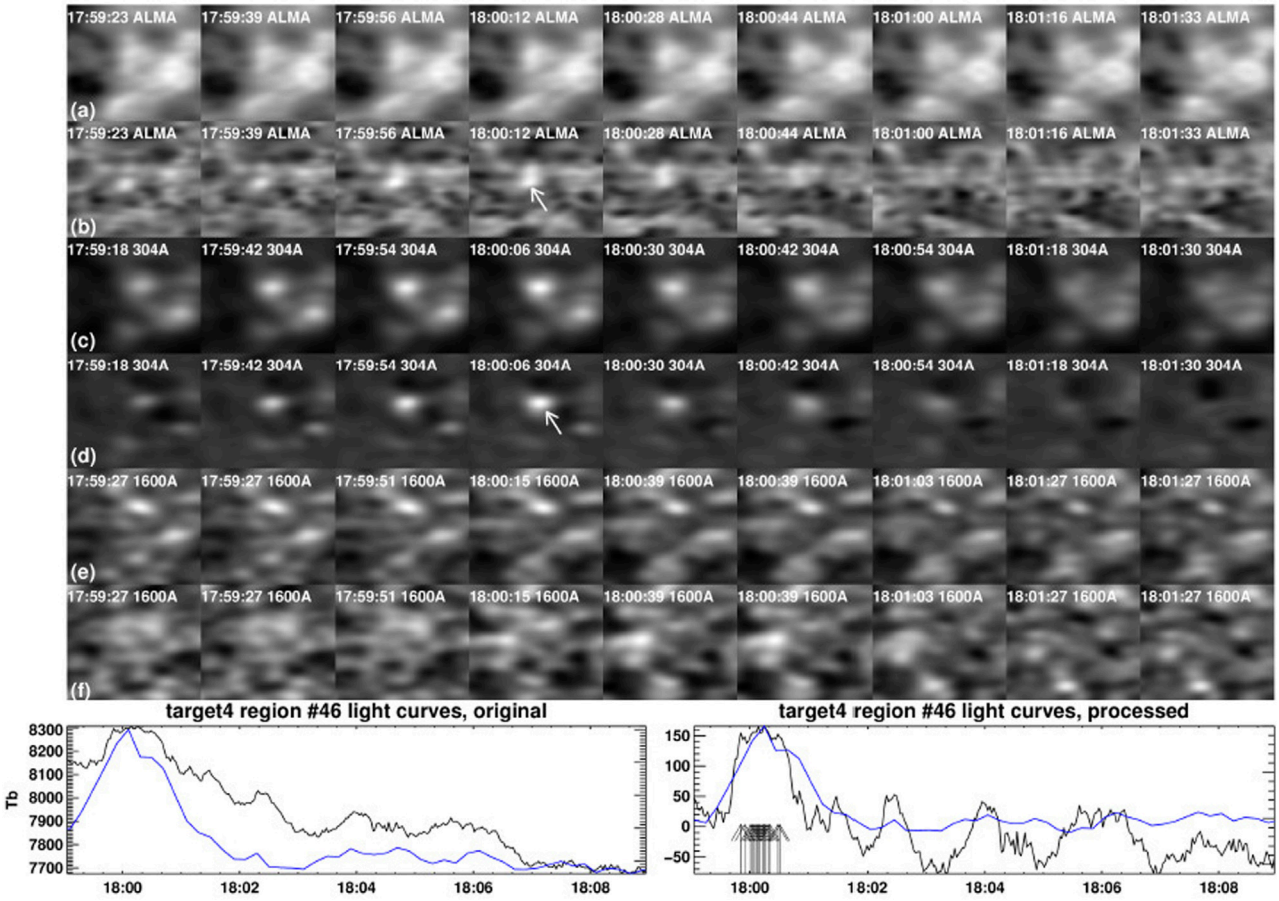

FIGURE 7
A quiet Sun transient event observed at 3 mm and 304 Å. Panel **(A)** shows characteristic ALMA snapshots while panel **(B)** shows the same snapshots after the average 3 mm image has been subtracted. Rows c–f: same as **(A,B)** but for the 304 **(C,D)** and the 1600 Å data **(E,F)**. The white arrows mark the transient brightening. The field of view is 35″ × 35″. Bottom row: light curves of the event emission at 3 mm (black) and 304 Å (blue) before and after processing (left and right panel, respectively) (from Nindos et al., 2020). Reproduced with permission © ESO.

considered or differences in the detection algorithms (for example Eklund et al., 2020, might have not removed oscillations prior to the application of their search criteria).

It is worth mentioning that the number of ALMA detected events in the publications mentioned above could be considered as lower limits to their actual numbers due to smearing introduced to the data by the finite spatial resolution (*see* Eklund et al., 2021b), thus leaving some of the weak events undetectable. The simulations performed by Eklund et al. (2021b) indicate that the situation improves as spatial resolution becomes better; therefore it is advisable to search for weak transient brightenings using the wider ALMA array configurations.

In contrast to the events discussed above, the active-region transient events studied by da Silva Santos et al. (2020) were EUV-selected, i.e. they were first identified in AIA EUV images and then their 3 mm counterparts were detected in ALMA data. da Silva Santos et al. (2020) reported the detection of nine transient ALMA events in a field of view of 60″ throughout their 60-min observing run. Their occurrence rate per unit area is about two to eight times higher than the occurrence rate per unit area of the ALMA-AIA paired events that were registered by Nindos et al. (2020, 2021).

In the above studies, the locations of the ALMA transients show diversity which is related to different properties of the target regions. The 3 mm events detected by Nindos et al. (2020, 2021) show a weak tendency (about 70%) to appear at the boundaries of network cells in agreement with the visual inspection of Figure 6C. The situation is somehow different in the 1.25 mm events detected by Nindos et al. (2021) where more than half of the events are located in internetwork regions. This difference is a natural consequence of the fact that much of the

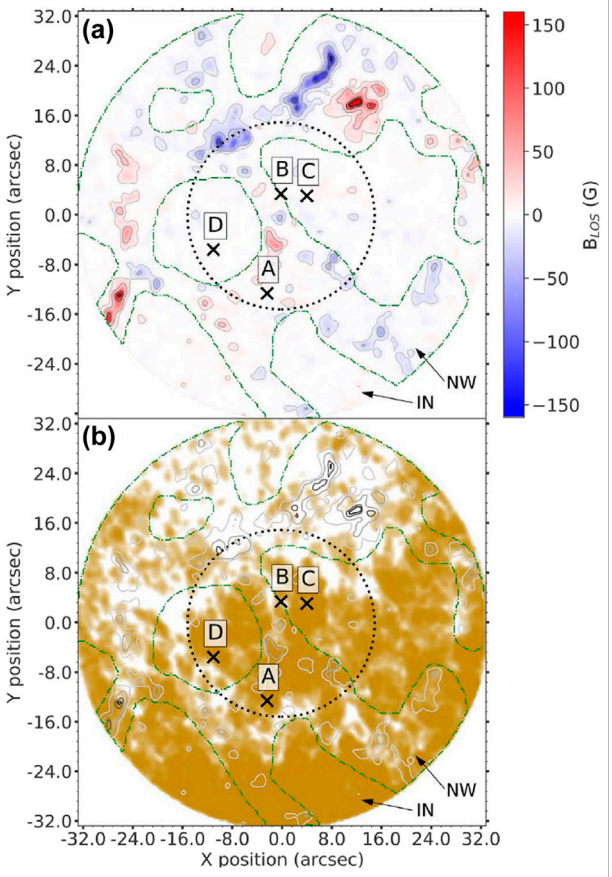

FIGURE 8
(a) HMI magnetogram of a quiet Sun region with the magnetic field displayed in gray contours as well as blue, white, and red shades. The green dashed-dotted curves distinguish network regions from internetwork regions. The dotted circle marks the 30″-diameter region whose transients were analyzed. (b) The color marks the pixels participating in transient events with a brightness temperature >400 K and duration shorter than 200 s. The contours have the same meaning as in panel (a) (from Eklund et al., 2020). Reproduced with permission © ESO.

field of view of the 1.25 mm observations by Nindos et al. (2021) was covered by the interior of a supergranular cell whereas that was not the case for the 3-mm observations by Nindos et al. (2020, 2021).

The quiet Sun events detected by Eklund et al. (2020) show a tendency to occur in regions of lower magnetic field strength. This is obvious in Figure 8 where the white spaces of panel (b) that are not associated with any events correspond to the stronger magnetic field concentrations that appear in panel (a). This was one of the arguments used by Eklund et al. (2020) to interpret the origin of their events in terms of propagating shock waves (*see* Section 3.4).

The region studied by da Silva Santos et al. (2020) was centered at a group of pores in the periphery of a large sunspot (*see* Figure 9); part of that region was the site of magnetic flux emergence during the ALMA observations. These authors identified Ellerman bombs in their 1700 Å AIA data but did not find any conspicuous brightenings associated with them in the ALMA data. This result may indicate that Ellerman bombs are reconnection events that are formed at heights around temperature minimum (e.g. *see* Georgoulis et al., 2002; Archontis and Hood, 2009; Watanabe et al., 2011; Hansteen et al., 2019), that is, well below the formation height of the 3-mm continuum emission. It appears that ALMA 0.86 mm observations that may probe lower heights than Band 6 might be more appropriate to search for mm-λ counterparts of Ellerman bombs.

Contrary to the null detection of Ellerman bombs, da Silva Santos et al. (2020) reported the detection of bright (above 9000 K and up to 14,200 K corresponding to excess emissions of up to ~5000 K above background) 3-mm events that were better correlated with transient EUV brightenings than UV ones (*see* Figure 10). This may indicate that these 3 mm-λ brightenings may probe material from the upper chromosphere with overlapping contributions from the transition region and even the corona. Therefore these transients are more reminiscent of the UV bursts identified by Guglielmino et al. (2018), that is small, bright transients occurring higher than the photospheric/low chromospheric layers where the usual small-scale UV active region transient brightenings occur (e.g. *see* the review by Young et al., 2018, and references therein).

3.2 Morphology of transient activities

Most studies of ALMA transient brightenings have come out of observations obtained with a 3-mm spatial resolution of ~ 2″, and the detected transients are unresolved (*see* Figure 7 for a typical example) with sizes comparable to the size of the synthesized beam. This indicates that the typical size of the mm-λ transients should be smaller than ~ 2″, and that the few resolved ones may, on average, represent rather energetic events.

The first detection of a resolved transient brightening has been reported by Shimojo et al. (2017b) (*see* Figure 11 for a snapshot around the peak of the event). The event was associated with an X-ray bright point near a sunspot. The bright point was visible in soft X-ray, EUV, and 3-mm images. The location of the brightest part of the 3-mm source (left box of the top left panel of Figure 11) matches the loop top of the X-ray bright point. Hence, it is hard to think that the 3-mm source is located in the chromosphere, and the source might not be optically thick.

The time evolution of the event in the EUV and soft X-ray images is similar to that of coronal jets (e.g. *see* Shimojo et al., 2007; Moore et al., 2010; Raouafi et al., 2016). At first, the X-ray bright point flares up, small flare loops are created, and an elongated jet structure develops simultaneously from near the loop top. Then a plasmoid blob ejects from the bright point.

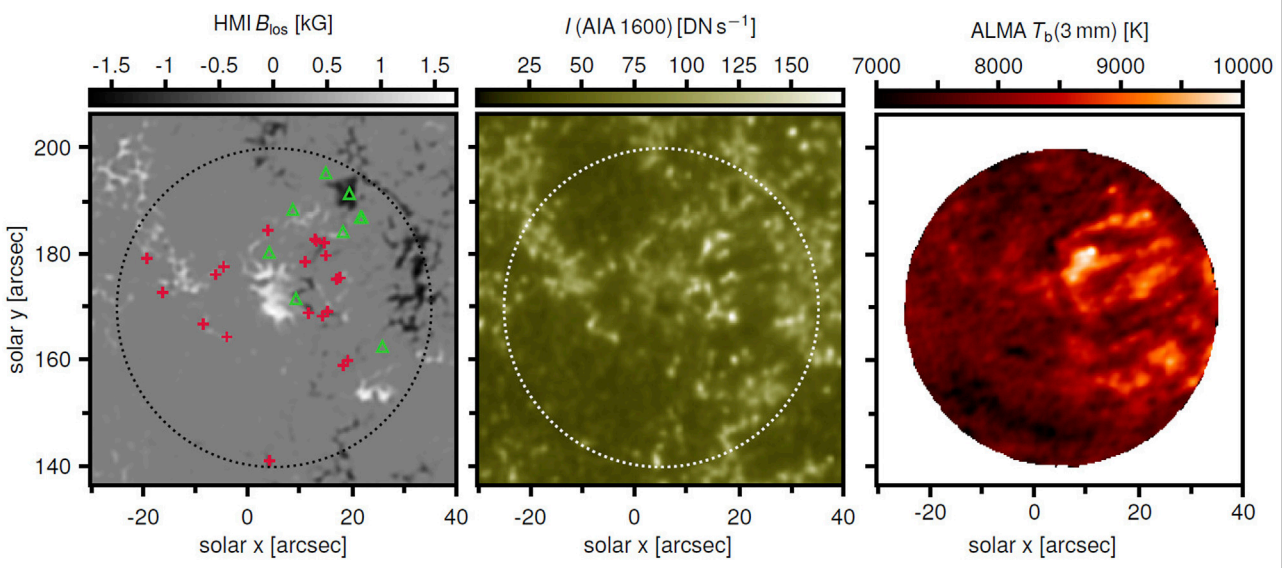

FIGURE 9
A small active region observed by SDO and ALMA. The left image is a longitudinal magnetogram from HMI/SDO, the middle image has been obtained by AIA/SDO while the right image shows the ALMA 3 mm emission. The dotted circles show the ALMA field of view. In the magnetogram the crosses mark the locations of Ellerman bombs. The triangles indicate locations of transient brightenings detected by both AIA and ALMA (adapted from da Silva Santos et al., 2020). Reproduced with permission © ESO.

Interestingly, the apparent direction of motion of the plasmoid is slightly different from the direction of motion of the jet. In the 3-mm images, emission from both the flaring bright point and the plasmoid can be seen (*see* Figure 11). Shimojo et al. (2017b) argued that the plasmoid was neither a chromospheric object nor was it optically thick. Their analysis indicated that the plasmoid consisted either of isothermal $\sim 10^5$ K plasma which was optically thin at 3 mm, or a 10^4 core with a hot envelope. Subsequent spectral analysis has favored the latter conditions as opposed to the fully optically thin case (Rodger et al., 2019).

Transient ejecta have also been revealed in other ALMA observations. For example Yokoyama et al. (2018) presented the ejection of a small blob at 3 mm which was associated with a spicule appearing in Mg II images obtained with the Interface Region Imaging Spectrograph (IRIS De Pontieu et al., 2014). This may suggest a relationship between the ejection of plasmoids and the development of spicules. We note that the mm-λ emission from solar structures mainly arises from continuum processes (*see* Section 1). Therefore even when the velocity of the emitting structure increases rapidly, we will still be able to track its motion in contrast to what might happen in spectral line observations due to their narrow band-pass. In this respect, ALMA images may serve as a valuable tool for tracing ejecta.

We note in passing that Yokoyama et al. (2018) also revealed that there is a correspondence in the solar limb location between 3-mm ALMA images and 171 Å images obtained by AIA/SDO. Since the limb is populated by dynamic structures like spicules, this result can be used both for the coalignment of ALMA and EUV images and for constraining the variation of their density with height.

Figure 10 indicates that some of the events detected by da Silva Santos et al. (2020) (*see* Section 3.1) were also resolved and showed an elongated shape bridging regions of opposite magnetic polarities and exhibiting proper motions with high apparent velocities (37–340 km s^{-1}). da Silva Santos et al. (2020) compared their results with a snapshot from a radiative MHD (r-MHD) simulation of magnetic flux emergence (*see* top part of right column of Figure 10). The simulation region contained an Ellerman bomb and an UV burst marked by the top and bottom arrows in panels (a)-(j), respectively. In agreement with the observations there is no signature of the Ellerman bomb in the simulated 3-mm emission but the presence of the UV burst, probably a signature of magnetic reconnection following flux emergence, is captured as a rather elongated structure in good qualitative agreement with the UV and 3-mm observations that appear in the left column of Figure 10.

3.3 Energetics of transient brightenings

The importance of transient brightenings as potential contributors to the heating of the upper layers of the solar atmosphere has been highlighted in Section 1. Therefore it is not a surprise that in some of the papers reporting on ALMA transient brightenings, estimates of their energy content are provided. The mm-λ emission is considered to arise from

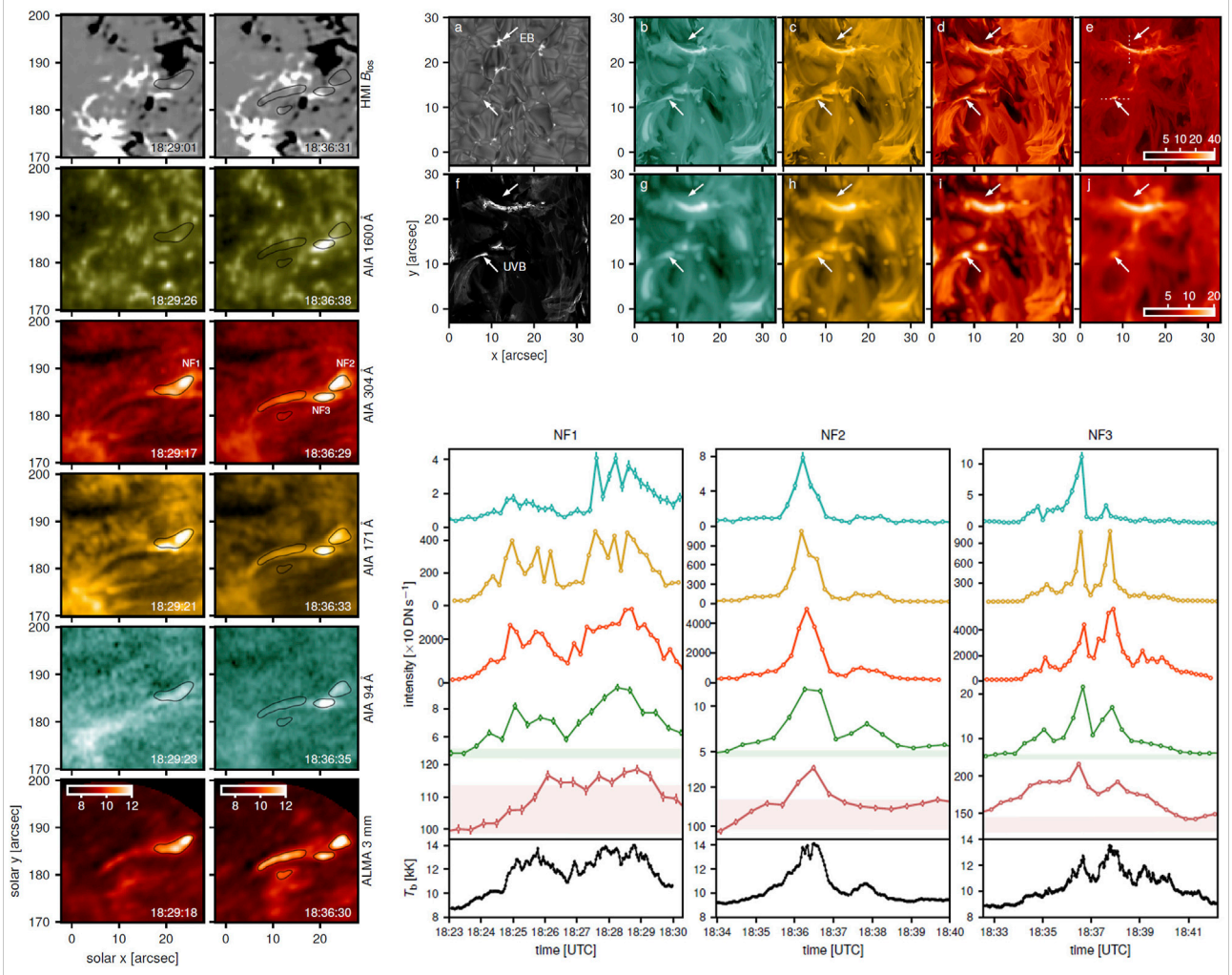

FIGURE 10
The two leftmost columns show characteristic snapshots of flaring fibrils in an HMI magnetogram, several AIA channels and ALMA 3 mm data. The contours mark a 3-mm brightness temperature of 10^4 K. The two rows at the top-right part of the figure show results from an r-MHD simulation. Panels **(A,F)** show Hα line wing and integrated Si IV 1393 Å intensity while panels **(B–E)** show the simulation's emission in AIA 94, 171, 304 Å and 3 mm, at its original spatial scale. In panels **(G–J)** the spatial resolution of the simulation has been degraded resulting to pixel size of 0.3″. The top and bottom arrows mark the locations of an Ellerman bomb and a UV burst, respectively. The remaining columns at the bottom-right part of the figure show time profiles (3 mm, 1700, 1600, 304, 171, and 94 Å from bottom to top) of the events marked NF1, NF2, NF3 at the two left columns (adapted from da Silva Santos et al., 2020). Reproduced with permission © ESO.

thermal free-free emission. Three approaches to the subject have been developed: *1*) Direct use of the ALMA brightness temperature enhancements for the calculation of the thermal energy supplied to the chromosphere by the transients (Nindos et al., 2020, 2021; Shimizu et al., 2021). *2*) Combine ALMA data with EUV or soft X-ray data to constrain the temperature and density of the event's plasma and then use these results to estimate its thermal energy content (Shimojo et al., 2017b). *3*) Calculate heating rates from a pertinent MHD simulation and compare the results with ALMA observations (da Silva Santos et al., 2022a).

In approach *1*) the mm-λ brightness temperature enhancement is considered to be equal to the electron temperature increase of the plasma which is correct only if the mm-λ emission is optically thick. Nindos et al. (2020, 2021) and Shimizu et al. (2021) used the electron temperature values resulted from invertions of center-to-limb variation curves performed by Alissandrakis et al. (2017, 2020) with the corresponding model densities from pertinent Fontenla et al. (1993) models and verified that that was indeed the case in their events. In these studies it was assumed that the density did not change during the events and was taken from models (Fontenla

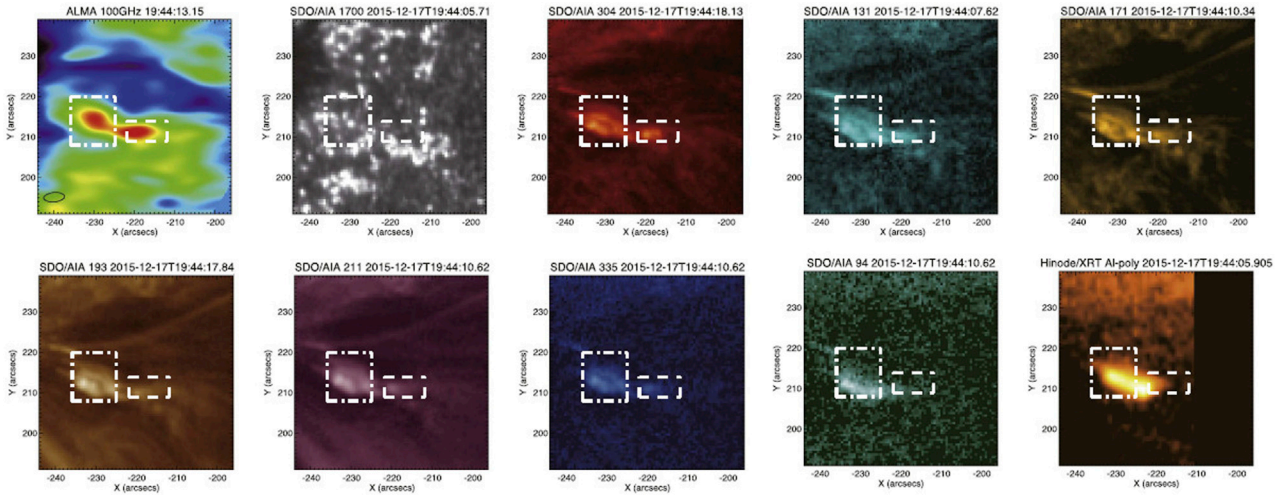

FIGURE 11
Images of a plasmoid ejection close to the time of its maximum emission. From left to right and top to bottom we present images at 3 mm (ALMA), 1700, 304, 131, 171, 193, 211, 335, and 94 Å (all from AIA), and Al-poly filter soft X-rays (from Hinode XRT) (from Shimojo et al., 2017b). © AAS. Reproduced with permission.

et al., 1993; Loukitcheva et al., 2015). That is a rather crude treatment of the problem which, however, is justified by the lack of appropriate data to perform differential emission measure (DEM) analysis.

Nindos et al. (2020, 2021) found that the thermal energies of their transient brightenings ranged from ~ 10^{24} to ~ 2×10^{26} erg at 3 mm and from ~ 2×10^{23} to ~ 10^{26} erg at 1.25 mm. At both frequencies power laws with indices of 1.65–1.75 were established for the frequency distribution of the events versus energy (*see* Figure 12). These indices are well below values of ≥ 2 which should appear if the energy released by weak events could heat the upper layers of the atmosphere (e.g., Hudson, 1991). Furthermore, the above properties are consistent with those of quiet Sun EUV events reported in previous publications (e.g. *see* Joulin et al., 2016, and references therein). We note that the lower end of the energy distribution of the 1.25 mm events detected by Nindos et al. (2021) is among the smallest ever reported irrespective of the observing wavelength. The power per unit area of their events was ~ $1 - 2 \times 10^4$ erg cm^{-2} s^{-1} which can account for about 1% of the radiative losses from the quiet low chromosphere (e.g. *see* Withbroe and Noyes, 1977).

Shimizu et al. (2021) performed an in-depth analysis of a microflare event observed at 3 mm as well as in UV, EUV, and soft X-rays. The thermal energy supplied to the chromosphere by the event was 2.2×10^{24} erg. This estimate was derived from the 3 mm emission at the footpoint of a (micro-)flaring loop that emitted in soft X-rays. The soft X-ray data were used to estimate the event's thermal energy that was supplied to the corona. It was found that the coronal excess energy was about 100 times larger than the chromospheric one. The fact that compared to the soft X-ray emission, the event's emission at 3 mm was *1*) more impulsive, *2*) clearly reached its peak before the soft X-ray emission, and *3*) was associated with a microflare's footpoint while the soft X-ray emission came from the loop led Shimizu et al. (2021) to argue that the energy measured from the 3 mm data can be viewed as a proxy to the energy carried by the non-thermal electrons that impinge deeper and denser atmospheric layers. This result may reflect that the non-thermal energy is not adequate to account for the thermal component in this event because of a deficit of such energetic electrons. Warmuth and Mann (2020) reached a similar conclusion for a set of weak flares they analyzed.

When an event's mm-λ emission is optically thin, the observed excess brightness temperature is not equal to the plasma electron temperature increase. In such case if the event has been co-observed in EUV or soft X-rays, the variation of the assumed electron density and temperature may reveal parameter spaces that can reconcile the intensity enhancements in both EUV/soft X-rays and mm-λ. That was the strategy adopted by Shimojo et al. (2017b) who found that in their plasmoid event (*see* Section 3.2) the appropriate pair of electron temperature and density (10^5 K and 3×10^9 cm^{-3}, respectively) yields a thermal energy of 5×10^{24} erg.

An alternative, albeit less straightforward approach, is to constrain the energetics of mm-λ transient events by comparing their observations with MHD simulations. This path was followed by da Silva Santos et al. (2022a) who found enhanced heating rate of up to 5 kW m^{-2} in the upper

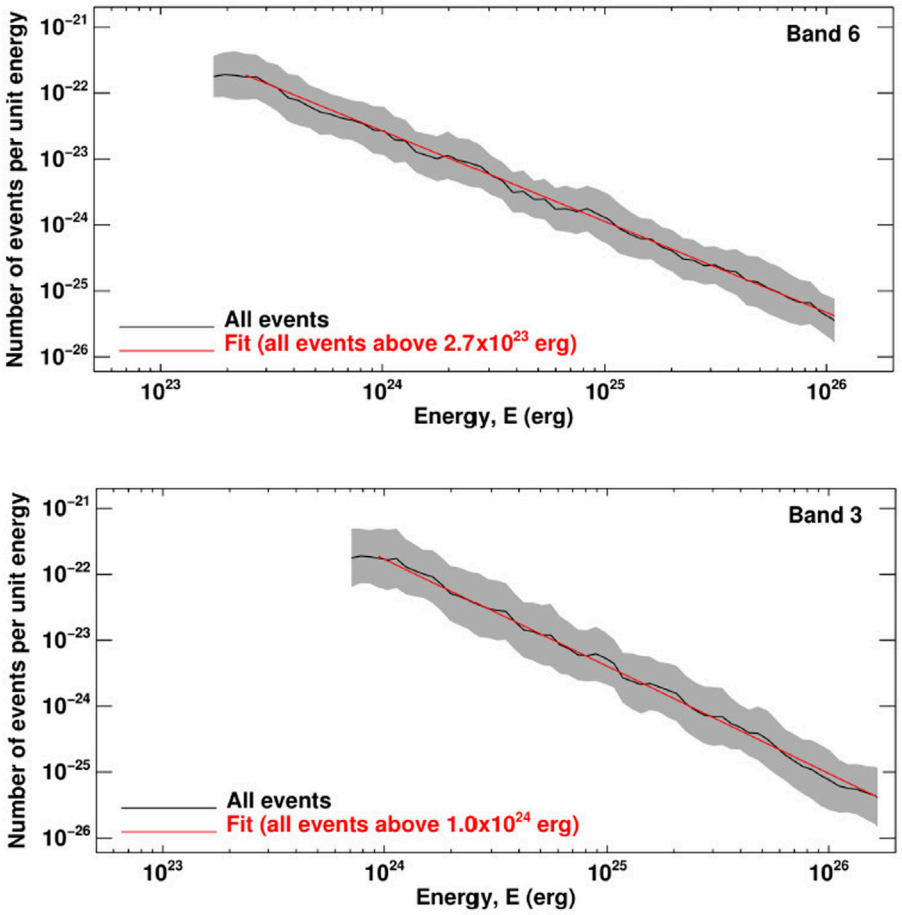

FIGURE 12
Energetics of quiet Sun ALMA transients. In the top panel, the black curve outlines the frequency distribution of 1.25-mm transients. The gray band marks the uncertainties while the red line represents the power-law fit (with index of 1.64) of the frequency distribution for energies $>2.7 \times 10^{23}$ erg. In the bottom panel the energetics of 3-mm transients are shown with a layout indentical to the top panel. The only exception is that the red line represents the power-law fit (with index of 1.73) of the frequency distribution for energies $>10^{24}$ erg (from Nindos et al., 2021). Reproduced with permission © ESO.

chromosphere part of a simulation box that contained small emerging loops interacting with the overlying canopy field in a situation that resembles the events studied by da Silva Santos et al. (2020) (*see* also Figure 10). The simulation reproduced well the observations and indicated that the observed 3 mm brightness temperature may form as a weighted average of significant contributions from different layers along the line of sight (*see* Martínez-Sykora et al., 2020).

3.4 Detection of shock waves

Significant attention has been drawn to the detection of possible signatures of propagating shock waves in ALMA data because: *1*) dissipation of shock waves may have a bearing on the heating of the chromosphere and corona, and *2*) 1D hydrodynamic simulations (*see* Loukitcheva et al., 2004, 2006) as well as 3D radiative MHD simulations (*see* Wedemeyer-Böhm et al., 2007; Loukitcheva et al., 2015; Eklund et al., 2020, 2021a, and also the review by Wedemeyer et al. included in this special Research Topic collection) have revealed that the signatures of such shocks could be identified in ALMA data.

Typically, snapshots from 3D simulations of propagating shock waves show, especially in regions of small magnetic field strength, a pronounced small-scale mesh-like pattern of elongated structures which is produced by propagating shock waves. Wedemeyer et al. (2016) (*see* also Wedemeyer-Böhm et al., 2007) concluded that the larger building blocks of such pattern can still be visible at a spatial resolution of 0.9″. However, such resolution, although feasible with ALMA at 1.25 mm, is probably at or beyond the instrument's capabilities at 3 mm where most of solar observing programs have been executed; the so-far most used Band 3 antenna

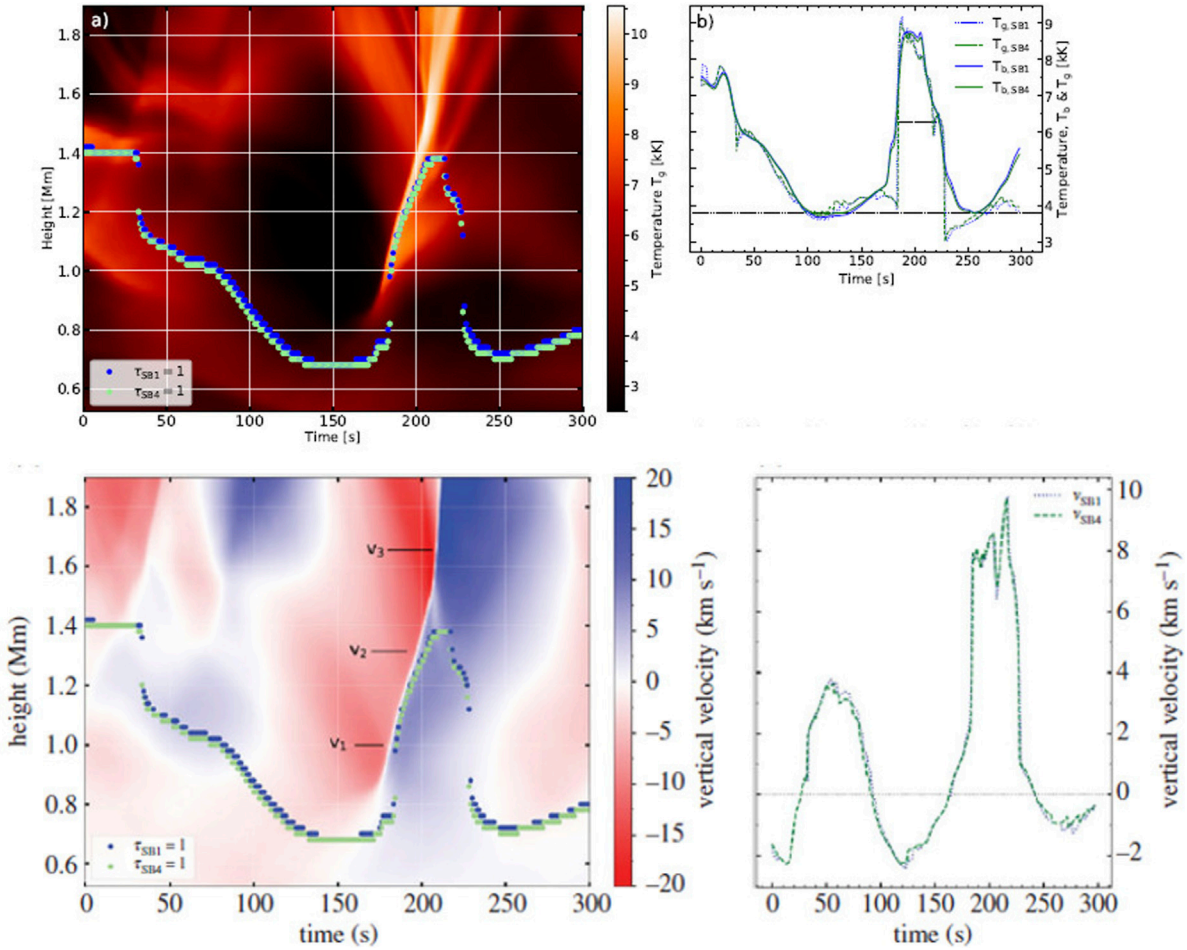

FIGURE 13
Top left [panel **(A)**]: Gas temperature as a function of time and height for a simulated shock wave. The blue and green dots indicate the formation heights for emission at 1.309 (SB1) and 1.204 mm (SB4), respectively. Top right [panel **(B)**]: Time profile of the brightness temperature at SB1 (solid blue) and SB4 (solid green) as well as of the gas temperature at the $\tau = 1$ heights of the corresponding wavelengths (blue/green dotted). Bottom panels: same as top panels but for the vertical velocity of the gas (from Eklund et al., 2021a).

configuration, C3, yields spatial resolution of ~ 2″. Therefore, it is not a surprise that the predicted shock-induced spatial pattern has yet to be identified with clarity in ALMA images.

Simulations also show how a number of plasma and radiation macroscopic parameters may change with height and time during the propagation of a shock wave. As an example in Figure 13 (top left panel) we show the gas temperature as a function of time and height at the location of a shock wave detected in the simulations by Eklund et al. (2021a). In the same panel the formation heights at optical depth $\tau = 1$ for two ALMA Band 6 sub-bands (SB1, 1.298–1.309 mm, and SB4 1.204–1.214 mm) are also plotted (*see* the blue and green circles). It is clear that the ~1.25 mm emission tracks well the shock front as it propagates from about 1 Mm up to about 1.4 Mm where it decouples from it. Note, however, that the shock front keeps moving upward. The decoupling occurs due to the lower opacities for the 1.25 mm emission at heights above ~1.4 Mm. Panel (b) of Figure 13 shows the corresponding time profiles of the SB1-SB4 brightness temperatures as well as the associated gas temperature time profiles at heights where $\tau = 1$. The event's FWHM is 41 s and the shock-related increase of brightness temperature is about 5000 K.

In the left bottom panel of Figure 13 we show the material's vertical velocity associated with the same simulated shock as a function of time and height. The pre-shock region is dominated by a bulk downflow of relatively cool material which is followed by the upflow of hotter material that is associated with the development of the shock. The upflow velocity reaches a value of ~10 km s^{-1} at the formation heights of the 1.25 mm radiation but velocities as double as that are registered higher up. On the other hand, the velocity of the vertical propagation of the shock front as can be depicted along the sharp shock-related height-

time slopes in the left panels of Figure 13 lies in the range of ~20–80 km s^{-1}.

The shock-related excess brightness temperature in the simulation we presented in Figure 13 is similar to those reported in other simulations (e.g. *see* Wedemeyer-Böhm et al., 2007) whereas the transient brightenings detected by Eklund et al. (2020) showed lower excess brightness temperatures up to 1200 K with typical values in the range 450–750 K. However, such discrepancies can be largely reconciled when the simulation results are degraded to the inferior ALMA spatial resolution (*see* Eklund et al., 2021b). Furthermore, Eklund et al. (2021b) reported that the degraded spatial resolution also affects the lifetime (i.e. FWHM) of shock-related transients because the 3 mm emission is not sensitive to some of the cooler pre-shock material; therefore the ALMA events will tend to be shorter than those detected by simulations. However, these discrepancies (differences on the order of about 15%) should not be as serious as those associated with their brightness temperatures.

Overall, the comparison of the simulation results with ALMA data may lead to the following criteria for the identification of shock signatures in mm-λ transient brightenings (*see* also Eklund et al., 2020; Chintzoglou et al., 2021b)

- Excess brightness temperature on order from a few hundred to more than a thousand degrees Kelvin.
- Temporal FWHM on the order of tens of seconds.
- Small lateral motions (i.e. with speeds smaller than the local sonic and Alfven speeds) during their lifetime since they are supposed to represent upward-propagating disturbances along magnetic field lines of minimal inclination.
- Occurrence in regions of relatively small magnetic field strength.
- Brightness temperature increases and decreases which should be consistent with undulatory intensity changes recorded in wavelegth-time cuts of the emission from chromospheric lines. This criterion probably provides the most compelling evidence for the presence of a shock wave (*see* below for the discussion of a particular example).

Eklund et al. (2020) concluded that most of the 552 transients events they detected were consistent with the first four of the criteria listed above (no spectroscopic data were available to them). As an example, in Figure 14 we show one of their best events. The event was largely spatially unresolved, its lifetime was 67 s and the brightness temperature increased by ~1100 K. Its location corresponds to the cross marked "A" in Figure 8, i.e. it was associated with small magnetic fields. Furthermore, the space-time cuts (panels f–g of Figure 14) yielded an apparent motion of the brightest pixel at the peak of the event (which coincided with the center of the field of view) of about 22 km s^{-1}. This value is somewhat larger that the nominal chromospheric sound and Alfven speeds (which are on the order of ~10 km s^{-1}, e.g. *see* Priest, 2014, and references therein) and, in any case, lies toward the high-end limit of the lateral apparent velocities registered by these authors.

When a shock passes through the chromosphere one expects wavelength-time (λ-t) cuts of chromospheric line emission to show a repetitive pattern of a blueshifted excursion that gradually drifts toward the red wing of the line. Such pattern should yield a "sawtooth" modulation in the λ-t cuts. That is exactly what was observed by Chintzoglou et al. (2021b) (*see* Figure 15) who studied coordinated ALMA 1.25 mm and IRIS UV observations of a plage region. In Figure 15 the time profile of the 1.25 mm emission for the same location of the plage is also displayed; its behavior is similar to the UV wavelength-time drift trends attributed to the propagation of shocks in the chromosphere; note in particular the correlation of 1.25-mm brightness temperature increases and UV blueshifts.

Chintzoglou et al. (2021b) concluded that the 1.25-mm plage emission was sensitive to localized heating of the upper chromosphere by propagating shocks. The pertinent brightness temperature jumps were of the order of 10–20% from a reference value of about 7500 K with a decay time of about 60–120 s and a recurrence at about 120 s. This temporal behavior may indicate that multiple shocks from different directions and at different timings could have passed through the specific plage location they considered.

4 Conclusions and prospects for the future

Oscillations, wave phenomena, and transient brightenings, along with turbulence, non-periodic temporal variations, and instrumental noise, all contribute to the observed time variability at any location in the chromosphere. Therefore, for any meaningful study of chromospheric dynamics care must be taken to separate these components. Despite the difficulties several important new results about the dynamic chromosphere have come out since the relatively recent (2016) initiation of regular solar observations with ALMA. The most important findings are summarized below.

- Magnetic field strength and topology largely influence the oscillatory behavior of the chromosphere; the traditional 3-min p-mode oscillations appear at mm-λ only above regions showing small amounts of overlying horizontal magnetic flux, i.e. over weak-field quiet Sun regions.
- When the p-modes are present, they represent brightness fluctuations of about 1–2% with respect to the average quiet Sun. But they correspond to ~0.5–0.6 of the spectrum-integrated power, i.e. they represent a significant fraction of the observed mm-λ

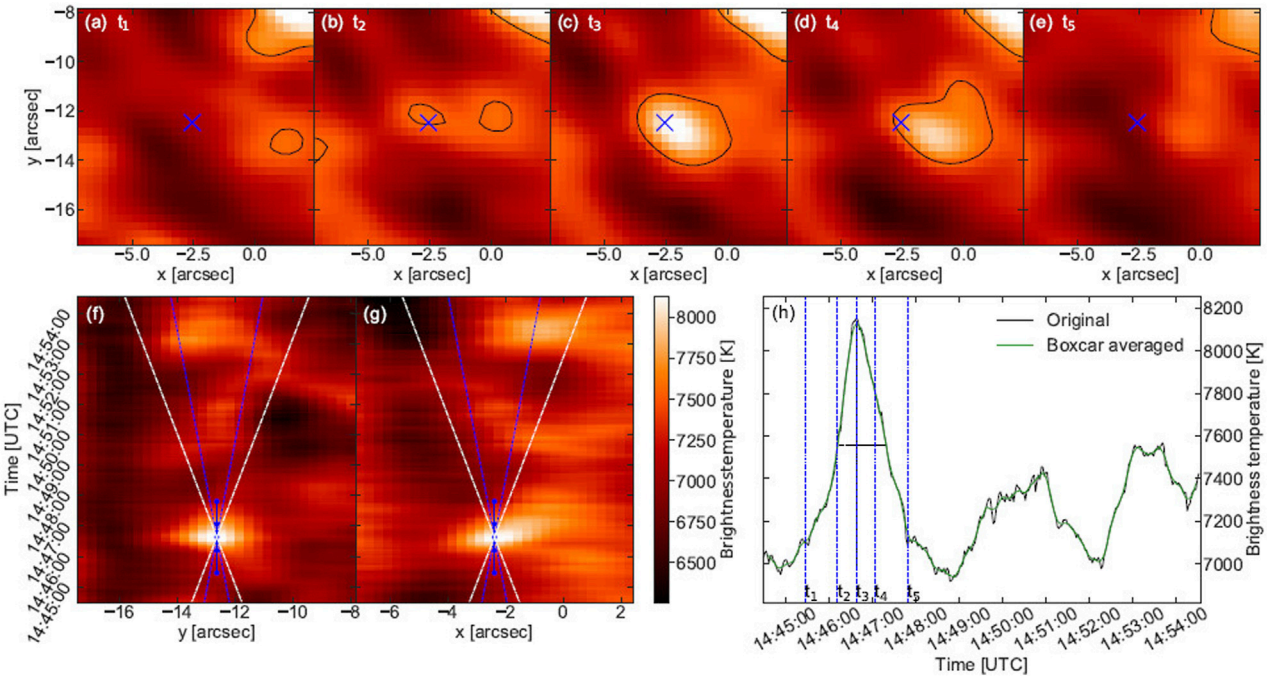

FIGURE 14
Panels **(A–E)** show characteristic snapshots of a transient brightening attributed to a propagating shock wave. The center of the field of view is marked by the blue "x." Panels **(F,G)** show vertical and horizontal cuts, respectively, across the center of the field of view which is indicated by blue dots for the times of panels **(A–E)**. Blue and white lines indicate apparent velocity slopes for 10 and 20 km s^{-1}, respectively. Panel **(H)** shows the brightness temperature time profile of the center of the field of view (from Eklund et al., 2020). Reproduced with permission © ESO.

brightness temperature fluctuations. For the first time, their power has been spatially resolved, thanks to the unprecedented ALMA's spatial resolution. Similar *p*-mode frequencies have been established both in the network and cell interior.

- High frequency (periods of 66–90 s) oscillations in brightness temperature, size, and horizontal motion of small-scale bright features have been detected for the first time in mm-λ observations.
- The first detection of spatially resolved mm-λ oscillations above a sunspot exhibited properties consistent with the propagation of magneto-acoustic waves above the umbra with some indications of nonlinear steepening.
- A multitude of weak transient brightenings, both in the quiet Sun and active regions, has been detected in ALMA data. Their excess brightness temperature may lie from about 40 K up to about 5000 K above background. Most of them are spatially unresolved. Some of the resolved ones are associated with ejecta that are likely caused by magnetic reconnection.
- The thermal energy of the transient brightenings is between 2×10^{23} and 10^{24} erg. The computed lower end of their energy distribution is among the smallest ever reported irrespective of the observing wavelength. However, their power per unit area can account for only ~1% of the radiative losses from the quiet low chromosphere.
- Brightness temperature increases in mm-λ transient brightenings could result from acoustic/magnetoacoustic shocks or from magnetic reconnection. Those associated with ejecta are probably induced by reconnection while those showing brightness temperature modulations that are consistent with undulatory intensity changes recorded in λ-*t* cuts of the emission from chromospheric lines may arise from shocks. A multitude of transients has been attributed to propagating shocks.

The above list highlights ALMA's great potential to address open issues in chromospheric physics. The major advantage of ALMA data is probably their ability to directly probe the spatial distribution and temporal variability of the electron temperature of the plasma without the need to address complicated effects arising from the non-LTE conditions prevailing in the formation of chromospheric spectral lines.

On the other hand, the major difficulties associated with solar ALMA observations include the small field of view, relatively low spatial resolution compared to state-of-the-art observations in

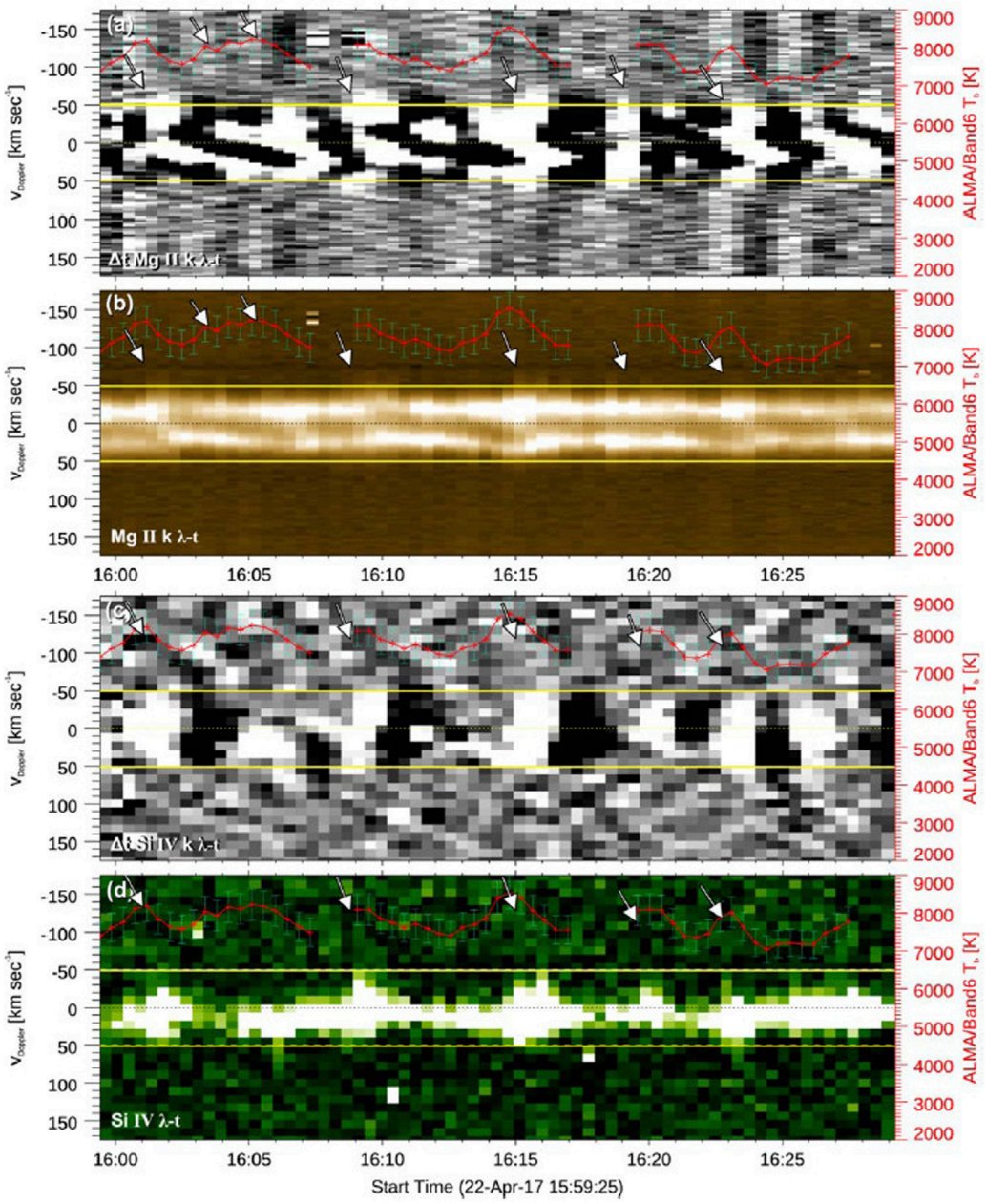

FIGURE 15
Wavelegth-time plot for Mg II k (panel **B**) and its temporal derivative (panel **A**) of a 1″ × 1″ area above a plage with recurrent shock waves. Panels **(C,D)** same as panels **(A,B)** but for Si IV. In all panels the 1.25 mm emission is overplotted (red curves). The rest-wavelegth position is marked with a dotted line. The arrows point to blueshifts and correlated 1.25-mm emission increases (from Chintzoglou et al., 2021b). © AAS. Reproduced with permission.

other wavelengths, the availability of a small number of frequency bands, as well as the demanding processing of the visibility data. The field of view can be enlarged by invoking mosaicking techniques at the cost of reduced cadence. With such a setup, only slowly varying phenomena can be tracked and this partly explains why in most of the studies that we reviewed in this paper, Band 3 data were analyzed; it is the frequency band providing the largest FOV, nominally 60″, for solar observing (the other part of the explanation is that, due to weather/atmospheric conditions, the execution of observations becomes increasingly demanding with frequency).

The study of the height dependence of dynamic phenomena requires observations at as many frequencies as possible. Currently ALMA is capable of observing one frequency band at a time. Things will improve by using subarrays, i.e. splitting an array configuration into pieces that observe different frequency bands at the same time or/and by adding new frequency bands to the solar observing programs. For example, the recent addition of Band 7 (0.86 mm) will help us probe lower heights than Band 6. At lower frequencies, a possible future addition of Band 1 (7.25 mm) will probe higher layers where the impact of oscillations should be lower, and thus the detection of weaker transient brightenings could be facilitated. Currently, making snapshot images at different spectral windows within the same ALMA band (*see* Jafarzadeh et al., 2019; Rodger et al., 2019) could act as a feasible, albeit not completely satisfactory (due to the limited range of sampled heights) alternative, to obtain spectral information about dynamic phenomena. Guevara Gómez et al. (2022b) and also in a work in preparation Guevara Gómez et al. (2022a) have shows that the combination of such spectral windows (to improve the signal-to-noise ratio) at two separate spectral regions within Band 3 yields height separations on the order of 70 km, as well as the approximate determination of propagating speeds of transverse waves identified in ALMA sub-bands and in synthetic data.

Throughout this paper the need for observations with the highest possible spatial resolution has been highlighted because several of the phenomena we discussed (for example transient brightenings) exhibit spatial scales at or below ALMA's current spatial resolution. Since ALMA's Cycle 7 (October 2019–October 2021, which includes the observatory's shutdown period due to the COVID-19 pandemic) the C4 antenna configuration array, whose most extended baseline is over 700 m, has been enabled for solar observations. With the C4 configuration a spatial resolution of about $1''$ can be achieved at 3 mm, which constitutes an improvement of a factor of two over the resolution of the Band 3 observations reviewed in this paper. Unfortunately, there has been no paper yet reporting observations of waves or transient events with the C4 configuration. However, the potential to observe with ALMA at sub-arcsecond resolution has been demonstrated by da Silva Santos et al. (2022b) who reported on the fine structure of a filament.

The implementation of circular polarization (Stokes parameter, V) measurements to future solar ALMA observing programs is anticipated to help constraining the magnetic field in the chromosphere. However, we note that the expected low degree of circular polarization outside of active regions demands high sensitivity and will certainly require the development of advanced calibration and imaging procedures. At the time of writing of this paper it is not yet known when solar V ALMA observations will become available. However, synergies between ALMA and high-sensitivity, high spatial and spectral polarimetric observations of photospheric and chromospheric magnetic fields (like the ones that will become available by the Daniel K. Inouye Solar Telescope, DKIST, instrumentation Rimmele et al., 2020) will certainly advance our knowledge on the topics discussed in this paper by shedding light on the upward propagation of waves through the magnetized solar atmosphere and by constraining the magnetic configuration where transient brightenings occur.

We also tried to emphasize that an important ingredient of the recent advances in the study of the dynamic chromosphere is the synergy between the ALMA observations and observations at (E)UV and X-rays. In particular, several spectral lines observed by IRIS (e.g., Mg II h and k) are formed at about the same height as the mm-λ continua observed with ALMA, but probe different plasma properties, thereby providing a highly complementary dataset to the ALMA data (e.g. *see* Bastian et al., 2017). Last but not least, the coordination of the anticipated sub-arcsecond DKIST and Solar Orbiter (Müller et al., 2020) observations with ALMA has the potential to provide information on the small-scale structure of several chromospheric dynamic phenomena together with their photospheric and transition region counterparts in an unprecentedly long wavelength range from UV to mm-λ.

Author contributions

All authors have contributed to preparing this article.

Acknowledgments

ALMA is a partnership of ESO (representing its member states), NSF (USA) and NINS (Japan), together with NRC (Canada) and NSC and ASIAA (Taiwan), and KASI (Republic of Korea), in co-operation with the Republic of Chile. The Joint ALMA Observatory is operated by ESO, 654 AUI/NRAO, and NAOJ. The National Radio Astronomy Observatory is a facility of the National Science Foundation operated under cooperative agreement by Associated Universities, Inc.

Conflict of interest

The authors declare that the research was conducted in the absence of any commercial or financial relationships that could be construed as a potential conflict of interest.

Publisher's note

References

Alissandrakis, C. E., Nindos, A., Bastian, T. S., and Patsourakos, S. (2020). Modeling the quiet Sun cell and network emission with ALMA. *Astron. Astrophys.* 640, A57. doi:10.1051/0004-6361/202038461

Alissandrakis, C. E., Patsourakos, S., Nindos, A., and Bastian, T. S. (2017). Center-to-limb observations of the Sun with ALMA . Implications for solar atmospheric models. *Astron. Astrophys.* 605, A78. doi:10.1051/0004-6361/201730953

Archontis, V., and Hood, A. W. (2009). Formation of Ellerman bombs due to 3D flux emergence. *Astron. Astrophys.* 508, 1469–1483. doi:10.1051/0004-6361/200912455

Baker, D., Stangalini, M., Valori, G., Brooks, D. H., To, A. S. H., van Driel-Gesztelyi, L., et al. (2021). Alfvénic perturbations in a sunspot chromosphere linked to fractionated plasma in the corona. *Astrophys. J.* 907, 16. doi:10.3847/1538-4357/abcafd

Bastian, T. S., Chintzoglou, G., De Pontieu, B., Shimojo, M., Schmit, D., Leenaarts, J., et al. (2017). A first comparison of millimeter continuum and Mg II ultraviolet line emission from the solar chromosphere. *Astrophys. J.* 845, L19. doi:10.3847/2041-8213/aa844c

Beckers, J. M., and Schultz, R. B. (1972). Oscillatory motions in sunspots. *Sol. Phys.* 27, 61–70. doi:10.1007/BF00151770

Beckers, J. M., and Tallant, P. E. (1969). Chromospheric inhomogeneities in sunspot umbrae. *Sol. Phys.* 7, 351–365. doi:10.1007/BF00146140

Bogdan, T. J., Carlsson, M., Hansteen, V. H., McMurry, A., Rosenthal, C. S., Johnson, M., et al. (2003). Waves in the magnetized solar atmosphere. II. Waves from localized sources in magnetic flux concentrations. *Astrophys. J.* 599, 626–660. doi:10.1086/378512

Bogdan, T. J., and Judge, P. G. (2006). Observational aspects of sunspot oscillations. *Phil. Trans. R. Soc. A* 364, 313–331. doi:10.1098/rsta.2005.1701

Carlsson, M., De Pontieu, B., and Hansteen, V. H. (2019). New view of the solar chromosphere. *Annu. Rev. Astron. Astrophys.* 57, 189–226. doi:10.1146/annurev-astro-081817-052044

Carlsson, M., and Stein, R. F. (2002). Dynamic hydrogen ionization. *Astrophys. J.* 572, 626–635. doi:10.1086/340293

Carlsson, M., and Stein, R. F. (1992). Non-LTE radiating acoustic shocks and CA II K2V bright points. *Astrophys. J.* 397, L59. doi:10.1086/186544

Centeno, R., Collados, M., and Trujillo Bueno, J. (2006). Spectropolarimetric investigation of the propagation of magnetoacoustic waves and shock formation in sunspot atmospheres. *Astrophys. J.* 640, 1153–1162. doi:10.1086/500185

Chae, J., and Goode, P. R. (2015). Acoustic waves generated by impulsive disturbances in a gravitationally stratified medium. *Astrophys. J.* 808, 118. doi:10.1088/0004-637X/808/2/118

Chai, Y., Gary, D. E., Reardon, K. P., and Yurchyshyn, V. (2022). A study of sunspot 3 minute oscillations using ALMA and GST. *Astrophys. J.* 924, 100. doi:10.3847/1538-4357/ac34f7

Chintzoglou, G., De Pontieu, B., Martínez-Sykora, J., Hansteen, V., de la Cruz Rodríguez, J., Szydlarski, M., et al. (2021a). ALMA and IRIS observations of the solar chromosphere. I. An on-disk type II spicule. *Astrophys. J.* 906, 82. doi:10.3847/1538-4357/abc9b1

Chintzoglou, G., De Pontieu, B., Martínez-Sykora, J., Hansteen, V., de la Cruz Rodríguez, J., Szydlarski, M., et al. (2021b). ALMA and IRIS observations of the solar chromosphere. II. Structure and dynamics of chromospheric plages. *Astrophys. J.* 906, 83. doi:10.3847/1538-4357/abc9b0

Cirtain, J. W., Golub, L., Winebarger, A. R., de Pontieu, B., Kobayashi, K., Moore, R. L., et al. (2013). Energy release in the solar corona from spatially resolved magnetic braids. *Nature* 493, 501–503. doi:10.1038/nature11772

Cooley, J. W., and Tukey, J. W. (1965). An algorithm for the machine calculation of complex Fourier series. *Math. Comput.* 19, 297–301. doi:10.1090/s0025-5718-1965-0178586-1

Cram, L. E. (1978). High resolution spectroscopy of the disk chromosphere. VI. Power, phase and coherence spectra of atmospheric oscillations. *Astron. Astrophys.* 70, 345.

da Silva Santos, J. M., Danilovic, S., Leenaarts, J., de la Cruz Rodríguez, J., Zhu, X., White, S. M., et al. (2022a). Heating of the solar chromosphere through current dissipation. *Astron. Astrophys.* 661, A59. doi:10.1051/0004-6361/202243191

da Silva Santos, J. M., de la Cruz Rodríguez, J., White, S. M., Leenaarts, J., Vissers, G. J. M., and Hansteen, V. H. (2020). ALMA observations of transient heating in a solar active region. *Astron. Astrophys.* 643, A41. doi:10.1051/0004-6361/202038755

da Silva Santos, J. M., White, S. M., Reardon, K., Cauzzi, G., Gunár, S., Heinzel, P., et al. (2022b). Subarcsecond imaging of a solar active region filament with ALMA and IRIS. *Front. Astron. Space Sci.* 9, 898115. doi:10.3389/fspas.2022.898115

De Pontieu, B., Hansteen, V. H., Rouppe van der Voort, L., van Noort, M., and Carlsson, M. (2007a). High-resolution observations and modeling of dynamic fibrils. *Astrophys. J.* 655, 624–641. doi:10.1086/509070

De Pontieu, B., McIntosh, S. W., Carlsson, M., Hansteen, V. H., Tarbell, T. D., Schrijver, C. J., et al. (2007b). Chromospheric alfvénic waves strong enough to power the solar wind. *Science* 318, 1574–1577. doi:10.1126/science.1151747

De Pontieu, B., Title, A. M., Lemen, J. R., Kushner, G. D., Akin, D. J., Allard, B., et al. (2014). The Interface region imaging Spectrograph (IRIS). *Sol. Phys.* 289, 2733–2779. doi:10.1007/s11207-014-0485-y

Eklund, H., Wedemeyer, S., Snow, B., Jess, D. B., Jafarzadeh, S., Grant, S. D. T., et al. (2021a). Characterization of shock wave signatures at millimetre wavelengths from Bifrost simulations. *Phil. Trans. R. Soc. A* 379, 20200185. doi:10.1098/rsta.2020.0185

Eklund, H., Wedemeyer, S., Szydlarski, M., Jafarzadeh, S., and Guevara Gómez, J. C. (2020). The Sun at millimeter wavelengths. II. Small-scale dynamic events in ALMA Band 3. *Astron. Astrophys.* 644, A152. doi:10.1051/0004-6361/202038250

Eklund, H., Wedemeyer, S., Szydlarski, M., and Jafarzadeh, S. (2021b). The Sun at millimeter wavelengths. III. Impact of the spatial resolution on solar ALMA observations. *Astron. Astrophys.* 656, A68. doi:10.1051/0004-6361/202140972

Felipe, T., Khomenko, E., Collados, M., and Beck, C. (2010). Multi-layer study of wave propagation in sunspots. *Astrophys. J.* 722, 131–144. doi:10.1088/0004-637X/722/1/131

Felipe, T. (2021). Signatures of sunspot oscillations and the case for chromospheric resonances. *Nat. Astron.* 5, 2–4. doi:10.1038/s41550-020-1157-5

Fleck, B., Carlsson, M., Khomenko, E., Rempel, M., Steiner, O., and Vigeesh, G. (2021). Acoustic-gravity wave propagation characteristics in three-dimensional radiation hydrodynamic simulations of the solar atmosphere. *Phil. Trans. R. Soc. A* 379, 20200170. doi:10.1098/rsta.2020.0170

Fleck, B., and Schmitz, F. (1991). The 3-min oscillations of the solar chromosphere - a basic physical effect? *Astron. Astrophys.* 250, 235–244.

Fontenla, J. M., Avrett, E. H., and Loeser, R. (1993). Energy balance in the solar transition region. III. Helium emission in hydrostatic, constant-abundance models with diffusion. *Astrophys. J.* 406, 319. doi:10.1086/172443

Gabriel, A. H. (1976). A magnetic model of the solar transition region. *Philosophical Trans. R. Soc. Lond. Ser. A* 281, 339–352. doi:10.1098/rsta.1976.0031

Gafeira, R., Jafarzadeh, S., Solanki, S. K., Lagg, A., van Noort, M., Barthol, P., et al. (2017). Oscillations on width and intensity of slender Ca II H fibrils from sunrise/SuFI. *Astrophys. J. Suppl. Ser.* 229, 7. doi:10.3847/1538-4365/229/1/7

Gary, D. E., Hartl, M. D., and Shimizu, T. (1997). Nonthermal radio emission from solar soft X-ray transient brightenings. *Astrophys. J.* 477, 958–968. doi:10.1086/303748

Georgoulis, M. K., Rust, D. M., Bernasconi, P. N., and Schmieder, B. (2002). Statistics, morphology, and energetics of ellerman bombs. *Astrophys. J.* 575, 506–528. doi:10.1086/341195

Giovanelli, R. G., and Jones, H. P. (1982). The three-dimensional structure of atmospheric magnetic fields in two active regions. *Sol. Phys.* 79, 267–278. doi:10.1007/BF00146244

Giovanelli, R. G. (1972). Oscillations and waves in a sunspot. *Sol. Phys.* 27, 71–79. doi:10.1007/BF00151771

Guevara Gómez, J. C., Jafarzadeh, S., Wedemeyer, S., Grant, S. D. T., Eklund, H., and Szydlarski, M. (2022a). The Sun at millimeter wavelengths. IV. Magnetohydrodynamic waves in small-scale bright features. *Astron. Astrophys.* in prep.

Guevara Gómez, J. C., Jafarzadeh, S., Wedemeyer, S., and Szydlarski, M. (2022b). Propagation of transverse waves in the solar chromosphere through ALMA sub-bands. *Astron. Astrophys.* 665, L2.

Guevara Gómez, J. C., Jafarzadeh, S., Wedemeyer, S., Szydlarski, M., Stangalini, M., Fleck, B., et al. (2021). High-frequency oscillations in small chromospheric bright features observed with Atacama Large Millimetre/Submillimetre Array. *Phil. Trans. R. Soc. A* 379, 20200184. doi:10.1098/rsta.2020.0184

Guglielmino, S. L., Zuccarello, F., Young, P. R., Murabito, M., and Romano, P. (2018). IRIS observations of magnetic interactions in the solar atmosphere between preexisting and emerging magnetic fields. I. Overall evolution. *Astrophys. J.* 856, 127. doi:10.3847/1538-4357/aab2a8

Hansteen, V., Ortiz, A., Archontis, V., Carlsson, M., Pereira, T. M. D., and Bjørgen, J. P. (2019). Ellerman bombs and UV bursts: Transient events in chromospheric current sheets. *Astron. Astrophys.* 626, A33. doi:10.1051/0004-6361/201935376

Heggland, L., Hansteen, V. H., De Pontieu, B., and Carlsson, M. (2011). Wave propagation and jet formation in the chromosphere. *Astrophys. J.* 743, 142. doi:10.1088/0004-637X/743/2/142

Henriques, V. M. J., Kuridze, D., Mathioudakis, M., and Keenan, F. P. (2016). Quiet-sun Hα transients and corresponding small-scale transition region and coronal heating. *Astrophys. J.* 820, 124. doi:10.3847/0004-637X/820/2/124

Hollweg, J. V. (1981). Alfvén waves in the solar atmosphere. *Sol. Phys.* 70, 25–66. doi:10.1007/BF00154391

Howe, R., Jain, K., Bogart, R. S., Haber, D. A., and Baldner, C. S. (2012). Two-Dimensional helioseismic power, phase, and coherence spectra of solar dynamics observatory photospheric and chromospheric observables. *Sol. Phys.* 281, 533–549. doi:10.1007/s11207-012-0097-3

Hudson, H. S. (1991). Solar flares, microflares, nanoflares, and coronal heating. *Sol. Phys.* 133, 357–369. doi:10.1007/BF00149894

Jafarzadeh, S., Cameron, R. H., Solanki, S. K., Pietarila, A., Feller, A., Lagg, A., et al. (2014). Migration of Ca II H bright points in the internetwork. *Astron. Astrophys.* 563, A101. doi:10.1051/0004-6361/201323011

Jafarzadeh, S., Rutten, R. J., Solanki, S. K., Wiegelmann, T., Riethmüller, T. L., van Noort, M., et al. (2017a). Slender Ca II H fibrils mapping magnetic fields in the low solar chromosphere. *Astrophys. J. Suppl. Ser.* 229, 11. doi:10.3847/1538-4365/229/1/11

Jafarzadeh, S., Solanki, S. K., Gafeira, R., van Noort, M., Barthol, P., Blanco Rodríguez, J., et al. (2017b). Transverse oscillations in slender Ca II H fibrils observed with sunrise/SuFI. *Astrophys. J. Suppl. Ser.* 229, 9. doi:10.3847/1538-4365/229/1/9

Jafarzadeh, S., Solanki, S. K., Stangalini, M., Steiner, O., Cameron, R. H., and Danilovic, S. (2017c). High-frequency oscillations in small magnetic elements observed with sunrise/SuFI. *Astrophys. J. Suppl. Ser.* 229, 10. doi:10.3847/1538-4365/229/1/10

Jafarzadeh, S., Wedemeyer, S., Fleck, B., Stangalini, M., Jess, D. B., Morton, R. J., et al. (2021). An overall view of temperature oscillations in the solar chromosphere with ALMA. *Phil. Trans. R. Soc. A* 379, 20200174. doi:10.1098/rsta.2020.0174

Jafarzadeh, S., Wedemeyer, S., Szydlarski, M., De Pontieu, B., Rezaei, R., and Carlsson, M. (2019). The solar chromosphere at millimetre and ultraviolet wavelengths. I. Radiation temperatures and a detailed comparison. *Astron. Astrophys.* 622, A150. doi:10.1051/0004-6361/201834205

Jefferies, S. M., McIntosh, S. W., Armstrong, J. D., Bogdan, T. J., Cacciani, A., and Fleck, B. (2006). Magnetoacoustic portals and the basal heating of the solar chromosphere. *Astrophys. J.* 648, L151–L155. doi:10.1086/508165

Jess, D. B., Morton, R. J., Verth, G., Fedun, V., Grant, S. D. T., and Giagkiozis, I. (2015). Multiwavelength studies of MHD waves in the solar chromosphere. An overview of recent results. *Space Sci. Rev.* 190, 103–161. doi:10.1007/s11214-015-0141-3

Jess, D. B., Snow, B., Fleck, B., Stangalini, M., and Jafarzadeh, S. (2021). Reply to: Signatures of sunspot oscillations and the case for chromospheric resonances. *Nat. Astron.* 5, 5–8. doi:10.1038/s41550-020-1158-4

Jess, D. B., Snow, B., Houston, S. J., Botha, G. J. J., Fleck, B., Krishna Prasad, S., et al. (2020). A chromospheric resonance cavity in a sunspot mapped with seismology. *Nat. Astron.* 4, 220–227. doi:10.1038/s41550-019-0945-2

Joulin, V., Buchlin, E., Solomon, J., and Guennou, C. (2016). Energetic characterisation and statistics of solar coronal brightenings. *Astron. Astrophys.* 591, A148. doi:10.1051/0004-6361/201526254

Khomenko, E., and Collados, M. (2015). Oscillations and waves in sunspots. *Living Rev. Sol. Phys.* 12, 6. doi:10.1007/lrsp-2015-6

Klimchuk, J. A. (2006). On solving the coronal heating problem. *Sol. Phys.* 234, 41–77. doi:10.1007/s11207-006-0055-z

Krucker, S., Benz, A. O., Bastian, T. S., and Acton, L. W. (1997). X-ray network flares of the quiet Sun. *Astrophys. J.* 488, 499–505. doi:10.1086/304686

Kubo, M., Katsukawa, Y., Suematsu, Y., Kano, R., Bando, T., Narukage, N., et al. (2016). Discovery of ubiquitous fast-propagating intensity disturbances by the chromospheric lyman alpha spectropolarimeter (CLASP). *Astrophys. J.* 832, 141. doi:10.3847/0004-637X/832/2/141

Kuridze, D., Morton, R. J., Erdélyi, R., Dorrian, G. D., Mathioudakis, M., Jess, D. B., et al. (2012). Transverse oscillations in chromospheric mottles. *Astrophys. J.* 750, 51. doi:10.1088/0004-637X/750/1/51

Leighton, R. B., Noyes, R. W., and Simon, G. W. (1962). Velocity fields in the solar atmosphere. I. Preliminary report. *Astrophys. J.* 135, 474. doi:10.1086/147285

Lemen, J. R., Title, A. M., Akin, D. J., Boerner, P. F., Chou, C., Drake, J. F., et al. (2012). The atmospheric imaging assembly (AIA) on the solar dynamics observatory (SDO). *Sol. Phys.* 275, 17–40. doi:10.1007/s11207-011-9776-8

Löhner-Böttcher, J., Bello González, N., and Schmidt, W. (2016). Magnetic field reconstruction based on sunspot oscillations. *Astron. Nachr.* 337, 1040–1044. doi:10.1002/asna.201612430

Lomb, N. R. (1976). Least-squares frequency analysis of unequally spaced data. *Astrophys. Space Sci.* 39, 447–462. doi:10.1007/BF00648343

Loukitcheva, M. (2019). First solar observations with ALMA. *Adv. Space Res.* 63, 1396–1403. doi:10.1016/j.asr.2018.08.030

Loukitcheva, M., Solanki, S. K., Carlsson, M., and Stein, R. F. (2004). Millimeter observations and chromospheric dynamics. *Astron. Astrophys.* 419, 747–756. doi:10.1051/0004-6361:20034159

Loukitcheva, M., Solanki, S. K., Carlsson, M., and White, S. M. (2015). Millimeter radiation from a 3D model of the solar atmosphere. I. Diagnosing chromospheric thermal structure. *Astron. Astrophys.* 575, A15. doi:10.1051/0004-6361/201425238

Loukitcheva, M., Solanki, S. K., and White, S. (2006). The dynamics of the solar chromosphere: Comparison of model predictions with millimeter-interferometer observations. *Astron. Astrophys.* 456, 713–723. doi:10.1051/0004-6361:20053171

Martínez-Sykora, J., De Pontieu, B., de la Cruz Rodriguez, J., and Chintzoglou, G. (2020). the formation height of millimeter-wavelength emission in the solar chromosphere. *Astrophys. J.* 891, L8. doi:10.3847/2041-8213/ab75ac

McIntosh, S. W., de Pontieu, B., Carlsson, M., Hansteen, V., Boerner, P., and Goossens, M. (2011). Alfvénic waves with sufficient energy to power the quiet solar corona and fast solar wind. *Nature* 475, 477–480. doi:10.1038/nature10235

Moore, R. L., Cirtain, J. W., Sterling, A. C., and Falconer, D. A. (2010). Dichotomy of solar coronal jets: Standard jets and blowout jets. *Astrophys. J.* 720, 757–770. doi:10.1088/0004-637X/720/1/757

Moretti, P. F., Jefferies, S. M., Armstrong, J. D., and McIntosh, S. W. (2007). Observational signatures of the interaction between acoustic waves and the solar magnetic canopy. *Astron. Astrophys.* 471, 961–965. doi:10.1051/0004-6361:20077247

Müller, D., Cyr, St.O. C., Zouganelis, I., Gilbert, H. R., Marsden, R., Nieves-Chinchilla, T., et al. (2020). The solar orbiter mission. *Astron. Astrophys.* 642, A1. doi:10.1051/0004-6361/202038467

Nindos, A., Alissandrakis, C. E., Bastian, T. S., Patsourakos, S., De Pontieu, B., Warren, H., et al. (2018). First high-resolution look at the quiet Sun with ALMA at 3mm. *Astron. Astrophys.* 619, L6. doi:10.1051/0004-6361/201834113

Nindos, A., Alissandrakis, C. E., Patsourakos, S., and Bastian, T. S. (2020). Transient brightenings in the quiet Sun detected by ALMA at 3 mm. *Astron. Astrophys.* 638, A62. doi:10.1051/0004-6361/202037810

Nindos, A. (2020). Incoherent solar radio emission. *Front. Astron. Space Sci.* 7, 57. doi:10.3389/fspas.2020.00057

Nindos, A., Kundu, M. R., and White, S. M. (1999). A study of microwave-selected coronal transient brightenings. *Astrophys. J.* 513, 983–989. doi:10.1086/306886

Nindos, A., Patsourakos, S., Alissandrakis, C. E., and Bastian, T. S. (2021). ALMA observations of the variability of the quiet Sun at millimeter wavelengths. *Astron. Astrophys.* 652, A92. doi:10.1051/0004-6361/202141241

Nutto, C., Steiner, O., and Roth, M. (2012). Revealing the nature of magnetic shadows with numerical 3D-MHD simulations. *Astron. Astrophys.* 542, L30. doi:10.1051/0004-6361/201218856

Okamoto, T. J., and De Pontieu, B. (2011). Propagating waves along spicules. *Astrophys. J.* 736, L24. doi:10.1088/2041-8205/736/2/L24

Orozco Suárez, D., Katsukawa, Y., and Bellot Rubio, L. R. (2012). The connection between internetwork magnetic elements and supergranular flows. *Astrophys. J.* 758, L38. doi:10.1088/2041-8205/758/2/L38

Parker, E. N. (1988). Nanoflares and the solar X-ray corona. *Astrophys. J.* 330, 474. doi:10.1086/166485

Patsourakos, S., Alissandrakis, C. E., Nindos, A., and Bastian, T. S. (2020). Observations of solar chromospheric oscillations at 3 mm with ALMA. *Astron. Astrophys.* 634, A86. doi:10.1051/0004-6361/201936618

Pereira, T. M. D., De Pontieu, B., and Carlsson, M. (2012). Quantifying spicules. *Astrophys. J.* 759, 18. doi:10.1088/0004-637X/759/1/18

Pesnell, W. D., Thompson, B. J., and Chamberlin, P. C. (2012). The solar dynamics observatory (SDO). *Sol. Phys.* 275, 3–15. doi:10.1007/s11207-011-9841-3

Priest, E. (2014). *Magnetohydrodynamics of the sun*. Cambridge: Cambridge University Press. doi:10.1017/CBO9781139020732

Raouafi, N. E., Patsourakos, S., Pariat, E., Young, P. R., Sterling, A. C., Savcheva, A., et al. (2016). Solar coronal jets: Observations, theory, and modeling. *Space Sci. Rev.* 201, 1–53. doi:10.1007/s11214-016-0260-5

Rimmele, T. R., Warner, M., Keil, S. L., Goode, P. R., Knölker, M., Kuhn, J. R., et al. (2020). The Daniel K. Inouye solar telescope - observatory overview. *Sol. Phys.* 295, 172. doi:10.1007/s11207-020-01736-7

Rodger, A. S., Labrosse, N., Wedemeyer, S., Szydlarski, M., Simões, P. J. A., and Fletcher, L. (2019). First spectral analysis of a solar plasma eruption using ALMA. *Astrophys. J.* 875, 163. doi:10.3847/1538-4357/aafdfb

Rosenthal, C. S., Bogdan, T. J., Carlsson, M., Dorch, S. B. F., Hansteen, V., McIntosh, S. W., et al. (2002). Waves in the magnetized solar atmosphere. I. Basic processes and internetwork oscillations. *Astrophys. J.* 564, 508–524. doi:10.1086/324214

Rutten, R. J. (2007). "Observing the solar chromosphere," in *The physics of chromospheric plasmas. Vol. 368 of astronomical society of the pacific conference series*. Editors P. Heinzel, I. Dorotovič, and R. J. Rutten, 27.

Rutten, R. J. (2017). Solar H-alpha features with hot onsets. III. Long fibrils in Lyman-alpha and with ALMA. *Astron. Astrophys.* 598, A89. doi:10.1051/0004-6361/201629238

Scargle, J. D. (1982). Studies in astronomical time series analysis. II. Statistical aspects of spectral analysis of unevenly spaced data. *Astrophys. J.* 263, 835–853. doi:10.1086/160554

Schou, J., Scherrer, P. H., Bush, R. I., Wachter, R., Couvidat, S., Rabello-Soares, M. C., et al. (2012). Design and ground calibration of the helioseismic and magnetic imager (HMI) instrument on the solar dynamics observatory (SDO). *Sol. Phys.* 275, 229–259. doi:10.1007/s11207-011-9842-2

Shibasaki, K., Alissandrakis, C. E., and Pohjolainen, S. (2011). Radio emission of the quiet Sun and active regions (invited review). *Sol. Phys.* 273, 309–337. doi:10.1007/s11207-011-9788-4

Shimizu, T. (2015). 3D magnetic field configuration of small-scale reconnection events in the solar plasma atmosphere. *Phys. Plasmas* 22, 101207. doi:10.1063/1.4933056

Shimizu, T., Shimojo, M., and Abe, M. (2021). Simultaneous ALMA-hinode-IRIS observations on footpoint signatures of a soft X-ray loop-like microflare. *Astrophys. J.* 922, 113. doi:10.3847/1538-4357/ac27a4

Shimojo, M., Bastian, T. S., Hales, A. S., White, S. M., Iwai, K., Hills, R. E., et al. (2017a). Observing the Sun with the Atacama large millimeter/submillimeter array (ALMA): High-resolution interferometric imaging. *Sol. Phys.* 292, 87. doi:10.1007/s11207-017-1095-2

Shimojo, M., Hudson, H. S., White, S. M., Bastian, T. S., and Iwai, K. (2017b). The first ALMA observation of a solar plasmoid ejection from an X-ray bright point. *Astrophys. J.* 841, L5. doi:10.3847/2041-8213/aa70e3

Shimojo, M., Narukage, N., Kano, R., Sakao, T., Tsuneta, S., Shibasaki, K., et al. (2007). Fine structures of solar X-ray jets observed with the X-ray telescope aboard Hinode. *Publ. Astron. Soc. Jpn. Nihon. Tenmon. Gakkai.* 59, S745–S750. doi:10.1093/pasj/59.sp3.S745

Solanki, S. K., Steiner, O., and Uitenbroeck, H. (1991). Two-dimensional models of the solar chromosphere. I - the CA II K line as a diagnostic: 1.5-D radiative transfer. *Astron. Astrophys.* 250, 220–234.

Stangalini, M., Baker, D., Valori, G., Jess, D. B., Jafarzadeh, S., Murabito, M., et al. (2021). Spectropolarimetric fluctuations in a sunspot chromosphere. *Phil. Trans. R. Soc. A* 379, 20200216. doi:10.1098/rsta.2020.0216

Title, A. M., Topka, K. P., Tarbell, T. D., Schmidt, W., Balke, C., and Scharmer, G. (1992). On the differences between plage and quiet Sun in the solar photosphere. *Astrophys. J.* 393, 782. doi:10.1086/171545

Tsiropoula, G., Tziotziou, K., Kontogiannis, I., Madjarska, M. S., Doyle, J. G., and Suematsu, Y. (2012). Solar fine-scale structures. I. Spicules and other small-scale, jet-like events at the chromospheric level: Observations and physical parameters. *Space Sci. Rev.* 169, 181–244. doi:10.1007/s11214-012-9920-2

Vial, J.-C., and Engvold, O. (2015). "Solar prominences," in *Solar prominences. Vol. 415 of astrophysics and space science library*. doi:10.1007/978-3-319-10416-4

Warmuth, A., and Mann, G. (2020). Thermal-nonthermal energy partition in solar flares derived from X-ray, EUV, and bolometric observations. Discussion of recent studies. *Astron. Astrophys.* 644, A172. doi:10.1051/0004-6361/202039529

Watanabe, H., Vissers, G., Kitai, R., Rouppe van der Voort, L., and Rutten, R. J. (2011). Ellerman bombs at high resolution. I. Morphological evidence for photospheric reconnection. *Astrophys. J.* 736, 71. doi:10.1088/0004-637X/736/1/71

Wedemeyer, S., Bastian, T., Brajša, R., Hudson, H., Fleishman, G., Loukitcheva, M., et al. (2016). Solar science with the Atacama large millimeter/submillimeter array—a new view of our Sun. *Space Sci. Rev.* 200, 1–73. doi:10.1007/s11214-015-0229-9

Wedemeyer, S., Szydlarski, M., Jafarzadeh, S., Eklund, H., Guevara Gomez, J. C., Bastian, T., et al. (2020). The Sun at millimeter wavelengths. I. Introduction to ALMA Band 3 observations. *Astron. Astrophys.* 635, A71. doi:10.1051/0004-6361/201937122

Wedemeyer-Böhm, S., Lagg, A., and Nordlund, Å. (2009). Coupling from the photosphere to the chromosphere and the corona. *Space Sci. Rev.* 144, 317–350. doi:10.1007/s11214-008-9447-8

Wedemeyer-Böhm, S., Ludwig, H. G., Steffen, M., Leenaarts, J., and Freytag, B. (2007). Inter-network regions of the Sun at millimetre wavelengths. *Astron. Astrophys.* 471, 977–991. doi:10.1051/0004-6361:20077588

White, S. M., Iwai, K., Phillips, N. M., Hills, R. E., Hirota, A., Yagoubov, P., et al. (2017). Observing the Sun with the Atacama large millimeter/submillimeter array (ALMA): Fast-scan single-dish mapping. *Sol. Phys.* 292, 88. doi:10.1007/s11207-017-1123-2

White, S. M., and Kundu, M. R. (1992). Solar observations with a millimeter wavelength Array. *Sol. Phys.* 141, 347–369. doi:10.1007/BF00155185

White, S. M., Loukitcheva, M., and Solanki, S. K. (2006). High-resolution millimeter-interferometer observations of the solar chromosphere. *Astron. Astrophys.* 456, 697–711. doi:10.1051/0004-6361:20052854

Withbroe, G. L., and Noyes, R. W. (1977). Mass and energy flow in the solar chromosphere and corona. *Annu. Rev. Astron. Astrophys.* 15, 363–387. doi:10.1146/annurev.aa.15.090177.002051

Yokoyama, T., Shimojo, M., Okamoto, T. J., and Iijima, H. (2018). ALMA observations of the solar chromosphere on the polar limb. *Astrophys. J.* 863, 96. doi:10.3847/1538-4357/aad27e

Young, P. R., Tian, H., Peter, H., Rutten, R. J., Nelson, C. J., Huang, Z., et al. (2018). Solar ultraviolet bursts. *Space Sci. Rev.* 214, 120. doi:10.1007/s11214-018-0551-0

Zirin, H. (1988). *Astrophysics of the sun*. Cambridge: Cambridge University Press.

frontiers | Frontiers in Astronomy and Space Sciences

TYPE Original Research
PUBLISHED 17 November 2022
DOI 10.3389/fspas.2022.967878

OPEN ACCESS

EDITED BY
Masumi Shimojo,
National Astronomical Observatory of Japan (NINS), Japan

REVIEWED BY
Haruhisa Iijima,
Nagoya University, Japan
Kevin Reardon,
National Solar Observatory, United States

*CORRESPONDENCE
Sven Wedemeyer,
sven.wedemeyer@astro.uio.no

SPECIALTY SECTION
This article was submitted to Stellar and Solar Physics, a section of the journal Frontiers in Astronomy and Space Sciences

RECEIVED 13 June 2022
ACCEPTED 24 October 2022
PUBLISHED 17 November 2022

CITATION
Wedemeyer S, Fleishman G, de la Cruz Rodríguez J, Gunár S, da Silva Santos JM, Antolin P, Guevara Gómez JC, Szydlarski M and Eklund H (2022), Prospects and challenges of numerical modeling of the Sun at millimeter wavelengths.
Front. Astron. Space Sci. 9:967878.
doi: 10.3389/fspas.2022.967878

Prospects and challenges of numerical modeling of the Sun at millimeter wavelengths

Sven Wedemeyer[1,2]*, Gregory Fleishman[3], Jaime de la Cruz Rodríguez[4], Stanislav Gunár[5], João M. da Silva Santos[6], Patrick Antolin[7], Juan Camilo Guevara Gómez[1,2], Mikolaj Szydlarski[1,2] and Henrik Eklund[1,2,4]

[1]Rosseland Centre for Solar Physics, University of Oslo, Oslo, Norway, [2]Institute of Theoretical Astrophysics, University of Oslo, Oslo, Norway, [3]Center for Solar-Terrestrial Research, New Jersey Institute of Technology, Newark, NJ, United States, [4]Department of Astronomy, Institute for Solar Physics, Stockholm University, AlbaNova University Centre, Stockholm, Sweden, [5]Astronomical Institute, The Czech Academy of Sciences, Ondřejov, Czechia, [6]National Solar Observatory, Boulder, CO, United States, [7]Department of Mathematics, Physics, and Electrical Engineering, Northumbria University, Newcastle Upon Tyne, United Kingdom

The Atacama Large Millimeter/submillimeter Array (ALMA) offers new diagnostic possibilities that complement other commonly used diagnostics for the study of the Sun. In particular, ALMA's ability to serve as an essentially linear thermometer of the chromospheric gas at unprecedented spatial resolution at millimeter wavelengths and future polarization measurements has great diagnostic potential. Solar ALMA observations are therefore expected to contribute significantly to answering long-standing questions about the structure, dynamics, and energy balance of the outer layers of the solar atmosphere. In this regard, current and future ALMA data are also important for constraining and further developing numerical models of the solar atmosphere, which in turn are often vital for the interpretation of observations. The latter is particularly important given the Sun's highly intermittent and dynamic nature that involves a plethora of processes occurring over extended ranges in spatial and temporal scales. Realistic forward modeling of the Sun therefore requires time-dependent three-dimensional radiation magnetohydrodynamics that account for non-equilibrium effects and, typically as a separate step, detailed radiative transfer calculations, resulting in synthetic observables that can be compared to observations. Such artificial observations sometimes also account for instrumental and seeing effects, which, in addition to aiding the interpretation of observations, provide instructive tools for designing and optimizing ALMA's solar observing modes. In the other direction, ALMA data in combination with other simultaneous observations enable the reconstruction of the solar atmospheric structure *via* data inversion techniques. This article highlights central aspects of the impact of ALMA for numerical modeling of the Sun and their potential and challenges, together with selected examples.

KEYWORDS

radio radiation, atmosphere, magnetic fields, radiative transfer, magnetohydrodynamics (MHD), millimeter and submillimeter astronomy, solar physics, chromosphere and corona

1 Introduction

When pointed at the Sun, the Atacama Large Millimeter/submillimeter Array (ALMA, Wootten and Thompson, 2009) mostly observes radiation that originates from the solar chromosphere. This atmospheric layer, which is situated between the photosphere below and the transition region and the corona above, is highly dynamic and intermittent and shows variations on a large range of spatial and temporal scales. Plasma with chromospheric conditions can also be found in the corona in the form of prominences and coronal rain. These structures are integral components of the solar corona in the sense that they not only reflect specific physical processes of the corona but also influence its evolution (Vial and Engvold, 2015; Antolin and Froment, 2022). The investigation of the thermodynamic conditions and morphology of these dense and cool structures supported by the magnetic field is therefore also a major field to which ALMA can make a major contribution.

Despite very active research regarding the chromosphere, which involves observations at many different wavelength ranges supported by numerical simulations, many fundamental questions concerning this layer remain open. The main reason is that the chromosphere is notoriously difficult to observe. Only a small number of spectral lines and continua are formed in the chromosphere, usually across extended height ranges. The formation of chromospheric spectral lines involves non-equilibrium effects such as non-local thermodynamic equilibrium (NLTE[1], see Unsöld, 1955; Mihalas, 1978; Carlsson and Stein, 1992, and references therein) and time-dependent hydrogen ionization (Carlsson and Stein, 2002). Consequently, the few currently available diagnostics like the spectral lines of singly ionized calcium and magnesium are difficult to interpret, in particular, in combination with instrumental limitations. As a result, the physical properties of the observed atmospheric region can only be derived with rather large uncertainties, hampering the progress in understanding this important part of the solar atmosphere.

Observations of the solar continuum radiation using ALMA, as offered on a regular basis since 2016, provide unprecedented diagnostic possibilities that are complementary to other chromospheric diagnostics (Bastian, 2002; Karlický et al., 2011; Benz et al., 2012; Wedemeyer et al., 2016; Bastian et al., 2018). The radiation continuum at submillimeter/millimeter ((sub-)mm) wavelengths, including the range accessed by ALMA, forms essentially under conditions of local thermodynamic equilibrium (LTE) so that the observed brightness temperature, T_b, is closely related to the actual (electron) temperature of the chromospheric gas in a (corrugated) layer whose average height roughly increases with the selected observing wavelength. Unfortunately, observations at (sub-)mm wavelengths prior to the use of ALMA had too low spatial and temporal resolution for resolving the small spatial and short temporal scales on which the intricate chromospheric dynamics occur. For instance, the Berkeley–Illinois–Maryland Array (BIMA) had a spatial resolution corresponding to a restored beam size of ∼10 at a wavelength of $\lambda = 3.5$ mm (White et al., 2006; Loukitcheva et al., 2009). The full diagnostic potential of millimeter wavelengths has therefore only been unlocked by ALMA because of its high temporal and (comparatively high) spatial resolution, which significantly exceeds the resolution achieved by previous millimeter and radio observatories. It should be noted that the millimeter wavelengths addressed in this article are also referred to in terms of their corresponding frequencies (a few 10 s GHz up to ∼1 THz) and as (ALMA) receiver bands[2] that covered the discussed wavelength range. In particular, ALMA bands 3 and 6, which have been used most frequently for solar observations so far, refer to (central) wavelengths of 3.0 mm and 1.3 mm and corresponding frequencies of 100 GHz and 230–240 GHz, respectively.

Because ALMA is relatively new as a diagnostic tool for the solar chromosphere, many aspects are not understood well yet. For instance, the exact formation heights and, thus, the layers sampled by the different receiver bands of ALMA and, likewise, the oscillatory behavior seen in the ALMA observations are still debated (Jafarzadeh et al., 2021; Patsourakos et al., 2020; Narang et al., 2022; Nindos et al., 2021). On the other hand, as solar observing using ALMA is still in its infancy, its capabilities will continue to improve in the near future. However, any new ability to obtain unprecedented observations in any part of the spectrum always brings its own challenges in the interpretation of the resulting data. Fortunately, diagnostics and understanding of ALMA observations and their relationship

1 In this context, NLTE or non-LTE describes deviations from LTE conditions for the atomic-level populations (which can then be calculated under the assumption of statistical equilibrium), the electron density (mostly due to non-equilibrium hydrogen ionisation), and the radiative source function that is no longer given by the Boltzmann function.

2 https://www.eso.org/public/teles-instr/alma/receiver-bands/.

to the coordinated observations in other spectral domains can benefit from dedicated numerical modeling.

Like in many other fields of astrophysics, numerical simulations have developed into an essential tool in solar physics. Also, in the context of solar observations with ALMA, simulations help to interpret observational data but can also be used to develop and optimize new observing strategies (Wedemeyer-Böhm et al., 2007; Loukitcheva et al., 2015; Fleishman et al., 2021a). In return, comparisons with observations provide crucial tests for the veracity of existing models of the solar atmosphere. In this brief overview article, the potential value of numerical simulations for solar science with ALMA is explored, ranging from forward modeling of thermal and non-thermal mm continuum radiation and the impact of magnetic fields (**Section 2**) to data inversion techniques and modeling of instrumental and seeing effects (**Section 3**). Examples of scientific applications are given in **Section 4**, followed by a summary and outlook in **Section 5**.

2 Forward modeling and artificial observations

Forward modeling of the solar atmosphere is typically split into the following steps: (i) radiation (magneto) hydrodynamics simulations (**Section 2.1**), (ii) synthesis of observables *via* radiative transfer calculations (**Section 2.2**), and (iii, optional) application of simulated observational effects (e.g., limited angular resolution, see **Section 2.3**).

2.1 Radiation magnetohydrodynamics simulations

Semi-empirical models of the solar atmosphere like those by created by Vernazza et al. (1981), Fontenla et al. (1993), and Avrett and Loeser (2008) have been an important milestone and are still widely used for reference. Millimeter continuum observations were also used for the construction of these models, which therefore, give a first idea of where and under which conditions radiation continuum at different millimeter wavelengths is formed—on average. While the employed radiative transfer modeling, which even accounts for NLTE, is elaborate, this class of models can by nature not account for the pronounced temporal and spatial variations seen at the much increased resolution of modern observations.

The next step in the development toward realistic models was therefore to account for temporal variations in the chromosphere. The time-dependent one-dimensional simulations by Carlsson and Stein (1995) and variations therefore capture well the dynamics introduced by shock waves that propagate through the solar atmosphere and the resulting implications for the chromospheric plasma properties, i.e., the ionization degree of hydrogen and, thus, the (non-equilibrium) electron density (Carlsson and Stein, 2002). These simulations have been used for the synthesis of the millimeter continuum and thus provided first predictions of the brightness temperature variations that a telescope with sufficient resolution would be able to observe (Loukitcheva et al., 2008).

However, the solar atmosphere and, in particular, the highly dynamic and intermittent chromosphere is a truly time-dependent three-dimensional phenomenon, which poses significant challenges for realistic modeling capable of reproducing observational findings. Also, temporal variations on short timescales are typically connected to spatial variations across short-length scales. Consequently, accounting for the full time-dependence and multi-dimensionality of the solar chromosphere is a substantial step forward from one-dimensional approaches. In view of limited computational resources, early 3D simulations were restricted in the overall number of grid cells, seeking a compromise between the required resolution and the extent of the computational domain, and the physical processes that could be numerically treated (Skartlien et al., 2000; Wedemeyer et al., 2004). The enormous increase in computational power over the last decades now enables simulations with much higher numbers of grid cells and, thus, a better representation of the chromospheric small-scale structure and larger extents of the modeled region. However, self-consistent numerical simulations of whole active regions are still at the modeling frontier (Rempel et al., 2009).

Numerical two-dimensional (2D) and three-dimensional (3D) models produced using the radiation magnetohydrodynamics (rMHD) simulation codes Bifrost (Gudiksen et al., 2011) and CO^{5}BOLD (Freytag et al., 2012) have already been used as the basis for the synthesis of mm continuum radiation (Wedemeyer-Böhm et al., 2007; Loukitcheva et al., 2015) but an increasing number of codes is developing the necessary functionality, e.g., MURaM (Przybylski et al., 2022). Both Bifrost and CO^{5}BOLD solve the equations of magnetohydrodynamics and radiative energy transfer together with a realistic equation of state and realistic opacities and further relevant physics. A typical model includes a small part of the solar atmosphere (from a few Mm to a few 10 Mm, *cf.* Wedemeyer et al., 2016, and references therein) and extends from the upper convection zone into the chromosphere and/or low corona (**Figure 1A**). This way, the dynamics in the model are driven self-consistently and all layers mapped using ALMA are included. A simulation typically starts with an evolved model snapshot (or any other initial condition) and is evolved in time step-by-step, where the computational time steps are of the order of 1 ms–100 ms, depending on the magnetic field strength in the model. Simulation snapshots of the physical parameters can be output at a freely selectable cadence. Modeling the layers of the solar atmosphere above the temperature

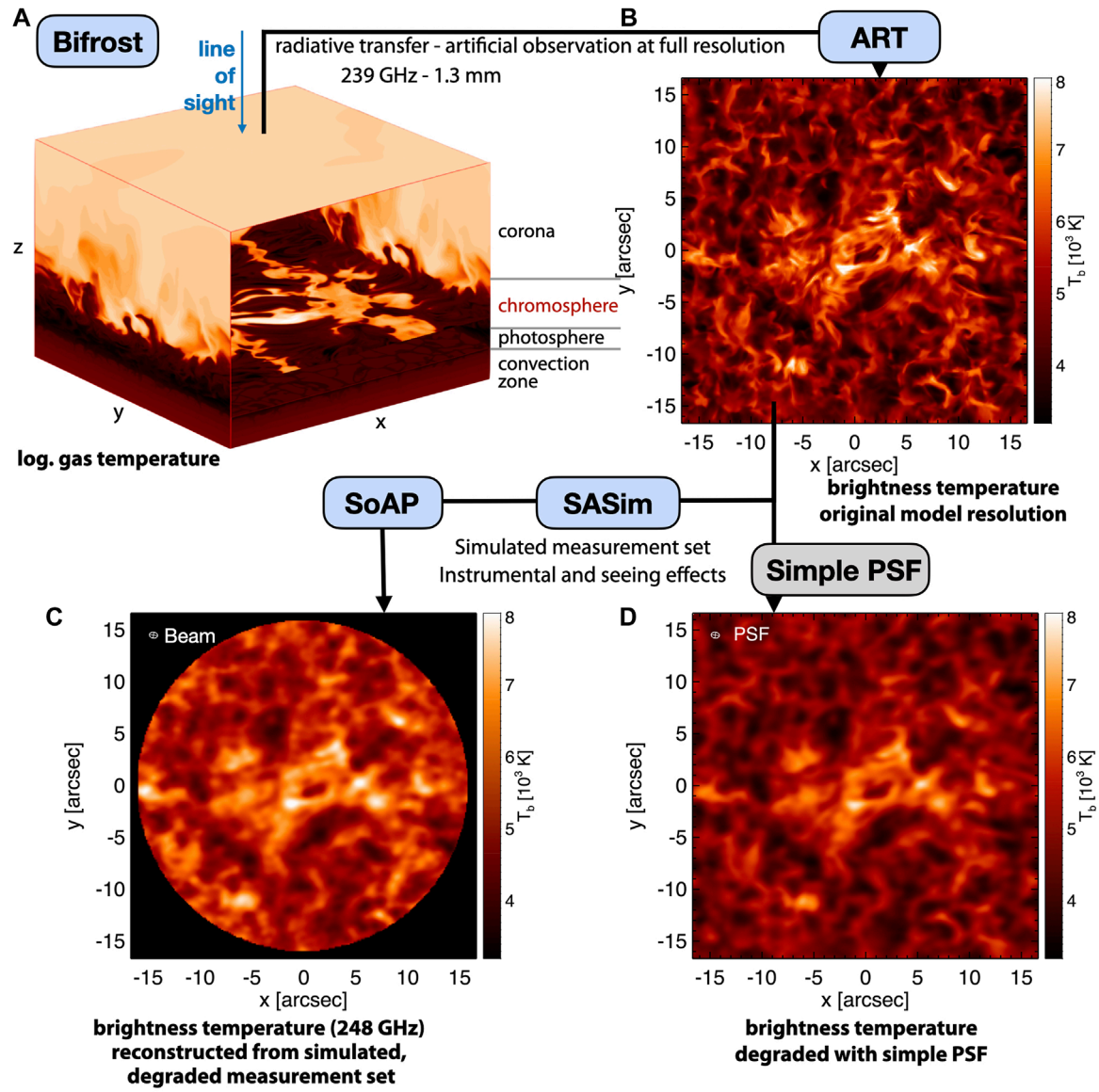

FIGURE 1
Forward modeling of synthetic brightness temperatures at millimeter wavelengths starting with a 3D model snapshot (or a time series of such) from a Bifrost simulation **(A)**. The model features an enhanced network region in the center surrounded by quiet Sun. The radiative transfer calculations with ART produce a brightness temperature map for the selected frequencies [shown here: 239 GHz, **(B)**] to which then a simple point spread function (PSF) equivalent to an idealized synthesized beam for ALMA can be applied **(C)**. The PSF is shown in the top left corner of the panel. A more realistic simulation of atmospheric seeing and instrumental effects as performed using SASim (and then reconstructed using SoAP) results in stronger degradation **(D)** of the original image than the simple PSF. It is to be noted that only a moderate example is shown that corresponds to good observing conditions. The synthesized beam is shown in the corner of the reconstructed image in panel **(D)**.

minimum in a realistic way requires the inclusion of additional physical processes and deviations from equilibrium conditions that are usually computationally expensive. As discussed in Section 2.2.1, the detailed treatment of time-dependent non-equilibrium hydrogen ionization, like it is implemented in Bifrost, is of particular importance for the continuum radiation at millimeter wavelengths. Also, adding non-equilibrium ionization of helium and ion-neutral interactions (ambipolar diffusion) significantly increases the computational costs. Consequently, so far, only a small number of models can account for these additional ingredients and are necessarily limited to 2.5D in order to render such modeling computationally feasible (Martínez-Sykora et al., 2020). These models suggest that the effective formation heights of the millimeter continuum in

both the ALMA bands 3 and 6 are similar in active regions (ARs) and network regions, which contradicts results from previous simulations (see Wedemeyer et al., 2016, and references therein) and actual ALMA observations (Hofmann et al., 2022). Clearly, the inclusion of more physical processes relevant under chromospheric conditions as implemented in the 2.5D simulations conducted by Martínez-Sykora et al. (2020) is an essential step in the right direction. However, given the complicated small-scale dynamics of the chromosphere, modeling this layer in full 3D at sufficient resolution is a critical requirement that comes with high computational costs.

2.2 Spectrum synthesis

In the Sun, continuum radiation is mostly due to thermal emission mechanisms as discussed in **Section 2.2.1** but non-thermal emission needs to be taken into account in flares (see **Section 2.2.2**). As discussed in the following section, this results in particular requirements for the forward modeling of meaningful millimeter radiation.

2.2.1 Thermal radiation

At (sub-)mm wavelengths, the main source of opacity is due to thermal free-free absorption (bremsstrahlung) from electron-ion free–free encounters and H^- (see, e.g., Dulk, 1985; White et al., 2006; Wedemeyer et al., 2016). In other words, the free–free emission originates when free thermal electrons collide with ambient ions and atoms, the total amount of which depends on the electron and ion density, chemical composition, and temperature. All these three inputs vary strongly in the solar atmosphere. In particular, the thermal radiation continuum is sensitively dependent on the local electron density (or line-of-sight electron density). In the presence of a strong magnetic field, additional contribution from gyro emission (Anfinogentov et al., 2019) needs to be taken into account (see the following section).

Many radiative transfer codes commonly use electron densities derived from local plasma properties such as the gas temperature to calculate the thermal free–free emission under the assumption of instantaneous LTE conditions. As demonstrated convincingly by Carlsson and Stein (2002), the rapid variations of the plasma properties in the solar chromosphere due to propagating shock waves in combination with finite hydrogen ionization and recombination time scales result in significant deviations of the electron density from equilibrium values. A realistic calculation of synthetic continuum intensity maps at millimeter wavelengths therefore requires detailed non-equilibrium electron densities as input (see, e.g., Leenaarts and Wedemeyer-Böhm, 2006). However, including non-equilibrium hydrogen ionization in numerical 3D rMHD simulations is computationally expensive, resulting in only a small number of adequate simulations so far (Gudiksen et al., 2011; Loukitcheva et al., 2015; Carlsson et al., 2016).

Figures 2, **3** show the formation of the thermal continuum along vertical slices of two snapshots from publicly available[3] Bifrost simulations: *en_024048_hion*—an enhanced network simulation, including non-equilibrium hydrogen ionization, and *ch024031*—a coronal hole simulation with LTE ionization. The heights at which the optical depth (τ) equals one are marked as a proxy for the formation height for simplicity. We note that, however, the contribution functions of the (sub-)mm continuum can potentially be wider and consist of several peaks due to the often complicated structure of the chromosphere leading to multiple optically thin contributions along the line of sight. Some ALMA observations indeed show occasional contributions from several layers (Wedemeyer et al., 2020a). For a detailed insight into the layers that actually contribute to the emission at any given wavelength, these more detailed contribution functions should be considered (e.g., Loukitcheva et al., 2015). The corrugated surfaces of optical depth unity—as corrugated as the chromosphere itself—underscore that the frequencies observed using ALMA probe different heights of the atmospheres at different spatial locations. Therefore, classical semi-empirical models of averaged spectra should be used with caution when interpreting spatially/temporally resolved data. The histograms in **Figure 3** show that the formation heights $[z(\tau = 1)]$ are, on average, lower in the coronal hole atmosphere than in the enhanced network. Both the magnetic topology and detailed ionization balance influence the formation of the millimeter continuum through changes in the electron/proton densities and temperature, directly affecting the free–free opacities. Simulations of more active conditions naturally lead to higher formation heights than in quiet conditions (Martínez-Sykora et al., 2020). This is true even if non-equilibrium effects are not taken into account because the higher densities in ARs lead to higher (sub-)mm opacities (e.g., da Silva Santos et al., 2022a).

Interestingly, even though the Bifrost-enhanced network simulation includes much of the relevant chromospheric physics, the averaged synthetic brightness temperatures in *en_024048_hion* are lower than what ALMA observations suggest. Loukitcheva et al. (2015) reported that $<T_b(1.25\,\mathrm{mm})> \sim 4{,}800$ K and $<T_b(3\,\mathrm{mm})> \sim 6{,}100$ K in that simulation, whereas White et al. (2017) obtained $<T_b(1.25\,\mathrm{mm})> \sim 5{,}900$ K and $<T_b(3\,\mathrm{mm})> \sim 7{,}300$ K from quiet Sun (QS) observations, values which, for the time being, are set as reference values for observational ALMA brightness temperatures. Alissandrakis et al. (2020) suggested an even higher value:

3 http://sdc.uio.no/search/simulations.

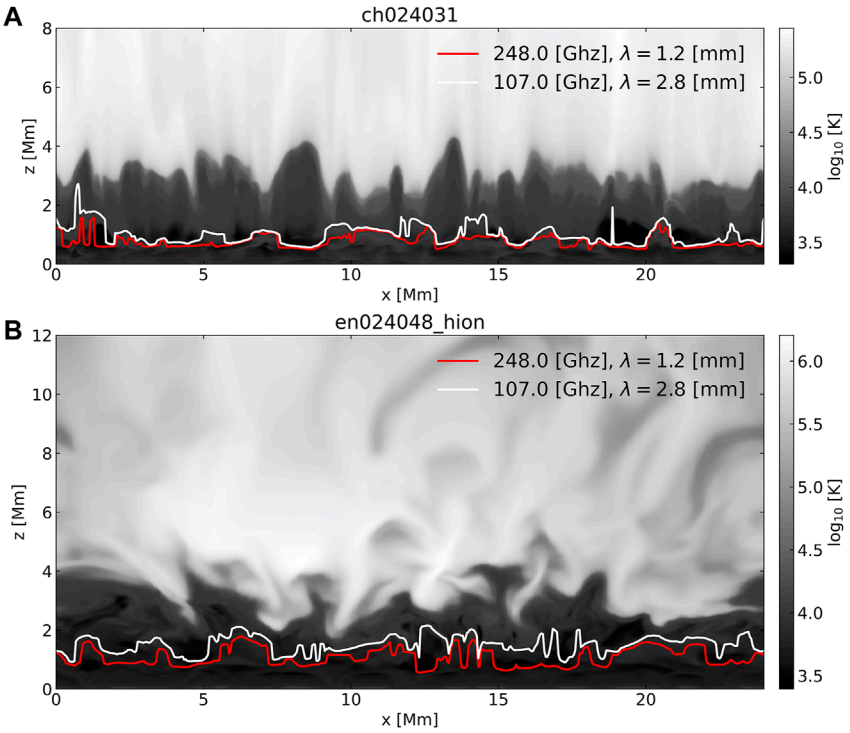

FIGURE 2
Simulated logarithmic gas temperature (gray-scale) in vertical slices of two 3D rMHD Bifrost simulations: **(A)** coronal hole and **(B)** enhanced network region. The solid lines represent the heights at which the optical depth is in unity at a wavelength of 1.2 mm (red) and 2.8 mm (white), which correspond to ALMA bands 6 and 3, respectively (see also **Figure 3**). It is to be noted that these heights are only rough proxies of typical formation heights, whereas the contribution functions can have multiple peaks along the line-of-sight as a result of the complicated thermal structure as can also be seen from the temperature response functions in **Figure 4**.

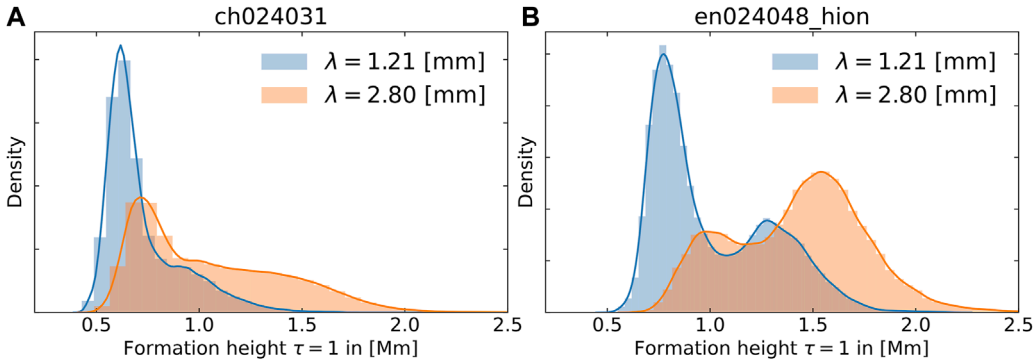

FIGURE 3
Distributions of the heights of optical depth unity [z ($\tau = 1$)] for the two Bifrost models shown in **Figure 2** for the continuum at 1.2 mm (blue) and at 2.8 mm (orange): **(A)** coronal hole and **(B)** enhanced network region.

$<T_b(1.25\,\mathrm{mm})> \sim 6{,}300$ K for the QS. We note that it has also been shown that the simulation produces, for UV and visible chromospheric lines, widths and intensities weaker than the observed values in the QS regions, which suggests that the simulated chromosphere is overall cooler or/and less dense than the real Sun (e.g., Leenaarts et al., 2013). As already stated in **Section 2.1**, the inclusion of more physical processes relevant under chromospheric conditions as implemented by Martínez-Sykora et al. (2020) is an essential step in the right direction, albeit computationally costly.

While there are several codes that can be used for the synthesis of millimeter continuum radiation, the Advanced Radiative Transfer (ART; de la Cruz Rodríguez et al., 2021) code was developed with the aim of providing a very fast tool for the synthesis of millimeter continuum maps. ART uses non-equilibrium electron densities as provided by 3D simulations with Bifrost (Gudiksen et al., 2011) and 1D RADYN simulations (Carlsson and Stein, 1992), but otherwise assumes LTE conditions. The high computational throughput of ART makes it possible to quickly produce time series, even for all individual spectral channels of ALMA instead of just one representative wavelength per (sub-)band. ART has been used by Wedemeyer et al. (2020a) and Eklund et al. (2021a,b). An example is given in **Figure 1B**. As a comparison, RH 1.5D (Uitenbroek, 2001; Pereira and Uitenbroek, 2015), MULTI (Carlsson, 1986), and ART were used to synthesize ALMA band 3 radiation from a 1D RADYN simulation. The simulation, which was intended as a first experiment toward nano-flares, included a beam of electrons injected during a time interval of 10 s in an initial atmosphere which is then left to evolve. The differences in brightness temperatures between the results from the three codes, which for this experiment did not contain any non-thermal contributions, agreed within $\lesssim 15\%$ while the beam was injected and on average less than 6% during the rest of the time.

Fleishman et al. (2021a) extended the theory of free–free emission to the case where the plasma can be composed of many chemical elements in various temperature-dependent ionization states. The theory takes into account that the plasma, in any resolution element (voxel), can have a distribution of the temperature described by the differential emission measure (DEM), rather than a single value of the temperature. Fleishman et al. (2021a) found that the chemical elements can enhance the free–free emission intensity by up to 30% depending on the plasma temperature. In the relatively cool chromosphere, where the plasma is only partly ionized, the code takes into account collisions of free electrons with neutral hydrogen and helium. The effect of the magnetic field on free–free polarization is also taken into account according to the exact magneto-ionic theory, which is important for modeling free–free emission from the chromosphere (Loukitcheva M. et al., 2017). Another effect controlled by the magnetic field is gyroresonant emission due to enhanced opacity of the emission at several gyroharmonics—integer multiples of the gyrofrequency (that is proportional to the ambient magnetic field). Fleishman et al. (2021a) extended the theory of gyroresonant emission to the case of multi-temperature plasma, which required introducing an additional differential density metrics (DDM) complementary to DEM. The code is fully open and available (see Kuznetsov et al., 2021). Although the main contribution to the radio emission at frequencies greater than ~ 100 GHz (ALMA band 3 and above) comes from the chromosphere, coronal contributions are not negligible in ALMA bands 1 and 2, and the described code is needed to properly model and isolate the coronal contributions. In particular, the gyroresonant contribution can be strong at 34 GHz and above (Anfinogentov et al., 2019). In addition, the coronal contribution dominates at microwave frequencies, which bear extremely useful complementary information.

2.2.2 Non-thermal radiation

Non-thermal radiation is emitted by non-thermal electrons accelerated in solar flares or relativistic positrons produced due to nuclear interactions (Fleishman et al., 2013). The dominant emission mechanism is gyrosynchrotron emission due to spiraling of charged particles in the ambient magnetic field, while free–free emission is often important as well (see Fleishman et al. in this special issue). The theory of gyrosynchrotron emission is well-developed, but the expressions for the emissivity and absorption coefficients are cumbersome and computationally expensive. To facilitate the computation of gyrosynchrotron emission, Fleishman and Kuznetsov (2010) developed fast gyrosynchrotron codes that programmatically increase the computation speed by orders of magnitude. The initial versions of the codes permitted only a limited set of analytical distribution functions of the electrons over energy and pitch-angle to be employed in the computations. To facilitate numerical modeling with a broader range of numerically defined distribution functions, Kuznetsov AA. and Fleishman GD. (2021) extended the codes for the case of distribution functions defined by numerical arrays. This new version of the code (Kuznetsov A. and Fleishman G., 2021) also employs the improved treatment of the free–free emission described in **Section 2.2.1**.

2.3 Simulation of atmospheric seeing and instrumental effects

In order to ensure a fair and meaningful comparison between observations and synthetic observables based on numerical models, in principle, all effects due to the telescope and instrument, data processing, and Earth's atmosphere must be considered in detail. Typically, for simplicity but often also *in lieu* of insufficient knowledge of the aforementioned factors, just the (modeled) telescope point spread function (PSF) is applied to synthetic intensity images, resulting in the degradation of the image to the same angular resolution as in the observations. Moreover, such PSFs are often very simplified as contributions such as stray light are usually not known (Wedemeyer-Böhm and Rouppe van der Voort, 2009). For such comparisons, it should therefore be kept in mind that the degradation effects applied to synthetic images tend to underestimate their effect.

Properly taking into account instrumental and seeing effects is even more challenging for interferometric imaging

as performed with ALMA. For solar observations, ALMA's 12-m array with up to 50 12-m antennas and the Atacama Compact Array (ACA) with up to 12 7-m antennas are correlated, including heterogeneous baselines, resulting in time series or mosaics. At the same time, the up to 4 total power (TP) antennas scan the whole disk of the Sun. The obtained visibility data are later calibrated before the brightness temperature maps are reconstructed *via* an involved deconvolution and imaging process, which is typically based on the CLEAN algorithm (Högbom, 1974; Rau and Cornwell, 2011). The resulting final synthesized beam, which is a byproduct of the CLEAN procedure, typically has an elliptical shape that changes with time as a result of the changing position of the Sun in the sky and, thus, the corresponding varying viewing angles of the array. While the synthesized beam is equivalent to a PSF and can thus be applied to synthetic intensity maps to match the resolution (see **Figure 1C**), it is still a simplification of the complicated instrumental setup described previously. An even more severe instrumental effect is the sparse sampling of the spatial Fourier space ("(u,v)-plane"), which is a direct result of the limited number of baselines between antennas. This effect is often compensated by following the source as it moves over the sky with time, thus filling different components in the *uv*-space. For the Sun, which changes on short time scales, this so-called rotation synthesis technique is not an option as the small structure would effectively be blurred out. Instead, brightness temperature maps of the Sun have to be reconstructed solely on the interferometric information retrieved over a very short time ("snapshot imaging"). The cadence of solar observations with ALMA has decreased from 2 s to only 1, which is a great capability for observing the highly dynamic chromosphere but is challenging for imaging based on sparse *uv*-sampling.

The Solar ALMA Simulator (SASim), which was developed in connection with the ESO-funded ALMA development study, "High-cadence Imaging of the Sun" (Wedemeyer, 2019), addresses this problem by aiming at a more realistic simulation of the degradation effects, including the atmosphere above ALMA, interferometric observations, and the imaging process. As input, the SASim uses currently synthetic millimeter brightness temperature maps that are produced with ART from a Bifrost simulation with snapshot output at 1 s cadence. Based on the simobserve task as part of CASA[4], the maps are then converted into measurements set similar to what is produced from real ALMA observations of the Sun. In the process, the antenna configuration and the degradation properties of Earth's atmosphere are prescribed. The resulting synthetic measurement set, which is an artificial ALMA observation of the Sun, is then used as input for the same deconvolution and imaging tool as real observations. For this purpose, the Solar ALMA Pipeline (SoAP) is used (Wedemeyer et al., 2020a; Henriques et al., 2022). An example is given in **Figure 1D**. Such artificial simulation-based observations enable the optimization of the imaging process as the resulting reconstructed images can be compared to the original (i.e., the SASim input) images for different imaging parameter combinations until the best match between the input and output is found. While this procedure is still computationally expensive, it will support the development of new and/or improved observing modes in the future and provide more realistic means for comparing observations with adequately degraded synthetic brightness temperature images.

4 Common Astronomy Software Applications (CASA): http://casa.nrao.edu.

3 Advanced reconstruction of model atmospheres from ALMA observations

3.1 Data inversion

Modern inversion techniques allow inferring the physical parameters of model atmospheres from the reconstruction of observed spectropolarimetric data. The model typically includes the stratification of temperature, line-of-sight velocity, microturbulence, and the three components of the magnetic field as a function of column-mass or continuum optical-depth at a reference wavelength. Inversion techniques have been applied systematically to study photospheric datasets with different levels of complexity (Ruiz Cobo and del Toro Iniesta, 1992; van Noort, 2012; Ruiz Cobo and Asensio Ramos, 2013; Scharmer et al., 2013; Pastor Yabar et al., 2021) under the assumption of LTE.

The extension of such inversion methods to chromospheric applications was possible by the assumption of statistical equilibrium and plane-parallel geometry in order to calculate the atom population densities (Socas-Navarro et al., 2000). The most used diagnostic has been the Ca II 8542 Å line (e.g., Pietarila et al., 2007; de la Cruz Rodríguez et al., 2013; Henriques et al., 2020). More recently, the inclusion of lines originating from multiple species and the inclusion of partial redistribution effects have been made possible with the STiC code (de la Cruz Rodríguez et al., 2019), which has enabled the application of inversion methods to datasets including the Mg II h&k lines (e.g., de la Cruz Rodríguez et al., 2016; Gošić et al., 2018; Sainz Dalda et al., 2019) and Ca II H&K lines (Esteban Pozuelo et al., 2019; Vissers et al., 2019; Morosin et al., 2022).

The depth-resolution that can be achieved by inversions greatly depends on the number of spectral diagnostics (lines and continua) included as constraints in the process, as well as their sensitivities to the different regions represented in the model. The inclusion of more diagnostics improves the depth resolution and reduces potential degeneracies in the reconstructed model. However, because of the non-locality of

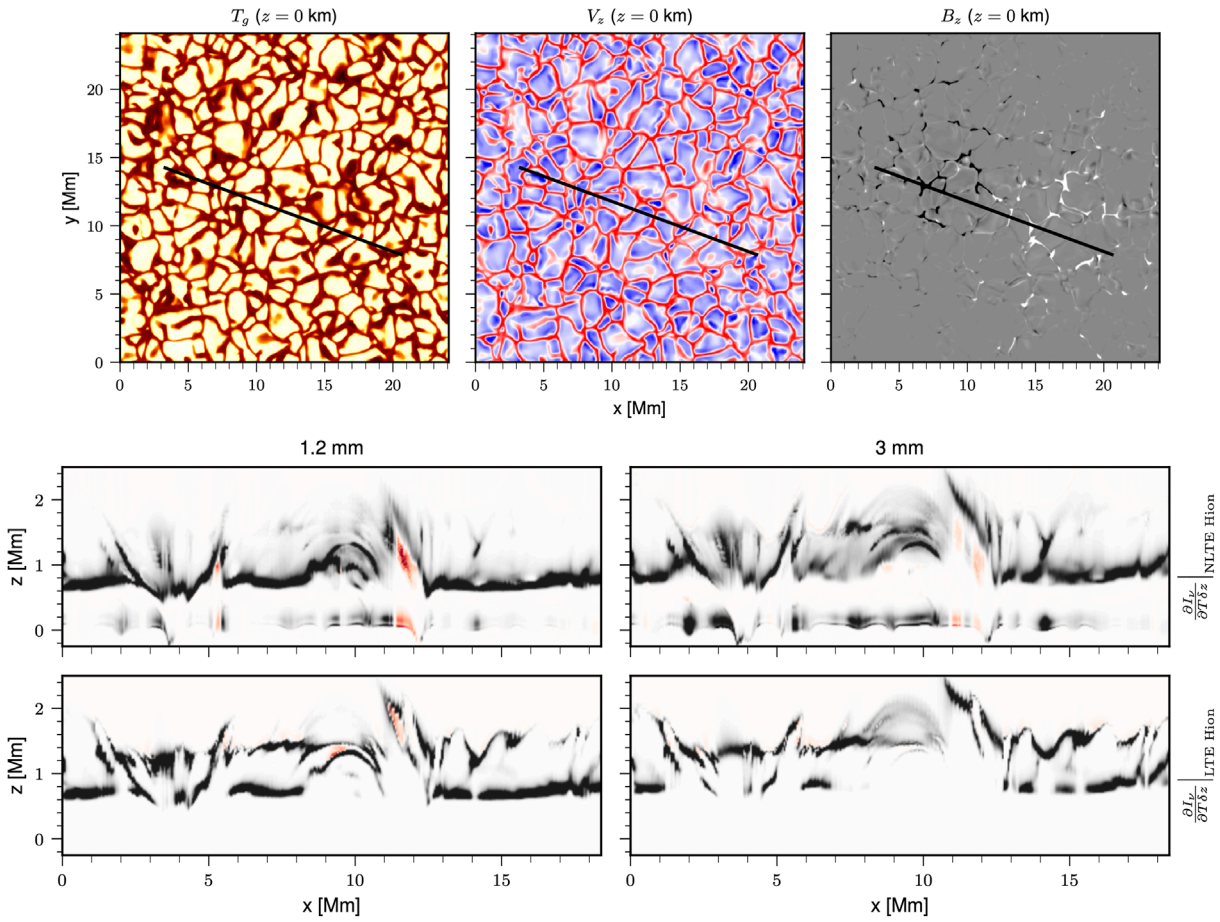

FIGURE 4
Temperature response function computed with the STiC code at 1.2 mm and 3 mm from a vertical slice of a 3D MHD model (Carlsson et al., 2016). In the middle row, the response function has been calculated with an NLTE equation-of-state where the hydrogen population densities are calculated in statistical equilibrium and charge conservation has been imposed in order to calculate the electron density. In the bottom row, an LTE case is shown. For context, we have indicated the location of the slice in the upper row over-imposed on the photospheric temperature, the line-of-sight velocity, and the vertical component of the magnetic field vector.

the radiation field in the chromosphere and the consequent decoupling of the source function from the local temperature stratification, NLTE inversions can fail to accurately constrain temperature stratification in the chromosphere, especially when only one spectral line is included in the inversion.

ALMA millimeter observations provide a powerful diagnostic for chromospheric inversions (da Silva Santos et al., 2018). At those wavelengths, the background continuum samples the chromosphere and the source function can be described by the Planck function. However, while ALMA radiation can be described in LTE, the continuum opacity is set by the electron density and the hydrogen ionization/recombination balance, which are far from LTE in the chromosphere, and time-dependent NLTE hydrogen ionization should be included in the calculations (Leenaarts and Wedemeyer-Böhm, 2006; Leenaarts et al., 2007, see also **Section 2.2.1**). Inversion methods are not sufficiently developed to include time-dependent hydrogen ionization yet. An alternative approach, which is more accurate than assuming LTE, is to calculate H ionization in statistical equilibrium and account for this NLTE contribution in the electron densities by imposing charge conservation in each NLTE iteration. The STiC inversion code (de la Cruz Rodríguez et al., 2019) allows performing such calculations as part of the spectroscopic inversion process. To illustrate the importance of this effect, we have calculated the temperature response function (RF) along a vertical slice from a 3D rMHD simulation (*cf.* **Section 2.1**) in LTE, using the proposed statistical equilibrium approach (see **Figure 4**). The response function is representative of the sensitivity of each grid cell to temperature perturbations. For both receiver bands, the LTE response function has significant peaks around heights of 0.8 and 1.2 Mm. While the peak at the lower height tends to

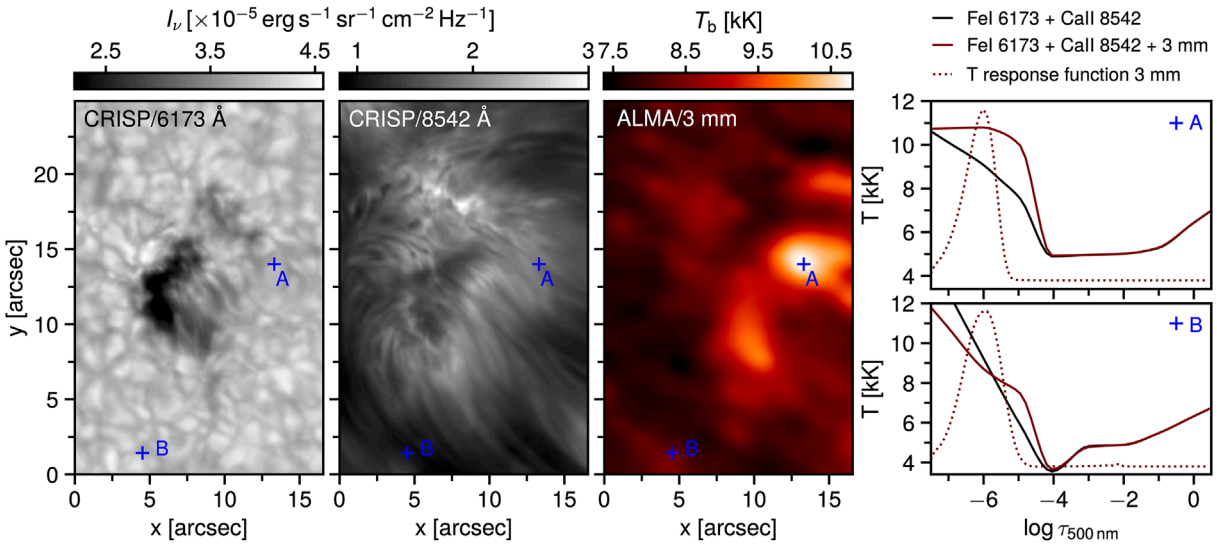

FIGURE 5
NLTE inversions of SST/CRISP and ALMA observations of an active region (da Silva Santos et al., 2022a). From the left to the right: intensities in the continuum at 6173 Å and in the core of the Ca II 8542 Å line, ALMA band 3 brightness temperature map, temperature as a function of the logarithmic optical depth (solid lines) derived from CRISP and CRISP + ALMA inversions at the locations A and B, and temperature response functions at 3 mm in arbitrary units (dotted lines) for the CRISP + ALMA models.

be more prominent for band 6 than for band 3, there are many locations for both bands where peaks at both heights occur, resulting in bimodal RFs. When NLTE H ionization is included in the calculation, the response function generally becomes less localized, basically extending across a height range from as high as 1.8–2.0 Mm to as low as ∼0.1 Mm for both receiver bands. Also, within this range, the NLTE RF often shows multiple peaks. The computationally easier LTE approach is clearly less accurate, particularly in cold atmospheric pockets after the passage of a shock wave, where a full time-dependent treatment would allow for higher ionization fractions than those predicted by statistical equilibrium. A detailed treatment of time-dependent hydrogen ionization is therefore essential for modeling chromospheric emission at mm wavelengths.

While it is not possible to constrain all the inversion parameters using ALMA continuum observations alone, the combination of ALMA data with spectroscopic/spectropolarimetric datasets from other facilities such as DKIST, the 1-m Swedish Solar Telescope (SST), BBSO, or NASA's IRIS satellite is extremely powerful in inferring atmospheric models. For example, da Silva Santos et al. (2020a) utilized datasets from the IRIS and ALMA to constrain the average value of microturbulence in plage down to approximately 5 km s^{-1} within the range of the optical depths probed by the Mg II h and k lines (log $\tau_{500\,nm} = [-6, -4]$) using STiC. Furthermore, da Silva Santos et al. (2022b) used co-temporal SST/CRISP and ALMA observations to reconstruct a model atmosphere of an AR undergoing magnetic reconnection (**Figure 5**). The rightmost panels in **Figure 5** show that the addition of the continuum intensities at 3 mm to NLTE inversions of the Fe I 6173 Å and Ca II 8542 Å lines observed by CRISP has a significant impact on the inverted temperatures in the chromosphere (log $\tau_{500\,nm} < -4$) where the temperature response functions at 3 mm peaks, and thus, provides more accurate models for, in this case, comparisons with rMHD simulations of magnetic flux emergence into the chromosphere. Hofmann et al. (2022) investigated inversion strategies for co-temporal ALMA and IBIS observations in the Na I 5896 Å and Ca II 8542 Å lines using STiC and showed that performing the inversions on a column-mass scale, instead of an optical depth scale, helps to resolve the chromosphere, while the inclusion of the NLTE electron densities as described previously leads to a warmer chromosphere (by ∼1,000 K) than un the LTE case. ALMA band 3 continuum measurements were successfully inverted together with the spectral lines, but band 6 temperatures were difficult to reproduce. The latter could be due to the multi-modal contribution function at 1.2 mm (Loukitcheva et al., 2015) shown in **Figure 3**, introducing uncertainties in the determination of the height of the observed emission and the time-dependent opacity effects (mostly as a result of the variations of the electron density, see **Section 2.2.1**) not accounted for in the code.

Inverse modeling of ALMA brightness temperature maps along with spectroscopic or spectropolarimetric observations at higher frequencies entails several challenges in data acquisition and analysis, such as the non-simultaneity of the observations at different wavelengths, significant differences in spatial

resolution, the uncertainties in the absolute flux calibration, and the simplifying assumptions in inversion codes, namely, hydrostatic equilibrium and 1D radiative transfer. Therefore, improving data inversions is ongoing work with large scientific potential but also requires further coordinated campaigns between ALMA and other observatories in order to produce the needed datasets.

3.2 Magnetic field reconstructions

Probing and modeling the coronal magnetic field is a key challenge in solar physics. Measurements of the coronal magnetic field are difficult and yet very rare (e.g., Lin et al., 2004; Brosius and White, 2006; Wiegelmann et al., 2014; Schad et al., 2016; Casini et al., 2017; Kuridze et al., 2019), giving modeling of the coronal magnetic field an even more important role. The most easily accessible, routine approach to this modeling is the use of nonlinear force-free field (NLFFF) reconstruction (e.g., Wiegelmann and Sakurai, 2012; Wiegelmann et al., 2014). Typically, such reconstructions are initiated with a vector boundary condition derived from a routine Zeeman diagnostics at photospheric heights. A challenge associated with this boundary condition is that the magnetic field is not necessarily in a force-free state in the photosphere, which is in conflict with the assumption that the field is force-free.

Fleishman et al. (2019) developed an advanced NLFFF code that can use additional (to the photospheric ones) magnetic constraints at various locations and various heights in the chromosphere and/or corona while performing the NLFFF reconstruction. The quality of the NLFFF reconstruction increases notably the more complete the set of additional constraints is. In this regard, multifrequency imaging spectropolarimetry in various ALMA spectral bands would enable measurements of the LOS magnetic field component at different chromospheric heights (Loukitcheva M. et al., 2017). Adding these measurements to the NLFFF reconstruction code promises a much improved magnetic model of a given AR. The necessary observing modes and post-processing steps are still under development but might be offered in the coming years, possibly starting with full polarization observations of the Sun in band 3 from as early as cycle 10 (i.e., 2023–24).

4 Examples of scientific applications

4.1 Atmospheric stratification and center-to-limb variation

When observing the solar atmosphere not directly from the top but at an inclined viewing angle (i.e., $\mu = \cos\theta < 1$), the line-of-sight traverses a longer path through the solar atmosphere for a given height difference, resulting in optical depth unity higher up in the atmosphere. As the change in viewing angle corresponds to the variation from observations at different distances from the disk-center ($\mu = 1$) toward the limb ($\mu = 0$), observations of the center-to-limb variation of the continuum emission contain information about atmospheric stratification (i.e., the height dependence of the underlying plasma properties) and can thus be used to constrain models of the solar atmosphere (see, e.g., Brajša et al., 2018). Alissandrakis et al. (2017, 2020) used ALMA brightness temperatures maps in the range ∼1–3 mm at different positions on the solar disk to infer a relation between kinetic temperature and optical depth, which was shown to be consistent with the widely used FALC QS model (Fontenla et al., 1993) within uncertainties. Using ALMA observations, Sudar et al. (2019) determined lower limits for the limb-brightening effect on the order of 10% in band 3 and 15% in band 6. These results agree with the range of values independently derived by Menezes et al. (2022). Such empirically derived model atmospheres provide crucial tests for numerical models (**Section 2.1**) for which the center-to-limb variation of the (sub-)mm can be computed by repeating the radiative transfer calculations (**Section 2.2**) under varying viewing angles.

4.2 Small-scale dynamics in quiet Sun regions

As established by observations using other chromospheric diagnostics such as the Ca II K line, internetwork QS regions exhibit a highly dynamic mesh-like pattern produced by the interaction of ubiquitous propagating shock waves (e.g., Wöger et al., 2006), unless obscured by overlying fibrilar structures outlining the magnetic field. The expected appearance of these signatures of chromospheric shock waves at (sub-)mm wavelengths had already been simulated based on 1D simulations (Loukitcheva et al., 2004) and 3D simulations (Wedemeyer-Böhm et al., 2005, 2007) before the advent of ALMA. The simulations confirmed that sufficient spatial resolution, which is particularly challenging at (sub-)mm wavelengths, and a high temporal cadence are essential for enabling the detection of shock waves. However, the viewing angle and, thus, the location on the solar disk also impact the detectability of shock waves due to the potential superposition of structures at different heights along inclined lines of sight (*cf.* **Section 4.1**). As a consequence, ALMA is expected to observe the ubiquitous chromospheric shocks in the QS regions with higher contrast at the disk center than closer to the limb (Wedemeyer-Böhm et al., 2007).

As shown in **Figure 2** for a Bifrost simulation, the formation height of the millimeter continuum varies significantly when the atmosphere is buffeted by shock waves. Consequently, the brightness temperature increases temporarily by up to several

thousand kelvin, as long as the shock structure remains optically thick at a given wavelength (Eklund et al., 2021b). Comparable ALMA observations show bright small-scale features in the QS regions with typical lifetimes of ∼ 1–2 min and amplitudes of a few hundred kelvin above the background (Eklund et al., 2020; Nindos et al., 2021). Taking into account the impact of ALMA's limited spatial resolution on the appearance of small-scale structures and the resulting reduction of the amplitudes of the dynamic bright features, the detected bright features are consistent with upward propagating shocks as predicted by numerical simulations (Eklund et al., 2020). **Figure 1** shows the shock-induced chromospheric pattern before and after applying the effects of limited spatial resolution to simulated millimeter continuum images. The amplitude reduction of bright features in the Bifrost simulation at wavelengths corresponding to all ALMA receiver bands 3–10 (0.34 mm–3.22 mm) and the corresponding spatial resolutions with different ALMA antenna configurations were studied by Eklund et al. (2021a), providing conversion factors that could, in principle, be used to correct the amplitudes of bright features in observational data on a statistical basis, although with large uncertainties. Furthermore, propagating shocks create steep temperature gradients in the atmosphere. As numerical simulations show, the slope of the brightness temperature continuum can, in principle, be used to identify signatures of shocks and also the potential existence of multiple shock components propagating at different velocities as shown by Eklund et al. (2021b). The diagnostic potential of splitting ALMA datasets into sub-bands has recently been shown for the study of propagating transverse waves by Guevara Gómez et al. (2022) and for propagating shock waves by Eklund et al. (Forthcoming 2022).

Shocks may play a significant role in the heating of the quiet chromosphere, but addressing this science case with ALMA beyond pure detection requires follow-up observations with higher spatial resolution than the ones available so far. The use of a wider array of configurations in combination with improved imaging routines has the potential to reach a resolution of a few $0.1''$ for ALMA's higher receiver bands. Determining the exact requirements could be achieved through the modeling approach shown in **Figure 1**. In addition, studying the propagation of shock waves through the (sub-)mm continuum forming layers by means of the methods introduced in **Sections 2**, **3**, which includes, in particular, inversions and detailed (statistical) comparisons of high-quality ALMA observations and artificial observations based on state-of-the art numerical 3D simulations, promises essential insights into the formation heights of the (sub-)mm continuum as a function of the wavelength and the atmospheric stratification for different regions on the Sun. da Silva Santos et al. (2020a) and Eklund et al. (2020, 2021a) conducted recent studies employing these methods.

4.3 Active regions and flares

Well-developed ALMA diagnostics could contribute significantly to progressing our understanding of the thermal and magnetic properties of ARs and flares. Modeling the magnetic topology of a steady-state AR is now routinely possible based on NLFFF reconstructions constrained by routinely available photospheric vector magnetograms (Fleishman et al., 2015; Fleishman et al., 2021b). At the same time, dynamic phenomena are particularly hard to reproduce in numerical simulations for several reasons: the time scales that need to be resolved span the evolution of ARs (from hours to days) to the rapid changes that occur during flares (i.e., to the fractions of seconds). The spatial scales, likewise, span a large range of values from the large extent of ARs (up to several 10 Mm) to the small computational cell size that is needed to adequately model all relevant processes (on the order of km toward sub-grid modeling at even much smaller scales). Finally, the presence of a stronger-than-average magnetic field, the occurrence of magnetic reconnection across different scales, the resulting impact on the chromospheric dynamics and, of particular relevance here, the emission at (sub-)mm wavelengths pose particularly challenging demands to numerical modeling (*cf.* **Section 2**). Consequently, forward modeling of the (sub-)mm continuum intensities emerging from semi-empirical models is therefore a natural starting point and, despite the obvious limitations, a complementary way of gaining an insight into the physics of AR phenomena through detailed comparisons between synthetic and observed brightness temperatures. Currently, there are a few examples of the application of this methodology in the literature. For instance, Loukitcheva MA. et al. (2017) compared brightness temperature measurements of a sunspot at two different wavelengths with the expected values computed from several 1D static, semi-empirical models in the literature and concluded that none of the models provided a good fit for the penumbra. This means that ALMA can provide constraints on the temperature gradient in those structures. Semi-empirical models have also been used to investigate the observed correlation between the width of the H α line and the brightness temperatures at 3 mm in the plage—which was explained based on the mutual dependence of both diagnostics on the hydrogen atom-level populations (Molnar et al., 2019). The agreement between empirical models and ALMA observations can also be improved in an automatic or iterative way using NLTE inversion codes (**Section 3.1**) when co-temporal spectroscopic observations at optical or ultraviolet (UV) wavelengths are likewise available (da Silva Santos et al., 2020a; de Oliveira e Silva et al., 2022; Hofmann et al., 2022; de Oliveira e Silva et al., 2022). Moreover, one-dimensional time-dependent simulations have been used to study the response of the solar atmosphere to flares. For instance, Simões et al, (2017) used RADYN simulations to evaluate the

diagnostic potential of flare emission in the thermal infrared and sub-millimeter range.

As an example of the applications of multi-dimensional numerical models in the context of interpreting ALMA observations of the Sun, the comparison between ALMA band 6 observations of the AR plage supported by IRIS UV spectroscopy and synthetic spectra from a 2.5D Bifrost simulation suggests that an observed bright linear feature emanating from the plage region is an on-disk type-II spicule, confirming their multithermal nature (Chintzoglou et al., 2021a), while other small-scale plage brightenings at 1.25 mm could be signatures of magnetoacoustic shocks (Chintzoglou et al., 2021b). ALMA band 3 observations of the same plage region also show out-of-phase oscillations in brightness temperature, feature size, and horizontal velocities, which are evidence of sausage-mode and kink-mode waves (Guevara Gómez et al., 2021). AR transients akin to UV-bursts (Young et al., 2018) with nanoflare-like energies have been observed in a flux emergence region with band 3, and their characteristics agree with synthetic thermal emission from a 3D Bifrost simulation of flux emergence, showing several magnetic reconnection events (da Silva Santos et al., 2020b). For a microflare detected at 3 mm in coordination with the IRIS and Hinode/XRT by Shimizu et al. (2021), the timing of millimeter brightening with respect to the soft X-rays indicated that the upper chromosphere was being heated by non-thermal particles in this event. Such an effect has also been pointed out by Valle Silva et al. (2019) using lower resolution observations at 1.4 mm with the Solar Submillimeter Telescope. It should be noted that the formation of millimeter continuum emission under flaring conditions, similarly to what has been conducted for quiet conditions (**Section 2.2.1**), and the interpretation of those diagnostics have been addressed previously within the given instrumental capabilities (see, e.g., Stepanov et al., 1992; Kundu et al., 1993; Silva et al., 1996; Krucker et al., 2013).

Finally, full 3D modeling of ARs and flares requires a 3D model of the magnetic structure to start with, which can be obtained from an NLFFF reconstruction or other means. To make the modeling with such 3D data cubes realistic, a magnetic "skeleton" must be supplied by thermal plasma, non-thermal particles (in case of flares), placed at the right location at the Sun, and supplied by various means for emission computation and meaningful data-to-model comparison. Nita et al. (2015, 2018) developed a powerful dedicated tool, the GX Simulator, designed specifically for the aforementioned goals. More than that, the GX Simulator includes an integrated mean to create a 3D model and an automated model production pipeline (AMPP) with minimal input from the user: only the date and time of the event have to be defined along with the anticipated resolution and sizes of the data cube. Once specified, the AMPP will download all the required magnetic maps obtained with SDO/HMI and other context data and perform magnetic reconstruction, as well as several other steps that are needed to create a 3D model. Then, magnetic flux tube(s) can be interactively created and designated to serve as the model flare loop(s). The user can control the properties of the thermal and non-thermal components in these flaring loops, compute mm/radio, EUV, and X-ray emissions from the model, and compare the synthetic images and spectra with the observed ones, in particular, with ALMA data.

As outlined previously, there are many ways in which the ALMA observations of flares and corresponding numerical models could complement each other in order to advance our understanding of this intricate process that is essential for the heating of the solar atmosphere over a large range of scales from nano-flares to X-class flares and, for stars other than the Sun, even toward mega-flares. Owing to the complexity and still insufficient knowledge regarding central aspects, many simulations necessarily focus on particular parts of the flare phenomenon and/or have to make simplifying assumptions. There are, however, efforts to capture flares self-consistently in full 3D time-dependent simulations as those as attempted with the MURaM simulations by Cheung et al. (2019). Such simulations could be used for calculating the corresponding (sub-)mm emission as it could be observed with ALMA, though they do not include non-thermal particles responsible for a good portion of the flare emission in the ALMA bands yet. The comparison of both would then, as for the other examples described in this article, allow identifying potential shortcomings of the models, which is necessary for future improvements toward a more detailed and complete picture. ALMA observations of flare emission, either with the already available continuum mapping capabilities and even more so with future full polarization capabilities, would provide valuable information complementary to existing flare diagnostics. Unfortunately, to the authors' knowledge at the time of writing, there are no good examples of flare observations with ALMA yet, maybe except for one microflare reported by Shimizu et al. (2021). Refer to Fleishman et al. in this issue for more information about how ALMA observations could advance our understanding of solar flares.

4.4 Solar prominences

In the field of prominence research, numerical simulations of (sub-)mm radiation observed using ALMA can help in two areas. The first is the visibility of large and small-scale structures of prominences and filaments in the ALMA observations and the connection between the structures observed at (sub-)mm wavelengths and in other parts of the spectrum. Methods that generate such simulated ALMA observations can be based on actual data observed at different wavelengths—e.g., the simulations of prominence fine structure visibility based on Hα observations performed by Heinzel et al. (2015)—or on the

synthesis of the radiation at (sub-)mm wavelengths emerging from models of prominence plasma (*cf.* **Section 2**). The first synthetic ALMA-like imaging of simulated prominences was conducted by Gunár et al. (2016). These simulated ALMA data represent the way in which the 3D whole-prominence fine structure (WFPS) model of Gunár and Mackay (2015) would appear in different ALMA bands. This model combines realistic 3D magnetic field configurations with a detailed description of the prominence plasma located in the magnetic dips. In doing so, the 3D WPFS model emulates entire prominences with their numerous fine structures and offers high spatial resolution reaching the best potential capabilities of ALMA. However, we should note that the current ALMA observations of prominences (Heinzel et al. (2022a); Labrosse et al., 2022) or filaments (da Silva Santos et al. (2022b), in this special issue) do not reach such a resolution. This is because ALMA has not achieved yet its full potential for solar observations and offers only more compact antenna configurations for solar targets. For more details on the actual and simulated observations of prominences and the predictions of the visibility of prominence fine structures, see the review by Heinzel et al. (2022b) in this special issue.

The second area where numerical simulations can help the prominence research is the understanding of the potential of ALMA observations as diagnostics for the kinetic temperature of the solar plasma. It has been known for some time that a measure of the kinetic temperature of the observed plasma can be derived from simultaneous observations in at least two different (sub-)mm wavelengths (see, e.g., Loukitcheva et al., 2004; Heinzel and Avrett, 2012; Heinzel et al., 2015). However, only recent modeling efforts demonstrated that such a derivation is not entirely straightforward and that in order to achieve sufficient precision, the observed plasma needs to be optically thick at one of those wavelengths and optically thin at the other. It must be noted here that such observations would require a new capability that ALMA is currently not offering and likely will not offer in the near future, namely simultaneous solar observing with two sub-arrays, each in a different receiver band. In the absence of such simultaneous multi-band ALMA observations, thermal properties of the observed plasma can be derived from a combination of ALMA observations and observations in other wavelength ranges, e.g., in the Hα line (see Heinzel et al., 2022a; Labrosse et al., 2022).

The first study of ALMA's diagnostic potential for determining the properties of prominence plasma was conducted by Rodger and Labrosse (2017). These authors used 2D cylindrical prominence models created by Gouttebroze and Labrosse (2009), both in the iso-thermal iso-baric configuration and in the configuration incorporating the prominence-corona transition region (PCTR). The study by Rodger and Labrosse (2017) showed that the realistic assumption of the presence of multi-thermal plasma along a line-of-sight leads to uncertainties in the determination of the kinetic temperature of the observed plasma. The authors then demonstrated that such uncertainties can be minimized by using ALMA observations at longer wavelengths (e.g., at 9 mm). At such wavelengths, the observed prominence plasma can be expected to be mostly optically thick, leading to reliable diagnostics of its thermal properties.

The relationship between the observed brightness temperature in various ALMA bands and the actual kinetic temperature of the observed plasma was further investigated by Gunár et al. (2018). To do so, these authors used the simulated ALMA observations of Gunár et al. (2016) at wavelengths at which the prominence plasma is optically thin (0.45 mm, corresponding to 666 GHz in band 9) and optically thick (9.0 mm, corresponding to 33 GHz in band 1). The resulting brightness temperature maps and the optical thickness maps are shown in **Figure 6**. The 0.45 mm and 9.0 mm wavelengths were chosen to assure that the studied plasma is completely optically thin (at 0.45 mm) and, at the same time, that a significant portion of the analyzed prominence is optically thick (at 9.0 mm). However, we should note that at the time of writing, solar observations with ALMA are offered only in bands 3, 5, 6, and 7, while bands 9 and 1 are not available yet. We also note that the current status of the development of band 1 indicates that it will reach a slightly shorter wavelength of 8.6 mm (35 GHz) instead of the 9.0 mm (33 GHz) used here. Moreover, ALMA band 10 will provide access to even shorter wavelengths than those covered by band 9 assumed here.

The results of the study by Gunár et al. (2018) confirmed that the brightness temperature simultaneously measured by ALMA in the aforementioned bands can be used to derive the kinetic temperature in every pixel of the observed prominences, e.g., using the method described in **Section 3** of Gunár et al. (2018). However, not all of the derived values of kinetic temperature accurately represent the thermal conditions of the plasma distributed along the lines-of-sight passing through individual pixels because the observed prominence cannot be generally assumed to be optically thick (i.e., have optical thickness above unity) in all pixels, even at the 9.0 mm wavelength. This can be clearly seen in the optical thickness map in **Figure 6D**, where large parts of the modeled prominence have an optical depth of $\tau_{9.0\,\mathrm{mm}} < 1$. Therefore, without the added information about the actual optical thickness, which is in this case provided by the model, the derived values of the kinetic temperature cannot be automatically assumed to be accurate in all pixels. This is because the basic approximation of the method used to derive the kinetic temperature is not valid if the plasma is not optically thick. Owing to the use of numerical simulations, Gunár et al. (2018) determined that the kinetic temperature values obtained in pixels with an optical thickness larger than 2 typically have an accuracy better than 1,000 K compared to the true kinetic temperature of the studied plasma. Such a study was possible because the

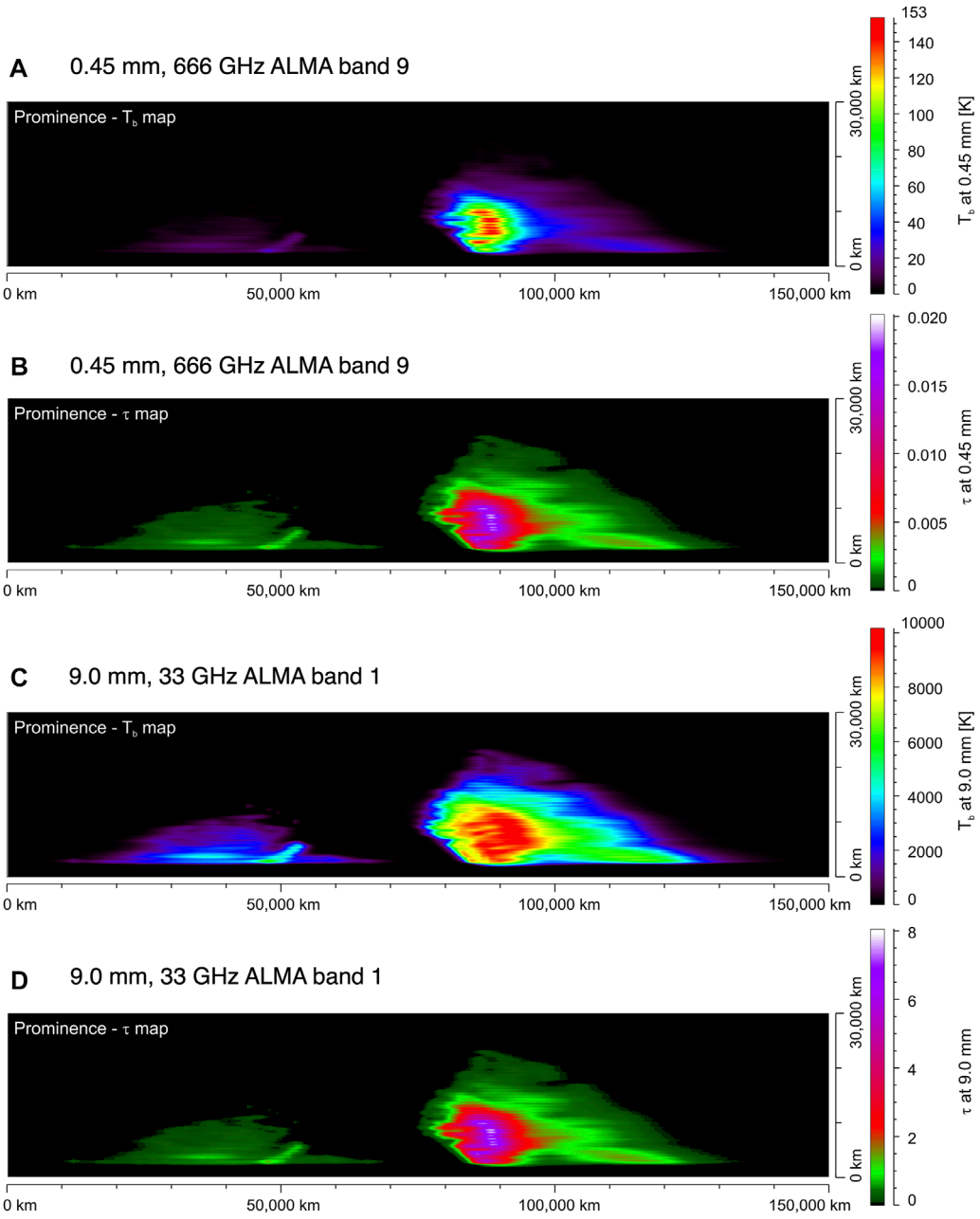

FIGURE 6
Synthetic brightness temperature maps [panels **(A, C)**] and optical thickness maps [panels **(B, D)**] showing the 3D whole-prominence fine structure model of Gunár and Mackay (2015) in a prominence view. The top two panels were obtained at a wavelength of 0.45 mm, which corresponds to the 666 GHz ALMA band 9. The bottom two panels were obtained at a wavelength of 9.0 mm (33 GHz ALMA band 1). Displayed color scales are unique for each panel. Adapted from Gunár et al. (2016).

authors used realistic numerical simulations, demonstrating the essential value of simulations for testing adequate methods for the interpretation of observations.

The 3D WPFS model of Gunár and Mackay (2015) contains detailed information about the properties of the prominence plasma including its kinetic temperature. Using the (sub-)mm radiation synthesis method described by Gunár et al. (2016), the authors could synthesize the specific intensities at any wavelength along any LOS crossing the simulated prominence. That led to an ideal set of co-spatial simulated observations (**Figures 6A, C**) coupled with the implicit knowledge of the corresponding optical thickness (**Figures 6B, D**). A major problem lies in

the fact that the optical thickness values are not explicitly known based on ALMA observations alone—but can be derived from other observations, such as those in the Hα line (see Heinzel et al., 2015; Heinzel et al., 2022a; Labrosse et al., 2022). However, Gunár et al, (2018) showed that with the use of numerical simulations, it is possible to determine a criterion for the minimum value of the measured brightness temperature in the optically thin wavelengths (in this case, at 0.45 mm) above which the optical thickness at the optically thick wavelengths is, with great confidence, higher than the required value. The second part of the study conducted by Gunár et al. (2018) showed that the values of the kinetic temperature derived from the ALMA observations correspond to the mean kinetic temperature of the observed plasma weighted by the contribution function of the emission in the optically thick wavelengths. For more details see Sections 5–7 of the study by Gunár et al. (2018).

4.5 Coronal rain

In addition to the large prominence structures discussed in **Section 4.4**, condensation phenomena occur far more frequently in the solar corona in the form of coronal rain. This phenomenon, which is also thought to be the seeds leading to prominences, corresponds to cool (10^3–10^5 K) and dense (10^{10}–10^{12} cm^{-3}) plasma occurring in a timescale of minutes seemingly condensing out of nowhere at coronal heights, and flowing predominantly downward along loop-like trajectories under the action of gravity and gas pressure mainly (Kawaguchi, 1970; Leroy, 1972; Foukal, 1978; Antolin and Rouppe van der Voort, 2012). The leading explanation for coronal rain is thermal instability (TI) within a structure in thermal non-equilibrium and, therefore, reflects mostly the MHD thermal mode becoming unstable and generating a condensation from the localized loss of pressure (Antiochos et al., 1999; Antolin, 2020). Numerical simulations have shown that the easiest path toward thermal instability within a structure such as a coronal loop is to have strongly stratified and high-frequency heating (Klimchuk and Luna, 2019). This state, known as thermal non-equilibrium (TNE), leads to TNE cycles for heating that remain largely unchanged over time. The details of this process and the various observable signatures can be found in the study by Antolin and Froment (2022).

Various properties of coronal rain remain poorly understood. Similar to prominences, the observed rain morphology is filamentary (also known as multi-stranded) and clumpy, whose widths (a few hundred km size) are interestingly very similar to the smallest widths detected for EUV strands in high-resolution observations with Hi-C (Williams et al., 2020). It has been hypothesized that such sizes are set by granular spatial scales (Martínez-Sykora et al., 2018). This is supported by self-consistent 2.5D rMHD numerical simulations with Bifrost (see **Figure 7** and also **Section 2.1**) but the details of this process remain unclear (Antolin et al., 2022). Observational validation could come from multi-instrument observations with ALMA (using extended array configurations with correspondingly high angular resolution) and IRIS simultaneously observing a bright point and its indirect effects (coronal rain) on the upper atmosphere. While dense, the very small sizes of the clumps make them optically thin most of the time in spectral lines in the optical and UV spectrum such as Hα and Mg II k&h line (Antolin and Rouppe van der Voort, 2012; Antolin et al., 2021), and cannot be resolved in the present ALMA configuration. However, extended array configurations with higher resolution should allow their detection. This can be confirmed by forward modeling of Bifrost simulations with coronal rain (see **Figure 7**), demonstrating once more the essential role of numerical simulations for developing adequate observing modes.

Most coronal rain clumps do not occur in isolation independently from each other. Rain clumps are produced in groups called showers (Antolin and Rouppe van der Voort, 2012) due to a syncing cross-field mechanism known as sympathetic cooling (Fang et al., 2013). These showers have been found to successfully identify coronal loops in the "coronal veil" produced by optically thin radiation (Sahin and Antolin, 2022; Malanushenko et al., 2022). The detection and quantification of rain showers is important for coronal heating since it is a proxy for the coronal volume in TNE (and thus subject to specific spatial and temporal heating conditions). The detection of showers using ALMA remains a target that should be feasible at medium resolution as it is currently offered. The fact that no rain showers have been detected using ALMA so far may be simply due to a lack of off-limb observations (with good seeing conditions) of an AR and the additional complexity of interferometric imaging off-limb. Also, low opacity of rain showers at ALMA wavelengths might prevent their detection. The latter can and should be checked through forward modeling of numerical simulations with, e.g., Bifrost.

Coronal rain has been shown to be largely multi-thermal with probably high ionization levels due to its relatively low lifetime. A very thin corona condensation transition region (CCTR) is expected at the boundaries of rain clumps (similar to the PCTR for prominences), with different plasma conditions ahead and behind the condensation due to a piston-like effect produced by the downward motion (Antolin et al., 2022). Accordingly, the pressure restructuring is expected to be the leading cause for the observed lower than free-fall speeds (Schrijver, 2001). An interesting mass–velocity relation has been numerically obtained but remains to be observationally validated (Oliver et al., 2014). The good correlation between Hα intensity and brightness temperature measured by ALMA in prominences

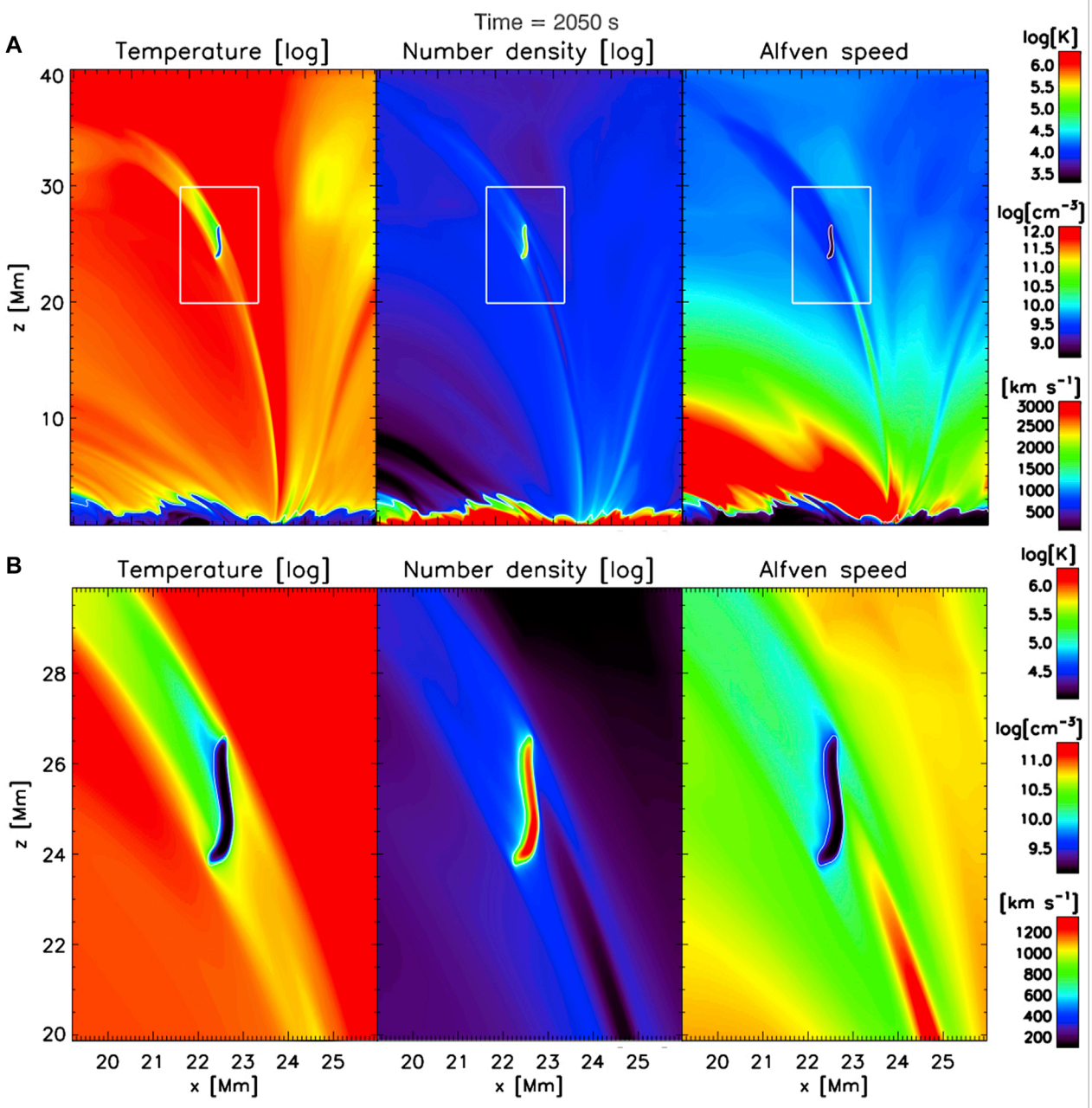

FIGURE 7
Coronal rain event self-consistently produced in a 2.5D rMHD simulation with Bifrost (**Section 2.1**). **(A)** (Left to right): snapshot of the temperature (log), mass density (log), and Alfvén speed in a portion of the modeled atmosphere. Thermal instability occurs locally in a coronal loop that is in a state of thermal non-equilibrium, thereby leading to the formation of a condensation (coronal rain clump) falling toward the loop footpoint. **(B)** (same quantities in same order) shows the white rectangular inset seen in the upper panels (the three color bars on the right of each row correspond uniquely to that particular row). Taken and adapted from **Figures 2**, **3** of Antolin et al. (2022).

(Heinzel et al., 2022a; Labrosse et al., 2022) suggests that ALMA could also serve as a proxy for prominence and coronal rain mass, and therefore, shed light into the mass–velocity relation. Indeed, the emission measure in Hα is known to be strongly correlated to the absolute intensity in Hα (Gouttebroze et al., 1993), and this has been used to infer the densities of rain clumps in Hα observations with the SST (Froment et al., 2020).

Future ALMA observations may be able to provide detailed measurements of the morphological, thermodynamic, and

kinematic properties of coronal rain. Such measurements can serve as unique proxies for coronal heating conditions and improve our understanding of fundamental plasma and MHD processes such as thermal instability. As outlined previously, numerical simulations would be essential for several aspects, ranging from the development of adequate observing modes and capabilities to supporting the detailed interpretation of ALMA observations.

5 Summary and outlook

Synthetic brightness temperature maps for millimeter wavelengths based on 3D numerical simulations of the solar atmosphere play an important role in several aspects of solar science with ALMA. First of all, such synthetic observables, for which the connection to the underlying plasma properties in the model is accurately known, have already proven their value for supporting the interpretation of ALMA observations, very much as for other chromospheric diagnostics previously. Another important application of simulation-based observables is the development of (sub-)mm continua as a diagnostic tool for the solar atmosphere. Surprisingly though, the first ALMA observations raised questions regarding even rather fundamental properties such as the exact formation height ranges and their possible variations in time and space, locally and for different types of region. Also, the chromospheric temperatures in 3D simulations (see a comparison in Wedemeyer et al., 2016) tend to be lower than the brightness temperatures observed with ALMA (e.g., Bastian et al., 2017; White et al., 2017; Nindos et al., 2018; Wedemeyer et al., 2020a) although some cooler regions have been observed too (Loukitcheva et al., 2019). The apparent differences with respect to numerical models highlight potentially missing physical ingredients and the need for the further development of models to higher levels of realism as far as computational costs allow. To what extent simulations can reproduce observations and, thus, aid their interpretation depends ultimately on the accessible computational resources and the implementation of efficient and stable numerical schemes and the resulting affordable sizes of computational boxes, grid resolution, and the considered physical processes. An important example in this regard is the need to account for time-dependent hydrogen ionization as it impacts the electron densities in the chromosphere on which the millimeter continuum as mapped by ALMA sensitively depends. Clearly, detailed comparisons to observations, to which solar ALMA observations add a new suite of complementary diagnostics, either directly or with the powerful help of data inversion techniques, serve as crucial tests of models and, as such, of our current understanding of the solar chromosphere. In this regard, it should be noted that such comparisons are limited by the realism of the instrumental models that are used to produce artificial observations. Degradation of synthetic brightness temperature maps with a simple Gaussian would correspond to an ideal telescope with a filled aperture and ignores ALMA's sparse *uv*-sampling as an interferometer and also degradation effects due to Earth's atmosphere (i.e., phase errors) and the handling of noise during the imaging stage. As pointed out in **Section 2.3**, such tools are under development but also require notable computational effort.

Another valuable application of simulation-based synthetic observables is the justification of resource investments for the development of additional diagnostics and observing modes, e.g., additional ALMA receiver bands and more extended array configurations for, in principle, higher angular resolution. A much awaited capability of ALMA will be full polarization measurements that would facilitate the determination of the magnetic field in the chromosphere. Detailed knowledge of the 3D magnetic field structure of the solar chromosphere (or chromospheric plasma in the corona such as coronal rain) as a function of time at high resolution would be a fundamental game-changer for understanding the dynamics, energy transport, and (local) heating of this still largely elusive but yet important atmospheric layer inside ARs, QS regions, and prominences alike. A fundamental challenge of polarization measurements is, among other things, the low expected degree of polarization outside of ARs, which thus demands high sensitivity and accuracy and a well-developed observing mode, reliable calibration, and advanced processing/imaging routines (see, e.g., Grebinskij et al., 2000; Fleishman et al., 2015; Loukitcheva M. et al., 2017; Wedemeyer et al., 2020b, and references therein). The development of these components is usually hampered by the insufficiently known "ground truth" against which the data should be compared to. Forward modeling of artificial polarization measurements based on numerical 3D rMHD simulations would also play a very important role here, similar to what is attempted for continuum brightness temperatures.

The scientific potential of ALMA observations of the Sun is promising but requires significant effort and resources to be fully unlocked due to the complexity of the instrument and the observational targets, namely, the dynamic and intermittent chromosphere, both in a quiescent and active state, the atmosphere above ARs including the often dramatically evolving coronal magnetic field (Fleishman et al., 2020), and non-thermal electrons in solar flares (Fleishman et al., 2021b). The resulting challenges for numerical modeling of the chromosphere, prominences, and the flaring corona, their appearances at the wavelengths observed using ALMA, and not least, the impact of ALMA's complex instrumental properties pose critical tests of our current understanding that will inspire future progress.

Data availability statement

Publicly available datasets were analyzed in this study. These data can be found at: Atacama Large Millimeter/submillimeter Array (ALMA), https://almascience.nrao.edu/aq/, Solar ALMA Science Archive (SALSA), http://sdc.uio.no/salsa/ and Hinode Science Data Centre Europe, http://sdc.uio.no/sdc/.

Author contributions

All authors listed have made a substantial, direct, and intellectual contribution to the work and approved it for publication.

Funding

MS, JG, and SW were supported by the SolarALMA project, which received funding from the European Research Council (ERC) under the European Union's Horizon 2020 research and innovation program (grant agreement No. 682462), and by the Research Council of Norway through its Centers of Excellence scheme, project number 262622. GF was supported in part by NSF grants AGS-2121632, AST-2206424, and AST-1820613, and NASA grants 80NSSC20K0718, and 80NSSC23K0090 to New Jersey Institute of Technology. SG acknowledges the support from grant No. 19-16890S of the Czech Science Foundation (GA ČR) and from project RVO:67985815 of the Astronomical Institute of the Czech Academy of Sciences. PA acknowledges funding from the STFC Ernest Rutherford Fellowship (No. ST/R004285/2). HE was supported through the CHROMATIC project (2016.0019) funded by the Knut and Alice Wallenberg Foundation. This project received funding from the European Research Council (ERC) under the European Union's Horizon 2020 research and innovation program (SUNMAG, grant agreement 759548). The Swedish 1-m Solar Telescope is operated on the island of La Palma by the Institute for Solar Physics of Stockholm University in the Spanish Observatorio del Roque de los Muchachos of the Instituto de Astrofísica de Canarias. The Institute for Solar Physics was supported by a grant for research infrastructures of national importance from the Swedish Research Council (registration number 2021-00169).

Acknowledgments

This paper makes use of the following ALMA data: ADS/JAO.ALMA#2011.0.00020.SV and ADS/JAO.ALMA#2018.1.01518.S. ALMA is a partnership of ESO (representing its member states), NSF (United States), and NINS (Japan), together with NRC (Canada) and NSC and ASIAA (Taiwan), and KASI (Republic of Korea), in co-operation with the Republic of Chile. The Joint ALMA Observatory is operated by ESO, AUI/NRAO, and NAOJ. The National Radio Astronomy Observatory is a facility of the National Science Foundation operated under cooperative agreement by Associated Universities, Inc. CGGC is grateful with FAPESP (2013/24155-3), CAPES (88887.310385/2018-00), and CNPq (307722/2019-8). The NSO is operated by the Association of Universities for Research in Astronomy, Inc., under cooperative agreement with the National Science Foundation. Part of this work was carried out in connection with the ESO-funded development study for the Atacama Large Millimeter/submillimeter Array (ALMA) High-cadence imaging of the Sun (agreement no. 80738/18/87966/ASP). **Figure 7** was obtained through computational time granted from the Greek Research and Technology Network (GRNET) in the National HPC facility ARIS. Part of the numerical computations was also carried out on the Cray XC50 at the Center for Computational Astrophysics, NAOJ.

Conflict of interest

The authors declare that the research was conducted in the absence of any commercial or financial relationships that could be construed as a potential conflict of interest.

Publisher's note

References

Alissandrakis, C. E., Nindos, A., Bastian, T. S., and Patsourakos, S. (2020). Modeling the quiet Sun cell and network emission with ALMA. *Astron. Astrophys.* 640, A57. doi:10.1051/0004-6361/202038461

Alissandrakis, C. E., Patsourakos, S., Nindos, A., and Bastian, T. S. (2017). Center-to-limb observations of the Sun with ALMA. Implications for solar atmospheric models. *Astron. Astrophys.* 605, A78. doi:10.1051/0004-6361/201730953

Antolin, P., Pagano, P., Testa, P., Petralia, A., and Reale, F. (2021). Reconnection nanojets in the solar corona. *Nat. Astron.* 5, 54–62. doi:10.1038/s41550-020-1199-8

Anfinogentov, S. A., Stupishin, A. G., Mysh'yakov, I., and Fleishman, G. D. (2019). Record-breaking coronal magnetic field in solar active region 12673. *Astrophys. J.* 880, 880L29. doi:10.3847/2041-8213/ab3042

Antiochos, S. K., MacNeice, P. J., Spicer, D. S., and Klimchuk, J. A. (1999). The dynamic formation of prominence condensations. *Astrophys. J.* 512, 985–991. doi:10.1086/306804

Antolin, P., and Froment, C. (2022). Multi-scale variability of coronal loops set by thermal non-equilibrium and instability as a probe for coronal heating. *Front. Astron. Space Sci.* 9. doi:10.3389/fspas.2022.820116

Antolin, P., Martínez-Sykora, J., and Şahin, S. (2022). Thermal instability-induced fundamental magnetic field strands in the solar corona. *Astrophys. J. Lett.* 926, L29. doi:10.3847/2041-8213/ac51dd

Antolin, P., and Rouppe van der Voort, L. (2012). Observing the fine structure of loops through high-resolution spectroscopic observations of coronal rain with the CRISP instrument at the Swedish solar telescope. *Astrophys. J.* 745, 152. doi:10.1088/0004-637X/745/2/152

Antolin, P. (2020). Thermal instability and non-equilibrium in solar coronal loops: From coronal rain to long-period intensity pulsations. *Plasma Phys. control. Fusion* 62, 014016. doi:10.1088/1361-6587/ab5406

Avrett, E. H., and Loeser, R. (2008). Models of the solar chromosphere and transition region from SUMER and HRTS observations: Formation of the extreme-ultraviolet spectrum of hydrogen, carbon, and oxygen. *Astrophys. J. Suppl. Ser.* 175, 229–276. doi:10.1086/523671

Bastian, T. S. (2002). ALMA and the sun. *Astron. Nachr.* 323, 271–1.

Bastian, T. S., Bárta, M., Brajša, R., Chen, B., Pontieu, B. D., Gary, D. E., et al. (2018). Exploring the sun with ALMA. *Messenger* 171, 25–30.

Bastian, T. S., Chintzoglou, G., De Pontieu, B., Shimojo, M., Schmit, D., Leenaarts, J., et al. (2017). A first comparison of millimeter continuum and Mg II ultraviolet line emission from the solar chromosphere. *Astrophys. J.* 845, L19. doi:10.3847/2041-8213/aa844c

Benz, A. O., Brajsa, R., Shimojo, M., Karlicky, M., and Testi, L. (2012). Observing the sun with ALMA. *IAU Spec. Sess.* 6, E2.

Brajša, R., Kuhar, M., Benz, A. O., Skokić, I., Sudar, D., Wedemeyer, S., et al. (2018). A comparison of solar ALMA observations and model based predictions of the brightness temperature. *Cent. Eur. Astrophys. Bull.* 42, 1.

Brosius, J. W., and White, S. M. (2006). Radio measurements of the height of strong coronal magnetic fields above sunspots at the solar limb. *Astrophys. J.* 641, L69–L72. doi:10.1086/503774

Carlsson, M. (1986). A computer program for solving multi-level non-LTE radiative transferproblems in moving or static atmospheres. *Upps. Astron. Obs. Rep.* 33.

Carlsson, M., Hansteen, V. H., Gudiksen, B. V., Leenaarts, J., and De Pontieu, B. (2016). A publicly available simulation of an enhanced network region of the Sun. *Astron. Astrophys.* 585, A4. doi:10.1051/0004-6361/201527226

Carlsson, M., and Stein, R. F. (1995). Does a nonmagnetic solar chromosphere exist? *Astrophys. J.* 440, L29. doi:10.1086/187753

Carlsson, M., and Stein, R. F. (2002). Dynamic hydrogen ionization. *Astrophys. J.* 572, 626–635. doi:10.1086/340293

Carlsson, M., and Stein, R. F. (1992). Non-LTE radiating acoustic shocks and CA II K2V bright points. *Astrophys. J.* 397, L59. doi:10.1086/186544

Casini, R., White, S. M., and Judge, P. G. (2017). Magnetic diagnostics of the solar corona: Synthesizing optical and radio techniques. *Space Sci. Rev.* 210, 145–181. doi:10.1007/s11214-017-0400-6

Cheung, M. C. M., Rempel, M., Chintzoglou, G., Chen, F., Testa, P., Martínez-Sykora, J., et al. (2019). A comprehensive three-dimensional radiative magnetohydrodynamic simulation of a solar flare. *Nat. Astron.* 3, 160–166. doi:10.1038/s41550-018-0629-3

Chintzoglou, G., De Pontieu, B., Martínez-Sykora, J., Hansteen, V., de la Cruz Rodríguez, J., Szydlarski, M., et al. (2021a). ALMA and IRIS observations of the solar chromosphere. I. An on-disk type II spicule. *Astrophys. J.* 906, 82. doi:10.3847/1538-4357/abc9b1

Chintzoglou, G., De Pontieu, B., Martínez-Sykora, J., Hansteen, V., de la Cruz Rodríguez, J., Szydlarski, M., et al. (2021b). ALMA and IRIS observations of the solar chromosphere. II. Structure and dynamics of chromospheric plages. *Astrophys. J.* 906, 83. doi:10.3847/1538-4357/abc9b0

da Silva Santos, J. M., Danilovic, S., Leenaarts, J., de la Cruz Rodríguez, J., Zhu, X., White, S. M., et al. (2022b). Heating of the solar chromosphere through current dissipation. *Astron. Astrophys.* 661, A59. doi:10.1051/0004-6361/202243191

da Silva Santos, J. M., de la Cruz Rodríguez, J., Leenaarts, J., Chintzoglou, G., De Pontieu, B., Wedemeyer, S., et al. (2020a). The multi-thermal chromosphere. Inversions of ALMA and IRIS data. *Astron. Astrophys.* 634, A56. doi:10.1051/0004-6361/201937117

da Silva Santos, J. M., de la Cruz Rodríguez, J., and Leenaarts, J. (2018). Temperature constraints from inversions of synthetic solar optical, UV, and radio spectra. *Astron. Astrophys.* 620, A124. doi:10.1051/0004-6361/201833664

da Silva Santos, J. M., de la Cruz Rodríguez, J., White, S. M., Leenaarts, J., Vissers, G. J. M., and Hansteen, V. H. (2020b). ALMA observations of transient heating in a solar active region. *Astron. Astrophys.* 643, A41. doi:10.1051/0004-6361/202038755

da Silva Santos, J. M., White, S. M., Reardon, K., Cauzzi, G., Gunár, S., Heinzel, P., et al. (2022a). Subarcsecond imaging of a solar active region filament with ALMA and IRIS. *Front. Astron. Space Sci.* 9. doi:10.3389/fspas.2022.898115

de la Cruz Rodríguez, J., Szydlarski, M., and Wedemeyer, S. (2021). *Art: Advanced (and fast!) radiative transfer code for solar physics*. doi:10.5281/zenodo.4604825

de la Cruz Rodríguez, J., Leenaarts, J., and Asensio Ramos, A. (2016). Non-LTE inversions of the Mg II h & k and UV triplet lines. *Astrophys. J.* 830, L30. doi:10.3847/2041-8205/830/2/L30

de la Cruz Rodríguez, J., Leenaarts, J., Danilovic, S., and UitenbroekSTiC, H. (2019). STiC: A multiatom non-LTE prd inversion code for full-Stokes solar observations. *Astron. Astrophys.* 623, A74. doi:10.1051/0004-6361/201834464

de la Cruz Rodríguez, J., Rouppe van der Voort, L., Socas-Navarro, H., and van Noort, M. (2013). Physical properties of a sunspot chromosphere with umbral flashes. *Astron. Astrophys.* 556, A115. doi:10.1051/0004-6361/201321629

de Oliveira e Silva, A. J., Selhorst, C. L., Costa, J. E. R., Simões, P. J. A., Giménez de Castro, C. G., Wedemeyer, S., et al. (2022). A genetic algorithm to model solar radio active regions from 3D magnetic field extrapolations. *Front. Astron. Space Sci.* 9, 911118. doi:10.3389/fspas.2022.911118

Dulk, G. A. (1985). Radio emission from the sun and stars. *Annu. Rev. Astron. Astrophys.* 23, 169–224. doi:10.1146/annurev.aa.23.090185.001125

Eklund, H., Szydlarski, M., and Wedemeyer, S. (Forthcoming 2022). Utilizing the slope of the brightness temperature continuum as a diagnostic tool of solar ALMA observations. *Astron. Astrophys.*

Eklund, H., Wedemeyer, S., Snow, B., Jess, D. B., Jafarzadeh, S., Grant, S. D. T., et al. (2021b). Characterization of shock wave signatures at millimetre wavelengths from Bifrost simulations. *Phil. Trans. R. Soc. A* 379, 20200185. doi:10.1098/rsta.2020.0185

Eklund, H., Wedemeyer, S., Szydlarski, M., Jafarzadeh, S., and Guevara Gómez, J. C. (2020). The Sun at millimeter wavelengths. II. Small-scale dynamic events in ALMA Band 3. *Astron. Astrophys.* 644, A152. doi:10.1051/0004-6361/202038250

Eklund, H., Wedemeyer, S., Szydlarski, M., and Jafarzadeh, S. (2021a). The Sun at millimeter wavelengths. III. Impact of the spatial resolution on solar ALMA observations. *Astron. Astrophys.* 656, A68. doi:10.1051/0004-6361/202140972

Esteban Pozuelo, S., de la Cruz Rodríguez, J., Drews, A., Rouppe van der Voort, L., Scharmer, G. B., and Carlsson, M. (2019). Observationally based models of penumbral microjets. *Astrophys. J.* 870, 88. doi:10.3847/1538-4357/aaf28a

Fang, X., Xia, C., and Keppens, R. (2013). Multidimensional modeling of coronal rain dynamics. *Astrophys. J.* 771, L29. doi:10.1088/2041-8205/771/2/L29

Fleishman, G., Loukitcheva, M., and Nita, G. (2015). "Solar ALMA: Observation-based simulations of the mm and sub-mm emissions from active regions," in *Revolution in Astronomy with ALMA: The third year*. Editors D. Iono, K. Tatematsu, A. Wootten, and L. Testi (San Francisco, United States: Astronomical Society of the Pacific Conference Series), 499, 351.

Fleishman, G., Myshyakov, I., Stupishin, A., Loukitcheva, M., and Anfinogentov, S. (2019). Force-free field reconstructions enhanced by chromospheric magnetic field data. *Astrophys. J.* 870, 101. doi:10.3847/1538-4357/aaf384

Fleishman, G. D., Altyntsev, A. T., and Meshalkina, N. S. (2013). Microwave signature of relativistic positrons in solar flares. *Publ. Astron. Soc. Jpn. Nihon. Tenmon. Gakkai.* 65, S7. doi:10.1093/pasj/65.sp1.S7

Fleishman, G. D., Anfinogentov, S. A., Stupishin, A. G., Kuznetsov, A. A., and Nita, G. M. (2021b). Coronal heating law constrained by microwave gyroresonant emission. *Astrophys. J.* 909, 89. doi:10.3847/1538-4357/abdab1

Fleishman, G. D., Gary, D. E., Chen, B., Kuroda, N., Yu, S., and Nita, G. M. (2020). Decay of the coronal magnetic field can release sufficient energy to power a solar flare. *Science* 367, 278–280. doi:10.1126/science.aax6874

Fleishman, G. D., and Kuznetsov, A. A. (2010). Fast gyrosynchrotron codes. *Astrophys. J.* 721, 1127–1141. doi:10.1088/0004-637X/721/2/1127

Fleishman, G. D., Kuznetsov, A. A., and Landi, E. (2021a). Gyroresonance and free-free radio emissions from multithermal multicomponent plasma. *Astrophys. J.* 914, 52. doi:10.3847/1538-4357/abf92c

Fontenla, J. M., Avrett, E. H., and Loeser, R. (1993). Energy balance in the solar transition region. III. Helium emission in hydrostatic, constant-abundance models with diffusion. *Astrophys. J.* 406, 319. doi:10.1086/172443

Foukal, P. (1978). Magnetic loops, downflows, and convection in the solar corona. *Astrophys. J.* 223, 1046–1057. doi:10.1086/156338

Freytag, B., Steffen, M., Ludwig, H. G., Wedemeyer-Böhm, S., Schaffenberger, W., and Steiner, O. (2012). Simulations of stellar convection with CO5BOLD. *J. Comput. Phys.* 231, 919–959. doi:10.1016/j.jcp.2011.09.026

Froment, C., Antolin, P., Henriques, V. M. J., Kohutova, P., and Rouppe van der Voort, L. H. M. (2020). Multi-scale observations of thermal non-equilibrium cycles in coronal loops. *Astron. Astrophys.* 633, A11. doi:10.1051/0004-6361/201936717

Gošić, M., de la Cruz Rodríguez, J., De Pontieu, B., Bellot Rubio, L. R., Carlsson, M., Esteban Pozuelo, S., et al. (2018). Chromospheric heating due to cancellation of quiet sun internetwork fields. *Astrophys. J.* 857, 48. doi:10.3847/1538-4357/aab1f0

Gouttebroze, P., Heinzel, P., and Vial, J. C. (1993). The hydrogen spectrum of model prominences. *A&AS* 99, 513–543.

Gouttebroze, P., and Labrosse, N. (2009). Radiative transfer in cylindrical threads with incident radiation. VI. A hydrogen plus helium system. *Astron. Astrophys.* 503, 663–671. doi:10.1051/0004-6361/200811483

Grebinskij, A., Bogod, V., Gelfreikh, G., Urpo, S., Pohjolainen, S., and Shibasaki, K. (2000). Microwave tomography of solar magnetic fields. *Astron. Astrophys. Suppl. Ser.* 144, 169–180. doi:10.1051/aas:2000202

Gudiksen, B. V., Carlsson, M., Hansteen, V. H., Hayek, W., Leenaarts, J., and Martínez-Sykora, J. (2011). The stellar atmosphere simulation code Bifrost. Code description and validation. *Astron. Astrophys.* 531, A154. doi:10.1051/0004-6361/201116520

Guevara Gómez, J. C., Jafarzadeh, S., Wedemeyer, S., and Szydlarski, M. (2022). Propagation of transverse waves in the solar chromosphere probed at different heights with ALMA sub-bands. *Astron. Astrophys.* 665, L2. doi:10.1051/0004-6361/202244387

Guevara Gómez, J. C., Jafarzadeh, S., Wedemeyer, S., Szydlarski, M., Stangalini, M., Fleck, B., et al. (2021). High-frequency oscillations in small chromospheric bright features observed with Atacama Large Millimetre/Submillimetre Array. *Phil. Trans. R. Soc. A* 379, 20200184. doi:10.1098/rsta.2020.0184

Gunár, S., Heinzel, P., Anzer, U., and Mackay, D. H. (2018). Quiescent prominences in the era of ALMA. II. Kinetic temperature diagnostics. *Astrophys. J.* 853, 21. doi:10.3847/1538-4357/aaa001

Gunár, S., Heinzel, P., Mackay, D. H., and Anzer, U. (2016). Quiescent prominences in the era of ALMA: Simulated observations using the 3D whole-prominence fine structure model. *Astrophys. J.* 833, 141. doi:10.3847/1538-4357/833/2/141

Gunár, S., and Mackay, D. H. (2015). 3D whole-prominence fine structure modeling. *Astrophys. J.* 803, 64. doi:10.1088/0004-637X/803/2/64

Heinzel, P., and Avrett, E. H. (2012). Optical-to-Radio continua in solar flares. *Sol. Phys.* 277, 31–44. doi:10.1007/s11207-011-9823-5

Heinzel, P., Bárta, M., Gunár, S., Labrosse, N., and Vial, J. C. (2022b). Prominence observations with alma. *Front. Astron. Space Sci.* 9. doi:10.3389/fspas.2022.983707

Heinzel, P., Berlicki, A., Bárta, M., Karlický, M., and Rudawy, P. (2015). On the visibility of prominence fine structures at radio millimeter wavelengths. *Sol. Phys.* 290, 1981–2000. doi:10.1007/s11207-015-0719-7

Heinzel, P., Berlicki, A., Bárta, M., Rudawy, P., Gunár, S., Labrosse, N., et al. (2022a). ALMA as a prominence thermometer: First observations. *Astrophys. J. Lett.* 927, L29. doi:10.3847/2041-8213/ac588f

Henriques, V. M. J., Jafarzadeh, S., Guevara Gómez, J. C., Eklund, H., Wedemeyer, S., Szydlarski, M., et al. (2022). The Solar ALMA Science Archive (SALSA). First release, SALAT, and FITS header standard. *Astron. Astrophys.* 659, A31. doi:10.1051/0004-6361/202142291

Henriques, V. M. J., Nelson, C. J., Rouppe van der Voort, L. H. M., and Mathioudakis, M. (2020). Umbral chromospheric fine structure and umbral flashes modelled as one: The corrugated umbra. *Astron. Astrophys.* 642, A215. doi:10.1051/0004-6361/202038538

Hofmann, R. A., Reardon, K. P., Milic, I., Molnar, M. E., Chai, Y., and Uitenbroek, H. (2022). *Evaluating non-LTE spectral inversions with ALMA and IBIS*. APJ 933 (2), 244. doi:10.3847/1538-4357/ac6f00

Högbom, J. A. (1974). Aperture synthesis with a non-regular distribution of interferometer baselines. *A&AS* 15, 417.

Jafarzadeh, S., Wedemeyer, S., Fleck, B., Stangalini, M., Jess, D. B., Morton, R. J., et al. (2021). An overall view of temperature oscillations in the solar chromosphere with ALMA. *Phil. Trans. R. Soc. A* 379, 20200174. doi:10.1098/rsta.2020.0174

Karlický, M., Bárta, M., Dabrowski, B. P., and Heinzel, P. (2011). Solar research with ALMA. *Sol. Phys.* 268, 165–173. doi:10.1007/s11207-010-9671-8

Kawaguchi, I. (1970). Observed interaction between prominences. *PASJ* 22, 405.

Klimchuk, J. A., and Luna, M. (2019). The role of asymmetries in thermal nonequilibrium. *Astrophys. J.* 884, 68. doi:10.3847/1538-4357/ab41f4

Krucker, S., Giménez de Castro, C. G., Hudson, H. S., Trottet, G., Bastian, T. S., Hales, A. S., et al. (2013). Solar flares at submillimeter wavelengths. *Astron. Astrophys. Rev.* 21, 58. doi:10.1007/s00159-013-0058-3

Kundu, M. R., White, S. M., Gopalswamy, N., and Lim, J. (1993). Interferometric observations of solar flares at 3 mm wavelength. *Adv. Space Res.* 13, 289–293. doi:10.1016/0273-1177(93)90492-T

Kuridze, D., Mathioudakis, M., Morgan, H., Oliver, R., Kleint, L., Zaqarashvili, T. V., et al. (2019). Mapping the magnetic field of flare coronal loops. *Astrophys. J.* 874, 126. doi:10.3847/1538-4357/ab08e9

Kuznetsov, A., and Fleishman, G. (2021b). *Ultimate fast gyrosynchrotron codes: The first release*. Genève, Switzerland: Zenodo. doi:10.5281/zenodo.5139156

Kuznetsov, A., Fleishman, G., and Landi, E. (2021). *Codes for computing the solar gyroresonance and free-free radio emissions: The first release*. Genève, Switzerland: Zenodo. doi:10.5281/zenodo.4625572

Kuznetsov, A. A., and Fleishman, G. D. (2021a). Ultimate fast gyrosynchrotron codes. *Astrophys. J.* 922, 103. doi:10.3847/1538-4357/ac29c0

Labrosse, N., Rodger, A. S., Radziszewski, K., Rudawy, P., Antolin, P., Fletcher, L., et al. (2022). First high resolution interferometric observation of a solar prominence with ALMA. *MNRAS* 513, L30–L34. doi:10.1093/mnrasl/slac021

Leenaarts, J., Carlsson, M., Hansteen, V., and Rutten, R. J. (2007). Non-equilibrium hydrogen ionization in 2D simulations of the solar atmosphere. *Astron. Astrophys.* 473, 625–632. doi:10.1051/0004-6361:20078161

Leenaarts, J., Pereira, T. M. D., Carlsson, M., Uitenbroek, H., and De Pontieu, B. (2013). the formation of IRIS diagnostics. II. The formation of the Mg II h&k lines in the solar atmosphere. *Astrophys. J.* 772, 90. doi:10.1088/0004-637X/772/2/90

Leenaarts, J., and Wedemeyer-Böhm, S. (2006). Time-dependent hydrogen ionisation in 3D simulations of the solar chromosphere. Methods and first results. *Astron. Astrophys.* 460, 301–307. doi:10.1051/0004-6361:20066123

Leroy, J. (1972). Emissions 'froides' dans la couronne solaire. *Sol. Phys.* 25, 413–417. doi:10.1007/BF00192338

Lin, H., Kuhn, J. R., and Coulter, R. (2004). Coronal magnetic field measurements. *Astrophys. J.* 613, L177–L180. doi:10.1086/425217

Loukitcheva, M., Solanki, S. K., Carlsson, M., and Stein, R. F. (2004). Millimeter observations and chromospheric dynamics. *Astron. Astrophys.* 419, 747–756. doi:10.1051/0004-6361:20034159

Loukitcheva, M., Solanki, S. K., Carlsson, M., and White, S. M. (2015). Millimeter radiation from a 3D model of the solar atmosphere. I. Diagnosing chromospheric thermal structure. *Astron. Astrophys.* 575, A15. doi:10.1051/0004-6361/201425238

Loukitcheva, M., Solanki, S. K., and White, S. M. (2009). The relationship between chromospheric emissions and magnetic field strength. *Astron. Astrophys.* 497, 273–285. doi:10.1051/0004-6361/200811133

Loukitcheva, M., White, S. M., Solanki, S. K., Fleishman, G. D., and Carlsson, M. (2017a). Millimeter radiation from a 3D model of the solar atmosphere. II. Chromospheric magnetic field. *Astron. Astrophys.* 601, A43. doi:10.1051/0004-6361/201629099

Loukitcheva, M. A., Iwai, K., Solanki, S. K., White, S. M., and Shimojo, M. (2017b). Solar ALMA observations: Constraining the chromosphere above sunspots. *Astrophys. J.* 850, 35. doi:10.3847/1538-4357/aa91cc

Loukitcheva, M. A., Solanki, S. K., and White, S. (2008). ALMA as the ideal probe of the solar chromosphere. *Astrophys. Space Sci.* 313, 197–200. doi:10.1007/s10509-007-9626-1

Loukitcheva, M. A., White, S. M., and Solanki, S. K. (2019). ALMA detection of dark chromospheric holes in the quiet sun. *Astrophys. J.* 877, L26. doi:10.3847/2041-8213/ab2191

Malanushenko, A., Cheung, M. C. M., DeForest, C. E., Klimchuk, J. A., and Rempel, M. (2022). The coronal veil. *Astrophys. J.* 927, 1. doi:10.3847/1538-4357/ac3df9

Martínez-Sykora, J., De Pontieu, B., de la Cruz Rodriguez, J., and Chintzoglou, G. (2020). the formation height of millimeter-wavelength emission in the solar chromosphere. *Astrophys. J.* 891, L8. doi:10.3847/2041-8213/ab75ac

Martínez-Sykora, J., De Pontieu, B., De Moortel, I., Hansteen, V. H., and Carlsson, M. (2018). Impact of type II spicules in the corona: Simulations and synthetic observables. *Astrophys. J.* 860, 116. doi:10.3847/1538-4357/aac2ca

Menezes, F., Selhorst, C. L., Giménez de Castro, C. G., and Valio, A. (2022). Subterahertz radius and limb brightening of the Sun derived from SST and ALMA. *Mon. Not. R. Astron. Soc.* 511, 877–885. doi:10.1093/mnras/stab3501

Mihalas, D. (1978). *Stellar atmospheres*.

Molnar, M. E., Reardon, K. P., Chai, Y., Gary, D., Uitenbroek, H., Cauzzi, G., et al. (2019). Solar chromospheric temperature diagnostics: A joint ALMA-hα analysis. *Astrophys. J.* 881, 99. doi:10.3847/1538-4357/ab2ba3

Morosin, R., de la Cruz Rodríguez, J., Díaz Baso, C. J., and Leenaarts, J. (2022). *Spatio-temporal analysis of chromospheric heating in a plage region. arXiv e-prints*arXiv:2203.01688.

Narang, N., Chandrashekhar, K., Jafarzadeh, S., Fleck, B., Szydlarski, M., and Wedemeyer, S. (2022). Power distribution of oscillations in the atmosphere of a plage region. Joint observations with ALMA, IRIS, and SDO. *Astron. Astrophys.* 661, A95. doi:10.1051/0004-6361/202142080

Nindos, A., Alissandrakis, C. E., Bastian, T. S., Patsourakos, S., De Pontieu, B., Warren, H., et al. (2018). First high-resolution look at the quiet Sun with ALMA at 3mm. *Astron. Astrophys.* 619, L6. doi:10.1051/0004-6361/201834113

Nindos, A., Patsourakos, S., Alissandrakis, C. E., and Bastian, T. S. (2021). ALMA observations of the variability of the quiet Sun at millimeter wavelengths. *Astron. Astrophys.* 652, A92. doi:10.1051/0004-6361/202141241

Nita, G. M., Fleishman, G. D., Kuznetsov, A. A., Kontar, E. P., and Gary, D. E. (2015). Three-dimensional radio and X-ray modeling and data analysis software: Revealing flare complexity. *Astrophys. J.* 799, 236. doi:10.1088/0004-637X/799/2/236

Nita, G. M., Viall, N. M., Klimchuk, J. A., Loukitcheva, M. A., Gary, D. E., Kuznetsov, A. A., et al. (2018). Dressing the coronal magnetic extrapolations of active regions with a parameterized thermal structure. *Astrophys. J.* 853, 66. doi:10.3847/1538-4357/aaa4bf

Oliver, R., Soler, R., Terradas, J., Zaqarashvili, T. V., and Khodachenko, M. L. (2014). Dynamics of coronal rain and descending plasma blobs in solar prominences. I. Fully ionized case. *Astrophys. J.* 784, 21. doi:10.1088/0004-637X/784/1/21

Pastor Yabar, A., Borrero, J. M., Quintero Noda, C., and Ruiz Cobo, B. (2021). Inference of electric currents in the solar photosphere. *Astron. Astrophys.* 656, L20. doi:10.1051/0004-6361/202142149

Patsourakos, S., Alissandrakis, C. E., Nindos, A., and Bastian, T. S. (2020). Observations of solar chromospheric oscillations at 3 mm with ALMA. *Astron. Astrophys.* 634, A86. doi:10.1051/0004-6361/201936618

Pereira, T. M. D., and Uitenbroek, H. (2015). RH 1.5D: A massively parallel code for multi-level radiative transfer with partial frequency redistribution and zeeman polarisation. *Astron. Astrophys.* 574, A3. doi:10.1051/0004-6361/201424785

Pietarila, A., Socas-Navarro, H., and Bogdan, T. (2007). Spectropolarimetric inversions of the Ca II 8498 and 8542 Å lines in the quiet sun. *Astrophys. J.* 670, 885–902. doi:10.1086/521271

Przybylski, D., Cameron, R., Solanki, S. K., Rempel, M., Leenaarts, J., Anusha, L. S., et al. (2022). *Chromospheric extension of the MURaM code. arXiv e-prints*arXiv:2204.03126.

Rau, U., and Cornwell, T. J. (2011). A multi-scale multi-frequency deconvolution algorithm for synthesis imaging in radio interferometry. *Astron. Astrophys.* 532, A71. doi:10.1051/0004-6361/201117104

Rempel, M., Schüssler, M., and Knölker, M. (2009). Radiative magnetohydrodynamic simulation of sunspot structure. *Astrophys. J.* 691, 640–649. doi:10.1088/0004-637X/691/1/640

Rodger, A., and Labrosse, N. (2017). Solar prominence modelling and plasma diagnostics at ALMA wavelengths. *Sol. Phys.* 292, 130. doi:10.1007/s11207-017-1161-9

Ruiz Cobo, B., and Asensio Ramos, A. (2013). Returning magnetic flux in sunspot penumbrae. *Astron. Astrophys.* 549, L4. doi:10.1051/0004-6361/201220373

Ruiz Cobo, B., and del Toro Iniesta, J. C. (1992). Inversion of Stokes profiles. *Astrophys. J.* 398, 375. doi:10.1086/171862

Sahin, S., and Antolin, P. Prevalence of thermal-non-equilibrium over an active region. ApJ Accepted (2022).doi:10.3847/2041-8213/ac6fe9

Sainz Dalda, A., de la Cruz Rodríguez, J., De Pontieu, B., and Gošić, M. (2019). Recovering thermodynamics from spectral profiles observed by IRIS: A machine and deep learning approach. *Astrophys. J.* 875, L18. doi:10.3847/2041-8213/ab15d9

Schad, T. A., Penn, M. J., Lin, H., and Judge, P. G. (2016). Vector magnetic field measurements along a cooled stereo-imaged coronal loop. *Astrophys. J.* 833, 5. doi:10.3847/0004-637X/833/1/5

Scharmer, G. B., de la Cruz Rodriguez, J., Sütterlin, P., and Henriques, V. M. J. (2013). Opposite polarity field with convective downflow and its relation to magnetic spines in a sunspot penumbra. *Astron. Astrophys.* 553, A63. doi:10.1051/0004-6361/201220899

Schrijver, C. J. (2001). Catastrophic cooling and high-speed downflow in quiescent solar coronal loops observed with TRACE. *Sol. Phys.* 198, 325–345. doi:10.1023/A:1005211925515

Shimizu, T., Shimojo, M., and Abe, M. (2021). Simultaneous ALMA-hinode-IRIS observations on footpoint signatures of a soft X-ray loop-like microflare. *Astrophys. J.* 922, 113. doi:10.3847/1538-4357/ac27a4

Silva, A. V. R., White, S. M., Lin, R. P., de Pater, I., Shibasaki, K., Hudson, H. S., et al. (1996). First images of a solar flare at millimeter wavelengths. *Astrophys. J.* 458, L49–L52. doi:10.1086/309918

Simões, P. J. A., Kerr, G. S., Fletcher, L., Hudson, H. S., Giménez de Castro, C. G., and Penn, M. (2017). Formation of the thermal infrared continuum in solar flares. *Astron. Astrophys.* 605, A125. doi:10.1051/0004-6361/201730856

Skartlien, R., Stein, R. F., and Nordlund, Å. (2000). Excitation of chromospheric wave transients by collapsing granules. *Astrophys. J.* 541, 468–488. doi:10.1086/309414

Socas-Navarro, H., Trujillo Bueno, J., and Ruiz Cobo, B. (2000). Non-LTE inversion of Stokes profiles induced by the zeeman effect. *Astrophys. J.* 530, 977–993. doi:10.1086/308414

Stepanov, A. V., Urpo, S., and Zaitsev, V. V. (1992). Diagnostics of solar flare and evaporated plasma using mm-wave emission. *Sol. Phys.* 140, 139–148. doi:10.1007/BF00148434

Sudar, D., Brajša, R., Skokić, I., and Benz, A. O. (2019). Centre-to-Limb brightness variations from the Atacama large millimeter-submillimeter array (ALMA) full-disk solar images. *Sol. Phys.* 294, 163. doi:10.1007/s11207-019-1556-x

Uitenbroek, H. (2001). Multilevel radiative transfer with partial frequency redistribution. *Astrophys. J.* 557, 389–398. doi:10.1086/321659

Unsöld, A. (1955). *Physik der Sternatmospharen*. MIT besonderer Berucksichtigung der Sonne.

Valle Silva, J. F., Giménez de Castro, C. G., Simões, P. J. A., and Raulin, J. P. (2019). Submillimeter radiation as the thermal component of the neupert effect. *Sol. Phys.* 294, 150. doi:10.1007/s11207-019-1542-3

van Noort, M. (2012). Spatially coupled inversion of spectro-polarimetric image data. I. Method and first results. *Astron. Astrophys.* 548, A5. doi:10.1051/0004-6361/201220220

Vernazza, J. E., Avrett, E. H., and Loeser, R. (1981). Structure of the solar chromosphere. III. Models of the EUV brightness components of the quiet sun. *Astrophys. J. Suppl. Ser.* 45, 635–725. doi:10.1086/190731

J. C. Vial, and O. Engvold (Editors) (2015). *Solar prominences, astrophysics and space science library* (Springer International Publishing Switzerland), 415. doi:10.1007/978-3-319-10416-4

Vissers, G. J. M., de la Cruz Rodríguez, J., Libbrecht, T., Rouppe van der Voort, L. H. M., Scharmer, G. B., and Carlsson, M. (2019). Dissecting bombs and bursts: Non-LTE inversions of low-atmosphere reconnection in SST and IRIS observations. *Astron. Astrophys.* 627, A101. doi:10.1051/0004-6361/201833560

Wedemeyer, S., Bastian, T., Brajša, R., Hudson, H., Fleishman, G., Loukitcheva, M., et al. (2016). Solar science with the Atacama large millimeter/submillimeter array - a new view of our sun. *Space Sci. Rev.* 200, 1–73. doi:10.1007/s11214-015-0229-9

Wedemeyer, S., Freytag, B., Steffen, M., Ludwig, H. G., and Holweger, H. (2004). Numerical simulation of the three-dimensional structure and dynamics of the non-magnetic solar chromosphere. *Astron. Astrophys.* 414, 1121–1137. doi:10.1051/0004-6361:20031682

Wedemeyer, S. (2019). "High-cadence imaging of the sun," in ALMA Development Workshop, ESO Garching, Germany, June 3 - 5, 2019 (Genève, Switzerland: Zenodo), 47. doi:10.5281/zenodo.3240401

Wedemeyer, S., Szydlarski, M., Jafarzadeh, S., Eklund, H., Guevara Gomez, J. C., Bastian, T., et al. (2020a). The Sun at millimeter wavelengths. I. Introduction to ALMA Band 3 observations. *Astron. Astrophys.* 635, A71. doi:10.1051/0004-6361/201937122

Wedemeyer, S., Szydlarski, M., Rodriguez, JdlC., and Jafarzadeh, S. (2020b). "Observing the sun with the Atacama large millimeter/submillimeter array - from continuum to magnetic fields," in *Solar and stellar magnetic fields: Origins and manifestations*. Editors A. Kosovichev, S. Strassmeier, and M. Jardine, 354, 24–37. doi:10.1017/S174392131900 9906

Wedemeyer-Böhm, S., Ludwig, H. G., Steffen, M., Freytag, B., and Holweger, H. (2005). "The shock-patterned solar chromosphere in the light of ALMA," in *13th cambridge workshop on cool stars, stellar systems and the Sun*. Editors F. Favata, G. A. J. Hussain, and B. Battrick (Noordwijk, Netherlands: ESA Special Publication), 560, 1035.

Wedemeyer-Böhm, S., Ludwig, H. G., Steffen, M., Leenaarts, J., and Freytag, B. (2007). Inter-network regions of the Sun at millimetre wavelengths. *Astron. Astrophys.* 471, 977–991. doi:10.1051/0004-6361:20077588

Wedemeyer-Böhm, S., and Rouppe van der Voort, L. (2009). On the continuum intensity distribution of the solar photosphere. *Astron. Astrophys.* 503, 225–239. doi:10.1051/0004-6361/200911983

White, S. M., Iwai, K., Phillips, N. M., Hills, R. E., Hirota, A., Yagoubov, P., et al. (2017). Observing the sun with the Atacama large millimeter/submillimeter array (ALMA): Fast-scan single-dish mapping. *Sol. Phys.* 292, 88. doi:10.1007/s11207-017-1123-2

White, S. M., Loukitcheva, M., and Solanki, S. K. (2006). High-resolution millimeter-interferometer observations of the solar chromosphere. *Astron. Astrophys.* 456, 697–711. doi:10.1051/0004-6361:20052854

Wiegelmann, T., and Sakurai, T. (2012). Solar force-free magnetic fields. *Living Rev. Sol. Phys.* 9, 5. doi:10.12942/lrsp-2012-5

Wiegelmann, T., Thalmann, J. K., and Solanki, S. K. (2014). The magnetic field in the solar atmosphere. *Astron. Astrophys. Rev.* 22, 78. doi:10.1007/s00159-014-0078-7

Williams, T., Walsh, R. W., Winebarger, A. R., Brooks, D. H., Cirtain, J. W., De Pontieu, B., et al. (2020). Is the high-resolution coronal imager resolving coronal strands? Results from AR 12712. *Astrophys. J.* 892, 134. doi:10.3847/1538-4357/ab6dcf

Wöger, F., Wedemeyer-Böhm, S., Schmidt, W., and von der Lühe, O. (2006). Observation of a short-lived pattern in the solar chromosphere. *Astron. Astrophys.* 459, L9–L12. doi:10.1051/0004-6361:20066237

Wootten, A., and Thompson, A. R. (2009). The Atacama large millimeter/submillimeter array. *Proc. IEEE* 97, 1463–1471. doi:10.1109/JPROC.2009.2020572

Young, P. R., Tian, H., Peter, H., Rutten, R. J., Nelson, C. J., Huang, Z., et al. (2018). Solar ultraviolet bursts. *Space Sci. Rev.* 214, 120. doi:10.1007/s11214-018-0551-0

frontiers | Frontiers in Astronomy and Space Sciences

TYPE Review
PUBLISHED 07 October 2022
DOI 10.3389/fspas.2022.983707

OPEN ACCESS

EDITED BY
Costas E. Alissandrakis,
University of Ioannina, Greece

REVIEWED BY
Debi Prasad Choudhary,
California State University, United States
Baolin Tan,
National Astronomical Observatories (CAS), China

*CORRESPONDENCE
Petr Heinzel,
pheinzel@asu.cas.cz

SPECIALTY SECTION
This article was submitted to Stellar and Solar Physics, a section of the journal Frontiers in Astronomy and Space Sciences

RECEIVED 01 July 2022
ACCEPTED 14 September 2022
PUBLISHED 07 October 2022

CITATION
Heinzel P, Bárta M, Gunár S, Labrosse N and Vial J-C (2022), Prominence observations with ALMA. *Front. Astron. Space Sci.* 9:983707. doi: 10.3389/fspas.2022.983707

Prominence observations with ALMA

Petr Heinzel[1,2]*, Miroslav Bárta[1], Stanislav Gunár[1], Nicolas Labrosse[3] and Jean-Claude Vial[4]

[1]Astronomical Institute, The Czech Academy of Sciences, Ondřejov, Czechia, [2]Centre of Scientific Excellence–Solar and Stellar Activity, University of Wrocław, Wrocław, Poland, [3]SUPA, School of Physics & Astronomy, University of Glasgow, Glasgow, United Kingdom, [4]Institut d'Astrophysique Spatiale, CNRS/Univ. Paris-Sud, Université Paris-Saclay, Orsay, France

This review comes at the time when ALMA successfully obtained the first regular observations of both a prominence and a filament. These observations have a spatial resolution of 1-2 arcsec, far better than previous prominence observations in the mm/sub-mm radio domain. The achieved resolution is compatible with the cotemporal ground-based coronagraphic observations in the hydrogen Hα line that accompany the ALMA Band 3 prominence observations. A core part of this review is the description and analysis of these pioneering ALMA observations of a quiescent prominence, focusing on various physical and geometrical properties of the observed prominence fine structures. We also summarize the basic physical processes behind the formation of mm/sub-mm continua under prominence conditions and describe the plasma diagnostics potential of ALMA solar observations. Finally, we discuss future prospects of ALMA prominence observations and the value of coordinated optical and UV spectra and images.

KEYWORDS

prominences, mm/sub-mm observations, ALMA, plasma diagnostics, temperature structure

1 Introduction

The Atacama Large Millimeter/submillimeter Array (ALMA) currently offers an unprecedented spatial resolution for solar observations in the radio domain. These ALMA capabilities will be further improved and exploited for the study of extended sources in the solar atmosphere including cool coronal structures like prominences. One of the primary interests of the solar physics community in ALMA observations is the ability to diagnose the kinetic temperature of the observed plasma from the measurements of the brightness temperature provided by ALMA. As is described, for example, in Wedemeyer et al. (2016), under specific conditions the plasma kinetic temperature can be directly derived from the measured brightness temperature. However, in the general case, the derivation of the kinetic temperature is not straightforward because the studied solar plasma is typically in the non-LTE state, i.e. departing from the Local Thermodynamic Equilibrium (Labrosse et al., 2010; Heinzel, 2015). This means that even though the free-free emission processes have a Planckian source function, the opacity depends on the ionisation state of the plasma which strongly departs from LTE and may be even time-dependent. In the special

case of prominences, which we focus on here, there are not only observational difficulties related to ALMA observations performed above the solar limb but also increased non-LTE effects due to the critical importance of the spectral line scattering in optical and ultraviolet (UV) domains. The latter affects the ionisation in the multilevel hydrogen which in the case of prominences is dominated by Lyman and Balmer continuum photoionisation. However, the free-free opacity, which is proportional to the emission measure (see below), can be independently derived from the hydrogen Hα line intensity obtained simultaneously with the ALMA observations in a single band, or from spectral radio measurements themselves once ALMA will be able to provide near-simultaneous observations in more than one band.

Thanks to the advent of specific ALMA observations of prominences and filaments, we can review here not only the procedures leading to ALMA prominence observations and the diagnostic potential of ALMA data, but also the results of the first analyses of a quiescent prominence (Heinzel et al., 2022; Labrosse et al., 2022) and filament (da Silva Santos et al., 2022) observations. The first prominence observations were obtained only in Band 3 but, thanks to a dedicated coordinated observing campaign, are accompanied by Hα and Mg II h&k spectra. The first observations of an (active region) filament were also obtained in a single ALMA band (Band 6), accompanied by simultaneous Mg II h&k spectral observations. In the frame of this review, we address in detail the difficulties encountered in the ALMA observations of prominences and discuss various aspects of ALMA data interpretation. Of particular interest is the development of relevant multi-spectral inversion techniques.

The paper is organized as follows. In Section 2, we present a historical overview of prominence observations in mm/sub-mm domain. In Section 3 we provide a brief description of ALMA with the emphasis on solar observations. Section 4 describes the formation mechanisms of the ALMA continua under the conditions of solar prominences. The issues of the visibility of quiescent prominences in the ALMA bands are addressed in Section 5. Section 6 is devoted to a thorough discussion of the plasma diagnostic capabilities of ALMA. In Section 7 we present the set-up of the current ALMA prominence observations, together with a discussion of the complexity of the data reduction of ALMA off-limb observations and the results of the analysis of these first ALMA prominence observations. Our conclusions and the future prospects of ALMA prominence observations are addressed in Section 8.

2 Historical overview of mm prominence observations

Up to now, observations of prominences and filaments in the mm-continuum have been limited by low spatial resolution, making it difficult to accurately infer their temperatures or densities due to constrained information about the size of the observed structures and the filling factor (Heinzel et al., 2015; Rodger, 2019). Depending on the exact wavelength, filaments were found to be generally nearly invisible or slightly dark against the disk at 1.3 mm while becoming much darker at 3 mm (Hiei et al., 1986; Lindsey et al., 1992). Vrsnak et al. (1992) analysed maps of the solar disk at wavelengths between 4 and 26 mm using a beam size of 2.4 arcmin (at λ = 8 mm). They looked for correlations between low temperature regions and various structures including disk filaments. They did not find an obvious relationship, as many filaments did not present a discernable reduction in the mm-continuum temperature maps. Bastian et al. (1993) conducted a study of prominences using the Caltech submillimeter observatory. The resolution was between 20 and 30 arcsec for observations at 0.85 and 1.25 mm. They concluded that filaments and prominences were optically thin at 0.85 mm. Hα filaments were found to have a brightness temperature comparable to or below that of the disk centre. Harrison et al. (1993) caught a large erupting prominence with the James Clerk Maxwell Telescope on Mauna Kea, Hawaii, at the wavelength of 1.3 mm during the total solar eclipse of 11 July 1991. The lack of complementary observations did not allow the authors to make an accurate diagnostic, though they found that assuming a 33% filling factor, a density of 10^{10} cm^{-3} and a temperature of 6000 K was consistent with their observations. Limitation to a single band was not the case in the observations of Irimajiri et al. (1995) who presented the first simultaneous measurements of an eruptive prominence at multiple millimetre wavelengths of 2.7 mm (110 GHz), 3.4 mm (89 GHz), and 8.3 mm (36 GHz) with spatial resolutions of 15, 19, and 46 arcsec respectively. This allowed the authors to measure the spectral index for the prominence, and thus its optical thickness in each observing band. The optical thickness was of the order of unity up to about 6 at 8.3 mm. Clearly, all these observations did not reach a spatial resolution capable of revealing prominence fine structures, which are found from the optical observations down to sub-arcsecond scales (Engvold, 2015). As demonstrated in this review, ALMA enables us to address this issue.

3 ALMA

Because of the diffraction law, it may seem an illogical idea to use an interferometer in mm (and even submm) wavelengths in order to reach an excellent spatial resolution on an extended object such as the Sun. But because of the large-scale interferometer arms possible on the ground, on one hand, and because of the properties of the emitted radiation in these bands, on the other hand, solar physicists have been very interested in the brand new instrument ALMA. Of course, radio observations of the quiet chromosphere are not a new fact and interferometers working from a few mm to a few cm (WSRT, BIMA, VLA) have

paved the way to ALMA. But neither interferometers nor single dish telescopes could catch up with the permanently increasing spatial resolution of UV and optical instruments. The challenge is now to match the expected DKIST resolution of 0.15 arcsec (Rast et al., 2021).

The 66 antennas of ALMA are organized as follows: The 12-m array (50 movable antennas with 12 m diameter) and the Acatama Compact Array (ACA) which combines 12 antennas with 7 m diameter for interferometry. The set-up is completed with 4 antennas with 12 m diameter for single dish observations referred to as the ACA Total Power (TP) Array. As seen later, this set-up is necessary for having a large field of view (FOV) from which it is possible to derive the background emission. Current estimates based on numerical simulations of ALMA's imaging capabilities (e.g., Wedemeyer and Parmer, 2015) imply a spatial resolution of (0.3–0.4) × λ/1 mm [arcsec]. In principle, every antenna will eventually be equipped with receivers covering ten frequency bands in the range from 35 to 950 GHz, corresponding to wavelengths from 8.6 to 0.3 mm, according to Wedemeyer et al. (2016). Presently, ALMA is working in 8 bands centered from 3.1 to 0.35 mm, but not all are yet available for solar observations.

4 Formation of ALMA continua in solar prominences and filaments

In this section, we describe the formation mechanisms of the ALMA continua with a focus on prominence observations. More details can be found in Heinzel et al. (2015).

In solar prominences the principal source of opacity is the hydrogen free-free continuum. Other emission processes in the mm-continuum such as gyrosynchrotron emission can be safely neglected in the absence of strong-enough magnetic fields and of particles accelerated to relativistic speeds. Thus, the absorption coefficient at frequency ν is

$$\kappa_\nu(\mathrm{H}) = 3.7\times10^{8}T^{-1/2}n_\mathrm{e}n_\mathrm{p}\nu^{-3}g_\mathrm{ff}, \tag{1}$$

where n_e and n_p are the electron and proton densities, respectively, T the kinetic temperature, and $g_\mathrm{ff} \approx 1$ is the Gaunt factor which is of the order of unity but depends generally on the kinetic temperature and frequency (see, e.g., Rodger, 2019). Note that we use the cgs units throughout this section. At low temperatures, H^- free-free opacity is

$$\kappa_\nu(\mathrm{H}^-) = \frac{n_\mathrm{e}n_\mathrm{HI}}{\nu}x, \tag{2}$$

with n_HI being the neutral hydrogen density and x takes the form

$$x = \left(1.3727\times10^{-25} + \left(4.3748\times10^{-10} - 2.5993\times10^{-7}/T\right)/\nu\right). \tag{3}$$

The total free–free absorption coefficient, corrected for stimulated emission, is then

$$\kappa_\nu = [\kappa_\nu(\mathrm{H}) + \kappa_\nu(\mathrm{H}^-)]\left(1 - \mathrm{e}^{-h\nu/kT}\right), \tag{4}$$

where h and k are the Planck and Boltzmann constants, respectively. Contrary to UV, the stimulated emission is non-negligible in the ALMA domain.

At low temperatures the hydrogen is much less ionized and the ionization degree $i = n_\mathrm{p}/n_\mathrm{H}$ goes to zero (here n_H is the total hydrogen number density). Let's express the ratio $r = \kappa_\nu(\mathrm{H}^-)/\kappa_\nu(\mathrm{H})$ as

$$r = 2.7\times10^{-9}\nu^2T^{1/2}x(1-i)/i. \tag{5}$$

Gouttebroze et al. (1993) computed a set of low-temperature isothermal-isobaric models with T = 4300 K, which may correspond to the radiative-equilibrium conditions (Heinzel et al., 2014). At this extremely low temperature, i decreases with increasing gas pressure and for the highest considered pressure p = 1 dyn cm^{-2}, $i = 2.3\times10^{-2}$. But even under such extreme conditions, r is of the order of 10^{-4} in the wavelength range 1–9 mm and therefore we can neglect the H^- free-free opacity in prominences, contrary to solar temperature minimum where the density is very high.

In the literature some authors use the form

$$\kappa_\nu(\mathrm{H}) = \alpha n_\mathrm{e}n_\mathrm{p}T^{-3/2}\nu^{-2} \tag{6}$$

where $\alpha = 0.018g_\mathrm{ff}$. In the radio domain where $h\nu/kT \ll 1$, the stimulated emission term can be written as $h\nu/kT$. This then gives the above alternative form which already includes the stimulated emission.

The synthetic intensity I_ν, emergent from the prominence on the limb, is in general obtained as

$$I_\nu = \int B_\nu(T)\mathrm{e}^{-t_\nu}\mathrm{d}t_\nu = \int \eta_\nu\mathrm{e}^{-t_\nu}\mathrm{d}l \quad \eta_\nu = \kappa_\nu B_\nu \quad \mathrm{d}t_\nu = \kappa_\nu\mathrm{d}l, \tag{7}$$

where $B_\nu(T)$ is the source function, η_ν the emission coefficient, t_ν the optical depth, and l is the geometrical path length along the LOS. The free-free processes are collisional processes and therefore the source function is Planckian, whereas n_e and n_p result from the non-LTE ionization equilibria mainly in hydrogen and helium continua where the photoionizations and spontaneous recombinations dominate.

Using the Rayleigh–Jeans law, I_ν and B_ν are directly proportional to the brightness temperature T_b and to the kinetic temperature T, respectively

$$I_\nu = \frac{2\nu^2k}{c^2}T_\mathrm{b} \quad B_\nu = \frac{2\nu^2k}{c^2}T, \tag{8}$$

where c is the speed of light. Then we get from Eq. 7

$$T_\mathrm{b} = \int T\mathrm{e}^{-t_\nu}\mathrm{d}t_\nu = \int T\mathrm{e}^{-t_\nu}\kappa_\nu\mathrm{d}l. \tag{9}$$

Assuming an isothermal prominence we have

$$T_\mathrm{b} = T(1-\mathrm{e}^{-\tau_\nu}), \tag{10}$$

where $\tau_\nu = \kappa_\nu L$ is the total optical thickness and L is the *effective* geometrical thickness of the prominence along the LOS representing the absorbing path. In the optically-thin case $T_b = T\tau(\nu)$, or equivalently

$$T_b = \alpha \nu^{-2} T^{-1/2} EM, \tag{11}$$

where $EM = n_e^2 L$ is called here the emission measure. The brightness temperature of a prominence thus depends on the kinetic temperature and optical thickness. The latter is directly proportional to the emission measure, provided that $n_e = n_p$ (this applies to a pure hydrogen plasma).

5 Visibility of quiescent prominences in ALMA bands

Based on the calculations described in Section 4, the ideal brightness temperature ($\boldsymbol{T_b}$) maps at mm wavelengths can be inferred from the Hα integrated intensity, see e.g. the study by Heinzel et al. (2015). Such maps played an important role in the period of 2015–2017 prior to the actual solar ALMA observations when prominences were evaluated as a prospective science case for ALMA. However, for accurate prediction of the visibility of prominences in ALMA, the non-ideal effects introduced by the instrument and Earth's atmosphere have to be included and applied to the ideal T_b maps. From all possible degradations, two play the most important role: 1) the incomplete coverage of the Fourier space due to the limited number of interferometric visibilities and 2) the random phase errors of those visibilities caused by atmospheric turbulence. These effects can be included in the synthetic T_b maps thanks to the simulation toolkit contained in the standard CASA (Common Astronomy Software Applications, see http://casa.nrao.edu/) package. The simulated degraded visibilities can be obtained from ideal T_b maps using the *simobserve*() task. Afterwards, the visibility synthesis and image analysis (namely the comparison with the initial ideal model and the fidelity estimation) can be performed by *simanalyze*().

The results are presented in Figure 1. The left part shows the ideal T_b map at 100 GHz (i.e., 3 mm) used as an input model for visibility simulations. It has been computed using the observed Hα integrated intensity as described in Heinzel et al. (2015). Its resolution is $\approx 1-2$ arcsec. Overlaid are the pointings (white crosses) of ALMA 12 m array for a mosaic that is able to sample the displayed part of the prominence and field of view for the single pointing (a white circle). The displayed part of the prominence represents a trade-off between larger total field of view and cadence of mosaicing since the full scan over 49 pointings takes more than 6 min of on-source time. The atmosphere-degraded interferometric visibilities at 100 GHz have been calculated from this model for the combined 12 m+7 m ALMA array in one of its compact configurations. The configuration has been selected in line with the sub-set allowed so far for the solar research and with respect to the resolution provided by the input model–ALMA resolution at 3 mm is similar for the compact array. Realistic atmospheric parameters and elevation in line with the Solar ALMA Observing Mode specifications have been selected for simulating the phase distortions. A synthetic image obtained from the simulated interferometric visibilities is presented in the right panel of Figure 1. Simulations have shown that the multi-frequency synthesis (i.e. combining the visibilities for all available frequency channels) used for the continuum imaging slightly improves the *uv* coverage and thus the fidelity of the image. Clearly, the effect of the intensity jump at the solar limb remains visible in the simulated ALMA interferometric image (repeating structures parallel to the limb in the corona). This has to be fixed by proper combination of the interferometric image with its complementary single-dish low-resolution counterpart, in order to complete the missing flux density at the *uv* scales not covered by the interferometer (see Section 7). Nevertheless, the described study has demonstrated the feasibility of solar-prominence observations by ALMA and provided estimates of reachable brightness temperatures and plausible value-ranges for other parameters necessary for the correct setup of the ALMA observing procedure. This knowledge has been later used in actual ALMA solar science observations.

5.1 Simulated imaging of prominences in ALMA bands

High-resolution interferometric observations in the mm/sub-mm wavelengths open an entirely new door for the investigation of solar prominences. However, at the same time, such a new type of data brings challenges in how we can understand and interpret them. While ALMA has the potential to improve the spatial resolution in the mm/sub-mm domain by an order of magnitude, or more (see e.g. the discussion in Wedemeyer et al., 2016), we need to understand to what extent the prominences at the limb and on the disk (filaments) will be visible in the ALMA observations and how well their fine structures will be resolved. Moreover, to correctly interpret the ALMA prominence observations we need to understand how the thermal structure of the prominence plasma will appear in various ALMA bands.

As we discuss above, Heinzel et al. (2015) used the Hα coronagraphic observations of a quiescent prominence obtained by the Multichannel Subtractive Double Pass (MSDP) spectrograph to determine the visibility of the prominence fine structures at various ALMA wavelengths. The spatial resolution that can be achieved by this technique depends on the original resolution of the used Hα observations. Therefore, the spatial resolution of the synthetic ALMA images obtained by Heinzel et al. (2015) was of the order of 1 arcsec. While this does not reach the best potential resolution of ALMA,

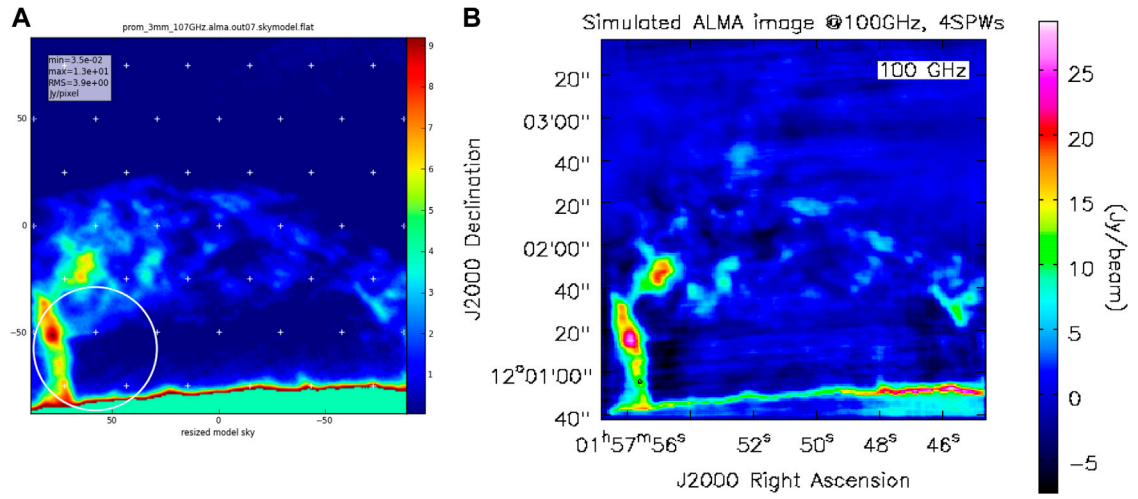

FIGURE 1
(A): Modelled (ideal) brightness temperature map at 100 GHz. The white circle shows ALMA field-of-view for single pointing, the crosses are the centres of pointing for interferometric mosaic. Fourty-nine pointings are necessary for Nyquist sampling of the displayed part of the prominence. **(B)**: Corresponding image as seen by ALMA at 3 mm in Band 3 simulated with the CASA:*simobserve*() task. Reproduced from Heinzel et al. (2015).

it is similar to the resolution that was achieved in the current ALMA solar observations. Of course, the solar ALMA observations mode is being continually developed and the capabilities of ALMA will thus improve over the coming years. If we want to address the issues of the visibility of prominence and filament fine structures in the future ALMA observations, we can harness the power of simulated ALMA-like prominence observations based on visualizations of prominence models.

The first simulated high-resolution ALMA observations of a modelled prominence were produced by Gunár et al. (2016). These authors used the detailed 3D WPFS (Whole-Prominence Fine Structure) model of Gunár and Mackay (2015) to show to what extent both the large-scale and small-scale structures of prominences at the limb and filaments on the disk might be visible in the ALMA observations. For this purpose, the authors used a visualization method adapted from Heinzel et al. (2015) to construct synthetic images at mm/sub-mm wavelengths covering the entire ALMA range. It is worth noting that this visualization method, which is described in Gunár et al. (2016), can be applied to any model with prominence-like conditions to produce synthetic images at the wavelengths covered by ALMA. The synthetic brightness temperature maps adapted from Gunár et al. (2016) are shown in Figure 2. These simulated observations represent both the prominence at the limb and the filament on the disk in ALMA bands 6 and 3. The work of Gunár et al. (2016) showed that in prominences the large-scale structures visible at the ALMA wavelengths appear similar to those visible in the Hα line. The cool and dense prominence fine structures are well visible in the simulated ALMA images, which offer even better contrast than the Hα images (for more details see Figures 1–5 in Gunár et al., 2016). The situation becomes more complex in the case of filaments observed against the solar disk. There, in an optically rather thick case of Band 3, the filament appears as two parallel structures that are brighter than the background (see the bottom panel of Figure 2). The central region between these bright structures exhibits the same brightness temperature T_b as the (simulated) background photosphere. However, this region actually corresponds to the densest part of the simulated filament. That is obvious, for example, from the Hα image of the same filament (Figure 5 of Gunár et al., 2016). The coincidence in the similar T_b values is due to the fact that the simulated plasma has a kinetic temperature of 7,000 K, which is very close to the background brightness temperature T_b^{bcg} in Band 3 (see Gunár et al., 2016, for more details). However, without prior knowledge of the structure and temperature of the observed plasma, it would be difficult to correctly interpret similar ALMA filament observations on their own. Access to complementary observations, for example in the Hα line would be in such a case necessary.

6 Plasma diagnostics potential of ALMA

As is described in Section 4, the observed specific intensity at the mm/sub-mm wavelengths can be used to derive the kinetic temperature of the solar plasma (see also Loukitcheva et al., 2004; Heinzel and Avrett, 2012). However, such derivation of the kinetic temperature is not entirely straightforward. Without

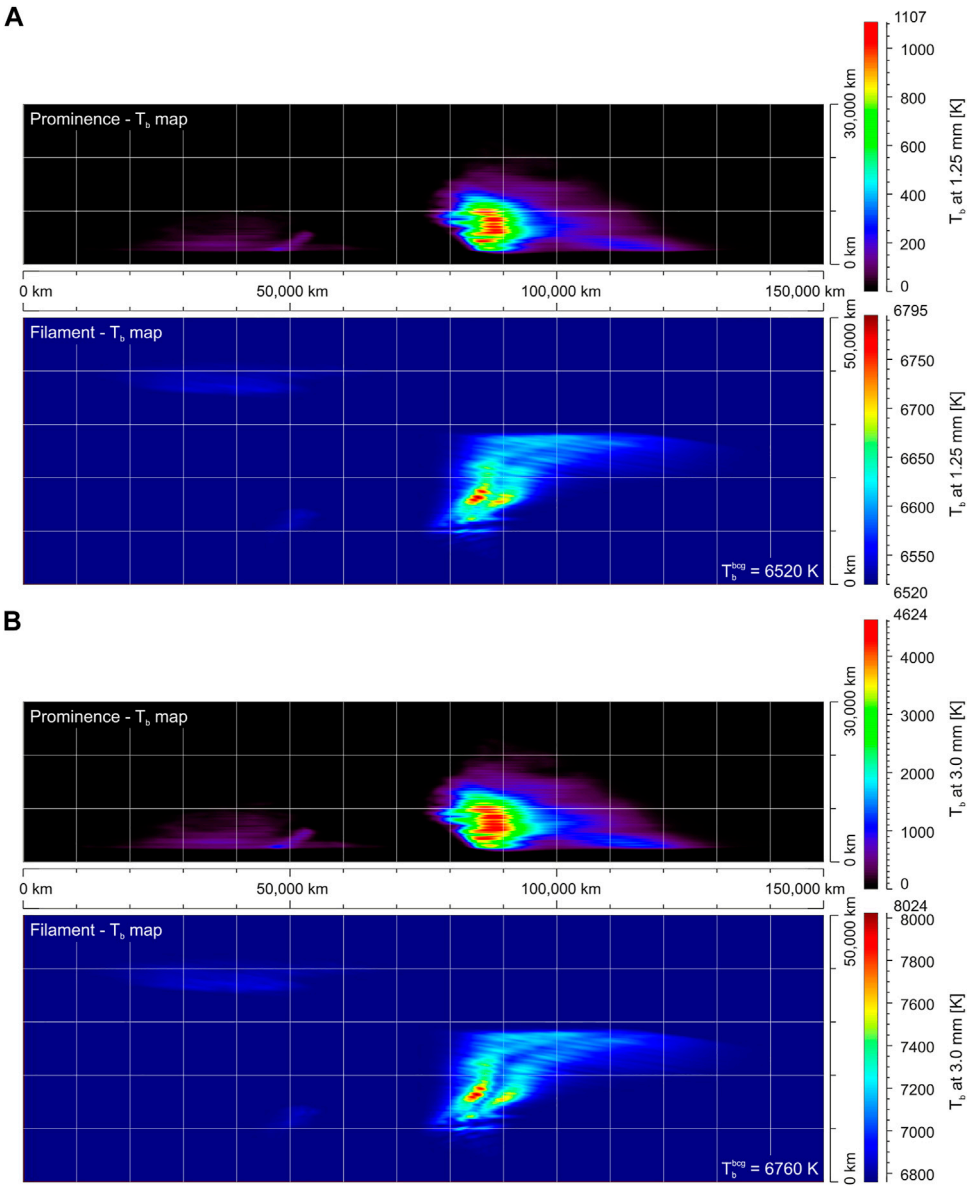

FIGURE 2
Visualization of the 3D WPFS model. **(A)**: synthetic images obtained in Band 6 at 1.25 mm wavelength (240 GHz). **(B)**: synthetic images obtained in Band 3 at 3.0 mm wavelength (100 GHz). Each pair of panels shows the brightness temperature map for the prominence view (top) and the brightness temperature map for the filament view (bottom). Displayed color scales are unique for each panel. The value of the background brightness temperature T_b^{bcg} is indicated in the panels showing the filament view. Adapted from Gunár et al. (2016).

modelling, it can only be performed in cases where at least two simultaneous observations are obtained at mm/sub-mm wavelengths where at one the observed prominence is optically thin and at the other it is optically thick. The kinetic temperature can also be derived from a single mm/sub-mm wavelength observation if simultaneous observations in a different spectral range–e.g. the Hα line in the optical domain–are available (see Heinzel et al., 2015, 2022). Fortunately, to study the relationship between the brightness and kinetic temperature we can also use the simulated ALMA observations produced by prominence models.

The potential of ALMA as a plasma diagnostics tool was explored by Rodger and Labrosse (2017) using 2D cylindrical models based on the code presented in Gouttebroze and Labrosse (2009). In their approach, Rodger and Labrosse (2017) self-consistently included the ionization of hydrogen and helium to compute electron densities and intensities at ALMA wavelengths. The authors investigated in detail how brightness

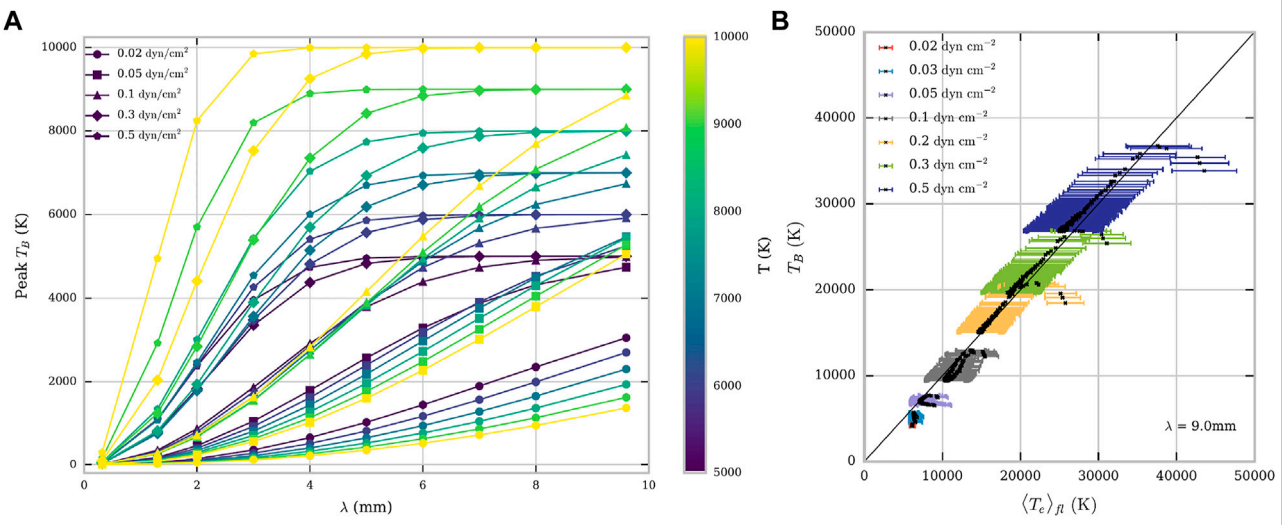

FIGURE 3
(A): Brightness temperature as a function of wavelength for isothermal isobaric prominence models. Colours correspond to plasma temperature (see colour bar on the right) and different symbols indicate different pressures. The grey-shaded areas show ALMA Bands 3 and 6. **(B)**: Brightness temperature as a function of plasma temperature averaged over the formation layer of the 9 mm radiation. The error bars show the standard error in the mean for the average plasma temperature. Colours correspond to different pressures, as indicated in the legend. Adapted from Rodger and Labrosse (2017).

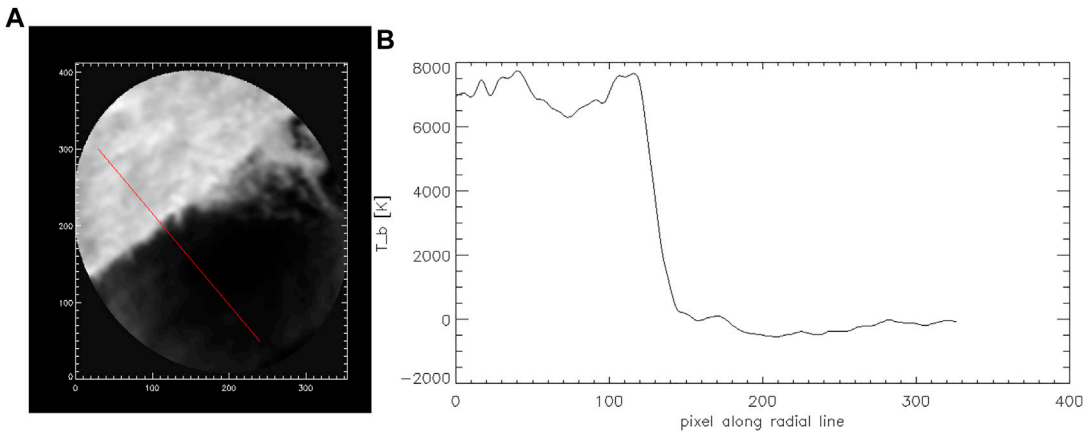

FIGURE 4
(A): Prominence analysed in Section 7.2 with red-marked radial line. **(B)**: A profile of the brightness temperature along the radial line in the **(A)**. The parameters *in feather()* has been selected such a way that the coronal brightness temperature is close to zero and the brightness of the solar disk corresponds to that observed by the TP scan.

temperature and optical thickness vary with plasma temperature and pressure at different wavelengths across the ALMA spectral bands, and how the ratio of brightness temperatures in two bands can be used to estimate the optical thickness and the emission measure. For this investigation, Rodger and Labrosse (2017) used both the isothermal–isobaric models and models with the prominence-corona transition region (PCTR) representing the gradient of the temperature between cool prominence cores and their hot coronal environment. Not surprisingly, the presence of a non-isothermal plasma along the line of sight renders the diagnostic less straightforward and these calculations once again demonstrated the necessity of

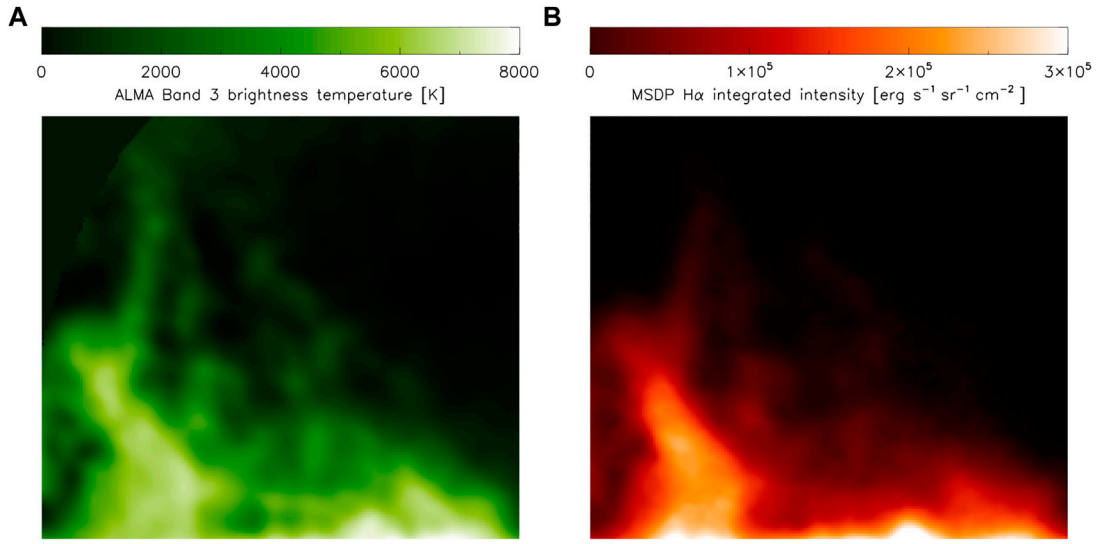

FIGURE 5
Coaligned maps of the brightness temperature T_b obtained from calibrated ALMA Band 3 INT mosaic **(A)** and Hα integrated intensities from MSDP Wrocław/Białków **(B)**. The spatial resolution of both images is comparable. ALMA and MSDP data was recorded simultaneously, at 15:38:07 UT (start of ALMA mozaic) and 15:37:56 UT (start of MSDP Hα scan). Individual fine structures are well recognized. Reproduced from Heinzel et al. (2022)

complementing the observations with competent radiative transfer calculations. To illustrate this, the left panel of Figure 3 shows the relation between brightness temperature and wavelength of observation for small-scale isothermal threads.It can be seen that for optically thin emission (mostly, shorter wavelengths and lower pressures), the brightness temperature decreases with the temperature, as noted also by Gunár et al. (2016). On the contrary, the brightness temperature will be a direct measure of the plasma temperature if the plasma is optically thick at the observed wavelength. This is visible in the left panel of Figure 3 where the T_B curves flatten at longer wavelengths and higher pressures. The behaviour of the absorption coefficient depends not only on wavelength but also on temperature, electron density, and ion density. This leads to the more complex variations seen in the central section of the plot where the plasma is neither optically thin nor optically thick. The left panel of Figure 3 thus shows that ALMA observations obtained at longer wavelengths (e.g., at 9 mm) would have a good potential to diagnose regions which are close to isothermal as the plasma is mostly optically thick at those wavelengths. For larger non-isothermal threads, the relation between brightness temperature measured at 9 mm and plasma temperature averaged over the region of formation of the continuum at that wavelength is shown in the right panel of Figure 3. Each point on the plot represents one optically thick line of sight going through the modeled prominence thread. The plot indicates that ALMA 9 mm observations allow a reliable measurement of the mean electron temperature in the region of the prominence where the radiation is formed. For more details see Rodger and Labrosse (2017).

To provide deeper theoretical insight into the diagnostics of the thermal properties of solar prominences observed by ALMA, the relationship between the observed brightness temperature and the actual kinetic temperature of the studied prominence plasma was further investigated by Gunár et al. (2018). These authors used two sets of synthetic brightness temperature maps of the 3D WPFS model–one at a wavelength at which the simulated prominence is completely optically thin and another at a wavelength at which a significant portion of the simulated prominence is optically thick. Because the 3D WPFS model contains detailed information about the distribution of the kinetic temperature and the optical thickness along any line of sight, it was possible to assess whether the kinetic temperature derived from observations accurately represents the actual kinetic temperature properties of the observed plasma. Gunár et al. (2018) similarly found that the derived kinetic temperature represents an average of the actual kinetic temperature distribution along the given LOS, where it is weighted by the distribution of the opacity along that LOS. This study also confirmed that in a given pixel the optical thickness at the wavelength at which the prominence plasma is optically thick needs to be above unity or even larger to achieve sufficient accuracy of the derived information about the kinetic temperature of the analyzed plasma. However, information about the optical thickness is difficult to obtain from observations at the mm/sub-mm wavelengths alone. As the study by Rodger and Labrosse (2017) illustrates, we can speak about optically thin plasma diagnostic for $\tau \lesssim 0.1$ and optically thick plasma diagnostic for $\tau \gtrsim 10$. Where the optical thickness

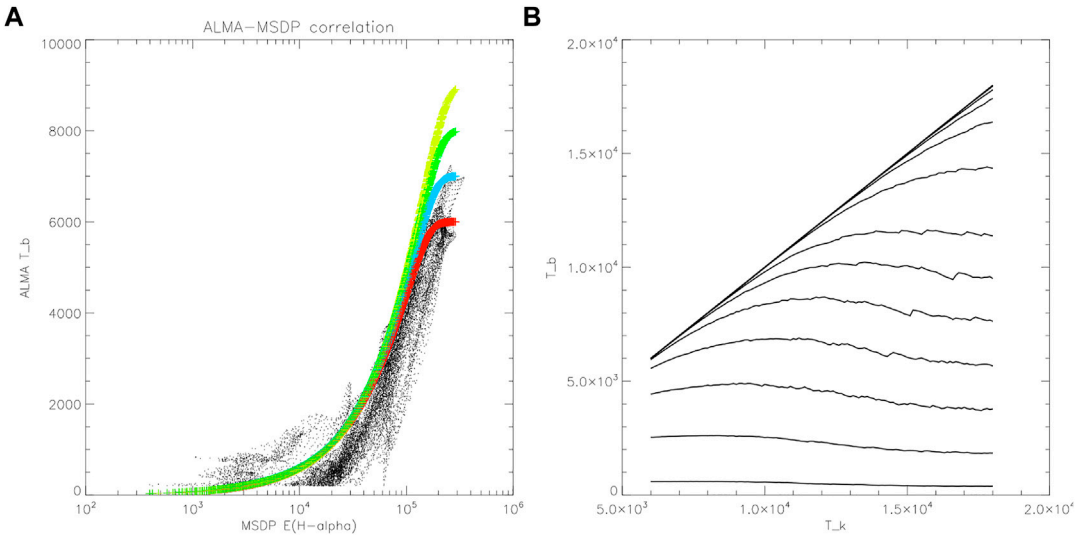

FIGURE 6
(A) - relation between observed T_b and $E(H\alpha)$ in units of erg s^{-1} cm^{-2} sr^{-1} for all pixels from Figure 5 (dots). Color curves indicate the same relation constructed from non-LTE models and assuming a uniform distribution of kinetic temperature in the whole FOV (yellow - 9000 K, green - 8000 K, blue - 7000 K, red - 6000 K). **(B)** - theoretical variations of Band 3 brightness temperature T_b *versus* 1D-slab kinetic temperature T_k for several values of the Hα line integrated intensity. This plot was constructed from the used grid of models (small kinks on some curves are due to finite separation between the models in the grid). The individual curves correspond (from below) to $E(H\alpha)$ from 10^4 up to 10^6 erg cm^{-2} s^{-1} sr^{-1}. Reproduced from Heinzel et al. (2022).

lies between 0.1 and 10 it is more difficult to assign an optically "thin" or "thick" tag to the plasma. This stresses the importance of making available the longest wavelengths of ALMA observations to solar observers in order to have a clear, unambiguously optically thick emission regime. Rodger and Labrosse (2017) also presented a study of the diagnostic potential of the brightness temperature ratio in Bands 3 and 6 (the first two bands available to solar observers) for optical thickness and average emission measure along the line of sight.

Later, Gunár et al. (2018) showed that an empirical criterion which can identify those pixels in which the derived kinetic temperature values correspond well to the actual thermal properties of the observed prominence can be established. More details are presented in the review of numerical modelling of the Sun in mm/sub-mm wavelengths by Wedemeyer et al. (2022), which is part of this special issue.

7 ALMA prominence observations

7.1 Observational setup and data reduction

The feasibility of prominence observations above the limb has been demonstrated by CASA simulations (see Section 5) and demonstrated during the Solar ALMA observing campaigns in 2014 and 2015 (Shimojo et al., 2017; White et al., 2017; Bastian et al., 2018). The ALMA observing setup for prominences typically includes a small mosaic (as a result of the trade-off between full-scan cadence and the FOV), sometimes accompanied by a high-cadence single-FOV observations performed as close as possible to the mosaic (so called back-to-back execution blocks). The latter serves for studies of fast dynamic phenomena on small spatial scales. The observations may be performed at a single ALMA frequency band or in multiple bands, again, in a back-to-back manner. However, truly synchronous multi-band observations are not currently possible. Because the brightness temperature measured in prominences is rather low with respect to the solar disk, the weaker MD1 attenuation mode (see, e.g., Shimojo et al., 2017) is used in order to suppress the brightness of the portion of solar disc present in the FOV. Because interferometric observations lack the flux at low spatial frequencies (a hole around zero in the *uv*-space), they essentially provide just the differences with respect to the average brightness. For that reason each solar interferometric (INT) observation is accompanied by a single-dish full-disk image performed by the total-power (TP) antenna synchronously with the INT execution block. The TP observation is performed using the fast-scanning method (see White et al., 2017) in order to complete the full-disk scan in a relatively short time interval. Unlike the INT observations, where the direct result of the measurement is represented by interferometric visibilities (i.e. samples of the spatial Fourier components of the image), the TP scan provides the flux density convolved with

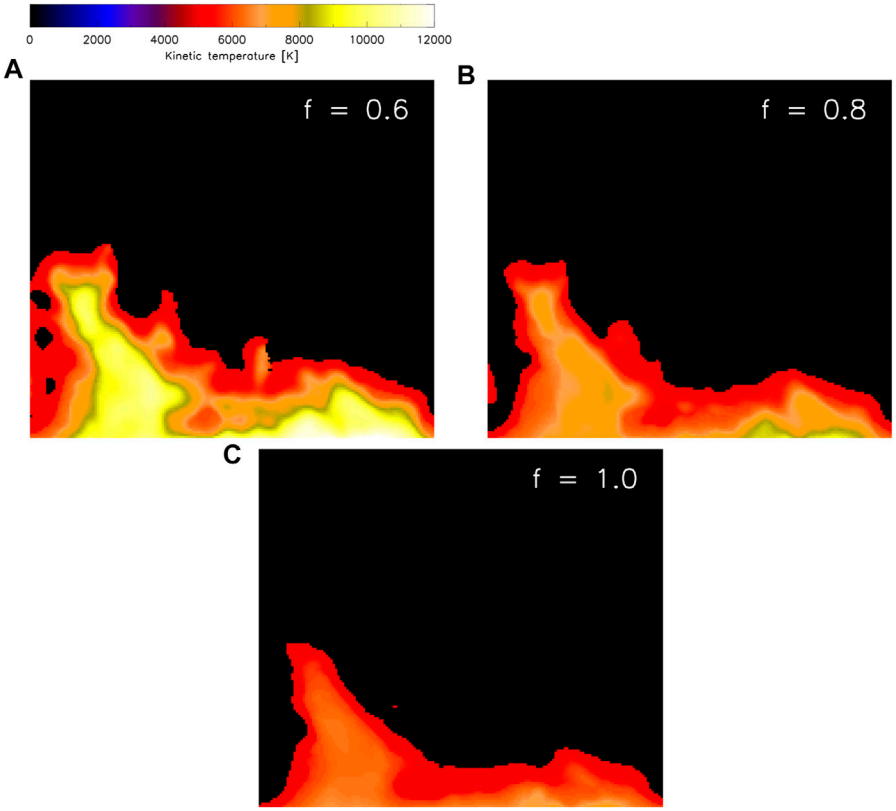

FIGURE 7
Inverted maps of kinetic temperatures for different values of the filling factor: **(A)** $f = 0.6$, **(B)** $f = 0.8$, **(C)** $f = 1.0$. The field-of-view is the same as in Figure 5. Reproduced from Heinzel et al. (2022).

the TP-antenna primary beam at a given AzEl coordinate. This means that the TP scan produces direct low-resolution image in the absolute brightness temperature scale. The INT and TP observations have to be combined during the data-reduction process to get the complete reconstruction of the brightness map. The basic data reduction of ALMA observations is performed at ALMA Regional Centers (ARCs) as part of the Quality Assurance level 2 procedure (QA2). The standard procedures for solar INT and TP data are described in Shimojo et al. (2017) and White et al. (2017), respectively. This prominence (as all the European solar data) has been processed by the EU ARC node in Ondřejov.

It is worth noting that the combination of INT and TP solar data has caveats, especially for limb observations. The disparity between the two signals and the necessity to scale them properly has been reported in Alissandrakis et al. (2017). The CASA *feather*() task allows to match the INT and TP data by fitting two free parameters. Alissandrakis et al. (2017) recommend that this is done in such a way that the combined image: 1) has the average brightness temperature in the quiet solar region selected further from the limb corresponding to that obtained from the purely TP data, and 2) the average brightness temperature of corona (i.e., the small off-limb region selected further from the prominence) is approximately zero (specifically, that it is not significantly negative). An example of the results of this INT/TP matching procedure for the prominence analyzed in Section 7.2 is presented in Figure 4. It shows a profile of the brightness temperature (center-limb-corona brightness variation) along the mostly radial line crossing the solar limb. The above two conditions are mostly matched.

7.2 Observations and plasma diagnostics

The derivation of the kinetic or electron temperature of the prominence plasma (here we assume that the kinetic temperature of all particles is the same) is a key subject of the ALMA science as far as the solar atmosphere is concerned. The reason is that standard spectroscopic diagnostics of the temperature is based on analysis of spectral-line intensities and line shapes which represents a difficulty because of various competing processes. The line intensities depend on prominence thermodynamic parameters, but also to a large extent on the external illumination. On the other hand, the line shapes are sensitive

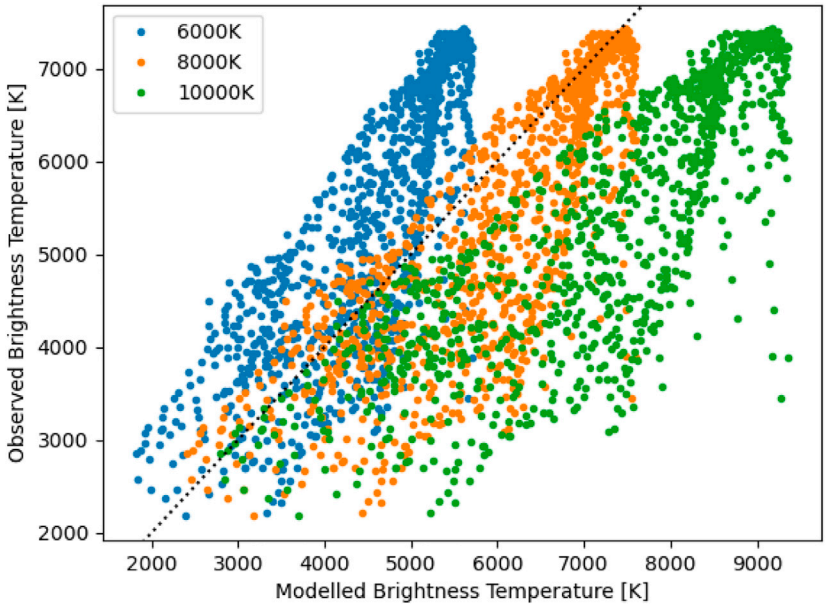

FIGURE 8
Relationship between observed brightness temperature from ALMA and that modelled using the Hα MSDP data. The modelled brightness temperatures are estimated at 6000, 8000, and 10000 K. The dotted line shows when the observed and estimated brightness temperatures are equal. Reproduced from Labrosse et al. (2022).

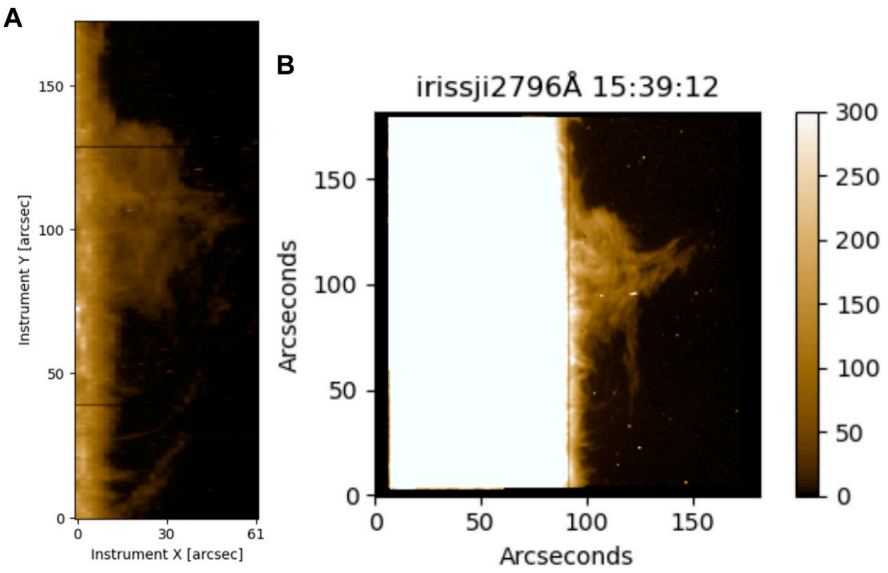

FIGURE 9
IRIS observations of the ALMA prominence: raster of the Mg II h line intensity taken at 14:14UT **(A)** and slit-jaw image at 2796 Å **(B)**. Adapted from Peat et al. (2021).

not only to temperature, but to other non-thermal broadening processes like the microturbulence or fine-structure dynamics, not speaking about the pressure broadening which is less important in low-density prominences. Realistic knowledge of the kinetic temperature is key for discrimination between various processes of heating and cooling which are still far from being

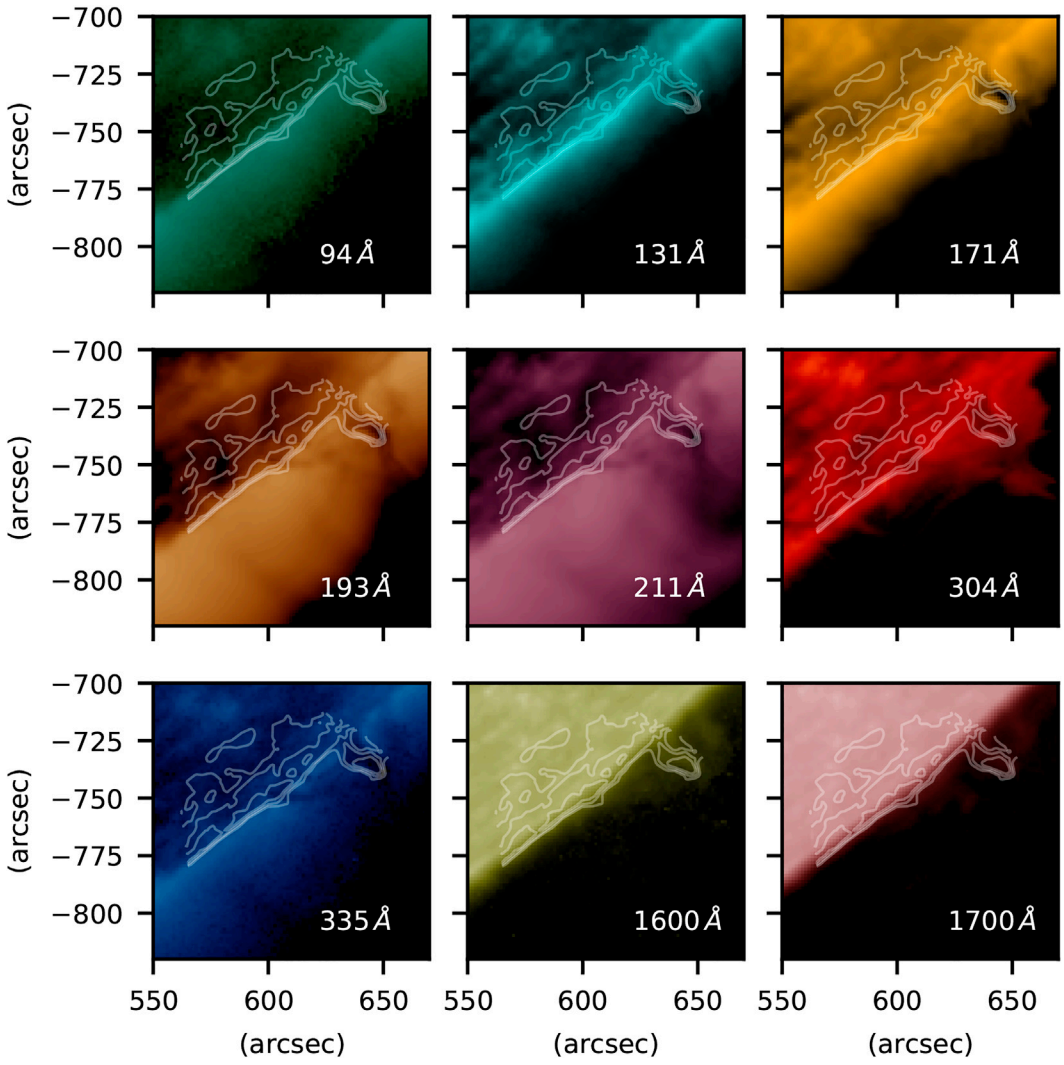

FIGURE 10
Co-aligned images of the ALMA prominence (shown as white contours at relative brightness temperatures of 1000, 2000, and 3000 K) observed with AIA. Reproduced from Labrosse et al. (2022).

well understood under the prominence conditions (Gilbert, 2015). A reliable knowledge of the temperature distribution within the prominence fine structures and its temporal evolution will also help our understanding of the magneto-thermal convection processes discussed in Berger et al. (2011). A more straightforward way of determining temperature is to use continuum observations in the mm or sub-mm domain now provided by ALMA with unprecedented resolution.

The first prominence observations with ALMA were obtained in Band 3 (ALMA project 2017.01138.S) when a quiescent prominence was observed on 19 April 2018 (Heinzel et al., 2022; Labrosse et al., 2022). The prominence was also observed (Peat et al., 2021) by the Interface Region Imaging Spectrograph (IRIS, De Pontieu et al., 2014) and in the Hα line by MSDP instruments in Bialków (Poland) and Meudon (France).

In the following we will describe the analysis performed by Heinzel et al. (2022) and Labrosse et al. (2022) who independently demonstrated the ability of ALMA to deduce the prominence kinetic temperatures. First of all, we show in Figure 5 two co-aligned images of the brightness-temperature distribution in Band 3 and of the integrated Hα emission from Białków MSDP. Although the contrast is different in these two spectral bands, we clearly see, for the first time, a detailed prominence structure in 3 mm band consistent with that in Hα, both at spatial resolution between 1 - 2 arcsec. This is quite unique thanks to interferometric capabilities of ALMA. We immediately see that many areas have T_b rather low, around

4000 K or even less which indicates that in those areas the prominence is optically thin so that $T_b \approx T_k\tau$, neglecting the filling factor (see below). In Figure 6 we plot for all observed pixels the correlation between observed T_b and MSDP integrated Hα intensity E(Hα). If we overplot the synthetic color curves using the grid of non-LTE models, we see a reasonable fit. The curves split according to their kinetic temperature for highest values of E, this happens close to the saturation limit i.e. for $\tau \geq 1$. However, at lower τ the curves become indistinguishable so that it is difficult to find a unique solution for the kinetic temperature. At low intensities, the curves are rather flat and do not provide reasonable solutions for T_k, namely when one adds a noise in the observed T_b. This is the problem found by Heinzel et al. (2022) by analyzing ALMA and MSDP data and because of that they restricted themselves only to brighter areas where the intensity is larger than 10^5 cgs. For such areas they produced maps of the kinetic temperature, by inverting Band 3 and Hα. However, Heinzel et al. (2022) discovered another, even more critical problem. In Figure 6A we see that for $E \leq 10^5$ cgs almost all pixels lay below color-coded curves which merge together in this region as discussed above. T_b along these color-coded curves represents, for a given E, a maximum value which is achieved assuming that the plane-of-sky (POS) filling factor $f = 1$. For lower values of f all points will have lower T_b - see also Irimajiri et al. (1995). Therefore, it seems that the scatter of pixels below the color-coded curves in fact indicates a variety of f-values within the prominence. To demonstrate the effect on inverted T_k, Heinzel et al. (2022) used three characteristic values of f being uniform in the whole FOV and produced temperature maps shown in Figure 7 We clearly see how lowering of f increases T_k. For $f = 1$ temperatures seem to be very low, between 5000–6000 K, but they increase to more realistic values for lower f. A surprising feature is a low temperature at borders of the prominence where one normally expects higher ones. However, these are not true borders because all weaker prominence parts were excluded for reasons explained above and, moreover, these less bright regions can be more heterogeneous and may have much lower f than that assumed. Finally, allowing the inversion to give higher-temperature solutions (in the maps the range of unique solutions was limited to 12000 K), one could have these regions hotter. All these aspects will require further detailed analysis and new ALMA observations.

The analysis by Labrosse et al. (2022), see Figure 8, shows a comparison between the brightness temperatures observed by ALMA and those derived using the Hα MSDP data, for three temperatures between 6000 and 10000 K. In this case, the non-LTE calculations were similar to those used by Rodger and Labrosse (2017). This figure reveals a very good correlation at a temperature of 8000 K–with nevertheless some scatter which could be explained by a non-uniform plasma temperature along the line of sight, and/or by a filling factor f less than 1.

The very close resemblance of the prominence appearance in Hα and in ALMA Band 3 can be understood by studying the contribution functions at both wavelengths. Labrosse et al. (2022) showed that they both have a clear and consistent overlap across a wide range of pressures. The width of the 3 mm contribution function inside the 2D cylindrical prominence model used by these authors is larger than that of the Hα contribution function, which suggests that the emission detected by ALMA has a contribution from hotter plasma at the base of the PCTR. However, an obvious similarity of fine structures seen in both ALMA Band 3 and in Hα (Figure 5) can be understood in terms of the analysis made by Heinzel et al. (2015). The ratio between the integrated Hα intensity and brightness temperature (both shown in Figure 5) is proportional to a temperature-dependent factor

$$10^3\, b_3\,(T)\, \mathrm{e}^{17534/T}/T, \tag{12}$$

assuming that the fine structures are optically thin in both Hα and Band 3. Here we used the Eqs 6, 12 from Heinzel et al. (2015). For three different temperatures 6000 K, 8000 K, and 10000 K, the non-LTE departure factor b_3 amounts to 0.75, 1.67, and 2.97, respectively (Jejčič and Heinzel, 2009) and corresponding values of the above factor are 2.32, 1.87, and 1.72. Therefore the ratio between the integrated Hα intensity and brightness temperature does not depend on the emission measure (which cancels there) and is only weakly dependent on the kinetic temperature. This then leads to a close resemblance between well coaligned and calibrated images in Figure 5.

It is also very interesting to compare the ALMA images with the observations by the Atmospheric Imaging Assembly (AIA; Lemen et al., 2012) on the Solar Dynamics Observatory (SDO; Pesnell et al., 2012) and with IRIS. This is presented in Figures 9, 10.

Both figures show a high degree of similarity in the overall morphology of the prominence (as expected based on well-known comparisons between Hα and IRIS or AIA observations), but of course the details depend on the wavelengths used in the comparisons. A detailed analysis was carried out by Labrosse et al. (2022) with the AIA observations. These authors found that the dark structures seen in AIA 171, and more particularly at AIA 193 and AIA 211, correspond to the contours of the prominence spine seen by ALMA in Band 3. This is not surprising as we know that the optical thickness of ALMA Band 3 and of Hα are similar, and Heinzel et al. (2008) have shown that the opacity of the hydrogen and helium continua at 195 Å (responsible for the dark appearance of the prominence above the limb) is also comparable to that in the Hα line center. On the other hand, a large optical thickness of the He II 304 Å line explains the more extended structure at that wavelength as compared to ALMA Band 3—allowing fine structures to be more easily observed away from the prominence spine (the same applies to Mg II lines observed by IRIS). Correlations with

ALMA Band 3 at other AIA wavelengths can also be seen in Figure 10 but the prominence is much fainter.

The first ALMA observations of a disk filament (an active region, non-eruptive filament) are reported and analyzed in the paper by da Silva Santos et al. (2022), which is part of this special issue on solar observations by ALMA. This active region filament was observed simultaneously in ALMA Band 6 and by the IRIS, SDO/AIA and the Solar Optical Telescope (SOT, Suematsu et al., 2008) on the Hinode satellite. In the absence of simultaneous observations in the Hα line or in other ALMA bands, quantitative thermal diagnostics of this filament is not possible. However, da Silva Santos et al. (2022) could conclude that some of the darkest features visible in the ALMA Band 6 ($T_b < 5000$ K) coincide with dark filament threads visible in the AIA 304 Å channel and in the cores of the Mg II h and k lines observed by IRIS.

8 Conclusion

In this review we addressed various aspects of the prominence physics from the point of view of radio mm/sub-mm observations. Historically, such observations have been carried out at rather low spatial resolution which did not allow the study of prominence fine structures, contrary to high-resolution observations available in optical and UV. When ALMA was going to be operational during the last decade, a hope arose that we will be ultimately able to resolve the fine structures in solar prominences and filaments in the radio domain. Based on data-driven simulations (Heinzel et al., 2015) and other modeling work (Rodger and Labrosse, 2017), several proposals have been submitted to facilitate prominence observations with ALMA. As a result, one prominence was observed still at the moderate ALMA resolution of 1-2 arcsec and the data was recently analyzed - we provide an overview of obtained results. We also mention one disk filament observation, the analysis is presented in another paper in this volume. We discussed in detail all aspects, but also caveats, of prominence plasma diagnostics using ALMA. Since only one band was used so far in prominence observations, the temperature diagnostics was possible only thanks to simultaneous ground-based observations in the hydrogen Hα line with a comparable spatial resolution. In future prominence/filament observations a quasi-simultaneous detection in more than one ALMA band will significantly enhance the ALMA diagnostical potential as a prominence plasma 'thermometer'. The ultimate goal is to get much higher spatial resolution in the near future, at least comparable to current optical instruments such as DKIST or even better. ALMA co-observation with DKIST is very challenging because both instruments can in principle reach the so-far best spatial resolution. However, a problem can be the time difference between instrument locations (6 h) and exact coaligned pointing. DKIST can provide spectral-line diagnostics in blue, red and IR, complementary to ALMA multi-band imaging. On the other hand, there is a recent proposal for other coordinated observations with ALMA in the frame of the SOLARNET programme which includes large European facilities. And one should also consider UV/EUV spectral observations from space instruments like IRIS, SPICE on Solar Orbiter, or coming MUSE and Solar-C/EUVST. A complex spectral inversion of plasma parameters based on ALMA and multi-wavelength spectra is a highly challenging task.

Author contributions

All authors listed have made a substantial, direct, and intellectual contribution to the work and approved it for publication.

Funding

SG and PH acknowledge support by the grant 19-16890S and 19-17102S of the Czech Science Foundation (GA ČR) and by the project RVO:67985815 of the Astronomical Institute of the Czech Academy of Sciences. MB acknowledges support by the grants 20-09922J and 21-16808J of the Czech Science Foundation, and by the project LM2015067 from the Ministry of education of the Czech Republic. Support from STFC grant ST/T000422/1 (NL) is also gratefully acknowledged. This work was partially supported by the program 'Excellence Initiative–Research University' for years 2020-2026 at the University of Wrocław, Poland.

Conflict of interest

The authors declare that the research was conducted in the absence of any commercial or financial relationships that could be construed as a potential conflict of interest.

Publisher's note

References

Alissandrakis, C. E., Patsourakos, S., Nindos, A., and Bastian, T. S. (2017). Center-to-limb observations of the sun with ALMA . Implications for solar atmospheric models. *Astron. Astrophys.* 605, A78. doi:10.1051/0004-6361/201730953

Bastian, T. S., Bárta, M., Brajša, R., Chen, B., Pontieu, B. D., Gary, D. E., et al. (2018). Exploring the sun with ALMA. *Messenger* 171, 25. doi:10.18727/0722-6691/5065

Bastian, T. S., Ewell, J., and Zirin, H. (1993). A study of solar prominences near lambda = 1 millimeter. *Astrophys. J.* 418, 510. doi:10.1086/173413

Berger, T., Testa, P., Hillier, A., Boerner, P., Low, B. C., Shibata, K., et al. (2011). Magneto-thermal convection in solar prominences. *Nature* 472, 197–200. doi:10.1038/nature09925

da Silva Santos, J. M., White, S. M., Reardon, K., Cauzzi, G., Gunár, S., Heinzel, P., et al. (2022). Subarcsecond imaging of a solar active region filament with alma and iris. *Front. Astron. Space Sci.* 9. doi:10.3389/fspas.2022.898115

De Pontieu, B., Title, A. M., Lemen, J. R., Kushner, G. D., Akin, D. J., Allard, B., et al. (2014). The Interface region imaging spectrograph (IRIS). *Sol. Phys.* 289, 2733–2779. doi:10.1007/s11207-014-0485-y

Engvold, O. (2015). "Description and classification of prominences," in *Solar prominences*. Cham: Springer. Editors J.-C. Vial and O. Engvold (Astrophysics and Space Science Library), 41531. doi:10.1007/978-3-319-10416-4_2

Gilbert, H. (2015). "Energy balance," in *Solar prominences*. Cham: Springer. Editors J.-C. Vial and O. Engvold (Astrophysics and Space Science Library), 415157. doi:10.1007/978-3-319-10416-4_7

Gouttebroze, P., Heinzel, P., and Vial, J. C. (1993). The hydrogen spectrum of model prominences. *Astron. Astrophys.* 99, 513

Gouttebroze, P., and Labrosse, N. (2009). Radiative transfer in cylindrical threads with incident radiation. VI. A hydrogen plus helium system. *Astron. Astrophys.* 503, 663–671. doi:10.1051/0004-6361/200811483

Gunár, S., Heinzel, P., Anzer, U., and Mackay, D. H. (2018). Quiescent prominences in the era of ALMA. II. Kinetic temperature diagnostics. *Astrophys. J.* 853, 21. doi:10.3847/1538-4357/aaa001

Gunár, S., Heinzel, P., Mackay, D. H., and Anzer, U. (2016). Quiescent prominences in the era of ALMA: Simulated observations using the 3D whole-prominence fine structure model. *Astrophys. J.* 833, 141. doi:10.3847/1538-4357/833/2/141

Gunár, S., and Mackay, D. H. (2015). 3D whole-prominence fine structure modeling. *Astrophys. J.* 803, 64. doi:10.1088/0004-637X/803/2/64

Harrison, R. A., Carter, M. K., Clark, T. A., Lindsey, C., Jefferies, J. T., Sime, D. G., et al. (1993). An active solar prominence in 1.3 MM radiation. *Astron. Astrophys.* 274, L9.

Heinzel, P., and Avrett, E. H. (2012). Optical-to-Radio continua in solar flares. *Sol. Phys.* 277, 31–44. doi:10.1007/s11207-011-9823-5

Heinzel, P., Berlicki, A., Bárta, M., Karlický, M., and Rudawy, P. (2015). On the visibility of prominence fine structures at radio millimeter wavelengths. *Sol. Phys.* 290, 1981–2000. doi:10.1007/s11207-015-0719-7

Heinzel, P., Berlicki, A., Bárta, M., Rudawy, P., Gunár, S., Labrosse, N., et al. (2022). ALMA as a prominence thermometer: First observations. *Astrophys. J. Lett.* 927, L29. doi:10.3847/2041-8213/ac588f

Heinzel, P. (2015). "Radiative transfer in solar prominences," in *Solar prominences*. Cham: Springer. Editors J.-C. Vial and O. Engvold (Astrophysics and Space Science Library), 415103. doi:10.1007/978-3-319-10416-4_5

Heinzel, P., Schmieder, B., Fárník, F., Schwartz, P., Labrosse, N., Kotrč, P., et al. (2008). Hinode, TRACE, SOHO, and ground-based observations of a quiescent prominence. *Astrophys. J.* 686, 1383–1396. doi:10.1086/591018

Heinzel, P., Vial, J. C., and Anzer, U. (2014). On the formation of Mg ii h and k lines in solar prominences. *Astron. Astrophys.* 564, A132. doi:10.1051/0004-6361/201322886

Hiei, E., Shimizu, Y., Miyazaki, H., Imai, H., Sato, K., Kuji, S., et al. (1986). Coronal structure observed at the total solar eclipse of 11 June, 1983 in Indonesia. *Astrophys. Space Sci.* 119, 9–15. doi:10.1007/BF00648803

Irimajiri, Y., Takano, T., Nakajima, H., Shibasaki, K., Hanaoka, Y., and Ichimoto, K. (1995). Simultaneous multifrequency observations of an eruptive prominence at millimeter wavelengths. *Sol. Phys.* 156, 363–375. doi:10.1007/BF00670232

Jejčič, S., and Heinzel, P. (2009). Electron densities in quiescent prominences derived from eclipse observations. *Sol. Phys.* 254, 89–100. doi:10.1007/s11207-008-9289-2

Labrosse, N., Heinzel, P., Vial, J. C., Kucera, T., Parenti, S., Gunár, S., et al. (2010). Physics of solar prominences: I—spectral diagnostics and non-LTE modelling. *Space Sci. Rev.* 151, 243–332. doi:10.1007/s11214-010-9630-6

Labrosse, N., Rodger, A. S., Radziszewski, K., Rudawy, P., Antolin, P., Fletcher, L., et al. (2022). First high resolution interferometric observation of a solar prominence with ALMA. *MNRAS* 513, L30–L34. doi:10.1093/mnrasl/slac021

Lemen, J. R., Title, A. M., Akin, D. J., Boerner, P. F., Chou, C., Drake, J. F., et al. (2012). The atmospheric imaging assembly (AIA) on the solar dynamics observatory (SDO). *Sol. Phys.* 275, 17–40. doi:10.1007/s11207-011-9776-8

Lindsey, C., Jefferies, J. T., Clark, T. A., Harrison, R. A., Carter, M. K., Watt, G., et al. (1992). Extreme-infrared brightness profile of the solar chromosphere obtained during the total eclipse of 1991. *Nature* 358, 308–310. doi:10.1038/358308a0

Loukitcheva, M., Solanki, S. K., Carlsson, M., and Stein, R. F. (2004). Millimeter observations and chromospheric dynamics. *Astron. Astrophys.* 419, 747–756. doi:10.1051/0004-6361:20034159

Peat, A. W., Labrosse, N., Schmieder, B., and Barczynski, K. (2021). Solar prominence diagnostics from non-LTE modelling of Mg II h&k line profiles. *Astron. Astrophys.* 653, A5. doi:10.1051/0004-6361/202140907

Pesnell, W. D., Thompson, B. J., and Chamberlin, P. C. (2012). The solar dynamics observatory (SDO). *Sol. Phys.* 275, 3–15. doi:10.1007/s11207-011-9841-3

Rast, M. P., Bello González, N., Bellot Rubio, L., Cao, W., Cauzzi, G., Deluca, E., et al. (2021). Critical science plan for the daniel K. Inouye solar telescope (DKIST). *Sol. Phys.* 296, 70. doi:10.1007/s11207-021-01789-2

Rodger, A., and Labrosse, N. (2017). Solar prominence modelling and plasma diagnostics at ALMA wavelengths. *Sol. Phys.* 292, 130. doi:10.1007/s11207-017-1161-9

Rodger, A. (2019). *Millimetre-continuum diagnostics and non-LTE radiative transfer modelling of solar prominences*. UK: Ph.D. thesis, University of Glasgow.

Shimojo, M., Bastian, T. S., Hales, A. S., White, S. M., Iwai, K., Hills, R. E., et al. (2017). Observing the sun with the Atacama large millimeter/submillimeter array (ALMA): High-resolution interferometric imaging. *Sol. Phys.* 292, 87. doi:10.1007/s11207-017-1095-2

Suematsu, Y., Tsuneta, S., Ichimoto, K., Shimizu, T., Otsubo, M., Katsukawa, Y., et al. (2008). The solar optical telescope of solar-B (Hinode): The optical telescope assembly. *Sol. Phys.* 249, 197–220. doi:10.1007/s11207-008-9129-4

Vrsnak, B., Pohjolainen, S., Urpo, S., Terasranta, H., Brajsa, R., Ruzdjak, V., et al. (1992). Large-scale patterns on the Sun observed in the millimetric wavelength range. *Sol. Phys.* 137, 67–86. doi:10.1007/BF00146576

Wedemeyer, S., Bastian, T., Brajša, R., Hudson, H., Fleishman, G., Loukitcheva, M., et al. (2016). Solar science with the Atacama large millimeter/submillimeter array – a new view of our sun. *Space Sci. Rev.* 200, 1–73. doi:10.1007/s11214-015-0229-9

Wedemeyer, S., Fleishman, G., De La Cruz Rodríguez, J., Gunár, S., da Silva Santos, J. M., Antolin, P., et al. (2022). Prospects and challenges of numerical modelling of the sun at millimetre wavelengths. *Front. Astronomy Space Sci.* 9.

Wedemeyer, S., and Parmer, A. (2015). "ALMA's high-cadence imaging capabilities for solar observations," in *Revolution in Astronomy with ALMA: The third year*. San Francisco. Editors D. Iono, K. Tatematsu, A. Wootten, and L. Testi (Astronomical Society of the Pacific Conference Series), 499, 343.

White, S. M., Iwai, K., Phillips, N. M., Hills, R. E., Hirota, A., Yagoubov, P., et al. (2017). Observing the sun with the Atacama large millimeter/submillimeter array (ALMA): Fast-scan single-dish mapping. *Sol. Phys.* 292, 88. doi:10.1007/s11207-017-1123-2

frontiers | Frontiers in Astronomy and Space Sciences

BRIEF RESEARCH REPORT
published: 23 May 2022
doi: 10.3389/fspas.2022.898115

Subarcsecond Imaging of a Solar Active Region Filament With ALMA and IRIS

J. M. da Silva Santos[1]*, *S. M. White*[2], *K. Reardon*[1], *G. Cauzzi*[1], *S. Gunár*[3], *P. Heinzel*[3] and *J. Leenaarts*[4]

[1]National Solar Observatory, Boulder, CO, United States, [2]Space Vehicles Directorate, Air Force Research Laboratory, Albuquerque, NM, United States, [3]Astronomical Institute of the Czech Academy of Sciences, Ondřejov, Czechia, [4]Department of Astronomy, Institute for Solar Physics, Stockholm University, Stockholm, Sweden

Quiescent filaments appear as absorption features on the solar disk when observed in chromospheric lines and at continuum wavelengths in the millimeter (mm) range. Active region (AR) filaments are their small-scale, low-altitude analogues, but they could not be resolved in previous mm observations. This spectral diagnostic can provide insight into the details of the formation and physical properties of their fine threads, which are still not fully understood. Here, we shed light on the thermal structure of an AR filament using high-resolution brightness temperature (T_b) maps taken with ALMA Band 6 complemented by simultaneous IRIS near-UV spectra, Hinode/SOT photospheric magnetograms, and SDO/AIA extreme-UV images. Some of the dark threads visible in the AIA 304 Å passband and in the core of Mg II resonance lines have dark (T_b < 5,000 K) counterparts in the 1.25 mm maps, but their visibility significantly varies across the filament spine and in time. These opacity changes are possibly related to variations in temperature and electron density in filament fine structures. The coolest T_b values (< 5,000 K) coincide with regions of low integrated intensity in the Mg II h and k lines. ALMA Band 3 maps taken after the Band 6 ones do not clearly show the filament structure, contrary to the expectation that the contrast should increase at longer wavelengths based on previous observations of quiescent filaments. The ALMA maps are not consistent with isothermal conditions, but the temporal evolution of the filament may partly account for this.

Keywords: Sun, radio, ultraviolet, chromosphere, active regions, filaments, prominences

OPEN ACCESS

Edited by:
Alexander Nindos, University of Ioannina, Greece

Reviewed by:
Maria Loukitcheva, Special Astrophysical Observatory (RAS), Russia
Susanna Parenti, UMR8617 Institut d'Astrophysique Spatiale (IAS), France

***Correspondence:**
J. M. da Silva Santos
jdasilvasantos@nso.edumailto: jdasilvasantos@nso.edu

Specialty section:
This article was submitted to Stellar and Solar Physics, a section of the journal Frontiers in Astronomy and Space Sciences

Received: *17 March 2022*
Accepted: *19 April 2022*
Published: *23 May 2022*

Citation:
da Silva Santos JM, White SM, Reardon K, Cauzzi G, Gunár S, Heinzel P and Leenaarts J (2022) Subarcsecond Imaging of a Solar Active Region Filament With ALMA and IRIS. Front. Astron. Space Sci. 9:898115. doi: 10.3389/fspas.2022.898115

1 INTRODUCTION

Dark filaments on the solar disk and bright prominences at the limb are homologous structures filled with cool ($\lesssim 10^4$ K), dense plasma suspended by the Lorentz force against gravity above polarity-inversion lines in the photosphere. They are generally separated into two categories: the larger (~10 – 100 Mm), long-lived, high-altitude (> 10 Mm) quiescent filaments and the smaller (~10 Mm), more dynamic, lower-altitude (< 10 Mm) active region (AR) filaments. The magnetic field in the former is essentially horizontal with field strengths of ~3–80 G (Leroy, 1989; Casini et al., 2005; Orozco Suárez et al., 2014), but AR filaments may show flux rope structure and field strengths that can be an order of magnitude higher than in the quiescent ones (Kuckein et al., 2009, 2012; Guo et al., 2010; Xu et al., 2012; Díaz Baso et al., 2019). Estimates of (core) kinetic temperatures in prominences lie within the range ~ 5,000 – 9,000 K for microturbulence values within ~ 3 – 16 km s^{-1} (e.g., Stellmacher et al., 2003; Jejčič

et al., 2018; Ruan et al., 2019). While the general properties of filaments are well understood, there are open questions pertaining to their fine structure and magnetic configuration (Chen et al., 2020, and references therein). Furthermore, they may become unstable and erupt, leading to coronal mass ejections, hence their relevance in the context of solar activity and space weather (see reviews by Parenti, 2014; Gibson, 2018).

Observational studies have mainly used spectral lines such as Ly α, H α, Ca II H, 8,542 Å, He I D_3, 10,830 Å, and He II 304 Å to investigate prominence/filament thermodynamics and to infer the magnetic field topology (e.g., Labrosse et al., 2010, and references therein). These structures have also been routinely observed in the last decade by the Interface Region Imaging Spectrograph (IRIS, De Pontieu et al., 2014) in the Mg II h and k resonance lines, which have been used to investigate dynamics in prominences (e.g., Schmieder et al., 2014) and constrain nonlocal thermodynamic equilibrium (non-LTE) models (Heinzel et al., 2015b; Vial et al., 2019; Levens and Labrosse, 2019; Peat et al., 2021). Similar studies have yet to be conducted for AR filaments.

At the other end of the wavelength spectrum, low-resolution ($>\mathbf{20}''$) radio observations have shown that quiescent filaments appear as depressions of the background brightness temperatures on disk at continuum wavelengths between 3 and 8 mm, possibly due to free-free absorption by dense, cool material, and as emission features at the limb (Kundu, 1972; Raoult et al., 1979; Schmahl et al., 1981; Vrsnak et al., 1992). At wavelengths around 1 mm, prominences are still well visible at the limb (Harrison et al., 1993), but they are practically invisible on disk (Bastian et al., 1993; Lindsey, 1994). Under certain conditions, brightness measurements at different mm wavelengths can be used to constrain the optical thickness and kinetic temperature of such structures (Heinzel et al., 2015a; Rodger and Labrosse, 2017; Gunár et al., 2018).

The Atacama Large Millimeter/submillimeter Array (ALMA, Wootten and Thompson, 2009) provides an opportunity to investigate filament substructure in the (thermal) millimeter continuum at a much higher spatial resolution than before (see review by Wedemeyer et al., 2016). These capabilities have been recently demonstrated for a prominence at the limb (Heinzel et al., 2022; Labrosse et al., 2022). The only ALMA observations of filaments available until now have been taken with single dishes with a beam size of approximately 25″ at 1.25 mm (Alissandrakis et al., 2017; White et al., 2017; Brajša et al., 2018). Here, we use interferometry maps with a significantly improved spatial resolution (~ 0.6″ at 1.25 mm) that show considerably lower brightness temperatures in an AR filament compared to the background. Because of their smaller spatial scales, AR filaments had not yet been observed in this wavelength range. We compare the ALMA maps to UV imagery provided by IRIS and the Solar Dynamics Observatory (SDO, Pesnell et al., 2012) and magnetograms obtained by the Solar Optical Telescope (SOT, Tsuneta et al., 2008) onboard Hinode.

2 OBSERVATIONS

We observed NOAA AR 12738 on 13 April 2019, with ALMA Band 6 (240 GHz or 1.25 mm) in two execution blocks between 14:15-15:10 UT and 16:52-17:47 UT in mosaic mode and with Band 3 (100 GHz or 3 mm) in two execution blocks between 18:19-18:54 UT and 19:15-19:50 UT in single-pointing mode. The target was a group of pores and plage region near the disk center at $\mu \approx 0.98$ (the cosine of the heliocentric angle), west of a leading sunspot, where an AR filament was also visible for most of the observing campaign. We obtained co-temporal observations with IRIS and Hinode for the first Band 6 block and part of the second block. There are no IRIS nor Hinode supporting observations to the ALMA Band 3 data. We also use full-disk images in the ultraviolet range taken by the Atmospheric Imaging Assembly (AIA, Lemen et al., 2012) and continuum images at 6,163 Å obtained by the Helioseismic and Magnetic Imager (HMI, Scherrer et al., 2012) on SDO. We use one H α image taken by the Global Oscillation Network Group (GONG, Harvey et al., 2011).

2.1 Data Reduction and Calibration

The ALMA array consisted of 9 × 7 m and 40 × 12 m functioning antennas, with a maximum baseline length of about 700 m. In order to cover a significant region of plage, a mosaic of ten different pointings was carried out using Band 6, covering a region slightly larger than one arcminute across, which is comparable to the Band 3 field of view (FOV). The FOV of a 12 m antenna is 25″ at 230 GHz, and the centers of adjacent mosaic fields have a separation of 12″. The observation cycled through the ten mosaic fields in order, acquiring three 2 s integrations at each visit. The duration of a full mosaic cycle was 85 s; these were repeated during scans on the Sun approximately 7-min long alternating with 2-min calibration scans.

We attempted to make time-resolved images of complete mosaic cycles using the standard Common Astronomy Software Applications (CASA, McMullin et al., 2007) package, applying the recommended "mosaic" gridding option, but we found that most of the resulting images were corrupted by bright or dark features at the edges of the mosaic. This did not occur when the full-time range was mapped. To get around this problem, we mapped and self-calibrated every integration in every field separately without primary beam correction, including the four base bands at 230, 232, 245 and 247 GHz to improve uv coverage, and then combined them in a linear mosaic in the image plane, weighting overlapping regions of the image using the appropriate primary beam response for the 12 m antennas. The single-field images were restored with a Gaussian beam with full-width-at-half-maximum of 0.6″. The three consecutive integrations at each pointing were combined, and at each step, the time-dependent mosaic image was created by replacing the previous image of the current field with the new image, appropriately weighted by the primary beam, and recalculating the mosaic. This resulted in a sequence of 280 mosaic images for each of the two observations with a time separation of 9 s between mosaics within a scan, but the true time resolution is more complicated due to the overlapping nature of the fields. Comparison of the resulting images with cases where CASA successfully imaged a full 85 s mosaic cycle indicated good agreement.

The Band 6 mosaics were scaled to T_b units, and a value of 6,600 K was added to the mosaics to compensate for the background level not observable by the interferometer, derived by inspection of the corresponding FOV in single-dish images (taken with the total-power array) that measure the full solar disk temperatures. The typical temperature range in individual mosaic images is from ~ 4,000 to ~ 8,500 K.

The Band 3 data consists of single-pointing maps at 2-s cadence, maximum spatial resolution of 1.2″, and noise level of 20 K. We refer to da Silva Santos et al. (2020) for a detailed explanation of the data reduction, which includes self-calibration, primary beam correction, and absolute flux calibration.

The SDO level 1 data were converted into level 1.5 using the `aia_prep` routine in SolarSoftWare (`SSW`, Freeland and Handy, 1998). Further processing including coaligment, resampling, and derotation was performed using the `SunPy` package (The SunPy Community et al., 2020). The HMI 6173 Å continuum images were deconvolved using the `Enhance` deep learning code[1] (Díaz Baso and Asensio Ramos, 2018). The AIA 304 Å images were corrected for stray light using semi-empirical point-spread functions (Poduval et al., 2013) and instrumental degradation. The data cadences are 12 and 24 s in the EUV and UV.

The IRIS data comprises a time series of dense 64-step raster scans in the near-UV and far-UV wavelength ranges. Here we only use the spectral data around the Mg II h and k lines that probe the chromosphere; there is no signal in the far-UV lines in the filament. The pixel scale is 0.166″ along the slit and the size of the FOV is 22″ × 67″. The integration time was 1 s and the raster cadence was about 2.3 min. The level 2 data were converted from data units into intensity in physical units using version five of the spectrograph effective areas obtained through the `iris_get_response` routine in `SSW`.

The Hinode/SOT data consists of level 2 products, which include the magnetic field strength ($|\boldsymbol{B}|$), the stray-light filling factor ($1-f$), inclination (γ), and azimuth (ϕ) angles derived from Milne-Eddington inversions of the Fe I 6,301.5 and 6,302.5 Å Zeeman sensitive lines (Lites and Ichimoto, 2013). The line of sight (LOS) component of the magnetic field vector is given by $B_{\rm LOS} = (1-f)|\boldsymbol{B}|\cos(\gamma)$. The slit step is ~ 0.297″ and the pixel scale is ~ 0.319″ along the slit. The size of the FOV is approximately 60 × 61″ The exposure time was 1.6 s and the raster cadence was ~13 min.

The co-aligment of the IRIS and Hinode data was improved by cross-correlation with the HMI continuum images. The ALMA Band 6 maps were cross-correlated with AIA 304 Å images taken at an instant close to the middle of each ALMA mosaic sampled at the same spatial resolution. This allowed a proper coalignment of the EUV and mm brightenings recurring near the pore at the center of the FOV (not displayed; see also da Silva Santos et al., 2020).

2.2 Data Clustering

To investigate the spatial correlation between the Mg II h and k profiles and the mm continuum emission, we applied an agglomerative hierarchical clustering method to the former using the `hierarchy` library in `Scipy` (Virtanen et al., 2020) wherein profiles are grouped based on a distance metric. We used Ward's linkage method, which minimizes the within-cluster variance (Ward, 1963), that is the spread in the euclidean distances between each cluster member and the centroid. This technique can be interpreted as a type of dimensionality reduction in that the information in the IRIS spectra with hundreds of wavelength points is condensed into a single number, which can then be compared to the 1.25 mm continuum brightness. The number of clusters was decided upon visual inspection of the dendrogram. While that choice is arbitrary, we concluded that 15 clusters were a good compromise between limiting the impact of noise and being able to identify sufficient spatial structure within the filament while tracking its time evolution. The clustering is based on 20,475 spectral profiles of the wavelength window between 2,791.2 and 2,809.6 Å, which includes the Mg II h, k, and UV triplet lines.

3 RESULTS

Figure 1 shows the target as observed by the different instruments at the start of the coordinated campaign. Observations of this AR with ALMA have shown that T_b(3, mm) correlates poorly with AIA 1,600 Å intensity ($r = 0.34$, da Silva Santos et al., 2020). Here, we find that T_b(1.25 mm) correlates slightly better with AIA 1,600 Å emission ($r = 0.45$), which is consistent with lower formation heights of shorter mm wavelengths. An overall better agreement is found with the AIA 304 Å intensities, especially during small-scale transient brightenings similarly to the ones observed with Band 3 (da Silva Santos et al., 2020), but we did not quantify this correlation as the main focus of this paper is the AR filament described below.

The observations also reveal a dark filamentary structure that can be identified in all of the chromospheric diagnostics in the upper part of the FOV. However, the filament appears fragmented into pieces at 1.25 mm in contrast with the more uniform dark structures seen in Hα, He I 304Å, and Mg II k. Brightness values as low as T_b (1.25 mm) ~ 2,800 K can be found at certain locations, but other parts of the filament cannot be distinguished from the background, suggesting either significant opacity variations or temperature variations if the filament threads are optically thick. Other dark Hα fibrils near the center of the ALMA FOV appear to have no counterpart at 1.25 mm.

Figure 2 shows the temporal evolution of the filament as seen by the different instruments. The y-axes in all panels are aligned with solar north. The appearance of the filament in the Band 6 maps changes dramatically over 1 hour as parts of it practically vanish and reappear, whereas the filament spine remains well visible in the Mg II core images throughout. The dark Band 6 structures thin out around 14:36 UT when a bright thread forms in the 304 Å images, following a brightening at the eastern footpoint of the filament. The lowest T_b (1.25 mm) values (< 5,000 K) are located near the widest part of the filament

[1]https://github.com/cdiazbas/enhance

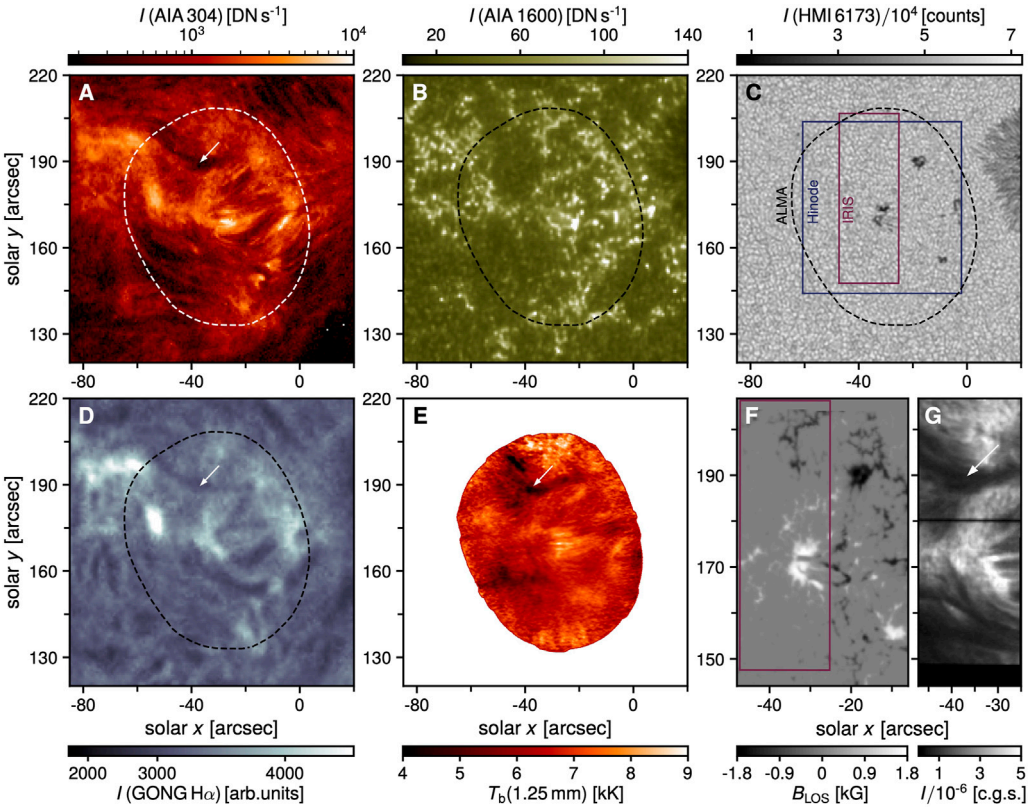

FIGURE 1 | Overview of NOAA AR 12738 by different instruments on 13 April 2019, around 14:15 UT. Panel **(A)** SDO/AIA 304 Å intensity in logarithmic scale; panel **(B)** SDO/AIA 1,600 Å intensity (capped); panel **(C)** deconvolved SDO/HMI 6173 Å continuum intensity; panel **(D)** gamma-adjusted and unsharpened GONG H α; panel **(E)** ALMA Band 6 brightness temperature mosaic; panel **(F)** Hinode/SOT line-of-sight magnetogram; panel **(G)** IRIS intensity in the core of Mg II k (in units of erg $s^{-1}sr^{-1}cm^{-2}Hz^{-1}$). The dashed lines show the ALMA field of view, and the boxes in panel C show the area covered by the Hinode and IRIS raster scans. The arrows indicate the location of an AR filament.

but usually offset from the darkest regions in the 304 Å images. We find that the coolest T_b (1.25 mm) values correlate with the darkest features in the k2v and k2r images, whereas the dark clouds in the core of the h and k lines (as indicated by the arrows), which probes higher heights, are indistinguishable from the background at 1.25 mm. Note that depending on the phase of the IRIS slit-scan, there could be a time lag of up to ~1.5 min between the latter and ALMA. Even in the darkest part of the filament, the intensities in the core of the Mg II lines are about 10–15% brighter than the mean QS profile at disk center, yet the filament contrast is high owing to the bright surrounding plage. The SOT magnetograms do not show a significant change in the photospheric magnetic flux underneath the filament spine over time.

Figure 3 shows the results of the clustering algorithm on the IRIS spectra. To create smooth spatial maps of cluster types, profiles belonging to a particular cluster were averaged, and the 15 mean spectra were sorted in terms of integrated intensity (within ± 50 km s^{-1} from line center) and labeled from A to O; a few of those profiles are displayed for comparison. A simple intensity threshold of 650 DN s^{-1} separates well the filament structure from the background in the AIA 304 Å passband. The coolest T_b (1.25 mm) values (< 5,000 K contours) occur in regions where, on average, the Mg II h and k lines are the narrowest, the central reversals are the shallowest, and the h and k double peaks are more symmetric, which suggests small velocity gradients. The average k line width measured at half intensity between the averaged k2v and k2r peaks and the averaged k1r and k1v dips is ≈0.31 Å compared to ≈0.54 Å in the nearby plage (e.g., profile N). The filament body north of the Band 6 contours shows Mg II profiles that are just as dark in the h and k cores as in the lower part (cf. **Figure 2**), but they are broader and show stronger, more asymmetrical, and separated k2v and k2r (or h2v, h2r) peaks, so they are classified as a different type. This implies that the coolest Band 6 temperatures coincide with the regions of lower integrated intensity in the h and k lines where the coolest and densest material may be located.

The aforementioned trend generally holds at different times but the time lag between the mm and NUV diagnostics has to be taken into consideration. At 14:26, low T_b (1.25 mm) values coincide with locations with A- and B-type IRIS profiles–they are essentially of the same kind but B-types are only slightly broader and brighter. These profiles practically disappear at 14:35, so do T_b (1.25 mm) < 5,000 K; this appears to be related to the heating event that occurs along the filament spine as shown

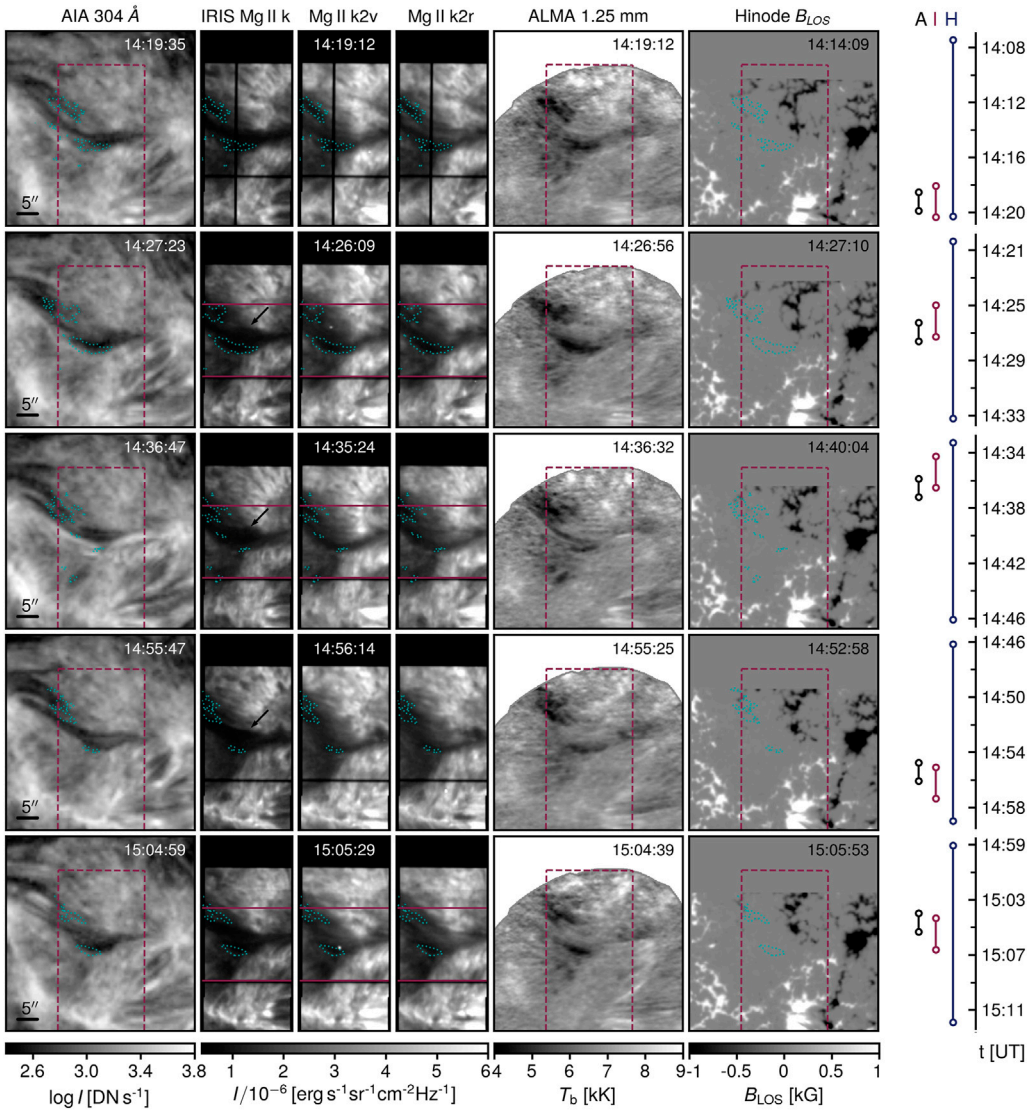

FIGURE 2 | Time evolution of the AR filament. The AIA 304 Å images have been averaged within the time span needed by ALMA to mosaic the filament. The intensities are capped for display purposes. The time stamps on the IRIS and Hinode raster images correspond to the central slit position. The dashed boxes show the IRIS FOV. The cyan contours show T_b (1.25 mm) = 5,000 K. The horizontal magenta lines delimit the area displayed in **Figure 3**. The data acquisition times are shown on the right.

by the 304 Å image; both signatures reappear at 15:05. We note that there are locations outside of the filament that show A- or B-type profiles where low T_b (1.25 mm) values are not found, and vice-versa, which just indicates relative, spatially-dependent opacity variations in both diagnostics.

Figure 4 shows selected ALMA Band 3 maps obtained after the Band 6 mosaics. The AIA images show a more dramatic evolution of the filament compared to an earlier time in the day (cf. **Figure 2**), to the point that the filament practically vanished towards the end of the second observing block. Unlike the 1.25 mm maps, the 3 mm maps do not show the same dark features against the background. This is interesting in that the optical thickness is expected to increase with wavelength, so the absorbing features in Band 6 should appear even darker in Band 3, that is the contrast is expected to slightly increase at longer wavelengths by extrapolation of the contrast curve obtained from previous low-resolution observations of quiescent filaments in the mm and cm ranges (Raoult et al., 1979). Therefore, it is somewhat surprising that the filament shows higher contrast in Band 6 than in Band 3. However, the dynamic nature of AR filaments may play a role here. The mean T_b (3 mm) values within the filament identified in the 304 Å images are around 7,700 K with a few hundred-kelvin variations, which is slightly higher than the average QS level (~ 7,500 (±100) K, White et al., 2017), but these values may be contaminated by the bright plage background because the Band 3 contours overlap with the plage as shown by the AIA 1,600 Å images. We note that the non-simultaneity of the Band 6 and

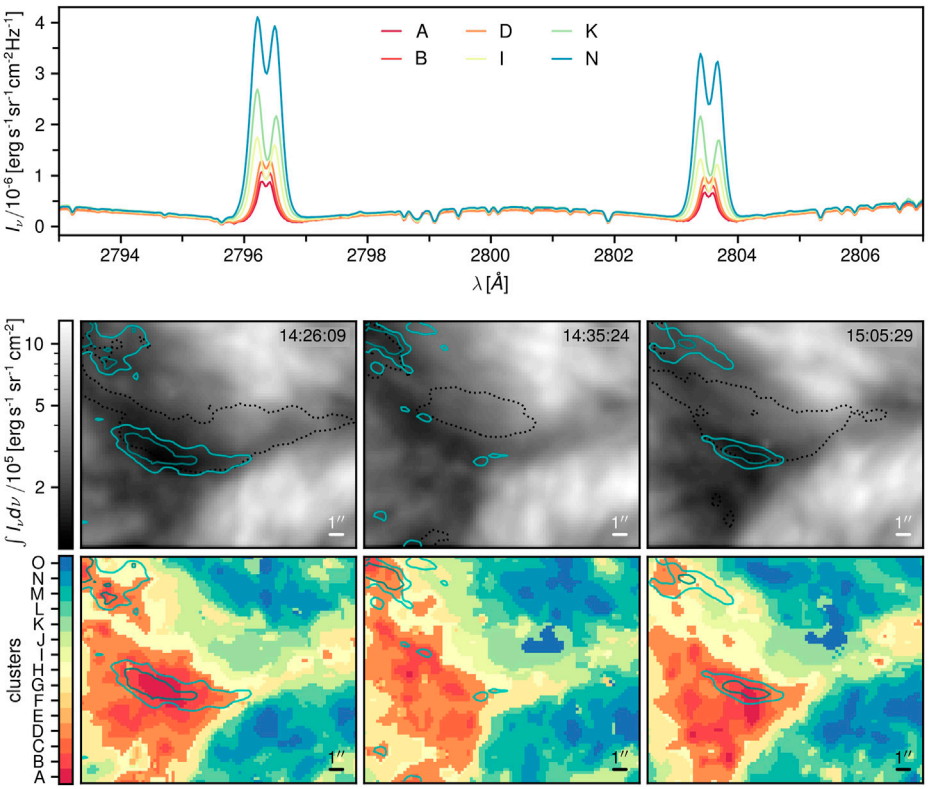

FIGURE 3 | Clustering of Mg II h and k profiles in an AR filament. Upper panel: mean spectral profiles of selected clusters. Middle panel: integrated intensity in the k line in logarithmic scale within the region delimited by the horizontal lines in **Figure 2**. Lower panel: clusters of Mg II h and k profiles. The light and dark blue contours correspond to T_b (1.25 mm) = 5,000 and 4,500 K, and the dotted black contours outline the filament boundary in the AIA 304 Å images.

Band 3 maps is relevant for interpreting relative brightness ratios.

4 DISCUSSION AND CONCLUSION

This paper presents ALMA observations of an AR filament at 2 mm wavelengths supported by SDO and partly by IRIS and Hinode. The filament shows substantial temporal variability in the AIA 304 Å passband, the Mg II h and k lines, and in ALMA Band 6. Brightness variations are also detected in Band 3 but they are more difficult to discern from the background fluctuations. As anticipated, the ALMA Band 6 interferometric T_b maps show dark/cool features with much higher contrast relative to the background than the single-dish observations reported thus far (Alissandrakis et al., 2017; Brajša et al., 2018). Very fine dark threads can be seen at certain times (e.g., **Figure 2**, 14:36 UT), but they do not last more than a few minutes. However, not all of the filament body (as seen by IRIS or AIA 304 Å) appears dark, but there are significant brightness variations across the filament spine. We note that the filament is also visible in the second Band 6 observing block until 17:47 UT (not displayed). We did not identify significant changes in the photospheric magnetic field that we could relate to the filament variability, but we would need field extrapolations to study the topology of the filament itself to investigate a possible correlation between "magnetic dips" and the mm continuum brightness distribution, similarly to what has been done based on H α observations (e.g., Aulanier et al., 1999; van Ballegooijen, 2004; Guo et al., 2010; Li et al., 2017).

We find a spatial association between the integrated k line intensity and T_b (1.25 mm) in the filament that is consistent in time. This suggests that both diagnostics are coupled through changes in temperature and electron density. The Mg II lines are narrower and the central reversals are shallower than the average QS profile at those locations. The coolest T_b (1.25 mm) values coincide with the dark structures that are visible away from the k (and h) line center and thus extend down to lower heights in the atmosphere. The lower atmosphere may be filled with low-lying dense cool threads where the absorption is high but the emissivity is low, hence the weak Mg II lines. However, interpreting the Mg II line shapes is not trivial as they depend on the interplay between the incident radiation, gas pressure, filament thickness, and the properties of the prominence-corona transition region (Heinzel et al., 2014), and thus require a follow-up investigation.

Detailed radiative transfer models of AR filaments are scarce in the literature. The spectral synthesis based on a 3D whole-

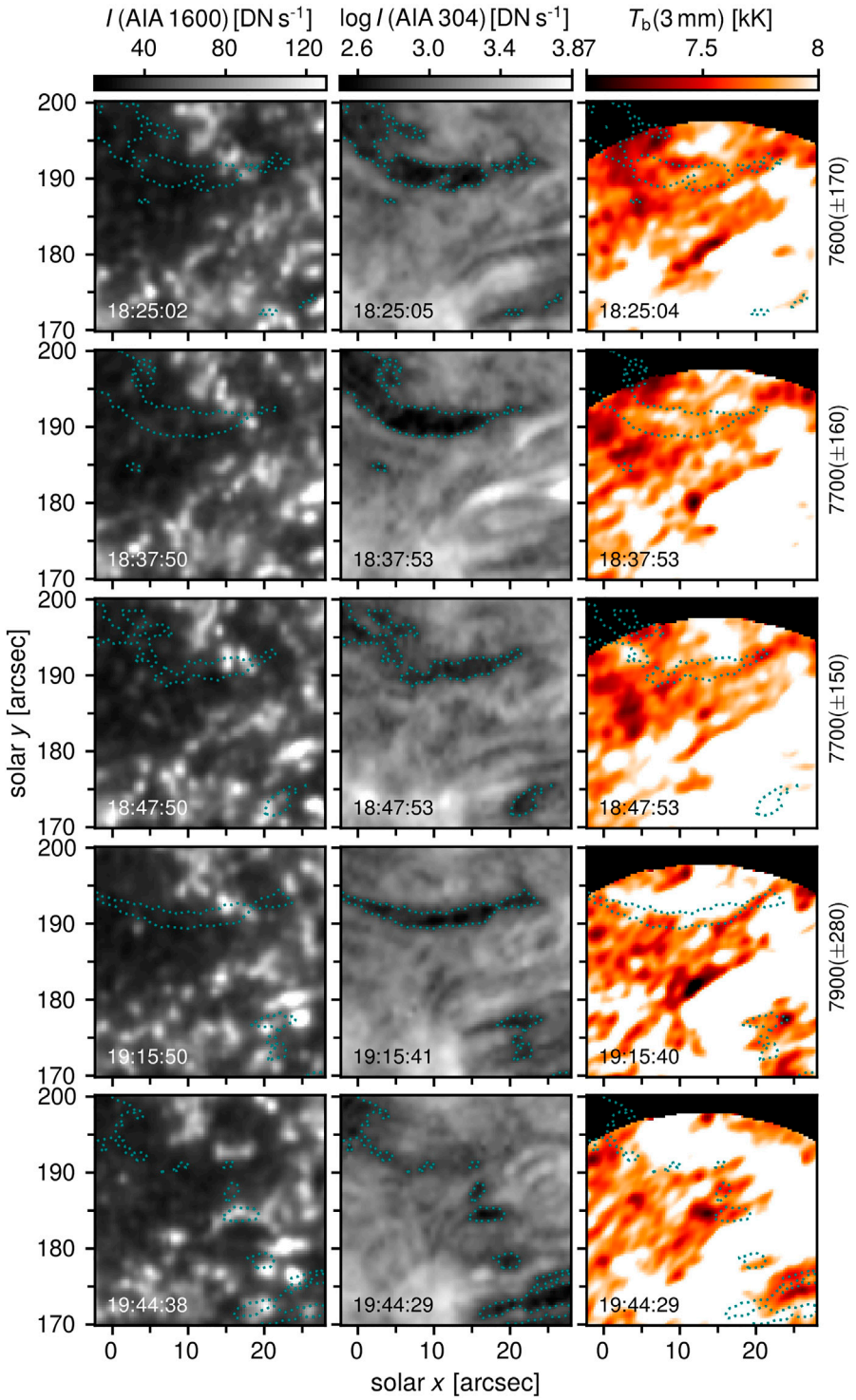

FIGURE 4 | AIA and ALMA Band 3 observations at a later time on 13 April 2019. The Band 3 colormap range is capped at 8 kK to enhance small T_b variations within the filament. Images in the AIA 1600 Å passband are displayed for context. The cyan contours delimit the filament structure in the AIA 304 Å images. The values on the right indicate the mean (±standard deviation) T_b (3 mm) within the filament.

prominence fine structure model presented by Gunár et al. (2016) shows filament threads in emission by a few hundred kelvins above a uniform disk background at 1.25 mm unlike what we observed; the simulated filament is optically thin ($\tau_\nu <$ 1) at this wavelength. The emerging brightness temperature is the result of the absorbed background brightness

temperature, T_b^{bcg}, plus the integrated emission along a geometrical path of length L:

$$T_b(\nu) = T_b^{bcg}(\nu)\, e^{-\tau_\nu} + \int_0^L T \kappa_\nu\, e^{-\int_0^l \kappa_\nu dl'}\, dl, \quad (1)$$

where κ_ν is the frequency-dependent absorption coefficient (e.g., Gunár et al., 2016). Brightness temperature values lower than the background level require kinetic temperatures, T, lower than background temperatures. However, the observed AR filament and background certainly have different properties than the simulated ones. Dedicated simulations with more realistic AR conditions are needed to investigate this.

Constraining both the kinetic temperature and thickness of the prominence is not possible using single-band data but it requires simultaneous observations at two wavelengths and the assumption of isothermal conditions (e.g., Heinzel et al., 2015a; Rodger and Labrosse, 2017). In that case, Eq. 1 simplifies to

$$T_b(\nu) = T_b^{bcg}(\nu)\, e^{-\tau_\nu} + T(1 - e^{-\tau_\nu}). \quad (2)$$

An hour after the Band 6 observations, the filament is still visible in the AIA 304 Å images, but it is indiscernible from the background in Band 3. This cannot be attributed to a difference in spatial resolution (by a factor of ~2) because the dark threads in the Band 6 with the typical sizes of a few arcseconds would be well resolved with Band 3. Instead, it could imply that the filament temperature is similar to the background. We note that the background is far from uniform, which makes it complicated to interpret T_b variations within the filament. Assuming that the average properties of the filament did not significantly change between the time the Band 6 and Band 3 maps were taken, which is a reasonable assumption at least for the first Band 3 observing block (**Figure 4**), it is difficult to reconcile these observations with an isothermal model since we would expect even stronger absorption features at 3 mm than at 1.25 mm (see also Rodger et al., 2019). Following Dulk (1985), the opacity ratio in both bands is given by

$$\frac{\kappa_3}{\kappa_{1.25}} = \left[\frac{\nu_{1.25}}{\nu_3}\right]^2 \frac{18.2 + \ln\left(T^{3/2}\right) - \ln \nu_3}{18.2 + \ln\left(T^{3/2}\right) - \ln \nu_{1.25}}, \quad \left(T < 2 \times 10^5\ \mathrm{K}\right). \quad (3)$$

An optically thick plasma at 3 mm with a kinetic temperature of 7,500 K (equal to the mean QS background at 3 mm) would show a higher mean T_b (1.25 mm) than what we have observed. For example, $\tau_{3\ mm} = 1$ implies $\tau_{1.25\ mm} = 0.15$ and T_b (1.25 mm) ~ 6,100 K, which would make the filament stand out above the background. Therefore, these two wavelengths are more likely sensitive to different layers of the filament with different temperature and density conditions, or there is a temperature gradient spanning their formation heights, with Band 6 probing closer to the lowest temperatures of the filament, and Band 3 sensing warmer filament plasma or possibly the outermost shell that separates it from the corona if the optical thickness is large. Simultaneous observations of AR filaments in both ALMA bands are needed to clarify these findings.

Combined non-LTE radiative transfer modeling of the Mg II h and k lines and the radio continua will be required to diagnose the properties of the observed filament. Using such an approach, ALMA observations will allow us to constrain the plasma temperature, while the IRIS spectra can provide information about the pressure/density and the LOS velocity gradients.

DATA AVAILABILITY STATEMENT

The SDO data can be obtained from the Joint Science Operations Center (http://jsoc.stanford.edu). The IRIS data can be downloaded from the Heliophysics Events Knowledgebase Coverage Registry (https://www.lmsal.com/hek/hcr). The Hinode data can be obtained from the Community Spectro-polarimetric Analysis Center (http://www2.hao.ucar.edu/csac). The GONG data can be fetched from Data Archive (https://gong2.nso.edu/archive). The raw ALMA data can be found at the ALMA Science Archive (https://almascience.nrao.edu/aq).

AUTHOR CONTRIBUTIONS

JS, SW, and JL contributed to the ALMA research proposal and data acquisition. SW performed the ALMA data reduction. JS conducted the analysis. JS, SW, KR, GC, SG, PH, and JL contributed to the discussion and writing.

FUNDING

SG and PH acknowledge support from the grants 19-16890S and 19-17102S of the Czech Science Foundation (GAČR).

ACKNOWLEDGMENTS

This paper makes use of the following ALMA data: ADS/JAO.ALMA#2018.1.01518.S. ALMA is a partnership of ESO (representing its member states), NSF (USA) and NINS (Japan), together with NRC (Canada), MOST and ASIAA (Taiwan), and KASI (Republic of Korea), in cooperation with the Republic of Chile. The Joint ALMA Observatory is operated by ESO, AUI/NRAO and NAOJ. IRIS is a NASA small explorer mission developed and operated by LMSAL with mission operations executed at NASA Ames Research center and major contributions to downlink communications funded by ESA and the Norwegian Space Centre. Hinode is a Japanese mission developed and launched by ISAS/JAXA, with NAOJ as domestic partner and NASA and STFC (UK) as international partners. It is operated by these agencies in co-operation with ESA and NSC (Norway). Data were acquired by GONG instruments operated by NISP/NSO/AURA/NSF with contribution from NOAA. The NSO is operated by the Association of Universities for Research in Astronomy, Inc.,

under cooperative agreement with the National Science Foundation. This research has made use of `Astropy` (https://astropy.org) – a community-developed core Python package for Astronomy (Astropy Collaboration et al., 2018), `SunPy` (https://sunpy.org) – an open-source and free community-developed solar data analysis Python package (The SunPy Community et al., 2020), and MATLAB and the Image Processing Toolbox release 2021b (The Mathworks, Inc., Natick, MA, USA). SG and PH thank for the support from project RVO:67985815 of the Astronomical Institute of the Czech Academy of Sciences.

REFERENCES

Alissandrakis, C. E., Patsourakos, S., Nindos, A., and Bastian, T. S. (2017). Center-to-limb Observations of the Sun with ALMA. *A&A* 605, A78. doi:10.1051/0004-6361/201730953

Aulanier, G., Démoulin, P., Mein, N., van Driel-Gesztelyi, L., Mein, P., and Schmieder, B. (1999). 3-D Magnetic Configurations Supporting Prominences. III. Evolution of Fine Structures Observed in a Filament Channel. *A&A* 342, 867–880.

Astropy CollaborationPrice-Whelan, A. M., Price-Whelan, A. M., Sipőcz, B. M., Günther, H. M., and Lim, P. L. (2018). The Astropy Project: Building an Open-Science Project and Status of the v2.0 Core Package. *AJ* 156, 123. doi:10.3847/1538-3881/aabc4f

Bastian, T. S., Ewell, J., and Zirin, H. (1993). A Study of Solar Prominences Near Lambda = 1 Millimeter. *ApJ* 418, 510. doi:10.1086/173413

Brajša, R., Sudar, D., Benz, A. O., Skokić, I., Bárta, M., De Pontieu, B., et al. (2018). First Analysis of Solar Structures in 1.21 Mm Full-Disc ALMA Image of the Sun. *A&A* 613, A17. doi:10.1051/0004-6361/201730656

Casini, R., Bevilacqua, R., and López Ariste, A. (2005). Principal Component Analysis of the He I D_3 Polarization Profiles from Solar Prominences. *ApJ* 622, 1265–1274. doi:10.1086/428283

Chen, P.-F., Xu, A.-A., and Ding, M.-D. (2020). Some Interesting Topics Provoked by the Solar Filament Research in the Past Decade. *Res. Astronomy Astrophysics* 20, 166. doi:10.1088/1674-4527/20/10/166

da Silva Santos, J. M., de la Cruz Rodríguez, J., White, S. M., Leenaarts, J., Vissers, G. J. M., and Hansteen, V. H. (2020). ALMA Observations of Transient Heating in a Solar Active Region. *A&A* 643, A41. doi:10.1051/0004-6361/202038755

De Pontieu, B., Title, A. M., Lemen, J. R., Kushner, G. D., Akin, D. J., Allard, B., et al. (2014). The Interface Region Imaging Spectrograph (IRIS). *Sol. Phys.* 289, 2733–2779. doi:10.1007/s11207-014-0485-y

Díaz Baso, C. J., and Asensio Ramos, A. (2018). Enhancing SDO/HMI Images Using Deep Learning. *A&A* 614, A5. doi:10.1051/0004-6361/201731344

Díaz Baso, C. J., Martínez González, M. J., Asensio Ramos, A., and de la Cruz Rodríguez, J. (2019). Diagnostic Potential of the Ca II 8542 Å Line for Solar Filaments. *A&A* 623, A178. doi:10.1051/0004-6361/201834793

Dulk, G. A. (1985). Radio Emission from the Sun and Stars. *ARA&A* 23, 169–224. doi:10.1146/annurev.aa.23.090185.001125

Freeland, S. L., and Handy, B. N. (1998). Data Analysis with the SolarSoft System. *Sol. Phys.* 182, 497–500. doi:10.1023/A:1005038224881

Gibson, S. E. (2018). Solar Prominences: Theory and Models. Fleshing Out the Magnetic Skeleton. *Living Rev. Sol. Phys.* 15, 7. doi:10.1007/s41116-018-0016-2

Gunár, S., Heinzel, P., Anzer, U., and Mackay, D. H. (2018). Quiescent Prominences in the Era of ALMA. II. Kinetic Temperature Diagnostics. *ApJ* 853, 21. doi:10.3847/1538-4357/aaa001

Gunár, S., Heinzel, P., Mackay, D. H., and Anzer, U. (2016). Quiescent Prominences in the Era of ALMA: Simulated Observations Using the 3D Whole-Prominence Fine Structure Model. *ApJ* 833, 141. doi:10.3847/1538-4357/833/2/141

Guo, Y., Schmieder, B., Démoulin, P., Wiegelmann, T., Aulanier, G., Török, T., et al. (2010). Coexisting Flux Rope and Dipped Arcade Sections along One Solar Filament. *ApJ* 714, 343–354. doi:10.1088/0004-637X/714/1/343

Harrison, R. A., Carter, M. K., Clark, T. A., Lindsey, C., Jefferies, J. T., Sime, D. G., et al. (1993). An Active Solar Prominence in 1.3 MM Radiation. *A&A* 274, L9.

Harvey, J. W., Bolding, J., Clark, R., Hauth, D., Hill, F., Kroll, R., et al. (2011). Full-disk Solar H-Alpha Images from GONG, *AAS/Solar Phys. Div. Abstr. #42* 4217. 45.

Heinzel, P., Berlicki, A., Bárta, M., Karlický, M., and Rudawy, P. (2015a). On the Visibility of Prominence Fine Structures at Radio Millimeter Wavelengths. *Sol. Phys.* 290, 1981–2000. doi:10.1007/s11207-015-0719-7–

Heinzel, P., Berlicki, A., Bárta, M., Rudawy, P., Gunár, S., Labrosse, N., et al. (2022). *ALMA as a Prominence Thermometer: First Observations*. *arXiv e-prints*arXiv:2202.12761.

Heinzel, P., Schmieder, B., Mein, N., and Gunár, S. (2015b). Understanding the Mg II and Hα Spectra in a Highly Dynamical Solar Prominence. *ApJ* 800, L13. doi:10.1088/2041-8205/800/1/L13

Heinzel, P., Vial, J. C., and Anzer, U. (2014). On the Formation of Mg Ii H and K Lines in Solar Prominences. *A&A* 564, A132. doi:10.1051/0004-6361/201322886

Jejčič, S., Schwartz, P., Heinzel, P., Zapiór, M., and Gunár, S. (2018). Statistical Analysis of UV Spectra of a Quiescent Prominence Observed by IRIS. *A&A* 618, A88. doi:10.1051/0004-6361/201833466

Kuckein, C., Centeno, R., Martínez Pillet, V., Casini, R., Manso Sainz, R., and Shimizu, T. (2009). Magnetic Field Strength of Active Region Filaments. *A&A* 501, 1113–1121. doi:10.1051/0004-6361/200911800

Kuckein, C., Martínez Pillet, V., and Centeno, R. (2012). An Active Region Filament Studied Simultaneously in the Chromosphere and Photosphere. I. Magnetic Structure. *A&A* 539, A131. doi:10.1051/0004-6361/201117675

Kundu, M. R. (1972). Observations of Prominences at 3.5 Millimeter Wavelength. *Sol. Phys.* 25, 108–115. doi:10.1007/BF00155749

Labrosse, N., Heinzel, P., Vial, J. C., Kucera, T., Parenti, S., Gunár, S., et al. (2010). Physics of Solar Prominences: I—Spectral Diagnostics and Non-LTE Modelling. *Space Sci. Rev.* 151, 243–332. doi:10.1007/s11214-010-9630-6

Labrosse, N., Rodger, A. S., Radziszewski, K., Rudawy, P., Antolin, P., Fletcher, L., et al. (2022). *First High Resolution Interferometric Observation of a Solar Prominence with ALMA*. *arXiv e-prints*arXiv:2202.12434.

Lemen, J. R., Title, A. M., Akin, D. J., Boerner, P. F., Chou, C., Drake, J. F., et al. (2012). The Atmospheric Imaging Assembly (AIA) on the Solar Dynamics Observatory (SDO). *Sol. Phys.* 275, 17–40. doi:10.1007/s11207-011-9776-8

Leroy, J. L. (1989). "Observation of Prominence Magnetic Fields," in *Dynamics and Structure of Quiescent Solar Prominences*. Editor E. R. Priest (of Astrophysics and Space Science Library), 150, 77–113. doi:10.1007/978-94-009-3077-3_13

Levens, P. J., and Labrosse, N. (2019). Modelling of Mg II Lines in Solar Prominences. *A&A* 625, A30. doi:10.1051/0004-6361/201833132

Li, S., Su, Y., Zhou, T., van Ballegooijen, A., Sun, X., and Ji, H. (2017). High-resolution Observations of Sympathetic Filament Eruptions by NVST. *ApJ* 844, 70. doi:10.3847/1538-4357/aa78f5

Lindsey, C. (1994). "The Sun in Submillimeter Radiation,". *Infrared Solar Physics C. Lindsey*. Editors D. M. Rabin and J. T. Jefferies, 154, 85. doi:10.1007/978-94-011-1926-9_12

Lites, B. W., and Ichimoto, K. (2013). The SP_PREP Data Preparation Package for the Hinode Spectro-Polarimeter. *Sol. Phys.* 283, 601–629. doi:10.1007/s11207-012-0205-4

McMullin, J. P., Waters, B., Schiebel, D., Young, W., and Golap, K. (2007). "CASA Architecture and Applications,". Editors R. A. Shaw, F. Hill, and D. J. Bell (Astronomical Society of the Pacific Conference Series), 376, 127.

Orozco Suárez, D., Asensio Ramos, A., and Trujillo Bueno, J. (2014). The Magnetic Field Configuration of a Solar Prominence Inferred from Spectropolarimetric Observations in the He I 10 830 Å Triplet. *A&A* 566, A46. doi:10.1051/0004-6361/201322903

Parenti, S. (2014). Solar Prominences: Observations. *Living Rev. Sol. Phys.* 11, 1. doi:10.12942/lrsp-2014-1

Peat, A. W., Labrosse, N., Schmieder, B., and Barczynski, K. (2021). Solar Prominence Diagnostics from Non-LTE Modelling of Mg II H&k Line Profiles. *A&A* 653, A5. doi:10.1051/0004-6361/202140907

Pesnell, W. D., Thompson, B. J., and Chamberlin, P. C. (2012). The Solar Dynamics Observatory (SDO). *Sol. Phys.* 275, 3–15. doi:10.1007/s11207-011-9841-3

Poduval, B., DeForest, C. E., Schmelz, J. T., and Pathak, S. (2013). Point-spread Functions for the Extreme-Ultraviolet Channels of SDO/AIA Telescopes. *ApJ* 765, 144. doi:10.1088/0004-637X/765/2/144

Raoult, A., Lantos, P., and Fuerst, E. (1979). Prominences at Centrimetric and Millimetric Wavelengths. I. Size and Spectrum of the Radio Filaments. *Sol. Phys.* 61, 335–343. doi:10.1007/BF00150418

Rodger, A., and Labrosse, N. (2017). Solar Prominence Modelling and Plasma Diagnostics at ALMA Wavelengths. *Sol. Phys.* 292, 130. doi:10.1007/s11207-017-1161-9

Rodger, A. S., Labrosse, N., Wedemeyer, S., Szydlarski, M., Simões, P. J. A., and Fletcher, L. (2019). First Spectral Analysis of a Solar Plasma Eruption Using ALMA. *ApJ* 875, 163. doi:10.3847/1538-4357/aafdfb

Ruan, G., Jejčič, S., Schmieder, B., Mein, P., Mein, N., Heinzel, P., et al. (2019). Diagnostics of the Prominence Plasma from Hα and Mg II Spectral Observations. *ApJ* 886, 134. doi:10.3847/1538-4357/ab4b50

Scherrer, P. H., Schou, J., Bush, R. I., Kosovichev, A. G., Bogart, R. S., Hoeksema, J. T., et al. (2012). The Helioseismic and Magnetic Imager (HMI) Investigation for the Solar Dynamics Observatory (SDO). *Sol. Phys.* 275, 207–227. doi:10.1007/s11207-011-9834-2

Schmahl, E. J., Bobrowsky, M., and Kundu, M. R. (1981). Observations of Solar Filaments at 8-GHZ 15-GHZ 22-GHZ and 43-GHZ. *Sol. Phys.* 71, 311–328. doi:10.1007/BF00167554

Schmieder, B., Tian, H., Kucera, T., López Ariste, A., Mein, N., Mein, P., et al. (2014). Open Questions on Prominences from Coordinated Observations by IRIS, Hinode, SDO/AIA, THEMIS, and the Meudon/MSDP. *A&A* 569, A85. doi:10.1051/0004-6361/201423922

Stellmacher, G., Wiehr, E., and Dammasch, I. E. (2003). Spectroscopy of Solar Prominences Simultaneously from Space and Ground. *Sol. Phys.* 217, 133–155. doi:10.1023/A:1027310303994

The SunPy CommunityBarnes, W. T., Bobra, M. G., Christe, S. D., Freij, N., Hayes, L. A., et al. (2020). The Sunpy Project: Open Source Development and Status of the Version 1.0 Core Package. *Astrophysical J.* 890, 68. doi:10.3847/1538-4357/ab4f7a

Tsuneta, S., Ichimoto, K., Katsukawa, Y., Nagata, S., Otsubo, M., Shimizu, T., et al. (2008). The Solar Optical Telescope for the Hinode Mission: An Overview. *Sol. Phys.* 249, 167–196. doi:10.1007/s11207-008-9174-z

van Ballegooijen, A. A. (2004). Observations and Modeling of a Filament on the Sun. *ApJ* 612, 519–529. doi:10.1086/422512

Vial, J. C., Zhang, P., and Buchlin, É. (2019). Some Relationships between Radiative and Atmospheric Quantities through 1D NLTE Modeling of Prominences in the Mg II Lines. *A&A* 624, A56. doi:10.1051/0004-6361/201834249

Virtanen, P., Gommers, R., Oliphant, T. E., Haberland, M., Reddy, T., Cournapeau, D., et al. (2020). SciPy 1.0: Fundamental Algorithms for Scientific Computing in Python. *Nat. Methods* 17, 261–272. doi:10.1038/s41592-019-0686-2

Vrsnak, B., Pohjolainen, S., Urpo, S., Terasranta, H., Brajsa, R., Ruzdjak, V., et al. (1992). Large-scale Patterns on the Sun Observed in the Millimetric Wavelength Range. *Sol. Phys.* 137, 67–86. doi:10.1007/BF00146576

Ward, J. H. (1963). Hierarchical Grouping to Optimize an Objective Function. *J. Am. Stat. Assoc.* 58, 236–244. doi:10.1080/01621459.1963.10500845

Wedemeyer, S., Bastian, T., Brajša, R., Hudson, H., Fleishman, G., Loukitcheva, M., et al. (2016). Solar Science with the Atacama Large Millimeter/Submillimeter Array—A New View of Our Sun. *Space Sci. Rev.* 200, 1–73. doi:10.1007/s11214-015-0229-9

White, S. M., Iwai, K., Phillips, N. M., Hills, R. E., Hirota, A., Yagoubov, P., et al. (2017). Observing the Sun with the Atacama Large Millimeter/submillimeter Array (ALMA): Fast-Scan Single-Dish Mapping. *Sol. Phys.* 292, 88. doi:10.1007/s11207-017-1123-2

Wootten, A., and Thompson, A. R. (2009). The Atacama Large Millimeter/Submillimeter Array. *IEEE Proc.* 97, 1463–1471. doi:10.1109/JPROC.2009.2020572

Xu, Z., Lagg, A., Solanki, S., and Liu, Y. (2012). Magnetic Fields of an Active Region Filament from Full Stokes Analysis of Si I 1082.7 Nm and He I 1083.0 Nm. *ApJ* 749, 138. doi:10.1088/0004-637X/749/2/138

Conflict of Interest: The authors declare that the research was conducted in the absence of any commercial or financial relationships that could be construed as a potential conflict of interest.

Publisher's Note: All claims expressed in this article are solely those of the authors and do not necessarily represent those of their affiliated organizations, or those of the publisher, the editors and the reviewers. Any product that may be evaluated in this article, or claim that may be made by its manufacturer, is not guaranteed or endorsed by the publisher.

frontiers | Frontiers in Astronomy and Space Sciences

TYPE Review
PUBLISHED 20 October 2022
DOI 10.3389/fspas.2022.1025368

OPEN ACCESS

EDITED BY
Alexander Nindos,
University of Ioannina, Greece

REVIEWED BY
Jorrit Leenaarts,
Stockholm University, Sweden
Adriana Valio,
Mackenzie Presbyterian University, Brazil

*CORRESPONDENCE
Maria Loukitcheva,
lukicheva@mps.mpg.de

SPECIALTY SECTION
This article was submitted to Stellar and Solar Physics, a section of the journal Frontiers in Astronomy and Space Sciences

RECEIVED 22 August 2022
ACCEPTED 04 October 2022
PUBLISHED 20 October 2022

CITATION
Loukitcheva M and Reardon KP (2022), First looks at solar active regions with ALMA.
Front. Astron. Space Sci. 9:1025368.
doi: 10.3389/fspas.2022.1025368

First looks at solar active regions with ALMA

Maria Loukitcheva[1,2,3]* and Kevin P. Reardon[4,5]

[1]Max Planck Institute for Solar System Research, Goettingen, Germany, [2]Special Astrophysical Observatory, Russian Academy of Science, Nizhniy Arkhyz, Russia, [3]Department of Mathematics and Mechanics, Saint-Petersburg State University, Saint-Petersburg, Russia, [4]National Solar Observatory, Boulder, CO, United States, [5]Department of Astrophysical and Planetary Sciences, University of Colorado, Boulder, CO, United States

During the first few years of observing the Sun with the Atacama Large Millimeter/submillimeter Array (ALMA), the scientific community has acquired a number of observational datasets targeting various structures in active regions, including sunspot umbra and penumbra, active region pores, and plages. In this paper we review the results obtained from the extensive analysis of these interferometric millimeter data, together with the coordinated observations from IRIS, SDO, IBIS, and Hinode, that reveal information on the chromospheric thermal structure above active regions and properties of small-scale heating events near magnetic field concentrations. We discuss the properties of waves (especially the three-minute oscillations) in sunspots, plage, and network. We speculate how high-resolution millimeter data can supplement spectral line observations in the visible and UV and can improve chromospheric spectroscopic inversions. We identify challenges in the interpretation of the millimeter continuum emission due to the complex, non-local and time-dependent processes that determine the electron density through the chromosphere. Finally we overview the prospects for future active regions observations with ALMA during the ascending phase of the solar cycle.

KEYWORDS

ALMA, Sun, Sun—active regions, solar radio astronomy, millimeter (mm) and submillimeter (sub-mm) waves

1 Solar active regions

"Solar active regions" (hereafter ARs) is an observational term referring to the regions in the atmosphere of the Sun, spanning from the photosphere up to the solar corona, where a whole variety of phenomena related to strong concentrations of magnetic fields takes place. Principal structures of active regions, such as sunspots, plages, and pores, are all associated with magnetic field bundles of typically kiloGauss strength. These features are the primary source for a broad range of solar activity phenomena, especially transient events such as small-scale brightenings, dynamic loops, streamers, jets, flares, and coronal mass ejections (CMEs), which heat and shape the outermost solar atmospheric layers, and can drive the space weather.

This solar activity results in the emission from a wide range of wavelengths: from the X-ray to radio, and the most effective way to exploit diagnostic capabilities of each wavelength regime lies in the synergy between the observations at different wavelengths. In this respect, the complementary use of radio data is particularly valuable for diagnostics of the physical conditions in the solar atmosphere. In particular, the bulk of the millimeter continuum emission originates from the chromospheric heights (Kundu, 1965) and allows a rather straightforward measurements of the gas temperature across these heights, as the radiation is coupled linearly to the temperature owing to its formation in local thermodynamic equilibrium (LTE) and is in the Rayleigh-Jeans limit. Thereby, observations at mm wavelengths provide strong constraints to the thermal structure of the chromosphere in ARs. Furthermore, the solar chromosphere harbors plenty of highly nonlinear phenomena that result in local heating (e.g., magneto-acoustic waves and shocks, wave dissipation events, reconnection along magnetic field lines (see, e.g., Carlsson et al., 2019). Observations at mm wavelengths with sufficiently high spatial and temporal resolution would be able to diagnose the thermodynamic changes in the rapid, small-scale events.

The slowly-varying component of the solar radio emission from active regions was termed the S-component (Krueger, 1979) to distinguish it from emission from sporadic events, e.g. flares, radio bursts and storms). It gained a lot of interest starting from the early radio measurements, as it reflects the atmospheric structuring of solar activity features in the chromosphere and corona, which can exhibit very different physical characteristics. The single-dish observations of the Sun at mm and short cm wavelengths (Kundu, 1970; Efanov et al., 1972) provided the first radio maps of the solar chromosphere and transition region. Enhanced radio brightness from solar ARs (compared to the quiet-Sun level), showing good correspondence with the calcium plage regions as well as with the regions of enhanced magnetogram signals, were detected in the two-dimensional solar maps. But the spatial resolution of the single-dish antennas (typically not exceeding 1 arcmin) was not enough to resolve individual sunspots, pores and plage elements, and isolate their radio brightness from the surroundings. Since the first observations of the Sun at radio wavelengths the techniques of radio measurements have made a big leap forward and the greatest breakthrough originated with the start of solar observing with the Atacama Large Millimeter-Submillimeter Array (ALMA, Wootten and Thompson, 2009) in 2016. ALMA has proven to be a unique instrument that is capable of providing the required spatial, temporal and spectral resolution to contribute to solving some of the central questions of solar physics, like the energy transport and mechanisms of its deposition in the solar corona.

Mapping of the Sun with spatial resolution of order of arcseconds has revealed the fine structure of the solar radio emission from ARs. With ALMA it became possible to distinguish and describe sunspot umbra and penumbra in the mm images (Iwai et al., 2017; Loukitcheva et al., 2017), to study signatures of the three-minute oscillations and wave propagation in the mm brightness of sunspot umbra (Chai et al., 2022a), to detect oscillations of mm brightness in small bright features in a plage (Guevara Gómez et al., 2021), to study spatial association of the observed oscillations through the atmosphere mapped by the different passbands (Narang et al., 2022), and evaluate the contribution from detected high-frequency acoustic waves to the chromospheric heating in plages (Molnar et al., 2021), to explore AR small-scale transient brightenings as signatures of heating linked to magnetic reconnection events (da Silva Santos et al., 2020b) and to provide further evidence for heating in the upper chromosphere through current dissipation (da Silva Santos et al., 2022a), to image a solar active region filament at sub-arcsecond resolution with the Interface Region Imaging Spectrograph (IRIS, De Pontieu et al., 2014) and ALMA (da Silva Santos et al., 2022b), to explore the structure and the dynamics of chromospheric plages, namely, of fibrils (Chintzoglou et al., 2021a) and jet-like features (Type II spicules) (Chintzoglou et al., 2021b), to perform quantitative comparison between the mm continuum brightness and the chromospheric diagnostics from observations, e.g., with Hα (Molnar et al., 2019), and Mg II line (Bastian et al., 2017; Bastian et al., 2018; Jafarzadeh et al., 2019), to constrain the thermodynamical properties of the plage atmosphere using ALMA and IRIS data from a NLTE inversion code (da Silva Santos et al., 2020a), and finally, to identify small-scale bright features in the ALMA images and study their relation to the chromospheric structures seen in the EUV, UV and Hα images (Brajša et al., 2018, 2021), and to employ ALMA measurements in a data-constrained model of the sunspot's atmosphere (de Oliveira e Silva et al., 2022). Below we provide more details about these observational results.

2 ALMA observations of solar active regions

Regular solar ALMA observations have became possible since 2016 (ALMA Cycle 4). They were preceded by six solar test campaigns, run by solar radio astronomy experts, as part of Commissioning and Science Verification/Extension of Capabilities (CSV/EOC) activities, that were summarized in (Shimojo et al., 2017; White et al., 2017).

The observational data, obtained during the CSV/EOC phase, were released to the scientific community in early 2017. The ALMA data sets consist of calibrated visibility data and scripts to synthesize images for a number of solar targets, including both single-pointing and mosaic observations of solar active regions (ARs).[1] The following AR data were released: 149-pointing mosaics of the active region NOAA

1 The science verification data are available for download at .https://almascience.nrao.edu/alma-data/science-verification.

TABLE 1 Successful AR observational projects that have resulted in at least one publication.

Project ID	Bands	Date of obs	Co-observations	AR structures
2011.0.00020.SV	3, 6	2015-12-16-2015-12-18	IRIS, GST	umbra, penumbra, plage
2016.1.00030.S	3, 6	2017-03-19	IRIS, IBIS, Hinode	plage, tiny bipolar AR
2016.1.00050.S	3, 6	2017-04-22	IRIS, Hinode, IBIS	plage
2016.1.01129.S	3, 6	2017-04-23, 2017-04-18	IBIS, IRIS, Hinode	plage
2017.1.001672.S	3, 6	2018-08-23, 2018-04-26	IRIS, Hinode	small pores
2018.1.01518.S	3, 6	2019-04-13	SST, IRIS, Hinode	pores, plage

12470 (hereafter AR 12470) in Band 3 (a frequency of 100 GHz, corresponding to a wavelength $\lambda = 3$ mm) and Band 6 (230 GHz, $\lambda \approx 1.3$ mm) obtained on 16 December 2015 and 18 December, respectively (Table 1); single-pointing observations of the west side of the active region AR 12470 in Band 3 recorded with a cadence of 2 s (16–17 December 2015). The interferometric maps synthesized from the mosaic observations sampled a field of view (FOV) of 300″ x300 ″ in Band 3, covering the sunspot umbra and penumbra as well as the surrounding AR plage. In the Band 6 mosaic the FOV is limited to 140″ × 140″, covering mostly the sunspot with only a small portion of the surrounding plage. The observations were performed in the compact array configuration involving 36 antennas with a maximum baseline of ≃ 300 m, resulting in the full-width at half maximum (FWHM) of the synthesized beam of 4.9″ × 2.2″ in Band 3 and of 2.4″ × 0.9″ in Band 6.

The interferometric measurements are limited to observing areas of the solar surface limited by the field of view of a single dish (typically ≈60 ″ in diameter at 3 mm, or ≈25 ″ in diameter at 1.3 mm). While multiple pointings can be used to build up mosaic images, up to 10 s are required for each pointing. This makes it impractical to cover large regions of the Sun on reasonable timescales. Instead, a method was developed for fast-scan solar imaging using a single 12-meter dish with a "double-circle" continuous circular scanning pattern (White et al., 2017). While only achieving the spatial resolution of a single disk (50 and 22 ″ for 3 and 1.3 mm, respectively), this approach allows the full solar disk to be scanned in approximately 15 min, depending on the ALMA Band being used, and generates low-resolution observations of many active regions at once.

Up to the present day (August 2022), due to the declining of phase of the solar cycle from 2017–2020 and the low number of executed solar programs between 2019 and 2022, the science verification data on the sunspot in AR 12470 from 2015 remain the only successfully recorded ALMA interferometric measurements of sunspots. During periods of low activity, it was difficult to successfully propose observations of active regions due to uncertainties about their occurrence during those intervals when the array would be in configurations appropriate for solar observing. However the CSV/EOC data were extensively used for various studies resulting in new insights into the sunspot atmospheres.

ALMA observing of AR plages appeared to be more fortunate and successful in this period. During ALMA cycles 4-7 (2017–2019) at least five datasets of successful AR observations were acquired (Table 1) and are available *via* the ALMA Data Archive[2] for download. The effective spatial resolution varies quite significantly between the datasets, as it depends on the wavelength, array configuration (maximum baseline), and the position of the target on the sky. Further information about the observational datasets can be found in (Jafarzadeh et al., 2021; Henriques et al., 2022).

3 Results on active regions from ALMA observations

3.1 Full-disk solar images

A first comparison of the full-disk solar images observed with ALMA with those observed in other UV and visible wavelengths was first presented in Alissandrakis et al. (2017) and further explored by Brajša et al. (2018). These authors utilized full-disk images obtained in Bands 3 and 6 (100 and 239 mHz, respectively), following the method of White et al. (2017), in the period 17–20 December 2015. They were able to compare these ALMA brightness temperature maps with simultaneous full-disk solar images using an Hα filter (NISP/NSO at the Cerro Tololo Observatory), in the He I 1083 nm line core (SOLIS/NSO), and with the AIA/SDO UV images and HMI/SDO magnetograms. The FWHM of the beam of these single-disk observations is 27″ at 239 GHz and 60″ at 100 GHz. At this resolution, in agreement with previous observations with similar or better resolution (Bastian et al., 1993; Lindsey and Kopp, 1995; Loukitcheva et al., 2014; Iwai and Shimojo, 2015), plages are the most prominent feature on the disk at 239 GHz, and only slightly

2 ALMA data are available for download at https://almascience.nrao.edu/aq/.

less so at 100 GHz. Active regions were found to be brighter than the surrounding quiet Sun, as also expected from the theoretical modeling. Alissandrakis et al. (2017) noted that the one large sunspot visible on the disk was easily visible at 239 GHz but only barely detectable at 100 GHz, perhaps in part due to the lower spatial resolution. Brajša et al. (2018) found that the sunspot was not only cooler than the surrounding plage, but also than the quiet Sun regions. At wavelengths around ~(1–5) mm, the brightness temperature of sunspots is expected to rise above that of the quiet Sun and the wavelength of this transition in the temperature contrast can be used to validate the temperature profiles of the various 1-D sunspot models (Loukitcheva et al., 2014).

de Oliveira e Silva et al. (2022) (this volume) used the brightness temperatures of AR 12470 obtained at 17 mm with the Nobeyama Radioheliograph (NoRH), and in Band 3 (3 mm) and Band6 (1.3 mm) derived from ALMA full-disk single-dish data, to construct a data-constrained model of the solar AR atmosphere. By modifying 5 parameters in the standard quiet Sun atmospheric model: the chromospheric gradients of temperature and electron density, the coronal temperature and density, and the TR height, the authors achieved a general agreement between the sunspot brightness synthesized from the model height profiles and the brightness values measured from the full-disk ALMA images. Their model indicates that the chromosphere above the sunspot umbra is compressed and the rise to transition region temperatures begins at about 1000 km above the surface. Instead above the penumbra and plage regions, the chromosphere is more extended and the transition region begins at 1800–2000 km .

3.2 Sunspots

3.2.1 Thermal structure

Single-dish measurements at mm wavelengths are not able to provide sufficient spatial resolution required to isolate brightness temperature of sunspots from their surroundings due to limitations of the antenna size. Previously, the highest spatial resolution with a single antenna was achieved in sunspot observations with the James Clerk Maxwell Telescope (JCMT) at 0.35, 0.85, and 1.2 mm by Lindsey and Kopp (1995), with spatial resolutions ranging from 6″ FWHM at the shorter wavelengths up to 16″ at 1.2 mm (analogous to ALMA's Band 6). These observations found that sunspot umbrae at these wavelengths appeared colder than the surrounding quiet Sun, with temperatures below 4000 K at 0.35 mm, rising to 5000 K at 1.2 mm, indicating the presence of a positive temperature gradient in the upper atmosphere of the umbra and penumbra, similar to the quiet Sun.

However, much improved spatial resolution can be achieved by employing interferometric observations. White et al. (2006) reported observations of a sunspot with the 10-element Berkeley-Illinois-Maryland Array (BIMA) at 3.5 mm where the spatial resolution of $\approx 10''$ was achieved. In this interferometric observations the sunspot was found to be the darkest feature in the map, but the resolution was not enough to resolve the umbra (Loukitcheva et al., 2014). They also observed fluctuations in the active region with the predominant periods in the 400–900 s range, but the spatial smearing meant it was not possible to spatially separate oscillatory signals. Only with ALMA, an interferometric system consisting of many elements, did it become feasible to study the sunspot's chromospheric structure with greater detail.

Iwai et al. (2017) presented the first analysis of the ALMA Band 3 mosaic image of the large sunspot in AR 12470 obtained with the spatial resolution of $4.9'' \times 2.2''$ at the wavelength of 3 mm. The map of the sunspot with clearly distinguished umbra and penumbra was compared with UV, EUV, and optical images observed by IRIS, AIA, and HMI.

The achieved spatial resolution allowed for the first time the fine structure of a sunspot's umbra to be resolved with mm observations of the chromosphere and these authors detected a surprising umbral brightening, nearly as bright as the surrounding plage, in the core of the large sunspot umbra (Figure 1A). The enhanced central emission was found to correspond to a temperature excess of 800 K relative to the surrounding penumbral region. Similar bright features near the center of the umbra, adjacent to a partial lightbridge, were detected in the 1330 and 1,400 Å IRIS images, their location was found to be close but not identical to the mm feature. The lightbridge itself was not apparent in the ALMA Band 3 image. Surprisingly, no clear cospatial counterpart of the mm umbral enhancement was found in the AIA 1700A, 304A, or 171A channels, although they showed generally similar large-scale structure of the AR plage as in the mm image. Brajša et al. (2021) analyzed the same active region mosaic and confirmed the umbral brightening. These authors also identified several correspondences between temperature enhancements in the region surrounding the sunspot and chromospheric fibrils and coronal bright points seen in several AIA/SDO channels (Figure 2).

However, Iwai et al. (2017) could not make clear conclusions about the origin of the central brightness from the available observational data. The authors suggest at least three possible explanations of the discovered brightness feature were proposed. According to a first explanation, the observed central brightness could be an intrinsic property of sunspots, not detected before only because of the insufficient resolution of earlier observations. In favor of this explanation is the fact that similar brightness enhancement in the umbral center was also seen in the Band 3 observations on the following day, implying that it is a steady or recurrent phenomenon. Moreover, the brightness of the central umbral feature is in agreement with some of the umbral atmospheric models (see, e.g., Loukitcheva et al., 2017, and

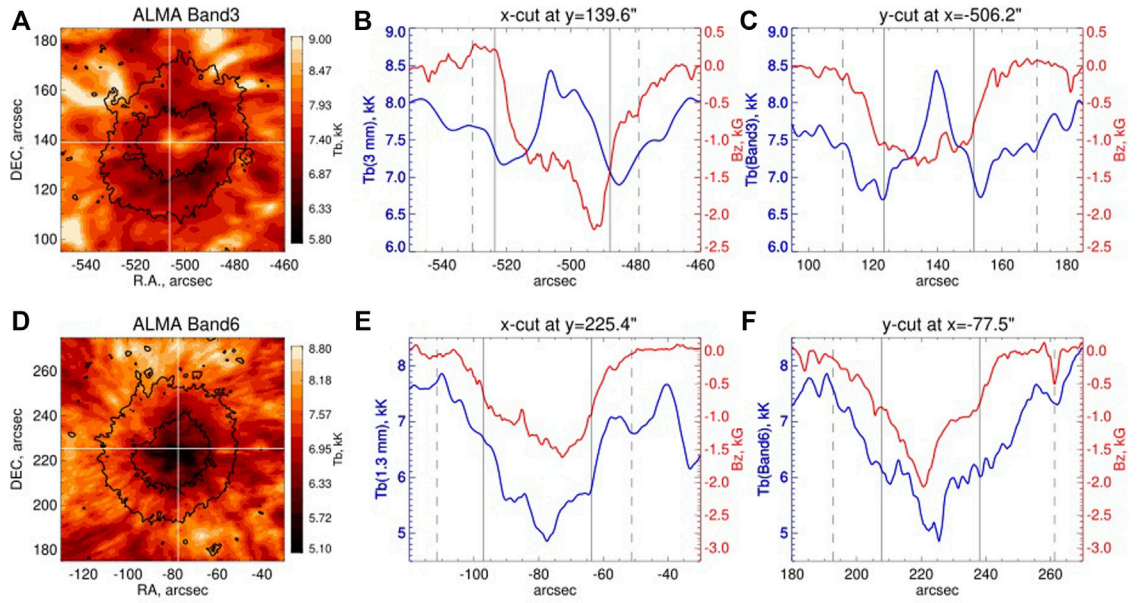

FIGURE 1
ALMA mosaic images of the sunspot in AR 12470 at 3 mm **(A)** and at 1.3 mm **(D)**. The color bars correspond to the displayed range of mm brightness. Profiles of the mm brightness (blue, left axis) and of the longitudinal component of the magnetic field (red, right axis) for **(B)** the x-cut at y = 139.6, **(C)** the y-cut at x = −506.2 through the brightest umbral pixel at 3 mm; **(E)** the x-cut at y = 225.4, **(F)** the y-cut at x = −77.5 through the darkest umbral pixel at 1.3 mm. The black lines indicate the positions of umbral and penumbral boundaries along the cuts. Adapted from Loukitcheva et al. (2017).

below). Terminologically this would mean that not an "umbral brightness enhancement" but rather a "penumbral darkening" was observed. These different brightness temperatures do not necessarily indicate relative temperatures at the same height in the atmosphere for these features, but may be a manifestation of the difference in heights of formations of the millimeter continuum in the sunspot and penumbra due to distinct electron density profiles in the various structures.

The observed brightness enhancement could also be a signature of dynamic umbral flashes, often seen as brightenings in the cores of chromospheric spectral lines, such as Hα and the Ca II IR triplet, due to the passage of the shock waves in the umbral chromosphere. This scenario is supported by a recent study of Chai et al. (2022a), Chai et al. (2022b), (see Sect. 3.2.2), who detected the presence of the 3-min oscillations in the umbra analyzing the 1-hour observational set in Band 3 from the following day, 17 December 2015. The observed temperature fluctuations in the sunspot of as much as ± 500 K, comparable to the magnitude of the temperature excess seen in the snapshot observation from the mosaic.

And the final explanation proposed in (Iwai et al., 2017) was that the observed umbral brightness enhancement is related to signatures of downflowing coronal material interacting with the dense lower atmosphere (seen in coronal plumes), as its location corresponded to footpoints of coronal loops seen at 171A inside the umbra, and inside the umbra there was also a region bright at 1330 and 1400A. Finally, it was concluded that additional millimeter observations with better spatial and temporal resolution are required to understand the detected umbral brightness enhancement.

Loukitcheva et al. (2017) extended the study of Iwai et al. (2017) by analyzing the observations of the same sunspot but in Band 6 (a wavelength of 1.3 mm), and by comparing ALMA observations at the two wavelengths with the predictions of sunspot umbral and penumbral models. To account for radial brightness inhomogeneities seen in the structure of sunspot umbra and penumbra in both Band 3 and Band 6, the authors distinguished between inner and outer umbra, as well as between inner and outer penumbra when analyzing ALMA images. The distribution of brightness in the umbra in Band 6 was found to differ significantly from the distribution in Band 3 (Figure 1). In contrast to the Band 3 central brightness enhancement, the central part of umbra showed a temperature depression of 700 K relative to the QS level in Band 6, making it the coolest (≈5300 K) feature of the sunspot in Band 6 maps, while the outer umbra is significantly (≈1000 K) brighter.

ALMA sunspot observations have also resolved for the first time the penumbral structure in both bands. In Band 6 the penumbra was, on average, ≈ 1000 K hotter than the umbra with the larger difference between the inner and the outer parts of the penumbra (≈500 K) than between the outer penumbra and the surrounding plage (≈150 K). This result agrees with the presence

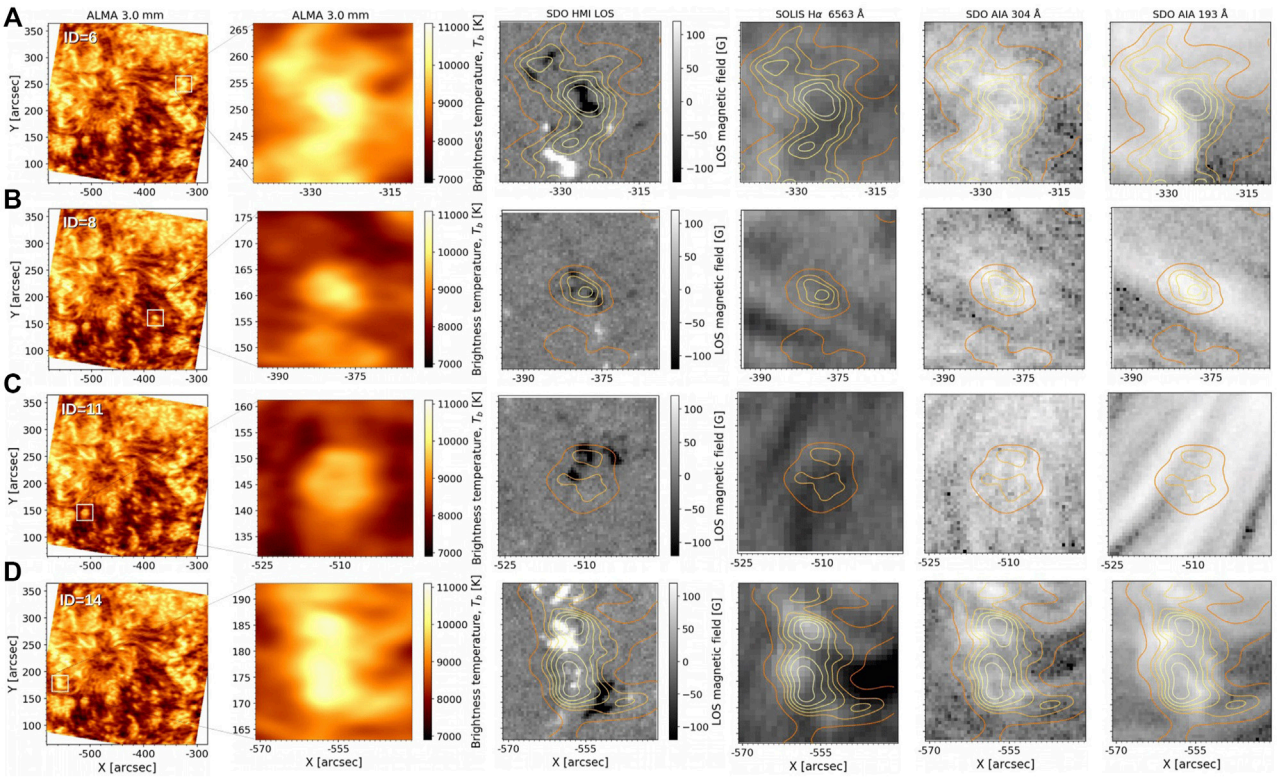

FIGURE 2
(A–D) four examples of comparison between ALMA Band 3 brightness structures (second column) observed within the FOV of the AR 12470 on 16 December 2015 (first column) and HMI/SDO magnetogram (third column), SOLIS Hα core 6563A (fourth column), AIA/SDO 304 and 193A (fifth and sixth columns, respectively). ALMA contours at 9000, 9500, 9750, 10000, 10250 and 10500 K are overlaid in each panel. White rectangles in the first column mark the structures of interest. From Brajša et al. (2021). Reproduced with permission © ESO.

of the superpenumbra (see, e.g. Giovanelli and Jones, 1982; Leka and Metcalf, 2003; Solanki, 2003), the idea that at chromospheric heights the sunspot's magnetic field expands significantly beyond the photospheric boundary of the sunspot, so that there is essentially no difference in the appearance of the outer penumbra and the adjacent AR plage, which is dominated by sunspot magnetic fields. In Band 3 the penumbra shows up as a dark ring surrounding the umbra, with the inner part ≈100 K cooler than the outer part of the umbra and cooler than the QS. A clear brightness temperature gradient was found within the penumbra at both wavelengths (Figure 1) with brightness increasing from inside to outside by ≈ (400–500) K. In addition, the structure of the outer penumbra at both wavelengths was similar to that of the surrounding plage region.

The measured brightness temperatures for different parts of umbra and penumbra at the two ALMA wavelengths were compared with the expected mm brightness calculated from a number of selected sunspot models (Figures 3, 4). The models differ from each other, as well as from the reference QS model of Fontenla et al. (1993), in the location and extension of the temperature minimum region and in the height of the transition region. For improved wavelength coverage, the observed ALMA brightness in the two bands was supplemented with the earlier measurements at a number of other mm wavelengths.

None of the analyzed umbral models provided an outstanding fit to the observations. However, the umbral model of (Severino et al., 1994) showed the best agreement for the ALMA observations of the inner umbrae in both bands among the models considered in this work. It also provided the best fit to the sunspot data from the earlier works (Figure 3). The authors concluded that the chromospheric temperature gradient in the model resembles the actual temperature gradient in the umbral chromosphere. According to this model, the bulk of the emission in Bands 6 and 3 comes from the heights of 1100 km and 1500 km in the umbral chromosphere, respectively, while the QS emission, estimated from the FALC model, is formed ≈500 km higher at both wavelengths. This model is consistent with that derived by de Oliveira e Silva et al. (2022) (2022, see Section 3.1) using a data-constrained model based on three different millimeter wavelengths and extrapolated chromospheric magnetic fields.

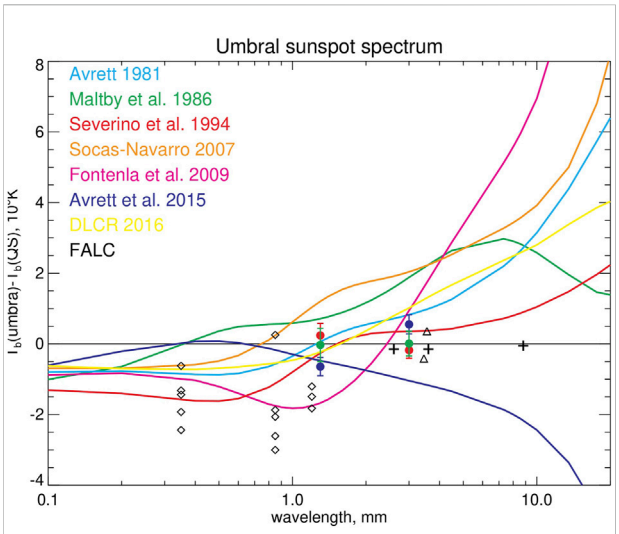

FIGURE 3
Difference between the umbral brightness (in temperature units) and the QS brightness, plotted as a function of wavelength for the umbral models, including the models of Avrett (1981), of Maltby et al. (1986), of Severino et al. (1994), of Socas-Navarro (2007), of Fontenla et al. (2009), of Avrett et al. (2015), and of de la Cruz Rodríguez et al. (2016), marked as DLCR 2016. The individual models are identified by color as indicated in the figure. The solid black line is the reference QS atmosphere FALC. The colored filled circles and error bars indicate the umbral ALMA mean brightness values together with the rms values for the inner umbra (blue), outer umbra (red), and the whole umbra (green) at 1.3 and 3 mm. The figure also depicts the BIMA measurements obtained at 3.5 mm by Loukitcheva et al. (2014) at a resolution of 12″ (triangles), the measurements at 0.35, 0.85, and 1.2 mm (diamonds) made by Lindsey and Kopp (1995) at a resolution of 14″–17″; and brightness observations at 2.6 and 3.5 mm obtained from the Nobeyama 45 m telescope by Iwai and Shimojo (2015) at a resolution of 15″, and at 8.8 mm from the NoRH by Iwai et al. (2016) at a resolution of 5″–10″ (plus signs). From Loukitcheva et al. (2017). Reproduced by permission of the AAS.

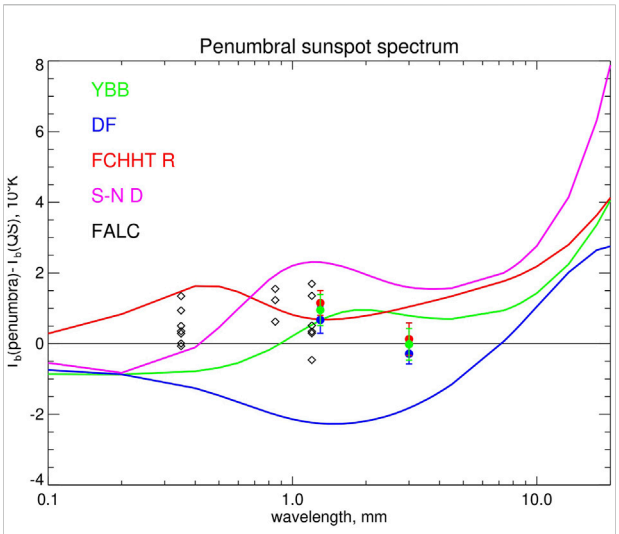

FIGURE 4
Same as in Figure 3 for the penumbral models of Yun et al. (1984) (1984; green), Ding and Fang (1989) (1989; blue), Fontenla et al. (2009) model R (red), and Socas-Navarro (2007) model D (violet). The colored filled circles and error bars indicate the observational penumbral mean values with the rms values for the inner penumbra (blue), the outer penumbra (red), and the whole penumbra (green) at 1.3 and 3 mm. The diamonds indicate the brightness measurements at 0.35, 0.85, and 1.2 mm from Lindsey & Kopp (1995). From Loukitcheva et al. (2017). Reproduced by permission of the AAS.

One notable difference is that their model does not reach the same low temperatures in the sunspot umbra (T_{min} of 4900 vs. 2900 K). Further work by Bogod et al. (2019) combined the ALMA sunspot observations with data from RATAN-600 in the frequency range 3–17 GHz and showed that the crucial wavelengths for capturing the transition region temperature rise lie between 3 and 18 mm.

In contrast to the numerous umbral models, only a few penumbral models that include the chromosphere have been published. The authors used four penumbral models from the literature for comparison with the observed brightness at the two ALMA wavelengths and also the penumbral measurements at short wavelengths from Lindsey and Kopp (1995). No penumbral model gave a really satisfactory fit to the analyzed measurements (Figure 4). Interestingly, the two models that came closest to being consistent with the data were found to be quite distinct in their thermal profiles and in the heights at which the 1.3 and 3 mm radiation is emitted. These results prevented the authors from making any certain conclusion about the best model fit to the penumbral data. The penumbral model derived by de Oliveira e Silva et al. (2022) reaches a similar minimum temperature as their umbral model, but a much slower decrease in density which correspondingly pushes the transition region ~800 km higher.

The work of Loukitcheva et al. (2017) demonstrated that multi-wavelength ALMA data can be used to validate or rule out models of the umbral/penumbral atmospheres, and can also add important constraints to any new empirical models. At the same time, for a definite determination of the temperature gradient in the solar chromosphere at the heights where mm emission is formed, additional ALMA sunspot observations are required.

3.2.2 Sunspot oscillations

Observations of the same AR 12470 were used by Chai et al. (2022a,b) to study oscillations and wave propagation in sunspots for the first time. The one-hour ALMA Band 3 sequence acquired with a cadence of 2 s on 2015 December 17 was analyzed together with Hα spectral imaging observations from the Goode Solar Telescope (GST) operating at the Big Bear Solar Observatory, AIA/SDO and IRIS. Prominent 3-minute oscillation power was detected within the umbral boundaries in the ALMA data (Figure 5D), being stronger in the western part and weaker in the eastern part of the umbra. ALMA temperature variations

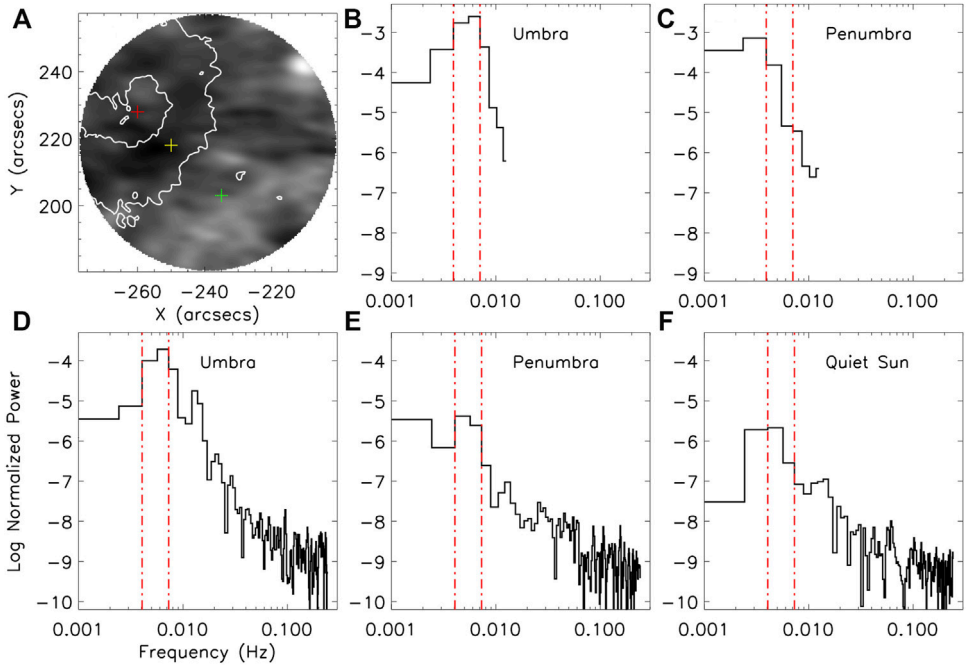

FIGURE 5
(A) ALMA Band 3 image of AR 12470 with 3 marked locations: in the sunspot umbra (a red plus sign), penumbra (yellow), and a quiet-Sun region (green); and **(B–F)** corresponding Fourier power spectra. The white contours in panel **(A)** mark the boundaries of the umbra and the penumbra, respectively. Panels **(B,C)** display the Fourier power spectra of GST Hα near blue wing (–0.4 **(A)**. **(D–F)** of ALMA Band 3 data. The 3 min oscillation range is marked with red dotted–dashed lines. From Chai et al. (2022a). Reproduced by permission of the AAS.

demonstrated a sawtooth pattern (a tendency for a gradual rise and a steeper drop), which together with the amplitudes of brightness variations and phase relative to Hα Doppler velocity from GST, provided new exciting information about the three-minute-oscillatory behavior in sunspots. The authors concluded that the mm temperature fluctuations are in general consistent with propagating acoustic waves, although the nature of the asymmetry (gradual rise, steeper fall) was opposite what would be expected due to simple nonlinear steepening. Interestingly, penumbral 5 min oscillations, that were found in Hα (Figure 5C), were not detected in the ALMA Band 3 data (Figure 5E).

3.3 Comparison of ALMA brightness with other chromospheric diagnostics

Comparisons between different observational parameters provide a key to the assessment of the diagnostic power, as well as to studying the physics of the observed solar structures. For the chromospheric diagnostics, good agreement is expected between the gas (radiation) temperatures deduced from the intensities of the millimeter and UV measurements, based on earlier low-resolution observations and expectations about the heights of formation from solar atmospheric models. With the onset of high-resolution and high-cadence ALMA observations, detailed comparison of spatially resolved morphological features within active regions has also become possible.

Bastian et al. (2017), Bastian et al. (2018) presented the first quantitative comparison between ALMA mm and IRIS UV chromospheric emissions from the sunspot umbra, plage, and quiet-Sun regions observed in AR 12470 on 2015 December 18 in Band 6. The authors reported a clear correlation between ALMA Band 6 (1.25 mm) brightness temperatures and radiation temperatures inferred from IRIS/Mg II h2v and h2r peak intensities, although with significant scatter (Figure 6). Additionally, a compressed range of radiation temperatures of Mg II lines as compared to the Band 6 brightness temperatures and an offset between the temperatures at the two wavelengths were detected. Among the considered AR features, the correlation coefficient was found to be higher in the umbra and plage, and lower in the quiet Sun. They attributed some of the scatter in the between this ALMA and IRIS diagnostics to the decoupling of the Mg II source function from the local conditions, as well as differences in the heights of formation of the different spectral lines and continuum emissions.

Using the same ALMA and IRIS observations Jafarzadeh et al. (2019) obtained similar results, comparing ALMA Band

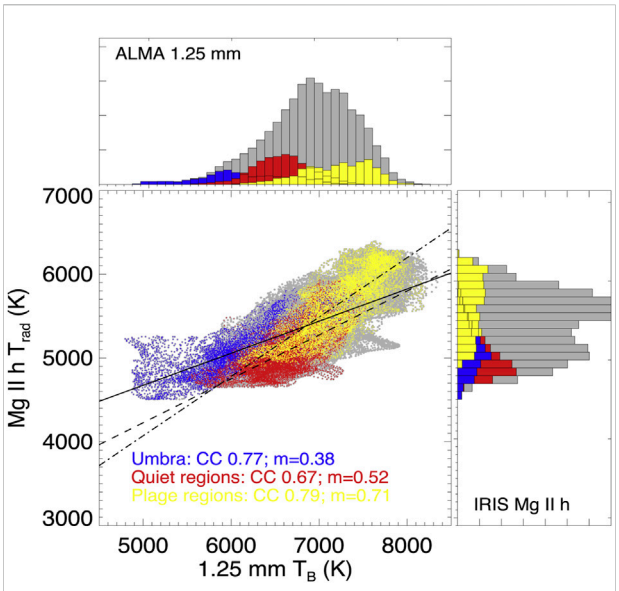

FIGURE 6
A scatter plot of IRIS Mg II h line radiation temperatures versus the ALMA 1.25 mm brightness temperatures together with the corresponding histograms. Gray points represent all pixels; blue points for the umbra; red for the quiet-Sun areas; and yellow for the plage. Linear fits to pixels in the umbra, quiet, and plage pixels are shown with a solid, dashed, and dotted–dashed line, respectively. From Bastian et al. (2018). Reproduced by permission of the AAS.

6 brightness temperatures with radiation temperatures from Mg II for each of its h and k line features individually. They took into account the observation times for each location in the IRIS slit raster and ALMA mosaic, which sampled the region with overlapping but different patterns. For their analysis, they considered subsets of pixels where the sampling time difference in the pixel-to-pixel relationships was smaller than 2 or 0.5 min. As a result, the authors used only 28% and 8% of the spatial pixels, respectively, with only very few data points for analysis in the umbra itself. Good pixel-to-pixel correlations were found between most of the IRIS UV channels and ALMA Band 6 in all active region features (except the umbra), with the strongest correlation for the pair C II line in the FUV - ALMA Band 6. The authors concluded that the spatial variation of the UV radiation temperatures is similar to that of the ALMA Band 6 in these regions. However, we note that many of these active region features have relatively high brightness temperatures at 1.25 mm compared to quiet Sun regions, where the correlation between temperatures derived from Mg II and ALMA Band 6 might not be so strong.

In the umbral pixels, Jafarzadeh et al. (2019) found a very low correlation between the temperatures derived from Band 6 and Mg II h, much lower than what was found by Bastian et al. (2017, 2018), 0.04 vs. 0.77, respectively. Moreover, improved but still low correlations were detected for all the considered IRIS diagnostics (Figure 7). The authors speculated that such a significant difference in the umbral correlation coefficients could be due to a large uncertainty arising from the very few data points used. It might be important that the exact criteria for selecting umbral regions is somewhat different between these two works, and the mask used by Bastian et al. (2017) might have included some of the inner penumbral regions. However, Jafarzadeh et al. (2019) noted that in the umbra the time differences between diagnostics can be particularly essential, since dynamic events, e.g., umbral oscillations, can produce changes in the umbra on time scales shorter than 2 min, with their Band 6 vs. Mg II h correlation coefficients showing a slight improvement in the umbra when the allowable time differences between observables were reduced from 2 to 0.5 min (but interestingly no change for the Mg II k or C II correlation coefficients).

Recently Chintzoglou et al. (2021a) reported much lower correlation coefficients found between Mg II and ALMA Band 6 in the leading part of NOAA AR 12651 observed on 2017 April 22. The observed FOV contained parts of a plage region with strong magnetic flux that included impulsive behavior such as dynamic fibrils. The authors employed an empirical approach and isolated plage elements from their surroundings using a magnetogram signal threshold of 100 G and also excluded such elements as pores and cool features in the superpenumbra. After applying these strict segmentation criteria and achieving very high time synchronization between IRIS and ALMA observations, the highest correlations were obtained for the combinations of ALMA Band 6 with Si IV or C II, but the degree of correlation between Mg II k and ALMA Band 6 was found to be relatively poor (~0.5). The authors claimed that the scatter in the chromospheric diagnostics comparison is more significant than was previously thought and based on the obtained correlation coefficients speculated that even though both Mg II and ALMA Band 6 are sensitive to a similar range of temperatures, the formation height for ALMA Band 6 emission is above that of Mg II for most wavelengths along the Mg II line. Chintzoglou et al. (2021a) concluded that all three diagnostics, ALMA Band 6, C II, and Si IV, have formation heights relatively close to one another and are sampling similar parts of structures in the plage.

However, Hofmann et al. (2022) showed evidence based on spectroscopic inversions of the Ca II 8542 Å and Na I D_1 5,896 Å lines compared with simultaneous ALMA observations that the height of formation of the Band 6 line can be highly variable, as was already explored using simulations by Loukitcheva et al. (2015). In particular, the authors suggest that relatively high temperatures (> 7500 K) observed in Band 6 are observed in regions where the height of formation of the continuum emission is relatively high in the atmosphere, while cooler temperatures arise when the opacity along a given line-of-sight is lower and the emission arises from deeper in the atmosphere. Thus correlations, or the lack thereof, found for selected types of

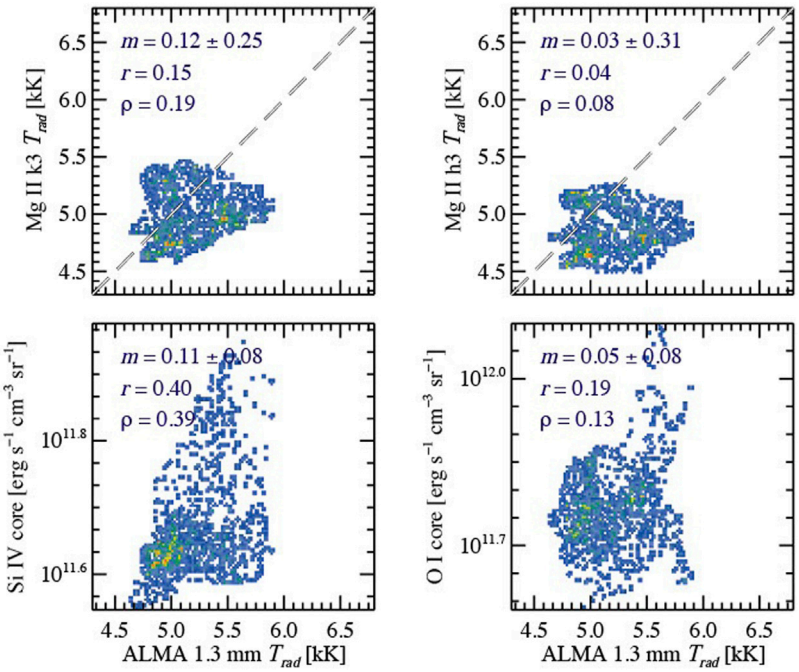

FIGURE 7
Scatter plots of radiation temperatures for IRIS NUV and FUV line features versus the ALMA 1.25 mm brightness temperatures limited to pixels in the umbral region. The density of the scatter points is denoted with the colours: the highest density number is coloured in red, the lowest density in dark blue. The regression slope of the linear fit (m), the Pearson correlation coefficient (r), and the Spearman's rank correlation coefficient are listed for each relationship. From Jafarzadeh et al. (2019).Reproduced with permission © ESO.

solar features, or that tend to isolate a specific range of brightness temperatures, do not necessarily apply to other regions or define an overall height of formation for the millimeter continuum at a given wavelength. This may be part of the underlying discrepancies in the measured correlations among these different studies.

3.4 Thermal diagnostic of plages

While the characterization of the thermal structure above sunspots needs more observations, sampling multiple sunspots, our understanding of the temperature above strong magnetic field concentrations above plages and network regions has been informed by multiple ALMA observations (see Jafarzadeh et al., 2021, for an overview of several plage observations). In general, above strong concentrations of magnetic fields, the brightness temperature in Band 3 tends to show regions of high temperatures, reaching up to 10–12 kK in isolated regions of a few arcseconds in diameter (i.e., marginally resolved with typical beam widths), embedded by a generally diffuse area of temperatures of 8–10 kK (above the quiet Sun average of 7.3 kK). In Band 6, similar locations with high temperatures (up to 9–10 kK) are sometimes seen above strong magnetic network. There have been a few cases where the same region was observed with both Bands in sequence, and a similar distribution of hot features can be seen in both bands (see Hofmann et al., 2022, for a direct comparison of a plage in both ALMA bands).

One notable feature of the plage and network observations is that features with high brightness temperatures are seen to extend away from the photospheric magnetic field concentrations. These features are seen to project approximately 10 arcseconds (7 Mm) into the internetwork. Beyond or in between these features, the brightness temperatures drop down to 6 kK or lower. They are most easily seen in the Band 3 observations, but are also sometimes present in Band 6 as well.

By comparing these features with simultaneous observations of the Hα line obtained with IBIS, Molnar et al. (2019) showed that these features correspond to the chromospheric fibrils extending outward from the magnetic concentrations and expanding into a more horizontal canopy. Even more intriguing, they showed a very direct relationship between the ALMA fibrils and the structures seen in maps of the width of the Hα line profile (see Figure 8). This was not entirely unexpected based on earlier studies showing the temperature sensitivity of

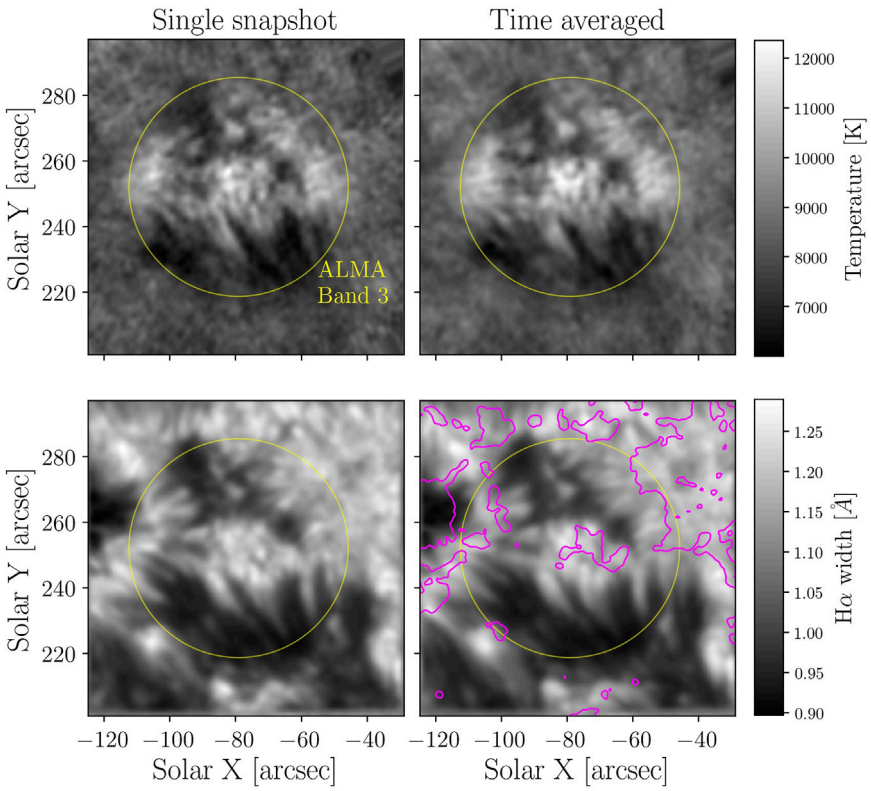

FIGURE 8
Maps of ALMA intensity (top row) and IBIS Hα line width (bottom row), the latter smoothed to match the resolution of the ALMA data. The left column shows the two parameters at single time step of the observations, while the right column shows the same two parameters averaged over the 10 minutes of a continuous ALMA observation block. The yellow circle has a diameter of 66″, slightly larger than the usable FOV of ALMA. The purple contours show areas with magnetic field strength above 500 Gauss, as measured by HMI. From Molnar et al. (2019). Reproduced by permission of the AAS.

the Hα line width (Cauzzi et al., 2009) and theoretical investigations of Hα line formation in the solar chromosphere (Leenaarts et al., 2012). The point-wise relationship between the brightness temperatures and the line widths was essentially linear, but the magnitude of the broadening of the Hα line (ranging from 0.9–1.25 Å) was greater than what would be produced by the temperature range indicated by the ALMA observations (6–12 kK). The authors use the 1-D FAL model to synthesize the millimeter continuum and Hα line profile, essentially reproducing the observed relationship. They find the observed coupling between these two diagnostics is in large part driven by changes in the $n = 2$ level population of hydrogen. As this parameter increases in the atmosphere, it also leads to and increased ionization fraction of hydrogen, a greater electron density, and a higher height of formation of the 3 mm continuum, closer to the steep temperature rise of the transition region. At the same time, a larger column mass of $n = 2$ hydrogen atoms leads to an opacity broadening of the Hα line (similar to a curve-of-growth effect). Tarr et al. in this collection reproduce the strong correlation between the Band 3 brightness temperature and Hα line width in their data set, but observe a more bimodal distribution, with two different slopes.

In general, higher temperatures are seen above and around plages and magnetic network, compared to internetwork and the quiet Sun average. Disentangling the extent this reflects an actual increased temperature at comparable densities to the quiet Sun, or whether it is the result of a larger electron density and a corresponding increase in the height of formation of the millimeter continuum, will require additional multiwavelength observations and improved modelling.

3.5 Active region transient brightening and heating events

The two most widely discussed mechanisms for chromospheric heating include magneto-acoustic wave dissipation and small-scale magnetic reconnection (Carlsson et al., 2019). Possible signatures of both mechanisms have been reported in ALMA active region observations in the

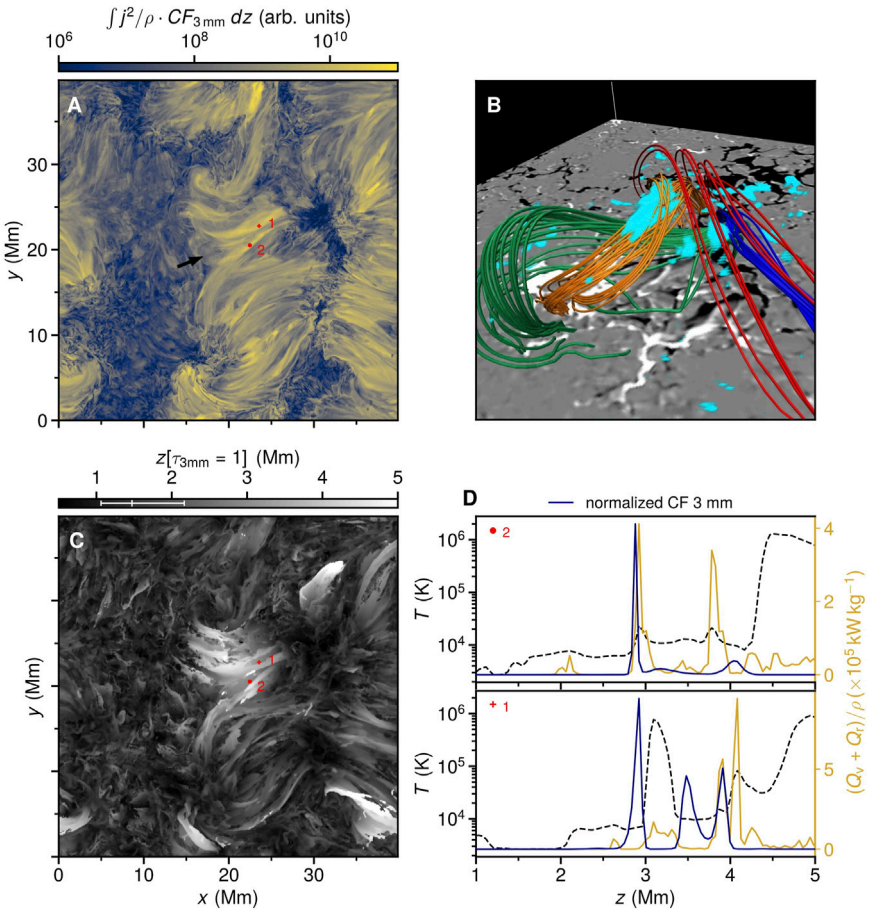

FIGURE 9
(A) Integrated j^2/ρ weighted by the contribution function of the Band 3 emission (CF3mm); **(B)** Extrapolated magnetic field lines overlying photospheric magnetogram with the CF3mm depicted with blue shade from the region indicated by the arrow in **(A)**; **(C)** heights of formation of the Band 3 emission; **(D)** temperature (dashed lines), total heating rates per mass (yellow lines), and normalized CF3mm (dark blue lines) as a function of height at two locations indicated in **(A)** and **(C)**. From da Silva Santos et al. (2022a). Reproduced with permission © ESO.

form of brightness enhancements, some of them quasi-periodic, with spatial scales at the limit of the current ALMA resolution for solar observations (~ 1″) and timescales ranging from tens of seconds to minutes. When combining ALMA observations with chromospheric diagnostics formed in the UV or visible, the physical interpretation often relies on the techniques of spectroscopic inversions or by comparison with the synthetic output of advanced 2D or 3D r-MHD models that correspond to the observed features.

Signatures of magnetic reconnection at the heights of the chromosphere and transition region might be present for features such as Ellerman bombs (EBs), ultraviolet bursts (UVBs), and flaring (dynamic) AR fibrils (FAFs). Some of these were studied by da Silva Santos et al. (2020b) in ALMA Band 3 observations of a group of pores and an arch-filament system south-west of a large sunspot in NOAA AR 12738 on 13 April 2019. The visibility of reconnection events at mm wavelengths, their formation heights, as well as their role in the energy balance in the chromosphere, were investigated using a snapshot of a Bifrost 3D r-MHD simulation of flux emergence. The authors found multiple bright compact mm-bursts (analogues of small nanoflares) with the temperatures above 9 kK up to 14 kK, with corresponding brightenings seen in the AIA EUV images from transition region and coronal heights (e.g. 304, 171 Å), but not the UV continuum at 1600 and 1700 Å. They suggest that these heating events could be the millimeter emission from UVBs, but did not have simultaneous IRIS observations to confirm that possibility. They used the temperature profiles derived from the AIA images to estimate that up to 5% of the signal at 3 mm could come from higher-temperature coronal plasma along the line of sight. They also detected FAF-like events in the Band 3 brightness, showing up as rapid motions of hot (over 10 kK) plasma launched from bright kernels with the visible velocities of 40–300 km/s. The mm FAFs were found

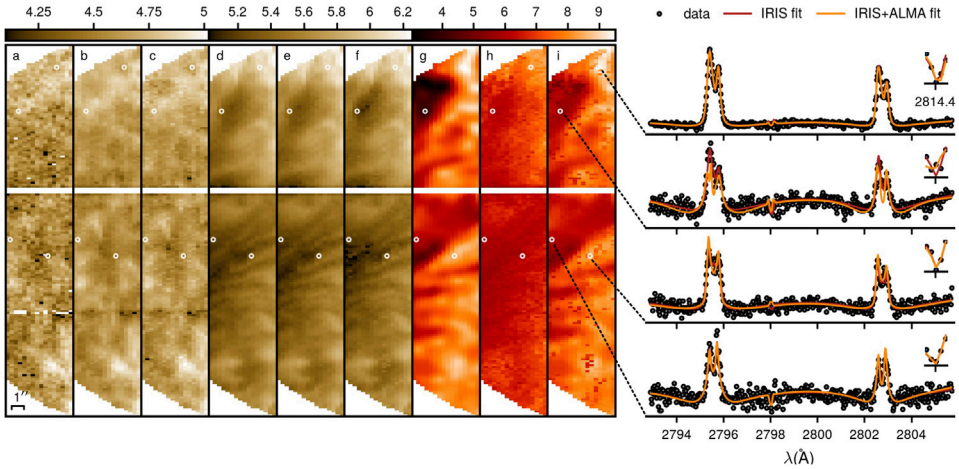

FIGURE 10
Comparison of the observed **(a,d,g)**, synthetic from IRIS fit **(b,e,i)** and synthetic from IRIS + ALMA fit **(c,f,i)** temperature maps (kK) as a function of optical depth in a plage region: for averaged continuum at 2800 A **(a–C)**, for averaged k core wavelengths **(D–F)**, and for Band 6 **(G–I)**. The panels on the right depict observed and synthetic IRIS spectra at selected locations. From da Silva Santos et al. (2020a). Reproduced with permission © ESO.

to correspond to warm canopy fibrils connecting magnetic regions of opposite polarities. At the same time, no EBs were detected in the ALMA Band 3 images at the resolution of the observations (≃ 1.2″).

In a follow-up study, da Silva Santos et al. (2022a) analyzed the same ALMA Band 3 observations together with the optical spectropolarimetric observations from the CRISP instrument (Scharmer et al., 2008) at the Swedish Solar Telescope (SST) in the Fe I 6173A and the Ca II 8542A lines. The authors employed non-LTE STiC inversion package, field extrapolations using a magnetohydrostatic model based on the SST and HMI data, and the 3D r-MHD numerical simulation based on the MURaM code to study the processes of ongoing magnetic flux emergence into a preexisting arch-filament system of AR 12738. They found elongated patches of enhanced (over 3 kK relative to QS values) Band 3 brightness temperatures and bright Ca II 8542A lines profiles at the location of short low-lying chromospheric fibrils, where overlying arch-filament system is seen in absorption in the AIA 304 Å channel. From the computed heating rates and their comparison with the chromospheric diagnostics, the authors concluded that dissipation in current sheets might be, at least, a locally dominant source of atmospheric heating, producing brightenings in chromospheric diagnostics within ARs (Figure 9). The radiative energy losses were estimated to be in the range from 3 to 5 kW/m^2 in regions where the 3 mm brightness temperature is over 9 kK. Although da Silva Santos et al. (2022a) could not unambiguously link the observed millimeter emission to heating in current sheets based on the analyzed data alone, they demonstrated that the ALMA Band 3 emission in their observations forms above Ca II 8542A line, but below the He II 304 Å line, strongly suggesting that it originates in this shear layer. The heating itself occurs on spatial scales that are not resolved with the ~ 1.2″ FWHM beam size of their observations.

3.5.1 (Magneto-)acoustic shocks

The diagnostic value of the ALMA measurements in the framework of spectroscopic inversions using some of the first ALMA data in Bands 3 and 6 was studied by da Silva Santos et al. (2020a). The authors performed inversions of IRIS Mg II observations and used ALMA data as an additional constraint for the STiC non-local thermodynamic equilibrium (NLTE) inversion code. ALMA and IRIS co-observed part of a plage in active region NOAA AR 12651 on 22 April 2017. The work demonstrated that the combination of IRIS and ALMA is a powerful tool for diagnosing a wider range of physical conditions in the atmosphere than IRIS alone, and the Mg II lines alone may not be sufficient to infer accurate chromospheric temperatures and microturbulence due to well-known NLTE effects (Figure 10). The presence of localized enhanced brightness in ALMA maps of plage was explained as non-equilibrium hydrogen ionization effects following acoustic shocks in the chromosphere driven by the 3–4 min wave oscillations detected in the Mg II lines. Hofmann et al. (2022) performed tests that showed that the non-LTE hydrogen ionization effects need to be taken into account when performing spectroscopic inversions to better estimate the temperatures at chromospheric heights. In their analysis, the authors used only an approximation to the full non-equilibrium

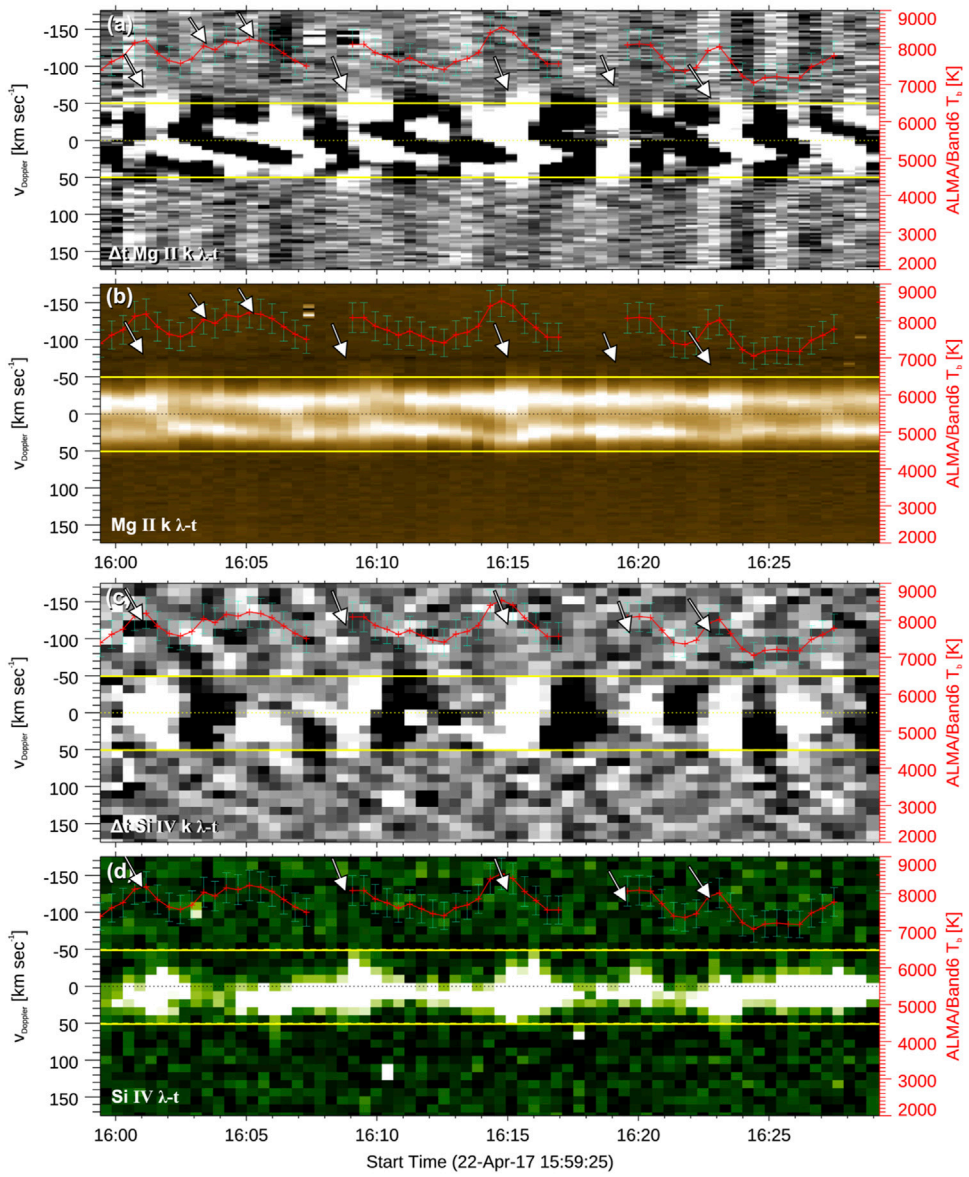

FIGURE 11
Signatures of recurrent shocks in the selected 1″ × 1″ area in plage in the form of the wavelength–t plots for **(B)** Mg II k and **(A)** its time derivative, **(D)** Si IV and **(C)** its time derivative. ALMA Band 6 brightness temperature is overplotted in red in all panels. The rest-wavelength position is plotted with a dotted line in all panels. The increases in mm brightness correlate with blueshifts, suggesting chromospheric heating due to the passing of shocks in Si IV and Mg II (indicated by arrows). From Chintzoglou et al. (2021a). Reproduced by permission of the AAS.

ionisation balance, namely statistical equilibrium, and thus the results of their inversions of ALMA data still have an appreciable uncertainty in the heights of formation. This uncertainty is greater for the millimeter continuum than for spectral lines, since the opacity for the latter is much less sensitive to the electron density. They further showed that the ALMA Band 3 brightness temperatures improved inversion outputs, essentially by enforcing a temperature rise at the top of the chromosphere. However, the inclusion of Band 6 often led to unrealistic atmospheres, likely because poorly constrained estimates of the electron density led to errors in reconciling the height of formation of the 1.2 mm continuum with the overlapping contribution function of the Ca II 8542 Å line.

The work of (Chintzoglou et al., 2021a) also explored the potential of ALMA Band 6 observations for measuring

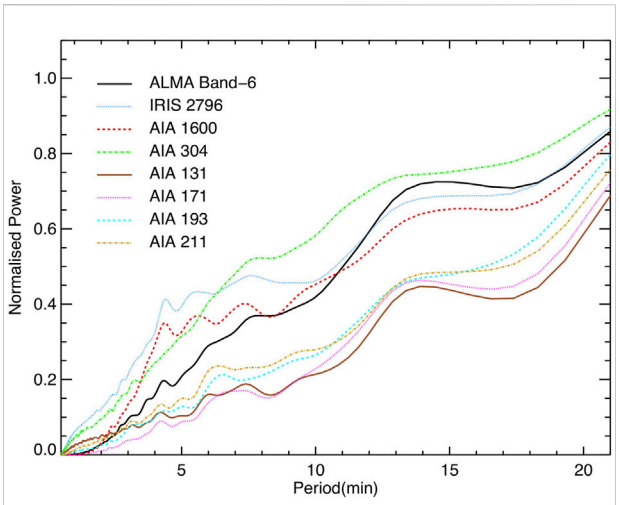

FIGURE 12
Average power spectra of the ALMA Band 6, IRIS 2796 A, and 6 selected AIA passbands in a plage region. From Narang et al. (2022). Reproduced with permission © ESO.

the temporal evolution of plasma temperature in regions dominated by the passage of chromospheric oscillations and presented indications of heating by shocks propagating in the plage chromosphere. In ALMA Band 6 measurements of the brightness temperature in dynamic fibrils with the resolution of $0.7'' \times 0.8''$, the authors detected intensity enhancements of the order of 10%–20% above a basal value of 7500 K with a decay time back down to the basal levels of about 60–120 s. Sometimes these brightenings recurred with withing ≃120 s, and in some cases corresponded to times of blueshift excursions seen in the Mg II k and Si IV lines observed with IRIS (Figure 11).

Recently (Narang et al., 2022), have presented a statistical comparison of oscillations in a plage region with focus on the correlation of power distribution of ALMA oscillations with the oscillations detected in the coordinated observations from IRIS and SDO obtained on 22 April 2017 (2016.1.00050.S.). A presence of oscillations in a wide range of periods (up to 35 min) was found in the

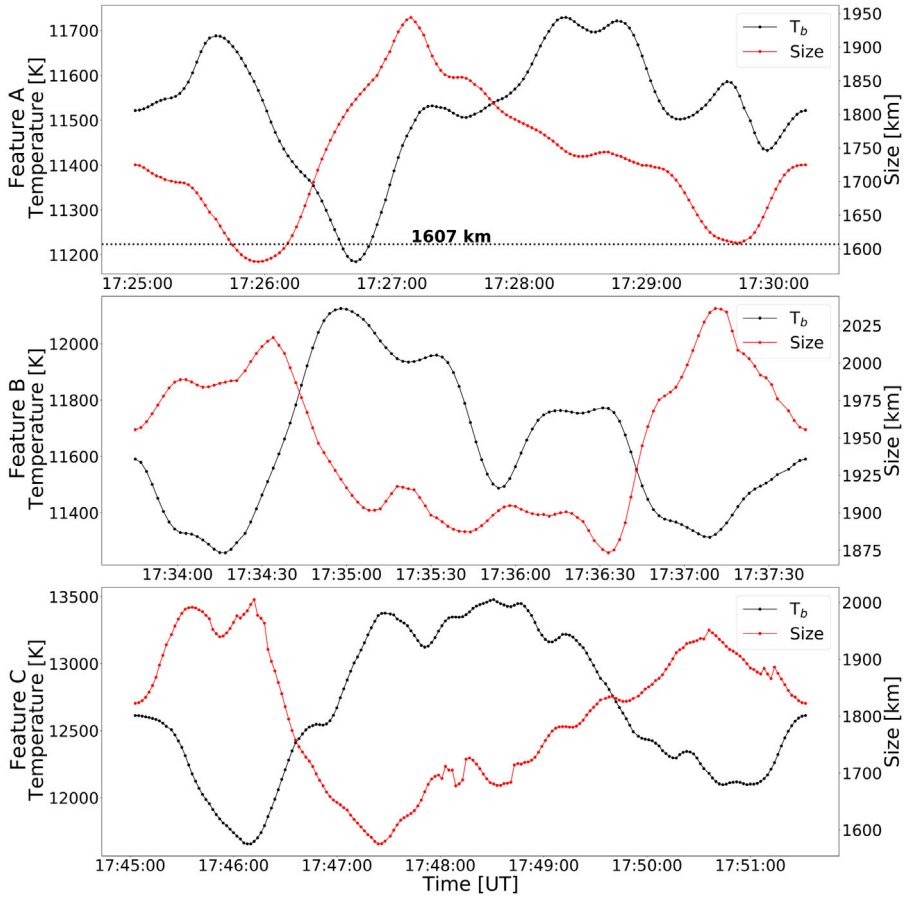

FIGURE 13
Temporal variations in brightness temperature (black, left axis) and size (red, right axis) of the three small bright features detected in a plage region. The horizontal dotted line marks the size of a spatial-resolution element. From Guevara Gómez et al. (2021).

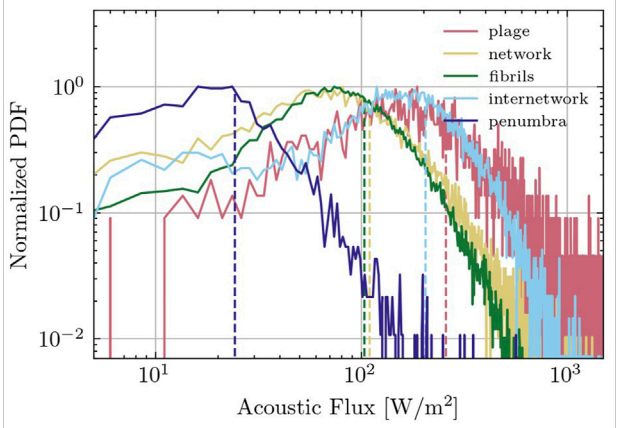

FIGURE 14
Acoustic flux distributions derived from ALMA Bands 3 and 6 brightness data and from the Ca II 854.2 nm line Doppler velocity data based on the RADYN models. The vertical lines mark the medians of the distributions. From Molnar et al. (2021). Reproduced by permission of the AAS.

ALMA and the AIA EUV images, with 12–14 min periods being the most prominent, while shorter dominant periods of 4–7 min were found for the AIA UV images (Figure 12). At the same time, no correlation was found in the spatial distribution of dominant periods and in the power in the considered intervals of periods between ALMA and any other considered diagnostics. The authors speculated that the result could be due to the large variations in the height of formation in the 1.25 mm continuum observed by ALMA. Analyzing the same ALMA plage data, Guevara Gómez et al. (2021) detected high-frequency brightness oscillations with periods less that 2 min in the three small bright features within the Band 3 FOV. The noted an anti-correlation between fluctuations in brightness temperature and variations of size of three features with changes below the resolution of the Band 3 data (Figure 13). The authors suggested that this could indicate the presence of MHD fast sausage-mode waves in them, but such a correlation could also be produced by a time varying beam size during the ALMA time series.

Observational constraints on the chromospheric heating contribution from acoustic waves with frequencies between 5 and 50 mHz were presented in Molnar et al. (2021). The authors studied high frequency dynamics of the chromosphere using coordinated observations from ALMA and the Interferometric Bidimensional Imaging Spectrograph (IBIS) at the Dunn Solar Telescope (DST, Dunn and Smartt, 1991) on 23 April 2017. The obtained high-cadence data set contain spectral observations covering from the upper photosphere and the middle (Ca II 854.2 nm, Hα, and ALMA Band 6) and upper chromosphere (ALMA Band 3). They focused on the velocity diagnostics derived from Ca II 854.2 nm, as tracers of upward propagating compressive waves, and on the brightness temperature fluctuations from ALMA Bands 3 and 6 as indicators of local heating from those waves. The FOV was partitioned into five different classes solar structures: penumbra, internetwork, fibrils, network and plage. The authors found a very similar power-law behavior in the high-frequency Fourier Power Spectrum Densities (PSDs) from 5 to 50 mHz in all the considered chromospheric observables: namely velocity measurements of the Hα and Ca II 854.2 nm line core intensities and velocities, and ALMA Bands 3 and 6 brightness temperatures. The authors found that the slopes of the spectral diagnostics' power laws depend on the observed solar region, in particular, hotter regions (network and plage) exhibit less steep power law slopes than was found in cooler, more dynamic, regions. Tarr et al. in this collection find a similar power law behavior at high temporal frequencies and explore the effects of spatial downsampling and intermittent, ALMA-like temporal sampling on the measured power-spectral density.

Molnar et al. (2021) then used RADYN model runs to generate synthetic observables, after accounting for a frequency-dependent transmission coefficient that accounts for power attenuation due to radiative transfer effects, and identify the range models with input power that matched the Ca II 8542 Å velocities and ALMA brightness temperature fluctuations. Using the model-derived transmission coefficient and assumptions about the local densities, they inferred and average acoustic flux from the Band 6 time series of 0.7 kW/m^2 (with spatially resolved values ranging from ~200–2000 kW/m^2). For the Band 3 time series, observing emission expected to be formed higher in the atmosphere, the average flux was only 0.03 kW/m^2, perhaps indicating the significant dissipation of the wave in between the two regions of formation (Figure 14). Using instead the Ca II 854.2 nm line Doppler velocity measurements, the estimations of the derived acoustic flux were in the range from 0.1 to 1.0 kW/m^2. The amount of flux was the highest in the internetwork and plage regions, and the lowest in the penumbra and fibril regions, potentially due to the dissipation of waves lower down, below the inclined magnetic canopy, or the conversion of the waves to other wave modes. The average acoustic flux dissipated between the two layers probed by ALMA was found to be insufficient for heating of the middle chromosphere, but could potentially be a significant contribution to its energy budget, especially in localized regions where the acoustic flux was estimated to exceed 2 kW/m^2.

4 Conclusion: Prospects for future observations and use of ALMA data

The main goal of this review was to demonstrate that, despite limited availability of appropriate observations, ALMA solar science of active regions has transformed from estimations and expectations to observational results and their quantitative interpretation. The applicability of solar ALMA data is extensive and their potential is huge (see, e.g. Wedemeyer et al., 2016). The presented here results have demonstrated that the best of the solar ALMA potential can be achieved when high-resolution ALMA data are paired with other spectral diagnostics, in particular in the ultraviolet and visible wavelength ranges. The synergy between ALMA and other chromospheric observations effectively expands the diagnostic capabilities of each wavelength and instrument.

Simulations and observations have shown that the typical heights of formation of the millimeter continuum at different wavelengths are highly variable, both spatially and temporally. The locations of the sources of the millimeter continuum emissions are more sensitive to the electron density profile than spectral lines which have been predominantly used in the past. This complicates the interpretation of the ALMA observations, but it also provides a critical test for advanced numerical simulations (motivating the inclusion non-equilibrium ionization of both hydrogen and helium (see, e.g. Golding et al. (2016)) in the chromosphere and incorporating the effect of the strong sunspot magnetic fields). In particular, the formation heights (and there must be an expectation that there may be a broad averaging of temperatures through multiple locations even along a single line of sight) of the millimeter continuum is strongly dependent on the run of electron density in the atmosphere, a parameter that is highly dependent on many of these hard-to-model physical processes and may not be well constrained by other diagnostics. Properly accounting for these effects in spectroscopic inversions will be challenging but will be essential to recovering fully realistic atmospheres above the photosphere (including constraining both the chromospheric temperature and turbulent motions over a wide range of heights). The possibility that some millimeter emission above sunspots is coming from transition region and coronal plasma will introduce additional complications in our interpretation of these observations.

As solar activity has returned and the 25th solar activity cycle is progressing, the hope of getting new AR observations, including more time sequences and a broader sampling of multiple sunspots, is growing. At the same time, ALMA capabilities for solar observations are getting more advanced: additional frequency bands providing diagnostics at both lower and higher heights, than the initial bands, are being added. The achievable spatial resolutions with ALMA in the allowed bands and array configurations is approximately one arcsecond, up to 0.6″ at the shortest wavelengths, which is still larger than the characteristic sizes of events we observe in the visible and UV at higher resolution. It would be advantageous to make possible the use of larger-baseline array configurations as well as to develop further interferometric reconstruction techniques for an extended object like the Sun, in order to archive higher spatial resolution and probe heating and temperature variations on smaller, more relevant scales. Capturing sporadic, impulsive events such as energetic flares would be highly valuable (Stepanov et al., 1992; Kundu et al., 1993) but will be a challenge given the small fields of view provided by the interferometric observations, especially for a facility under high observing pressure. Observations of flares will require the development (currently underway) of methods to avoid saturation or non-linear response of the receivers. The new fast-region-mapping mode for continuous active region scanning (albeit at low spatial resolution, 15–60″) with cadences of 10–30 s has been introduced, which may allow for more opportunities to capture flare profiles in these wavelengths (especially given the possibility for its independent use). The availability of circular polarization measurements is expected in the coming observing cycles, opening the possibility of direct evaluation of the magnetic field strength in the upper atmosphere.

Significant effort is being taken to make ALMA data practical and easy to exploit for scientists not specializing in radio interferometry. To this end, Henriques et al. (2022) released the first version of SALSA (The Solar ALMA Science Archive), a database of 26 science ready data sets of ALMA observations of the Sun obtained in 2017–2019. In the future, great benefits for solar AR science are expected from ALMA observations combined with multiwavelength spectropolarimetric capabilities in the photosphere and the chromosphere offered by Daniel K. Inouye Solar Telescope (DKIST, Rast et al., 2021). However, ALMA's available observing windows are constrained by pointing limitations and typical weather conditions, making coordinated observations between ALMA and DKIST, as well as with the other solar observatories at different latitudes (and different weather conditions), severely time constrained. This will require efficient communication among facilities, as well as effective strategies to make reliable statistical comparisons when strict simultaneity is not possible.

Author contributions

All authors listed have made a substantial, direct, and intellectual contribution to the work and approved it for publication.

Funding

KR was supported by the National Solar Observatory (NSO). NSO is managed by the Association of Universities for Research in Astronomy, Inc., and is funded by the National Science Foundation (NSF). KR also acknowledges the support of NASA under the grant 80NSSC20K1282.

Acknowledgments

This paper makes use of the following ALMA data: ADS/JAO.ALMA#2011.0.000020.SV, ADS/JAO.ALMA#2016.1.00423.S, ADS/JAO.ALMA#2016.1.00050.S, ADS/JAO.ALMA#2016.1.00202.S, ADS/JAO.ALMA#2016.1.00788.S, ADS/JAO.ALMA#2016.1.01129.S, ADS/JAO.ALMA#2016.1.01532.S, ADS/JAO.ALMA#2017.1.00653.S, ADS/JAO.ALMA#2017.1.01672.S, and ADS/JAO.ALMA#2018.1.01518.S. ALMA is a partnership of ESO (representing its member states), NSF (United States), and NINS (Japan), together with NRC (Canada), MOST and ASIAA (Taiwan), and KASI (South Korea), in cooperation with the Republic of Chile. The Joint ALMA Observatory is operated by ESO, AUI/NRAO, and NAOJ.

Conflict of interest

The authors declare that the research was conducted in the absence of any commercial or financial relationships that could be construed as a potential conflict of interest.

Publisher's note

References

Alissandrakis, C. E., Patsourakos, S., Nindos, A., and Bastian, T. S. (2017). Center-to-limb observations of the Sun with ALMA . Implications for solar atmospheric models. *Astron. Astrophys.* 605, A78. doi:10.1051/0004-6361/201730953

Avrett, E. H. (1981). "Reference model atmosphere calculation-the sunspot sunspot model," in *The physics of sunspots* Editors Cram, L. E., and Thomas, J. H. 235–255.

Avrett, E., Tian, H., Landi, E., Curdt, W., and Wuelser, J. P. (2015). Modeling the chromosphere of a sunspot and the quiet sun. *ApJ* 811, 87. doi:10.1088/0004-637X/811/2/87

Bastian, T. S., Chintzoglou, G., De Pontieu, B., Shimojo, M., Schmit, D., Leenaarts, J., et al. (2017). A first comparison of millimeter continuum and Mg II ultraviolet line emission from the solar chromosphere. *Astrophys. J.* 845, L19. doi:10.3847/2041-8213/aa844c

Bastian, T. S., Chintzoglou, G., De Pontieu, B., Shimojo, M., Schmit, D., Leenaarts, J., et al. (2018). Erratum: "A first comparison of millimeter continuum and Mg II ultraviolet line emission from the solar chromosphere" (2017, ApJL, 845, L19). *Astrophys. J.* 860, L16. doi:10.3847/2041-8213/aac8dc

Bastian, T. S., Ewell, M. W., and Zirin, H. (1993). The center-to-limb brightness variation of the sun at lambda = 850 microns. *Astrophys. J.* 415, 364. doi:10.1086/173170

Bogod, V. M., Kal'tman, T. I., and Lukicheva, M. A. (2019). Millimeter observations at alma and in the microwave range with ratan-600. comparison for active regions on the sun. *Geomagn. Aeron.* 59, 783–788. doi:10.1134/s0016793219070077

Brajša, R., Skokić, I., Sudar, D., Benz, A. O., Krucker, S., Ludwig, H. G., et al. (2021). ALMA small-scale features in the quiet Sun and active regions. *Astron. Astrophys.* 651, A6. doi:10.1051/0004-6361/201936231

Brajša, R., Sudar, D., Benz, A. O., Skokić, I., Bárta, M., De Pontieu, B., et al. (2018). First analysis of solar structures in 1.21 mm full-disc ALMA image of the Sun. *Astron. Astrophys.* 613, A17. doi:10.1051/0004-6361/201730656

Carlsson, M., De Pontieu, B., and Hansteen, V. H. (2019). New view of the solar chromosphere. *Annu. Rev. Astron. Astrophys.* 57, 189–226. doi:10.1146/annurev-astro-081817-052044

Cauzzi, G., Reardon, K., Rutten, R. J., Tritschler, A., and Uitenbroek, H. (2009). The solar chromosphere at high resolution with ibis. iv. dual-line evidence of heating in chromospheric network. *Astron. Astrophys.* 503, 577–587. doi:10.1051/0004-6361/200811595

Chai, Y., Gary, D. E., Reardon, K. P., and Yurchyshyn, V. (2022a). A study of sunspot 3 minute oscillations using ALMA and GST. *Astrophys. J.* 924, 100. doi:10.3847/1538-4357/ac34f7

Chai, Y., Gary, D. E., Reardon, K. P., and Yurchyshyn, V. (2022b). Erratum: "A study of sunspot 3 minute oscillations using ALMA and GST" (2022, ApJ, 924, 100). *Astrophys. J.* 933, 247. doi:10.3847/1538-4357/ac7c1c

Chintzoglou, G., De Pontieu, B., Martínez-Sykora, J., Hansteen, V., de la Cruz Rodríguez, J., Szydlarski, M., et al. (2021b). ALMA and IRIS observations of the solar chromosphere. I. An on-disk type II spicule. *Astrophys. J.* 906, 82. doi:10.3847/1538-4357/abc9b1

Chintzoglou, G., De Pontieu, B., Martínez-Sykora, J., Hansteen, V., de la Cruz Rodríguez, J., Szydlarski, M., et al. (2021a). ALMA and IRIS observations of the solar chromosphere. II. Structure and dynamics of chromospheric plages. *Astrophys. J.* 906, 83. doi:10.3847/1538-4357/abc9b0

da Silva Santos, J. M., Danilovic, S., Leenaarts, J., de la Cruz Rodríguez, J., Zhu, X., White, S. M., et al. (2022a). Heating of the solar chromosphere through current dissipation. *Astron. Astrophys.* 661, A59. doi:10.1051/0004-6361/202243191

da Silva Santos, J. M., de la Cruz Rodríguez, J., Leenaarts, J., Chintzoglou, G., De Pontieu, B., Wedemeyer, S., et al. (2020a). The multi-thermal chromosphere. Inversions of ALMA and IRIS data. *Astron. Astrophys.* 634, A56. doi:10.1051/0004-6361/201937117

da Silva Santos, J. M., de la Cruz Rodríguez, J., White, S. M., Leenaarts, J., Vissers, G. J. M., and Hansteen, V. H. (2020b). ALMA observations of transient heating in a solar active region. *Astron. Astrophys.* 643, A41. doi:10.1051/0004-6361/202038755

da Silva Santos, J. M., White, S. M., Reardon, K., Cauzzi, G., Gunár, S., Heinzel, P., et al. (2022b). Subarcsecond imaging of a solar active region filament with ALMA and IRIS. *Front. Astron. Space Sci.* 9, 898115. doi:10.3389/fspas.2022.898115

de la Cruz Rodríguez, J., Leenaarts, J., and Asensio Ramos, A. (2016). Non-LTE inversions of the Mg II h & k and UV triplet lines. *ApJL* 830, L30. doi:10.3847/2041-8205/830/2/L30

de Oliveira e Silva, A. J., Selhorst, C. L., Costa, J. E. R., Simões, P. J. A., Giménez de Castro, C. G., Wedemeyer, S., et al. (2022). A genetic algorithm to model solar radio active regions from 3D magnetic field extrapolations. *Front. Astron. Space Sci.* 9, 911118. doi:10.3389/fspas.2022.911118

De Pontieu, B., Title, A. M., Lemen, J. R., Kushner, G. D., Akin, D. J., Allard, B., et al. (2014). The interface region imaging spectrograph (IRIS). *Sol. Phys.* 289, 2733–2779. doi:10.1007/s11207-014-0485-y

Ding, M. D., and Fang, C. (1989). A semi-empirical model of sunspot penumbra. *A&A* 225, 204–212.

Dunn, R. B., and Smartt, R. N. (1991). High resolution telescopes at the national solar observatory. *Adv. Space Res.* 11, 139–148. doi:10.1016/0273-1177(91)90371-P

Efanov, V. A., Kislyakov, A. G., and Moiseev, I. G. (1972). Slowly varying component Spectrum of the solar radio emission at millimetre wavelengths. *Sol. Phys.* 24, 142–153. doi:10.1007/BF00231092

Fontenla, J. M., Avrett, E. H., and Loeser, R. (1993). Energy balance in the solar transition region. III. Helium emission in hydrostatic, constant-abundance models with diffusion. *Astrophys. J.* 406, 319. doi:10.1086/172443

Fontenla, J. M., Curdt, W., Haberreiter, M., Harder, J., and Tian, H. (2009). Semiempirical models of the solar atmosphere. III. set of non-LTE models for far-ultraviolet/extreme-ultraviolet irradiance computation. *ApJ* 707, 482–502. doi:10.1088/0004-637X/707/1/482

Giovanelli, R. G., and Jones, H. P. (1982). The three-dimensional structure of atmospheric magnetic fields in two active regions. *Sol. Phys.* 79, 267–278. doi:10.1007/BF00146244

Golding, T. P., Leenaarts, J., and Carlsson, M. (2016). Non-equilibrium helium ionization in an MHD simulation of the solar atmosphere. *ApJ* 817, 125. doi:10.3847/0004-637X/817/2/125

Guevara Gómez, J. C., Jafarzadeh, S., Wedemeyer, S., Szydlarski, M., Stangalini, M., Fleck, B., et al. (2021). High-frequency oscillations in small chromospheric bright features observed with Atacama Large Millimetre/Submillimetre Array. *Phil. Trans. R. Soc. A* 379, 20200184. doi:10.1098/rsta.2020.0184

Henriques, V. M. J., Jafarzadeh, S., Guevara Gómez, J. C., Eklund, H., Wedemeyer, S., Szydlarski, M., et al. (2022). The Solar ALMA Science Archive (SALSA). First release, SALAT, and FITS header standard. *Astron. Astrophys.* 659, A31. doi:10.1051/0004-6361/202142291

Hofmann, R. A., Reardon, K. P., Milic, I., Molnar, M. E., Chai, Y., and Uitenbroek, H. (2022). Evaluating non-LTE spectral inversions with ALMA and IBIS. *Astrophys. J.* 933, 244. doi:10.3847/1538-4357/ac6f00

Iwai, K., Koshiishi, H., Shibasaki, K., Nozawa, S., Miyawaki, S., and Yoneya, T. (2016). Chromospheric sunspots in the millimeter range as observed by the Nobeyama radioheliograph. *ApJ* 816, 91. doi:10.3847/0004-637X/816/2/91

Iwai, K., Loukitcheva, M., Shimojo, M., Solanki, S. K., and White, S. M. (2017). ALMA discovery of solar umbral brightness enhancement at $\lambda = 3$ mm. *Astrophys. J.* 841, L20. doi:10.3847/2041-8213/aa71b5

Iwai, K., and Shimojo, M. (2015). Observation of the chromospheric sunspot at millimeter range with the Nobeyama 45 m telescope. *Astrophys. J.* 804, 48. doi:10.1088/0004-637X/804/1/48

Jafarzadeh, S., Wedemeyer, S., Fleck, B., Stangalini, M., Jess, D. B., Morton, R. J., et al. (2021). An overall view of temperature oscillations in the solar chromosphere with ALMA. *Phil. Trans. R. Soc. A* 379, 20200174. doi:10.1098/rsta.2020.0174

Jafarzadeh, S., Wedemeyer, S., Szydlarski, M., De Pontieu, B., Rezaei, R., and Carlsson, M. (2019). The solar chromosphere at millimetre and ultraviolet wavelengths. I. Radiation temperatures and a detailed comparison. *Astron. Astrophys.* 622, A150. doi:10.1051/0004-6361/201834205

Krueger, A. (1979). *Introduction to solar radio astronomy and radio physics*. Netherland: Springer.

Kundu, M. R. (1970). Solar active regions at millimeter wavelengths. *Sol. Phys.* 13, 348–356. doi:10.1007/BF00153556

Kundu, M. R. (1965). *Solar radio astronomy*. New Jersey, United States: John Wiley & Sons.

Kundu, M. R., White, S. M., Gopalswamy, N., and Lim, J. (1993). Interferometric observations of solar flares at 3 mm wavelength. *Adv. Space Res.* 13, 289–293. doi:10.1016/0273-1177(93)90492-T

Leka, K. D., and Metcalf, T. R. (2003). Active-region magnetic structure observed in the photosphere and chromosphere. *Sol. Phys.* 212, 361–378. doi:10.1023/A:1022996404064

Leenaarts, J., Carlsson, M., and Rouppe van der Voort, L. (2012). The formation of the Hα line in the solar chromosphere. *ApJ* 749, 136. doi:10.1088/0004-637X/749/2/136

Lindsey, C., and Kopp, G. (1995). Submillimeter radiometry of sunspots. *Astrophys. J.* 453, 517. doi:10.1086/176413

Loukitcheva, M. A., Iwai, K., Solanki, S. K., White, S. M., and Shimojo, M. (2017). Solar ALMA observations: Constraining the chromosphere above sunspots. *Astrophys. J.* 850, 35. doi:10.3847/1538-4357/aa91cc

Loukitcheva, M., Solanki, S. K., Carlsson, M., and White, S. M. (2015). Millimeter radiation from a 3D model of the solar atmosphere. I. Diagnosing chromospheric thermal structure. *Astron. Astrophys.* 575, A15. doi:10.1051/0004-6361/201425238

Loukitcheva, M., Solanki, S. K., and White, S. M. (2014). The chromosphere above sunspots at millimeter wavelengths. *Astron. Astrophys.* 561, A133. doi:10.1051/0004-6361/201321321

Maltby, P., Avrett, E. H., Carlsson, M., Kjeldseth-Moe, O., Kurucz, R. L., and Loeser, R. (1986). A new sunspot umbral model and its variation with the solar cycle. *ApJ* 306, 284. doi:10.1086/164342

Molnar, M. E., Reardon, K. P., Chai, Y., Gary, D., Uitenbroek, H., Cauzzi, G., et al. (2019). Solar chromospheric temperature diagnostics: A joint ALMA-hα analysis. *Astrophys. J.* 881, 99. doi:10.3847/1538-4357/ab2ba3

Molnar, M. E., Reardon, K. P., Cranmer, S. R., Kowalski, A. F., Chai, Y., and Gary, D. (2021). High-frequency wave power observed in the solar chromosphere with IBIS and ALMA. *Astrophys. J.* 920, 125. doi:10.3847/1538-4357/ac1515

Narang, N., Chandrashekhar, K., Jafarzadeh, S., Fleck, B., Szydlarski, M., and Wedemeyer, S. (2022). Power distribution of oscillations in the atmosphere of a plage region. Joint observations with ALMA, IRIS, and SDO. *Astron. Astrophys.* 661, A95. doi:10.1051/0004-6361/202142080

Rast, M. P., Bello González, N., Bellot Rubio, L., Cao, W., Cauzzi, G., Deluca, E., et al. (2021). Critical science plan for the Daniel K. Inouye solar telescope (DKIST). *Sol. Phys.* 296, 70. doi:10.1007/s11207-021-01789-2

Scharmer, G., Henriques, V., Hillberg, T., Kiselman, D., Löfdahl, M., Narayan, G., et al. (2008). "Spectropolarimetry of sunspots at 0.16 ARCSEC resolution," in 12th European Solar Physics Meeting, Freiburg, Germany, September, 8-12, 2008.

Severino, G., Gomez, M. T., and Caccin, B. (1994). "Modelling umbrae," in *Solar surface magnetism*. Editors R. J. Rutten and C. J. Schrijver (Dordrecht: Kluwer Academic Publishers), 433, 169.

Shimojo, M., Bastian, T. S., Hales, A. S., White, S. M., Iwai, K., Hills, R. E., et al. (2017). Observing the sun with the Atacama large millimeter/submillimeter array (ALMA): High-resolution interferometric imaging. *Sol. Phys.* 292, 87. doi:10.1007/s11207-017-1095-2

Socas-Navarro, H. (2007). Semiempirical models of solar magnetic structures. *ApJS* 169, 439–457. doi:10.1086/510336

Solanki, S. K. (2003). Sunspots: An overview. *Astronomy Astrophysics Rev.* 11, 153–286. doi:10.1007/s00159-003-0018-4

Stepanov, A. V., Urpo, S., and Zaitsev, V. V. (1992). Diagnostics of solar flare and evaporated plasma using mm-wave emission. *Sol. Phys.* 140, 139–148. doi:10.1007/BF00148434

Wedemeyer, S., Bastian, T., Brajša, R., Hudson, H., Fleishman, G., Loukitcheva, M., et al. (2016). Solar science with the Atacama large millimeter/submillimeter array—a new view of our sun. *Space Sci. Rev.* 200, 1–73. doi:10.1007/s11214-015-0229-9

White, S. M., Iwai, K., Phillips, N. M., Hills, R. E., Hirota, A., Yagoubov, P., et al. (2017). Observing the sun with the Atacama large millimeter/submillimeter array (ALMA): Fast-scan single-dish mapping. *Sol. Phys.* 292, 88. doi:10.1007/s11207-017-1123-2

White, S. M., Loukitcheva, M., and Solanki, S. K. (2006). High-resolution millimeter-interferometer observations of the solar chromosphere. *Astron. Astrophys.* 456, 697–711. doi:10.1051/0004-6361:20052854

Wootten, A., and Thompson, A. R. (2009). The Atacama large millimeter/submillimeter array. *Proc. IEEE* 97, 1463–1471. doi:10.1109/JPROC.2009.2020572

Yun, H. S., Beebe, H. A., and Baggett, W. E. (1984). A model of a penumbral chromosphere. *Sol. Phys.* 92, 145–151. doi:10.1007/BF00157241

frontiers | Frontiers in Astronomy and Space Sciences

ORIGINAL RESEARCH
published: 13 June 2022
doi: 10.3389/fspas.2022.908249

An ALMA Observation of Time Variations in Chromospheric Temperature of a Solar Plage Region

Masashi Abe[1,2], *Toshifumi Shimizu*[1,2]* *and Masumi Shimojo*[3,4]

[1]Department of Earth and Planetary Science, School of Science, The University of Tokyo, Tokyo, Japan, [2]Institute of Space and Astronautical Science, Japan Aerospace Exploration Agency, Kanagawa, Japan, [3]National Astronomical Observatory of Japan, Tokyo, Japan, [4]Department of Astronomical Science, SOKENDAI (The Graduate University for Advanced Studies), Tokyo, Japan

Nanoflares and the shock formation of magnetohydrodynamic waves in the solar chromosphere have been considered as key physical mechanisms of the heating of the chromosphere and corona. To investigate candidates of their signature in the mm-wavelength, a tiny active region located on the solar disk was observed with the Atacama Large millimeter and sub-millimeter Array (ALMA) at 3 mm, coordinated with observatories on orbit including Hinode SOT spectro-polarimeter in the Cycle 4 solar campaign (19 March 2017). ALMA's spatial resolution was moderate, far from the best performance, but it provided stable conditions that are suitable to investigate temporal variations in the mm-wavelength. We determined that the noise level is less than 20 K (σ) over 1 hour in the 20-s cadence time series of synthesized ALMA images. The time variations with amplitudes above the noise level were observed throughout the field of view, but variations exceeding 200 K, corresponding to energy input to the chromosphere on the order of $10^{20\text{-}22}$ erg, were localized in two locations. One location was on the polarity inversion line, where tiny concentrated magnetic patches exist in weak field and a tiny magnetic flux may be emergent. The other location was at the outer edge of a bipolar magnetic region, which was under development with a successive series of magnetic flux emergence. This observation suggests that nanoflare-class energy inputs in the chromosphere can occur associated with emerging flux activities.

Keywords: the sun, radio radiation, alma, chromosphere, magnetic field, nanoflare

OPEN ACCESS

Edited by:
Mario J. P. F. G. Monteiro, University of Porto, Portugal

Reviewed by:
João M. da Silva Santos, National Solar Observatory, United States
Peng-Fei Chen, Nanjing University, China

***Correspondence:**
Toshifumi Shimizu
shimizu@solar.isas.jaxa.jp

Specialty section:
This article was submitted to Stellar and Solar Physics, a section of the journal Frontiers in Astronomy and Space Sciences

Received: *30 March 2022*
Accepted: *09 May 2022*
Published: *13 June 2022*

Citation:
Abe M, Shimizu T and Shimojo M (2022) An ALMA Observation of Time Variations in Chromospheric Temperature of a Solar Plage Region. Front. Astron. Space Sci. 9:908249. doi: 10.3389/fspas.2022.908249

1 INTRODUCTION

The solar chromosphere is the interface layer connecting the solar surface (photosphere) to the corona. The corona is permeated with bundles of both open and closed magnetic fields that are rooted in the photosphere. The corona is heated to over 1 MK, whereas the temperature of the photosphere is 6,000 K. The chromosphere has a temperature of approximately 10,000 K; however, because of its high density, it requires heat input that is one order of magnitude higher than that of the corona. The energy is believed to transfer through chromospheric structures towards the corona. Thus, much attention has been given recently to the dynamical behaviors of chromospheric structures. Observationally, high spatial and temporal resolution observations, provided by space-borne observatories, such as the Hinode Solar Optical Telescope (Kosugi et al., 2007; Ichimoto et al., 2008; Shimizu et al., 2008; Suematsu et al., 2008; Tsuneta et al., 2008; Lites et al., 2013) and Interface Region Imaging Spectrograph (IRIS) (De Pontieu et al., 2014), and

recent 1-m class ground-based telescopes, such as Swedish Solar Telescope (Scharmer et al., 2003) and Goode Solar Telescope (Cao et al., 2010), have revealed propagating magnetohydrodynamics (MHD) waves (e.g., De Pontieu et al., 2007; Okamoto et al., 2007; Okamoto and De Pontieu, 2011; Stangalini et al., 2011; Martínez-Sykora et al., 2017; Abbasvand et al., 2020) and the ubiquitous occurrence of small-scale magnetic reconnection events in the chromosphere (Katsukawa et al., 2007; Shibata et al., 2007; Shimizu et al., 2009). Meanwhile, significant progress has been made recently in modeling the three-dimensional chromospheric structures and their dynamics with sophisticated radiative MHD models, helping to capture a physical picture of the chromospheric fine structures and their dynamics (e.g., Martínez-Sykora et al., 2017). It has been considered that MHD waves excited by the convective gas motions at the photosphere propagate through the chromosphere toward the corona and are also dissipated in the chromosphere by the formation of shocks (e.g., Carlsson and Stein, 1997). As an alternate model, the convective gas motions generate tangential discontinuity and braiding in magnetic field lines in the corona, leading to numerous numbers of tiny magnetic reconnection events, so-called nanoflares (Parker, 1988). It is noted that the terminology nanoflare in Parker (1988) represents a swarm of tiny energy releases in order of 10^{24} erg produced in coronal loops, but hereafter we will use the terminology nanoflare for a transient release in nanoflare energy range, i.e., $10^{22} - 10^{24}$ erg.

Most of the solar radiation at millimeter (mm) wavelengths comes from the chromosphere, providing a unique diagnostic for the chromosphere (Vernazza et al., 1981). The mm-wavelength emission is free-free emission (thermal bremsstrahlung), produced by free electrons scattering off ions without being captured. Assuming the free electrons to be in local thermodynamic equilibrium (LTE), the source function is equivalent to the Planck function. In the mm wavelengths, the Rayleigh–Jeans law is an approximation to the Plank function, giving a linear relation from the emission intensity to the brightness temperature (Kraus, 1986). However, the electrons are mostly regulated by the ionization degree of hydrogen atoms that significantly departs from LTE in the chromosphere. 3D non-LTE radiative MHD simulations show that the formation height range of the radiation at millimeter wavelengths depends on the location in the simulation domain and is related to the underlying magnetic structure (Loukitcheva et al., 2015; Martínez-Sykora et al., 2020). Nonetheless, millimeter emission can image the chromospheric thermal structure at the height at which the radiation is formed. This suggests that the radiation at mm wavelengths can be used as a thermometer to probe the chromospheric temperature. The thermometer provides a useful tool to detect changes in chromospheric temperature. Variations in brightness temperature could be due to variations in formation height depending on the chromospheric structure. For large class of variations to be examined in this paper, however, it would be plausible that brightness variations are caused dominantly by changes in chromospheric temperature. Therefore, transient energy inputs in the chromosphere either by nanoflare and microflare (da Silva Santos et al., 2020; Shimizu et al., 2021) or by shock formation (Eklund et al., 2020; Nindos et al., 2021a; Chintzoglou et al., 2021) may be identified by monitoring transient increases in the thermometer.

The Atacama Large millimeter and sub-millimeter Array (ALMA) (ALMA Partnership et al., 2016) is capable of performing interferometric observations of the Sun at mm wavelengths, allowing both high spatial and temporal resolution imaging observations of a few arcsec or higher spatial resolution (Shimojo et al., 2017a). Using ALMA observations in early phase, transient time variability was studied primarily in the quiet Sun (Nindos et al., 2021a; Nindos et al., 2021b). The number of studies addressing temporal variations of brightness temperature associated with strong magnetic flux concentrations is increasing; for example, a solar plasmoid ejection from an X-ray bright point (Shimojo et al., 2017b), tiny brightenings in a group of pores (da Silva Santos et al., 2020), oscillations in chromospheric plage regions (Chintzoglou et al., 2021; Narang et al., 2022), and the ALMA counterpart at the footpoints of a soft X-ray loop-type microflare observed in a tiny active region (Shimizu et al., 2021). The objective of this article is to present the temporal variations in mm-wavelength data recorded with an ALMA observation for a small active region. **Section 2** describes observations and data analysis. **Section 3** presents the results of the data analysis, followed by discussions in **Section 4** and a summary in **Section 5**.

2 OBSERVATIONS AND DATA ANALYSIS

The ALMA observation was coordinated with Hinode from 13: 36-19:41 UT on 19 March 2017, as an execution of the ALMA Project code 2016.1.00030.S (PI: Shimizu). The Hinode program was numbered as IHOP 327. The target region was a tiny active region located on the solar disk at (-495, -40) arcsec on the heliocentric coordinate seen as a compact bright region in soft X-rays with a magnetic bipolar distribution on photospheric SDO/HMI magnetograms. It is noted that no any NOAA number was designated to this region. The ALMA performed its observations at 100 GHz (3 mm, Band 3) with the C40-1 antenna configuration, which is the most compact layout in the solar observing mode, giving a spatial resolution of 5".0, ×, 3".9. See Shimizu et al. (2021) for further details of the observations and data processing. It should be noted that no single-dish (total power) data were acquired to calibrate the absolute brightness temperature in this observation. Thus, the temporal profiles presented in this article show the deviation from the averaged brightness temperature in the observation field of view. Time variations in temperature brightness can be derived even without absolute temperature information. The co-alignment of the data from the different instruments was carefully investigated to identify a better method among alignment methods examined, and we finally appear to achieve a precision better than 2". Details of the co-alignment procedure are also described in Shimizu et al. (2021).

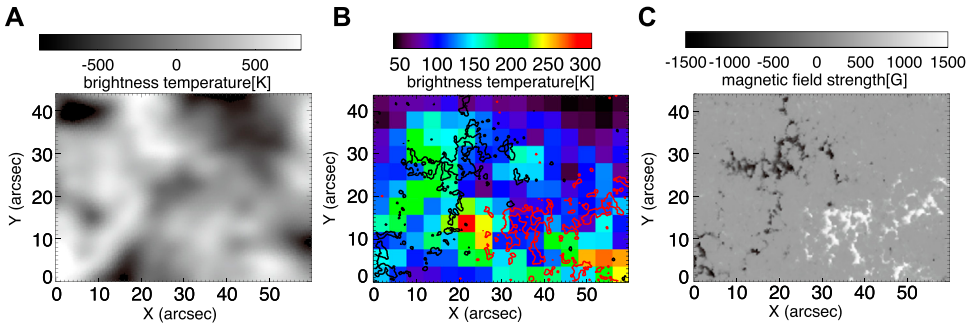

FIGURE 1 | The spatial distribution of **(A)** the mean brightness temperature and **(B)** the standard deviation in the time series of ALMA data. The contours represent the spatial distribution of **(C)** magnetic flux density: positive 300 gauss in red and negative 300 gauss in black.

3 RESULTS

3.1 Noise Level in ALMA Time Series

We use the method described in Shimojo et al. (2017a) to evaluate the noise level in the ALMA time series. ALMA Band 3 has two receivers sensitive to orthogonal components of the linear polarization (ALMA Partnership et al., 2016). The interferometric measurements in each component can be used independently to synthesize an image and the two synthesized images should be identical to each other if no noise is included in the data. Thus, the noise level was estimated from the difference between the two polarizations for a 20 s integration. The difference should be zero for thermal emission from optically-thick chromospheric plasma in the absence of flare emission. Furthermore, circularly polarized light due to the presence of strong magnetic fields (Miyawaki et al., 2016) may produce net linear polarization due to differential Faraday rotation; however, it is negligibly small at 100 GHz (Iwai et al., 2017; Loukitcheva et al., 2017). The difference in two synthesized images, which were generated independently with interferometric measurements by the two receivers sensitive to orthogonal components of the linear polarization, gives the standard deviation smaller than 20 K for the entire period. Weak spatial dependence may be visible when it is compared to the brightness temperature derived from the ALMA data, although the dependence is small in magnitude and may be roughly regarded as random distribution. Therefore, we set 20 K as the noise level in σ in the subsequent results, although this would represent the most conservative evaluation.

3.2 Spatial Distribution of Large Time Variability

Figure 1B is the spatial distribution of time variations detected in the ALMA brightness temperature map in panel (a). For each location, the standard deviation was derived from the time series of brightness temperature. The map is shown at 4 arcsec/pixel. The contours in **Figure 1B** represent the spatial distribution of magnetic flux density: positive 300 gauss in red and negative 300 gauss in black, from **Figure 1C**. Time variations with amplitudes much larger than the noise level (20 K in σ) are observed in most of the binned pixels. The variations exceeding 200 K are observed in the lower middle (around X = 22, Y = 13; area A1 hereafter) and the lower right (around X = 54, Y = 6; area A2 hereafter), both of which are located at or close to polarity inversion lines. **Figure 2** shows the time profile of ALMA brightness temperature at these locations. At area A1, the brightness temperature is gradually decreased with some enhancements during the observation. The largest enhancement is about 400 K increase from the base brightness just before the enhancement. The appearance of the observed enhancement looks periodic, but the interval exceeds 10 min, which is different from 3 to 5 min expected from p-mode oscillations. The temporal profile of enhancements shows an increase in relatively short timescale (100–200 s) and gradual decrease after the peak. At area A2, a large enhancement is observed at the latter half of the observation and its duration is about 1,000 s.

The magnitude of the time variations is compared to the time-averaged brightness temperature in **Figure 3A**. The figure shows a fairly dispersive distribution between them. The binned pixels with large variation over 200 K are widely distributed from -300 to 500 K. The correlation coefficient is 0.34, suggesting poor correspondence. In **Figure 3B**, the magnitude of time variations is compared with the magnetic flux density at the photosphere. Large variations over 200 K are observed in the regions where the magnetic flux density is less than 200 gauss. At the magnetic flux concentrations (higher than 300 gauss) in the photosphere, large variations over 200 K are not observed and dominant variations have a standard deviation of 90-170 K.

3.3 Magnetic Flux Evaluation at the Photosphere

According to the previous subsection, two areas showed large temperature variations exceeding 200 K. **Figure 4** is the magnetic flux distribution at the photospheric level, measured with the Hinode/SOT Spectro-Polarimeter (SP) during the first and last half of the ALMA observing period. The two areas are marked by yellow squares in **Figure 4**.

The large variations observed in area A1 (around X = 30, Y = 30 arcsec in **Figure 4**) are located in a weak-field area at the polarity inversion. Positive polarity patches are dominant at the

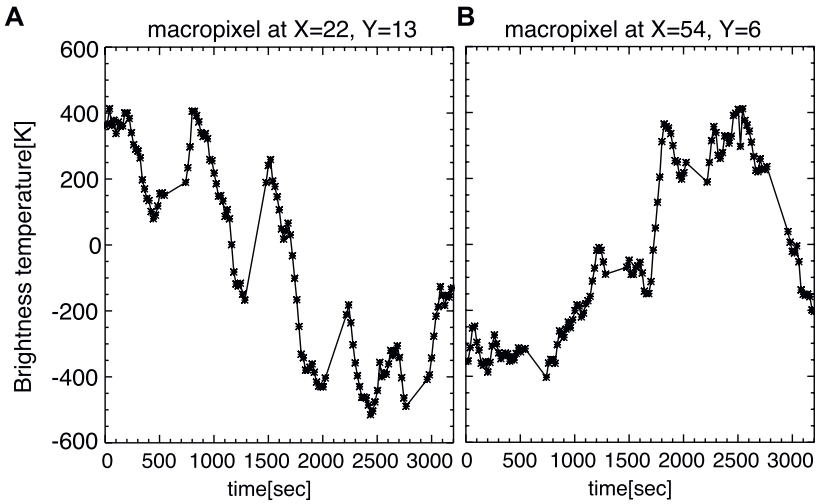

FIGURE 2 | Time profile of ALMA brightness temperature at two locations: **(A)** area A1 **(B)** area A2.

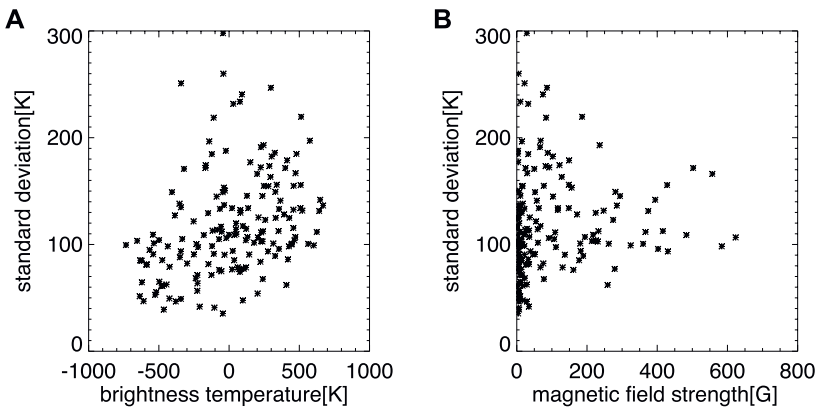

FIGURE 3 | The magnitude of time variations measured as the standard deviation in the time series of ALMA data is compared **(A)** to the time-averaged brightness temperature and **(B)** to the magnetic flux density in the photosphere. The value of magnetic flux density (magnetic strength) is derived from the magnetic flux density map binned to 4 arcsec/pixel.

right of this area, whereas negative polarity patches are distributed at the left. In the square, a tiny negative polarity patch exists and shows an increase in the magnetic flux. Positive and negative magnetic patches located around the square also show changes their locations and shapes, as well as strength within about 30 min. As given by arrows in the second map, a small negative polarity patch and a small positive polarity patch appeared, indicating emergence of tiny magnetic flux around the polarity inversion line. Note that it is difficult to look into the temporal evolution of such a tiny magnetic patch in the time series of HMI magnetograms (Scherrer et al., 2012; Schou et al., 2012).

The large variations at area A2 are located at the outer edge of a small bipolar magnetic region that is under development with successive series of magnetic flux emergence from below the photosphere. A group of positive polarity fluxes moves toward the upper left direction. The ALMA pixels showing large variations are located near the front side of this moving positive polarity flux. Weak signals for negative polarity flux can be recognized there in the SP maps, suggesting that a mixed polarity or polarity inversion configuration is formed. It should also be noted that the brightness temperature is high in this emerging flux region, as shown in **Figure 1A**.

4 DISCUSSIONS

In this study, we synthesized time series of ALMA maps by integrating the data acquired over each 20 s and investigated the temporal variations in the brightness temperature for a tiny active region with a magnetic bipolar distribution at the photosphere (**Figure 1**). Following the method described in Shimojo et al.

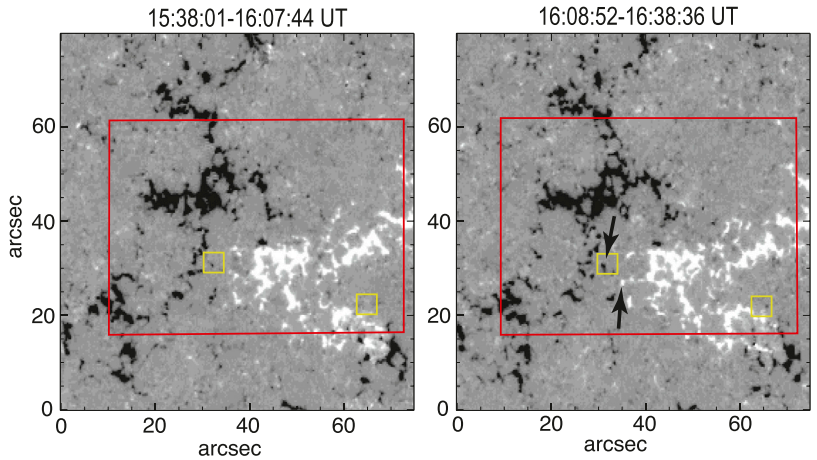

FIGURE 4 | Stokes V amplitude maps from two Hinode/SOT Spectro-Polarimeter's scans during the ALMA observing period. The field of view is 75 × 80 arcsec, where the slit is moved from the left to the right. The left map was recorded from 15:38:01-16:07:44 UT and the right from 16:08:52-16:38:36 UT. The red rectangle gives the field of view used in **Figure 1**. The yellow squares are the location of two macro-pixels where large variations exceeding 200 K are observed. The arrows specify newly appeared magnetic flux patches.

(2017a), we derived the noise level of the examined data less than 20 K, which is similar to that derived by Shimojo et al. (2017a) for verification data acquired in December 2015. Moreover, the level of noise is quite stable for about 1 h, indicating that the examined ALMA data are valuable for investigating temporal variations in brightness temperature.

Time variations above the noise level can be recognized in most of regions, even when the spatial resolution of the synthesized images (4 arcsec/pixel) is lower than the best resolution ALMA can achieve (ALMA Partnership et al., 2016). The chromosphere is dynamic; there is consistently dynamic behavior of fine scale structures such as spicules and fibrils, and the height of the chromospheric structure is always changing (Pereira et al., 2012). Time variations in ALMA time series would reflect the dynamic nature of the chromosphere, and thus, it is not surprising to observe time variations above the noise level. In this study, we focused on significant variations, namely variations exceeding 200 K, which are ten times larger than the noise level. The emission of the chromosphere is closely related to magnetic field concentrations at the solar surface. It is well established that the relation between chromospheric emission and magnetic field is nonlinear (Barczynski et al., 2018). **Figure 3** shows that the magnitude of time variations is weakly correlated with the brightness temperature with a fairly board distribution. The brightness temperature is not enhanced in the locations where large time variations above 200 K are observed. This indicates that large time variations have no clear relationship with the heating level of the chromosphere. In terms of the relationship with the magnetic field strength, large time variations above 200 K are not observed in magnetic flux concentrations above 200 G, but occur above regions with weak magnetic fields below 100 G. This is not the case in magnetic flux concentrations, but in the geometry of the magnetic field expanding from the concentrations in the photosphere into the chromosphere, i.e., magnetic canopy structure. When a magnetic flux emerges from below the photosphere to the canopy structure, the sudden change in geometry, such as a sudden expansion or change in shape of the magnetic field lines that have emerged above the photosphere, may lead to magnetic reconnection with the pre-existing field, resulting in large time variations.

Pervasive presence of brightness temperature variations due to p-mode oscillations are expected in the examined time series. We applied an FFT analysis on the time series and found that the power of variations in 3–5 mHz is not significant and p-mode oscillations may contribute to time variations much smaller than the significant variations discussed. The time profiles shown in **Figure 2** do not show strong signals for oscillations in 3–5 mHz. In contrast, in a past observation, intensity oscillations with significant power in the frequency range 3–5 mHz were found in the quiet-Sun and active region (White et al., 2006). Recently, Jafarzadeh et al. (2021) have obtained the power spectra for 10 ALMA datasets (of which, 6 datasets for Band 3) and found a lack of dominant chromospheric oscillations within the frequency range of 3–7 mHz for most of the datasets. These datasets are largely influenced by the strong magnetic fields originating within the observed field of view, while clear power enhancements at around 4 mHz were observed for the magnetically quiescent datasets. The result from our FFT analysis for the data examined in this study seems to be in line with the Jafarzadeh et al. (2021)'s findings.

Time variations exceeding 200 K were dominantly observed at two locations; one is at the outer edge of a small emerging flux region, and the other is at the polarity inversion line where tiny concentrated magnetic flux patches exist in weak field. In the series of chromospheric images, such as AIA 1600 Å, SOT Ca II H, and IRIS 1400 Å slit jaw, many point-like transient brightenings are observed in emerging flux regions in general (e.g., Toriumi & Wang, 2019). They may correspond to Ellerman bombs, burst intensity enhancements in Hα line

wings (Ellerman, 1917), which may be caused by magnetic reconnection occurring at the magnetic flux dips (Bernasconi et al., 2002; Georgoulis et al., 2002; Pariat et al., 2004; Matsumoto et al., 2008). They may be formed by horizontal motions of magnetic flux driven either by the flux emergence or by gas convection. Small-scale transient brightenings are observed in common when opposite magnetic polarities come into contact with or cancel each other at the photospheric level (Shimizu, 2015). In particular, magnetic reconnection may occur when an emerging flux interacts with the pre-existing, overlying magnetic field, creating high-temperature plasma in localized volume with hot and cold ejections (e.g., Yokoyama and Shibata, 1995; Cheung and Isobe, 2014). In IRIS observations, high-temperature plasma in localized volume may appear as UV bursts (Peter et al., 2014). Many such bursts appear to be associated with the cancellation of magnetic fluxes. Tian et al. (2018) investigated the 3D magnetic field topology through a magnetohydrostatic model and found that a small fraction of the bursts are associated with bald patches (magnetic dips), which are similar to the magnetic configuration for Ellerman bombs. In active regions, newly emerging magnetic flux interacts with the pre-existing magnetic field, leading to magnetic reconnection events. Indeed, this scenario has been reported with high spatial resolution observations of granular-sized emerging fluxes and of their chromospheric response carried out in recent years (e.g., Guglielmino et al., 2008, 2010; Vargas Domínguez et al., 2012; Ortiz et al., 2014; de la Cruz Rodríguez et al., 2015; Centeno et al., 2017; Guglielmino et al., 2018; Díaz Baso et al., 2021). A complex fan-spine magnetic topology may be responsible for triggering UV bursts (Chitta et al., 2017; Smitha et al., 2018). The same scenario has also been considered as one of major magnetic configuration for producing coronal transient brightenings or microflares in active regions (Shimizu et al., 2002; Kano et al., 2010). Thus, it is natural that the time variations with relatively large amplitude in ALMA data can occur associated with small evolving magnetic flux driven by the flux emergence and may be a counterpart of magnetic reconnection events, such as Ellerman bombs, UV bursts and transient brightenings in active regions.

The ALMA data can be used as a thermometer to probe changes in the temperature of chromospheric plasma, at least in the range 6,500–12,000 K (Molnar et al., 2019). The 200 K increase may be interpreted as the thermal energy increase ($3nk_B\delta TV$) of approximately 10^{21-22} erg for a brightening at one pixel (4 arcsec), if we assume that the density (n) is 10^{10-11} cm^{-3} according to the standard solar atmospheric model in Fontenla et al. (1993). Here, k_B is the Boltzmann constant and δT is the temperature increase. The increased brightness temperature was used for the δT. This is valid when the optical thickness is unity or larger at 3 mm. If the optical thickness is much smaller than unity, the increased brightness temperature divided by the optical thickness should be used for the δT. As discussed in Shimizu et al. (2021), however, we have concluded that the optical thickness for the layer where the ALMA observes at 3 mm is about unity or higher. The volume V is simply given by multiplying the pixel size (4×4 arcsec^2) by the line-of-sight depth. We used 500 km for the line-of-sight depth, coming from the width of the contribution function, which describes how much of the emergent radiation is contributed over height, by Loukitcheva et al. (2015), who studied the formation height of the millimeter radiation with a snapshot of a 3D radiative MHD simulation performed with the Bifrost code (Gudiksen et al., 2011). It is noted that even the Bifrost simulation resembles quiet-Sun conditions despite the stronger magnetic fields, and that 500 km is only an average value. The width of the contribution function depends largely on the atmospheric structure; it ranges from 100 to 1,000 km. The contribution function can be quite localized (100 km in width) for Band 3 in active region conditions or shows multiple peaks (100 km in width each) from distinct layers with different electron densities and temperatures spanning several megameters, particularly during flux emergence (da Silva Santos et al., 2022), which may be relevant for the science case in this study. The actual width of the contribution function for the observed targets is unknown and thus when we used 100–1000 km for the line-of-sight depth, the thermal energy would be in a range between 4×10^{20} and 4×10^{22} ergs. This rough estimate indicates that transient variations with a temperature change of 200 K can be considered as nanoflare-class energy inputs to the chromosphere.

The amount of energy was estimated with the ALMA 3 mm data, which are sensitive to temperature changes in a limited line-of-sight depth at the chromosphere. Depending on the structure of an energy release event in the solar atmosphere, the energy of the time variation observed with ALMA may be only a small fraction of the energy release event. If it is a counterpart such as UV burst or Ellerman bomb, the overall energy content will be larger than the energy evaluated with ALMA. For example, if the energy is released deeper than the chromosphere, the energy will be larger; The total energy of the Ellerman bombs are estimated to be 10^{26} to 5×10^{27} ergs (Fang et al., 2006). More interestingly, semiempirical atmospheric models for Ellerman bombs indicate that the inclusion of nonthermal particles can reduce the temperature enhancement compared to the thermal only model (Fang et al., 2006). This situation is also the same even if an energy release occurs in the transition region above the chromosphere, as in the case of a UV burst. When the energy is released in the coronal loops, a counterpart can be observed at the loop footpoints as the transient response of the chromosphere with ALMA; Shimizu et al. (2021) have found that this transient response is caused by the non-thermal particles impinging to the footpoints and that its energy is much smaller than what is released in the corona. This tells that the overall energy content may be larger compared to the energy estimated with ALMA.

Energy evaluations are important for understanding the role of observed time variations in coronal and chromospheric heating. Nindos et al. (2020) performed a systematic survey for transient brightenings with ALMA data at 3 mm and found a significant number of weak brightenings everywhere (not only at network boundaries and in cell interiors) in the quiet solar chromosphere. Their brightness temperatures are from 70 K to more than 500 K, and they derived the energies between 1.5×10^{24} and 9.9×10^{25} ergs. As briefly discussed above, the energy estimate contains a significant uncertainty due to uncertainties in the input parameters, such as the electron density and line-of-sight depth for volume. To reduce the uncertainties, we need to

have additional modeling for the height of formation, especially on transient energy releases in the regions where successive series of magnetic flux bundles emerge from below the solar surface and develop the complex of magnetic structures in the chromosphere.

5 SUMMARY

We investigated time variations, especially those with relatively large amplitude, in series of ALMA synthesized maps, acquired for a small active region on 19 March 2017. We found several time variations exceeding 200 K, which is ten times larger than the noise level, in a 1-h observation. The 200 K variations correspond to energy input on the order of $10^{20\text{-}22}$ erg. Such large variations were observed at two locations; one is at the outer edge of a small emerging flux region, and the other is at the polarity inversion line where tiny concentrated magnetic patches exist in weak field and a tiny magnetic flux may be emergent. This observation suggests that nanoflare-class energy inputs in the chromosphere can occur associated with emerging flux activities.

DATA AVAILABILITY STATEMENT

The raw data supporting the conclusions of this article will be made available by the authors, without undue reservation.

AUTHOR CONTRIBUTIONS

Most of the results presented in this article were obtained by MA as a part of his master thesis with supervision of TS for science and Hinode data analysis and MS for ALMA data analysis. TS proposed this joint-observation project to ALMA and Hinode and led the observations for this study and wrote this article with help of MS.

FUNDING

This work was partially supported by JSPS KAKENHI Grant Number 15H05750, 15H05814, and 18H05234.

ACKNOWLEDGMENTS

ALMA is a partnership of ESO (representing its member states), NSF (United States) and NINS (Japan), together with NRC (Canada), MOST and ASIAA (Taiwan), and KASI (Republic of Korea), in cooperation with the Republic of Chile. The Joint ALMA Observatory is operated by ESO, AUI/NRAO and NAOJ. Hinode is a Japanese mission developed and launched by ISAS/JAXA, with NAOJ as domestic partner and NASA and STFC (United Kingdom) as international partners. It is operated by these agencies in co-operation with ESA and NSC (Norway).

REFERENCES

Abbasvand, V., Sobotka, M., Švanda, M., Heinzel, P., García-Rivas, M., Denker, C., et al. (2020). Observational Study of Chromospheric Heating by Acoustic Waves. *Astronomy Astrophysics* 642, A52. doi:10.1051/0004-6361/202038559

ALMA PartnershipAsayama, S., Biggs, A., de Gregorio, I., Dent, B., Di Francesco, J., Fomalont, E., et al. (2016). ALMA Cycle 4 Technical Handbook. Available at: http://almascience.org/documents-and-tools/cycle4/alma-technical-handbook. 978-3-923524-66-2.

Barczynski, K., Peter, H., Chitta, L. P., and Solanki, S. K. (2018). Emission of Solar Chromospheric and Transition Region Features Related to the Underlying Magnetic Field. *Astronomy Astrophysics* 619, A5. doi:10.1051/0004-6361/201731650

Bernasconi, P. N., Rust, D. M., Georgoulis, M. K., and Labonte, B. J. (2002). *Sol. Phys.* 209, 119–139. doi:10.1023/a:1020943816174

Cao, W., Gorceix, N., Coulter, R., Ahn, K., Rimmele, T. R., and Goode, P. R. (2010). Scientific Instrumentation for the 1.6 M New Solar Telescope in Big Bear. *Astron. Nachr.* 331, 636–639. doi:10.1002/asna.201011390

Carlsson, M., and Stein, R. F. (1997). Formation of Solar Calcium H and K Bright Grains. *Astrophysical J.* 481, 500–514. doi:10.1086/304043

Centeno, R., Rodríguez, J. B., Del Toro Iniesta, J. C., Solanki, S. K., Barthol, P., Gandorfer, A., et al. (2017). A Tale of Two Emergences: Sunrise II Observations of Emergence Sites in a Solar Active Region. *Astrophysical J. Suppl. Ser.* 229, 3. doi:10.3847/1538-4365/229/1/3

Cheung, M. C. M., and Isobe, H. (2014). *Living Rev. Sol. Phys.* 11, 3. doi:10.12942/lrsp-2014-3

Chintzoglou, G., De Pontieu, B., Martínez-Sykora, J., Hansteen, V., Cruz Rodríguez, J. d. l., Szydlarski, M., et al. (2021). ALMA and IRIS Observations of the Solar Chromosphere. II. Structure and Dynamics of Chromospheric Plages. *Astrophysical J.* 906, 83. doi:10.3847/1538-4357/abc9b0

Chitta, L. P., Peter, H., Young, P. R., and Huang, Y.-M. (2017). Compact Solar UV Burst Triggered in a Magnetic Field with a Fan-Spine Topology. *Astronomy Astrophysics* 605, A49. doi:10.1051/0004-6361/201730830

da Silva Santos, J. M., Danilovic, S., Leenaarts, J., de la Cruz Rodríguez, J., Zhu, X., White, S. M., et al. (2022). *arXiv:2202.03955*.

da Silva Santos, J. M., de la Cruz Rodríguez, J., White, S. M., Leenaarts, J., Vissers, G. J. M., and Hansteen, V. H. (2020). ALMA Observations of Transient Heating in a Solar Active Region. *Astronomy Astrophysics* 643, A41. doi:10.1051/0004-6361/202038755

de la Cruz Rodríguez, J., Hansteen, V., Bellot-Rubio, L., and Ortiz, A. (2015). *Astrophysical J.* 810, 145.

De Pontieu, B., McIntosh, S. W., Carlsson, M., Hansteen, V. H., Tarbell, T. D., Schrijver, C. J., et al. (2007). Chromospheric Alfve´nic Waves Strong Enough to Power the Solar Wind. *Science* 318, 1574–1577. doi:10.1126/science.1151747

De Pontieu, B., Title, A. M., Lemen, J. R., Kushner, G. D., Akin, D. J., Allard, B., et al. (2014). The Interface Region Imaging Spectrograph (IRIS). *Sol. Phys.* 289, 2733. doi:10.1007/s11207-014-0485-y

Díaz Baso, C. J., de la Cruz Rodríguez, J., and Leenaarts, J. (2021). An Observationally Constrained Model of Strong Magnetic Reconnection in the Solar Chromosphere. Atmospheric Stratification and Estimates of Heating Rates. *Astronomy Astrophysics* 647, 188. doi:10.1051/0004-6361/202040111

Eklund, H., Wedemeyer, S., Szydlarski, M., Jafarzadeh, S., and Guevara Gómez, J. C. (2020). The Sun at Millimeter Wavelengths. *Astronomy Astrophysics* 644, A152. doi:10.1051/0004-6361/202038250

Ellerman, F. (1917). Solar Hydrogen "bombs". *Astrophysical J.* 46, 298. doi:10.1086/142366

Fang, C., Tang, Y. H., Xu, Z., Ding, M. D., and Chen, P. F. (2006). Spectral Analysis of Ellerman Bombs. *Astrophysical J.* 643, 1325–1336. doi:10.1086/501342

Fontenla, J. M., Avrett, E. H., and Loeser, R. (1993). Energy Balance in the Solar Transition Region. III - Helium Emission in Hydrostatic, Constant-Abundance Models with Diffusion. *Astrophysical J.* 406, 319. doi:10.1086/172443

Georgoulis, M. K., Rust, D. M., Bernasconi, P. N., and Schmieder, B. (2002). Statistics, Morphology, and Energetics of Ellerman Bombs. *Astrophysical J.* 575, 506–528. doi:10.1086/341195

Gudiksen, B. V., Carlsson, M., Hansteen, V. H., Hayek, W., Leenaarts, J., and Martínez-Sykora, J. (2011). The Stellar Atmosphere Simulation codeBifrost. *Astronomy Astrophysics* 531, A154. doi:10.1051/0004-6361/201116520

Guglielmino, S. L., Bellot Rubio, L. R., Zuccarello, F., Aulanier, G., Vargas Domínguez, S., and Kamio, S. (2010). *Astrophysical J.* 724, 1098. doi:10.1088/0004-637x/724/2/1083

Guglielmino, S. L., Zuccarello, F., Romano, P., and Bellot Rubio, L. R. (2008). Hinode Observations of Chromospheric Brightenings in the Ca Ii H Line during Small-Scale Flux Emergence Events. *Astrophysical J.* 688, L111–L114. doi:10.1086/595657

Guglielmino, S. L., Zuccarello, F., Young, P. R., Murabito, M., and Romano, P. (2018). IRISObservations of Magnetic Interactions in the Solar Atmosphere between Preexisting and Emerging Magnetic Fields. I. Overall Evolution. *Astrophysical J.* 856, 127. doi:10.3847/1538-4357/aab2a8

Ichimoto, K., Lites, B., Elmore, D., Suematsu, Y., Tsuneta, S., Katsukawa, Y., et al. (2008). Polarization Calibration of the Solar Optical Telescope Onboard Hinode. *Sol. Phys.* 249, 233–261. doi:10.1007/s11207-008-9169-9

Iwai, K., Loukitcheva, M., Shimojo, M., Solanki, S. K., and White, S. M. (2017). ALMA Discovery of Solar Umbral Brightness Enhancement at λ = 3 Mm. *Astrophysical J.* 841, L20. doi:10.3847/2041-8213/aa71b5

Jafarzadeh, S., Wedemeyer, S., Fleck, B., Stangalini, M., Jess, D. B., Morton, R. J., et al. (2021). *Philosophical Trans. R. Soc. A* 379, 20200174.

Kano, R., Shimizu, T., and Tarbell, T. D. (2010). Hinode Observation of Photospheric Magnetic Activities Triggering X-Ray Microflares Around a Well-Developed Sunspot. *Astrophysical J.* 720, 1136–1145. doi:10.1088/0004-637x/720/2/1136

Katsukawa, Y., Berger, T. E., Ichimoto, K., Lites, B. W., Nagata, S., Shimizu, T., et al. (2007). Small-Scale Jetlike Features in Penumbral Chromospheres. *Sci* 318, 1594. doi:10.1126/science.1146046

Kosugi, T., Matsuzaki, K., Sakao, T., Shimizu, T., Sone, Y., Tachikawa, S., et al. (2007). The Hinode (Solar-B) Mission: An Overview. *Sol. Phys.* 243, 3–17. doi:10.1007/s11207-007-9014-6

Kraus, J. (1986). *Radio Astronomy*. 2nd Ed. Pawell, Ohio: Cygnus-Quasar Books. 1-882484-00-2.

Lites, B. W., Akin, D. L., Card, G., Cruz, T., Duncan, D. W., Edwards, C. G., et al. (2013). The Hinode Spectro-Polarimeter. *Sol. Phys.* 283, 579–599. doi:10.1007/s11207-012-0206-3

Loukitcheva, M. A., Iwai, K., Solanki, S. K., White, S. M., and Shimojo, M. (2017). Solar ALMA Observations: Constraining the Chromosphere above Sunspots. *Astrophysical J.* 850, 35. doi:10.3847/1538-4357/aa91cc

Loukitcheva, M., Solanki, S. K., Carlsson, M., and White, S. M. (2015). Millimeter Radiation from a 3D Model of the Solar Atmosphere. *Astronomy Astrophysics* 575, A15. doi:10.1051/0004-6361/201425238

Martínez-Sykora, J., De Pontieu, B., de la Cruz Rodriguez, J., and Chintzoglou, G. (2020). *Astrophysical J.* 891, L8.

Martínez-Sykora, J., De Pontieu, B., Hansteen, V. H., Rouppe van der Voort, L., Carlsson, M., and Pereira, T. M. D. (2017). On the Generation of Solar Spicules and Alfvénic Waves. *Sci* 356, 1269. doi:10.1126/science.aah5412

Matsumoto, T., Kitai, R., Shibata, K., Shin'ichi, N., Kenichi, O., Tahe i, N., et al. (2008). Cooperative Observation of Ellerman Bombs between the Solar Optical Telescope Aboard Hinode and Hida/Domeless Solar Telescope. *PASJ* 60, 577. doi:10.1093/pasj/60.3.577

Miyawaki, S., Iwai, K., Shibasaki, K., Shiota, D., and Nozawa, S. (2016). Coronal Magnetic Fields Derived from Simultaneous Microwave and Euv Observations and Comparison with the Potential Field Model. *Astrophysical J.* 818, 8. doi:10.3847/0004-637x/818/1/8

Molnar, M. E., Reardon, K. P., Chai, Y., Gary, D., Uitenbroek, H., Cauzzi, G., et al. (2019). *Astrophys. J.* 881, 99. doi:10.3847/1538-4357/ab2ba3

Narang, N., Chandrashekhar, K., Jafarzadeh, S., Fleck, B., Szydlarski, M., and Wedemeyer, S. (2022). *arXiv:2202.11547*.

Nindos, A., Alissandrakis, C. E., Patsourakos, S., and Bastian, T. S. (2021a). *Astronomy Astrophysics* 638, A62.

Nindos, A., Patsourakos, S., Alissandrakis, C. E., and Bastian, T. S. (2021b). ALMA Observations of the Variability of the Quiet Sun at Millimeter Wavelengths. *Astronomy Astrophysics* 652, A92. doi:10.1051/0004-6361/202141241

Okamoto, T. J., and De Pontieu, B. (2011). Propagating Waves along Spicules. *Astrophysical J.* 736, L24. doi:10.1088/2041-8205/736/2/l24

Okamoto, T. J., Tsuneta, S., Berger, T. E., Ichimoto, K., Katsukawa, Y., Lites, B. W., et al. (2007). Coronal Transverse Magnetohydrodynamic Waves in a Solar Prominence. *Science* 318, 1577–1580. doi:10.1126/science.1145447

Ortiz, A., Bellot Rubio, L. R., Hansteen, V. H., de la Cruz Rodríguez, J., and van der Voort, L. R. (2014). Emergence of Granular-Sized Magnetic Bubbles through the Solar Atmosphere. I. Spectropolarimetric Observations and Simulations. *Astrophysical J.* 781, 126. doi:10.1088/0004-637x/781/2/126

Pariat, E., Aulanier, G., Schmieder, B., Georgoulis, M. K., Rust, D. M., and Bernasconi, P. N. (2004). Resistive Emergence of Undulatory Flux Tubes. *Astrophysical J.* 614, 1099–1112. doi:10.1086/423891

Parker, E. N. (1988). Nanoflares and the Solar X-Ray Corona. *Astrophysical J.* 330, 474. doi:10.1086/166485

Pereira, T. M. D., De Pontieu, B., and Carlsson, M. (2012). Quantifying Spicules. *Astrophysical J.* 759, 18. doi:10.1088/0004-637x/759/1/18

Peter, H., Tian, H., Curdt, W., Schmit, D., Innes, D., De Pontieu, B., et al. (2014). Hot Explosions in the Cool Atmosphere of the Sun. *Science* 346 (6207), 1255726. doi:10.1126/science.1255726

Scharmer, G. B., Bjelksjo, K., Korhonen, T. K., Lindberg, B., and Petterson, B. (2003). *Proc. SPIE Conf. Ser.* 4853, 341.

Scherrer, P. H., Schou, J., Bush, R. I., Kosovichev, A. G., Bogart, R. S., Hoeksema, J. T., et al. (2012). The Helioseismic and Magnetic Imager (HMI) Investigation for the Solar Dynamics Observatory (SDO). *Sol. Phys.* 275, 207–227. doi:10.1007/s11207-011-9834-2

Schou, J., Scherrer, P. H., Bush, R. I., Wachter, R., Couvidat, S., Rabello-Soares, M. C., et al. (2012). Design and Ground Calibration of the Helioseismic and Magnetic Imager (HMI) Instrument on the Solar Dynamics Observatory (SDO). *Sol. Phys.* 275, 229. doi:10.1007/s11207-011-9842-2

Shibata, K., Nakamura, T., Matsumoto, T., Otsuji, K., Okamoto, T. J., Nishizuka, N., et al. (2007). Chromospheric Anemone Jets as Evidence of Ubiquitous Reconnection. *Sci* 318, 1591. doi:10.1126/science.1146708

Shimizu, T. (2015). 3D Magnetic Field Configuration of Small-Scale Reconnection Events in the Solar Plasma Atmosphere. *Phys. Plasmas* 22, 101207. doi:10.1063/1.4933056

Shimizu, T., Katsukawa, Y., Kubo, M., Lites, B. W., Ichimoto, K., Suematsu, Y., et al. (2009). Hinode Observation of the Magnetic Fields in a Sunspot Light Bridge Accompanied by Long-Lasting Chromospheric Plasma Ejections. *Astrophysical J.* 696, L66–L69. doi:10.1088/0004-637x/696/1/l66

Shimizu, T., Nagata, S., Tsuneta, S., Tarbell, T., Edwards, C., Shine, R., et al. (2008). Image Stabilization System for Hinode (Solar-B) Solar Optical Telescope. *Sol. Phys.* 249, 221–232. doi:10.1007/s11207-007-9053-z

Shimizu, T., Shimojo, M., and Abe, M. (2021). Simultaneous ALMA-Hinode-IRIS Observations on Footpoint Signatures of a Soft X-Ray Loop-like Microflare. *Astrophysical J.* 922, 113. doi:10.3847/1538-4357/ac27a4

Shimizu, T., Shine, R. A., Title, A. M., Tarbell, T. D., and Frank, Z. (2002). Photospheric Magnetic Activities Responsible for Soft X-Ray Pointlike Microflares. I. Identifications of Associated Photospheric/Chromospheric Activities. *Astrophysical J.* 574, 1074–1088. doi:10.1086/340998

Shimojo, M., Bastian, T. S., Hales, A. S., White, S. M., Iwai, K., Hills, R. E., et al. (2017a). *Sol. Phys.* 292, 87. doi:10.1007/s11207-017-1095-2

Shimojo, M., Hudson, H. S., White, S. M., Bastian, T. S., and Iwai, K. (2017b). The First ALMA Observation of a Solar Plasmoid Ejection from an X-Ray Bright Point. *Astrophysical J.* 841, L5. doi:10.3847/2041-8213/aa70e3

Smitha, H. N., Chitta, L. P., Wiegelmann, T., and Solanki, S. K. (2018). Observations of Solar Chromospheric Heating at Sub-arcsec Spatial Resolution. *Astronomy Astrophysics* 617, A128. doi:10.1051/0004-6361/201833276

Stangalini, M., Del Moro, D., Berrilli, F., and Jefferies, S. M. (2011). MHD Wave Transmission in the Sun's Atmosphere. *Astronomy Astrophysics* 534, A65. doi:10.1051/0004-6361/201117356

Suematsu, Y., Tsuneta, S., Ichimoto, K., Shimizu, T., Otsubo, M., Katsukawa, Y., et al. (2008). The Solar Optical Telescope of Solar-B (Hinode): The Optical Telescope Assembly. *Sol. Phys.* 249, 197–220. doi:10.1007/s11207-008-9129-4

Tian, H., Zhu, X., Peter, H., Zhao, J., Samanta, T., and Chen, Y. (2018). Magnetic Reconnection at the Earliest Stage of Solar Flux Emergence. *Astrophysical J.* 854, 174. doi:10.3847/1538-4357/aaaae6

Toriumi, S., and Wang, H. (2019). Flare-productive Active Regions. *Living Rev. Sol. Phys.* 16, 3. doi:10.1007/s41116-019-0019-7

Tsuneta, S., Ichimoto, K., Katsukawa, Y., Nagata, S., Otsubo, M., Shimizu, T., et al. (2008). The Solar Optical Telescope for the Hinode Mission: An Overview. *Sol. Phys.* 249, 167–196. doi:10.1007/s11207-008-9174-z

Vargas Domínguez, S., van Driel-Gesztelyi, L., and Bellot Rubio, L. R. (2012). *Sol. Phys.* 278, 99.

Vernazza, J. E., Avrett, E. H., and Loeser, R. (1981). Structure of the Solar Chromosphere. III - Models of the EUV Brightness Components of the Quiet-Sun. *Astrophysical J. Suppl. Ser.* 45, 635. doi:10.1086/190731

White, S. M., Loukitcheva, M., and Solanki, S. K. (2006). High-resolution Millimeter-Interferometer Observations of the Solar Chromosphere. *Astronomy Astrophysics* 456, 697–711. doi:10.1051/0004-6361:20052854

Yokoyama, T., and Shibata, K. (1995). Magnetic Reconnection as the Origin of X-Ray Jets and Hα Surges on the Sun. *Nature* 375 (6526), 42–44. doi:10.1038/375042a0

Conflict of Interest: The authors declare that the research was conducted in the absence of any commercial or financial relationships that could be construed as a potential conflict of interest.

frontiers | Frontiers in Astronomy and Space Sciences

ORIGINAL RESEARCH
published: 16 June 2022
doi: 10.3389/fspas.2022.911118

A Genetic Algorithm to Model Solar Radio Active Regions From 3D Magnetic Field Extrapolations

Alexandre José de Oliveira e Silva[1,2,3], Caius Lucius Selhorst[1], Joaquim E. R. Costa[3], Paulo J. A. Simões[4,5], Carlos Guillermo Giménez de Castro[4,6], Sven Wedemeyer[7], Stephen M. White[8], Roman Brajša[9] and Adriana Valio[4]*

[1]NAT–Núcleo de Astrofísica, Universidade Cidade de São Paulo, São Paulo, Brazil, [2]IP&–Instituto de Pesquisa e Desenvolvimento, Universidade do Vale do Paraíba, São José dos Campos, Brazil, [3]INPE–Instituto Nacional de Pesquisas Espaciais (DICEP), São José dos Campos, Brazil, [4]Centro de Rádio Astronomia e Astrofísica Mackenzie, Escola de Engenharia, Universidade Presbiteriana Mackenzie, São Paulo, Brazil, [5]SUPA School of Physics and Astronomy, University of Glasgow, Glasgow, United Kingdom, [6]Instituto de Astronomía y Física del Espacio, CONICET-UBA, Ciudad Universitaria, Buenos Aires, Argentina, [7]Rosseland Centre for Solar Physics, Institute of Theoretical Astrophysics, University of Oslo, Oslo, Norway, [8]Space Vehicles Directorate, Air Force Research Laboratory, Albuquerque, NM, United States, [9]Hvar Observatory, Faculty of Geodesy, University of Zagreb, Zagreb, Croatia

OPEN ACCESS

Edited by:
Masumi Shimojo, National Astronomical Observatory of Japan (NINS), Japan

Reviewed by:
Sijie Yu, New Jersey Institute of Technology, United States
Victor De La Luz, National Autonomous University of Mexico, Mexico

***Correspondence:**
Caius L. Selhorst
caiuslucius@gmail.com

Specialty section:
This article was submitted to Stellar and Solar Physics, a section of the journal Frontiers in Astronomy and Space Sciences

Received: *02 April 2022*
Accepted: *06 May 2022*
Published: *16 June 2022*

Citation:
de Oliveira e Silva AJ, Selhorst CL, Costa JER, Simões PJ, Giménez de Castro CG, Wedemeyer S, White SM, Brajša R and Valio A (2022) A Genetic Algorithm to Model Solar Radio Active Regions From 3D Magnetic Field Extrapolations. Front. Astron. Space Sci. 9:911118. doi: 10.3389/fspas.2022.911118

In recent decades our understanding of solar active regions (ARs) has improved substantially due to observations made with better angular resolution and wider spectral coverage. While prior AR observations have shown that these structures were always brighter than the quiet Sun at centimeter wavelengths, recent observations at millimeter and submillimeter wavelengths have shown ARs with well defined dark umbrae. Given this new information, it is now necessary to update our understanding and models of the solar atmosphere in active regions. In this work, we present a data-constrained model of the AR solar atmosphere, in which we use brightness temperature measurements of NOAA 12470 at three radio frequencies: 17, 100 and 230 GHz. The observations at 17 GHz were made by the Nobeyama Radioheliograph (NoRH), while the observations at 100 and 230 GHz were obtained by the Atacama Large Millimeter/submillimeter Array (ALMA). Based on our model, which assumes that the radio emission originates from thermal free-free and gyroresonance processes, we calculate radio brightness temperature maps that can be compared with the observations. The magnetic field at distinct atmospheric heights was determined in our modelling process by force-free field extrapolation using photospheric magnetograms taken by the Helioseismic and Magnetic Imager (HMI) on board the Solar Dynamics Observatory (SDO). In order to determine the best plasma temperature and density height profiles necessary to match the observations, the model uses a genetic algorithm that modifies a standard quiet Sun atmospheric model. Our results show that the height of the transition region (TR) of the modelled atmosphere varies with the type of region being modelled: for umbrae the TR is located at 1080 ± 20 km above the solar surface; for penumbrae, the TR is located at 1800 ± 50 km; and for bright regions outside sunspots, the TR is located at 2000 ± 100 km. With these results, we find good agreement with the observed AR brightness temperature maps. Our modelled AR can be used to estimate the emission at frequencies without observational coverage.

Keywords: Sun: radio radiation, Sun: atmosphere, Sun: magnetic fields, force-free field extrapolation, Sun–active regions

1 INTRODUCTION

Numerous semi-empirical models of the solar atmosphere are intended to reproduce solar active region (AR) observations with success in a specific wavelength range. Most of these efforts have been based on optical and UV line observations (e.g.: Vernazza et al., 1981; Fontenla et al., 1993, 1999, 2009) and have had success modelling the observations at these wavelengths. Nevertheless, these models are less successful in reproducing radio observations of ARs, perhaps due to the presence of distinct emission mechanisms at radio wavelengths and the lack of comparable spatial resolution.

In the last decades our knowledge of solar active regions has improved substantially due to observations made with better angular resolution. Recent observations at millimeter and submillimeter wavelengths have shown ARs with well defined dark umbrae (Loukitcheva et al., 2014; Iwai and Shimojo, 2015; Shimojo et al., 2017). Moreover, Iwai et al. (2016) suggested that even at radio frequencies as low as 34 GHz the observed brightness temperature (T_b) of the umbral region is almost the same as that of the quiet region, which indicates that the height (and therefore temperature) in the atmosphere at which its emission becomes optically thick should be lower than that predicted by the models.

Great advances in the understanding of AR behavior have been acquired with the daily NoRH (Nakajima et al., 1994) observations at 17 GHz since 1992, and also 34 GHz after 1996. Vourlidas et al. (2006) studied 529 ARs observed by the NoRH at 17 GHz (1992–1994), and concluded that the ARs with polarization greater than 30% contain a gyroresonance core that increases their brightness temperatures to $T_b \gtrsim 10^5$ K, well above the quiet Sun brightness temperature ($T_{b,QS}$) of 10000 K at 17 GHz. Moreover, they also argued that these high T_b values were due to opacity at the gyroresonance 3rd harmonic, requiring 2000 G of magnetic field intensity ($|\vec{B}|$) in the corona, and therefore at least $|\vec{B}| = 2200$ G at the photospheric level.

At submillimeter wavelenghts, Silva et al. (2005) analyzed a total of 23 ARs observed during 2002 at 212 and 405 GHz from the Submillimeter Solar Telescope (SST, Kaufmann et al., 2008) and combined with maps at 17 and 34 GHz from NoRH. The flux density spectra at these frequencies was found to increase with frequency with a slope of 2, indicating that the emission from these active regions is predominantly due to thermal bremsstrahlung. Moreover, Valle Silva et al. (2021) made a similar analyses with the inclusion of the ALMA single-dish data reaching the same conclusions.

Further advances in the study of ARs became possible in 2016, with the start of ALMA observations at millimeter/submillimeter wavelengths (Wedemeyer et al., 2016). During the Science Verification period, 2015 December 16–20, AR 12470, including a sunspot umbra, was observed by the ALMA interferometric array at Band 3 (84–116 GHz) and Band 6 (211–275 GHz). Whereas the sunspot umbra exhibited a continuous dark region at Band 6 (Shimojo et al., 2017), at Band 3 the center of the umbra showed a bright structure with T_b 800 K above the dark region around it (Iwai et al., 2017). This Band 3 brightness enhancement may be an intrinsic feature of the sunspot umbra at chromospheric heights, such as a manifestation of umbral flashes, or it could be related to a coronal plume.

Selhorst et al. (2008) were able to reproduce the brightness temperatures and the spatial structure of AR NOAA 10008 seen in NoRH observations at 17 and 34 GHz. That work used photospheric magnetic field extrapolation to derive $\vec{B}$ in the atmosphere[1] and suggested that the AR chromospheric temperature and density gradients were steeper than those proposed for the quiet Sun. Also, the temperature and density in the corona needed to be greater than expected in the quiet Sun, as expected. With these assumptions, the model was able to reproduce the high T_b observed in the 17 GHz gyroresonance core, and also the free-free emission observed in non-polarized areas at both 17 and 34 GHz.

Brajša et al. (2009) studied active regions observed at 37 GHz with the 14-m antenna of the Metsähovi Radio Observatory and compared the measured intensities with radiation models. They concluded that thermal bremsstrahlung can explain the observed radiation of ARs, while thermal gyromagnetic emission can, with high probability, be excluded as a possible radiation mechanism at the frequency considered (37 GHz). Further, Brajša et al. (2018) compared intensities measured in full-disc solar ALMA maps taken at 248 GHz with model-based prediction of the brightness temperatures. Again, they concluded that the thermal bremsstrahlung is the main radiation mechanism responsible for the AR emission, also at this observing frequency (248 GHz).

As an improvement of the AR modelling presented in Selhorst et al. (2008, 2009), in this work we apply a genetic algorithm (GA; Charbonneau, 1995) to modify a standard quiet Sun atmospheric model in order to determine the best plasma temperature and density height profiles necessary to match the observations of NOAA 12470 obtained by ALMA (single-dish maps at 100 and 230 GHz) and NoRH (17 GHz interferometric map).

Finally, we note that Brajša et al. (2020) performed a preliminary analysis of the magnetic structure above the same AR 12470 using LOS photospheric magnetograms and a potential-field source surface (PFSS) model to extrapolate magnetic fields into the solar chromosphere and corona. Results of the model were compared with the ALMA single-dish (248 GHz) and interferometric (100 GHz) measurements of the same AR. The general extrapolated magnetic structure is consistent with the ALMA observations, but a detailed analysis and comparison with ALMA small-scale features was not possible with the model used and requires a more detailed magnetic field extrapolation model, what is performed in the present work.

[1]The 3D magnetic field extrapolation used in Selhorst et al. (2008) has been integrated in the fast algorithm GX Simulator tool available in SolarSoft (Nita et al., 2015, 2018).

2 ATMOSPHERIC MODELLING *VIA* GENETIC ALGORITHM

The purpose of this study is to estimate the temperature and electron density as a function of height in the solar atmosphere, as constrained by brightness temperature T_b maps of radio observations. The different frequencies provide access to different layers of the atmosphere due to the frequency dependence of opacity. An initial 1D atmospheric model is used as a seed for the GA: at each step, T_b is obtained via the calculation of radiative transfer incorporating opacity from both the thermal bremsstrahlung and gyroresonance emission mechanisms. For these calculation, the 3D magnetic field structure above the AR is derived from linear force-free extrapolations (LFF) from photospheric magnetograms. The GA iteratively updates the atmospheric plasma trapped by magnetic field lines until a best model is found via χ^2 minimization of the calculated and observed T_b values. This process is run independently for each pixel of the observed radio maps, resulting in an atmospheric model (T and n versus height) for each line of sight. Together, the results for all pixels provide the 3D atmospheric model for the active region.

2.1 Genetic Algorithm Features

In order to determine the best plasma temperature and density height profiles necessary to match the observations, we employ the genetic algorithm Pikaia (Charbonneau, 1995).

The atmospheric model developed by Selhorst et al. (2005b, hereafter SSC) is used as the seed in the genetic algorithm, that changes the seed model to find the best fit for the observational measurements. Five free parameters are supplied to the GA representing the atmospheric model. These parameters are based on the ideas presented in Selhorst et al. (2008), as follows:

- ∇T–changes the AR temperature gradient in the chromosphere;
- ∇n_e–changes the AR electron density gradient in the chromosphere;
- N_T–changes the AR coronal temperature by a constant value, in which $N_T = \frac{T_{AR}}{T_{QS}}$;
- N_{n_e}—changes the AR coronal electron density by a constant value, in which $N_{n_e} = \frac{n_{e_{AR}}}{n_{e_{QS}}}$;
- Δh–changes the TR position.

These five free parameters combined build new electron density and temperature profiles, which are used, along with the magnetic field values for the line-of-sight column, to calculate the bremsstrahlung and gyroresonance absorption coefficients. The radiative transfer is then performed and the resulting T_b values are compared with the observations. Nevertheless, the GA used here is a mathematical solution and it does not verify if the atmospheric plasma is in local thermodynamic equilibrium (LTE) or not.

A generation of child atmospheric models is created by the algorithm based on the parent models with the lowest χ^2 values, using the genetic algorithm described in Charbonneau (1995). The GA starts with the choice of minimum and maximum values for each one of the five free parameters. The method used here was full-generation replacement using ten generations with one hundred children each. The crossover probability was 0.85 and the mutation mode was variable. The initial mutation rate, that is, the initial probability that any gene locus will mutate in any generation, was 0.005. Finally, the mutation rate range was between 0.0005 and 0.25. In our runs the χ^2 measure typically stabilizes to a minimum value by about the seventh generation.

2.2 Magnetic Field Extrapolation

Photospheric magnetograms are used as the boundary condition for an extrapolation of the field above the photosphere using the linear force-free field approximation. The fundamental equation that describes a force-free field (assuming that the current density is parallel to the magnetic field at any point in space) is

$$\vec{\nabla} \times \vec{B} = \alpha \vec{B} \tag{1}$$

where α is a proportionality function and represents the current density distribution, called a force-free function.

The extrapolation routine is based on the works of Nakagawa and Raadu (1972) and Seehafer (1978) and was previously implemented in IDL by J. E. R. Costa and T. S. N. Pinto (used in Selhorst et al., 2005a, 2008; Nita et al., 2018). The calculation starts from the line-of-sight magnetic field component at the photosphere and determines the magnetic field above it for both the potential field ($\alpha = 0$) and the force-free field ($\alpha \neq 0$). The result is three cubes of intensities, one for each component of the magnetic field vector (B_x, B_y, and B_z) and another data cube for the positions of the magnetic field lines. The positions of the magnetic field lines determine where the atmospheric plasma is changed with respect to the quiet Sun. Moreover, the x and y dimensions of the cubes have the same dimensions as the selected active region area. In this work, the extrapolated field lines were calculated only above positions with $|\vec{B}|_{\min} = 200$ G at the photosphere. A different minimum value could be chosen by the user, but we found that the inclusion of magnetic fields below this limit resulted in the simulated ARs appearing much larger than the observed ARs. This approach in effect determines one parameter, i.e., the lower limit of the field strength needed to best reproduce the observations.

2.3 Emission Mechanisms

The brightness temperature T_b is obtained by computing the radiative transfer along the line of sight for each column of the AR. At radio frequencies, in the quiescent solar atmosphere, the main emission mechanisms are bremsstrahlung and gyroresonance (Dulk, 1985). The thermal bremsstrahlung absorption coefficient (κ_b) is calculated by

$$\kappa_b \approx 9.78 \times 10^{-3} \frac{n_e}{\nu^2\ T^{3/2}} \sum_i Z_i^2\ n_i \times g(T, \nu) \tag{2}$$

where ν is the observed frequency (Hz), T is the plasma temperature and n_e is the electron density. Only the contributions of collisions with protons was considered, since its density is much larger than that of other ion species (n_i).

Following Zirin (1988), it was assumed $Z = 1.178$, if a fully hydrogen atmosphere was considered, i.e., $Z = 1$, the resulting T_b should be only ~ 3% smaller for all frequencies simulated here.

The Gaunt factor (g(T,ν)) used is as follow:

$$g(T,\nu) = \begin{cases} 18.2 + \ln T^{3/2} - \ln \nu & (T < 2 \times 10^5 \mathrm{K}) \\ 24.5 + \ln T - \ln \nu & (T > 2 \times 10^5 \mathrm{K}) \end{cases}$$

The gyroresonance absorption coefficient (κ_g) is

$$\begin{aligned} \kappa_g(s,\theta) &= \int_{-\infty}^{\infty} \kappa_g(s,\theta)\, \frac{d\nu}{\nu_b} \\ &= \left(\frac{\pi}{2}\right)^{\frac{5}{2}} \frac{2}{c}\, \frac{\nu_p^2}{\nu}\, \frac{s^2}{s!} \left(\frac{s^2\, \beta_o^2\, \sin^2\theta}{2}\right)^{s-1} \times (1 - \sigma|\cos\theta|)^2 \end{aligned} \tag{3}$$

where $\sigma = +1$ for the o-mode and $\sigma = -1$ for the x-mode, $\beta_o^2 = kT/mc^2$. The harmonic is defined as $s = \nu/\nu_B$, where ν_B is electron-cyclotron frequency and ν_p is the electron plasma frequency:

$$\begin{aligned} \nu_B &\approx 2.8 \times 10^6 B \\ \nu_p &\approx 9000\, n_e^{1/2} \end{aligned} \tag{4}$$

Since the contribution of higher harmonics to the radio emission is very small (Shibasaki et al., 1994), the gyroresonance emission was only calculated for harmonics smaller than 5 ($s \leq 5$).

Following Zirin (1988), radiative transfer yields the brightness temperature as a function of wavelength as:

$$T_b(\nu) = \int T \kappa_\nu\, e^{-\tau_\nu} dL \tag{4}$$

where $\kappa_\nu = \kappa_b + \kappa_g$, dL is the distance element towards the observer, and τ_ν is the optical depth

$$\tau_\nu = \int \kappa_\nu\, dL \tag{5}$$

3 OBSERVATIONS

In this work, we selected the active region AR NOAA 12470 to test our algorithm. This region was selected due to the availability of radio observations at three frequencies: 17 GHz, from the Nobeyama Radio Heliograph (NoRH), 100 and 230 GHz from the Atacama Large Millimetric and submillimetric Array (ALMA) (Shimojo et al., 2017; Valle Silva et al., 2021).

Here, the LFF extrapolations algorithm used the line-of-sight (LOS) magnetogram obtained by the Helioseismic and Magnetic Imager (HMI, Schou et al., 2012) on the Solar Dynamics Observatory (SDO, Pesnell et al., 2012), nevertheless, the LFF extrapolations could also be applied to vector magnetograms. HMI operates at wavelengths around 6173 Å (Fe I) and provides LOS magnetograms of 4096 × 4096 pixels with ~ 0.5 arcsec spatial resolution.

3.1 Magnetogram

Figure 1A shows the HMI line of sight (LOS) magnetogram obtained on 17 December 2015 at 14:51 UT. This full Sun image has an apparent radius of 975" and magnetic field intensities ($|\vec{B}|$) up to 2300 G. The active region is shown in detail in **Figure 1B**, centered in the point of greatest magnetic field intensity ($|\vec{B}|_{\max}$). The selected area included the whole AR NOAA 12470, and also part of the AR NOAA 12469 located to the northwest of the central umbra.

The line-of-sight magnetogram will underestimate field strengths in AR 12470 due to projection effects, since the region is significantly offset from disk center. To correct for this, the AR has been rotated to solar disk center, solar spherical curvature has been removed, and the magnetic field intensities have been corrected for projection. This increases the maximum field strength from 2,300 G to ~ 2500 G.

3.2 Radio Maps

The ALMA maps used here were obtained during the Science Verification period, 2015 December 16–20[2]. The maps were obtained by the fast-scan single-dish method described in White et al. (2017), at Band 3 (84–116 GHz) and Band 6 (211–275 GHz). Following Selhorst et al. (2019), we took 100 and 230 GHz as the reference frequencies for Bands 3 and 6, respectively. The maps were made from observations of a 12 m diameter antenna, resulting in nominal spatial resolutions of 25″ and 58" at 230 and 100 GHz, respectively.

Since the radio maps were not obtained at the same time as the magnetogram, it was necessary to take into account solar rotation when aligning the radio data with the magnetogram. The nominal time of the 230 GHz map is 14:52 UT, i.e., only 1 min difference from the nominal time of the HMI observation, requiring just −0.01° of longitudinal rotation. The nominal time of the 100 GHz map was 19:35 UT, requiring a longitudinal rotation of −2.85°. Moreover, the ALMA maps come in distinct sizes, 800 × 800 pixels^2 (3″ pixel) at 230 GHz and 400 × 400 pixels^2 (6" pixel) at 100 GHz. Thus for a better comparison with the model results they were resized to match the HMI magnetogram (4096 × 4096 pixels^2).

While the quiet Sun brightness temperature ($T_{b,QS}$) at 230 GHz is 6210 ± 110 K (Selhorst et al., 2019), the AR 12470 brightness temperature (T_b) varies from 5800 to 6600 K across locations with magnetic field intensities greater than 1500 G, i.e., the minimum intensity to form a sunspot (Livingston et al., 2012). At 100 GHz, T_{qS} = 7,110 ± 90 K (Selhorst et al., 2019) and AR 12470 showed T_b varying from 7,200 to 7,650 K where $|\vec{B}| > 1500$ G.

We also used 17 GHz radio maps obtained routinely by NoRH with resolution of 10–18 arcsec in intensity and circular polarization (Nakajima et al., 1994) and intensity maps at 34 GHz with 5–10″ spatial resolution (Takano et al., 1997). We used a 17 GHz map observed at 02:44 UT and available in 512 × 512 pixels^2 format (4.91" resolution), rotated longitudinally by 7.31° with respect to the HMI magnetogram. At 17 GHz, T_{qS}

[2]https://almascience.eso.org/alma-data/science-verification.

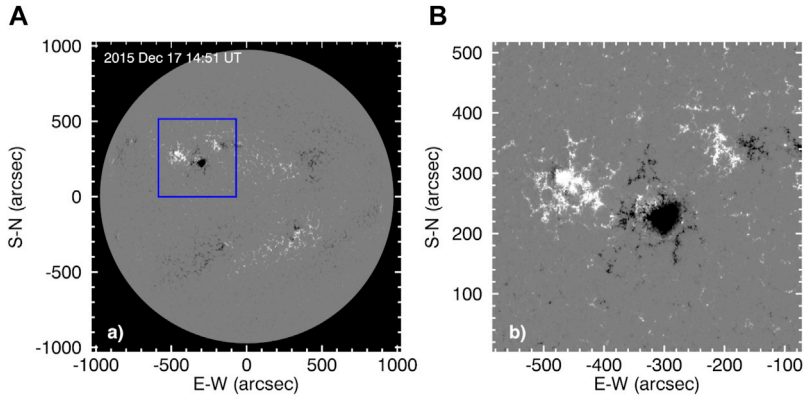

FIGURE 1 | The **(A)** image shows the SDO/HMI LOS magnetogram obtained on 2015 December 17 at 14:51 UT. The blue rectangle indicates the selected area of active region AR12470, shown in expanded form in the **(B)**. The region shown is 516.4″ × 516.4″, centered at 17.40°N,17.68°E.

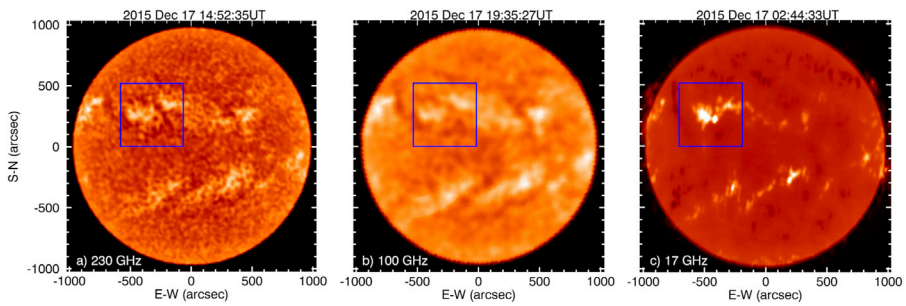

FIGURE 2 | Full disc solar maps obtained at **(A)** 230 GHz **(A)**, **(B)** 100 GHz and **(C)** the NoRH map at 17 GHz. The blue rectangle in each panel indicates the selected area of the active region AR12470, taking into account solar rotation given timing differences relative to the HMI magnetogram.

= 10050 ± 120 K, and AR 12470 has brightness temperatures varying from 5.3 × 10^4 to 6.8 × 10^4 K in the areas with $|\vec{B}| > 1500$ G. **Figure 2** shows the ALMA single dish maps obtained at 230 and 100 GHz, plus the NoRH map at 17 GHz. In contrast to the small levels of variability in the ALMA maps, at 17 GHz the active region T_b reached values almost 7 times the level of the quiet Sun. The bright compact source in the active region has a high polarization degree (~ 100%) indicating the presence of a gyroresonance core (Vourlidas et al., 2006; Selhorst et al., 2008) which is coincident with the sunspot umbra.

4 RESULTS

A low value for the α parameter in (1) does not significantly affect the extrapolated magnetic field configuration at low heights in the atmosphere: here α = −0.005 was chosen for the LFF extrapolation since it generated a greater number of closed magnetic field lines in the selected region than did the potential-field extrapolation (α = 0). **Figure 3** shows some of the magnetic field lines obtained in the extrapolation with α = −0.005 and $|\vec{B}|_{min}$ = 200 G.

To speed up the computational process, the datacubes and images were resized from 1024 × 1024 pixels^2 to 256 × 256 pixels^2, corresponding to a spatial resolution ~ 2″ per pixel. However, the radiative transfer calculations require better resolution in the height of the voxels (h_z) due to the relatively narrow width of the chromosphere, and they were re-scaled via interpolation from the resolution of the magnetogram to 50 km, similar to the resolution of the SSC model.

The GA optimizes the electron density and temperature profiles for each vertical column in the model cube by comparing the brightness temperatures obtained from the model with the observed maps, pixel by pixel. This procedure initially generated ~28 thousand different atmosphere profiles. These profiles were refined, in order to reduce the χ^2 between observed T_b values and those obtained from the model. The final model is obtained when the χ^2 from the GA process ceases to reduce further.

The resulting atmospheric profiles were grouped into four different classes corresponding to different atmospheric features: umbrae, penumbrae, plage and quiet Sun. To speed up the GA process, distinct initial seeds were used for each class. Each pixel in the magnetogram was classified as umbra, penumbra, or plage according to its intensity ($|\vec{B}|$), as follows: umbra, $|\vec{B}| \geq 1500$ G

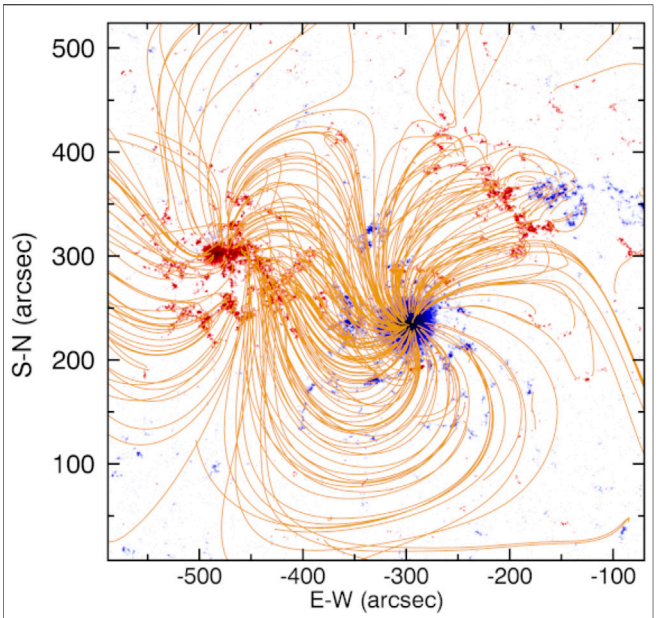

FIGURE 3 | Magnetic field lines obtained in a linear force-free extrapolation of the AR 12470 magnetogram, for $|\vec{B}|_{min}$ = 200 G and α = −0.005.

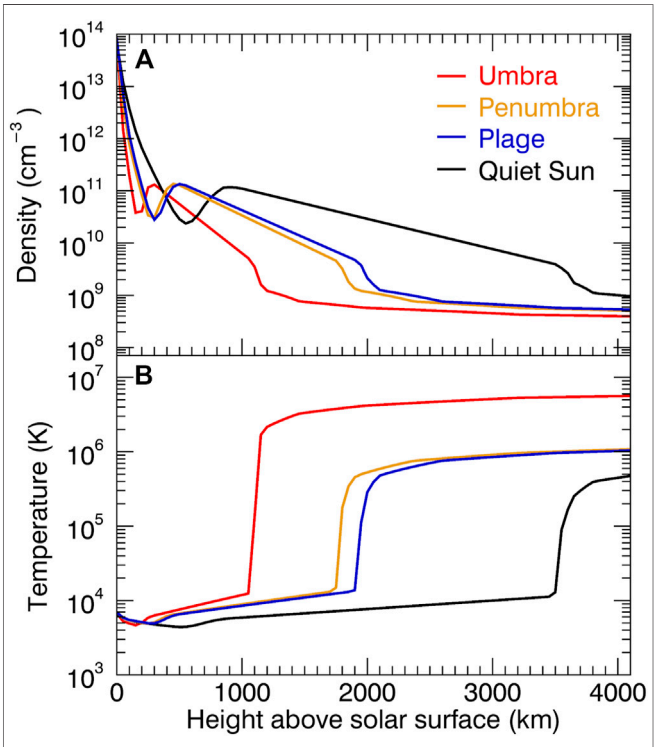

FIGURE 4 | Mean electron density **(A)** and temperature **(B)** profiles obtained for umbrae, penumbrae and plages. The SSC model (quiet Sun) is shown for comparison.

TABLE 1 | Average transition region heights in models of distinct atmospheric features.

AR region	$\|\vec{B}\|_0$ (G)	TR height (km)
Quiet Sun	$\|\vec{B}\|_0 < 200$	3,500
Umbra	$\|\vec{B}\|_0 \geq 1500$	1080 ± 20
Penumbra	$1000 \leq \|\vec{B}_0\| < 1500$	1800 ± 50
Plages	$200 \leq \|\vec{B}_0\| < 1000$	2000 ± 100

(~ 200 pixels); penumbra, $1000 \leq |\vec{B}_0| < 1500$ G (~230 pixels); plages, $200 \leq |\vec{B}_0| < 1000$ G (~27,200 pixels). All pixels with $|\vec{B}| \leq 200$ G were classified as quiet Sun (~38,000 pixels) and were assumed to have $T_B = T_{qS}$. We then obtained the average electron density and temperature profiles for each of the three AR classes by calculating the average of the profiles with the lowest χ^2 values in the T_b calculation, in relation to the observed values at the three distinct observing frequencies. These resulting models are shown in **Figure 4** along with the SSC quiet Sun, for comparison.

The $|\vec{B}|$ limits used to classify each pixel are based on studies by Livingston et al. (2012), who derived a minimum necessary value of 1500 G for sunspot formation. Moreover, the umbra is a compact source with a diameter ~ 25″ in its largest part. In Nita et al. (2018), the authors proposed a similar separation, however, in that work the separation was based on solar white light images instead of a magnetogram, which is not useful for faint or spotless ARs.

In **Table 1** we present the average height of the transition region (TR), which is one of the five free parameters fitted in the GA process, for each atmospheric class: thus, 1080 ± 20 km above the solar surface for umbrae, 1800 ± 50 km for penumbrae, and 2,000 ± 100 km for plages.

4.1 Free-Free Contribution

The GA is able to derive appropriate fits for the assumed basic structure of the solar atmosphere, i.e., fitting for the 5 free parameters yields satisfactory models. Although, the SSC model considers the plasma fully ionized above 1,000 km, i.e. $n_e = n_i$, to simplify the GA the densities were grouped in a single variable, that is $(n_e \times n_i)^{1/2}$. This variable was assumed as the density in **Table 2** and **Figure 4**. **Table 2** shows the variation of temperature and density as function of height for the distinct AR areas, moreover, the distinct atmospheric layer were displayed in different colors, that is salmon for photosphere, green for chromosphere and orange for TR and corona.

Comparison with the quiet-Sun model indicates that the umbrae, penumbrae and plages have a narrower temperature-minimum region and a thinner chromosphere than the quiet Sun, as can be seen in **Table 2** and **Figure 4**. Moreover, the compression of the temperature minimum and the chromosphere are most pronounced in umbral pixels, i.e., the region with more intense magnetic fields (**Figure 4**). The mean umbral model placed the transition region close to 1,000 km above the solar surface, in agreement with previous work (e.g., Fontenla et al., 1999, 2009; Selhorst et al., 2008; Nita et al., 2018, see also; Zlotnik et al., 1996). Furthermore, the umbral region is

TABLE 2 | Variation of temperature and density as function of height for the distinct AR areas. The distinct atmospheric layer were displayed in different colors, that is salmon for photosphere, green for chromosphere and orange for TR and corona.

	Quiet Sun		Plage		Penumbra		Umbra	
Height (km)	Temperature (K)	Density $[(n_e \times n_i)^{1/2}]$ (cm^{-3})	Temperature (K)	Density $[(n_e \times n_i)^{1/2}]$ (cm^{-3})	Temperature (K)	Density $[(n_e \times n_i)^{1/2}]$ (cm^{-3})	Temperature (K)	Density $[(n_e \times n_i)^{1/2}]$ (cm^{-3})
0.0	$6.5200E+03$	$6.7882E+13$	$6.9568E+03$	$7.9951E+13$	$6.9568E+03$	$8.0156E+13$	$6.6786E+03$	$8.0079E+13$
100.0	$5.4100E+03$	$3.7211E+12$	$5.4831E+03$	$1.1535E+12$	$5.4236E+03$	$7.8583E+11$	$4.9185E+03$	$1.9381E+11$
200.0	$4.9900E+03$	$6.5751E+11$	$5.1178E+03$	$1.2238E+11$	$5.0417E+03$	$8.2822E+10$	$5.0368E+03$	$4.0661E+10$
300.0	$4.7700E+03$	$2.0174E+11$	$4.9405E+03$	$2.7854E+10$	$5.0807E+03$	$3.0434E+10$	$6.2980E+03$	$1.3120E+11$
400.0	$4.5600E+03$	$6.9649E+10$	$5.8022E+03$	$7.6292E+10$	$6.1542E+03$	$1.0840E+11$	$6.9067E+03$	$8.5847E+10$
500.0	$4.4071E+03$	$2.8640E+10$	$6.5441E+03$	$1.3471E+11$	$6.6928E+03$	$1.2788E+11$	$7.5747E+03$	$5.5659E+10$
600.0	$4.5500E+03$	$2.6229E+10$	$6.9024E+03$	$1.1233E+11$	$7.0932E+03$	$9.8027E+10$	$8.2983E+03$	$3.6027E+10$
700.0	$5.0045E+03$	$5.2452E+10$	$7.2778E+03$	$8.8068E+10$	$7.5130E+03$	$7.5063E+10$	$9.0839E+03$	$2.3368E+10$
800.0	$5.4690E+03$	$9.4091E+10$	$7.6690E+03$	$6.8978E+10$	$7.9529E+03$	$5.7486E+10$	$9.9380E+03$	$1.5132E+10$
900.0	$5.7445E+03$	$1.1679E+11$	$8.0776E+03$	$5.4071E+10$	$8.4148E+03$	$4.4031E+10$	$1.0867E+04$	$9.8165E+09$
1000.0	$5.9000E+03$	$1.1000E+11$	$8.5048E+03$	$4.2397E+10$	$8.9001E+03$	$3.3727E+10$	$1.1879E+04$	$6.3579E+09$
1100.0	$6.0573E+03$	$9.6271E+10$	$8.9519E+03$	$3.3208E+10$	$9.4106E+03$	$2.5837E+10$	$1.3144E+05$	$3.5132E+09$
1200.0	$6.2188E+03$	$8.4253E+10$	$9.4201E+03$	$2.6047E+10$	$9.9479E+03$	$1.9794E+10$	$2.1610E+06$	$1.2177E+09$
1300.0	$6.3847E+03$	$7.3736E+10$	$9.9106E+03$	$2.0422E+10$	$1.0514E+04$	$1.5164E+10$	$2.5885E+06$	$1.0404E+09$
1400.0	$6.5549E+03$	$6.4532E+10$	$1.0425E+04$	$1.5996E+10$	$1.1109E+04$	$1.1618E+10$	$3.0181E+06$	$8.6324E+08$
1500.0	$6.7297E+03$	$5.6477E+10$	$1.0964E+04$	$1.2552E+10$	$1.1737E+04$	$8.9018E+09$	$3.3377E+06$	$7.4682E+08$
1600.0	$6.9092E+03$	$4.9427E+10$	$1.1529E+04$	$9.8406E+09$	$1.2398E+04$	$6.8206E+09$	$3.5101E+06$	$7.1085E+08$
1700.0	$7.0934E+03$	$4.3257E+10$	$1.2122E+04$	$7.7100E+09$	$1.3095E+04$	$5.2261E+09$	$3.6829E+06$	$6.7492E+08$
1800.0	$7.2825E+03$	$3.7857E+10$	$1.2744E+04$	$6.0504E+09$	$1.7611E+05$	$3.2130E+09$	$3.8559E+06$	$6.3902E+08$
1900.0	$7.4767E+03$	$3.3132E+10$	$1.3806E+04$	$4.7408E+09$	$4.5365E+05$	$1.3433E+09$	$4.0292E+06$	$6.0316E+08$
2000.0	$7.6761E+03$	$2.8996E+10$	$2.8696E+05$	$2.1365E+09$	$5.2845E+05$	$1.1619E+09$	$4.1805E+06$	$5.7397E+08$
2100.0	$7.8808E+03$	$2.5377E+10$	$4.7769E+05$	$1.2613E+09$	$5.8934E+05$	$1.0535E+09$	$4.2745E+06$	$5.6185E+08$
2200.0	$8.0909E+03$	$2.2209E+10$	$5.3609E+05$	$1.1487E+09$	$6.5039E+05$	$9.4510E+08$	$4.3686E+06$	$5.4974E+08$
2300.0	$8.3067E+03$	$1.9437E+10$	$5.9190E+05$	$1.0498E+09$	$7.1160E+05$	$8.3678E+08$	$4.4626E+06$	$5.3765E+08$
2400.0	$8.5282E+03$	$1.7010E+10$	$6.4785E+05$	$9.5113E+08$	$7.6257E+05$	$7.5280E+08$	$4.5566E+06$	$5.2557E+08$
2500.0	$8.7556E+03$	$1.4887E+10$	$7.0397E+05$	$8.5237E+08$	$7.8713E+05$	$7.3078E+08$	$4.6507E+06$	$5.1349E+08$
2600.0	$8.9890E+03$	$1.3029E+10$	$7.5755E+05$	$7.5985E+08$	$8.1172E+05$	$7.0878E+08$	$4.7448E+06$	$5.0143E+08$
2700.0	$9.2287E+03$	$1.1402E+10$	$7.8152E+05$	$7.3639E+08$	$8.3633E+05$	$6.8679E+08$	$4.8389E+06$	$4.8937E+08$
2800.0	$9.4748E+03$	$9.9791E+09$	$8.0406E+05$	$7.1633E+08$	$8.6098E+05$	$6.6481E+08$	$4.9330E+06$	$4.7733E+08$
2900.0	$9.7275E+03$	$8.7335E+09$	$8.2661E+05$	$6.9630E+08$	$8.8565E+05$	$6.4285E+08$	$5.0271E+06$	$4.6529E+08$
3000.0	$9.9868E+03$	$7.6433E+09$	$8.4920E+05$	$6.7627E+08$	$9.1035E+05$	$6.2090E+08$	$5.1213E+06$	$4.5325E+08$
3100.0	$1.0253E+04$	$6.6892E+09$	$8.7181E+05$	$6.5625E+08$	$9.3507E+05$	$5.9897E+08$	$5.2155E+06$	$4.4122E+08$
3200.0	$1.0527E+04$	$5.8542E+09$	$8.9443E+05$	$6.3625E+08$	$9.5982E+05$	$5.7704E+08$	$5.3098E+06$	$4.2920E+08$
3300.0	$1.0807E+04$	$5.1235E+09$	$9.1709E+05$	$6.1626E+08$	$9.7439E+05$	$5.6817E+08$	$5.3552E+06$	$4.2413E+08$
3400.0	$1.1095E+04$	$4.4839E+09$	$9.3976E+05$	$5.9627E+08$	$9.8782E+05$	$5.6076E+08$	$5.3896E+06$	$4.2060E+08$
3500.0	$1.2921E+04$	$3.9172E+09$	$9.6246E+05$	$5.7630E+08$	$1.0012E+06$	$5.5335E+08$	$5.4239E+06$	$4.1709E+08$
3600.0	$1.6723E+05$	$2.6584E+09$	$9.7625E+05$	$5.6767E+08$	$1.0147E+06$	$5.4595E+08$	$5.4581E+06$	$4.1357E+08$
3700.0	$2.9924E+05$	$1.5281E+09$	$9.8857E+05$	$5.6091E+08$	$1.0281E+06$	$5.3854E+08$	$5.4922E+06$	$4.1006E+08$
3800.0	$3.9164E+05$	$1.1247E+09$	$1.0009E+06$	$5.5416E+08$	$1.0415E+06$	$5.3115E+08$	$5.5263E+06$	$4.0655E+08$
3900.0	$4.2154E+05$	$1.0526E+09$	$1.0132E+06$	$5.4742E+08$	$1.0550E+06$	$5.2376E+08$	$5.5602E+06$	$4.0304E+08$
4000.0	$4.4674E+05$	$1.0055E+09$	$1.0255E+06$	$5.4067E+08$	$1.0684E+06$	$5.1637E+08$	$5.5941E+06$	$3.9953E+08$
4250.0	$5.0974E+05$	$8.8756E+08$	$1.0563E+06$	$5.2383E+08$	$1.1020E+06$	$4.9791E+08$	$5.6786E+06$	$3.9078E+08$
4500.0	$5.7275E+05$	$7.6965E+08$	$1.0871E+06$	$5.0701E+08$	$1.1356E+06$	$4.7948E+08$	$5.7628E+06$	$3.8203E+08$
4750.0	$6.3281E+05$	$6.5889E+08$	$1.1179E+06$	$4.9020E+08$	$1.1692E+06$	$4.6107E+08$	$5.8466E+06$	$3.7330E+08$
5000.0	$6.5724E+05$	$6.3504E+08$	$1.1488E+06$	$4.7341E+08$	$1.2028E+06$	$4.4267E+08$	$5.9301E+06$	$3.6457E+08$
5250.0	$6.8167E+05$	$6.1119E+08$	$1.1796E+06$	$4.5664E+08$	$1.2355E+06$	$4.2486E+08$	$6.0135E+06$	$3.5585E+08$
5500.0	$7.0610E+05$	$5.8734E+08$	$1.2104E+06$	$4.3988E+08$	$1.2479E+06$	$4.1947E+08$	$6.0966E+06$	$3.4714E+08$
5750.0	$7.3052E+05$	$5.6349E+08$	$1.2402E+06$	$4.2383E+08$	$1.2602E+06$	$4.1409E+08$	$6.1795E+06$	$3.3844E+08$
6000.0	$7.5495E+05$	$5.3964E+08$	$1.2515E+06$	$4.1892E+08$	$1.2724E+06$	$4.0872E+08$	$6.2623E+06$	$3.2975E+08$

the only one that presents a significant increase in the coronal temperature, which is necessary to reach the high T_b values observed in the gyroresonance source at 17 GHz (Selhorst et al., 2008, 2009).

In **Figure 5** we show, for each atmospheric class, the optical depth (τ, A row) and the contribution function (CF, B row), that represents the emission variation with the atmosphere height. The CF is defined as

$$\mathrm{CF}(h) = j_\nu e^{-\tau_\nu} \tag{6}$$

where $j_\nu = \kappa_\nu B_\nu(T)$ is the emission coefficient, and $B_\nu(T)$ is the Planck function. Following Tapia-Vázquez and De la Luz (2020), each CF shown in **Figure 4** was normalized by its maximum, for a better comparison of the formation height of the emission at each frequency.

As previously reported by Selhorst et al. (2019), the quiet Sun free-free emission at 230 GHz is formed mainly in two different layers: near the temperature-minimum region ($h \sim 400$ km), and in the chromosphere, with a peak around 900 km. Moreover, the contraction of the atmosphere does not change the CF double-peak structure, rather it just changes the heights of the two peaks and their contribution percentages (see red curves in **Figure 5**). On the other hand, the quiet Sun free-free emission at 100 and 17 GHz are completely formed in the chromosphere, with CF peaks, respectively, at 1,650 and 2,900 Km. These heights of the maximum of the CF are close to the atmosphere height at which τ

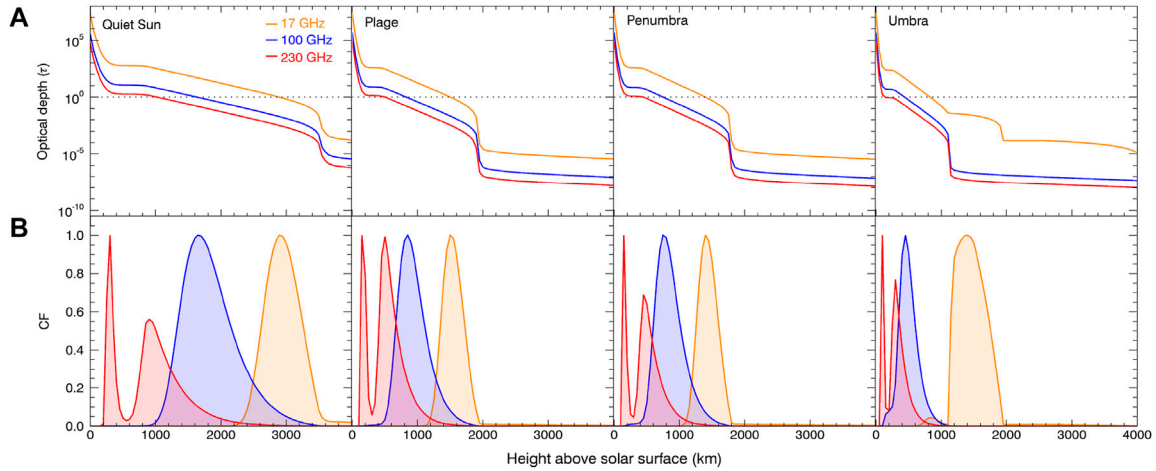

FIGURE 5 | (A): the panels show the optical depth (τ) variation with the height above the solar surface for the following areas: quiet Sun, plage, penumbra and umbra. The horizontal dotted line represents the $\tau = 1$ height. **(B):** the variation of the contribution function (CF) with the height above the solar surface. Each CF was normalized by its maximum for a better comparison of the formation height of the emission at each frequency.

= 1, as expected. Moreover, the atmospheric reduction of the AR active areas only moves the CF peaks closer to the solar surface. However, the 17 GHz τ results (orange curves) in the umbral region showed a huge change in the TR structure that cannot be attributed to free-free opacity and will be discussed in detail in the next **Section 4.2**. The chromospheric free-free contribution is still present at 17 GHz, but its CF peak is only 5% of the TR peak (see the small orange peak close to 800 km).

4.2 Gyroresonance Contribution

Several studies (e.g., Shibasaki et al., 1994; White and Kundu, 1997; Kundu et al., 2001; Vourlidas et al., 2006) have established that the gyroresonance radio emission is produced by opacity in harmonics 2, 3 and 4 of the electron cyclotron frequency, necessarily at TR or coronal heights in order to produce the brightness temperatures in excess of 10^5 K observed at 17 GHz. Moreover, Vourlidas et al. (2006) suggested that ARs with high polarization ($\gtrsim 30\%$) at 17 GHz have gyroresonance cores, and that $|\vec{B}| = 2200$ G is the minimum intensity to generate such a core. AR 12470 presented a component with high polarization degree (up to 94%) and $|\vec{B}| \sim 2500$ G that is likely to be due to a gyroresonance source.

To investigate the gyroresonance contribution, κ_g was calculated for harmonics $s \leq 5$, allowing for an uncertainty of 10% in the $|\vec{B}|$ values. That is, the 3rd harmonic was calculated where the magnetic field model showed intensities of $|\vec{B}| \simeq 2000 \pm 200$ G, the 4$^{\text{th}}$ harmonic was calculated where $|\vec{B}| \simeq 1500 \pm 150$ G, and the 5$^{\text{th}}$ harmonic where $|\vec{B}| \simeq 1200 \pm 120$ G. Due to the heliographic position of AR 12740 (17.40°N, 17.68°E), it is estimated that $|\vec{B}|$ is 7.5% greater than the observed B_z.

Figure 6A shows the variation in the absorption coefficient κ_ν with height along the line-of-sight to the location of maximum brightness temperature in AR 12470. The blue curve represents the magnetic field variation with height. The continuous black curve shows the absorption coefficient for bremsstrahlung (κ_b), and the dashed curve, in red, represents the contribution of gyroresonance ($\kappa_\nu = \kappa_b + \kappa_g$) and each of its respective harmonics (s). The 3$^{\text{rd}}$ harmonic occurs between 1,150 and 1,900 km in altitude, while the 4th harmonic occurs between 2,550 and 4,050 km. As for the 5$^{\text{th}}$ harmonic, it occurs between 4,250 and 5,950 km.

Figure 6B shows the τ variation with the height, where the 3rd and 4th harmonics effectively contribute to τ. The 3$^{\text{rd}}$ harmonic provides an optical depth of $\tau \sim 10^{-1}$ (**Figure 6B** red curve) that is three orders of magnitude greater than the free-free optical depth (**Figure 6B** black curve). The contribution from the 4th harmonic is an order of magnitude larger than the free-free τ. These results are in agreement with the studies of Shibasaki et al. (1994), who found that the 3rd harmonic contribution is approximately three orders of magnitude greater than the 4th harmonic. Despite being optically thin, the gyroresonance contribution of $\tau \sim 10^{-1}$ is able to increase the 17 GHz T_b from 10×10^3 K to almost 70×10^3 K thanks to the high temperature in the gyroresonance layers. To illustrate the contribution of each mechanism at 17 GHz, **Figure 6C** shows the free-free CF in black and the total CF in red (free-free plus gyroresonance). While the free-free CF shows a single peak at around 800 km (black curve), when the gyroresonance is included an intense peak appears at TR/coronal heights (red curve) that is ~ 20 times greater than the free-free contribution.

4.3 Comparison of the Synthetic and Observed Radio Images

The GA model images were generated with 2″ spatial resolution, which is much finer than the resolution of the radio observations. To compare the simulations with the observations, the model results were convolved with a 2D Gaussian beam that matches the resolution of the ALMA single-dish observations, i.e., 25″ and 58”

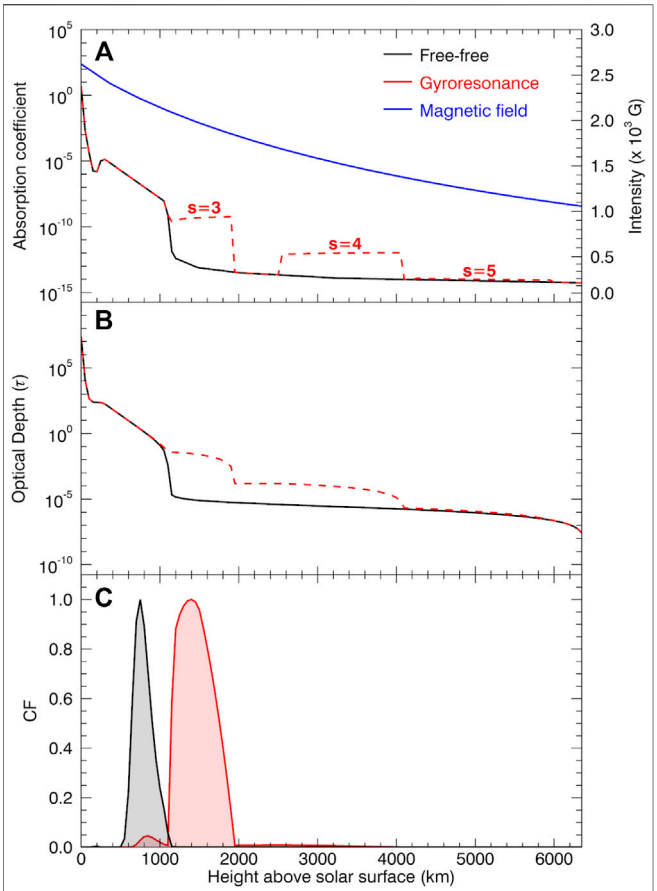

FIGURE 6 | (A) Absorption coefficient κ_ν obtained at 17 GHz for the free-free (black curve) and the gyroresonance (red curve) for the highest modelled T_b. The blue curve represents the magnetic field variation. **(B)** Variation of the optical depth for both emission mechanisms. **(C)** the variation of the contribution function (CF) with the height above the solar surface, in which the black curve represents the free-free emission, and the red curve represents the total emission, i.e., free-free plus gyroresonance ($\kappa_b + \kappa_g$).

at 230 and 100 GHz, respectively. In **Figure 7** the 2D structure of AR 12470 observed with ALMA at 230 and 100 GHz (left panels) is compared with the model results (right panels). The upper row shows the 100 GHz comparison, while the lower row shows the 230 GHz comparison.

Due to better spatial resolution, the 230 GHz map shows more detail than that observed at 100 GHz, in both observation and model. The bright features observed at both frequencies are in good agreement with the simulations. Moreover, due to the small size of the sunspot umbra (25" diameter at its widest), the dark umbral structure is readily seen at 230 GHz (see the center of panels **Figures 7C,D**), but completely masked in the 100 GHz simulations due to the convolution with the bright structures around it (see **Figures 7A,B**).

Even though dark when compared with the surrounding areas, the umbral T_b is only smaller than the $T_{b,QS}$ in the 230 GHz observation, and in the model result without the beam convolution, as shown in **Table 3**. When convolved to the observational resolution of 25", the modelled umbral T_b at 230 GHz is at the same level as $T_{b,QS}$. Furthermore, as shown in **Table 3**, the other AR areas (penumbra and plages) are brighter than the quiet Sun and showed a greater T_b variation than the umbra. All the simulated areas are consistent with the observations to within the uncertainties.

The resulting low contrast of the dark umbra with respect to the quiet Sun in the model is due to the low resolution of the ALMA single-dish observations. Since the umbral size is almost equal to the ALMA 230 GHz beam, the umbral T_b is smoothed with the bright surrounding areas. At the much better resolution of the ALMA interferometric array, the AR 12470 umbra presented brightness temperature as low as $\sim 0.90 \times T_{qS}$ (see Shimojo et al., 2017). Additionally, the 100 GHz ALMA interferometric observations obtained on 16 December 2015 showed a mysterious bright structure inside the umbra (Iwai et al., 2017; Brajša et al., 2021) that may still be present on December 17, increasing the umbral T_b and consequently the modeled value.

Figure 8 compares the observation obtained at 17 GHz by NoRH (8a) with the model results. Due to the high T_b in the polarized region ($\sim 7.0 \times T_{qS}$), to visualize the other regions the image display range was saturated at $3.0 \times T_{qS}$, allowing us to see bright free-free structures at positions consistent with those in the ALMA maps. Away from the polarized region, the maximum T_b was close to $2.8 \times T_{qS}$, and the average value was $1.58 \pm 0.32 \times T_{qS}$ (see **Table 4**).

At 17 GHz the non-polarized regions appear in the model at positions matching the observed ones. However, the modeled atmospheric profiles that achieved good agreement with the T_b observations at 230 and 100 GHz were not able to reach the high T_b values observed at 17 GHz. While these regions showed observational values as high as $2.8 \times T_{qS}$, the model was only able to reach a maximum T_b of $1.2 \times T_{qS}$ (**Figure 8B**). Moreover, since each modeled pixel used the same form of atmospheric profile to model the 3 frequencies (230, 100, and 17 GHz), we might expect the model to show good agreement with the bright and dark regions. The free-free regions bright at 17 GHz in the model (**Figure 8B**) have good spatial agreement with those ones modeled at 230 and 100 GHz (**Figures 7B,D**).

If only free-free emission is considered, at 17 GHz the umbra appears darker in the model than the surrounding area, with a brightness temperature of $1.06 \pm 0.02 \times T_{qS}$ at 10" resolution. When gyroresonance is included, the modeled T_b increased to values above $10 \times T_{qS}$. As summarized in **Table 4**, when gyroresonance is taken into account the T_b values obtained for the highly polarized region are in agreement with those observed. Nevertheless, as can be observed in **Figure 3**, the shape of the modelled polarized region is smaller and rounder, while the observed source appears elliptical.

5 CONCLUDING REMARKS

In this work, we present a data-constrained model of the solar atmosphere, in which we used the brightness temperatures of AR NOAA 12470 observed at three radio frequencies: 17 GHz

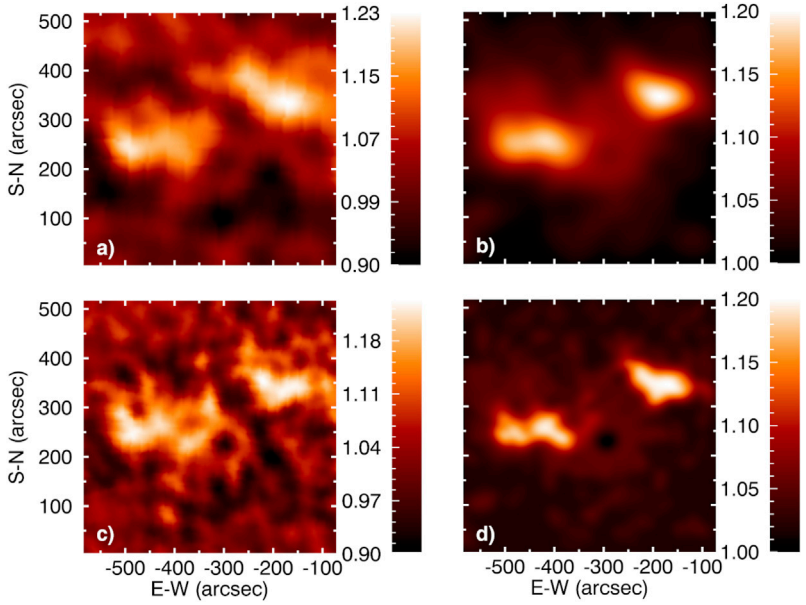

FIGURE 7 | Comparison between the observations and the model results at ALMA wavelengths. The upper panels show the 100 GHz comparison between the **(A)** ALMA observation and the **(B)** model results convolved with a gaussian beam of 58″ resolution. The lower panels show **(C)** the ALMA observation at 230 GHz and **(D)** the model results convolved with a 25″ gaussian beam. As in **Table 3**, the color bar scale is in multiples of the value of $T_{b,QS}$ appropriate for each frequency.

TABLE 3 | Comparison of the ALMA observations at 230 and 100 GHz and modeled averaged brightness temperatures of the distinct AR areas as compared with the quiet Sun temperature ($T_{b,QS}$).

AR region	Averaged brightness temperature (×T_{qS})					
	230 GHz			100 GHz		
	Obs	Model		Obs	Model	
		2”	25”		2”	58”
Umbra	0.99 ± 0.04	0.98 ± 0.01	1.00 ± 0.01	1.03 ± 0.01	1.02 ± 0.01	1.06 ± 0.01
Penumbra	1.05 ± 0.05	1.04 ± 0.01	1.02 ± 0.02	1.05 ± 0.02	1.07 ± 0.01	1.07 ± 0.02
Plages	1.07 ± 0.07	1.08 ± 0.05	1.04 ± 0.04	1.06 ± 0.04	1.10 ± 0.04	1.06 ± 0.03

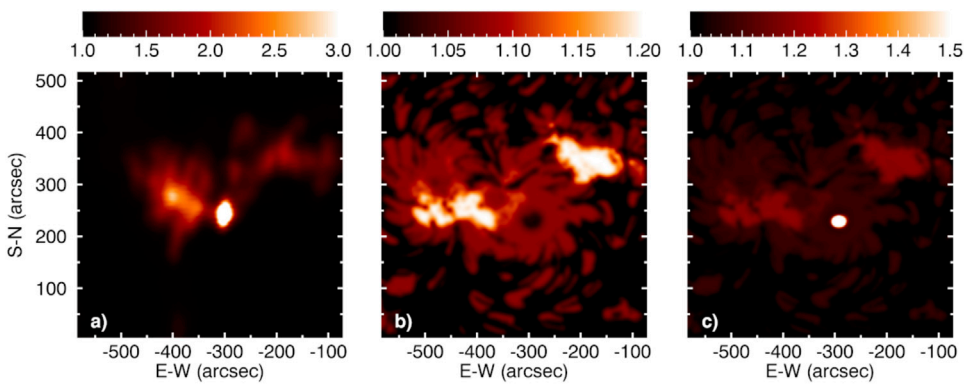

FIGURE 8 | (A) NoRH observation of AR 12470 at 17 GHz, with the displayed intensities saturating at 3 × T_{qS} K (i.e., well below the peak T_b of the highly polarized source). **(B)** The GA model image at 17 GHz with 10″ resolution based only on the free-free opacity, and **(C)** the GA model result when both free-free and gyroresonance are included. As in **Table 4**, the color bar scale is in multiples of $T_{b,QS}$ at 17 GHz (10,000 K).

TABLE 4 | Comparison of the 17 GHz observation and modeled averaged brightness temperatures of the polarized and non-polarized regions.

Bright region	Averaged brightness temperature at 17 GHz ($\times T_{qS}$)				
	κ_b			$\kappa_b + \kappa_g$	
	Obs	Model		Model	
		2"	10"	2"	10"
Polarized	3.69 ± 1.35	1.06 ± 0.03	1.06 ± 0.02	9.41 ± 3.51	4.08 ± 1.19
Non-polarized	1.58 ± 0.32	1.04 ± 0.06	1.04 ± 0.06	1.04 ± 0.06	1.04 ± 0.05

from NoRH, and 100 and 230 GHz from ALMA single-dish data. Under the assumption that the radio emission originates from the combination of thermal free-free and gyroresonance processes, our model allows for calculating radio brightness temperature maps that can be compared with the observations. The magnetic field at distinct atmospheric heights was determined by a force-free field extrapolation using HMI/SDO photospheric magnetograms. In order to determine the best plasma temperature and density height profiles necessary to match the observations, the Pikaia genetic algorithm (Charbonneau, 1995) is used to modify the standard quiet Sun atmospheric model characterized by 5 free parameters: the chromospheric gradients of temperature and electron density, the coronal temperature and density, and the TR height. The SSC (Selhorst et al., 2005b) was used as the basic quiet Sun model, however, other models could be chosen as the basic model. The GA modified the SSC model to fit three distinct classes of active region features, defined by their magnetic field intensities: umbrae, penumbrae, and plages.

As seen in **Figure 7** and **Table 3**, at the ALMA wavelengths the model was in general agreement with the observations. The umbral region looks dark at 230 GHz and the brighter regions match the positions seen in the observations at both frequencies (230 and 100 GHz). However, due to the small size of the umbra (diameter $\lesssim 25''$), it is not apparent in the 100 GHz data or model. Moreover, as shown by the ALMA interferometric observations at 230 GHz (Shimojo et al., 2017), the umbral region is darker ($\sim 0.90 \times T_{qS}$) than the single dish maps show ($0.99 \pm 0.04 \times T_{qS}$), implying that the umbra will be darker at 100 and 17 GHz. Nevertheless, there are no observational data to confirm that. While at 17 GHz the umbral free-free emission is masked by the bright source due to gyroresonance opacity, at 100 GHz, the interferometric image showed the presence of a bright structure inside the umbral region (Iwai et al., 2017), that may be produced higher in the atmosphere than the region where the umbral emission is formed.

Since the umbra is the region with the greatest magnetic field intensity ($|\vec{B}|$), it is also the location where the 17 GHz gyroresonance emission arises. As reported in previous works (Shibasaki et al., 1994; Vourlidas et al., 2006; Selhorst et al., 2008), gyroresonance emission at 17 GHz is typically formed at the 3rd harmonic ($|\vec{B}| = 2000$ G), and needs to be well above the TR where the free-free emission is optically thin. However, the free-free contribution function is much smaller than that of the gyroresonance (**Figure 6C**). Moreover, if only thermal free-free emission was contributing opacity at 17 GHz, the AR umbra should look darker than the surrounding region (see **Figure 8B**) and probably darker than the quiet Sun as the high resolution ALMA interferometric data suggest.

DATA AVAILABILITY STATEMENT

The original contributions presented in the study are included in the article/supplementary material, further inquiries can be directed to the corresponding author.

AUTHOR CONTRIBUTIONS

AJOS, CLS, and JERC contributed to conception and design of the study. CLS and PJAS wrote the first draft of the manuscript. All authors contributed to manuscript revision, read, and approved the submitted version.

FUNDING

This research was partially supported from the São Paulo Research Foundation (FAPESP) grant Nos. 2013/10559-5, 2013/24155-3 and 2019/03301-8. PJAS acknowledges support from CNPq (contract 307612/2019-8). SW was supported by the SolarALMA project, which has received funding from the European Research Council (ERC) under the European Union's Horizon 2020 research and innovation programme (grant agreement No. 682462), and by the Research Council of Norway through its Centres of Excellence scheme, project number 262622.

ACKNOWLEDGMENTS

This paper makes use of the following ALMA data: ADS/JAO. ALMA#2011.0.00020.SV. ALMA is a partnership of ESO (representing its member states), NSF (United States) and NINS (Japan), together with NRC (Canada) and NSC and ASIAA (Taiwan), and KASI (Republic of Korea), in co-operation with the Republic of Chile. The Joint ALMA Observatory is operated by ESO, AUI/NRAO, and NAOJ. The

National Radio Astronomy Observatory is a facility of the National Science Foundation operated under cooperative agreement by Associated Universities, Inc. AV acknowledges financial support from the FAPESP, grant No. 2013/10559-5 CGGC is grateful with FAPESP (2013/24155-3), CAPES (88887.310385/2018-00) and CNPq (307722/2019-8). RB acknowledges the support by the Croatian Science Foundation under the project 7549 "Millimeter and sub-millimeter observations of the solar chromosphere with ALMA."

REFERENCES

Brajša, R., Romštajn, I., Wöhl, H., Benz, A. O., Temmer, M., and Roša, D. (2009). Heights of Solar Tracers Observed at 8 Mm and an Interpretation of Their Radiation. *Astronomy Astrophysics* 493, 613–621. doi:10.1051/0004-6361:200810299

Brajsa, R., Skokic, I., Sudar, D., Benz, A. O., Krucker, S., Ludwig, H.-G., et al. (2021). ALMA Small-Scale Features in the Quiet Sun and Active Regions. *Astronomy Astrophysics* 651, A6. doi:10.1051/0004-6361/201936231

Brajša, R., Skokić, I., and Sudar, D. (2020). Magnetic Structure above Solar Active Regions. *Cent. Eur. Astrophys. Bull.* 44, 1.

Brajša, R., Sudar, D., Benz, A. O., Skokić, I., Bárta, M., De Pontieu, B., et al. (2018). First Analysis of Solar Structures in 1.21 Mm Full-Disc ALMA Image of the Sun. *Astronomy Astrophysics* 613, A17. doi:10.1051/0004-6361/201730656

Charbonneau, P. (1995). Genetic Algorithms in Astronomy and Astrophysics. *ApJS* 101, 309. doi:10.1086/192242

Dulk, G. A. (1985). Radio Emission from the Sun and Stars. *Annu. Rev. Astron. Astrophys.* 23, 169–224. doi:10.1146/annurev.aa.23.090185.001125

Fontenla, J. M., Avrett, E. H., and Loeser, R. (1993). Energy Balance in the Solar Transition Region. III - Helium Emission in Hydrostatic, Constant-Abundance Models with Diffusion. *ApJ* 406, 319–345. doi:10.1086/172443

Fontenla, J. M., Curdt, W., Haberreiter, M., Harder, J., and Tian, H. (2009). Semiempirical Models of the Solar Atmosphere. III. Set of Non-LTE Models for Far-Ultraviolet/Extreme-Ultraviolet Irradiance Computation. *ApJ* 707, 482–502. doi:10.1088/0004-637X/707/1/482

Fontenla, J., White, O. R., Fox, P. A., Avrett, E. H., and Kurucz, R. L. (1999). Calculation of Solar Irradiances. I. Synthesis of the Solar Spectrum. *ApJ* 518, 480–499. doi:10.1086/307258

Iwai, K., Koshiishi, H., Shibasaki, K., Nozawa, S., Miyawaki, S., and Yoneya, T. (2016). Chromospheric Sunspots in the Millimeter Range as Observed by the Nobeyama Radioheliograph. *ApJ* 816, 91. doi:10.3847/0004-637X/816/2/91

Iwai, K., Shimojo, M., Asayama, S., Minamidani, T., White, S., Bastian, T., et al. (2017). The Brightness Temperature of the Quiet Solar Chromosphere at 2.6 Mm. *Sol. Phys.* 292, 22. doi:10.1007/s11207-016-1044-5

Iwai, K., and Shimojo, M. (2015). Observation of the Chromospheric Sunspot at Millimeter Range with the Nobeyama 45 M Telescope. *ApJ* 804, 48. doi:10.1088/0004-637X/804/1/48

Kaufmann, P., Levato, H., Cassiano, M. M., Correia, E., Costa, J. E. R., Giménez de Castro, C. G., et al. (2008). "New Telescopes for Ground-Based Solar Observations at Submillimeter and Mid-infrared," in *Ground-based and Airborne Telescopes II. Vol. 7012 of Society of Photo-Optical Instrumentation Engineers (SPIE) Conference Series*. Editors L. M. Stepp and R. Gilmozzi, 70120L. doi:10.1117/12.788889

Kundu, M. R., White, S. M., Shibasaki, K., and Raulin, J. P. (2001). A Radio Study of the Evolution of Spatial Structure of an Active Region and Flare Productivity. *Astrophys. J. Suppl. S* 133, 467–482. doi:10.1086/320351

Livingston, W., Penn, M. J., and Svalgaard, L. (2012). Decreasing Sunspot Magnetic Fields Explain Unique 10.7 Cm Radio Flux. *ApJ* 757, L8. doi:10.1088/2041-8205/757/1/L8

Loukitcheva, M., Solanki, S. K., and White, S. M. (2014). The Chromosphere above Sunspots at Millimeter Wavelengths. *Astronomy Astrophysics* 561, A133. doi:10.1051/0004-6361/201321321

Nakagawa, Y., and Raadu, M. A. (1972). On Practical Representation of Magnetic Field. *Sol. Phys.* 25, 127–135. doi:10.1007/BF00155751

Nakajima, H., Nishio, M., Enome, S., Shibasaki, K., Takano, T., Hanaoka, Y., et al. (1994). The Nobeyama Radioheliograph. *Proc. IEEE* 82, 705–713. doi:10.1109/5.284737

Nita, G. M., Fleishman, G. D., Kuznetsov, A. A., Kontar, E. P., and Gary, D. E. (2015). Three-dimensional Radio and X-Ray Modeling and Data Analysis Software: Revealing Flare Complexity. *ApJ* 799, 236. doi:10.1088/0004-637X/799/2/236

Nita, G. M., Viall, N. M., Klimchuk, J. A., Loukitcheva, M. A., Gary, D. E., Kuznetsov, A. A., et al. (2018). Dressing the Coronal Magnetic Extrapolations of Active Regions with a Parameterized Thermal Structure. *ApJ* 853, 66. doi:10.3847/1538-4357/aaa4bf

Pesnell, W. D., Thompson, B. J., and Chamberlin, P. C. (2012). The Solar Dynamics Observatory (SDO). *Sol. Phys.* 275, 3–15. doi:10.1007/s11207-011-9841-3

Schou, J., Borrero, J. M., Norton, A. A., Tomczyk, S., Elmore, D., and Card, G. L. (2012). Polarization Calibration of the Helioseismic and Magnetic Imager (HMI) Onboard the Solar Dynamics Observatory (SDO). *Sol. Phys.* 275, 327–355. doi:10.1007/s11207-010-9639-8

Seehafer, N. (1978). Determination of Constant ? Force-free Solar Magnetic Fields from Magnetograph Data. *Sol. Phys.* 58, 215–223. doi:10.1007/bf00157267

Selhorst, C. L., Costa, J. E. R., and Silva, A. V. R. (2005a). "3-D Solar Atmospheric Model over Active Regions," in *ESA SP-600: The Dynamic Sun: Challenges for Theory and Observations*.

Selhorst, C. L., Silva, A. V. R., and Costa, J. E. R. (2005b). What Determines the Radio Polar Brightening? *Astronomy Astrophysics* 440, 367–371. doi:10.1051/0004-6361:20053083

Selhorst, C. L., Silva-Válio, A., and Costa, J. E. R. (2009). "17 GHz Active Region Model Using Magnetogram Extrapolation," in *The Second Hinode Science Meeting: Beyond Discovery-Toward Understanding. Vol. 415 of Astronomical Society of the Pacific Conference Series*. Editors B. Lites, M. Cheung, T. Magara, J. Mariska, and K. Reeves, 207.

Selhorst, C. L., Silva-Válio, A., and Costa, J. E. R. (2008). Solar Atmospheric Model over a Highly Polarized 17 GHz Active Region. *Astronomy Astrophysics* 488, 1079–1084. doi:10.1051/0004-6361:20079217

Selhorst, C. L., Simões, P. J. A., Brajša, R., Valio, A., de Castro, C. G. G., Costa, J. E. R., et al. (2019). Solar Polar Brightening and Radius at 100 and 230 GHz Observed by ALMA. *ApJ* 871, 45. doi:10.3847/1538-4357/aaf4f2

Shibasaki, K., Enome, S., Nakajima, H., Nishio, M., Takano, T., Hanaoka, Y., et al. (1994). A Purely Polarized S-Component at 17 GHz. *PASJ* 46, L17–L20.

Shimojo, M., Bastian, T. S., Hales, A. S., White, S. M., Iwai, K., Hills, R. E., et al. (2017). Observing the Sun with the Atacama Large Millimeter/submillimeter Array (ALMA): High-Resolution Interferometric Imaging. *Sol. Phys.* 292, 87. doi:10.1007/s11207-017-1095-2

Silva, A. V. R., Laganá, T. F., De Castro, C. G. G., Kaufmann, P., Costa, J. E. R., Levato, H., et al. (2005). Diffuse Component Spectra of Solar Active Regions at Submillimeter Wavelengths. *Sol. Phys.* 227, 265–281. doi:10.1007/s11207-005-2787-6

Takano, T., Nakajima, H., Enome, S., Shibasaki, K., Nishio, M., Hanaoka, Y., et al. (1997). "An Upgrade of Nobeyama Radioheliograph to a Dual-Frequency (17 and 34 GHz) System," in *Coronal Physics from Radio and Space Observations. Vol. 483 of Lecture Notes in Physics*. Editor G. Trottet (Berlin: Springer-Verlag), 183–191. doi:10.1007/BFb0106457

Tapia-Vázquez, F., and De la Luz, V. (2020). Nonlinear Convergence of Solar-like Stars Chromospheres Using Millimeter, Submillimeter, and Infrared Observations. *ApJS* 246, 5. doi:10.3847/1538-4365/ab5f0a

Valle Silva, J. F., Giménez de Castro, C. G., Selhorst, C. L., Raulin, J.-P., and Valio, A. (2020). Spectral Signature of Solar Active Region in Millimetre and Submillimetre Wavelengths. *MNRAS* 500, 1964–1969. doi:10.1093/mnras/staa3354

Vernazza, J. E., Avrett, E. H., and Loeser, R. (1981). Structure of the Solar Chromosphere. III - Models of the EUV Brightness Components of the Quiet-Sun. *ApJS* 45, 635–725. doi:10.1086/190731

Vourlidas, A., Gary, D. E., and Shibasaki, K. (2006). Sunspot Gyroresonance Emission at 17 GHz: A Statistical Study. *Publ. Astron Soc. Jpn.* 58, 11–20. doi:10.1093/pasj/58.1.11

Wedemeyer, S., Bastian, T., Brajša, R., Hudson, H., Fleishman, G., Loukitcheva, M., et al. (2016). Solar Science with the Atacama Large Millimeter/Submillimeter Array-A New View of Our Sun. *Space Sci. Rev.* 200, 1–73. doi:10.1007/s11214-015-0229-9

White, S. M., Iwai, K., Phillips, N. M., Hills, R. E., Hirota, A., Yagoubov, P., et al. (2017). Observing the Sun with the Atacama Large Millimeter/submillimeter Array (ALMA): Fast-Scan Single-Dish Mapping. *Sol. Phys.* 292, 88. doi:10.1007/s11207-017-1123-2

White, S. M., and Kundu, M. R. (1997). Radio Observations of Gyroresonance Emission from Coronal Magnetic Fields. *Sol. Phys.* 174, 31–52. doi:10.1023/a:1004975528106

Zirin, H. (1988). in *Astrophysics of the Sun* (New York, EUA: Cambridge University Press).

Zlotnik, E. Y., Kundu, M. R., and White, S. M. (1996). A Model of the Atmosphere above a Sunspot from Radio Observations. *Radiophys. Quantum Electron* 39, 255–267. doi:10.1007/BF02144449

Conflict of Interest: The authors declare that the research was conducted in the absence of any commercial or financial relationships that could be construed as a potential conflict of interest.

frontiers | Frontiers in Astronomy and Space Sciences

TYPE Mini Review
PUBLISHED 21 September 2022
DOI 10.3389/fspas.2022.966444

OPEN ACCESS

EDITED BY
Costas E. Alissandrakis,
University of Ioannina, Greece

REVIEWED BY
Fabio Lepreti,
University of Calabria, Italy

*CORRESPONDENCE
Gregory D. Fleishman,
gfleishm@njit.edu

SPECIALTY SECTION
This article was submitted to Stellar and Solar Physics,
a section of the journal
Frontiers in Astronomy and Space Sciences

RECEIVED 10 June 2022
ACCEPTED 19 August 2022
PUBLISHED 21 September 2022

CITATION
Fleishman GD, Martinez Oliveros JC, Landi E and Glesener L (2022), What aspects of solar flares can be clarified with mm/submm observations? *Front. Astron. Space Sci.* 9:966444. doi: 10.3389/fspas.2022.966444

What aspects of solar flares can be clarified with mm/submm observations?

Gregory D. Fleishman[1]*, Juan Carlos Martinez Oliveros[2], Enrico Landi[3] and Lindsay Glesener[4]

[1]Center for Solar-Terrestrial Research, New Jersey Institute of Technology, Newark, NJ, United States, [2]Space Sciences Laboratory, University of California, Berkeley, Berkeley, CA, United States, [3]Department of Climate and Space Sciences and Engineering, University of Michigan, Ann Arbor, MI, United States, [4]School of Physics and Astronomy, University of Minnesota, Minneapolis, MN, United States

This paper identifies several unsolved questions about solar flares, which can potentially be answered or at least clarified with mm/submm observations with ALMA. We focus on such questions as preflare phases and the initiation of solar flares and the efficiency of particle acceleration during flares. To investigate the preflare phase we propose to use the extraordinary sensitivity and high spatial resolution of ALMA, which promises to identify very early enhancements of preflare emission with high spatial resolution and link them to the underlying photospheric magnetic structure and chromospheric flare ribbons. In addition to revealing the flare onsets, these preflare measurements will aid in the investigation of particle acceleration in multiple ways. High-frequency imaging spectroscopy data in combination with the microwave data will permit the quantification of the high-energy cutoff in the nonthermal electron spectra, thus helping to constrain the acceleration efficiency. Detection and quantification of secondary relativistic positron (produced due to nonthermal accelerated ions) contribution using the imaging polarimetry data will help constrain acceleration efficiency of nonthermal nuclei in flares. Detection of a "mysterious" rising spectral component with high spatial resolution will help determine the emission mechanism responsible for this component, and will then help in quantifying this either nonthermal or thermal component of the flaring plasma. We discuss what ALMA observing mode(s) would be the most suitable for addressing these objectives.

KEYWORDS

flares, sun, submm interferometry, gyrosynchrotron emission, thermal, positron

1 Introduction

Solar flares are explosive transient phenomena, in which free magnetic energy accumulated in the solar corona is promptly released and converted to other forms of energy—kinetic, thermal, and nonthermal. This energy release manifests itself throughout the entire electromagnetic wavelength range, from radio waves to gamma-rays. These manifestations are highly different in the various wavelength regimes; thus, revealing

complementary facets of the solar flare. Flare manifestations in the radio domain are very diverse. At the meter and decimeter wavelengths, $\lesssim$ 1 GHz, radio emission is mainly produced by nonthermal electrons via coherent emission mechanisms. For example, such emissions can be produced by electron beams or shock waves. At higher frequencies, the flaring radio emission is dominated by the incoherent gyrosynchrotron emission produced by nonthermal electrons spiraling in the ambient magnetic field. Thermal free-free emission may also contribute, especially in the preflare and late decay phases. At the sub-THz range, observations of flare emission are limited. Several observed cases show that the sub-THz emission may represent a continuation of the nonthermal gyrosynchrotron spectrum, or show a distinct component that rises with frequency. Some contribution from thermal free-free emission is always present in the sub-THz range.

One chromospheric or photospheric manifestation of solar flares are the so-called white-light flares. These are defined as strong enhancements in the white-light continuum, associated with highly energetic flares, although white-light flares have also been observed during moderately energetic flares ~M5 (e.g. Svestka, 1976; Neidig and Cliver, 1983; Machado et al., 1989). Different mechanisms for their generation have been proposed, ranging from particle bombardment to wave-particle interactions. These mechanisms try to explain the sudden heating of the chromospheric/photospheric material to temperatures conducive to the emission in the white-light wavelength band. How the flare energy or at least a fraction of it is deposited in the lower atmospheric layers and converted into heat is still a topic of active research. Some of the proposed mechanisms are: bombardment by non-thermal electrons (e.g. Hudson, 1972; Aboudarham and Henoux, 1986), proton/ion bombardment Machado et al. (1978), soft X-ray and/or EUV irradiation, dissipation of Alfven waves and chromospheric backwarming Machado et al. (1989). The close spatial and temporal relation between the hard X-rays observed by the *Reuven Ramaty High Energy Spectroscopic Imager (RHESSI)* spacecraft and white-light emission (e.g. Battaglia and Kontar, 2011; Martínez Oliveros et al., 2011; Martínez Oliveros et al., 2012; Kuhar et al., 2016) suggest that non-thermal electron responsible for the hard X-ray emission are likely responsible for the white-light enhancements Ding (2007).

Flares have been associated with helioseismic signatures observed in the solar photosphere and propagating in the solar interior (Kosovichev and Zharkova, 1998). These helioseismic signatures, called sunquakes, are believed to be the photospheric and subphotospheric responses to flares and the changing magnetic and chromospheric conditions prompted by flares. Several mechanisms for their generation have been proposed. Some of these generation mechanisms can be grouped into the following: particle heating or bombardment (e.g. Kosovichev and Zharkova, 1998; Lindsey and Donea, 2008; Zharkova, 2008; Zharkov et al., 2013) and Lorentz force "induction" (e.g. Hudson et al., 2008; Alvarado-Gómez et al., 2012). It is still not clear if there is a unique generation mechanism or depending on chromospheric and photospheric conditions there is one more dominant. What is clear is that there is, in general, a spatial and temporal relation between enhancements in HXR and WL emissions and the location and timing of sunquakes (Buitrago-Casas et al., 2015).

In the ultraviolet (UV) range the emission is a combination of thermal free-free continuum and spectral lines produced by various ions in different ionization states. UV emission may form at various heights from the chromosphere to the corona, depending on the ion. For example, UV emission can trace flare ribbons formed due to precipitation of the nonthermal particles accelerated in the coronal portion of the flare to the dense and cool chromosphere. In the extreme UV (EUV) range, the emission is dominated by the hot corona. The EUV emission in the course of flares is mainly driven by the plasma response to the flaring energy deposition; this could be direct heating at or near reconnection sites, or heating due to Coulomb loss of the flare-accelerated particles. It is important to note that the EUV emission is dominated by spectral lines produced by ions; thus, the spectral shapes of these lines are sensitive to the ion velocity distributions including nonthermal broadening detected in some cases.

Next, the soft X-ray (SXR) spectral range is primarily dominated by thermal emission of the hot flaring plasma, hotter than the plasma producing the bulk of the EUV emission. The SXR-emitting plasma can either be heated directly or by the nonthermal particles accelerated in flares. The more energetic hard X-ray (HXR) emission is dominated by bremsstrahlung produced due to collisions of nonthermal electrons with ambient plasma. The highest energy photons, gamma-rays, are produced by several processes due to electrons or ions accelerated in flares. The nonthermal relativistic electrons (and positrons) produce a continuum component due to bremsstrahlung, while nonthermal ions/nuclei produce numerous gamma-ray lines and a continuum component due to decay of pions produced in nuclear collisions.

We see that each regime of the electromagnetic spectrum illuminates solar flares from its own perspective. Examining a flare in a particular energy range typically clarifies some scientific questions, but also produces new questions, which, in order to answer, often requires data taken in another range of the spectrum. This paper attempts to review what science questions can be solved or at least clarified by examining millimeter and sub-THz data obtained with high spatial, temporal, and spectral resolution, with an emphasize on ALMA solar capabilities.

2 Preflare phase of solar flares

Several previous studies hint at interesting physics in the early phases of flares, yet leave important questions unanswered. For instance, Hudson et al. (2021) find evidence using *GOES*/XRS

data for hot plasma emission in the soft X-ray (SXR) regime prior to the main flare impulsive phase, suggesting a separate precursor heating process. Battaglia et al. (2009) additionally find that flares observed in HXRs by *RHESSI* sometimes show thermal components much earlier than the nonthermal counterparts. This finding is inconsistent with the thick-target flare model, in which plasma is heated primarily due to energy deposition by energetic electrons. If this result should hold, it would require conduction or, alternatively, energetic ions, to be the primary means of energy transfer between the corona and the chromosphere early in the flare. However, microwave studies (e.g., Altyntsev et al., 2012) showed that such cases may be due to insufficient HXR sensitivity, and that there could be nonthermal electrons very early in the flare, as one of the first signatures of a flare in progress. There have been other detections (e.g., Asai et al., 2006) of nonthermal emission in the pre-flare phase for large flares using microwave and HXR observations. Some early impulsive ("cold") flares do not show any pre-flare phase, but do begin with a prominent nonthermal phase (Bastian et al., 2007; Lysenko et al., 2018). Evidence of superhot plasma arising near the reconnection site via direct heating has also been observed in early flare HXR measurements (Caspi and Lin, 2010; Caspi et al., 2014) as well as in the microwave measurements (Gary and Hurford, 1989; Fleishman et al., 2015).

Studies of EUV and UV emission show additional evidence of activity in the early flare phases. Certain EUV and UV lines in the chromosphere and transition region are highly responsive to the presence of accelerated electrons and can therefore provide an indirect, yet sensitive, measure of their presence (e.g., Testa et al., 2020). Panos and Kleint (2020), Panos et al. (2018), and Woods et al. (2021) provide further examples of early flare signatures, finding that there are distinct characteristics of the Mg II handk line features measured by the Interface Region Imaging Spectrograph (IRIS) during the pre-flare and impulsive phases compared to non-flaring intervals. Other studies using Hinode/SOT have found chromospheric indicators before the flare start (e.g., Bamba et al., 2013).

In short, previous studies are inconclusive as to whether the thick-target flare model holds in the early phases of flares. The high sensitivity of ALMA can potentially answer this question by picking out very faint signatures of plasma heating and nonthermal electrons in early flare and pre-flare phases, and also by identifying the location of these signatures. Spectral measurements permitting an unambiguous determination of the emission mechanism, thermal or nonthermal, are needed. Measurements in a single ALMA band or a combination of them could work here. The latter requires the use of subarrays, which is not yet offered at the time of this writing. Various ALMA bands could be helpful for preflare studies, although the lowest frequency bands one and two might be preferable as they provide the largest field of view, thus, maximizing chances to catch a flare.

3 Build up and dissipation of magnetic energy

Flares involve the major restructuring of active region magnetic field and are associated with the conversion of magnetic energy into thermal, non-thermal, and kinetic energy and high-energy electromagnetic radiation. The latter can have a significant impact on the ionization of the Earth's atmosphere and thus affect communications, alter satellite trajectories and even damage space-borne instrumentation. However, while the arrival time and, to some extent, geoeffectiveness of coronal mass ejections can be modeled and predicted, giving some form of early warning of the onset of a geomagnetic storm, this is not possible for flares (which have emission that reaches the near Earth environment very quickly), so that the only way to minimize their impact would be to forecast their occurrence before they happen.

Flares occur in active regions, following a slow build-up of magnetic energy which gets suddenly released in one or more flare reconnection events (Benz, 2017), but the precise location of these reconnections has not been identified. Various types of observations have shown that reconnection could happen in photospheric, chromospheric and coronal structures; the intrinsically small scale of reconnection provides an additional difficulty in directly observing it (Wang et al., 2017). Most studies have been directed towards identifying the conditions in which reconnection may happen, and identifying observational signatures of the build-up of either magnetic energy or the emergence of magnetic configurations that may lead to such events.

Significant efforts have been devoted towards identifying precursor signatures of flare events from ground-based and space observations, with varying degrees of success. There are three classes of precursors proposed (Aschwanden, 2020): 1) those involving the presence of specific features in photospheric magnetic structures (such as shear, penumbra type, length of polarity inversion line, etc); 2) those involving some type of magnetic configuration change observed in the photospheric magnetic field (such as helicity injection, new photospheric flux emergence and so on); and 3) direct observation of precursor activity in UV, EUV or X-ray observations, assumed to be related to the main flare itself (e.g. enhanced turbulence, brightenings at many wavelengths, line broadening, jets). More recently, machine learning techniques have also been applied in a two pronged effort aimed at both 1) identify precursor patterns not readily detectable in available data sets, and 2) at utilizing such precursors to glean information about which processes are responsible for flare triggering, and where do they take place (Chen et al. (2019); Bobra and Ilonidis (2016) and references therein).

The vast majority of the suggested precursors relies on some type of photospheric magnetic field observations for two reasons. First, flares being magnetic phenomena, it makes sense to utilize

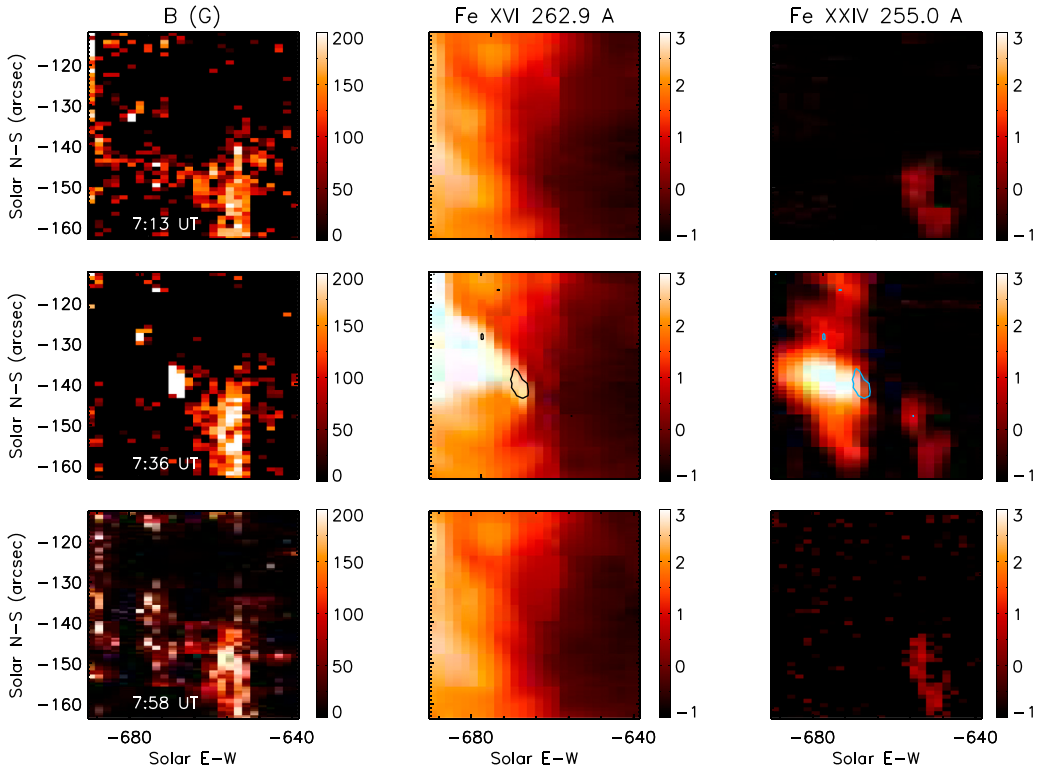

FIGURE 1
Maps of the magnetic field strength B (left column), and of the intensity ($\log_{10}$ values, in erg cm^{-2}s^{-1}sr^{-1}) of the Fe XVI 262.9 Å line (center column) and Fe XXIV 255.0 Å line (right column) as observed 22 min before the C2.0 flare on 24 Aug 2007 (top row), during the flare (middle row), and after the flare (bottom row). In the middle row, the magnetic field strength stronger than 250 G is superimposed as a contour plot in the Fe XVI and Fe XXIV images during the flare.

magnetic field observations; second, both line-of-sight and vector photospheric magnetic field observations at high resolution are routinely available from ground and space-based instrumentation. However, these observations are limited to the photosphere, and while they can determine photospheric field distribution, strength and structure, provide magnetic field boundaries to theoretical models, and detect the emergence of new flux from the solar interior, they fail to provide direct measurements at the reconnection locations, which are located at larger heights (e.g., Chen et al., 2020).

Magnetic field measurements in the solar corona might provide better tools for flare forecasting, but are far more scanty and difficult to obtain from ground-based or space-born observatories, so that they can not constitute a viable tool to identify precursors and build an active region monitoring system capable of forecasting flares (Landi et al., 2016). In fact, instruments observing in the visible and near-infrared wavelength range can only observe the solar corona at the limb; narrow-band EUV and X-ray imaging instruments do not have the diagnostic capabilities necessary to measure coronal magnetic fields, while among available or planned EUV high-resolution spectrometers, only Hinode/EIS includes a Magnetically Induced Transition (MIT) (Fe X 257.26 Å), which is the only spectral line in the EUV range capable of detecting magnetic fields in the solar corona (Li et al. (2015); Li et al. (2016)).

However, recent work suggested that the coronal magnetic field may indeed provide signatures that suggest the imminence of a solar flare. In fact, a new diagnostic technique which utilizes the Fe X MIT allows the use of EUV spectra to measure the strength of the magnetic field in the solar corona maintaining the arcsecond-size spatial resolution typical of high-resolution EUV spectrometers (Si et al. (2020); Landi et al. (2020)). Such a technique was applied by Landi et al. (2021) to a series of EIS spectrally-resolved images taken before, during and after a C2.0 flare. Landi et al. (2021) found that within 22 min of flare onset the magnetic field measured with the Fe X MIT line underwent a strong enhancement at a location which later corresponded to the footpoints of post-flare loops; also, this magnetic field enhancement stored enough magnetic energy to power then entire flare, and was completely dissipated during the flare (see Figure 1). A similar conclusion has been made for an X8.3 limb flare with the imaging microwave spectroscopy technique (Fleishman et al., 2020).

The results of Landi et al. (2021) raise more questions than they answer, due to their intrinsic limitations. They point to a new window where magnetic field energy build-up can be directly observed before the flare, possibly suggesting a precursor activity that can provide at the same time an early warning of possible flare activity, and an indication of the energy available to the flare. However, these results need to be confirmed with other flare observations, which however are not available yet. Furthermore, the EIS observations used by Landi et al. (2021) were taken with a rastering slit spectrometer, so that the field of view was limited, not observed simultaneously, and the cadence was slow (22 min). Also, Hinode/EIS only includes one magnetically-sensitive spectral line (Fe X 257.26 Å), which can provide measurements of the magnetic field only in the temperature range where the Fe X ion is formed, around 1 MK. What is really needed are measurements of the coronal magnetic field at multiple heights (and hence temperatures) spanning from the chromosphere to the lower corona, which can complement both Hinode/EIS measurement of the magnetic field at 1 MK on one side, and be associated to changes in photospheric and coronal plasma structures routinely observed in many wavelength ranges on the other.

Coronal magnetic field can be inferred from the microwave imaging observations due to sensitivity of the radio emission to the ambient magnetic field in two main radiation processes: the free-free emission and the gyroresonance (GR) emission. The latter may occur at the frequencies below ~40 GHz (Anfinogentov et al., 2019) at some rare cases, but typically at much lower frequencies. At the higher frequencies, the free-free emission from the chromosphere dominates, whose degree of polarization provides diagnostics of LOS component of the magnetic field. Free-free emission at various frequencies is formed at various heights of the solar chromosphere (Loukitcheva et al., 2017); thus, observing this emission at a range of ALMA frequencies will permit recovering the LOS B component over a corresponding range of heights.

Combining photospheric (optical), chromospheric (ALMA), and coronal (radio) measurements of the magnetic field, one can build an evolving height profile of the magnetic field over these three elements of the solar atmosphere. This will help determine where the preflare changes of the magnetic field are the most prominent and what dedicated observations could the optimal to address the fundamental physics that leads to the flare and then use this knowledge to forecast the flare. Measurements of the magnetic field with ALMA require polarimetric observations. The degree of polarization of the free-free emission increases with the magnetic field, while decreases with the frequency. This implies that observations in band one and two could be most favorable for this study. On the other hand, probing magnetic field in deeper chrompsphere may require higher-frequency bands to be used.

4 High-energy end of the accelerated electron spectra in solar flares

Nonthermal electrons accelerated in solar flares produce nonthermal emissions—primarily, HXR, gamma-ray, and radio. Of particular importance are the highest energy particles because these highest energies tell us about the acceleration efficiency and, thus, about the involved acceleration mechanism(s). The highest energy, relativistic electrons (and positrons if present) can be detected in the gamma-ray range and at the radio wavelengths. The diagnostic potential of the gamma-rays is somewhat limited because (i) there are other competing contributions in the gamma-ray range; (ii) only a minor subset of solar flares is detected in the gamma-ray range above background; and (iii) there are no gamma-ray instruments with high spatial resolution. The radio domain is free from these limitations.

The nonthermal radio emission is dominated by the gyrosynchrotron (GS) process, where the emission is produced by electrons spiraling in the ambient magnetic field. The GS emission in solar flares is characterized by a spectrum that typically has a spectral peak at the microwave range, while falls following roughly power-laws towards lower and higher frequencies. Supplementary videos to (Fleishman et al., 2020) display dependence of the GS spectrum on the key physical parameters including the high-energy cut-off of the nonthermal electron spectrum. This high-energy cut-off mainly affects the high-frequency end of the GS spectrum. Sometimes, even emission at microwave frequencies (dozens GHz or so) may be sensitive to the high-energy cutoff value (see, e.g., Fleishman et al., 2016), while in other cases the high-energy end of the nonthermal electron spectrum affects emission at higher frequencies at the mm/sub-mm range covered by ALMA.

Microwave spectroscopy observations permit measuring magnetic field, plasma density, and nonthermal electron properties with high spatial and temporal resolution (Fleishman et al., 2020). The available diagnostics employing the EOVSA data in 1–18 GHz range provide the number density, the spectral index, and (in some cases) the low-energy cut-off; however, the high-frequency cut-off cannot reliably be determined in most cases because of the lack of the high-frequency observations. To estimate the high-energy end of the electron spectrum, we need to combine EOVSA measurements in the microwave range and ALMA measurements in the mm or/and sub-mm range. ALMA spatial resolution in any configuration is sufficient to complement the EOVSA one. Yet, combining data from two different instruments represents a challenge as the maps from those instruments have to be carefully aligned and consistent calibrations and background subtractions performed. Once done, the combined EOVSA-ALMA data sets will help uniquely investigate the high-energy end of the nonthermal electron

spectrum, which is inconceivable with any other instrument or a combination thereof.

5 Are relativistic positrons produced in solar flares?

It is yet unclear how the flare energy is divided between nonthermal electrons and nuclei and also between different nucleus species. The diagnostics of the accelerated ions at the flare site is highly limited because of their big masses, which makes inefficient most of the radiative processes by the ions such as gyrosynchrotron radiation or bremsstrahlung. Some information about the accelerated ions is available from the deexcitation gamma-ray lines and from high-energy gamma-ray continuum produced by decay of π^0 particles produced in high-energy nuclear interactions.

Another product of the high-energy nuclear interactions is the relativistic positrons, which are low-mass particles and so are efficient emitters of the gyrosynchrotron radiation and bremsstrahlung. Thus, intensity of these continuum emissions from the positrons can be high enough to be detected in observations. However, there is a great challenge of how to distinguish the positron contributions from more well-known emissions produced by the electrons accelerated in the flare.

To address this challenge we note that the fast electrons and positrons are created differently in flares. The electrons are somehow accelerated from the original thermal Maxwellian distribution forming a nonthermal tail falling with energy from a few keV to a few Mev with a reasonably steep spectral slop. In contrast, the positrons are created as relativistic particles at or above 1 MeV from β^+ decay or at even higher energies from π^+ decay (Murphy et al., 2005). Some of flare-produced radioactive nuclei experience β^+ decay (Ramaty et al., 1979), $N \rightarrow N' + e^+ + \nu_e$, where N is the original radioactive nucleus, e.g. ^{11}C or ^{15}O, N' is the final nucleus, e^+ is the positron and ν_e is the electron neutrino. The β^+ decay time varies from a fraction of second to hours depending on the nucleus. Another option is the decay of π^+ particles (Dermer, 1986), $\pi^+ \rightarrow \mu^+ + \nu_\mu$, $\mu^+ \rightarrow e^+ + \nu_e + \overline{\nu_\mu}$, where μ^+ is anti mu–meson. The direct decay, $\pi^+ \rightarrow e^+ + \nu_e$, is also possible but has a smaller probability. Finally, some of excited nuclear states can relax to the ground state via production of the electron-positron pair. This implies that the composite electron-positron energy spectrum is strongly dominated by the electron contribution at low energies, say $E < 1$–10 MeV, but can be dominated by the positron contribution at the higher energies. Thus, the problem is to identify the emission produced by this high-energy positrons.

It is difficult to do using the gamma-ray continuum they generate because the positron-produced bremsstrahlung spectrum is indistinguishable from the electron-produced one. However, the situation with the gyrosynchrotron emission is remarkably much more promising, because this emission is circularly polarized with the senses opposite for oppositely charged particles, electrons and positrons. Fleishman et al. (2013) described a method of identification of the microwave emission produced by positrons and presented a 2000-Mar-13 flare in which the corresponding signature is detected.

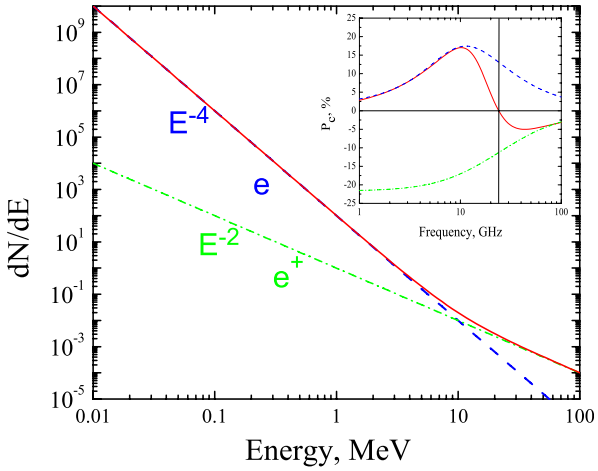

FIGURE 2
A cartoon illustrating a distinct contribution by relativistic positrons to GS emission. An assumed power-law energy spectrum of nonthermal electrons (dashed blue) with a typical spectral index of four and a schematic flat power-law energy spectrum of positrons (dash-dotted green) are shown in the main panel. Note that real spectra of relativistic positrons may deviate from the power-law, but contain a bump in the 1–10 MeV range. In this example, the total number of electrons is almost six orders of magnitude larger than the number of positrons. The red solid curve shows the composite spectrum dominated by electrons at low energies and by positrons at high energies. Circular polarization of the GS emission produced by these two components, appropriately color-coded, and by their composition is shown in the inset. The positron contribution results in the polarization reversal at a high frequency shown by red arrow. The demarcation frequency depends on the magnetic field at the radio source and the crossing point in the energy spectra and can vary between dozens and hundreds GHz.

Figure 2 illustrates the idea of the methodology: if a high-energy spectrum is dominated by positrons then a proportionally high-frequency GS emission will be dominated by the positrons, too. This GS component has the ordinary mode circular polarization in contrast to the extraordinary mode polarization produced by the electrons. The polarization of the radio emission is a standard observable in the form of the right-hand-side (RCP) or left-hand-site (LCP) circular polarization. The association between these observables and the ordinary and extraordinary modes depends on the direction of the line-of-sight (LOS) component of the magnetic field at the source. Thus, imaging radio data complemented by spatially resolved magnetic measurements are needed to distinguish the electron and positron contributions to the GS emission.

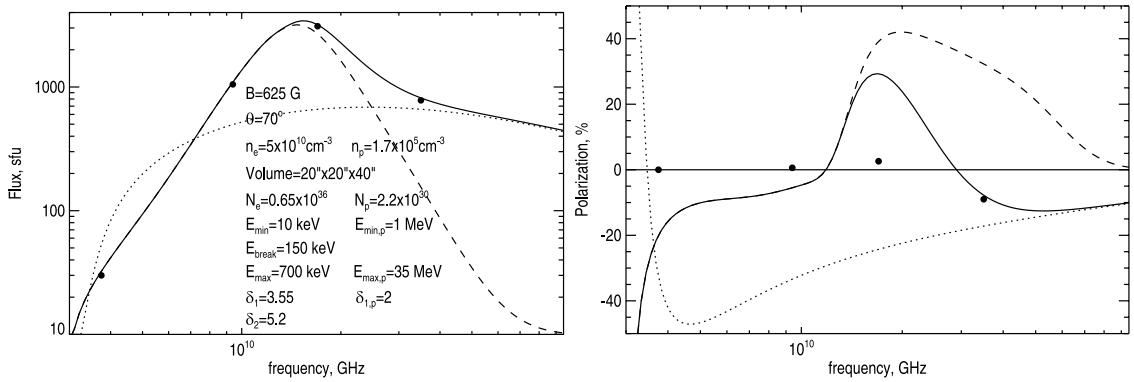

FIGURE 3
Microwave observations and a single-zone GS model (parameters of the model are printed in the left panel) for the 2000 March 13 event. The broken power-law spectrum of the nonthermal electrons is taken from Gan et al. (2001) derived from analysis of the HXR spectrum. The magnetic field value and the source dimensions are taken such as to match the low-frequency measurements. The resulting microwave spectrum (dashed curve) underestimates the emission at high frequencies. Adding emission produced by a relativistic positron component (dotted curve) offers a good match at all frequencies. Note that these two components are optically thin at high frequencies, so the contributions add up, while the opacity at tlow frequencies is solely determined by the electron contribution, so the positron component has no effect on the total spectrum at the low frequencies. The model also offers a correct sense and value of the polarization at the highest frequency, 35 GHz (see text for the details).

Fleishman et al. (2013) identified several events, where the microwave emission at 35 GHz was likely produced by the positrons. They described in some detail the cleanest 2000-Mar-13 case, where the wave-mode identification was straightforward because of simple on-disk source morphology. Additional evidence in favor of the positron origin of the high-frequency emission in this event comes from the quantitative modeling of its spectrum. Figure 3 presents the observed microwave spectrum (filled circles) at the peak flare time at 3.75–35 GHz. The dashed curve displays a model GS spectrum produced by nonthermal electrons with a broken power-law energy spectrum derived from spectral fit of the detected HXR spectrum (Gan et al., 2001). Other parameters of the model source are selected such as to match the low-frequency part of the radio spectrum. The high-frequency emission is underestimated by this model. To make up for this mismatch we added a relativistic positron population with the parameters printed in the left panel. This overall minor population is indeed capable of bringing the full spectrum in agreement with the observed one (note that radio emissions produced by electrons and positrons add together at high frequencies, where the emission is optically thin, but the spectrum is completely dominated by the electron opacity at low frequencies, where the emission is optically thick). The right panel of the Figure shows the measured and modeled polarization. The modeled polarization matches the observed one well at 35 GHz, while overestimates it at the lower frequencies. This is likely due to nonuniformity of the real source, which is ignored in the model.

In this example the positron contribution to the GS spectrum seems to dominate at a relatively low frequency, 35 GHz, although our estimates suggests that in more typical cases such contributions could become dominant at much higher frequencies, ~ 100 GHz or even above. This implies that ALMA could be an ideal instrument to detect radio emission produced by relativistic positrons in many flares. High spatial resolution of ALMA will permit studying spatial distribution of the relativistic positrons over the flare volume and address a question are they co-spatial with the nonthermal electrons accelerated in the flare or not. The sense of polarization needed for this analysis can be unambiguously determined provided the LOS component of the magnetic field is measured before the flare in the same ALMA observations—from the polarization of the thermal background emission. A more usual optical measurements of the photospheric magnetic field obtained from Zeeman diagnostics can also be employed. Thus, GS emission produced by relativistic positrons can be observed with ALMA in the mm or sub-THz range and provide highly useful information about flare-accelerated nuclei. Perhaps, observations in ALMA band three is most promising here.

6 Is the raising sub-THz flare component mysterious?

Spectrum of nonthermal gyrosynchrotron emission falls with frequency at the mm/sub-mm range; see the example in Figure 4. In such cases, the high-frequency source is rather compact, ~ $10''$ or so. However, in some powerful flares a raising with frequency sub-THz component has been observed (Kaufmann et al., 2001; Lüthi et al., 2004; Kaufmann et al., 2009) above 100–200 GHz. Although no reliable estimate of the source size has been reported

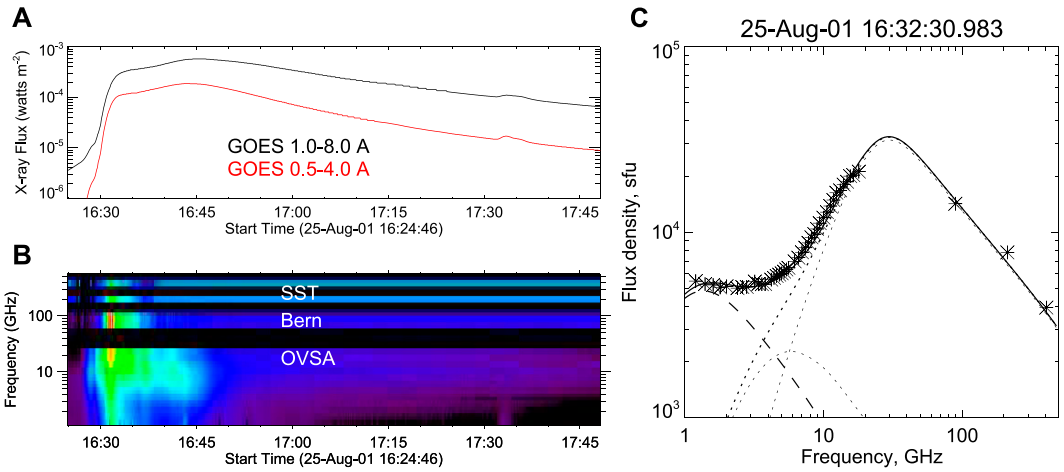

FIGURE 4
An example of a SOL 2001-08-25T16:23 flare with, perhaps, the most broadband nonthermal radio emission. **(A)** GOES light curves shown for the context; **(B)** the multi-instrument dynamic spectrum of the at 1–405 GHz; **(C)** the measured and model spectrum of the flare at the peak time 16:32:31 UT. The model assumes E_{max} =10 MeV. From Fleishman et al. (2017); reproduced by permission of the AAS.

in such cases, there were speculations that the corresponding source is too compact for the emission to be thermal. Accordingly, several nonthermal emission mechanisms were proposed (e.g., Krucker et al., 2013) including a number of exotic ones. Fleishman and Kontar (2010) discussed some of them and proposed a new one – Cherenkov emission at some spectral windows where the dielectric permeability is above one due to contributions of atomic or molecular transitions. Kontar et al. (2018) noted that the sub-mm radio flux is correlated with the area of the flare ribbons and proposed that the raising sub-mm component could be produced by thermal emission of these ribbons. This would imply that the sources must be rather large, larger than the nonthermal ones. None of those mechanisms has been generally adopted or proved for the raising sub-mm component. The key measure of the emission to be classified as thermal or nonthermal is its brightness temperature. ALMA offers observations with high spatial resolution sufficient for the source to be spatially resolved and, thus, brightness temperature to be unambiguously measured. Therefore, performing ALMA observations of the flaring emission with high spatial resolution is the key in specifying the responsible emission mechanism(s). If the emission proved thermal, ALMA will provide a valuable information about the chromosphere response on its bombardment by the precipitating nonthermal particles accelerated in flares. If proved nonthermal, say Cherenkov emission, the ALMA diagnostics will offer a unique diagnostics of the dielectric permeability and, thus, on the chemical composition of the chromosphere. Yet, no spatially resolved observations of the raising sub-mm component is available. Given that this raising sub-THz component has been reported between 100 and 400 GHz, ALMA bands three to seven would be the most appropriate to study this "mysterious" component.

7 Conclusion

We conclude that observing solar flares with ALMA can advance our understanding of the flare physics. We described several science questions, where we expect either incremental of breakthrough progress with the appropriately set up ALMA observations. We expect, however, that most impressive discoveries will made in areas, which we do not currently foresee.

Author contributions

All authors listed have made a substantial, direct, and intellectual contribution to the work and approved it for publication.

Funding

GF was supported in part by NSF grants AGS-2121632, and AST-1820613 80NSSC20K0627, 80NSSC19K0068, 80NSSC20K0718, and 80NSSC18K1128 to New Jersey Institute of Technology. EL was supported by NASA grants 80NSSC18K0647, 80NSSC18K1553, 80NSSC22K0750 and NSF grant AGS-1621686. JM was supported by NASA grants 80NSSC18K1250, NNX16AG89G, 80NSSC21K0521. LG was

supported by NSF CAREER grant AGS 1752268 and NASA grants 80NSSC20K0627 and 80NSSC20K0718.

Conflict of interest

The authors declare that the research was conducted in the absence of any commercial or financial relationships that could be construed as a potential conflict of interest.

Publisher's note

All claims expressed in this article are solely those of the authors and do not necessarily represent those of their affiliated organizations, or those of the publisher, the editors and the reviewers. Any product that may be evaluated in this article, or claim that may be made by its manufacturer, is not guaranteed or endorsed by the publisher.

References

Aboudarham, J., and Henoux, J. C. (1986). Non-thermal excitation and ionization of hydrogen in solar flares. I. Effects on a flaring chromosphere. *A&A* 168, 301–307.

Altyntsev, A. A., Fleishman, G. D., Lesovoi, S. V., and Meshalkina, N. S. (2012). Thermal to nonthermal energy partition at the early rise phase of solar flares. *ApJ* 758, 138. doi:10.1088/0004-637X/758/2/138

Alvarado-Gómez, J. D., Buitrago-Casas, J. C., Martínez-Oliveros, J. C., Lindsey, C., Hudson, H., and Calvo-Mozo, B. (2012). Magneto-acoustic energetics study of the seismically active flare of 15 february 2011. *Sol. Phys.* 280, 335–345. doi:10.1007/s11207-012-0009-6

Anfinogentov, S. A., Stupishin, A. G., Mysh'yakov, I. I., and Fleishman, G. D. (2019). Record-breaking coronal magnetic field in solar active region 12673. *ApJ* 880, L29. doi:10.3847/2041-8213/ab3042

Asai, A., Nakajima, H., Shimojo, M., White, S. M., Hudson, H. S., and Lin, R. P. (2006). Preflare nonthermal emission observed in microwaves and hard X-rays. *Publ. Astron Soc. Jpn.* 58, L1–L5. doi:10.1093/pasj/58.1.L1

Aschwanden, M. J. (2020). Global energetics of solar flares. XI. Flare magnitude predictions of the GOES class. *ApJ* 897, 16. doi:10.3847/1538-4357/ab9630

Bamba, Y., Kusano, K., Yamamoto, T. T., and Okamoto, T. J. (2013). Study on the triggering process of solar flares based onhinode/sot observations. *ApJ* 778, 48. doi:10.1088/0004-637X/778/1/48

Bastian, T. S., Fleishman, G. D., and Gary, D. E. (2007). Radio spectral evolution of an X-ray-poor impulsive solar flare: Implications for plasma heating and electron acceleration. *ApJ* 666, 1256–1267. doi:10.1086/520106

Battaglia, M., Fletcher, L., and Benz, A. O. (2009). Observations of conduction driven evaporation in the early rise phase of solar flares. *A&A* 498, 891–900. doi:10.1051/0004-6361/200811196

Battaglia, M., and Kontar, E. P. (2011). Height structure of X-ray, EUV, and white-light emission in a solar flare. *A&A* 533, L2. doi:10.1051/0004-6361/201117605

Benz, A. O. (2017). Flare observations. *Living Rev. Sol. Phys.* 14, 2. doi:10.1007/s41116-016-0004-3

Bobra, M. G., and Ilonidis, S. (2016). Predicting coronal mass ejections using machine learning methods. *ApJ* 821, 127. doi:10.3847/0004-637X/821/2/127

Buitrago-Casas, J. C., Martínez Oliveros, J. C., Lindsey, C., Calvo-Mozo, B., Krucker, S., Glesener, L., et al. (2015). A statistical correlation of sunquakes based on their seismic and white-light emission. *Sol. Phys.* 290, 3151–3162. doi:10.1007/s11207-015-0786-9

Caspi, A., Krucker, S., and Lin, R. P. (2014). Statistical properties of super-hot solar flares. *ApJ* 781, 43. doi:10.1088/0004-637X/781/1/43

Caspi, A., and Lin, R. P. (2010). RHESSI line and continuum observations of super-hot flare plasma. *ApJ* 725, L161–L166. doi:10.1088/2041-8205/725/2/L161

Chen, B., Shen, C., Gary, D. E., Reeves, K. K., Fleishman, G. D., Yu, S., et al. (2020). Measurement of magnetic field and relativistic electrons along a solar flare current sheet. *Nat. Astron.* 4, 1140–1147. doi:10.1038/s41550-020-1147-7

Chen, Y., Manchester, W. B., Hero, A. O., Toth, G., DuFumier, B., Zhou, T., et al. (2019). Identifying solar flare precursors using time series of SDO/HMI images and SHARP parameters. *Space weather.* 17, 1404–1426. doi:10.1029/2019SW002214

Dermer, C. D. (1986). Binary collision rates of relativistic thermal plasmas. II - Spectra. *ApJ* 307, 47. doi:10.1086/164391

Ding, M. D. (2007). The origin of solar white-light flares. In *Phys. Chromospheric Plasmas*, eds. P. Heinzel, I. Dorotovič, and R. J. Rutten (San Francisco: Astronomical Society of the Pacific Conference Series) 368, 417

Fleishman, G. D., Altyntsev, A. T., and Meshalkina, N. S. (2013). Microwave signature of relativistic positrons in solar flares. *Publ. Astron Soc. Jpn.* 65, S7. doi:10.1093/pasj/65.sp1.S7

Fleishman, G. D., Gary, D. E., Chen, B., Kuroda, N., Yu, S., and Nita, G. M. (2020). Decay of the coronal magnetic field can release sufficient energy to power a solar flare. *Science* 367, 278–280. doi:10.1126/science.aax6874

Fleishman, G. D., and Kontar, E. P. (2010). Sub-thz radiation mechanisms in solar flares. *ApJ* 709, L127–L132. doi:10.1088/2041-8205/709/2/L127

Fleishman, G. D., Nita, G. M., and Gary, D. E. (2017). A large-scale plume in an X-class solar flare. *ApJ* 845, 135. doi:10.3847/1538-4357/aa81d4

Fleishman, G. D., Nita, G. M., and Gary, D. E. (2015). Energy partitions and evolution in a purely thermal solar flare. *ApJ* 802, 122. doi:10.1088/0004-637X/802/2/122

Fleishman, G. D., Xu, Y., Nita, G. N., and Gary, D. E. (2016). Validation of the coronal thick target source model. *ApJ* 816, 62. doi:10.3847/0004-637X/816/2/62

Gan, W. Q., Li, Y. P., and Chang, J. (2001). Energy shortage of nonthermal electrons in powering a solar flare. *ApJ* 552, 858–862. doi:10.1086/320574

Gary, D. E., and Hurford, G. J. (1989). A simple solar microwave burst observed with high spectral resolution. *ApJ* 339, 1115. doi:10.1086/167366

Hudson, H. S., Fisher, G. H., and Welsch, B. T. (2008). "Flare energy and magnetic field variations,". Editors R. Howe, R. W. Komm, K. S. Balasubramaniam, and G. J. D. Petrie. *Subsurf. Atmos. Influ. Sol. Activity* (San Francisco, CA: Astronomical Society of the Pacific Conference Series), 383, 221.

Hudson, H. S., Simões, P. J. A., Fletcher, L., Hayes, L. A., and Hannah, I. G. (2020). Hot X-ray onsets of solar flares. *Mon. Not. R. Astron. Soc.* 501, 1273–1281. doi:10.1093/mnras/staa3664

Hudson, H. S. (1972). Thick-target processes and white-light flares. *Sol. Phys.* 24, 414–428. doi:10.1007/BF00153384

Kaufmann, P., Raulin, J.-P., Correia, E., Costa, J. E. R., de Castro, C. G. G., Silva, A. V. R., et al. (2001). Rapid submillimeter brightenings associated with a large solar flare. *Astrophys. J.* 548, L95–L98. doi:10.1086/318932

Kaufmann, P., Trottet, G., Giménez de Castro, C. G., Raulin, J.-P., Krucker, S., Shih, A. Y., et al. (2009). Sub-terahertz, microwaves and high energy emissions during the 6 december 2006 flare, at 18:40 UT. *Sol. Phys.* 255, 131–142. doi:10.1007/s11207-008-9312-7

Kontar, E. P., Motorina, G. G., Jeffrey, N. L. S., Tsap, Y. T., Fleishman, G. D., and Stepanov, A. V. (2018). Frequency rising sub-THz emission from solar flare ribbons. *A&A* 620, A95. doi:10.1051/0004-6361/201834124

Kosovichev, A. G., and Zharkova, V. V. (1998). X-ray flare sparks quake inside Sun. *Nature* 393, 317–318. doi:10.1038/30629

Krucker, S., Giménez de Castro, C. G., Hudson, H. S., Trottet, G., Bastian, T. S., Hales, A. S., et al. (2013). Solar flares at submillimeter wavelengths. *Astron. Astrophys. Rev.* 21, 58. doi:10.1007/s00159-013-0058-3

Kuhar, M., Krucker, S., Oliveros, J. C., Battaglia, M., Kleint, L., Casadei, D., et al. (2016). Correlation of hard X-ray and white light emission in solar flares. *ApJ* 816, 6. doi:10.3847/0004-637X/816/1/6

Landi, E., Habbal, S. R., and Tomczyk, S. (2016). Coronal plasma diagnostics from ground-based observations. *J. Geophys. Res. Space Phys.* 121, 8237–8249. doi:10.1002/2016JA022598

Landi, E., Hutton, R., Brage, T., and Li, W. (2020). Hinode/EIS measurements of active-region magnetic fields. *ApJ* 904, 87. doi:10.3847/1538-4357/abbf54

Landi, E., Li, W., Brage, T., and Hutton, R. (2021). Hinode/EIS coronal magnetic field measurements at the onset of a c2 flare. *ApJ* 913, 1. doi:10.3847/1538-4357/abf6d1

Li, W., Grumer, J., Yang, Y., Brage, T., Yao, K., Chen, C., et al. (2015). A novel method to determine magnetic fields in low-density plasma facilitated through accidental degeneracy of quantum states in Fe9+. *ApJ* 807, 69. doi:10.1088/0004-637X/807/1/69

Li, W., Yang, Y., Tu, B., Xiao, J., Grumer, J., Brage, T., et al. (2016). Atomic-level pseudo-degeneracy of atomic levels giving transitions induced by magnetic fields, of importance for determining the field strengths in the solar corona. *ApJ* 826, 219. doi:10.3847/0004-637X/826/2/219

Lindsey, C., and Donea, A. C. (2008). Mechanics of seismic emission from solar flares. *Sol. Phys.* 251, 627–639. doi:10.1007/s11207-008-9140-9

Loukitcheva, M., White, S. M., Solanki, S. K., Fleishman, G. D., and Carlsson, M. (2017). Millimeter radiation from a 3D model of the solar atmosphere. *A&A* 601, A43. doi:10.1051/0004-6361/201629099

Lüthi, T., Lüdi, A., and Magun, A. (2004). Determination of the location and effective angular size of solar flares with a 210 GHz multibeam radiometer. *A&A* 420, 361–370. doi:10.1051/0004-6361:20035899

Lysenko, A. L., Altyntsev, A. T., Meshalkina, N. S., Zhdanov, D., and Fleishman, G. D. (2018). Statistics of "cold" early impulsive solar flares in X-ray and microwave domains. *ApJ* 856, 111. doi:10.3847/1538-4357/aab271

Machado, M. E., Emslie, A. G., and Avrett, E. H. (1989). Radiative backwarming in white-light flares. *Sol. Phys.* 124, 303–317. doi:10.1007/BF00156272

Machado, M. E., Emslie, A. G., and Brown, J. C. (1978). The structure of the temperature minimum region in solar flares and its significance for flare heating mechanisms. *Sol. Phys.* 58, 363–387. doi:10.1007/BF00157282

Martínez Oliveros, J.-C., Hudson, H. S., Hurford, G. J., Krucker, S., Lin, R. P., Lindsey, C., et al. (2012). The height of a white-light flare and its hard X-ray sources. *ApJ* 753, L26. doi:10.1088/2041-8205/753/2/L26

Martínez Oliveros, J. C., Couvidat, S., Schou, J., Krucker, S., Lindsey, C., Hudson, H. S., et al. (2011). Imaging spectroscopy of a white-light solar flare. *Sol. Phys.* 269, 269–281. doi:10.1007/s11207-010-9696-z

Murphy, R. J., Share, G. H., Skibo, J. G., and Kozlovsky, B. (2005). The physics of positron annihilation in the solar atmosphere. *Astrophys. J. Suppl. S* 161, 495–519. doi:10.1086/452634

Neidig, D. F., and Cliver, E. W. (1983). The occurrence frequency of white-light flares. *Sol. Phys.* 88, 275–280. doi:10.1007/BF00196192

Panos, B., Kleint, L., Huwyler, C., Krucker, S., Melchior, M., Ullmann, D., et al. (2018). Identifying typical Mg II flare spectra using machine learning. *ApJ* 861, 62. doi:10.3847/1538-4357/aac779

Panos, B., and Kleint, L. (2020). Real-time flare prediction based on distinctions between flaring and non-flaring active region spectra. *ApJ* 891, 17. doi:10.3847/1538-4357/ab700b

Ramaty, R., Kozlovsky, B., and Lingenfelter, R. E. (1979). Nuclear gamma-rays from energetic particle interactions. *ApJS* 40, 487–526. doi:10.1086/190596

Si, R., Brage, T., Li, W., Grumer, J., Li, M., and Hutton, R. (2020). A first spectroscopic measurement of the magnetic-field strength for an active region of the solar corona. *ApJ* 898, L34. doi:10.3847/2041-8213/aba18c

Svestka, Z. (1976). *Solar flares.*

Testa, P., Polito, V., and Pontieu, B. (2020). IRIS observations of short-term variability in moss associated with transient hot coronal loops. *ApJ* 889, 124. doi:10.3847/1538-4357/ab63cf

Wang, H., Liu, C., Ahn, K., Xu, Y., Jing, J., Deng, N., et al. (2017). High-resolution observations of flare precursors in the low solar atmosphere. *Nat. Astron.* 1, 0085. doi:10.1038/s41550-017-0085

Woods, M. M., Sainz Dalda, A., and De Pontieu, B. (2021). Unsupervised machine learning for the identification of preflare spectroscopic signatures. *ApJ* 922, 137. doi:10.3847/1538-4357/ac2667

Zharkov, S., Green, L. M., Matthews, S. A., and Zharkova, V. V. (2013). Properties of the 15 february 2011 flare seismic sources. *Sol. Phys.* 284, 315–327. doi:10.1007/s11207-012-0169-4

Zharkova, V. V. (2008). The mechanisms of particle kinetics and dynamics leading to seismic emission and sunquakes. *Sol. Phys.* 251, 665–666. doi:10.1007/s11207-008-9266-9

frontiers | Frontiers in Astronomy and Space Sciences

ORIGINAL RESEARCH
published: 26 April 2022
doi: 10.3389/fspas.2022.832607

Estimating the Coronal Supra-Arcade Downflow Radio Emission: From Centimeter Through Submillimeter Wavelengths

Ernesto Zurbriggen[1*†], *C. Guillermo Giménez De Castro*[1,2†], *Andrea Costa*[3†], *Mariana Cécere*[3,4†] *and Caius L. Selhorst*[5]

[1]Centro de Rádio Astronomia e Astrofísica Mackenzie (CRAAM), Universidade Presbiteriana Mackenzie, São Paulo, Brazil, [2]Instituto de Astronomía y Física del Espacio (IAFE-UBA), Consejo Nacional de Investigaciones Científicas y Técnicas (CONICET), Buenos Aires, Argentina, [3]Instituto de Astronomía Teórica y Experimental (IATE), Consejo Nacional de Investigaciones Científicas y Técnicas, Córdoba, Argentina, [4]Observatorio Astronómico de Córdoba (OAC), Universidad Nacional de Córdoba (UNC), Córdoba, Argentina, [5]NAT—Núcleo de Astrofísica, Universidade Cidade de São Paulo, São Paulo, Brazil

Supra-arcade downflows (SADs) are infrequent, wiggly, and low-emission structures observed to descend through the solar corona, mostly in EUV and soft X-ray frequencies. Based on their physical characteristics, SADs have been interpreted as low-density bubbles and are related to magnetic reconnection processes during long-term erupting flares. In this work, we use numerical MHD simulations to compute flux density maps, which are convolved with telescope beams to synthesize images with the aim to assess the expected SAD emission in radio wavelengths. We assume that the emission is thermal bremsstrahlung from a fully ionized plasma and without any appreciable gyroresonance contribution since magnetic fields are of the order of 10 G. We find that SAD emission should be optically thin in the frequency range of [10–1,000] GHz, and the spatially integrated flux should be larger than 1 Jy. We conclude, therefore, that SADs consistently are less bright than the surrounding fan and that observing SADs in radio frequencies between [0.5–1,000] GHz is feasible with present instrumentation. The observing strategies are proposed, including the instruments that can be used. Moreover, since the emission is, for the most part, optically thin, the flux density is proportional to temperature, density, and line-of-sight depth and when combined with EUV and soft X-ray images may allow a better density and temperature determination of SADs.

Keywords: sun: corona, sun: flares, sun: magnetic fields, sun: radio radiation, MHD—instabilities

OPEN ACCESS

Edited by:
Masumi Shimojo, National Astronomical Observatory of Japan (NINS), Japan

Reviewed by:
Debi Prasad Choudhary, California State University, Northridge, United States
David McKenzie, National Aeronautics and Space Administration (NASA), United States

***Correspondence:**
Ernesto Zurbriggen
ernesto.zurbriggen@craam.mackenzie.br

†ORCID ID:
Ernesto Zurbriggen, orcid.org/0000-0002-3480-7107;
C. Guillermo Giménez De Castro, orcid.org/0000-0002-8979-3582;
Andrea Costa, orcid.org/0000-0002-4369-7392;
Mariana Cécere, orcid.org/0000-0002-9844-0033

Specialty section:
This article was submitted to Stellar and Solar Physics, a section of the journal Frontiers in Astronomy and Space Sciences

Received: *10 December 2021*
Accepted: *02 March 2022*
Published: *26 April 2022*

Citation:
Zurbriggen E, Giménez De Castro CG, Costa A, Cécere M and Selhorst CL (2022) Estimating the Coronal Supra-Arcade Downflow Radio Emission: From Centimeter Through Submillimeter Wavelengths. Front. Astron. Space Sci. 9:832607. doi: 10.3389/fspas.2022.832607

1 INTRODUCTION

In EUV and soft X-ray observations, coronal supra-arcade downflows (SADs) are seen as wiggly, low-emission structures leaving extended dark wakes during their descending motions toward the solar surface till they finally stop and gradually disappear. Often SAD descending motions resemble tadpoles swimming upstream through the fluid interstices that oppose less resistance. SADs have usually been detected during the early decay phases of long-term eruptive flares producing coronal mass ejections occurring many times during the first hour after the peak flare intensity. The SAD typical lifetime is of a few minutes. Today there exists a general consensus

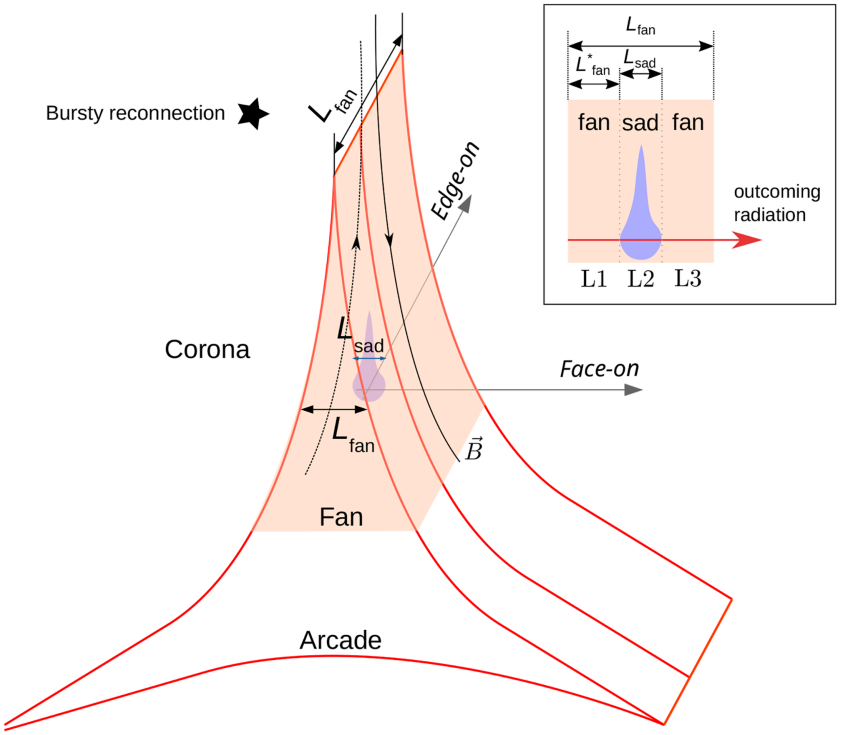

FIGURE 1 | Schematic scenario of a SAD (blue feature) embedded in the bright, hot, and dense fan plasma (shaded region). Below the fan lies the post-flare arcade, and the external coronal medium surrounds it. The fan in addition embeds the expected supra-arcade current-sheet (dark lines with arrows). The fan is represented as viewed by an observer to the limb with two particular line-of-sights of interest represented, the edge-on and face-on views. Given that the fan is a thin, linear, and long structure along the edge-on direction, when the fan is viewed edge-on, the line-of-sight depth L_{fan} is greater than when viewed face-on. (Inset) Sketches a three-layer scheme used to compute the outcoming radiation considering a SAD embedded in the fan for an observer in the arrow direction.

that SADs are subdense cavities of plasma, with densities lower than their surroundings and, thus, having an intrinsically lower brightness (Innes et al., 2003b). SADs have been reported in several events (McKenzie and Hudson, 1999; McKenzie and Savage, 2009; Savage and McKenzie, 2011; McKenzie and Savage, 2011; Warren et al., 2011; Hanneman and Reeves, 2014; Chen et al., 2017) and using different instruments and observational techniques: direct images, with TRACE in EUV and XRT/Hinode and AIA/SDO in soft X-rays; and spectra with SUMER/SOHO in EUV. SADs are observed to descend from the upper part of the fan, a region that lies above the post-flare arcade, which is formed after the eruption, and it is also known in the literature as post-eruption supra-arcade; plasma sheet; thermal halo; supra-arcade fan; or just fan (hereafter used, see the sketch of **Figure 1**). The fan is a dynamical region exhibiting turbulent motions with a relatively high plasma β parameter ($\gtrsim 1$; McKenzie, 2013; Freed and McKenzie, 2018), is bright in EUV and soft X-ray wavelengths, providing the necessary contrast for SAD detection; and is also hotter and denser than the external coronal medium by roughly an order of magnitude. SADs are observed in limb flares and generally when the fan is viewed face-on (i.e., perpendicular to the arcade axis, see **Figure 1**), whereas almost not in edge-on views. On the other hand, soft X-ray observations have provided evidence that the bright plasma of the fan surrounds a current sheet (Liu et al., 2013; Warren et al., 2018) that, in line with the classical model of eruptive flares, is expected to form behind the coronal mass ejection. In addition, there is observational evidence that the current sheet extends high in the corona with the fan just covering the lower part of it.

Despite the fact that several models of SADs have been proposed, the SAD origin and dynamics are not yet completely understood; therefore, the mechanism of their driving physical process is still open to further research. Based on observations and theoretical considerations, a common point among all proposed models is the association of possible SAD origins with post-eruption magnetic reconnection processes occurring inside the fan or in its upper coronal medium (**Figure 1**). Some models (Linton et al., 2009; Longcope et al., 2009; Scott et al., 2013; Guo et al., 2014; Longcope et al., 2018), have pointed out to reconnection downflows descending through the fan as the driven mechanism: considering the standard model of erupting flares, behind the coronal mass ejection, magnetic field lines of opposite polarities are swept together forming the supra-arcade current sheet where the lines reconnect. As a result, part of the reconnection outflows is propelled downward, *via* magnetic tension, to the already-formed underlying arcade, likely in the form of descending magnetic flux tubes or loops. With this picture in mind, Linton et al. (2009), see also Linton and Longcope (2006), carried out 3D MHD simulations considering

an intermittent burst of patchy reconnection in a Y-type current sheet, which supported the idea that SADs are descending reconnected flux tubes. Then, Savage et al. (2012) interpreted SADs as subdense wakes left by shrinking reconnected flux tubes by the observational analysis of one event. In turn, Guo et al. (2014), see also Innes et al. (2014), proposed that reconnected flux tubes in their retracting motions through the inhomogenous fan generate interfaces of plasma where Rayleigh–Taylor instabilities are developed and subsequently generate the SAD phenomenon. In these models, SADs are triggered in the current sheet neighborhood, that is, inside the fan or in its upper coronal region. A common issue with the reconnection downflow interpretation of SADs is the several-time reported discrepancy between the measured SAD speeds (often smaller than 200 km s^{-1}) and the theoretical reconnection downflow speeds, expected to be the Alfvén speed (~1,000 km s^{-1}) of the fan. Among the possible explanations to overcome this speed mismatch, it was proposed that drag forces could act on the descending motion of reconnection downflows (Longcope et al., 2018), slowing them down.

In contrast with the abovementioned reconnection downflow interpretation of SADs, Costa et al. (2009), Schulz et al. (2010), Maglione et al. (2011), Cécere et al. (2012), Cécere et al. (2015), and Zurbriggen et al. (2016) have assumed SADs to be generated by spontaneous, intermittent, and bursty magnetic reconnection processes taking place somewhere in the turbulent-like fan or in its upper coronal region. One of these bursty reconnection events injects energy in a localized fast way, resembling a spark or explosive event, generating shock and rarefaction nonlinear waves, leading to the formation of a subdense cavity, whose structure supports the external pressure because it is hotter than its surroundings, and which is then observed in EUV and soft X-rays as a low-emission structure moving down along the bright fan. These spontaneous reconnection drivers are considered local processes, which could be independent of the overall supra-arcade current sheet. A common characteristic of simulated SADs by Costa et al. (2009) and their subsequent works is that SADs are hotter than the fan. However, some observational studies (Hanneman and Reeves, 2014; Reeves et al., 2017; Xue et al., 2020) have pointed out that SADs are hotter than the upper coronal medium, but they do not seem to be hotter than the fan. This temperature discrepancy between SADs and the fan is due to simplifying assumptions on our modeling, which may be overcome by considering a more complex fan scenario. In addition, a questionable point related to the scenario proposed by Zurbriggen et al. (2016) is that the simulated SADs exhibited lack of elongated tadpole-like shapes during their descent; instead, they showed a more compact shape which opposes several observational reports. This issue is a consequence of considering explicitly anisotropic thermal conduction in the MHD simulations.

Finally, given that SADs are not usually detected during eruptive flares, an important question still remaining to be answered by observations and models is whether SADs are an infrequent phenomenon, and thus, rarely observed, or are they a common phenomenon usually not detected for some reason. SADs have been mainly detected and studied in EUV and soft X-ray frequencies, whereas in radio wavelengths, only indirect evidence have been reported, and, as far as we know, no attempt has been made to detect them directly. In this work, we compute the expected thermal bremsstrahlung emission produced by SADs in wavelengths from centimeter to submillimeter using the numerical MHD models presented by Guo et al. (2014), Cécere et al. (2015), and Zurbriggen et al. (2016). Moreover, we synthesize maps by convolving the telescope beams of the Atacama Large Millimeter/Submillimeter Array (ALMA) in Chajnantor (Chile) and the Karl G. Jansky Very Large Array (VLA) in Socorro (United States) with the MHD simulations of SADs carried out by Zurbriggen et al. (2016). The goal of this work is to motivate and identify the best strategy to observe in centimeter – submillimeter wavelengths these illusive structures triggered during long-term solar erupting flares.

2 REVIEW OF OBSERVATIONS

EUV and soft X-ray observations have reported that the fan is hotter and denser than the background coronal plasma in approximately an order of magnitude, with fan temperatures in the ~[10–20] MK range and ion number densities of ~10^9 cm^{-3}. In an observational study, Hanneman and Reeves (2014) measured plasma temperatures for the fan, SADs, and coronal background in four flare events using differential emission measures, briefly reporting that the peak temperatures of SADs are in the ~[2–12] MK range, with just one SAD being hotter than 10 MK; the fan temperatures are ~10 MK, except a temperature measurement of 20 MK, but having high uncertainty and background temperatures of ~[2–3] MK. In addition, in the literature, we find that SADs have been detected at heights ~[40–150] Mm above the solar surface, with an average height of ~80 Mm; descend distances of ~[10–20] Mm; have downward speeds in the ~[50–500] km s^{-1} range, but with a relatively low average speed of ~130 km s^{-1}; with SAD sizes between ~[1–10] Mm; and have lifetimes of around ~[5–10] min, although there have been few extreme exceptions. On the other hand, the emission contrast between the dark structure and surrounding bright fan is an essential parameter during SAD detection, where, for example, values of ~[2–4] were reported by Xue et al. (2020), see their Figure 4D. Less observational data about SAD properties are available in wavelengths other than EUV and soft X-rays. Among all limb flare events reported in the literature with SAD detection or any signature of their presence, four events extensively studied occurred on 21 April 2002 on the NOAA active region (AR) 9906 (e.g., see Innes et al., 2003a,b; Verwichte et al., 2005); 22 October 2011 on NOAA AR 11314 (McKenzie, 2013; Hanneman and Reeves, 2014; Reeves et al., 2017; Xue et al., 2020; Li et al., 2021); 19 July 2012 on NOAA AR 11520 (Liu, 2013; Liu et al., 2013; Innes et al., 2014); and 10 September 2017 on NOAA AR 12673 (Longcope et al., 2018; Warren et al., 2018; Cai et al., 2019; Hayes et al., 2019; Yu et al., 2020). While the fan view for the first two events was face-on, the view for the third and fourth ones was

edge-on. On the other hand, the fan is a linear-like, long column of plasma along the current sheet direction (edge-on view, see the sketch of **Figure 1**) with ~[3–30] Mm depths, and it is noted that it is considerably thinner in the perpendicular direction (face-on view).

So far, there has not been any direct SAD detection in radio or microwaves at any frequency. On the other hand, some observational studies of limb flaring events (Asai et al., 2004; Chen et al., 2015; Yu et al., 2020), preferably in edge-on views, revealed temporal and spatial correlations between EUV recurring downflow motions in the fan and subsequent detection of impulsive radio emission bursts on the top and/or leg of the lower arcade. In any case, the downflows had a counterpart in radio wavelengths. Assuming the reconnection downflow interpretation of SADs, these authors interpreted the radio impulsive emissions as a consequence of the presence of SADs.

3 MODELING THE EXPECTED EMISSION

3.1 Supra-Arcade Downflow Models Description

In order to calculate the thermal bremsstrahlung emissions of fans and SADs, we need to know their plasma temperatures and densities. Given that these data are not always provided by the models, we circumscribe to the numerical MHD scenarios presented by Guo et al. (2014), Cécere et al. (2015), and Zurbriggen et al. (2016). **Table 1** summarizes the relevant mean characteristics of each model: SAD size L_{sad}; SAD (inner) ion number density n_{sad} (also equivalent mass density ρ_{sad}) and temperature T_{sad}; and fan (outer) ion number density n_{fan}, temperature T_{fan}, and mean magnetic field intensity B_{fan}. Comparing the values of the models listed in **Table 1** and those reported by observations in **Section 2**, it is to be noted that all models predict SAD temperatures higher than the observationally reported ones, whereas the modeled fan temperatures and densities are in agreement with those in observations, except the fan densities of models 2 and 3 that seem to be a bit high.

Following the work of Costa et al. (2009) and motivated by the turbulent-like description of the fan provided by McKenzie (2013), Cécere et al. (2015) carried out 3D ideal MHD simulations to model a turbulent and dynamical fan as the medium where SADs descend. In order to generate this, a combination of tearing-mode and Kelvin–Helmholtz instabilities was used. It was argued that to obtain SADs compatible with observations, the activation of spontaneous bursty reconnection processes is required and that SADs support the external pressure because they are hotter than their surroundings. Moreover, for contrast requirements, Cécere et al. (2015) suggested that there must be a closed relation between SAD sizes and fan widths that should be satisfied for SADs to be observable. For this reason, SADs of two different characteristic sizes were generated with $L_{sad} = 4$ Mm and $L_{sad} = 12$ Mm (models 2 and 3 in **Table 1**, respectively).

Considering the scenario presented by Cécere et al. (2015), the 2D MHD simulations of Zurbriggen et al. (2016) considered the particular case of small SADs ($L \approx 2$Mm), where thermal conduction is expected to be more efficient and SADs fade away much faster than their typical lifetime. In this case, a properly turbulent fan was generated using a stirring force source. **Figure 2** shows images of density (**Figure 2A**) and temperature (**Figure 2B**) maps. The images display three SADs, two strongly faded away due to the thermal diffusion, and the third one at the bottom left corner with coordinates $(x,y) = (-3,-6)\times 10^8$ cm and size $\approx$2 Mm $\equiv 2.8''$ is the most intense. This SAD has a mean density $\rho_{sad} \approx 5.1\times 10^{-15}$ g cm^{-3}, while the fan is almost three times denser, $\rho_{fan} \approx 1.2\times 10^{-14}$ g cm^{-3}. On the other hand, the SAD inner temperature $T_{sad} \approx 19.2$ MK is three times greater than the outer $T_{fan} \approx 7$ MK. This model (model 1 in **Table 1**) represents the case of a fan viewed face-on.

Guo et al. (2014), performing 3D-resistive MHD simulations, generated SADs by means of Rayleigh–Taylor instabilities associated with shrinking motions of magnetic flux tubes. In their scenario, using constant magnetic resistivity, SADs have characteristic sizes within $[6'' - 15'']$ ($\equiv$ [4.7 – 11.6] Mm, see their Figure 2). Therefore, for models 4 and 5 listed in **Table 1**, the extreme values of this size range were adopted, and the remaining values of density and temperature required for our analysis were extracted by visual inspection from their **Figures 2B, C**.

3.2 Expected Total Flux

Hereafter, we will refer to models summarized in **Table 1** as model 1 to the smallest SAD (here considered) taken from the study by Zurbriggen et al. (2016); models 2 and 3 to the small and

TABLE 1 | Summary of relevant mean characteristics of different numerical MHD models. L_{sad} is the SAD size; n_{sad}, ρ_{sad}, and T_{sad} are the SAD (inner) average ion number densities, equivalent mass density, and temperature, respectively; n_{fan}, ρ_{fan}, and T_{fan} are the corresponding fan (outer) values; and B_{fan} [G] represents the mean magnetic field intensity of the fan. Data were taken from literature and here referred as model 1 from Zurbriggen et al. (2016); models 2–3 from Cécere et al. (2015); and models 4–5 from Guo et al. (2014).

Model	L_{sad} [Mm]	n_{sad} [cm^{-3}]	ρ_{sad} [g cm^{-3}]	n_{fan}	ρ_{fan}	T_{sad} [MK]	T_{fan}	B_{fan}
1	2	2.4×10^9	5.1×10^{-15}	5.8×10^9	1.2×10^{-14}	19.2	7	3
2	4	8.9×10^9	1.5×10^{-14}	20×10^9	3.3×10^{-14}	22.4	10	5.9
3	12	6.5×10^9	1.1×10^{-14}	20×10^9	3.3×10^{-14}	27	10	5.9
4	4.7	2.6×10^9	4.3×10^{-15}	3.3×10^9	5.5×10^{-15}	22	18	14
5	11.6	2.6×10^9	4.3×10^{-15}	3.3×10^9	5.5×10^{-15}	22	18	14

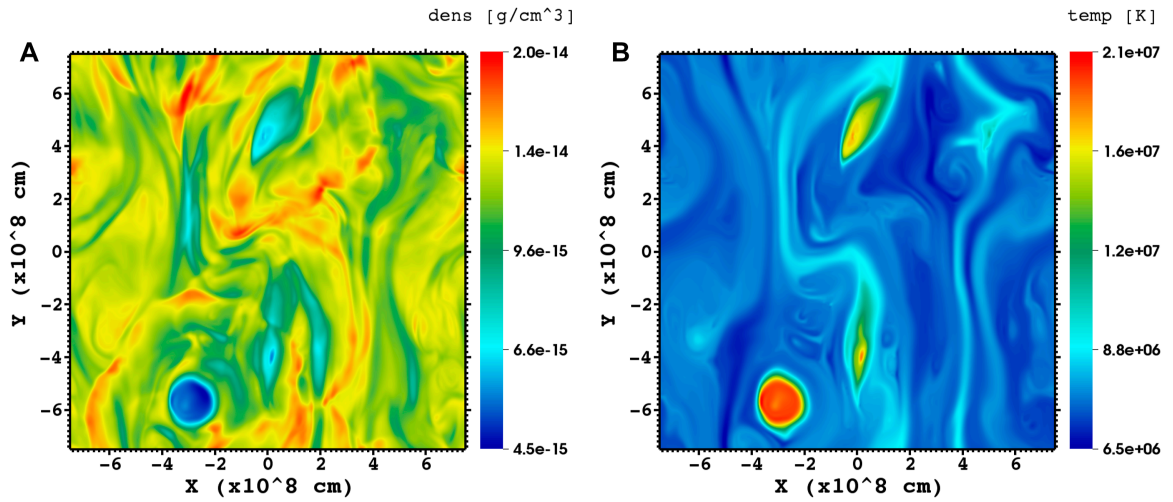

FIGURE 2 | 2D MHD numerical simulation of SADs descending through a turbulent fan explicitly considering thermal conduction (presented in Zurbriggen et al., 2016). **(A)** Density values are shown. **(B)** Corresponding temperature. This model represents a fan viewed face-on. It is to be noted that 10^8 cm ≡ 1 Mm.

big SADs simulated by Cécere et al. (2015); and models 4 and 5 to the extreme sizes (6″ and 15″) reported by Guo et al. (2014).

In order to compute the (free–free) thermal bremsstrahlung emission, we use the expression

$$F(\nu) = \frac{2k_B T \nu^2}{c^2}\left(1 - e^{-\tau_\nu}\right)\Omega \ , \tag{1}$$

where k_B is the Boltzmann constant and c is the speed of light. T_ν is the optical depth at frequency ν, which is approximated by Dulk (1985)

$$\tau_\nu = \kappa_\nu L \ ,$$
$$\kappa_\nu = 9.78 \times 10^{-3} \frac{n_e}{\nu^2 T^{3/2}} \left(\sum_i Z_i^2 n_i\right) G(T,\nu) \tag{2}$$

where κ_ν is the thermal bremsstrahlung opacity, L is the plasma line-of-sight depth considered, and $G(T,\nu)$ is the Gaunt factor that we obtain numerically from van Hoof et al. (2014). In addition, n_e and n_i are the number densities of free electrons and ions of specie i, respectively, and Z_i is the atomic number of specie i. As we consider a fully ionized, ideal plasma with a solar abundance of 70.7% H + 27.4% He + 1.9% heavier elements (Prialnik, 2000), we infer that $\sum_i Z_i^2 n_i = 3.703n$, with n the average total ion number density, and from which we derive the electron density $n_e = 1.445n$. Ω is the solid angle considered.

From **Eq. 2**, we compute the thermal bremsstrahlung opacities κ_ν as a function of the observing frequency ν for the SADs and fans of models 1–5. **Figure 3** shows the obtained results. Color-continuous lines represent the SAD opacities, while color-dashed

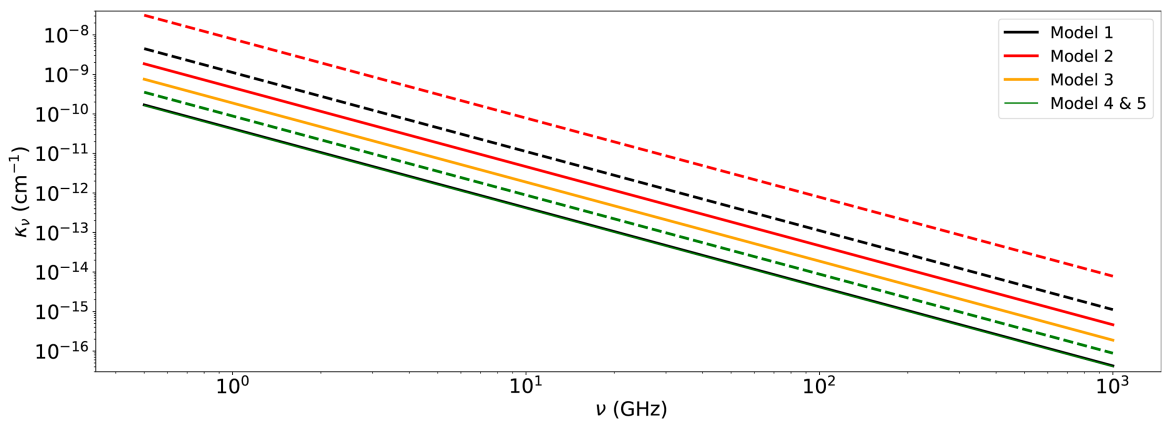

FIGURE 3 | Mean thermal bremsstrahlung opacities κ_ν for the different models (identified by colors) in the frequency range [0.5–1,000] GHz. Continuous lines correspond to inner (SAD) opacities, while dashed lines correspond to outer (fan) opacities. Fan opacities for models 2 and 3 are equal; the same happens for models 4 and 5. It is to be noted that SAD opacities for models 1, 4, and 5 are similar (lowest superimposed continuous lines).

lines represent the corresponding fan opacities, which in general are larger in values. For fans and SADs, the regime should be optically thin greater than 10 GHz. However, in some cases, that will be analyzed later, the transition from optically thick to thin regimes may happen at frequencies below 1 GHz.

We can now estimate the integrated flux density emitted by the whole SAD using **Eq. 1** and the mean values from **Table 1**. The intrinsically inhomogenous dynamics of the fan implies that random fluctuations cancel out when integrated over the line-of-sight, and therefore the use of mean values is appropriate for computing the outgoing radiation observed on Earth. In the calculation, we assume that all sources are cylindrical with a diameter equal to the SAD size, and the solid angle $\Omega = \pi L_{\rm sad}^2/4{\rm AU}^2$, with AU the mean Sun–Earth distance. The chromospheric contribution is not considered because we are considering an observer viewing the fan over the limb. As sketched in **Figure 1**, we assume an observer in the outcoming-radiation direction and that the SAD is embedded in the fan; thus, we consider the fan emission in front of and behind the SAD. Given that we are interested in the contrast, we want to compare the outgoing radiations coming from a direction, including the SAD, with another one just considering the surrounding fan. When the considered direction includes the SAD, a three-layer calculation is carried out (see the inset in **Figure 1**); otherwise, just one layer is considered. For all cases, the layers are assumed isothermal and homogenous. In the three-layer calculation of the flux density, the inner (L_1) and outer (L_3) layers are formed by the fan plasma, whereas the middle layer corresponds to the SAD (L_2). Here, we assume that in general $L_{\rm fan} > L_{\rm sad}$—although there is no conclusive observational data on this detail— and we suppose that the SAD layer is in the geometrical center of the fan, so the depth of the inner and outer layers are defined as $L_{\rm fan}^* = (L_{\rm fan} - L_{\rm sad})/2$. In this case, the final total flux density is then

$$F_{\rm sad}(\nu) = F_{\rm L_1}(\nu) + F_{\rm L_2}(\nu) + F_{\rm L_3}(\nu). \tag{3}$$

The emerging flux density from L_1, after traversing the SAD (L_2) and outer fan (L_3) layers, is

$$F_{\rm L_1}(\nu) = \frac{2k_{\rm B}T_{\rm fan}\nu^2}{c^2}\left(1 - e^{-\tau_{\rm L_1}(\nu)}\right)e^{-\tau_{\rm L_2}(\nu)}e^{-\tau_{\rm L_3}(\nu)}\Omega, \tag{4}$$

where $\tau_{\rm L_1}$, $\tau_{\rm L_2}$, and $\tau_{\rm L_3}$ are the opacities of the layers L_1, L_2, and L_3, respectively. In a similar way, the emerging flux density from the SAD layer is

$$F_{\rm L_2}(\nu) = \frac{2k_{\rm B}T_{\rm sad}\nu^2}{c^2}\left(1 - e^{-\tau_{\rm L_2}(\nu)}\right)e^{-\tau_{\rm L_3}(\nu)}\Omega. \tag{5}$$

Finally, for the outer layer, we have

$$F_{\rm L_3}(\nu) = \frac{2k_{\rm B}T_{\rm fan}\nu^2}{c^2}\left(1 - e^{-\tau_{\rm L_3}(\nu)}\right)\Omega. \tag{6}$$

On the other hand, the emerging radiation when observing the SAD direction has only the fan contribution (a one-layer calculation)

$$F_{\rm fan}(\nu) = \frac{2k_{\rm B}T_{\rm fan}\nu^2}{c^2}\left(1 - e^{-\tau_{\rm fan}(\nu)}\right)\Omega\ , \tag{7}$$

where $\tau_{\rm fan}(\nu)$ is the opacity of the whole fan line-of-sight depth $L_{\rm fan}$.

Figure 4 displays the resulting integrated flux densities and contrasts $Q = F_{\rm fan}(\nu)/F_{\rm sad}(\nu)$, dividing **Eq. 7** by **Eq. 3**. The results are displayed for the edge-on (**Figures 4A,B**) and face-on (**Figures 4C,D**) views of the fan, with line-of-sight depths $L_{\rm fan}$ = 30 Mm and $L_{\rm fan}$ = 5 Mm, respectively. It is to be noted that the flux density is almost constant for frequencies $\nu \gtrsim 5$ GHz, where the spectrum is optically thin. The SAD integrated flux densities $F_{\rm sad}(\nu)$ are in the range $\sim[10^2 - 10^4]$ Jy and are weaker than the fan flux densities $F_{\rm fan}(\nu)$. This is also evident in the right panels where we see contrasts $Q > 1$. Model 3 exhibits the highest contrasts, of 1.6 on the edge-on view and 6 on the face-on view, while model 1 exhibits the lowest, of 1.05 and 1.7, respectively. The remaining contrasts lie between these extremes. When the spectra become optically thick ($\nu \lesssim 5$ GHz), the contrasts tend to conform to unity, particularly in the edge-on view, meaning that the SAD layer contribution to the total flux density is negligible. Interestingly, for model 3 in the face-on view, we see $Q < 1$, implying that the SAD is brighter than the fan.

3.3 Gyroresonance

In the previous calculations of **Section 3.2**, we did consider gyroresonance radiation, an emission mechanism that depends on the magnetic field intensity, in addition to the temperature and density. The gyroresonance opacity at frequency ν depends on the harmonic number $s = \nu/\nu_B$, where $\nu_B = 2.8 \times 10^6 B$, with B the magnetic field intensity in G. The opacity at a given harmonic number τ_s (e.g., Casini et al., 2017) is proportional to $\tau_s \propto \frac{s^2}{s!}$. Because of this dependence, only the very first harmonics produce detectable emission. Indeed, usually, only the first three harmonics are considered (see, e.g., White, 2004; Selhorst et al., 2008). In the present case, where magnetic field intensities of the MHD simulations are $B \leq 14$ G, we have $\nu_B \leq 0.039$ GHz; therefore, for the lowest frequency, $\nu = 0.5$ GHz, $s \geq 13$, and $\tau_s \propto s^2/s! \lesssim 10^{-8}$. Since for higher frequencies the harmonic number s will be even larger, we can neglect the gyroresonance contribution from the emerging flux density in the frequency range [0.5–1,000] GHz used in our calculations.

3.4 2D Synthesized Radio Maps

Here, we use model 1 to synthesize images that we expect to observe with the present radio telescopes. Since model 1 is 2D, we do not include the fan contribution in front of or behind the SAD as was carried out previously in **Section 3.2**; instead, every grid cell is thought of as a homogenous source with a line-of-sight depth L = 5 Mm. This value for the line-of-sight depth is deduced from the fact that model 1 accounts for a fan viewed face-on. The solid angle $\Omega = \delta x^2/{\rm AU}^2$ is considered, which is defined by the grid resolution ($\delta x = \delta y = 5 \times 10^6$ cm) of the simulation. Using **Eq. 1**, we obtain the flux density emitted by every grid cell, and then to simulate observations, the resulting flux map is convolved with representations of instrument beams. In this case, due to the small size of the SAD, an instrument with high spatial resolution is needed to separate the SAD emission from the background

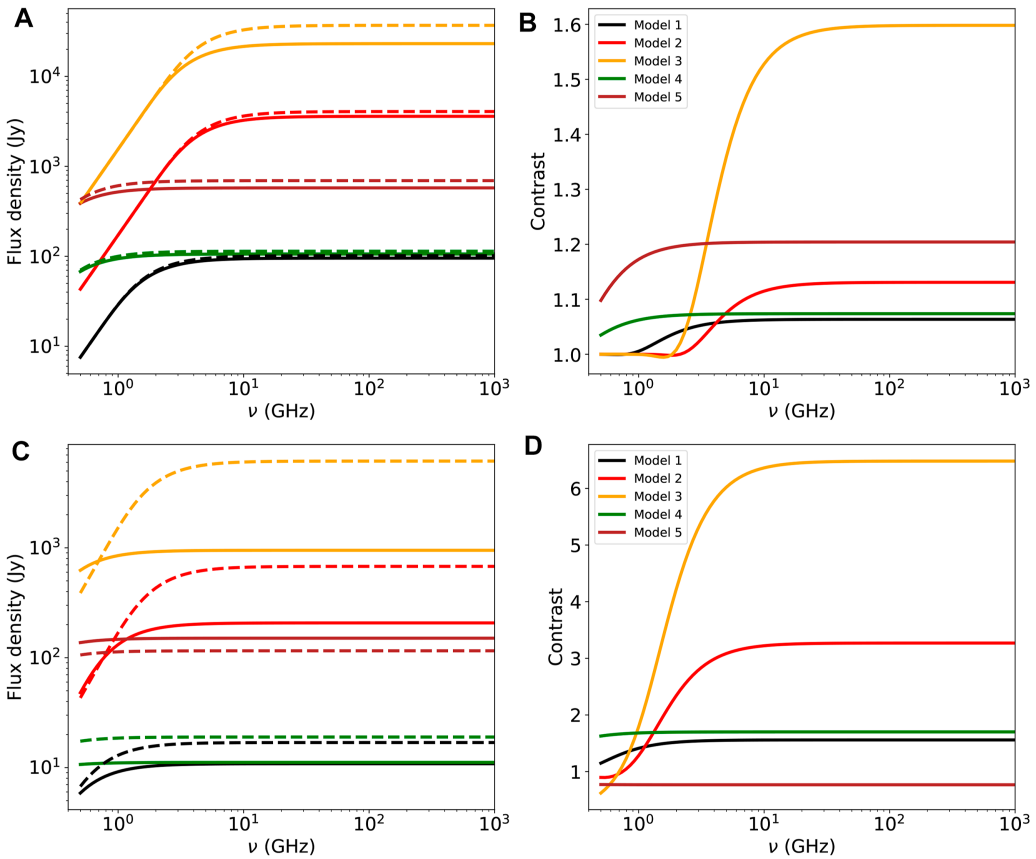

FIGURE 4 | Left panels show the expected flux density spectra incoming from the SADs (continuous lines) and for the fan (dashed lines). Right panels show the fan-SAD contrasts (flux density quotient between the fan and SADs). **(A,B)** Results for the fan viewed edge-on. **(C,D)** Results for the fan viewed face-on.

fan. Nowadays, there are only two instruments with arcsec spatial resolution in radio wavelengths and capable of observing the Sun: the VLA and ALMA. Both are interferometers with synthesized beams of the order of 1 arcsec and sensitivities below 1 mJy.

We compute the emissions for the VLA microwave band S (3 GHz) and also for the ALMA bands: 3 (100 GHz), 6 (230 GHz), and 9 (720 GHz). Since the spectrum is mostly optically thin, and aiming to display results for a low and high frequency in the thermal bremsstrahlung–opacity domain [0.5–1,000] GHz considered in **Figure 3**, we show in **Figure 5** the synthesized maps for the VLA band S at 3 GHz (**Figures 5A,B**) and the ALMA band 3 at 100GHz (**Figures 5C,D**). Left panels represent the flux densities with the simulation grid spatial resolution, while the right panels show the resulting flux densities convolved with the two instrument beams, at the top using the VLA band S with a half-power beamwidth HPBW = 0.65″ and at the bottom using the ALMA band 3 with HPBW = 0.3″. It is to be noted that the fan emission is always brighter than the SAD, with a contrast $Q \approx 6$. On the other hand, the convolved maps depend more on the spatial resolution (instrument beam) than on the flux density. For small SADs, such as that of model 1, using instruments with HPBW > 1″ will result in SADs spatially unresolved from the background fan emission. In terms of sensitivity, the expected flux detected by the instruments is in the order of or above 1 mJy/pixel.

In the 2D scenario, the order of magnitude for the emission contrast Q between the fan and SADs can be estimated straightforwardly in the optically thin regime. As was pointed out previously, the contrast depends on the model considered, for example, for models 1–3, the fan temperatures are roughly half of the SAD ones, whereas the fan densities are roughly twice of the SAD ones. Due to the fact that we are considering the optically thin regime, the opacity $\kappa_\nu \propto n^2 \nu^{-2} T^{-3/2}$ (**Eq. 2**); furthermore, the emission in the Rayleigh–Jeans approximation can be written as $F_\nu \propto T\nu^2 \kappa_\nu L\Omega \equiv n^2 T^{-1/2} L\Omega$; and thus, for these models, we obtain an order-of-magnitude contrast

$$Q = \frac{n_{\rm fan}^2 \; T_{\rm fan}^{-1/2} \; L \; \Omega}{n_{\rm sad}^2 \; T_{\rm sad}^{-1/2} \; L \; \Omega} = \left(\frac{n_{\rm fan}}{n_{\rm sad}}\right)^2 \left(\frac{T_{\rm sad}}{T_{\rm fan}}\right)^{1/2} \simeq 2^2 \cdot 2^{1/2} = 5.6. \quad (8)$$

This number is consistent with the contrast displayed by the flux densities in **Figure 5**. In addition, and as a support to the 2D-scenario results, the approximate contrast of **Eq. 8** is of the same order as that reported by Guo et al. (2014) in their **Figures 2D,E**, where 2D slices of the expected emissions were

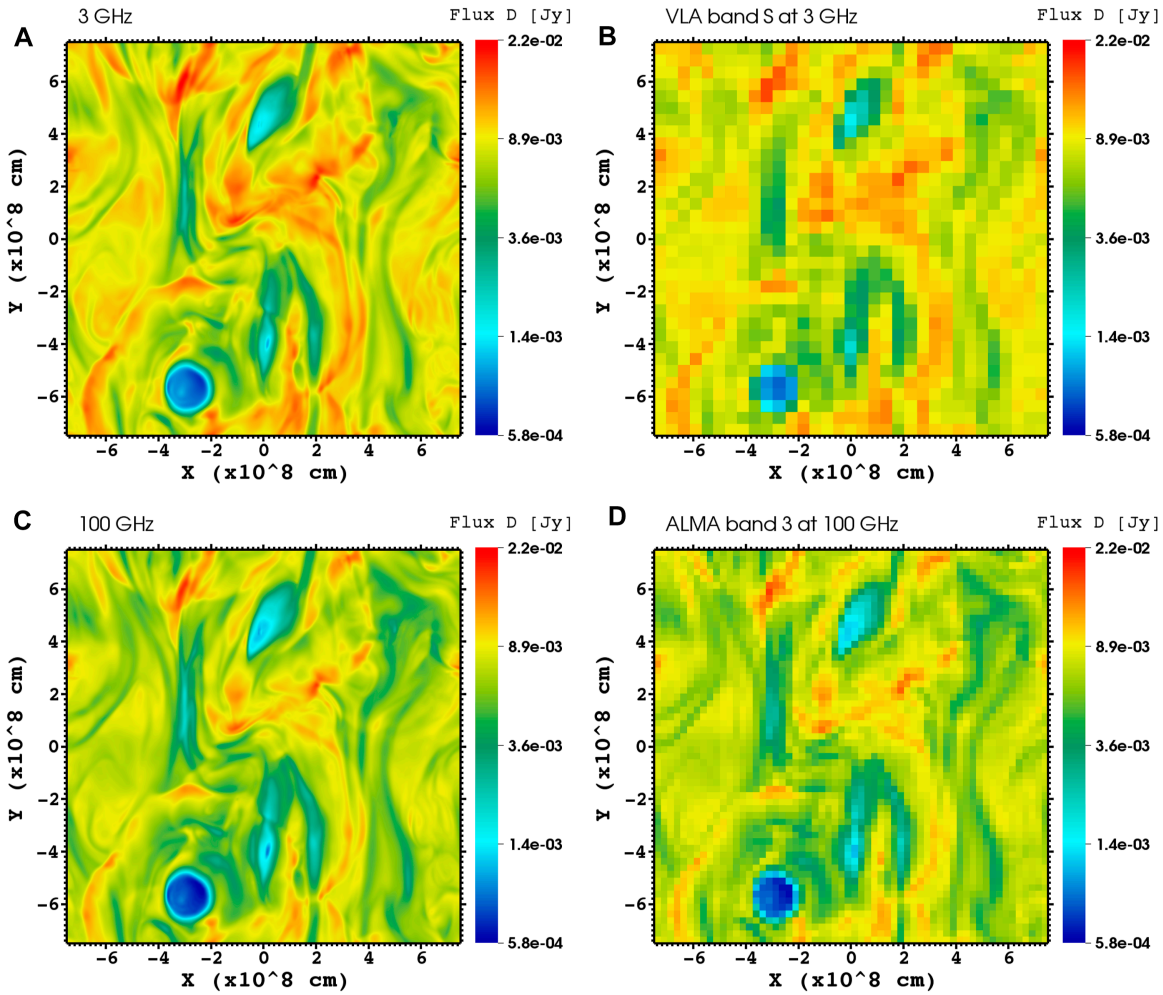

FIGURE 5 | (A) Expected flux density at 3 GHz obtained from an MHD simulation, and the flux density convolved with the VLA-band S beam of HPBW = 0.65″ **(B)**. **(C)** Simulated flux density at 100 GHz and the flux density convolved with the ALMA-band 3 beam of HPBW = 0.3″ **(D)**. It is to be noted that 10^8 cm ≡ 1 Mm.

shown to be corresponding to face-on views of the SDO/AIA Fe XXI and Fe XXIV channels, respectively. Finally, if we repeat the simple contrast calculation of **Eq. 8**, but instead using model 2 (see the 2D slices in density and temperature displayed in Figure 5 by Cécere et al. (2015), we again obtain a similar value. However, the contrast decrease is considerable when the plasma line-of-sight depth is taken into account, as illustrated in **Figure 4**.

3.5 Observational Strategies

It is evident from the flux density spectra displayed in **Figure 4** that observations with edge-on views produce lower contrasts than with face-on views, making SAD detection more difficult, which worsens in the optically thick regime. Since the emission from microwaves to submillimeter wavelengths is mostly optically thin, the best strategy to observe SADs is when the fan line-of-sight is over the dark limb and when the fan is viewed face-on. On the other hand, according to the models analyzed in this work, the spatially integrated flux emitted by SADs (**Figures 4A–C**) can be as low as ≈ 1 Jy and as high as ≈10^3 Jy. This means that a highly sensitive telescope is not required, although imaging capability is needed. The best instrument is an interferometer, for example, VLA has receivers in the low-frequency domain [1–18] GHz, and ALMA has receivers in the high-frequency domain [45–900] GHz. Both the instruments have adequate sensitivity and spatial resolution to observe even the smallest SAD (≈3 arcsec) of model 1, shown in **Figures 2**, **4**, **5**. Therefore, the best strategy would be to observe at different frequencies simultaneously with VLA and ALMA to cover the possible maximum frequency range. Moreover, instruments below the 1-GHz domain, such as Low-Frequency Array (van Haarlem et al., 2013) and Nançay Radioheliograph (Kerdraon and Delouis, 1997), can supply information in the optically thick spectral range, allowing better determination

of the density and temperature of the emitting sources. The Extended Owens Valley Array (EOVSA, Gary et al., 2018), with its spectral imager in [1–18] GHz range, could be used for the biggest SADs since its beam sizes are of the order of $\approx 54/\nu$[GHz]arcsec.

4 FINAL REMARKS

So far, SADs have been elusive structures likely produced by magnetic reconnection processes during solar flares. They have been detected only in EUV and soft X-ray emission, implying that currently known SAD characteristics, such as their temperatures, densities, and sizes, have been inferred using this wavelength range. The same thermal bremsstrahlung phenomenon that produces emission in EUV and soft X-ray should also produce emission in radio wavelengths. However, no direct observation of SADs in radio has been reported yet. Instead, in radio only were reported signatures of magnetic reconnection processes assumed to be responsible for SAD triggering, and also spatial/temporal correlations of SAD signatures with a burst of impulsive microwave emissions. Thus, the use of radio observations for SAD detection may help improve the estimations of SAD characteristics.

In order to contribute to the understanding of SAD nature, in this study, we produced spatially integrated spectra and synthesized images at selected radio frequencies. The spectra were obtained utilizing numerical MHD models of SADs based on the bursty localized reconnection interpretation by Costa et al. (2009) and subsequent works and the reconnection downflow interpretation by Guo et al. (2014). Here, we demonstrated that the fan emission should be detectable with current radio observatories and that the SADs should consistently be less bright than the surrounding fan. In the frequency range analyzed, [0.5–1,000] GHz, the spectra of SADs and fans show that the thermal bremsstrahlung emission greater than 10 GHz is mostly optically thin, and therefore proportional to the temperature, density, and line-of-sight depth. Furthermore, the gyroresonance contribution to the flux density is negligible. The fan emission and SAD sizes have a strong influence in their measured contrast Q. The contrast is a parameter that describes the detectability of a SAD, meaning that it is indistinguishable from the ambient-fan emission when it is close to unity. The fact that the contrast is not sufficiently high may be a reason why SADs are barely detected during eruptive events, particularly when the fan is viewed edge-on (as shown in **Figure 4**).

Despite our results being model-dependent, a strategic plan to increase chances of SAD detection in radio wavelengths is to first search for post-flare magnetic arcades over the limb, where a face-on view of the fan will be mostly desired; and second, to simultaneously observe at centimeter and millimeter wavelengths. Imaging SADs with arcsec resolution simultaneously at different radio wavelengths would be an excellent diagnostic to constraint models, with the VLA and ALMA interferometers being the best instruments to achieve this goal. Moreover, a combination of radio, EUV, and soft X-ray observations will enrich the description and deepen our understanding of the physical processes.

It is known that magnetic reconnection is in the origin of a great variety of phenomena: flares, CMEs, etc. Some of these phenomena are weak and, therefore, difficult to detect, as is the case with SADs. The SAD models used in this work consider that magnetic reconnection occurs at coronal heights, which is in line with the above-the-looptop hard X-ray source scenario (also known as Masuda flares, Masuda et al., 1994; Krucker et al., 2008) In order to fully understand the reconnection process and its consequences, we need to complete the SAD picture. Radio observations can be a key to having a more detailed image of them.

DATA AVAILABILITY STATEMENT

The original contributions presented in the study are included in the article/Supplementary Material, further inquiries can be directed to the corresponding author.

AUTHOR CONTRIBUTIONS

EZ, CC, and MC contributed to the conception and design of the study. CC carried out the analytical calculations, EZ performed the synthetic images, and CS assessed the radio emission mechanisms. AC contributed to the model and result discussions. EZ and CC led the manuscript writing. All the authors contributed to manuscript revision and read and approved the submitted version.

FUNDING

The research leading to these results has received funding from CAPES grant 88881.310386/2018-01, FAPESP grant 2013/24155-3. EZ, AC, and MC acknowledge support by CONICET grant number PIP No. 11220200103150CO.

ACKNOWLEDGMENTS

EZ is grateful to the FAPESP to have financed this research by the grant 2018/25177-4. GC thanks CNPq for support with a Productivity Research Fellowship. The authors are also grateful to Mackenzie Research Funding Mackpesquisa for the received support. GC is correspondent researcher of the Consejo Nacional de Investigaciones Científicas y Técnicas (CONICET) for the Instituto de Astronomía y Física del Espacio (IAFE), Argentina. MC and AC are members of the Carrera del Investigador Científico (CONICET). MC acknowledges support from ANPCyT under the grant PICT No. 2016-2480. MC also acknowledges support from the SECYT-UNC grant no. 33620180101147CB. We also thank the VisIt team–graphical tool (Harrison and Krishnan, 2012). The authors thank the editor and the referees for valuable and constructive comments and suggestions that helped improving this work significantly.

REFERENCES

Asai, A., Yokoyama, T., Shimojo, M., and Shibata, K. (2004). Downflow Motions Associated with Impulsive Nonthermal Emissions Observed in the 2002 July 23 Solar Flare. *ApJ* 605, L77–L80. doi:10.1086/420768

Cai, Q., Shen, C., Raymond, J. C., Mei, Z., Warmuth, A., Roussev, I. I., et al. (2019). Investigations of a Supra-arcade Fan and Termination Shock above the Top of the Flare-Loop System of the 2017 September 10 Event. *Mon. Not. Roy. Astron. Soc.* 489, 3183–3199. doi:10.1093/mnras/stz2167

Casini, R., White, S. M., and Judge, P. G. (2017). Magnetic Diagnostics of the Solar Corona: Synthesizing Optical and Radio Techniques. *Space Sci. Rev.* 210, 145–181. doi:10.1007/s11214-017-0400-6

Cécere, M., Schneiter, M., Costa, A., Elaskar, S., and Maglione, S. (2012). Simulation of Descending Multiple Supra-arcade Reconnection Outflows in Solar Flares. *ApJ* 759, 79. doi:10.1088/0004-637X/759/2/79

Cécere, M., Zurbriggen, E., Costa, A., and Schneiter, M. (2015). 3D MHD Simulation of Flare Supra-Arcade Downflows in a Turbulent Current Sheet Medium. *ApJ* 807, 6. doi:10.1088/0004-637X/807/1/6

Chen, B., Bastian, T. S., Shen, C., Gary, D. E., Krucker, S., and Glesener, L. (2015). Particle Acceleration by a Solar Flare Termination Shock. *Science* 350, 1238–1242. doi:10.1126/science.aac8467

Chen, X., Liu, R., Deng, N., and Wang, H. (2017). Thermodynamics of Supra-arcade Downflows in Solar Flares. *A&A* 606, A84. doi:10.1051/0004-6361/201629893

Costa, A., Elaskar, S., Fernandez, C. A., and Martinez, G. (2009). Simulation of Dark Lanes in post-flare Supra-arcade. *Mon. Not. Roy. Astron. Soc.* 400, L85–L89. doi:10.1111/j.1745-3933.2009.00769.x

Dulk, G. A. (1985). Radio Emission from the Sun and Stars. *Annu. Rev. Astron. Astrophys.* 23, 169–224. doi:10.1146/annurev.aa.23.090185.001125

Freed, M. S., and McKenzie, D. E. (2018). Quantifying Turbulent Dynamics Found within the Plasma Sheets of Multiple Solar Flares. *ApJ* 866, 29. doi:10.3847/1538-4357/aadee4

Gary, D. E., Chen, B., Dennis, B. R., Fleishman, G. D., Hurford, G. J., and Krucker, S. (2018). Microwave and Hard X-Ray Observations of the 2017 September 10 Solar Limb Flare. *Astrophys. J.* 863, 83. doi:10.3847/1538-4357/aad0ef

Guo, L. J., Huang, Y., Bhattacharjee, A., and Innes, D. E. (2014). Rayleigh-Taylor Type Instabilities in the Reconnection Exhaust Jet as a Mechanism for Supra-arcade Downflows in the Sun. *Astrophys. J. Lett.* 796, L29. doi:10.1088/2041-8205/796/2/l29

Hanneman, W. J., and Reeves, K. K. (2014). Thermal Structure of Current Sheets and Supra-arcade Downflows in the Solar Corona. *Astrophys. J.* 786, 95. doi:10.1088/0004-637X/786/2/95

Harrison, C., and Krishnan, H. (2012). "Python's Role in VisIt," in *11th Python in Science Conf. (Scipy 2012)*. Editors Ahmadia, A., Millman, J., and van der, S., 23–29. doi:10.25080/Majora-54c7f2c8-00d

Hayes, L. A., Gallagher, P. T., Dennis, B. R., Ireland, J., Inglis, A., and Morosan, D. E. (2019). Persistent Quasi-Periodic Pulsations during a Large X-Class Solar Flare. *Astrophys. J.* 875, 33. doi:10.3847/1538-4357/ab0ca3

Innes, D. E., Guo, L. J., Bhattacharjee, A., Huang, Y. M., and Schmit, D. (2014). Observations of Supra-arcade Fans: Instabilities at the Head of Reconnection Jets. *Astrophys. J.* 796, 27. doi:10.1088/0004-637X/796/1/27

Innes, D. E., McKenzie, D. E., and Wang, T. (2003a). Observations of 1000 Km S^{-1} Doppler Shifts in 10^7 K Solar Flare Supra-arcade. *Solar Phys.* 217, 267–279. doi:10.1023/b:sola.0000006874.31799.bc

Innes, D. E., McKenzie, D. E., and Wang, T. (2003b). SUMER Spectral Observations of post-flare Supra-arcade Inflows. *Solar Phys.* 217, 247–265. doi:10.1023/b:sola.0000006899.12788.22

Kerdraon, A., and Delouis, J.-M. (1997). "The Nançay Radioheliograph," in *Coronal Physics from Radio and Space Observations*. Editor Trottet, G. (Springer Berlin Heidelberg), 192–201. doi:10.1007/BFb0106458

Krucker, S., Battaglia, M., Cargill, P. J., Fletcher, L., Hudson, H. S., MacKinnon, A. L., et al. (2008). Hard X-ray Emission from the Solar corona. *Astron. Astrophys. Rev.* 16, 155–208. doi:10.1007/s00159-008-0014-9

Li, Z. F., Cheng, X., Ding, M. D., Reeves, K. K., Kittrell, D., Weber, M., et al. (2021). Thermodynamic Evolution of Solar Flare Supra-arcade Downflows. *Astrophys. J.* 915, 124. doi:10.3847/1538-4357/ac043e

Linton, M. G., Devore, C. R., and Longcope, D. W. (2009). Patchy Reconnection in a Y-type Current Sheet. *Earth, Planets, and Space* 61, 573–576. doi:10.1186/bf03352925

Linton, M. G., and Longcope, D. W. (2006). A Model for Patchy Reconnection in Three Dimensions. *Astrophys. J.* 642, 1177–1192. doi:10.1086/500965

Liu, R. (2013). Dynamical Processes at the Vertical Current Sheet behind an Erupting Flux Rope. *Mon. Not. Roy. Astron. Soc.* 434, 1309–1320. doi:10.1093/mnras/stt1090

Liu, W., Chen, Q., and Petrosian, V. (2013). Plasmoid Ejections and Loop Contractions in an Eruptive M7.7 Solar Flare: Evidence of Particle Acceleration and Heating in Magnetic Reconnection Outflows. *Astrophys. J.* 767, 168. doi:10.1088/0004-637X/767/2/168

Longcope, D., Unverferth, J., Klein, C., McCarthy, M., and Priest, E. (2018). Evidence for Downflows in the Narrow Plasma Sheet of 2017 September 10 and Their Significance for Flare Reconnection. *Astrophys. J.* 868, 148. doi:10.3847/1538-4357/aaeac4

Longcope, D. W., Guidoni, S. E., and Linton, M. G. (2009). Gas-dynamic Shock Heating of Post-flare Loops Due to Retraction Following Localized, Impulsive Reconnection. *Astrophys. J. Lett.* 690, L18–L22. doi:10.1088/0004-637x/690/1/l18

Maglione, L. S., Schneiter, E. M., Costa, A., and Elaskar, S. (2011). Simulation of Dark Lanes in post-flare Supra-arcades. III. A 2D Simulation. *Astron. Astrophys.* 527, L5. doi:10.1051/0004-6361/201015934

Masuda, S., Kosugi, T., Hara, H., Tsuneta, S., and Ogawara, Y. (1994). A Loop-Top Hard X-ray Source in a Compact Solar Flare as Evidence for Magnetic Reconnection. *Nature* 371, 495–497. doi:10.1038/371495a0

McKenzie, D. E., and Hudson, H. S. (1999). X-Ray Observations of Motions and Structure above a Solar Flare Arcade. *Astrophys. J. Lett.* 519, L93–L96. doi:10.1086/312110

McKenzie, D. E., and Savage, S. L. (2011). Distribution Functions of Sizes and Fluxes Determined from Supra-arcade Downflows. *Astrophys. J. Lett.* 735, L6. doi:10.1088/2041-8205/735/1/L6

McKenzie, D. E., and Savage, S. L. (2009). Quantitative Examination of Supra-arcade Downflows in Eruptive Solar Flares. *Astrophys. J.* 697, 1569–1577. doi:10.1088/0004-637X/697/2/1569

McKenzie, D. E. (2013). Turbulent Dynamics in Solar Flare Sheet Structures Measured with Local Correlation Tracking. *Astrophys. J.* 766, 39. doi:10.1088/0004-637X/766/1/39

Prialnik, D. (20002000). *An Introduction to the Theory of Stellar Structure and Evolution*". Cambridge: University Press. doi:10.1080/00107514.2011.580371

Reeves, K. K., Freed, M. S., McKenzie, D. E., and Savage, S. L. (2017). An Exploration of Heating Mechanisms in a Supra-arcade Plasma Sheet Formed after a Coronal Mass Ejection. *Astrophys. J.* 836, 55. doi:10.3847/1538-4357/836/1/55

Savage, S. L., and McKenzie, D. E. (2011). Quantitative Examination of a Large Sample of Supra-arcade Downflows in Eruptive Solar Flares. *Astrophys. J.* 730, 98. doi:10.1088/0004-637X/730/2/98

Savage, S. L., McKenzie, D. E., and Reeves, K. K. (2012). Re-interpretation of Supra-arcade Downflows in Solar Flares. *Astrophys. J. Lett.* 747, L40. doi:10.1088/2041-8205/747/2/L40

Schulz, W., Costa, A., Elaskar, S., and Cid, G. (2010). Simulation of Dark Lanes in post-flare Supra-arcades - II. A Contribution to the Remote Sensing of the Coronal Magnetic Field. *Mon. Not. Roy. Astron. Soc.* 407, L89–L93. doi:10.1111/j.1745-3933.2010.00911.x

Scott, R. B., Longcope, D. W., and McKenzie, D. E. (2013). Peristaltic Pumping Near Post-coronal Mass Ejection Supra-arcade Current Sheets. *Astrophys. J.* 776, 54. doi:10.1088/0004-637X/776/1/54

Selhorst, C. L., Silva-Válio, A., and Costa, J. E. R. (2008). Solar Atmospheric Model over a Highly Polarized 17 GHz Active Region. *Astron. Astrophys.* 488, 1079–1084. doi:10.1051/0004-6361:20079217

van Haarlem, M. P., Wise, M. W., Gunst, A. W., Heald, G., McKean, J. P., Hessels, J. W. T., et al. (2013). LOFAR: The LOw-Frequency ARray. *Astron. Astrophys.* 556. doi:10.1051/0004-6361/201220873

van Hoof, P. A. M., Williams, R. J. R., Volk, K., Chatzikos, M., Ferland, G. J. Lykins, M., et al. (2014). Accurate Determination of the Free-free Gaunt Factor - I. Non-relativistic Gaunt Factors. *Mon. Not. Roy. Astron. Soc.* 444, 420–428. doi:10.1093/mnras/stu1438

Verwichte, E., Nakariakov, V. M., and Cooper, F. C. (2005). Transverse Waves in a post-flare Supra-arcade. *Astron. Astrophys.* 430, L65–L68. doi:10.1051/0004-6361:200400133

Warren, H. P., Brooks, D. H., Ugarte-Urra, I., Reep, J. W., Crump, N. A., and Doschek, G. A. (2018). Spectroscopic Observations of Current Sheet

Formation and Evolution. *Astrophys. J.* 854, 122. doi:10.3847/1538-4357/aaa9b8

Warren, H. P., O'Brien, C. M., Sheeley, J., and Neil, R. (2011). Observations of Reconnecting Flare Loops with the Atmospheric Imaging Assembly. *Astrophys. J.* 742, 92. doi:10.1088/0004-637X/742/2/92

White, S. M. (2004). "Coronal Magnetic Field Measurements through Gyroresonance Emission,". *Astrophysics and Space Science Library*. Editors Gary, D. E., and Keller, C. U., 314, 89. doi:10.1007/1-4020-2814-8_5

Xue, J., Su, Y., Li, H., and Zhao, X. (2020). Thermodynamical Evolution of Supra-arcade Downflows. *Astrophys. J.* 898, 88. doi:10.3847/1538-4357/ab9a3d

Yu, S., Chen, B., Reeves, K. K., Gary, D. E., Musset, S., Fleishman, G. D., et al. (2020). Magnetic Reconnection during the Post-impulsive Phase of a Long-Duration Solar Flare: Bidirectional Outflows as a Cause of Microwave and X-Ray Bursts. *Astrophys. J.* 900, 17. doi:10.3847/1538-4357/aba8a6

Zurbriggen, E., Costa, A., Esquivel, A., Schneiter, M., and Cécere, M. (2016). MHD Simulations of Coronal Supra-arcade Downflows Including Anisotropic Thermal Conduction. *Astrophys. J.* 832, 74. doi:10.3847/0004-637X/832/1/74

Conflict of Interest: The authors declare that the research was conducted in the absence of any commercial or financial relationships that could be construed as a potential conflict of interest.

Frontiers in
Astronomy and Space Sciences

Explores planetary science and extragalactic astronomy in all wavelengths

Advances the understanding of our universe - from planetary science to extragalactic astronomy, to high-energy and astroparticle physics.

Discover the latest Research Topics

See more →

Frontiers

Avenue du Tribunal-Fédéral 34
1005 Lausanne, Switzerland
frontiersin.org

Contact us

+41 (0)21 510 17 00
frontiersin.org/about/contact